SEDIMENTOLOGY AND SOCIETY

EDITED BY: Amanda Owen, Michael Andrew Clare and Barbara Mauz
PUBLISHED IN: Frontiers in Earth Science

frontiers Research Topics

Frontiers eBook Copyright Statement

The copyright in the text of individual articles in this eBook is the property of their respective authors or their respective institutions or funders. The copyright in graphics and images within each article may be subject to copyright of other parties. In both cases this is subject to a license granted to Frontiers.

The compilation of articles constituting this eBook is the property of Frontiers.

Each article within this eBook, and the eBook itself, are published under the most recent version of the Creative Commons CC-BY licence. The version current at the date of publication of this eBook is CC-BY 4.0. If the CC-BY licence is updated, the licence granted by Frontiers is automatically updated to the new version.

When exercising any right under the CC-BY licence, Frontiers must be attributed as the original publisher of the article or eBook, as applicable.

Authors have the responsibility of ensuring that any graphics or other materials which are the property of others may be included in the CC-BY licence, but this should be checked before relying on the CC-BY licence to reproduce those materials. Any copyright notices relating to those materials must be complied with.

Copyright and source acknowledgement notices may not be removed and must be displayed in any copy, derivative work or partial copy which includes the elements in question.

All copyright, and all rights therein, are protected by national and international copyright laws. The above represents a summary only. For further information please read Frontiers' Conditions for Website Use and Copyright Statement, and the applicable CC-BY licence.

ISSN 1664-8714
ISBN 978-2-88963-572-6
DOI 10.3389/978-2-88963-572-6

About Frontiers

Frontiers is more than just an open-access publisher of scholarly articles: it is a pioneering approach to the world of academia, radically improving the way scholarly research is managed. The grand vision of Frontiers is a world where all people have an equal opportunity to seek, share and generate knowledge. Frontiers provides immediate and permanent online open access to all its publications, but this alone is not enough to realize our grand goals.

Frontiers Journal Series

The Frontiers Journal Series is a multi-tier and interdisciplinary set of open-access, online journals, promising a paradigm shift from the current review, selection and dissemination processes in academic publishing. All Frontiers journals are driven by researchers for researchers; therefore, they constitute a service to the scholarly community. At the same time, the Frontiers Journal Series operates on a revolutionary invention, the tiered publishing system, initially addressing specific communities of scholars, and gradually climbing up to broader public understanding, thus serving the interests of the lay society, too.

Dedication to Quality

Each Frontiers article is a landmark of the highest quality, thanks to genuinely collaborative interactions between authors and review editors, who include some of the world's best academicians. Research must be certified by peers before entering a stream of knowledge that may eventually reach the public - and shape society; therefore, Frontiers only applies the most rigorous and unbiased reviews.
Frontiers revolutionizes research publishing by freely delivering the most outstanding research, evaluated with no bias from both the academic and social point of view. By applying the most advanced information technologies, Frontiers is catapulting scholarly publishing into a new generation.

What are Frontiers Research Topics?

Frontiers Research Topics are very popular trademarks of the Frontiers Journals Series: they are collections of at least ten articles, all centered on a particular subject. With their unique mix of varied contributions from Original Research to Review Articles, Frontiers Research Topics unify the most influential researchers, the latest key findings and historical advances in a hot research area! Find out more on how to host your own Frontiers Research Topic or contribute to one as an author by contacting the Frontiers Editorial Office: researchtopics@frontiersin.org

SEDIMENTOLOGY AND SOCIETY

Topic Editors:
Amanda Owen, University of Glasgow, United Kingdom
Michael Andrew Clare, University of Southampton, United Kingdom
Barbara Mauz, University of Salzburg, Austria

Citation: Owen, A., Clare, M. A., Mauz, B., eds. (2020). Sedimentology and Society. Lausanne: Frontiers Media SA. doi: 10.3389/978-2-88963-572-6

Table of Contents

04 ***Editorial: Sedimentology and Society***
Amanda Owen, Michael Clare and Barbara Mauz

07 ***Complex and Cascading Triggering of Submarine Landslides and Turbidity Currents at Volcanic Islands Revealed From Integration of High-Resolution Onshore and Offshore Surveys***
Michael A. Clare, Tim Le Bas, David M. Price, James E. Hunt, David Sear, Matthieu J. B. Cartigny, Age Vellinga, William Symons, Christopher Firth and Shane Cronin

31 ***Dispersion, Accumulation, and the Ultimate Fate of Microplastics in Deep-Marine Environments: A Review and Future Directions***
Ian A. Kane and Michael A. Clare

58 ***Modern to Ancient Barrier Island Dimensional Comparisons: Implications for Analog Selection and Paleomorphodynamics***
Julia S. Mulhern, Cari L. Johnson and John M. Martin

80 ***Left High and Dry: Deglaciation of Dogger Bank, North Sea, Recorded in Proglacial Lake Evolution***
Andy R. Emery, David M. Hodgson, Natasha L. M. Barlow, Jonathan L. Carrivick, Carol J. Cotterill and Emrys Phillips

107 ***Where's the Carbon: Exploring the Spatial Heterogeneity of Sedimentary Carbon in Mid-Latitude Fjords***
Craig Smeaton and William E. N. Austin

123 ***Muddying the Picture? Forecasting Particulate Sources and Dispersal Patterns in Managed Catchments***
Janet Cristine Richardson, David Mark Hodgson, Paul Kay, Benjamin J. Aston and Andrew C. Walker

146 ***Event Stratigraphy in a Hadal Oceanic Trench: The Japan Trench as Sedimentary Archive Recording Recurrent Giant Subduction Zone Earthquakes and Their Role in Organic Carbon Export to the Deep Sea***
Arata Kioka, Tobias Schwestermann, Jasper Moernaut, Ken Ikehara, Toshiya Kanamatsu, Timothy I. Eglinton and Michael Strasser

170 ***Provenance and Sediment Maturity as Controls on CO_2 Mineral Sequestration Potential of the Gassum Formation in the Skagerrak***
Mette Olivarius, Anja Sundal, Rikke Weibel, Ulrik Gregersen, Irfan Baig, Tonny B. Thomsen, Lars Kristensen, Helge Hellevang and Lars Henrik Nielsen

frontiers in Earth Science

EDITORIAL
published: 11 February 2020
doi: 10.3389/feart.2020.00019

Editorial: Sedimentology and Society

Amanda Owen[1]*, *Michael Clare*[2] *and Barbara Mauz*[3]

[1] School of Geographical and Earth Sciences, University of Glasgow, Glasgow, United Kingdom, [2] National Oceanography Centre, University of Southampton Waterfront Campus, European Way, Southampton, United Kingdom, [3] Department of Geography and Geology, University of Salzburg, Salzburg, Austria

Keywords: sedimentology, society, natural hazards, pollutant dispersal, carbon transfer and storage, coastal change

Editorial on the Research Topic

Sedimentology and Society

Earth surface processes are increasingly affected by human activities, often resulting in complex, or unexpected consequences for society. The on-going effects of land-use changes and release of pollutants to the natural environment are of growing concern. Societal awareness of these environmental changes has grown rapidly over the past decade, prompting a need to better understand and predict the implications of future changes, and to inform adaptation and mitigation policies and strategies. Sedimentology is critical in understanding complex interplays between human activities and earth-surface processes by characterizing and quantifying the response of nature to human impact and vice versa, the impact of natural processes on society. Thus, while key challenges exist, there are many opportunities for sedimentologists to advance the understanding of the human-nature relationship (Hodgson et al., 2018) and thereby contribute to achieving the UN sustainability goals (United Nations Sustainable Development Goals, 2015). Research Topics of this contribution include natural hazards, pollutant dispersal, carbon transfer and storage, and Earth's surface response to changing climate and sea level. This Frontiers in Earth Science special issue brings together a collection of papers that bridge key knowledge gaps in these critical areas, and document the challenges and opportunities within the theme "Sedimentology and Society."

OPEN ACCESS

Edited and reviewed by:
David Mark Hodgson,
University of Leeds, United Kingdom

***Correspondence:**
Amanda Owen
amanda.owen@glasgow.ac.uk

Specialty section:
This article was submitted to Sedimentology, Stratigraphy and Diagenesis, a section of the journal Frontiers in Earth Science

Received: *07 January 2020*
Accepted: *22 January 2020*
Published: *11 February 2020*

Citation:
Owen A, Clare M and Mauz B (2020) Editorial: Sedimentology and Society. Front. Earth Sci. 8:19. doi: 10.3389/feart.2020.00019

NATURAL HAZARDS

Sedimentology plays a key role in improving our understanding of the frequency and impact of a wide range of geohazards that directly and indirectly impact communities. Five earthquakes with a magnitude >9 occurred in the last century, causing major economic damage and loss of life. The AD 2011 Tohoku-oki earthquake occurred along the hadal Japan Trench, generating the largest-ever recorded co-seismic slip and a tsunami with coastal run-up heights of up to 40 m, with more than 15,000 recorded fatalities (Bassett et al., 2016). Instrumental records of such events only extend c.100 years, while historical records lack detail on location, magnitude and mechanics. Subaqueous landslide deposits potentially provide a valuable archive of ancient earthquakes to extend such catalogs. Kioka et al. document >2000 years of earthquake activity along the hadal Japan Trench through detailed analysis of deposits across the trench, providing new insights into the behavior of earthquakes along the subduction zone, and how large volumes (>7 trillion grams) of organic carbon are mobilized during earthquakes. Besides earthquakes, natural hazards are created through other events such as volcanic or tropical cyclone activity (Pelling and Uitto, 2001). Small Island Developing States are particularly vulnerable to such natural hazards, partly owing to their remote location. Vanuatu has been described as the most disaster-prone nation in the South Pacific (Meheux and Parker, 2006); a location where Clare et al. document the complex and cascading interactions that can arise from volcanic activity, tropical cyclones, dam bursts and river floods. They discuss how

climatic and land-use changes may play a more important role than volcanic or tectonic events in preconditioning and triggering natural hazards on many small volcanic islands.

POLLUTANT DISPERSAL

As natural systems become modified and polluted by human activities, it is essential that we understand the complexities from source to sink in sedimentary routing systems; in particular how pollutants and particulates are liberated, transported and deposited within these systems. Fine-grained sediment can impact aquatic ecosystems, water quality, and increase flood risk. The implications of future climate change may also affect the rate and nature of such transport. Richardson et al. use a numerical model to simulate the effect of projected global warming and precipitation on the dispersal of fine-grained particles throughout the River Derwent (UK) catchment. They demonstrate how seasonal land-use can dramatically disrupt sediment transport, and alter the potential for erosion. The effect of plastic pollution in the natural environment is another growing concern (Eriksen et al., 2014). While many studies have focused on terrestrial aquatic systems (e.g., Lebreton et al., 2017), the deep sea is thought to be the ultimate sink for plastics (Woodall et al., 2014); much of which occurs in the form of tiny fragments and fibers (microplastics). Less than 1% of the plastic in the ocean floats on the surface (Jambeck et al., 2015; Van Sebille et al., 2015). Kane and Clare discuss where that missing plastic may accumulate, through a summary of the deep-sea processes that may transport this human-made particle, and lay out a number of future research directions to fill key but outstanding knowledge gaps in this field.

CARBON TRANSFER AND STORAGE

There has undoubtably been an increase in atmospheric CO_2 over the last century (Intergovernmental Panel on Climate Change, 2014; Abram et al., 2019). Understanding natural stores of CO_2 is critical as we try to reduce, and mitigate against, the release of natural carbon; however existing estimates of natural carbon sequestration still remain poorly constrained, which limits our understanding of the carbon cycle as a whole. Spatial heterogeneity of sedimentary deposits appears to be the dominant control on where organic carbon hotspots occur, as also suggested by Kioka et al.; hence future studies should aim to characterize such variability. Smeaton and Austin perform a detailed study in mid-latitude fjords, to better constrain the spatial and depth-related variability in natural organic carbon sequestration. Carbon Capture and Storage can offer a promising anthropogenic solution to mitigating against the release of CO_2, particularly as it can utilize existing petroleum fields. Olivarius et al. explore how sedimentological variations can influence the reactivity and storage potential of CO_2 within sandstone reservoirs using the Gassum Formation in Skagerrak as a case study example.

MANAGING THE COAST AND SHALLOW MARINE ENVIRONMENTS

Coastlines are often population density hotspots. With sea level rise being a real threat to many coastlines, understanding how systems migrate and adapt is key. Mulhern et al. analyse a dataset of modern and ancient barrier islands, to understand the linkages between processes and deposit architecture. The authors present a comprehensive and novel dataset of barrier island morphologies that allows conclusions on barrier island morphodynamics to be drawn upon. The authors show where linkages between modern and ancient deposits can, and importantly, cannot be drawn upon. Coastal and shallow marine environments are also key environments for the growth in renewable energy. Wind turbines are being installed in progressively deeper water, in larger arrays, to maximize energy yield and efficiency. Greater water depths and larger sites bring challenges for foundation design, particularly where the subsurface geology is complex. Emery et al. investigate one of the largest proposed offshore wind farm sites, at the Dogger Bank in the UK North Sea. The glacially generated highly variable stratigraphy of the Dogger Bank results from past phases of glaciation and ice-retreat. The paper improves our knowledge on ground conditions for designing wind turbines. Studies that link modern and ancient deposits can provide critical insights into how systems react to external forcing as well as gain insights into the three-dimensional form in the subsurface.

This collection of papers is designed to be a starting point of bringing together a variety of disciplines with the overarching aim of addressing how sedimentology can help better understand and mitigate against societal issues.

AUTHOR CONTRIBUTIONS

All authors listed have made a substantial, direct and intellectual contribution to the work, and approved it for publication.

FUNDING

MC acknowledges support from NERC National Capability project Climate Linked Atlantic Sector Science (NE/R015953/1).

REFERENCES

Abram, N., Gattuso, J. P., Prakash, A., Cheng, L., Chidichimo, M. P., Crate, S., et al. (2019). "Framing and context of the report," in *IPCC Special Report on the Ocean and Cryosphere in a Changing Climate,* eds H. O. Pörtner, D. C. Roberts, V. Masson-Delmotte, P. Zhai, M. Tignor, E. Poloczanska, K. Mintenbeck, A. Alegría, M. Nicolai, A. Okem, J. Petzold, B. Rama, and N. M. Weyer. Available online at: https://www.ipcc.ch/srocc/chapter/chapter-1-framing-and-context-of-the-report/ (accessed January 30, 2020).

Bassett, D., Sandwell, D. T., Fialko, Y., and Watts, A. B. (2016). Upper-plate controls on co-seismic slip in the 2011 magnitude 9.0 Tohoku-oki earthquake. *Nature* 531, 92–96. doi: 10.1038/nature16945

Eriksen, M., Lebreton, L. C., Carson, H. S., Thiel, M., Moore, C. J., Borerro, J. C., et al. (2014). Plastic pollution in the world's oceans: more than 5 trillion

plastic pieces weighing over 250,000 tons afloat at sea. *PLoS ONE* 9:e111913. doi: 10.1371/journal.pone.0111913

Hodgson, D. M., Bernhardt, A., Clare, M. A., Da Silva, A. C., Fosdick, J., Mauz, B., et al. (2018). Grand challenges (and great opportunities) in sedimentology, stratigraphy, and diagenesis research. *Front. Earth Sci.* 6:173. doi: 10.3389/feart.2018.00173

Intergovernmental Panel on Climate Change (2014) *Climate Change 2014: Synthesis Report. Contribution of Working Groups, I., II and III to the Fifth Assessment Report of the Intergovernmental Panel on Climate Change,* eds Core Writing Team, R. K. Pachauri and L. A. Meyer (Geneva: IPCC), 151. doi: 10.1017/CBO9781107415416

Jambeck, J. R., Geyer, R., Wilcox, C., Siegler, T. R., Perryman, M., Andrady, A., et al. (2015). Plastic waste inputs from land into the ocean. *Science* 347, 768–771. doi: 10.1126/science.1260352

Lebreton, L. C., Van der Zwet, J., Damsteeg, J. W., Slat, B., Andrady, A., and Reisser, J. (2017). River plastic emissions to the world's oceans. *Nat. Commun.* 8:15611. doi: 10.1038/ncomms15611

Meheux, K., and Parker, E. (2006). Tourist sector perceptions of natural hazards in Vanuatu and the implications for a small island developing state. *Tourism Manag.* 27, 69–85. doi: 10.1016/j.tourman.2004.07.009

Pelling, M., and Uitto, J. I. (2001). Small island developing states: natural disaster vulnerability and global change. *Global Environ. Change Part B* 3, 49–62. doi: 10.1016/S1464-2867(01)00018-3

United Nations Sustainable Development Goals (2015). *United Nations Sustainable Development Goals*. Available online at: http://www.un.org/sustainabledevelopment/sustainable-development-goals/ (accessed January 30, 2020).

Van Sebille, E., Wilcox, C., Lebreton, L., Maximenko, N., Hardesty, B. D., Van Franeker, J. A., et al. (2015). A global inventory of small floating plastic debris. *Environ. Res. Lett.* 10:124006. doi: 10.1088/1748-9326/10/12/124006

Woodall, L. C., Sanchez-Vidal, A., Canals, M., Paterson, G. L., Coppock, R., Sleight, V., et al. (2014). The deep sea is a major sink for microplastic debris. *R. Soc. Open Sci.* 1:140317. doi: 10.1098/rsos.140317

Conflict of Interest: The authors declare that the research was conducted in the absence of any commercial or financial relationships that could be construed as a potential conflict of interest.

Copyright © 2020 Owen, Clare and Mauz. This is an open-access article distributed under the terms of the Creative Commons Attribution License (CC BY). The use, distribution or reproduction in other forums is permitted, provided the original author(s) and the copyright owner(s) are credited and that the original publication in this journal is cited, in accordance with accepted academic practice. No use, distribution or reproduction is permitted which does not comply with these terms.

frontiers in Earth Science

ORIGINAL RESEARCH
published: 13 December 2018
doi: 10.3389/feart.2018.00223

Complex and Cascading Triggering of Submarine Landslides and Turbidity Currents at Volcanic Islands Revealed From Integration of High-Resolution Onshore and Offshore Surveys

Michael A. Clare[1], Tim Le Bas[1], David M. Price[1,2], James E. Hunt[1], David Sear[3], Matthieu J. B. Cartigny[4], Age Vellinga[2], William Symons[2], Christopher Firth[5] and Shane Cronin[6]*

[1] National Oceanography Centre, University of Southampton Waterfront Campus, Southampton, United Kingdom, [2] National Oceanography Centre, School of Ocean and Earth Science, University of Southampton, Southampton, United Kingdom, [3] Department of Geography & Environment, University of Southampton, Southampton, United Kingdom, [4] Department of Geography, Durham University, Durham, United Kingdom, [5] Department of Earth and Planetary Sciences, Macquarie University, Sydney, NSW, Australia, [6] School of Environment, University of Auckland, Auckland, New Zealand

OPEN ACCESS

Edited by:
Ivar Midtkandal, University of Oslo, Norway

Reviewed by:
Gijs Allard Henstra, University of Bergen, Norway
Miquel Poyatos Moré, University of Oslo, Norway

***Correspondence:**
Michael A. Clare
m.clare@noc.ac.uk

Specialty section:
This article was submitted to Sedimentology, Stratigraphy and Diagenesis, a section of the journal Frontiers in Earth Science

Received: *19 September 2018*
Accepted: *21 November 2018*
Published: *13 December 2018*

Citation:
Clare MA, Le Bas T, Price DM, Hunt JE, Sear D, Cartigny MJB, Vellinga A, Symons W, Firth C and Cronin S (2018) Complex and Cascading Triggering of Submarine Landslides and Turbidity Currents at Volcanic Islands Revealed From Integration of High-Resolution Onshore and Offshore Surveys. Front. Earth Sci. 6:223. doi: 10.3389/feart.2018.00223

Submerged flanks of volcanic islands are prone to hazards including submarine landslides that may trigger damaging tsunamis and sediment-laden seafloor flows (called "turbidity currents"). These hazards can break seafloor infrastructure which is critical for global communications and energy transmission. Small Island Developing States are particularly vulnerable to these hazards due to their remote and isolated nature, small size, high population densities, and weak economies. Despite their vulnerability, few detailed offshore surveys exist for such islands, resulting in a geohazard "blindspot," particularly in the South Pacific. Understanding how these hazards are triggered is important; however, pin-pointing specific triggers is challenging as most studies have been unable to link continuously between onshore and offshore environments, and focus primarily on large-scale eruptions with sudden production of massive volumes of sediment. We address these issues by integrating the first detailed (2×2 m) bathymetry data acquired from Tanna Island, Vanuatu with a combination of terrestrial remote sensing data, onshore and offshore sediment sampling, and documented historical events. Mount Yasur on Tanna has experienced low-magnitude Strombolian activity for at least the last 600 years. We find clear evidence for submarine landslides and turbidity currents, yet none of the identified triggers are related to major volcanic eruptions, in contrast to conclusions from several previous studies. Instead we find that cascades of non-volcanic events (including outburst floods with discharges of $>1{,}000$ m^3/s, and tropical cyclones), that may be separated by decades, are more important for preconditioning and triggering of landslides and turbidity currents in oversupplied sedimentary regimes such as at Tanna. We conclude with a general model for how submarine landslides and turbidity currents are triggered at volcanic and other heavily eroding mountainous islands. Our model

highlights the often-ignored importance of outburst floods, non-linear responses to land-use and climatic changes, and the complex interactions between a range of coastal and tectonic processes that may overshadow volcanic regimes.

Keywords: cascading hazards, turbidity current, submarine landslide, tropical cyclone, outburst flood, volcanic island, crescentic bedforms, Strombolian volcano

INTRODUCTION

Active volcanic islands can create a variety of subaerial hazards including explosive eruptions that disrupt air transport (e.g., Gudmundsson et al., 2012), emission of gases harmful to health (e.g., Horwell and Baxter, 2006), fast-moving pyroclastic flows and lahars (e.g., Cronin et al., 1997; Calder et al., 1999), and ash falls that destroy agriculture and pollute water supplies (e.g., Wilson et al., 2012). Given their high relief in the surrounding deep ocean (up to 7 km above the surrounding seafloor), the subaerial extents of volcanic islands are typically dwarfed by their submerged flanks (Watt et al., 2014). These submarine slopes are often affected by dynamic sediment transport processes that can also pose a major hazard (Watt et al., 2014). Subsea flank collapses can be prodigious in scale (>100 s of km^3) and trigger damaging tsunamis (Moore et al., 1989; Keating and McGuire, 2000; Carey et al., 2001; Tappin et al., 2001; Coussens et al., 2016). Strategically important seafloor infrastructure, such as the subsea telecommunications cable network that transmits more than 95% of all digital data traffic worldwide, is vulnerable to submarine landslides or powerful sediment avalanches (called "turbidity currents") that occur offshore from volcanic islands (Carter et al., 2014; Pope et al., 2017). Small Island Developing States are disproportionately vulnerable to both subaerial and submarine hazards; largely due to their remote and isolated nature, small size, high population densities at or near sea-level and weak economies (Briguglio, 1995; Pelling and Uitto, 2001; Cronin et al., 2004; Terry and Goff, 2012; Hodgson et al., 2018). Understanding the threats posed to seafloor cables is particularly important for these islands, as telecommunication links underpin many critical areas for development, including access to regional markets, overseas bank transactions and booking for tourism (ICPC, 2016). Despite their vulnerability, remarkably few detailed offshore surveys exist for Small Island Developing States in the South Pacific; largely due to geographic and economic constraints (CClare et al., 2018). Therefore, the South Pacific has been identified as a "hazard blind-spot" with respect to submarine landslides and associated tsunamis (Terry and Goff, 2012; Goff and Terry, 2016). Furthermore, the link between onshore and offshore sediment transport processes, and hence, identification of the triggers for offshore hazards, is often unclear as integrated subaerial and submarine surveys are limited to relatively few volcanic islands worldwide (e.g., Casalbore et al., 2010; Babonneau et al., 2013).

The advent of modern multibeam bathymetry has enabled detailed imaging of the seafloor, thus providing insights into submarine landslides at volcanic islands (e.g., Mitchell et al., 2002). In addition to evidence of past slope failures, deep-water seafloor surveys (>25 m cell size) of active volcanoes have revealed that previously undocumented, crescentic bedforms are common from shallow to deep-water modern marine volcaniclastic systems (Wright et al., 2006; Hoffmann et al., 2008; Silver et al., 2009; Gardner, 2010; Leat et al., 2013; Pope et al., 2018). These bedforms may be diagnostic of turbidity currents triggered by major, episodic volcanic events, including: (i) sector or flank collapse; (ii) powerful Vulcanian eruptions; or (iii) sustained Plinian eruptions that can produce high-flux, sustained pyroclastic density currents (Pope et al., 2018). These past studies focussed on large and powerful scenarios, but what should we expect if and when volcanoes erupt at lower rates or have long-term low but steady outputs? These cases are arguably most common, with large explosive volcanoes undergoing centuries or millennia of quiescence between events and many less-explosive volcanoes having regular small eruptions (e.g., throughout Vanuatu; Tonga, Solomon Islands, Papua New Guinea and New Zealand). Only one existing bathymetric study is known for a regularly erupting low-explosivity volcano (Stromboli: Aeolian Archipelago; Casalbore et al., 2010, 2014), which also reveals similar crescentic bedforms. Thus, it is plausible that crescentic bedforms offshore from volcanic islands may signify sudden catastrophic collapses that originate after long-term preconditioning and by a range of multiple possible triggering mechanisms—directly related to volcanism or otherwise. With smaller individual eruptions known at such sites, crescentic bedforms this bedforms thus may not constitute evidence for major volcanic events. Crescentic bedforms offshore from some volcanic islands have been tentatively linked to turbidity currents triggered by non-volcanic processes, with documented examples including ephemeral sediment-laden river floods that plunge directly into the sea (Babonneau et al., 2013; Quartau et al., 2018). Morphologically-similar crescentic bedforms have also been described in many other subaqueous, non-volcanic settings worldwide and have been related to a wide range of triggers, including: subaqueous delta collapses (Clare et al., 2016; Hughes Clarke, 2016); dense river-water plunging (Casalbore et al., 2011, 2017); settling of sediment from river plumes (Hizzett et al., 2018); wave and storm resuspension (Xu et al., 2004; Normandeau et al., 2016); and glacial outburst floods (Duller et al., 2008). Thus, there is a large degree of ambiguity in linking bedform morphology at volcanic islands with triggering mechanisms. One constraint to our understanding has been the challenge of acquiring detailed multibeam data in water depths of <100 m; hence, few studies have acquired data that extends shallow enough to link the subaerial volcano to offshore and of appropriate resolution

to image bedforms (Casalbore et al., 2010; Quartau et al., 2018).

There is a pressing need to acquire detailed data offshore from volcanic islands to better understand the nature and triggers of offshore hazards, and the link between terrestrial and marine environments; in particular at Small Island Developing States and offshore from long-lived volcanoes. Here, we present the first detailed survey (2 × 2 m cell size) offshore from Yasur volcano on Tanna Island, Vanuatu in the South Pacific. Typical volcanic activity at Yasur involves low-magnitude Strombolian eruptions (Nairn et al., 1988; Firth et al., 2014), making it an ideal location for this study.

AIMS

We integrate our offshore data with existing and new onshore data to address the following specific aims. First, what is the offshore morphology of a continuously active and rapidly uplifting volcanic island, and what processes caused that morphology? We investigate whether arcuate-bight like features can be linked to slope failure, as suggested previously by Goff and Terry (2016), and whether offshore sediment transport pathways can be identified, such as the trains of crescentic bedforms observed on other volcanic islands. Second, we ask whether submarine landslides and crescentic bedforms found offshore from volcanic islands are always directly linked to major eruptive volcanic activity or flank collapses? We identify possible volcanic and non-volcanic triggers for submarine landslides and turbidity currents offshore Tanna Island based on documented historical events, and through integration of onshore and offshore analysis. Third, we ask how important is the role of cascades of events, which may be separated by decades, compared to instantaneous triggers? Finally, we outline a general model for the preconditioning and triggering of submarine landslides and turbidity currents at volcanic islands worldwide, based on insights from this and other studies.

Geological and Physiographic Setting for Tanna Island, Vanuatu

Tanna is one of 83 islands making up the 1,200 km-long Vanuatu volcanic arc in the south-west Pacific (Brothelande et al., 2016; **Figure 1**). Vanuatu has been affected by a wide range of natural hazards in recent and historical times, including earthquakes, tropical cyclones, and tsunamis (Meheux and Parker, 2006). Given its vulnerability to these hazards, Vanuatu has been described as the most disaster-prone country in the South Pacific (Meheux and Parker, 2006). Tanna was formed approximately 2.5 Ma by successive episodes of volcanism and reef growth (Carney and Macfarlane, 1979). Volcanism is currently focussed on Yasur; one of the most active volcanoes in the archipelago. Yasur is a scoria cone, which formed from repeated strombolian- and vulcanian-style eruptions that occur every few minutes (Nairn et al., 1988; Merle et al., 2013). These are fed by a steady-state magma reservoir, which has been providing basaltic trachy-andesitic magma to drive eruptions at Yasur for at least the last 600 years (Nairn et al., 1988; Merle et al., 2013; Firth et al., 2014). Previous phases of volcanic activity in this vicinity were more dramatic, however. The Siwi ring fracture (**Figure 1**), defines the previous limit of a compound caldera, which collapsed during at least two major ignimbrite-forming eruptions at approximately 43 and 3–8 ka (Firth et al., 2015). In its lower-most course, the Siwi River drains along the northern edge of the Siwi ring fracture, until it reaches Sulfur Bay where it meets a back barrier-type beach (**Figure 1**). Until recently, the Siwi River fed into Lake Isiwi, which was dammed by a lava flow that was emplaced prior to 1800 A.D. (**Figure 1**; Firth et al., 2015). Heavy rainfall in 2000 A.D. led to the breaching of the dam, triggering a major outburst flood that cut a new channel and flowed into Sulfur Bay (Kanas et al., 2000).

The present-day eruptive activity of Mount Yasur shows continuous low-level explosivity; however, shallow magma intrusion drives significant post-caldera uplift on Tanna which may contribute to a range of potential geohazards (Merle et al., 2013). The Yenkahe Resurgent Dome is among the fastest resurgent calderas worldwide (Merle et al., 2013), with uplift rates of 156 mm/year calculated over the last 1,000 years from dating of uplifted coral terraces (Chen et al., 1995; **Figure 1**). Two strong earthquakes in 1878 A.D. caused up to 12 m of co-seismic uplift at the coast by Port Resolution (Nairn et al., 1988; Merle et al., 2013). Photogrammetric surveys provide possible evidence for several subaerial collapse scars, each with estimated volumes of a few million cubic meters (Brothelande et al., 2015). Some of these potential headscars abut the coastline between Sulfur Bay and Port Resolution, and form steep, often-overhanging cliffs cut into weathered basaltic sands (Brothelande et al., 2015; **Figure 1C**). Recommendations were made by Brothelande et al. (2015) to perform bathymetric surveys offshore from these features to understand whether such features, and their run-out, extend offshore. Our study focuses specifically on this area (**Figures 1**, **2**) to understand the links between onshore and offshore sediment transport at a dynamic volcanic island through integration with previous land-based studies.

Data

A multibeam survey was performed by EGS Survey on behalf of the UK Hydrographic Office in March 2017. The survey covers an area of ∼6.5 × 3.2 km, and extends from the coastline to 292 m water depth (**Figure 2A**). Multibeam bathymetry data were acquired using a Kongsberg EM2040 system (200–400 kHz range) and processed into 2 × 2 m bins; hence features smaller than 2 m across cannot be resolved. An onshore photogrammetry survey of the distal part of the Siwi River and the beach at Sulfur Bay (∼900 × 900 m composed from two flights) was performed in October 2017 using a DJI Phantom 4 unmanned aerial vehicle. Pix4Dcapture was used to predefine a flight plan at 100 m altitude. Agisoft Photoscan was used to create an orthomosaic with a pixel size of <4 cm. Offshore sediment sampling was performed using a two-disc grabber-cup (10 cm^3) mounted on a small portable Deep Trekker DTG2 Remotely

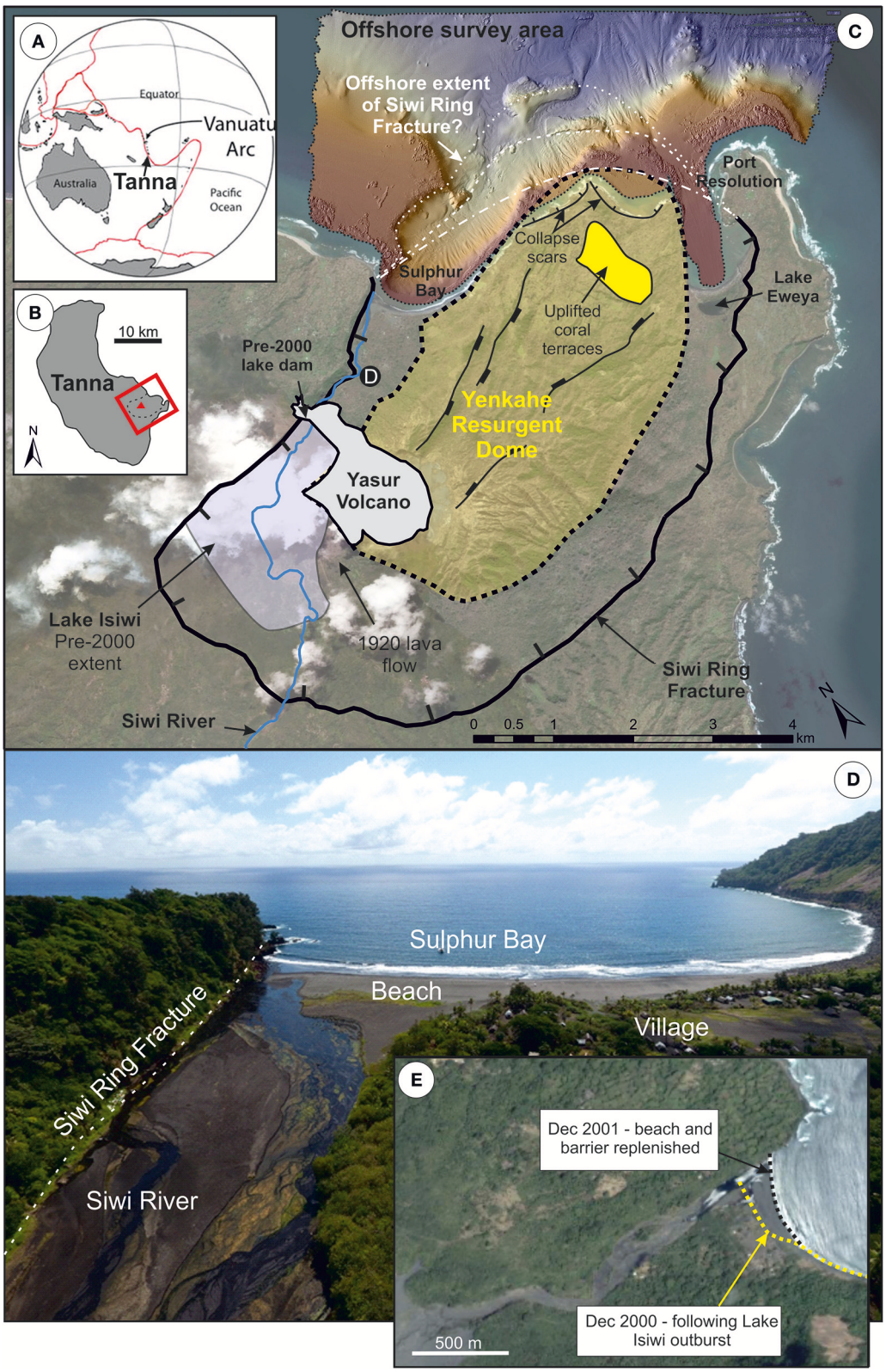


FIGURE 1 | (A) Location of Vanuatu Arc and **(B)** Tanna Island. Location and extent of survey area offshore Tanna Island, Vanuatu **(C)** shown in relation to onshore features. Onshore geomorphological and structural mapping based on Firth et al. (2014) and recreated under Copyright License 4433040166144. Three possible locations of the offshore extent of the Siwi Ring Fracture are annotated in white. Terrestrial photography from Google: Digital Globe. Aerial drone photograph **(D)** of Siwi River and Sulfur Bay taken toward the north-east at point D annotated on panel C. Satellite photograph **(E)** taken in 2001, following outburst flood in the Siwi River in 2000. December 2000 coastline is annotate in yellow.

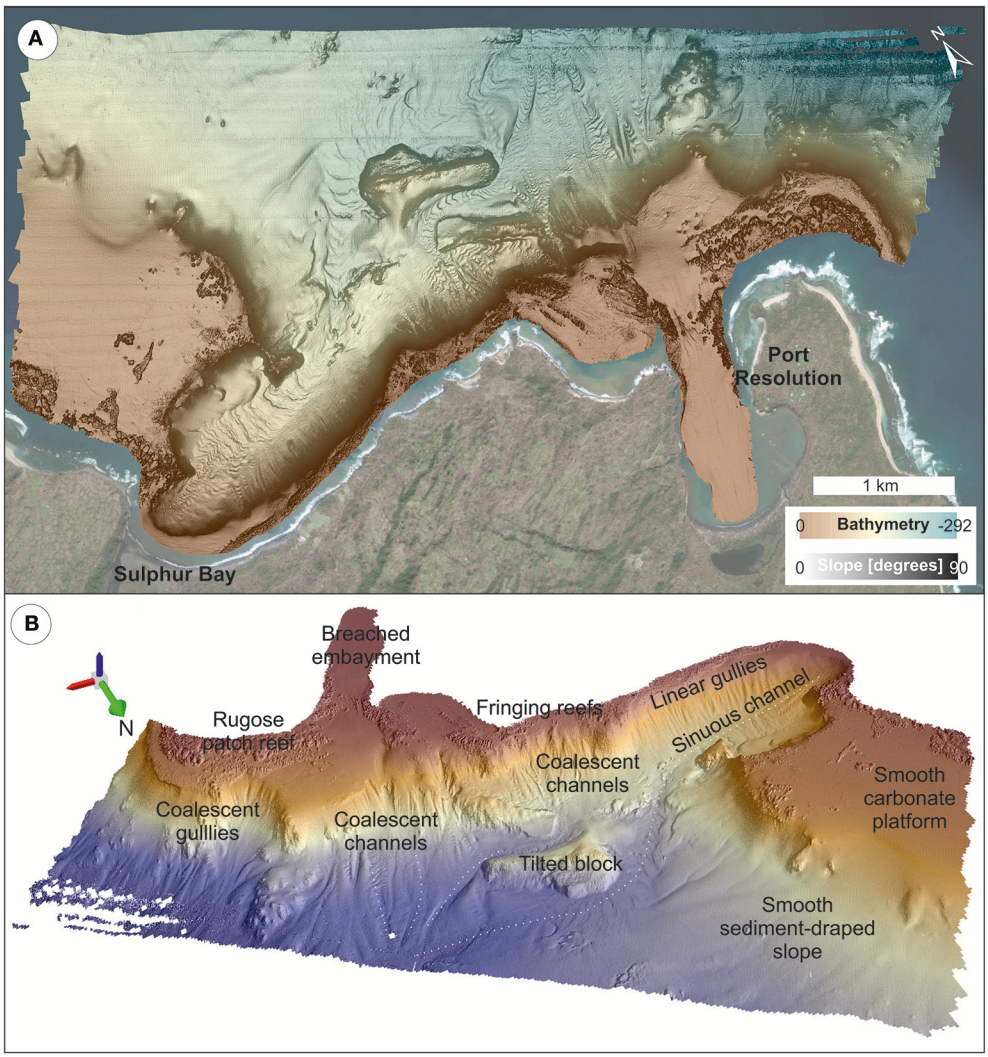


FIGURE 2 | Overview of seafloor topography and main features in the study area. **(A)** Colourwash bathymetry overlain on greyscale slope map. Terrestrial data from Google: Digital Globe. **(B)** 3D rendering (3 × vertical exaggeration) of hillshaded bathymetry (illumination from the north-west) annotated with main geomorphologic features and north-arrow (green).

Operated Vehicle (ROV) equipped with an additional high resolution camera (GoPro HERO4 silver) and deployed from the MV Escape (a 12.9 m catamaran) in October 2017. Offshore sediment samples were targeted within linear gullies (seven locations) and a submarine channel (three locations). Onshore sediment samples were hand-excavated from five locations in the Siwi River during the same survey in October 2017. Grain size analysis followed the procedures in Rothwell et al. (2006). Sediment was sieved at 2 mm to remove rare over-sized particles then three aliquots of each sub-sample were taken for measuring grain size. Aliquot samples (1 g) were dispersed in 30 ml 0.05% sodium hexametaphosphate solution and shaken for 24 h. Dispersed aliquots were analyzed using a Malvern Mastersizer 2000 using laser diffraction of suspended sediment grains (10,000 counts) to measure grain size distributions. Grain size distributions were measured three times per aliquot. Aliquots showed intra-sample variations of <3%. Standard reference materials showed intra-sample variations of up to 3% and accuracy toward reference values of 1.5%. Scanning Electron Microscopy (SEM) was performed using a Hitachi TM-1000 Microscope at the British Ocean Sediment Core Research Facility (BOSCORF) on selected samples to investigate micro-textural properties of the sediments.

RESULTS

Offshore Morphology of the Yenkahe Resurgent Dome, Tanna Island

Analysis of bathymetric data (ground-truthed based on observations made from video footage acquired from the ROV) generally reveals a smooth low-lying seafloor (carbonate platform) or a rougher, textured seafloor (fringing or patch

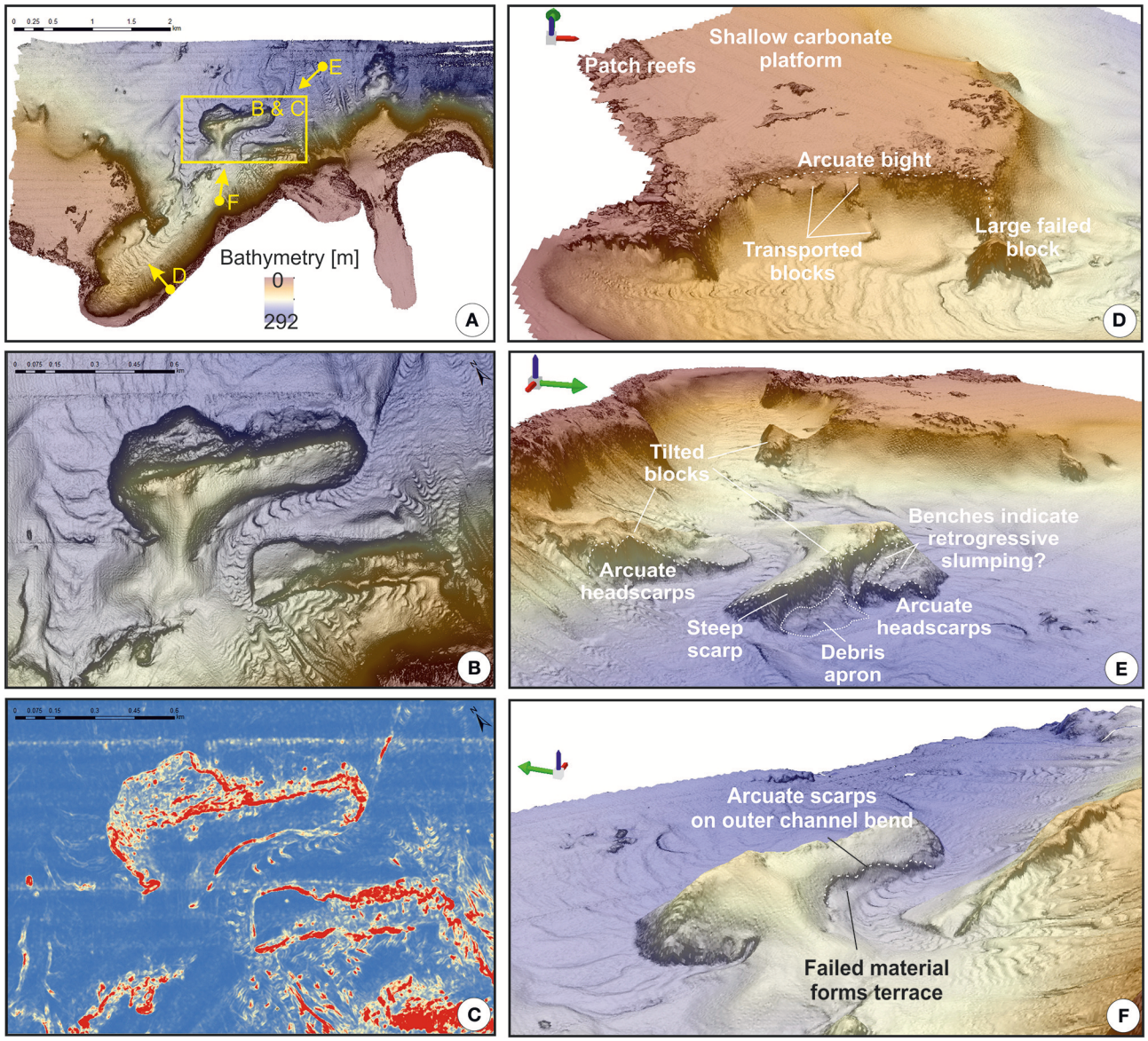


FIGURE 3 | Overview map **(A)** annotated with panels that illustrate evidence for localized slope instability. Line of sight is illustrated by yellow arrow for the following panels. Slope rendering (B, where black is steepest slope) and seafloor roughness (**C**, where red is roughest and blue is smoothest) maps show an elongated, tilted block that may be a failed slab of carbonate platform that has subsequently been eroded around. Arcuate bight-like structures may reflect past episodes of slope instability, and feature smaller blocks that appear to have slumped **(D)**. High slope angles **(B)** and roughness **(C)** on the flanks of the elongated, tilted block may indicate smaller-scale incipient slope failures, which are annotated in 3D renderings **(E,F)**.

reefs) in shallow (<60 m) waters to the north of Sulfur Bay and offshore from Port Resolution (**Figure 2**). Unlike its expression onshore, the edge of the Siwi Ring Fracture (i.e., the collapsed caldera margin) is difficult to trace offshore. Three different types of geomorphic character indicative of sediment transport are found locally obscuring the carbonate platform and extending into deeper water. These include: (i) arcuate bight-like features and tilted or displaced blocks (**Figure 3**); (ii) linear gullies, which are either isolated or coalescent in form (**Figure 2**); and (iii) trains of crescentic bedforms within sinuous channels, locally associated with scours (**Figures 4**, **5**). These three geomorphic characters now form the observational basis of this paper.

Arcuate Bight-Like Features and Tilted Blocks

Steep-flanked (up to 60°) arcuate bight-like features were identified locally cutting back into the carbonate platform (**Figure 3D**). At least five tilted blocks occur immediately downslope of an arcuate bight-like feature on the northern flank of

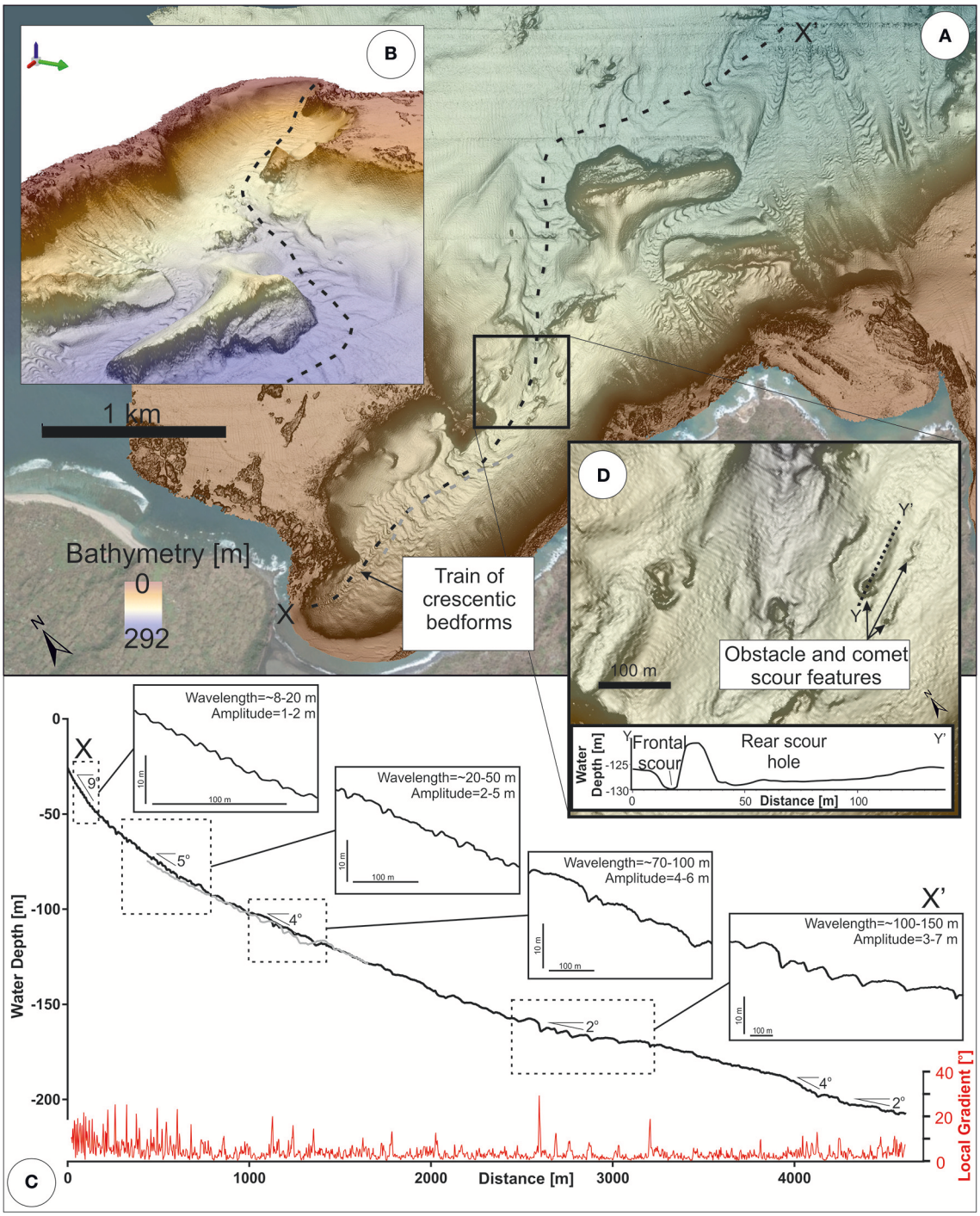


FIGURE 4 | Overview map **(A)** and 3D rendering **(B)** annotated with dashed line along the axis of sinuous channel with cresentic bedforms that originates in Sulfur Bay. Along-channel profile (black and gray lines in **C**) shows how bedforms generally increase in wavelength and amplitude with increasing water depth. Average slope gradients are annotated on the black profile, while local slope gradient that highlights bedforms and knickpoints is shown as a red line in **(C)**. Localized obstacle and scour features are shown in **(D)**.

the carbonate platform in Sulfur Bay (**Figure 3D**). The largest of these blocks has an estimated volume of 9.29×10^{-6} km^3, but all were significantly smaller than the scar from which they potentially originated. Three larger ($<3.82 \times 10^{-4}$ km^3) angular blocky features form localized prominent positive relief that deflect the course of seafloor channels (**Figures 3**B,E,F, **4**, **5**).

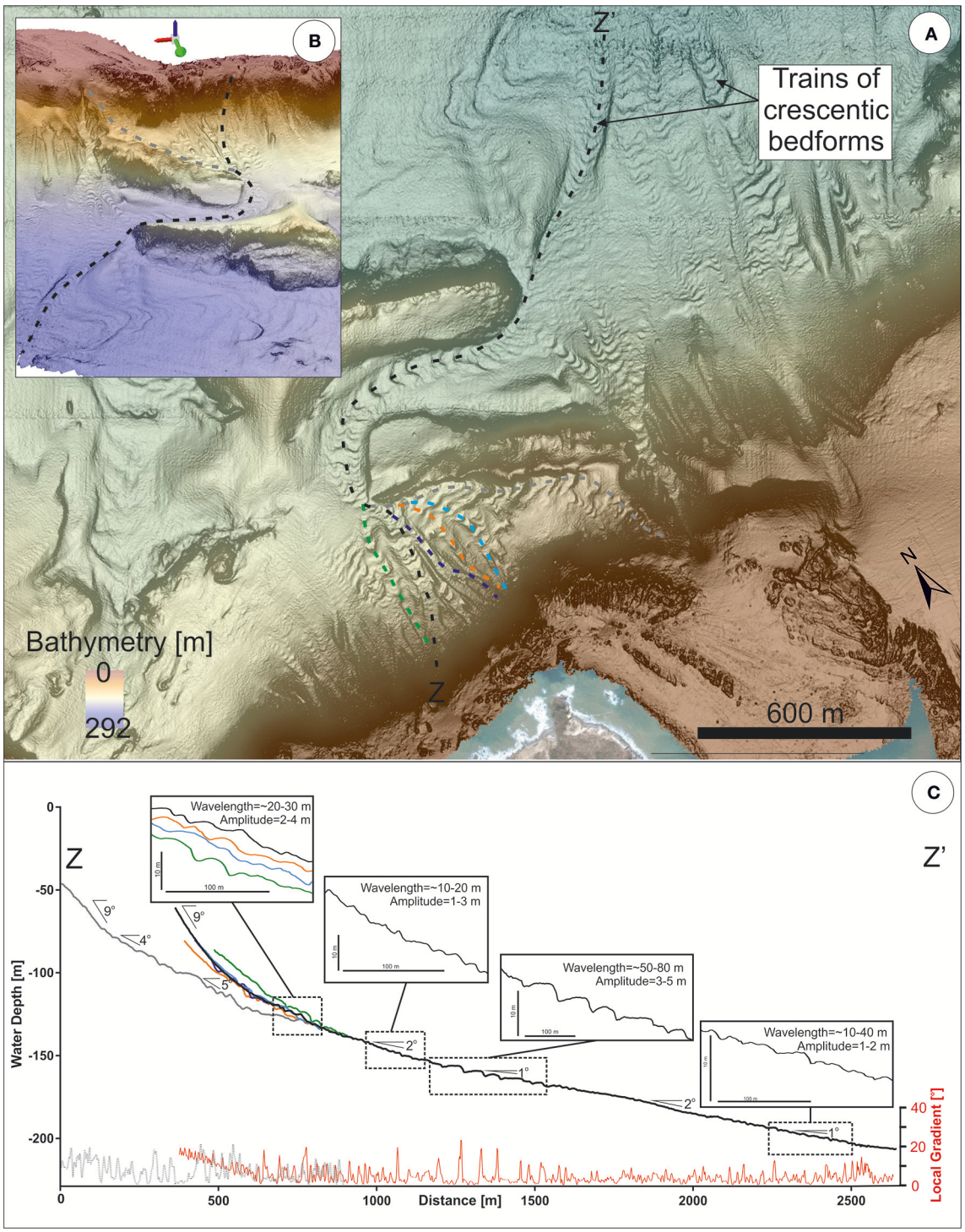


FIGURE 5 | Overview map **(A)** and 3D rendering **(B)** annotated with dashed lines along the axis of sinuous coalescent channels with cresentic bedforms that originate ~2.5 km to the east of Sulfur Bay. Along-channel profiles (black, gray, blue, orange and green lines in C) show how bedforms generally increase in wavelength and amplitude to 1,500 m water depth, but then decrease in response to the constriction of the channel. Average slope gradients are annotated on the black profile, while local slope gradient that highlights bedforms is shown as a red line in **(C)**.

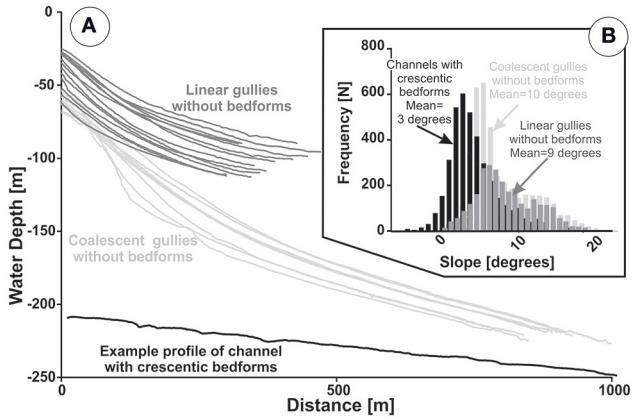


FIGURE 6 | Isolated linear gullies are much shorter in length than coalescent gullies, but attain similar slope angles, which are higher on average than those for channels with crescentic bedforms **(A)**. Local slope measurements along all mapped gullies and channels **(B)** shows that channels with crescentic bedforms only occur at much lower slope angles (mean of 3 degrees).

These blocky features have a low-angle, tilted upper surface (5–10°), which is otherwise similar in seafloor expression to the surrounding flat-lying carbonate platform. Their flanks are often steep (up to 60°) and are cut by arcuate incisions, downslope of which apron-like accumulations of roughly textured seafloor debris are found (**Figure 3E**). The largest of these blocky features has an estimated volume of 2.29×10^{-3} km^3. The two debris aprons have estimated volumes of 1.28×10^{-3} km^3 and 9.67×10^{-4} km^3, based on their planform area and assuming that they have a wedge-shaped cross-sectional geometry [in line with the approach used by McAdoo et al. (2000); Chaytor et al. (2009)].

Linear Gullies That Lack Bedforms

We observe two types of gully morphology: (i) isolated and (ii) coalescent forms. *Isolated linear gullies* initiate in water depths of 20–30 m on the steepest slopes in the survey area (**Figure 2**), with a mean slope of 9° but can locally reach up to 30–40° (**Figure 6A**). Such slopes are immediately downslope of areas with a limited extent of fringing coral (extending no more than 130–200 m seaward from the high water mark; **Figure 2A**) and with an abundance of boulders (observed from ROV dives). These gullies are most abundant on the eastern flank of Sulfur Bay; the flanks of the Yenkahe dome which is undergoing most rapid uplift (**Figure 1**; Chen et al., 1995). Linear gullies are up to 500 m in length, and terminate as slope angles reduce; typically where they intersect sinuous channels. Linear gullies maintain a near-continuous width along their straight course, which ranges from 20 to 60 m. Bedforms are absent from linear gullies. *Coalescent gullies* initiate at water depths of ∼50 m, to the north-east of Port Resolution, in an area of less dramatic uplift outside of the Yenkahe dome (**Figures 1**, **2**). Similarly to isolated linear gullies, they initiate on slopes of up to 30°, with a mean gradient of 10° (**Figure 6A**). Unlike isolated linear gullies, coalescent forms become adjoined downslope from their initiation points, in an amphitheater-shaped depression (**Figure 2**). Another difference is that they initiate >500 m offshore from the high water mark, downslope of a more extensive patch of coral reef (**Figure 2A**). Bedforms are also absent from these features.

Sinuous Channels With Crescentic Bedforms

One of the most extensive bathymetric features in the survey area is a sinuous channel that initiates as a series of small (8–20 m wavelength, 1–2 m amplitude) bedforms in 30 m water depth, immediately offshore from Siwi River at Sulfur Bay (**Figure 4**), and extends to the north-east beyond the limits of the survey area (**Figure 4**). Unlike linear gullies, this channel forms on much lower angle slopes (mean of 3°; **Figure 6A**). The channel contains abundant crescentic bedforms, which generally increase in wavelength and amplitude with increasing water depth, where the channel broadens out (to 200 m) on lower angle slopes (**Figure 4**). The bedforms show a backstepping asymmetry, featuring steep lee (down-stream) faces and lower angle back-angled stoss (up-stream) faces (**Figure 4C**). The channel is also punctuated by steeper and deeper scours with gradients of up to 20–30 degrees on their lee (down-stream) face, and obstacle and comet structures (Stow et al., 2009) oriented parallel with the axis of the channel.

A series of channels also initiates in water depths of between 40 and 50 m, to the west of Port Resolution. These commence individually as approximately 10 m-wide channels, until they coalesce at approximately 125 m water depth to form one channel that broadens to approximately 130 m (**Figure 5**). This combined channel then adjoins the single broad sinuous channel and extends beyond the limits of the survey area (**Figure 5**). In common with the broad sinuous channel (**Figure 4**), these channels feature an abundance of similar back-stepping crescentic bedforms (**Figure 5C**). The bedforms generally increase in size with increasing water depth; however, they locally attain lower amplitudes and wavelengths where the channel is constricted or steepened by seafloor relief. Channel orientation is strongly controlled by features that present prominent seafloor relief, such as tilted blocks.

Composition of Seafloor Sediments

Grain size analysis from crescentic bedforms in the submarine channel at Sulfur Bay reveals a very similar distribution to samples from the Siwi River, with clear bimodality at the most proximal location, becoming progressively finer offshore (**Figure 7**). The grain size within linear gullies is distinctly different to both samples from Siwi River and crescentic bedforms offshore Sulfur Bay, showing a finer and broader grain size distribution. Transmitted light and scanning electron microscopy show that sediment is dominantly comprised of basaltic lithics with a small component of volcanic glass. Small amounts of carbonate and coralline debris are incorporated further offshore. Samples were not taken from the arcuate bight-like features, tilted blocks, nor the coalescent sinuous channels to

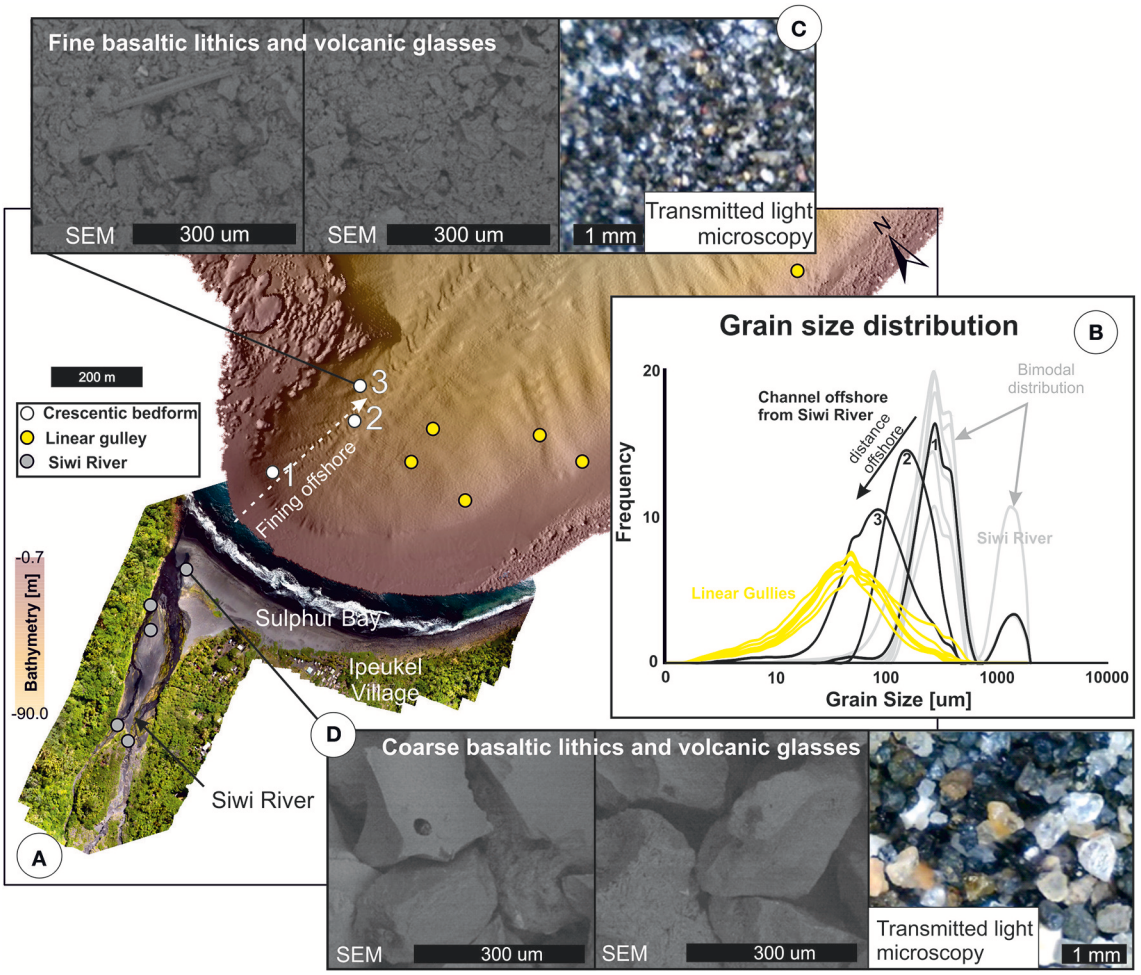


FIGURE 7 | Location of sediment samples presented in this study **(A)** overlain on drone-acquired photographic survey of Siwi River and multibeam bathymetry offshore. Grain size distributions **(B)** from Siwi River (gray lines) are similar to those from the proximal part of the sinuous channel with crescentic bedforms (black lines – 1–3), but distinct from samples from linear gullies (yellow lines). Details of SEM and transmitted light microscopy are shown for specific locations **(C,D)**.

the west of Port Resolution so no comment can be made on the seafloor sediments in those areas.

DISCUSSION

We first discuss the origin of the bathymetric features observed offshore Tanna and whether they relate to caldera collapse (along ring fractures due to catastrophic volcanic eruption) or offshore sediment transport processes. Second, based on the evidence for slope instability offshore Tanna, we discuss whether similar features on volcanic islands elsewhere in the world represent tsunamigenic collapse of carbonate platforms. Third, we discuss the potential triggers for slope instability and turbidity currents on volcanic islands, initially focusing on the range of plausible triggering events at Tanna. We conclude by proposing a general model for their preconditioning and triggering at volcanic islands worldwide, invoking a complex interplay of both volcanic and non-volcanic processes.

Challenges in Delineating the Offshore Extent of Caldera Margins

Caldera collapses at many volcanic islands have a distinct outer margin; the extent of which can be continuously mapped from onshore to offshore (e.g., Pantelleria, Italy; Nisyros and Santorini, Greece; Deception Island, Antarctica; Rabaul, Papua New Guinea; Aira, Japan - Walker, 1984; Nomikou et al., 2012). Such clarity is not apparent offshore Tanna, however. The submerged outline of the Siwi Ring Fracture is difficult to define (**Figure 1**). The overall morphological complexity of the caldera at Tanna is probably due to its formation by at least two major caldera-collapse episodes, with other modification possible during smaller intervening eruptions (Firth et al., 2014, 2015). In addition, the northern margin of the Siwi Ring Fracture is possibly erased by the rapid uplift of the Yenkahe block, with

higher uplift rates in the NE possibly "popping-out" the northern caldera margin (Brothelande et al., 2015). Resurgent calderas (pushed piston-like back up along or within caldera fractures) are common in submarine volcanic settings where magma rises into them following collapse (e.g., submarine Tonga arc; Graham et al., 2008), where crust is thin. They are also possible in other areas, e.g., Ischia Island off Naples is mapped as a fully resurgent caldera, where past caldera fill has been uplifted to form a steep island (Carlino et al., 2006). Furthermore, it is likely that the seafloor was strongly affected by a combination of sediment deposition, transport, and slope failures in the period since (or during) caldera-formation. These processes have sculpted and reworked both the caldera margin and carbonate platform. That a feature which is so distinct onshore, can be almost entirely reworked or masked by offshore sediment transport processes, has implications for the recognition and interpretation of partially or entirely submerged caldera collapses in areas of active seafloor sediment transport processes.

Are Arcuate Bight-Like Features Formed by Slope Failures and if So, Were They Single-Event or Multi-Phase in Nature?

Based on coarse resolution (>100 m) regional bathymetry, Terry and Goff (2013) identified arcuate bight-like features incised into carbonate platforms on a number of volcanic islands and atolls in the South Pacific, and proposed a submarine slope failure for their origin. They further suggested that such events may be very large in volume, and could trigger significant tsunamis if failure occurs in one displacement event. Indeed, many studies of volcanic islands have revealed prodigious-volume landslides of their submerged flanks (e.g., Moore et al., 1989; Masson, 1996; Coussens et al., 2016). The high resolution bathymetry offshore Tanna reveals arcuate bight-like features cut into the carbonate platform. Much of the large-scale (>km) "scalloping" of the carbonate platform is attributed here to caldera collapse, rather than slope failure. There is, however, compelling evidence of smaller-scale submarine slope failure within arcuate bights with perimeter lengths of 100–1,000s of meters. These slope failures are superimposed on the post-caldera collapse relief (**Figure 3D**). We interpret the arcuate bights to the north and east of Sulfur Bay as the up-slope limit of collapse events. The tilted blocks found downslope (partially-translated and/or rotated debris) are much smaller than the scars from which they originated (**Figure 3**). Thus, it is likely that submarine slope failures offshore from Tanna occurred progressively, as multiple phases of small volume collapses and partially-rotated blocks ($<2.9 \times 10^{-3}$ km^3). The heterogeneous nature of the mixed carbonate platform and patch reefs into which these bights are incised presumably results in localized zones of weaker material that may fail preferentially due to erosion, undercutting, or from external cyclic loading (e.g., earthquake, storm waves; Keating and McGuire, 2000). These smaller bights are interpreted to arise from a combination of retrogression and lateral unloading (when adjacent areas of seafloor are removed) during multiple phases of relatively small-scale slope collapses. Similar piecemeal failures of carbonate-dominated shelf breaks and slopes are common in the Bahama Banks, Great Barrier Reef and a number of volcanic-cored atolls in the South Indian Ocean (Puga-Bernabéu et al., 2013; Jo et al., 2015; Watson et al., 2017; Counts et al., 2018), suggesting that this situation may be similar for many other atolls and volcanic islands flanked by carbonate platform-reefs. The landslide-origin hypothesis for bight-like features (Terry and Goff, 2013) is generally supported by our findings; however, we suggest that landslide-related bights may form progressively in multiple stages rather than as one event. Multi-stage slope failures typically relate to a much lower tsunami hazard than one-off en-masse collapses, due to the smaller event volumes involved and the time elapsed between displacements (Hunt et al., 2013). Furthermore, without high resolution data, it may be challenging to attribute arcuate bight-like morphology to slope failure rather than caldera collapse. These complexities thus underline the importance of acquiring high resolution multi-beam bathymetry and the value of future efforts to map the offshore regions of Small Island Developing States for local and regional hazard assessments, particularly in the South Pacific.

What Processes Are Responsible for Creating Gullies and Submarine Channels With Crescentic Bedforms?

The linear gullies and seafloor channels observed offshore Tanna (**Figures 2**, **4**, **5**) are morphologically similar to those observed in many settings worldwide where density currents transport sediment to deeper waters (e.g., Micallef and Mountjoy, 2011; Babonneau et al., 2013; Lonergan et al., 2013; Symons et al., 2016; Casalbore et al., 2017; Covault et al., 2017). In particular, the scale, morphology and grain-size of the crescentic bedforms within the sinuous channels are very similar (i.e., meters in amplitude, tens of meters in wavelength, fine to coarse sand) to those where repeat seafloor surveys and direct flow monitoring have demonstrated the occurrence of density-stratified turbidity currents that undergo a series of hydraulic jumps (Hughes Clarke, 2016; Normandeau et al., 2016; Hage et al., 2018; Paull et al., 2018). In such sites, flows switch between super- and subcritical flow regimes that drive the up-stream migration of crescentic bedforms (Hughes Clarke, 2016; Normandeau et al., 2016; Hage et al., 2018). So why do linear gullies without bedforms occur, as well as channels with crescentic bedforms? Slope gradient appears to exert a strong control occur, as linear gullies have a significantly higher gradient (mean of 9–10°; **Figure 6**) than channels containing crescentic bedforms (mean of 3°). This is in line with observations by Micallef and Mountjoy (2011) who identified a minimum slope threshold (5°) for the formation of linear gullies, arguing that a critical bed shear stress can only be attained on such steep slopes. Quartau et al. (2018) only found linear gullies on the volcanic islands of the Madeira archipelago at slopes of >15°. On the submarine flanks of Stromboli volcano, Casalbore et al. (2010) only observed crescentic bedforms on slopes of <5°. We suggest therefore that both gullies and crescentic bedforms offshore Tanna were created by turbidity currents and that slope angle dictates the nature of the flow-seafloor interaction and thus the resultant morphology (Kostic, 2011; Zhong et al., 2015). But what processes were

responsible for triggering these flows? Were volcanic events solely responsible? We now explore these questions.

Do Gullies and Crescentic Bedforms on Volcanic Islands Only Result From Flows Triggered by Major Volcanic Events?

Trains of crescentic bedforms occur on the submarine flanks of many volcanic islands globally, including Stromboli, Reunion Island, the Canary Islands, and islands in the Bismark, West Mariana, Kermadec, and South Sandwich island arcs (see database in Symons et al., 2016; Pope et al., 2018 and references therein). At most of these sites, it has been inferred that these seafloor features result from major volcanic events: either large-magnitude explosive eruptions, or large flank/sector collapses (Pope et al., 2018). This is highly unlikely to be the case for the features observed offshore Tanna. The most recent Plinian eruption on Tanna occurred ∼3–8 ka, modifying the Siwi Caldera and emplacing widespread ignimbrite deposits (Firth et al., 2015). Onshore, these deposits radiate out from the Siwi Ring Fracture, but are absent within the caldera (Firth et al., 2015). Crescentic bedforms and linear gullies are found within the inferred offshore caldera margin, suggesting that they must post-date the caldera-modifying eruption. More recent volcanic activity from Yasur has involved continuous, low magnitude Strombolian and Vulcanian eruptions over at least the last 600 years (Nairn et al., 1988; Chen et al., 1995). This style of activity produces high rates of sediment input into the surrounding areas with ash fall and also contributes to a large, devegetated or sparsely vegetated area downwind of the volcano. Eruptions with major flow events powerful enough to scour gullies onshore Tanna have not been recorded in the recent geological record. Sea cliffs between Sulfur Bay and Port Resolution (**Figure 8A**) form the north and eastern margins of the rapidly uplifting Yenkahe Dome. Based on dating of uplifted coral terraces on this block (**Figure 1**) by Chen et al. (1995), these cliffs have formed over the last 1–2 ka. Sea cliffs to the north of the Siwi River incise into deposits from Plinian eruptions dated at 3–8 and ∼43 ka (Firth et al., 2015), hence must also significantly pre-date the features observed at seafloor. We can therefore rule out these Plinian eruptions as a trigger and conclude that bedforms on the flanks of volcanic islands do not necessarily relate to major volcanic events. If this is the case, then what are the other plausible triggers? We now explore potential mechanisms, initially considering those that are indirectly related to volcanic activity, and then those that are unrelated (**Table 1**).

Low Magnitude Volcanic Activity and Related Preconditioning Effects

While the effect of major eruptive volcanic activity may not necessarily be directly responsible, the cumulative or antecedent conditions resulting from past or ongoing low magnitude volcanic activity may play a key role in preconditioning slopes to failure or setting up a successive chain of events that may trigger turbidity currents at volcanic islands. For instance, the accumulation of relatively weak and laminated volcanic deposits, and the effects of shallow hydrothermal circulation, are plausible contributing factors to promote slope instability (Brothelande et al., 2015). Dynamic topographic changes also play a potentially important role. The uplift rates calculated for the Yenkahe Dome, abutting the area between Sulfur Bay and Port Resolution are among the highest for any resurgent dome worldwide (156 mm/year), with two earthquake events in 1878 A.D. leading to up to 10 m co-seismic uplift at Port Resolution (Chen et al., 1995). Elevation differences between a hydrographic survey performed in 1840 A.D. (Hydrographic Office of the Admiralty, 1843) and our 2017 A.D. survey, indicate the seafloor rose by between 2.6 and 11.3 m in Resolution Bay (an area located east of the even more rapidly uplifting Yenkahe Dome). This equates to an average rise of 40 mm /year; however, most of the elevation change was likely due to the 1878 A.D. earthquakes as evidenced by eye witness accounts. The Rev. Lawrie wrote in 1898: *"On the island of Tanna there was a great earthquake on the 10th January 1878, which caused a surge of the water at Port Resolution to rise forty feet, and to sweep everything before it, destroying all the canoes of the natives. Two minutes after the earthquake a rise of the land took place on the while west side of the harbour, to the extent of about twenty feet. This narrowed considerably the effective anchorage of the harbour, and a lost anchor came into view where a ship had ridden safely some years previously. About a month afterwards another earthquake caused a further elevation, so that rocks which were formerly covered with seven or eight fathoms of water are now above high-water mark"* (Lawrie, 1898). These uplift events caused the subaerial exposure of parts of Resolution Bay, forming the present day Lake Eweya (**Figure 9**). The coupling of geotechnically weak volcanic deposits and rapid uplift has been used to explain the presence of multiple onshore slope failures (Brothelande et al., 2016) and presumably explains the existence of steep, often-overhanging cliffs between Sulfur Bay and Port Resolution (**Figure 8A**). Underwater ROV-video footage reveals accumulations of boulders and other debris below these cliffs on the carbonate platform (**Figure 8B**), downslope of which a series of isolated linear gullies is found. Thus, cliff collapses may transition to sediment-laden density flows as they disaggregate and mix with seawater at the edge of the carbonate platform to create linear gullies.

The Role of Outburst Floods—An Under-appreciated Hazard at Volcanic Islands?

Crescentic bedforms similar to those observed offshore Tanna have been identified at many non-volcanic locations where rivers directly feed submarine canyons or channels (Symons et al., 2016 and references therein). At river-fed locations, it is hypothesized that turbidity currents initiate from a number of possible mechanisms, during, or shortly following periods of elevated river discharge. First, if sediment-laden river water is dense enough it may directly plunge upon entering the sea, initiating a hyperpycnal flow (Mulder et al., 2003). Second, settling from a buoyant sediment-laden river plume may settle more diffusively via a process known as convective fingering, periodically initiating turbidity currents (Parsons et al., 2001;

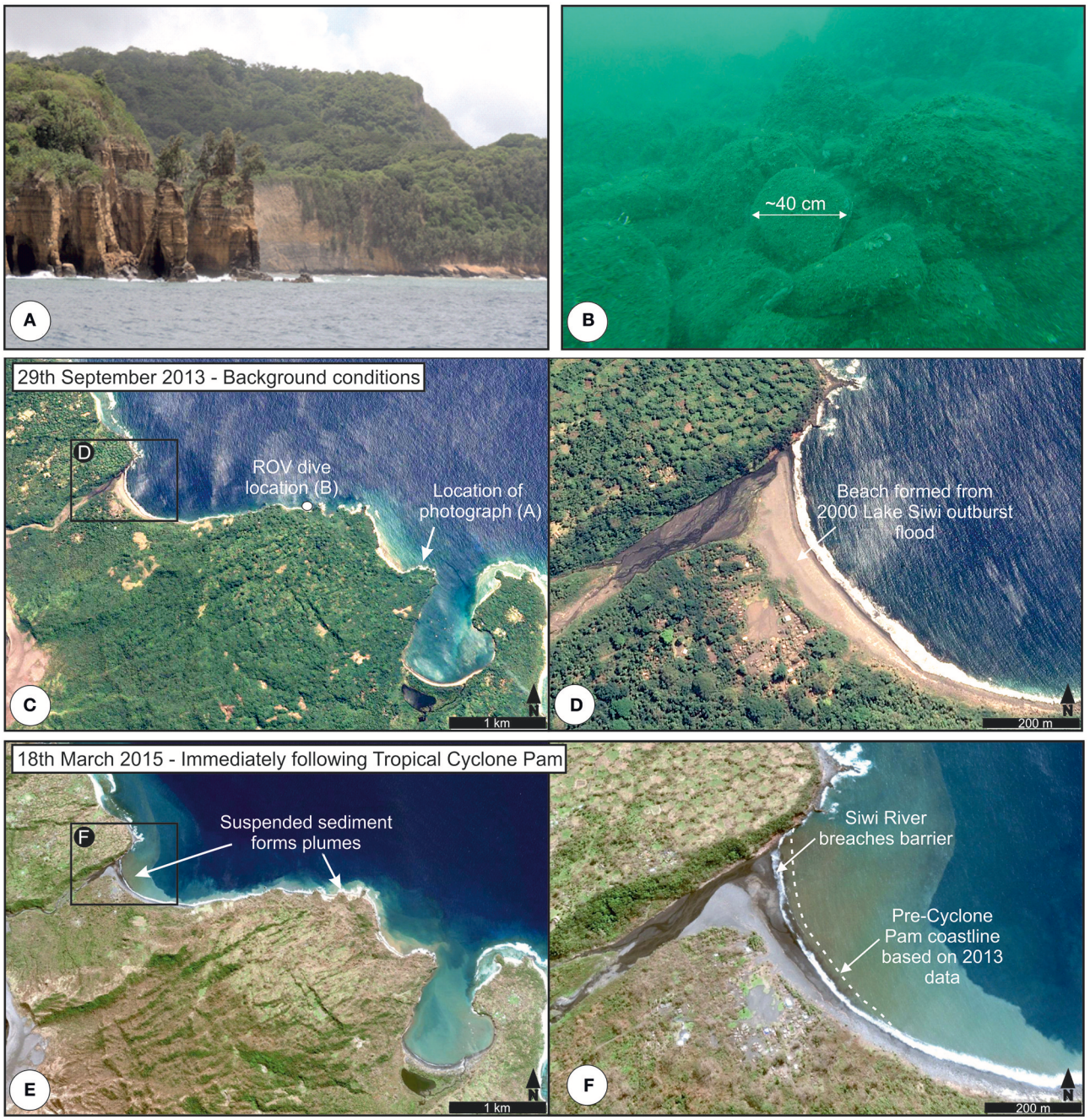


FIGURE 8 | Photograph **(A)** from survey vessel of steep coastal cliffs at location annotated on **(C)**. Photograph taken using ROV **(B)** showing boulders (~30–50 cm in diameter) below the cliffs. Satellite photography prior to **(C,D)** and immediately following **(E,F)** tropical cyclone Pam. **(D,F)** zoomed in to Siwi River and Sulfur Bay. Map images acquired by NASA and exported from Google: Digital Globe.

Hizzett et al., 2018; Jazi and Wells, 2018). Third, sediment delivered by a river flood rapidly accumulates at the river mouth and periodically becomes unstable, thus triggering a delayed slope failure that initiates a turbidity current (Clare et al., 2016; Hughes Clarke, 2016). Submarine channels with crescentic bedforms occur offshore from river outflows on volcanic islands in La Reunion and the Madeira Archipelago, and have been tentatively linked to ephemeral periods of flash flooding that may trigger hyperpycnal flow (Babonneau et al., 2013; Quartau et al., 2018). This may indicate that river floods are a potential trigger; however, Pope et al. (2018) explicitly ruled out river floods as a potential explanation for the formation of crescentic bedforms on volcanic islands of the Kermadec Arc, on the basis of a small hydrologic system that prevents

TABLE 1 | Review of possible triggers for turbidity currents and submarine landslides at volcanic islands, with specific reference to documented events at Tanna Island (parenthesized numbers are cross-references to **Figure 11**).

Event	Triggering mechanism	Known events on Tanna Island
DIRECTLY RELATED TO VOLCANIC ACTIVITY		
Eruption/pyroclastic flow	[1] Directly triggered as dense pyroclastic surge plunges into the sea or indirectly triggered from enhanced settling of grains by convective fingering due to [2] lofted surge cloud that overruns the sea or [3] tephra fallout from eruption cloud.	Last known pyroclastic-forming eruptions occurred at 3–8 ka and 34 ka (Firth et al., 2015) so unlikely to be responsible for features observed on present day seafloor.
Flank/dome/sector collapse	[4] Turbidity current evolves from slope failure or lava dome collapse due to eruption or growth of magma chamber.	Last major sector collapse was 34 ka so unlikely responsible for features on present day seafloor. No major collapses have occurred in recent times, but local slope failure may have been triggered due to fast uplift rates (156 mm/year, averaged over 2 ka) for the Yenkahe resurgent dome (Chen et al., 1995; Firth et al., 2015).
INDIRECTLY RELATED TO VOLCANIC ACTIVITY		
Crater lake or lava-dammed lake outburst flood	[5] Sudden discharge of heavily sediment-laden outwash [A] plunges to directly trigger hyperpycnal flow, [B] indirectly triggers turbidity current due to settling out of sediment from a sediment-laden plume, or [C] leads to rapid accumulation of sediment at shelf break setting up delayed slope failure.	Heavy rainfall in 2000 triggered outburst flood from Lake Isiwi releasing 4.1 million m^3 of water and erosion of 1.1 million m^3 of sediment that cut a new channel and flowed out to sea at Sulfur Bay (Kanas et al., 2000; Firth et al., 2014). Estimated peak discharge of >1,000 m^3/s (**Figure 11**).
Lahar	[6] Heavy rainfall mobilizes volcanic sediments and washes them offshore and triggers turbidity currents (in the same manner as 5A-C above).	No recorded evidence, but may occur due to tropical cyclone [8].
Earthquake/ground movement	[7] Ground shaking and/or uplift triggers slope or cliff collapse of weathered subaerial volcanic sediments or at the steep fringes of carbonate platform.	Strong ground movement (from witnesses) and co-seismic uplift of up to 12 m due to two earthquakes in 1878 (Chen et al.,1995).
UNRELATED TO VOLCANIC ACTIVITY		
Tsunami or storm surge	[8] Loading by waves triggers [A] slope instability or cliff collapse or [B] resuspension of seafloor sediments.	7.1-7.5 M_W earthquake triggered a tsunami on November 26th 1999 with 6.6 m run-up height on Tanna. Tsunamis also recorded in 1875, 1961, 1965 (Caminade et al., 2000).
Tropical cyclone	[9] Heavy rainfall triggers [A] enhanced sediment-laden surface water runoff that can trigger cliff collapse, or [B] dense river outflow that enters the sea. [C] Rapid accumulation of sediment at shelf break may lead to delayed slope failure.	Long history of cyclones at Tanna including Tropical Cyclone Pam (2015), Ivy (2004), Paula (2001), Prema (1993), Fran (1992), Uma (1987). Pam wind-speed up to 270 km/hour, up to 5.3 m maximum flow height, and triggered enhanced run-off (Hong et al., 2018).
Onshore failures/cliff collapse	[10] Onshore slope failures or collapse of coastal cliffs enters the sea triggered by climatic, erosion, or other non-volcanic processes (Terry and Goff, 2013).	Two historic landslides (1919 and 1975) occurred on the slopes of Yasur's cone but did not enter the sea (Carney and Macfarlane, 1979; Merle et al., 2013). Steep overhanging sea cliffs cut into weathered basalt may represent the headscars of subaerial failures (Brothelande et al., 2015) prone to incipient failure.

large-scale fluvial output to the ocean. At Tanna, we observe a submarine channel with crescentic bedforms offshore from the Siwi River, so are the two systems linked here? Grain size analysis points to a connection, given the similarities between samples hand-excavated from the river and those acquired from the submarine channel using an ROV (**Figure 7**). However, analysis of satellite photography since 2001, and our new aerial photography, does not indicate a river plume (with the exception of the aftermath of Tropical Cyclone Pam as discussed in the following section), and the river discharge is generally very low (based on visual observations and the presence of a back barrier at the river outflow). Therefore, it is unlikely that the background river discharge is capable of directly triggering turbidity currents (**Figures 8C,D**).

A series of events that culminated in May 2000 A.D. offers a likely mechanism for the submarine morphology (**Figure 10**). In 2000 A.D., above average rainfall triggered an outburst flood from Lake Isiwi, which was previously impounded by a tephra barrier on top of a lava flow (Kanas et al., 2000; Vanuatu Ministry of Lands and Natural Resources, 2014). The lake had no regular surface water outlet. The effect of heavy rainfall was exacerbated by the loss of storage capacity, caused by lake-wide deposition of over 1 m (average of 2.3 m) thickness of sediments that were eroded from the flanks of Mount Yasur and the upper reaches of the catchment during tropical cyclone Uma in 1987 (Kanas et al., 2000). The Vanuatu Ministry of Lands and Natural Resources provide a summary of observations from islanders: "*Water began overflowing the corner of the lake closest to Sulfur Bay (northeast).*

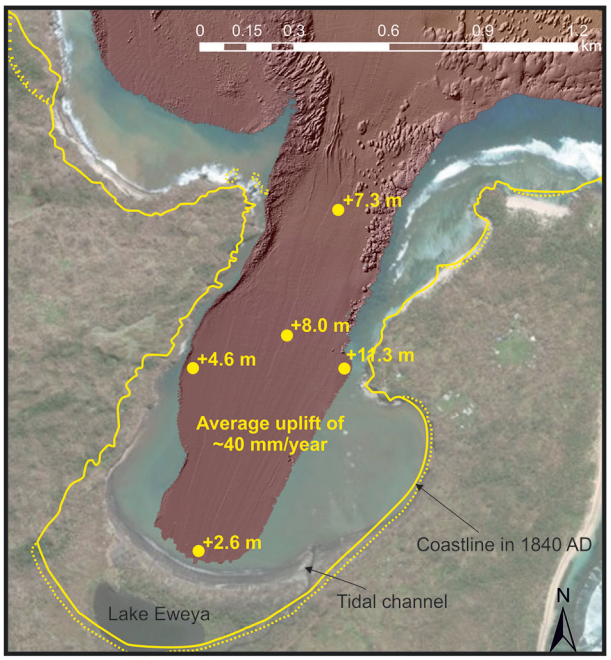


FIGURE 9 | Comparison of satellite photography and bathymetry of Resolution Bay acquired in 2017, compared with outline of coastline from mapping by Captain Belcher in 1840 in yellow (Hydrographic Office of the Admiralty, 1843). Filled circles illustrate comparison between bathymetric soundings in 1840 and 2017, which show an average elevation difference of +6.8 m; equating to an annual average rise of 40 mm/year.

On morning of May 2, Provincial Officials and the Local Police warned the residents of Sulfur Bay to move to higher ground to avoid flooding. Once the lake began overflowing its banks it quickly eroded through the soft volcanic deposits situated downgradient of the Lake. At approximately 6:00 pm on May 2 a huge volume of water began flowing from the Lake toward Sulphur Bay. The sound of the rushing water could be heard for miles. Villagers alerted by the roar of the flood waters, ran for higher ground. Luckily no lives were lost. Approximately 10 houses and a Nakamal were destroyed. An unknown number of livestock were reported to have been swept into the sea" (Vanuatu Ministry of Lands and Natural Resources, 2014). The outburst flood ran approximately along the course of the Siwi River, cutting a new channel of up to 40 m depth, until it reached the ocean at Sulfur Bay; washing several cattle and ten houses out to sea (Kanas et al., 2000). The village at Sulfur Bay was severely damaged by the outflow and was buried with up to 1.5 m of sediment (Kanas et al., 2000). Satellite data reveal that the back-barrier was breached, but reformed within at least a year (**Figure 1E**).

As the outburst flood discharged to the ocean at the outflow of the Siwi River, it is a highly plausible candidate for creating the crescentic bedforms in the submarine channel offshore of Sulfur Bay. So what were the likely flow conditions? The flood released 4.1 million m^3 of water over only 2 days, triggering catastrophic erosion of more than 1.1 million m^3 of sediment (Kanas et al., 2000; Firth et al., 2014). Based on these values, the flow averaged sediment concentration may have been up to 27% by volume (i.e., hyperconcentrated flow). This concentration is not unreasonable in light of estimates for glacial outbursts ("jokulhaups"; Russell, 1993; Duller et al., 2008), and direct measurements of subaerial debris flows (up to 60%–Weirich, 1989) and remobilised tephra lahars (up to 62% – Cronin et al., 1997; Lavigne and Thouret, 2003) triggered by heavy rainfall. Sediments from the flood, visited by Shane Cronin only months after the event were sand-dominated levees alongside the river, consistent with hyperconcentrated flow. No debris-flow deposits were found. Microscope and SEM analysis of river sediments indicate dominantly basaltic lithics with some volcanic glasses that have a density of 2,350–2,650 kg/m^3 (Wilson et al., 2012). A 73% freshwater (1,000 kg/m^3) and 27% sediment mixture equates to a flow density of 1,365–1,446 kg/m^3. Thus, should the flow have maintained this concentration when it entered the ocean, the density of the flow would have far exceeded the 40 kg/m^3 above seawater (~1,030 kg/m^3) required for hyperpycnal flow (Mulder et al., 2003). As a result the flow could have plunged directly to trigger a turbidity current; as observed from subaerial debris flows and lahars which transform into turbidity currents that last for many hours (Weirich, 1989; Mulder et al., 2003). Lahars can maintain hyperconcentrated conditions for over 40 km (Cronin et al., 1997), thus it is possible that the flow maintained this density to the coastline. We do not have a record of oceanographic conditions during the time of the flood, hence, it is unclear as to whether waves would have inhibited and/or dispersed the plunging of sediment-laden water.

Even if the flow had deposited much of the suspended sediment prior to reaching the ocean at Sulfur Bay, or it was partially redistributed as a homopycnal plume, it is likely that this outburst flood could still have triggered a turbidity current at lower concentrations, particularly given its discharge. Analysis of a global collation of outburst floods (that also includes jokulhaups, artificial dam, and moraine bursts) identified a power-law relationship between volume of water released and peak discharge (Manville, 2010; **Figure 11**). On the basis of the volume released from Lake Isiwi, a peak discharge of 1,000 m^3/s is estimated, with an upper bound (99th percentile) limit of 7,000 m^3/s (**Figure 11**). Turbidity currents (up to ~4 m/s) triggered by plume settling (with a density surfeit of <1 kg/m^3 above seawater) have been directly observed to occur frequently offshore from bedload-dominated rivers at a discharge threshold of >250 m^3/s and form similar bedforms (Bornhold et al., 1994; Clare et al., 2016; Hughes Clarke, 2016). Therefore, at its peak, the estimated discharge value for the outburst flood on Tanna is more than that required for triggering turbidity currents. The discharge of the turbidity current itself is more challenging to estimate, however. The cross-sectional area of the submarine channels proximal to the river mouth is ~70 m^2, which equates to a bankfull discharge of between 210 m^3/s and 630 m^3/s assuming velocities of turbidity currents based on measurements at locations with similar-scale bedforms (3 m/s at Squamish Delta – Hughes Clarke, 2016; 9 m/s at Fraser Delta – Lintern et al., 2016). These estimates may be supported by the localized presence of comet and tail scoured features within the sinuous

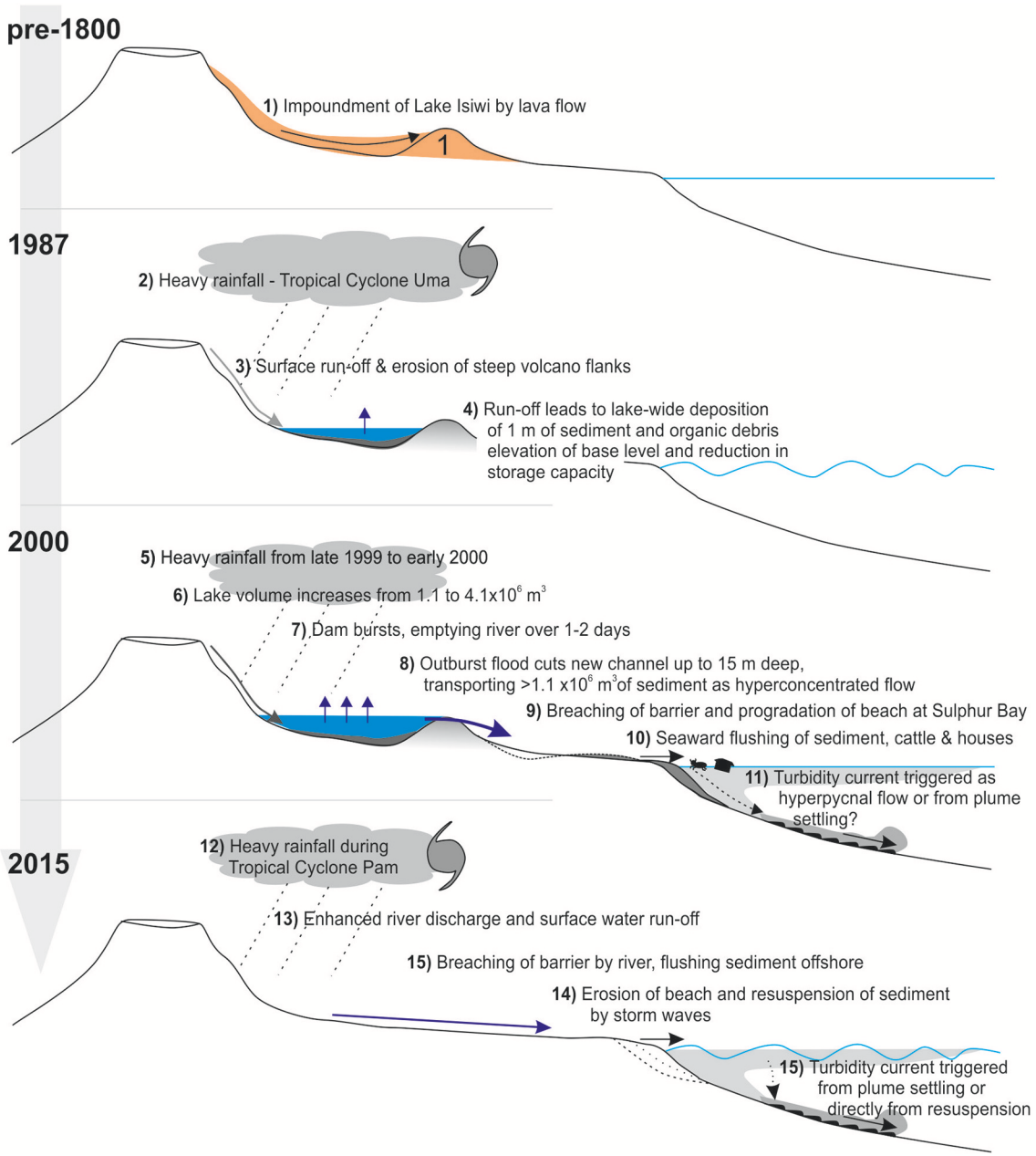


FIGURE 10 | Sequential chain of cascading effects (from 1 to 15) that may have led to the triggering of turbidity currents that formed crescentic bedforms offshore Sulfur Bay, Tanna Island.

channel offshore Sulfur Bay, which are similar to those associated with jokulhaups with observed peak discharges of ~1,000 m^3/s; Russell, 1993).

Evidence for outburst floods is increasingly being identified on volcanic islands, where craters, calderas, or past lava flows trap water without a surface outlet (Manville, 2010; Delmelle et al., 2015). These floods are only exceeded in discharge volume by the breaching of glacial impoundments, which are the largest known terrestrial floods on Earth (Manville, 2010). Intracaldera lakes have been identified from more than 100 Holocene volcanoes, with similar water storage volumes to that of the impounded Lake Isiwi (1–10 $\times$ 10^6 m^3; Manville, 2010). Caldera lakes can be larger still, such as Lake Toba in Indonesia (2.4 $\times$ 10^{11} m^3) or Lake Taupo in New Zealand (6 $\times$ 10^{10} m^3, where an outburst flood had an estimated peak discharge of 17,000–35,000 m^3/s in 232 AD; Manville et al., 1999), and result in far greater discharges than estimated for the outburst flood in 2000 A.D. on Tanna (**Figure 11**). While several studies have focused on the marine records of jokulhaups (e.g., Milliman et al., 1996; Maria et al., 2000; Willems et al., 2011; Gombiner et al., 2016),

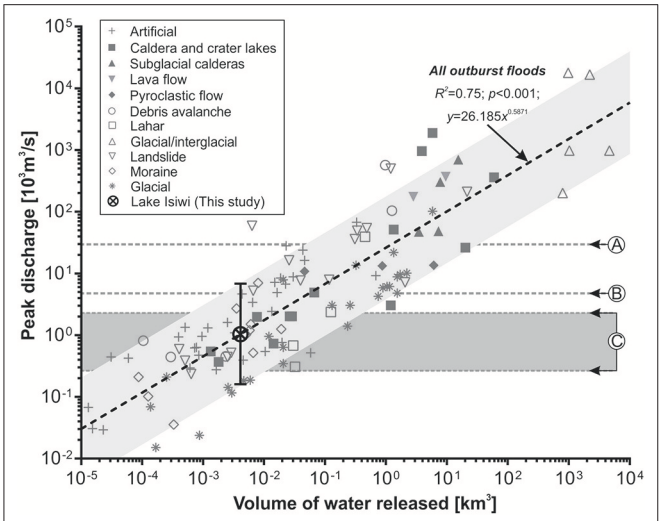


FIGURE 11 | Plot of peak discharge in relation to volume of water released from outburst floods based on global data from Manville (2010; reproduced under Copyright License 4433040862707. Black dashed lined is power-law trend for all outburst floods, and light gray parallel fill is the 99th percentile range. Lettered annotations refer to peak river discharges for: **(A)** Gaoping River following Typhoon Morakot in 2009 [28,000 m^3/s; (Carter et al., 2014)] when hyperpycnal flow triggered a turbidity current; **(B)** highest recorded river discharge in New Caledonia on Grand Terre due to Cyclone Anne in 1988 [4,583 m^3/s; (Terry et al., 2008)]; and (**C** and dark gray fill) the range of discharge on the Squamish River, British Columbia when turbidity currents are known to occur Clare et al. (2016). The estimated discharge for the 2,000 Lake Isiwi outburst flood is ∼1,000 m^3/s, with an upper bound estimate of 7,000 m^3/s.

to our knowledge, none have studied the offshore effects of non-glacial outburst floods at volcanic islands. Given the high discharges involved, we suggest that such outburst floods may be an under-appreciated hazard and a potentially important mechanism for initiating long run-out turbidity currents at many volcanic islands.

Triggers Unrelated to Volcanic Activity: Land Use, Extreme Weather Events and the Role of Climate Change

While volcanic processes may often be indirectly responsible, a number of non-volcanic events are also capable of providing the sediment discharges and preconditioning required for submarine landslides and turbidity currents to occur. Changes in land cover resulting from human activities in coastal tropical catchments substantially increase suspended sediment loads to the coastal zone (e.g., by 5.5 times, Kroon et al., 2012) and may dramatically increase the likelihood of hillslope failures and other terrestrial landslides (Froude and Petley, 2018). Historically, plantation growth and clearance by the arrival of humans on Pacific islands has increased sediment delivery from river systems as vegetation cover was disturbed by burning and cropping practices. Similarly, changes from forest cover to plantations or agriculture increase storm runoff (Comte et al., 2012). Persistent volcanism exacerbates this, attested by tens of square kilometers of de-vegetated areas in areas affected by volcanic ash and acid rains (Cronin and Sharp, 2002) in downwind areas of volcanoes such as Yasur and Ambrym in Vanuatu.

Tropical cyclones are an important type of non-volcanic event that can enhance preconditioning or directly trigger submarine landslides or turbidity currents due to: (i) storm wave-induced resuspension of shelf sediments; (ii) cyclic loading of unstable slope sediments; (iii) undercutting of coastal cliffs; or (iv) extreme rainfall triggering sediment-laden river floods and surface water run-off that discharge to the ocean (Kudrass et al., 1998; Liu et al., 2012; Carter et al., 2014; Pope et al., 2017). Recent analysis of a global database of telecommunications cable breaks revealed that the Pacific Ocean is a hotspot for tropical cyclone-triggered turbidity currents (Pope et al., 2017). Multiple powerful cyclones have been documented in Vanuatu in recent years, including tropical cyclones Uma in 1987 A.D., Fran in 1993 A.D., Prema in 1993 A.D., Paula in 2001 A.D. and Ivy in 2004 A.D. (Kosciuch et al., 2018). Most recently, tropical cyclone Pam (13th March 2015) made landfall on Tanna Island, traveling at up to 270 km/h with up to 5.3 m-high storm surges, resulting in up to $449M USD in damages Kosciuch et al., 2018. The direct impact of storm waves by events such as Pam is a further plausible explanation for downslope submarine sediment transport in the zone between Sulfur Bay and Port Resolution. Retrogressive or undercutting erosion of the steep coastal cliffs on Tanna by both storm waves and surface water run-off could result in cliff collapse and seaward transport of sediment; perhaps explaining the downslope location of linear gullies and coalescent sinuous channels. The power of such events is demonstrated by tropical cyclones on Fiji that were capable of eroding and transporting carbonate boulders (weighing up to 61 tons; Terry and Lau, 2018). Enhanced turbidity and the presence of a sediment-laden plume was visible around Sulfur Bay and Port Resolution from satellite photography in the days following tropical cyclone Pam, and the beach at Sulfur Bay was eroded landward by tens of meters (**Figures 8E,F**). Enhanced river outflow also caused breaching of the barrier at the mouth of the Siwi River. River discharges following tropical cyclones can be orders of magnitude higher than background conditions, such as Cyclone Anne in 1988 A.D. which triggered a peak river discharge of more than 4,500 m^3/s on Grand Terre in New Caledonia (**Figure 11**; Terry et al., 2008). Sediment loads during tropical cyclone floods have been recorded at 200–500 g/l in Fiji (Terry et al., 2002); far exceeding normal concentrations. Thus, it is likely that tropical cyclone Pam may also have contributed to, or triggered a turbidity current that formed or modified bedforms in the submarine channel initiating in Sulfur Bay (**Figure 10**). The increasing frequency of El-Nino-Southern Oscillation (ENSO) cycles due to climate change appear to be modifying the intensity of tropical cyclones, their migration tracks, and slowing the rate of their passage, which will result in increased surface water run-off and river discharge (Emanuel, 2005; Kossin et al., 2014; Lee et al., 2015; Mei and Xie, 2016; Chand et al., 2017; Gavey et al., 2017; Pope et al., 2017). Thus, we may expect such events to be a more likely preconditioning and/or triggering mechanism for submarine landslides and turbidity currents offshore from volcanic islands, at least in the Pacific.

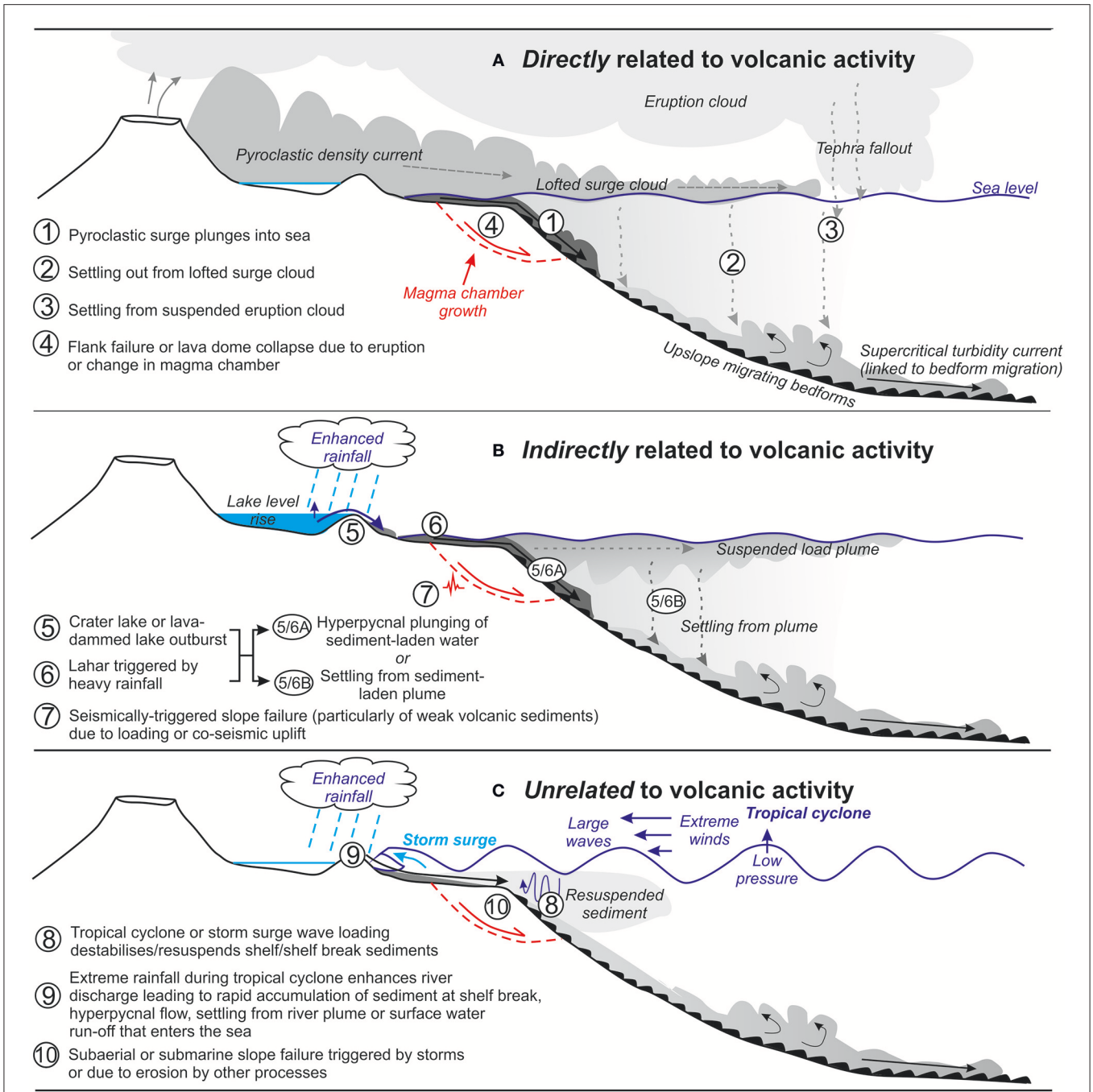


FIGURE 12 | General model of processes that contribute to preconditioning or drive triggering of submarine slope failures and turbidity currents at volcanic islands, related directly **(A)**, indirectly **(B)** and unrelated to volcanic processes. Unlike in **Figure 10**, the numbering here is not sequential and simply refers to isolated processes.

A General Model for Triggering Submarine Landslides and Turbidity Currents at Volcanic Islands

We found that a single triggering mechanism is often unlikely for submarine landslides and turbidity currents offshore from volcanic islands, and instead that a combination of preconditioning and triggering processes is responsible (**Figure 10**). On Tanna for example, the series of cascading events that commenced with the closure of Lake Isiwi by a lava flow (pre-1800 A.D.), was compounded by the rising of lake base-level due to sediment in-wash during tropical cyclone Uma in 1987 A.D., and culminated in the flushing of sediment to the ocean following the outburst flood triggered by elevated rainfall in 2000 A.D (Kanas et al., 2000). The outburst flood contributed to construction of the beach at Sulfur Bay, which was then eroded in 2015 A.D. during tropical cyclone Pam (**Figure 10**).

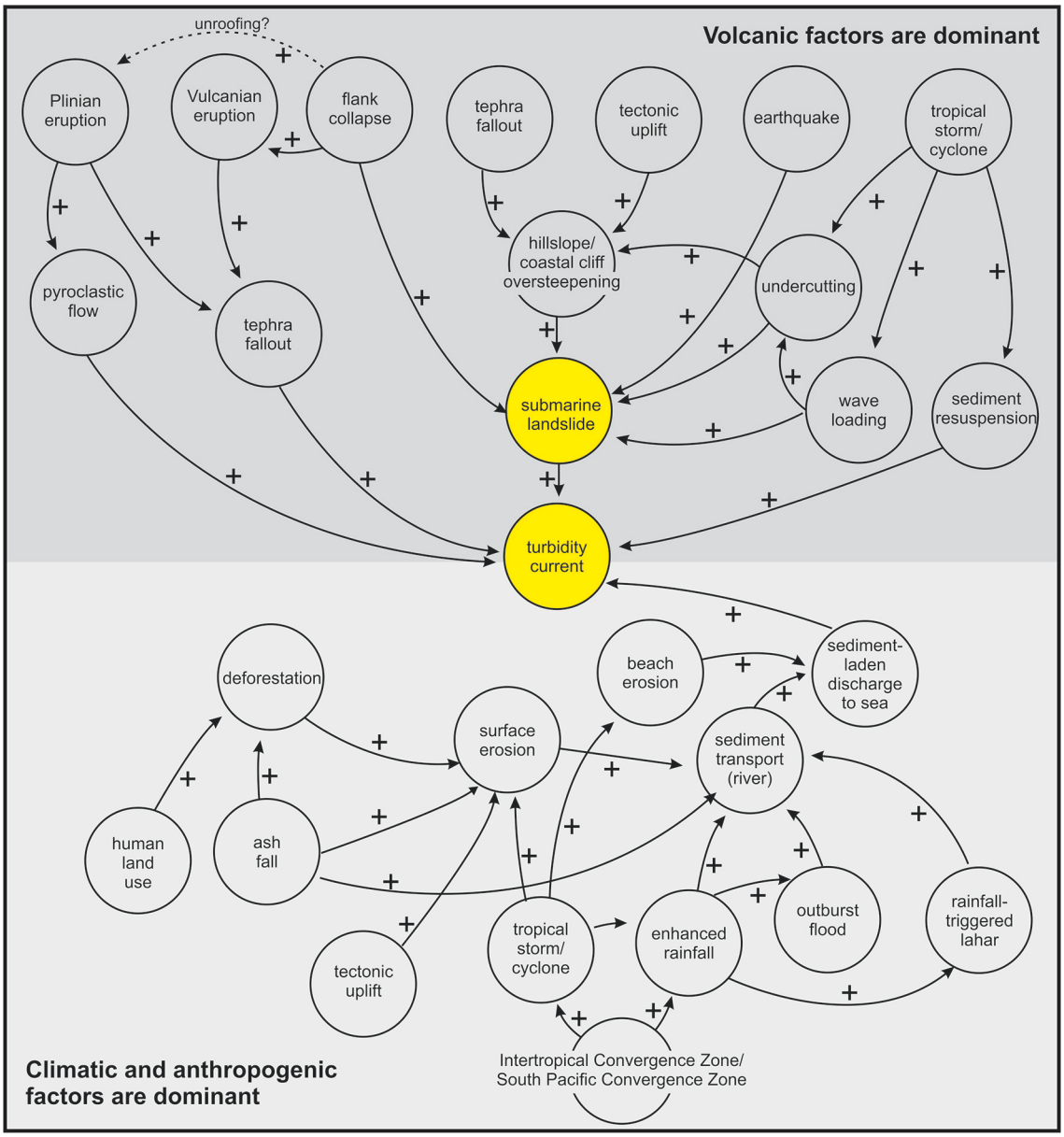


FIGURE 13 | Illustration of the potential complexity of interacting processes at volcanic islands that may precondition and trigger submarine landslides and turbidity currents. Plus signs and arrowed lines indicate how an increase in a variable may make a subsequent process more likely. Figure shows scenarios where volcanic factors may dominate (dark gray) and where climatic or anthropogenic factors may be more important (light gray). An animated version of this figure is available in the online material. Yellow circle refers to ultimately triggered event (landslide or turbidity current).

While separated by years to decades in time, these events each served to sequentially modify baseline conditions, setting up a cascade of hazards (Gill and Malamud, 2016). Similarly, the two earthquakes in 1878 A.D. that co-seismically uplifted sea cliffs by up to 12 m (Nairn et al., 1988; Merle et al., 2013), made them steeper, and more prone to wave erosion during severe storms and tropical cyclones in the following decades. Cascading or compound effects of volcanic, climatic and anthropogenic factors should therefore not be overlooked for the triggering of slope failures and turbidity currents offshore from volcanic islands. Land cover and climate changes, in particular, are relatively slow processes that change the background state of the land surface and runoff regime, and may be punctuated by extreme events such as cyclones, earthquakes and eruptions. The result is likely to be a non-linear response over time for given individual or multiple drivers for increased sediment delivery to the coast. Positive-phase Interdecadal Pacific Oscillation (IPO) countries such as Vanuatu, Fiji, and Samoa lie within the South Pacific

Convergence Zone under normal conditions (Partin et al., 2013). During El-Nino, however, IPO-positive phase regions experience markedly increased tropical cyclone activity (Kuleshov et al., 2008; Toomey et al., 2013; Stephens and and Ramsay, 2014). If periods of increased land use change (e.g., deforestation), or volcanic eruptions occur coincident with future enhanced ENSO and tropical cyclone intensity [as is predicted for Vanuatu and other Pacific SIDs (Partin et al., 2013; Stephens and and Ramsay, 2014)], we posit that the compounded increase in sediment loads from rivers discharging to the coastal zone will create hotspots for turbidity current generation.

We now conclude with a general model of processes that may contribute to preconditioning and instantaneous triggering of submarine landslides and turbidity currents at volcanic islands (**Figure 12**), that includes: (A) Processes that are directly related to volcanic activity that are mostly attributed to major eruptive or collapse events, e.g., Plinian eruptions (Manville et al., 1999; Pope et al., 2018); (B) Processes that are indirectly-related to volcanic activity that mostly relate to the preconditioning effects of past volcanism, or progressive ongoing low-magnitude events that may typify quiescent volcanoes and steady-state low-explosivity centers; and (C) Processes that are unrelated to volcanic activity, which include oceanographic and extreme weather events that can affect any type of volcanic island, but are most pronounced in tropical oceans. Each of these processes may play a contributing role in instantaneous triggering, or may continue to precondition the system to enhance the likelihood of offshore sediment transport; hence understanding those interplays is important. The role of cascading hazards may be much more important than that attributed to instantaneous events; particularly for volcanoes under constant low-explosivity conditions where climatic, oceanographic and anthropogenic processes may dominate. We highlight the potentially complex interrelationships between different processes in **Figure 13** (animated examples of feedback loops are shown in online **Video S1**). Because of these compound and/or cascading relationships, attempting to identify one specific triggering mechanism for submarine landslides or turbidity currents is challenging, and may be impossible in many cases. Therefore, determining links between triggers and offshore sediment transport requires careful integration of onshore and marine datasets, and may require direct monitoring of changes in onshore environmental baselines as well as offshore sediment transport processes. Such monitoring is challenging, but new technologies now enable measurement of both the environmental conditions and seafloor processes, thus opening up new opportunities to better understand these complex links to improve offshore hazard assessments in Small Island Developing States (Chouet, 1996; Lavigne et al., 2000; Clare et al., 2017; Zhang et al., 2018).

CONCLUSIONS

We presented the first detailed (2×2 m) bathymetric data acquired offshore from Tanna Island, Vanuatu and identified evidence for submarine slope failure and seafloor turbidity currents. These data, coupled with sediment sampling, help to address important knowledge gaps concerning seafloor hazards at Small Island Developing States in the South Pacific, and more generally on the flanks of Strombolian volcanoes, both of which are under-represented in the literature. We found that arcuate bight-like features, incised into the carbonate and reef platform, can be linked to slope collapses that occurred in multiple phases, and thus pose a lower tsunami hazard than if they occurred as one-off, larger failures. Integration of onshore and offshore surveys, with documented historical events, enabled identification of a number of potential triggers for slope failures and turbidity currents offshore Tanna. None of these triggers are related to major volcanic eruptions or collapses, in contrast to conclusions from several previous studies. One highly plausible triggering event was an outburst flood with an estimated discharge of $>1{,}000$ m^3/s. We suggest that outburst floods from crater lakes, caldera lakes and lava flow-impounded features may be under-recognized triggers at many other volcanic islands. Non-volcanic processes, such as tropical cyclones, were also identified as a plausible trigger for triggering slope collapses and turbidity currents, due to storm loading and elevated river discharge to the sea. Tropical cyclones may become more important triggers at islands such as Tanna, due to global warming-induced changes to the El-Nino Southern Oscillation. Finally, we presented a general model for the triggering of submarine landslides and turbidity currents at volcanic islands, underlining the often-ignored importance of non-volcanic processes, and the complex interactions between a range of processes that may precondition the system. We propose that compounding effects, and cascading chains of events, may be more important than instantaneous triggers in many volcanic islands; particularly those in quiescent or Strombolian regimes.

AUTHOR CONTRIBUTIONS

MC led the research, wrote the manuscript and created the figures. All authors contributed to discussions to form the basis of this paper, and provided feedback on the manuscript and figures. TL and DP performed offshore and onshore fieldwork. JH performed grain size, SEM and grain size analysis. DS assisted with analysis of outburst floods and links to river hydrology. MC, AV, and WS assisted with morphodynamic analysis. CF and SC assisted with analysis of the Lake Isiwi outburst flood and interpretation of volcanic aspects of the landscape.

ACKNOWLEDGMENTS

Fieldwork and analysis was supported by the Commonwealth Marine Economies Program which aims to enable safe and sustainable marine economies across Commonwealth Small Island Developing States. We thank EGS Survey Ltd, Justin Jenkin and the crew of the MV Escape, Camillia Garae of the Vanuatu Department of Geology and Mines, and

Douglas Kiri of the Vanuatu Environmental Science Society. We also thank the Department of Geology and Mines for support with fieldwork and logistics on Tanna. The staff of the BOSCORF are acknowledged for assistance with SEM analysis. We acknowledge NERC funding grants NE/M007138/1, NE/M017540/1, NE/P009190/1 and NE/P005780/1. MJB is supported by a Royal Society Dorothy Hodgkin Fellowship (RF1504449).

SUPPLEMENTARY MATERIAL

The Supplementary Material for this article can be found online at: https://www.frontiersin.org/articles/10.3389/feart.2018.00223/full#supplementary-material

Video S1 | Conceptual interplay of volcanic and non-volcanic processes on the preconditioning and triggering of offshore landslides and turbidity currents illustrated using a simple process interaction model. Model created using code at https://ncase.me/loopy/

REFERENCES

Babonneau, N., Delacourt, C., Cancouët, R., Sisavath, E., Bachèlery, P., Mazuel, A., et al. (2013). Direct sediment transfer from land to deep-sea: insights into shallow multibeam bathymetry at La Réunion Island. *Mar. Geol.* 346, 47–57. doi: 10.1016/j.margeo.2013.08.006

Bornhold, B. D., Ren, P., and Prior, D. B. (1994). High-frequency turbidity currents in British Columbia fjords. *Geo Mar. Lett.* 14, 238–243. doi: 10.1007/BF01274059

Briguglio, L. (1995). Small island developing states and their economic vulnerabilities. *World Dev.* 23, 1615–1632. doi: 10.1016/0305-750X(95)00065-K

Brothelande, E., Lénat, J. F., Normier, A., Bacri, C., Peltier, A., Paris, R., et al. (2015). Insights into the evolution of the Yenkahe resurgent dome (Siwi caldera, Tanna Island, Vanuatu) inferred from aerial high-resolution photogrammetry. *J. Volcanol. Geother. Res.* 322, 212–224. doi: 10.1016/j.jvolgeores.2015.04.006

Brothelande, E., Peltier, A., Got, J. L., Merle, O., Lardy, M., and Garaebiti, E. (2016). Constraints on the source of resurgent doming inferred from analogue and numerical modeling—Implications on the current feeding system of the Yenkahe dome–Yasur volcano complex (Vanuatu). *J. Volcanol. Geother. Res.* 322, 225–240. doi: 10.1016/j.jvolgeores.2015.11.023

Calder, E. S., Cole, P. D., Dade, W. B., Druitt, T. H., Hoblitt, R. P., Huppert, H. E., et al. (1999). Mobility of pyroclastic flows and surges at the Soufriere Hills Volcano, Montserrat. *Geophys. Res. Lett.* 26, 537–540. doi: 10.1029/1999GL900051

Caminade, P., Charlie, D., Kanoglu, U., Koshimura, S. I., Matsutomi, H., Moore, A., et al. (2000). Vanuatu earthquake and tsunami cause much damage, few casualties. *EOS Trans. Am. Geophys. Union* 81, 641–647. doi: 10.1029/EO081i052p00641-02

Carey, S., Morelli, D., Sigurdsson, H., and Bronto, S. (2001). Tsunami deposits from major explosive eruptions: an example from the 1883 eruption of Krakatau. *Geology* 29, 347–350. doi: 10.1130/0091-7613(2001)029andlt;0347:TDFMEEandgt;2.0.CO;2

Carlino, S., Cubellis, E., Luongo, G., and Obrizzo, F. (2006) On the mechanics of caldera resurgence of Ischia Island (southern Italy). *Geol. Soc. Lond. Spec. Public.* 269, 181–193. doi: 10.1144/GSL.SP.2006.269.01.12

Carney, J. N., and Macfarlane, A. (1979). *Geology of Tanna, Aneityum, Futuna and Aniwa.* Vila, New Hebrides Government.

Carter, L., Gavey, R., Talling, P. J., and Liu, J. T. (2014). Insights into submarine geohazards from breaks in subsea telecommunication cables. *Oceanography* 27, 58–67. doi: 10.5670/oceanog.2014.40

Casalbore, D., Chiocci, F. L., Mugnozza, G. S., Tommasi, P., and Sposato, A. (2011). Flash-flood hyperpycnal flows generating shallow-water landslides at Fiumara mouths in Western Messina Strait (Italy). *Mar. Geophys. Res.* 32:257. doi: 10.1007/s11001-011-9128-y

Casalbore, D., Ridente, D., Bosman, A., and Chiocci, F. L. (2017). Depositional and erosional bedforms in Late Pleistocene-Holocene pro-delta deposits of the Gulf of Patti (southern Tyrrhenian margin, Italy). *Mar. Geol.* 385, 216–227. doi: 10.1016/j.margeo.2017.01.007

Casalbore, D., Romagnoli, C., Bosman, A., and Chiocci, F. L. (2014). Large-scale seafloor waveforms on the flanks of insular volcanoes (Aeolian Archipelago, Italy), with inferences about their origin. *Mar. Geol.* 355, 318–329. doi: 10.1016/j.margeo.2014.06.007

Casalbore, D., Romagnoli, C., Chiocci, F., and Frezza, V. (2010). Morpho-sedimentary characteristics of the volcaniclastic apron around Stromboli volcano (Italy). *Mar. Geol.* 269, 132–148. doi: 10.1016/j.margeo.2010.01.004

Chand, S. S., Tory, K. J., Ye, H., and Walsh, K. J. (2017). Projected increase in El Nino-driven tropical cyclone frequency in the Pacific. *Nat. Climate Change* 7:123. doi: 10.1038/nclimate3181

Chaytor, J. D., Uri, S., Solow, A. R., and Andrews, B. D. (2009). Size distribution of submarine landslides along the US Atlantic margin. *Mar. Geol.* 264, 16–27. doi: 10.1016/j.margeo.2008.08.007

Chen, J. K., Taylor, F. W., Edwards, R. L., Cheng, H., and Burr, G. S. (1995). Recent emerged reef terraces of the Yenkahe resurgent block, Tanna, Vanuatu: implications for volcanic, landslide and tsunami hazards. *J. Geol.* 103, 577–590. doi: 10.1086/629777

Chouet, B. A. (1996). "New methods and future trends in seismological volcano monitoring," in *Monitoring and Mitigation of Volcano Hazards*, eds R. Scarpa and R. I. Tilling (Berlin; Heidelberg: Springer), 23–97.

Clare, M., Chaytor, J., Dabson, O., Gamboa, D., Georgiopoulou, A., Eady, H., et al. (2018). A consistent global approach for the morphometric characterization of subaqueous landslides. *Geol. Soc. Lond. Spec. Public* 477, SP477–15. doi: 10.1144/SP477.15

Clare, M. A., Clarke, J. H., Talling, P. J., Cartigny, M. J. B., and Pratomo, D. G. (2016). Preconditioning and triggering of offshore slope failures and turbidity currents revealed by most detailed monitoring yet at a fjord-head delta. *Earth Planetary Sci. Lett.* 450, 208–220. doi: 10.1016/j.epsl.2016.06.021

Clare, M. A., Vardy, M. E., Cartigny, M. J., Talling, P. J., Himsworth, M. D., Dix, J. K., et al. (2017). Direct monitoring of active geohazards: emerging geophysical tools for deep-water assessments. *Near Surface Geophys.* 15, 427–444. doi: 10.31223/osf.io/m3gkj

Comte, I., Colin, F., Whalen, J. K., Grünberger, O., and Caliman, J.-P. (2012), "Agricultural practices in oil palm plantations and their impact on hydrological changes, nutrient fluxes and water quality in indonesia: a review," in *Advances in Agronomy,* ed D. L. Sparks (Burlington: Academic Press), 71–124.

Counts, J. W., Jorry, S. J., Leroux, E., Miramontes, E., and Jouet, G. (2018). Sedimentation adjacent to atolls and volcano-cored carbonate platforms in the Mozambique Channel (SW Indian Ocean). *Mar. Geol.* 404, 41–59. doi: 10.1016/j.margeo.2018.07.003

Coussens, M., Wall-Palmer, D., Talling, P., Watt, S., Cassidy, M., Jutzeler, M., et al. (2016). The relationship between eruptive activity, flank collapse, and sea level at volcanic islands: a long-term (> 1 Ma) record offshore Montserrat, Lesser Antilles. *Geochem. Geophys. Geosyst.* 17, 2591–2611. doi: 10.1002/2015GC006053

Covault, J. A., Kostic, S., Paull, C. K., Sylvester, Z., and Fildani, A. (2017). Cyclic steps and related supercritical bedforms: building blocks of deep-water depositional systems, western North America. *Mar. Geol.* 393, 4–20. doi: 10.1016/j.margeo.2016.12.009

Cronin, S. J., Gaylord, D. R., Charley, D., Alloway, B. V., Wallez, S., and Esau, J. W. (2004). Participatory methods of incorporating scientific with traditional knowledge for volcanic hazard management on Ambae Island, Vanuatu. *Bull. Volcanol.* 66, 652–668. doi: 10.1007/s00445-004-0347-9

Cronin, S. J., Neall, V. E., Lecointre, J. A., and Palmer, A. S. (1997). Changes in Whangaehu River lahar characteristics during the 1995 eruption sequence,

Ruapehu volcano, New Zealand. *J. Volcanol. Geother. Res.* 76, 47–61. doi: 10.1016/S0377-0273(96)00064-9

Cronin, S. J., and Sharp, D. S. (2002). Environmental impacts on health from continuous volcanic activity at Yasur (Tanna) and Ambrym, Vanuatu. *Int. J. Environ. Health Res.* 12, 109–123. doi: 10.1080/0960312022012 9274

Delmelle, P., Henley, R. W., and Bernard, A. (2015). "Volcano-related lakes," in *The Encyclopedia of Volcanoes, 2nd Edn.*, eds H. Sigurdsson, B. Houghton, S. McNutt, H. Rymer and J. Stix (San Diego, CA: Elsevier) 851–864.

Duller, R. A., Mountney, N. P., Russell, A. J., and Cassidy, N. C. (2008). Architectural analysis of a volcaniclastic jökulhlaup deposit, southern Iceland: sedimentary evidence for supercritical flow. *Sedimentology* 55, 939–964. doi: 10.1111/j.1365-3091.2007.00931.x

Emanuel, K. (2005). Increasing destructiveness of tropical cyclones over the past 30 years. *Nature* 436:686. doi: 10.1038/nature03906

Firth, C. W., Cronin, S. J., Turner, S. P., Handley, H. K., Gaildry, C., and Smith, I. (2015). Dynamics and pre-eruptive conditions of catastrophic, ignimbrite-producing eruptions from the Yenkahe Caldera, Vanuatu. *J. Volcanol. Geother. Res.* 308, 39–60. doi: 10.1016/j.jvolgeores.2015.10.012

Firth, C. W., Handley, H. K., Cronin, S. J., and Turner, S. P. (2014). The eruptive history and chemical stratigraphy of a post-caldera, steady-state volcano: Yasur, Vanuatu. *Bull. Volcanol.* 76:837. doi: 10.1007/s00445-014-0837-3

Froude, M. J., and Petley, D. N. (2018). Global fatal landslide occurrence from 2004 to 2016. *Nat. Hazar. Earth Syst. Sci.* 18, 2161–2181. doi: 10.5194/nhess-18-2161-2018

Gardner, J. V. (2010). The West Mariana Ridge, western Pacific Ocean: geomorphology and processes from new multibeam data. *Bulletin* 122, 1378–1388. doi: 10.1130/B30149.1

Gavey, R., Carter, L., Liu, J. T., Talling, P. J., Hsu, R., Pope, E., et al. (2017). Frequent sediment density flows during 2006 to 2015, triggered by competing seismic and weather events: observations from subsea cable breaks off southern Taiwan. *Mar. Geol.* 384, 147–158. doi: 10.1016/j.margeo.2016.06.001

Gill, J. C., and Malamud, B. D. (2016). Hazard interactions and interaction networks (cascades) within multi-hazard methodologies. *Earth Syst Dyn.* 7, 659–679. doi: 10.5194/esd-7-659-2016

Goff, J., and Terry, J. P. (2016). Tsunamigenic slope failures: the Pacific Islands 'blind spot'?. *Landslides* 13, 1535–1543. doi: 10.1007/s10346-015-0649-3

Gombiner, J. H., Hemming, S. R., Hendy, I. L., Bryce, J. G., and Blichert-Toft, J. (2016). Isotopic and elemental evidence for Scabland Flood sediments offshore Vancouver Island. *Quat. Sci. Rev.* 139, 129–137. doi: 10.1016/j.quascirev.2016.02.026

Graham, I. J., A. G., Reyes, I. C., Wright, K. M., Peckett, I. E. M., and Smith, and, R. J., Arculus (2008), Structure and petrology of newly discovered volcanic centers in the northern Kermadec–southern Tofua arc, South Pacific Ocean, *J. Geophys. Res.* 113:B08SB02. doi:10.1029/2007JB005453.

Gudmundsson, M. T., Thordarson, T., Höskuldsson, A., Larsen, G., Björnsson, H., Prata, F. J., et al. (2012). Ash generation and distribution from the April-May 2010 eruption of Eyjafjallajökull, Iceland. *Sci. Rep.* 2:572. doi: 10.1038/srep00572

Hage, S., Cartigny, M. J., Clare, M. A., Sumner, E. J., Vendettuoli, D., Hughes Clarke, J. E., et al. (2018). How to recognize crescentic bedforms formed by supercritical turbidity currents in the geologic record: insights from active submarine channels. *Geology* 46, 563–566. doi: 10.1130/G40095.1

Hizzett, J. L., Hughes Clarke, J. E., Sumner, E. J., Cartigny, M. J. B., Talling, P. J., and Clare, M. A. (2018). Which triggers produce the most erosive, frequent, and longest runout turbidity currents on deltas?. *Geophys. Res. Lett.* 45, 855–863. doi: 10.1002/2017GL075751

Hodgson, D. M., Bernhardt, A., Clare, M. A., da Silva, A. C., Fosdick, J., Mauz, B., et al. (2018). Grand challenges (and Great Opportunities) in sedimentology, stratigraphy, and diagenesis research. *Front. Earth Sci.* 6:173. doi: 10.3389/feart.2018.00173

Hoffmann, G., Silver, E., Day, S., Morgan, E., Driscoll, N., and Orange, D. (2008). Sediment waves in the Bismarck volcanic arc, Papua New Guinea. *Spec. Papers Geol. Soc. Am.* 436:491. doi: 10.1130/2008.2436(05)

Hong, I., Pilarczyk, J. E., Horton, B. P., Fritz, H. M., Kosciuch, T. J., Wallace, D. J., et al. (2018). Sedimentological characteristics of the 2015 tropical cyclone pam overwash sediments from Vanuatu, South Pacific. *Mar. Geol.* 396, 205–214. doi: 10.1016/j.margeo.2017.05.011

Horwell, C. J., and Baxter, P. J. (2006). The respiratory health hazards of volcanic ash: a review for volcanic risk mitigation. *Bull. Volcanol.* 69, 1–24. doi: 10.1007/s00445-006-0052-y

Hughes Clarke, J. E. (2016). First wide-angle view of channelized turbidity currents links migrating cyclic steps to flow characteristics. *Nat Commun.* 7:11896. doi: 10.1038/ncomms11896

Hunt, J. E., Wynn, R. B., Talling, P. J., and Masson, D. G. (2013). Multistage collapse of eight western Canary Island landslides in the last 1.5 Ma: sedimentological and geochemical evidence from subunits in submarine flow deposits. *Geochem. Geophys. Geosyst.* 14, 2159–2181. doi: 10.1002/ggge.20138

Hydrographic Office of the Admiralty (1843), *New Hebrides – Resolution Bay in Tanna Island, Capt. Sir E. Belcher, 1840, Chart number 1508*, London.

International Cable Protection Committee (2016). *Submarine Cables and BBNJ.* Available online at: http://www.un.org/depts/los/biodiversity/prepcom_files/ICC_Submarine_Cables_&_BBNJ_August_2016.pdf

Jazi, S. D., and Wells, M. (2018). Settling-driven convection limits the spatial scale of deposition beneath sediment-laden buoyant flows in lakes and the coastal ocean. *EarthArXiv*. doi: 10.31223/osf.io/9xymn

Jo, A., Eberli, G. P., and Grasmueck, M. (2015). Margin collapse and slope failure along southwestern Great Bahama Bank. *Sediment. Geol.* 317, 43–52. doi: 10.1016/j.sedgeo.2014.09.004

Kanas, T., Nango, I., Fransser, J., and Morris, S. (2000). Lake Siwi to River Siwi. *Vanuatu. Dept. Land. Surv.* 27, 1–22.

Keating, B. H., and McGuire, W. J. (2000). Island edifice failures and associated tsunami hazards. *Pure Appl. Geophys.* 157, 899–955. doi: 10.1007/s000240050011

Kosciuch, T. J., Pilarczyk, J. E., Hong, I., Fritz, H. M., Horton, B. P., Rarai, A., et al. (2018). Foraminifera reveal a shallow nearshore origin for overwash sediments deposited by Tropical Cyclone Pam in Vanuatu (South Pacific). *Mar. Geol.* 396, 171–185. doi: 10.1016/j.margeo.2017.06.003

Kossin, J. P., Emanuel, K. A., and Vecchi, G. A. (2014). The poleward migration of the location of tropical cyclone maximum intensity. *Nature* 509:349. doi: 10.1038/nature13278

Kostic, S. (2011). Modeling of submarine cyclic steps: controls on their formation, migration, and architecture. *Geosphere* 7, 294–304. doi: 10.1130/GES00601.1

Kroon, F. J., Kuhnert, P. M., Henderson, B. L., Wilkinson, S. N., Kinsey-Henderson, A., Abbott, B., et al. (2012). River loads of suspended solids, nitrogen, phosphorus and herbicides delivered to the Great Barrier Reef lagoon. *Mar. Pollut. Bull.* 65, 167–181. doi: 10.1016/j.marpolbul.2011.10.018

Kudrass, H. R., Michels, K. H., Wiedicke, M., and Suckow, A. (1998). Cyclones and tides as feeders of a submarine canyon off Bangladesh. *Geology* 26, 715–718. doi: 10.1130/0091-7613(1998)026andlt;0715:CATAFOandgt;2.3.CO;2

Kuleshov, Y. L., Qui, L., Fawcett, R., and Jones, D., (2008). On tropical cyclone activity in the Southern Hemisphere: trends and the ENSO connection. *Geophys. Res. Lett.* 35, 1–5. doi: 10.1029/2007GL032983

Lavigne, F., and Thouret, J. C. (2003). Sediment transportation and deposition by rain-triggered lahars at Merapi Volcano, Central Java, Indonesia. *Geomorphology* 49, 45–69. doi: 10.1016/S0169-555X(02)00160-5

Lavigne, F., Thouret, J. C., Voight, B., Young, K., LaHusen, R., Marso, J., et al. (2000). Instrumental lahar monitoring at Merapi Volcano, Central Java, Indonesia. *J. Volcanol. Geother. Res.* 100, 457–478. doi: 10.1016/S0377-0273(00)00151-7

Lawrie, J. H. (1898). Transactions of the Edinburgh Field Naturalists' and Microscopical Society. *Corals Coral Islands* 3, 320–326.

Leat, P. T., Day, S. J., Tate, A. J., Martin, T. J., Owen, M. J., and Tappin, D. R. (2013). Volcanic evolution of the South Sandwich volcanic arc, South Atlantic, from multibeam bathymetry. *J. Volcanol. Geother. Res.* 265, 60–77. doi: 10.1016/j.jvolgeores.2013.08.013

Lee, T. Y., Huang, J. C., Lee, J. Y., Jien, S. H., Zehetner, F., and Kao, S. J. (2015). Magnified sediment export of small mountainous rivers in Taiwan: chain reactions from increased rainfall intensity under global warming. *PLoS ONE* 10:e0138283. doi: 10.1371/journal.pone.0138283

Lintern, D. G., Hill, P. R., and Stacey, C. (2016). Powerful unconfined turbidity current captured by cabled observatory on the Fraser River delta slope, British Columbia, Canada. *Sedimentology* 63, 1041–1064. doi: 10.1111/sed.12262

Liu, J. T., Wang, Y. H., Yang, R. J., Hsu, R. T., Kao, S. J., Lin, H. L., et al. (2012). Cyclone-induced hyperpycnal turbidity currents in a submarine canyon. *J. Geophys. Res.* 117:C4. doi: 10.1029/2011JC007630

Lonergan, L., Jamin, N. H., Jackson, C. A. L., and Johnson, H. D. (2013). U-shaped slope gully systems and sediment waves on the passive margin of Gabon (West Africa). *Mar. Geol.* 337, 80–97. doi: 10.1016/j.margeo.2013.02.001

Manville, V. (2010). An overview of break-out floods from intracaldera lakes. *Glob. Planet Change* 70, 14–23. doi: 10.1016/j.gloplacha.2009.11.004

Manville, V., White, J. D. L., Houghton, B. F., and Wilson, C. J. N. (1999). Paleohydrology and sedimentology of a post−1.8 ka breakout flood from intracaldera Lake Taupo, North Island, New Zealand. *Geol. Soc. Am. Bull.* 111, 1435–1447. doi: 10.1130/0016-7606(1999)111andlt;1435:PASOAPandgt;2.3.CO;2

Maria, A., Carey, S., Sigurdsson, H., Kincaid, C., and Helgadóttir, G. (2000). Source and dispersal of jokulhlaup sediments discharged to the sea following the 1996 Vatnajokull eruption. *Geol. Soc. Am. Bull.* 112, 1507–1521. doi: 10.1130/0016-7606(2000)112andlt;1507:SADOJKandgt;2.0.CO;2

Masson, D. G. (1996). Catastrophic collapse of the volcanic island of Hierro 15 ka ago and the history of landslides in the Canary Islands. *Geology* 24, 231–234.

McAdoo, B. G., Pratson, L. F., and Orange, D. L. (2000). Submarine landslide geomorphology, US continental slope. *Mar. Geol.* 169, 103–136. doi: 10.1016/S0025-3227(00)00050-5

Meheux, K., and Parker, E. (2006). Tourist sector perceptions of natural hazards in Vanuatu and the implications for a small island developing state. *Tour. Manage.* 27, 69–85. doi: 10.1016/j.tourman.2004.07.009

Mei, W., and Xie, S. P. (2016). Intensification of landfalling typhoons over the northwest Pacific since the late 1970s. *Nat. Geosci.* 9, 753–757. doi: 10.1038/ngeo2792

Merle, O., Brothelande, E., Lénat, J. F., Bachèlery, P., and Garaébiti, E. (2013). A structural outline of the Yenkahe volcanic resurgent dome (Tanna Island, Vanuatu Arc, South Pacific). *J. Volcanol. Geother. Res.* 268, 64–72. doi: 10.1016/j.jvolgeores.2013.10.009

Micallef, A., and Mountjoy, J. J. (2011). A topographic signature of a hydrodynamic origin for submarine gullies. *Geology* 39, 115–118. doi: 10.1130/G31475.1

Milliman, J. D., Snow, J., Jaeger, J., and Nittrouer, C. A. (1996). Catastrophic discharge of fluvial sediment to the ocean: evidence of Jökulhlaups events in the Alsek Sea Valley, southeast Alaska (USA). *IAHS Publications Series Proc. Rep. Int. Assoc. Hydrol. Sci.* 236, 367–380.

Mitchell, N. C., Masson, D. G., Watts, A. B., Gee, M. J., and Urgeles, R. (2002). The morphology of the submarine flanks of volcanic ocean islands: a comparative study of the Canary and Hawaiian hotspot islands. *J. Volcanol. Geother. Res.* 115, 83–107. doi: 10.1016/S0377-0273(01)00310-9

Moore, J. G., Clague, D. A., Holcomb, R. T., Lipman, P. W., Normark, W. R., and Torresan, M. E. (1989). Prodigious submarine landslides on the Hawaiian Ridge. *J. Geophys. Res.* 94, 17465–17484. doi: 10.1029/JB094iB12p17465

Mulder, T., Syvitski, J. P., Migeon, S., Faugeres, J. C., and Savoye, B. (2003). Marine hyperpycnal flows: initiation, behavior and related deposits. A review. *Mar. Petrol. Geol.* 20, 861–882. doi: 10.1016/j.marpetgeo.2003.01.003

Nairn, I. A., Scott, B. J., and Giggenbach, W. F. (1988). Yasur volcano investigations, Vanuatu, September 1988. *N. Z. Geol. Survey Rep.* G134:G174.

Nomikou, P., Carey, S., Papanikolaou, D., Bell, K. C., Sakellariou, D., Alexandri, M., et al. (2012). Submarine volcanoes of the Kolumbo volcanic zone NE of Santorini Caldera, Greece. *Glob Planet Change* 90, 135–151. doi: 10.1016/j.gloplacha.2012.01.001

Normandeau, A., Lajeunesse, P., Poiré, A. G., and Francus, P. (2016). Morphological expression of bedforms formed by supercritical sediment density flows on four fjord-lake deltas of the south-eastern Canadian Shield (Eastern Canada). *Sedimentology* 63, 2106–2129. doi: 10.1111/sed.12298

Parsons, J. D., Bush, J. W., and Syvitski, J. P. (2001). Hyperpycnal plume formation from riverine outflows with small sediment concentrations. *Sedimentology* 48, 465–478. doi: 10.1046/j.1365-3091.2001.00384.x

Partin, J. W., Quinn, T. M., Shen, C. C., Emile-Geay, J., Taylor, F. W., Maupin, C. R., et al. (2013). Multidecadal rainfall variability in South Pacific Convergence Zone as revealed by stalagmite geochemistry. *Geology* 41, 1143–1146. doi: 10.1130/H34718.1

Paull, C. K., Talling, P. J., Maier, K. L., Parsons, D., Xu, J., Caress, D. W., et al. (2018). Powerful turbidity currents driven by dense basal layers. *Nat. Commun.* 9:4114. doi: 10.1038/s41467-018-06254-6

Pelling, M., and Uitto, J. I. (2001). Small island developing states: natural disaster vulnerability and global change. *Glob. Environ Change Part B*3, 49–62. doi: 10.1016/S1464-2867(01)00018-3

Pope, E. L., Jutzeler, M., Cartigny, M. J., Shreeve, J., Talling, P. J., Wright, I. C., et al. (2018). Origin of spectacular fields of submarine sediment waves around volcanic islands. *Earth Planet. Sci. Lett.* 493, 12–24. doi: 10.1016/j.epsl.2018.04.020

Pope, E. L., Talling, P. J., Carter, L., Clare, M. A., and Hunt, J. E. (2017). Damaging sediment density flows triggered by tropical cyclones. *Earth Planet. Sci. Lett.* 458, 161–169. doi: 10.1016/j.epsl.2016.10.046

Puga-Bernabéu, Á., Webster, J. M., Beaman, R. J., and Guilbaud, V. (2013). Variation in canyon morphology on the Great Barrier Reef margin, north-eastern Australia: the influence of slope and barrier reefs. *Geomorphology* 191, 35–50. doi: 10.1016/j.geomorph.2013.03.001

Quartau, R., Ramalho, R. S., Madeira, J., Santos, R., Rodrigues, A., Roque, C., et al. (2018). Gravitational, erosional and depositional processes on volcanic ocean islands: Insights from the submarine morphology of Madeira Archipelago. *Earth Planet. Sci. Lett.* 482, 288–299. doi: 10.1016/j.epsl.2017.11.003

Rothwell, R. G., Hoogakker, B., Thomson, J., Croudace, I. W., and Frenz, M. (2006). Turbidite emplacement on the southern Balearic Abyssal Plain (western Mediterranean Sea) during Marine Isotope Stages 1–3: an application of ITRAX XRF scanning of sediment cores to lithostratigraphic analysis. *Geol. Soc. Lond. Spec. Public* 267, 79–98. doi: 10.1144/GSL.SP.2006.267.01.06

Russell, A. J. (1993). Obstacle marks produced by flow around stranded ice blocks during a glacier outburst flood (jökulhlaup) in west Greenland. *Sedimentology* 40, 1091–1111. doi: 10.1111/j.1365-3091.1993.tb01381.x

Silver, E., Day, S., Ward, S., Hoffmann, G., Llanes, P., Driscoll, N., et al. (2009). Volcano collapse and tsunami generation in the Bismarck volcanic arc, Papua New Guinea. *J. Volcanol. Geother. Res.* 186, 210–222. doi: 10.1016/j.jvolgeores.2009.06.013

Stephens,S. A., and and Ramsay, D. (2014). Extreme cyclone wave climate in the Southwest Pacific Ocean: influence of the El Niño Southern Oscillation and projected climate change. *Glob. Planet Change* 123, 13–26. doi: 10.1016/j.gloplacha.2014.10.002

Stow, D. A., Hernández-Molina, F. J., Llave, E., Sayago-Gil, M., Díaz del Río, V., and Branson, A. (2009). Bedform-velocity matrix: the estimation of bottom current velocity from bedform observations. *Geology* 37, 327–330. doi: 10.1130/G25259A.1

Symons, W. O., Sumner, E. J., Talling, P. J., Cartigny, M. J., and Clare, M. A. (2016). Large-scale sediment waves and scours on the modern seafloor and their implications for the prevalence of supercritical flows. *Mar. Geol.* 371, 130–148. doi: 10.1016/j.margeo.2015.11.009

Tappin, D. R., Watts, P., McMurtry, G. M., Lafoy, Y., and Matsumoto, T. (2001). The Sissano, Papua New Guinea tsunami of July 1998—offshore evidence on the source mechanism. *Mar. Geol.* 175, 1–23. doi: 10.1016/S0025-3227(01)00131-1

Terry, J. P., Garimella, S., and Kostaschuk, R. A. (2002). Rates of floodplain accretion in a tropical island river system impacted by cyclones and large floods. *Geomorphology* 42, 171–182. doi: 10.1016/S0169-555X(01)00084-8

Terry, J. P., and Goff, J. (2013). One hundred and thirty years since Darwin: 'reshaping' the theory of atoll formation. *Holocene* 23, 613–617. doi: 10.1177/0959683612463101

Terry, J. P., and Goff, J. R. (2012). The special vulnerability of Asia–Pacific islands to natural hazards. *Geol. Soc. Lond. Spec. Public* 361, 3–5. doi: 10.1144/SP361.2

Terry, J. P., Kostaschuk, R. A., and Wotling, G. (2008). Features of tropical cyclone-induced flood peaks on Grande Terre, New Caledonia. *Water Environ. J.* 22, 177–183. doi: 10.1111/j.1747-6593.2007.00098.x

Terry, J. P., and Lau, A. A. (2018). Magnitudes of nearshore waves generated by tropical cyclone Winston, the strongest landfalling cyclone in South Pacific records. Unprecedented or unremarkable? *Sediment. Geol.* 364, 276–285. doi: 10.1016/j.sedgeo.2017.10.009

Toomey, M., Donnelly, J., and Woodruff, J. (2013). Reconstructing mid-late Holocene cyclone variability in the Central Pacific using sedimentary records from Tahaa, French Polynesia. *Quat. Sci. Rev.* 77, 181–189. doi: 10.1016/j.quascirev.2013.07.019

Vanuatu Ministry of Lands and Natural Resources (2014). Available online at: https://web.archive.org/web/20171016152101/https://mol.gov.vu/index.php/en/water/223-the-lake-isiwi-disaster-sulfur-bay-tanna (Accessed November 5, 2018).

Walker, G. P. (1984). Downsag calderas, ring faults, caldera sizes, and incremental caldera growth. *J. Geophys. Res.* 89, 8407–8416. doi: 10.1029/JB089iB10p08407

Watson, S. J., Whittaker, J. M., Lucieer, V., Coffin, M. F., and Lamarche, G. (2017). Erosional and depositional processes on the submarine flanks of Ontong Java and Nukumanu atolls, western equatorial Pacific Ocean. *Mar. Geol.* 392, 122–139. doi: 10.1016/j.margeo.2017.08.006

Watt, S. F., Talling, P. J., and Hunt, J. E. (2014). New insights into the emplacement dynamics of volcanic island landslides. *Oceanography* 27, 46–57. doi: 10.5670/oceanog.2014.39

Weirich, F. H. (1989). The generation of turbidity currents by subaerial debris flows, California. *Geol. Soc. Am. Bull.* 101, 278–291. doi: 10.1130/0016-7606(1989)101andlt;0278:TGOTCBandgt;2.3.CO;2

Willems, B. A., Powell, R. D., Cowan, E. A., and Jaeger, J. M. (2011). Glacial outburst flood sediments within Disenchantment Bay, Alaska: implications of recognizing marine jökulhlaup deposits in the stratigraphic record. *Mar. Geol.* 284, 1–12. doi: 10.1016/j.margeo.2011.03.004

Wilson, T. M., Stewart, C., Sword-Daniels, V., Leonard, G. S., Johnston, D. M., Cole, J. W., et al. (2012). Volcanic ash impacts on critical infrastructure. *Phys. Chem. Earth Parts A B C* 45, 5–23. doi: 10.1016/j.pce.2011.06.006

Wright, I. C., Worthington, T. J., and Gamble, J. A. (2006). New multibeam mapping and geochemistry of the 30–35 S sector, and overview, of southern Kermadec arc volcanism. *J. Volcanol. Geother. Res.* 149, 263–296. doi: 10.1016/j.jvolgeores.2005.03.021

Xu, J. P., Noble, M. A., and Rosenfeld, L. K. (2004). *In-situ* measurements of velocity structure within turbidity currents. *Geophys. Res. Lett.* 31:9. doi: 10.1029/2004GL019718

Zhang, Y., Liu, Z., Zhao, Y., Colin, C., Zhang, X., Wang, M., et al. (2018). Long-term *in situ* observations on typhoon-triggered turbidity currents in the deep sea. *Geology* 46, 675–678. doi: 10.1130/G45178.1

Zhong, G., Cartigny, M. J., Kuang, Z., and Wang, L. (2015). Cyclic steps along the South Taiwan Shoal and West Penghu submarine canyons on the northeastern continental slope of the South China Sea. *Geol. Soc. Am. Bull.* 127, 804–824. doi: 10.1130/B31003.1

Conflict of Interest Statement: The authors declare that the research was conducted in the absence of any commercial or financial relationships that could be construed as a potential conflict of interest.

Copyright © 2018 Clare, Le Bas, Price, Hunt, Sear, Cartigny, Vellinga, Symons, Firth and Cronin. This is an open-access article distributed under the terms of the Creative Commons Attribution License (CC BY). The use, distribution or reproduction in other forums is permitted, provided the original author(s) and the copyright owner(s) are credited and that the original publication in this journal is cited, in accordance with accepted academic practice. No use, distribution or reproduction is permitted which does not comply with these terms.

frontiers in Earth Science

REVIEW
published: 30 April 2019
doi: 10.3389/feart.2019.00080

Dispersion, Accumulation, and the Ultimate Fate of Microplastics in Deep-Marine Environments: A Review and Future Directions

Ian A. Kane[1]* *and Michael A. Clare*[2]

[1] School of Earth and Environmental Sciences, University of Manchester, Manchester, United Kingdom, [2] National Oceanography Centre, University of Southampton, Southampton, United Kingdom

An estimated 8.3 billion tons of non-biodegradable plastic has been produced over the last 65 years. Much of this is not recycled and is disposed into the natural environment, has a long environmental residence time and accumulates in sedimentary systems worldwide, posing a threat to important ecosystems and potentially human health. We synthesize existing knowledge of seafloor microplastic distribution, and integrate this with process-based sedimentological models of particle transport, to provide new insights, and critically, to identify future research challenges. Compilation of published data shows that microplastics pervade the global seafloor, from abyssal plains to submarine canyons and deep-sea trenches (where they are most concentrated). However, few studies relate microplastic accumulation to sediment transport and deposition. Microplastics may enter directly into the sea as marine litter from shipping and fishing, or indirectly via fluvial and aeolian systems from terrestrial environments. The nature of the entry-point is critical to how terrestrially sourced microplastics are transferred to offshore sedimentary systems. We present models for physiographic shelf connection types related to the tectono-sedimentary regime of the margin. Beyond the shelf, the principal agents for microplastic transport are: (i) gravity-driven transport in sediment-laden flows; (ii) settling, or conveyance through biological processes, of material that was formerly floating on the surface or suspended in the water column; (iii) transport by thermohaline currents, either during settling or by reworking of deposited microplastics. We compare microplastic settling velocities to natural sediments to understand how appropriate existing sediment transport models are for explaining microplastic dispersal. Based on this analysis, and the relatively well-known behavior of deep-marine flow types, we explore the expected distribution of microplastic particles, both in individual sedimentary event deposits and within deep-marine depositional systems. Residence time within certain deposit types and depositional environments is anticipated to be variable, which has implications for the likelihood of ingestion and incorporation into the food chain, further transport, or deeper burial. We conclude that the integration of process-based sedimentological and stratigraphic knowledge with insights from modern sedimentary systems, and biological activity within them, will provide essential constraints on the transfer of microplastics to deep-marine

OPEN ACCESS

Edited by:
David Mark Hodgson, University of Leeds, United Kingdom

Reviewed by:
Rachel E. Brackenridge, Heriot-Watt University, United Kingdom
Aggeliki Georgiopoulou, University of Brighton, United Kingdom

***Correspondence:**
Ian A. Kane
ian.kane@manchester.ac.uk

Specialty section:
This article was submitted to Sedimentology, Stratigraphy and Diagenesis, a section of the journal Frontiers in Earth Science

Received: *02 March 2019*
Accepted: *03 April 2019*
Published: *30 April 2019*

Citation:
Kane IA and Clare MA (2019) Dispersion, Accumulation, and the Ultimate Fate of Microplastics in Deep-Marine Environments: A Review and Future Directions. Front. Earth Sci. 7:80. doi: 10.3389/feart.2019.00080

environments, their distribution and ultimate fate, and the implications that these have for benthic ecosystems. The dispersal of anthropogenic across the sedimentary systems that cover Earth's surface has important societal and economic implications. Sedimentologists have a key, but as-yet underplayed, role in addressing, and mitigating this globally significant issue.

Keywords: microplastic, microfiber, deep-marine, turbidite, sedimentology, contourite, submarine canyon, Anthropocene

INTRODUCTION: WHAT ARE MICROPLASTICS AND WHY DO WE CARE?

Plastic is an incredibly versatile and inexpensive material, which is ubiquitous in modern life. Since mass-produced plastics appeared in the 1950s, production has increased exponentially (Andrady and Neal, 2009; Andrady, 2011). It has been estimated that 8.3 billion tons of plastic has been produced over the last 65 years; 6.3 billion tons of which is now predicted to be waste (Geyer et al., 2017). In 2012 alone, it is estimated that 288 million tons of plastic was manufactured (Plastics Europe, 2013). Between 4.8 and 12.7 million tons of plastic entered the Earth's oceans in 2010, with this figure estimated to rise by one order of magnitude by 2025 (Jambeck et al., 2015; Geyer et al., 2017). At least 5.25 trillion pieces of plastic are estimated to be afloat in the world's oceans (Eriksen et al., 2014).

Microplastics are small plastic particles and fibers, which are found in the present and recent anthropogenically modified environment (**Figure 1**). Microplastics have been defined as ranging from <5 mm to 250 μm in diameter (Arthur et al., 2009; and many others), however, here we follow Browne et al. (2011) and Claessens et al. (2011), and other subsequent prominent investigations of microplastics (e.g., Van Cauwenberghe et al., 2013, 2015; Vianello et al., 2013; Dekiff et al., 2014) who suggested that <1 mm is more logical as this size class predominates in marine environments, and 'micro' generally refers to micrometer size range. Microfibers typically have lengths of 50 μm up to a few mm, and a diameter of <10 μm. Primary microplastic particles are either manufactured (e.g., microbeads in cosmetics, blasting media, and other industrial applications; Zitko and Hanlon, 1991; United States Environmental Protection Agency [USEPA], 1992; Fendall and Sewell, 2009; Mason et al., 2016), or secondary, when derived from the breakdown of larger plastic debris (e.g., Andrady, 2011; Cole et al., 2011; ter Halle et al., 2016). Microfibers are derived from synthetic textiles and are typically discharged from sewage plants (e.g., Browne et al., 2011; Dubaish and Liebezeit, 2013). As an illustration of the numbers of microfibers released, Browne et al. (2011) showed that up to 1,900 microplastic fibers can be shed from a single garment during one wash cycle.

Despite being documented since the 1970s (e.g., Buchanan, 1971; Carpenter and Smith, 1972; Colton et al., 1974; Gregory, 1978), plastic waste in the marine environment did not attract significant scientific or societal attention until later, when it became clear that plastic waste was having a deleterious effect on marine wildlife, particularly larger fauna such as dolphins and turtles (Barnes et al., 2009; Gall and Thompson, 2015). Microplastics were documented as early as 1972 on the surface of the Sargasso Sea (Carpenter et al., 1972); however, concern for the potential consequences for ocean life has only recently been raised. These small and light plastic particles are readily available to many organisms throughout the marine food-web. Furthermore, microplastics are preferential sites for the adhesion of organic pollutants, while their degradation can release toxic compounds (Teuten et al., 2009; Cole et al., 2011). Ongoing research is therefore required to quantify the risks posed to marine life (including fishing stocks), and potential knock on effects to human health (Van Cauwenberghe and Janssen, 2014; Galloway, 2015; Sharma and Chatterjee, 2017; Barboza et al., 2018).

Given their high mobility and long residence times, microplastics are found globally; from the beaches of isolated oceanic islands (Costa and Barletta, 2015; Lusher, 2015), within Antarctic currents (Lusher, 2015), to the seafloor of the Arctic (Bergmann and Klages, 2012; Bergmann et al., 2017; Kanhai et al., 2019) and the sea ice above it (Bergmann et al., 2017). In short, there appears to be no environment on Earth that has escaped microplastic pollution (Taylor et al., 2016). However, our knowledge of the locations of microplastic accumulation in the marine realm is presently incomplete, and in particular the distribution on the seafloor is poorly constrained (Thompson et al., 2004; Barnes et al., 2009; Ballent et al., 2013; Woodall et al., 2014; Martin et al., 2017). This is significant as it is estimated that approximately half of all plastics have a density greater than seawater (United States Environmental Protection Agency [USEPA], 1992; Morét-Ferguson et al., 2010). The seafloor is therefore considered a sink for global plastics, which could account for much of the 'missing' microplastic in global budgets (Goldberg, 1997; Thompson et al., 2004; Ballent et al., 2013; Van Cauwenberghe et al., 2013; Pham et al., 2014; Woodall et al., 2014; Fischer et al., 2015; Courtene-Jones et al., 2017; Hardesty et al., 2017; Underwood et al., 2017).

Challenges

Goldberg (1997) suggested that to better understand plastic accumulation on the seafloor required standardized monitoring to assess whether or not seafloor plastic contamination is increasing and whether or not it is affecting marine ecology. However, whilst seafloor microplastics have since been documented in an increasing number of studies, this has been done on a largely *ad hoc* basis, using existing cores and samples

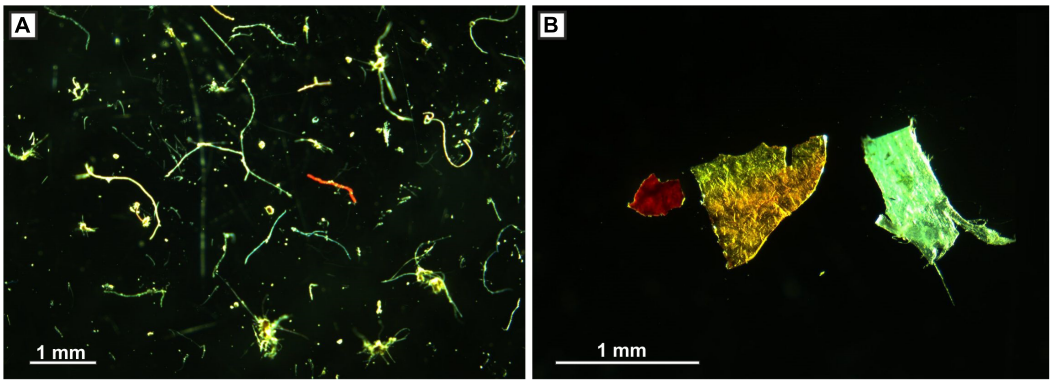


FIGURE 1 | (A) Microplastic fibers and **(B)** microplastic fragments; both from seafloor cores, c. 800 m water depth, Tyrrhenian Sea.

from older studies. Attention has been paid to ingestion of microplastics by seafloor organisms, however, there has been extremely limited attention paid to the physical mechanisms that control how microplastics reach the seafloor, how they are distributed and what governs their ultimate fate (e.g., Gregory, 2009; Corcoran et al., 2017; Graca et al., 2017; Horton and Dixon, 2017). Process-based sedimentological studies routinely relate sediment and other particulate accumulations to the processes that transport, deposit, and bury them. The present lack of characterization and quantification of the processes that control the influx, distribution, and ultimate burial of microplastics in the oceans, provides an opportunity for the application of process-based sedimentology to assess this globally significant issue (Hodgson et al., 2018a).

Aims

Here, we aim to synthesize existing knowledge on seafloor microplastic distribution, and integrate that with a process-based understanding of how particles are transported, and the known sedimentology of deep-marine systems. We do this in order to provide new insights from recent research and to identify future research challenges. We specifically address the following questions:

(1) What types of microplastics are found on the seafloor and where do they come from (see section "Where Do Microplastics Come From and What Types Are Found on the Seafloor?")?
(2) How are onshore microplastic transport pathways linked to offshore pathways? (see section "How Might Terrestrial Microplastics Be Introduced to Deep-Sea Environments?") This is currently a missing part of the microplastic cycle (Zalasiewicz et al., 2016). More specifically, are those pathways direct, or more complex with staggered transport and filtering mechanisms? Because of the dominance of river emissions in contributing microplastics to the world's oceans (Lebreton et al., 2017), here, we focus primarily on clastic systems, but many of our discussions will also relate to carbonate systems.
(3) Based on existing knowledge, where do microplastics accumulate on the seafloor, and is there disproportionality in where they are found (see section "In Which Physiographic Domains Have Microplastics Been Documented to Accumulate at Seafloor?")? How important for example are different physiographic domains such as submarine canyons, which are known conduits for sediment and organic carbon transport and nutrients, compared to, open continental slopes?
(4) Based on what we know of microplastic density, size and shape, what physical processes might be responsible for their transport and deposition on the seafloor (see sections "Settling Velocities of Microplastic Particles," "Enhanced Suspension Fall-Out Due to Reversing Buoyancy and Biological Modifications," "Inhibited Settling due to Thermohaline Stratification and Influence of Near-Bed Ocean Currents," and "Modified Settling in Sediment-Laden Fluids and the Importance of Sediment Gravity Flows")? What are the unique aspects of microplastics transport compared to natural sediments? Do microplastics accumulate within certain grain size ranges as a product of the environment in which they are found?
(5) Where should we expect microplastics to be deposited within individual deep-sea environments (see section "Where Should We Expect Microplastics to Be Deposited Within Individual Deep-Sea Deposits?"), i.e., do they have an affinity for different sedimentary facies, and how might they vary across and down systems such as submarine channels, levees and lobes? What are the implications of these predicted vertical and lateral distributions for deep-sea ecosystems?
(6) What is likely to be the ultimate fate of microplastics (see section "Implications for the Long-Term Distribution of Microplastics Within Depositional Settings and Their Ultimate Fate")? We explore the implications of deep-sea sediment transport that may initially result in preservation of microplastic-bearing deposits over short timescales, but over longer

time-scales may be subject to repeated re-exhumation and remobilization (e.g., canyon filling and flushing). We address this by comparing recent repeat seafloor surveys that span periods of days to decades in active settings, to consider the local residence time and ultimate fate of microplastics within the depositional record over anthropogenic timescales.

Objectives and Datasets

In order to address the questions outlined above, we synthesize the following datasets:

(1) Observations of microplastic distributions from various published studies.
(2) Process-based observations and models developed for distribution of lightweight, highly mobile particles in deep-sea systems such as organic carbon and pollutants.
(3) Experimental analysis of settling rates and settling behavior of microplastics.
(4) Measurements of sediment transport processes using recent direct monitoring technology (e.g., of river plumes, turbidity currents, internal tides).
(5) High resolution repeat seafloor surveys to understand the dynamic nature of active deep-sea sediment transport systems.
(6) Geological archives that demonstrate what is ultimately preserved in the depositional record, including sediment cores from modern systems and ancient outcrops that form the basis for the development of system-wide ecological models.

WHERE DO MICROPLASTICS COME FROM AND WHAT TYPES ARE FOUND ON THE SEAFLOOR?

The global production of plastic increased from approximately 30 million tons in the 1960s, to >140 million tons by the turn of the 21st Century (Goldberg, 1997; Thompson et al., 2004). It has proven challenging, however, to quantify the input rate of plastics to the oceans as there are only poor constraints on degradation rates in different environments, and plastic age does not necessarily reflect the age it was deposited (Ryan et al., 2009). In addition, there is a multitude of pathways for plastics to reach the seafloor and these may be heavily modulated by the effects of both surface and water-column currents (e.g., thermohaline currents) (Ryan et al., 2009; Cole et al., 2011; Doyle et al., 2011). A general trend of increasing macroplastic pollution has been observed in long term monitoring studies (e.g., Chiba et al., 2018; Maes et al., 2018); however, an encouraging decline in the occurrence of plastic bags has been noted in the North Sea, suggesting that legislation can have a positive impact (Maes et al., 2018). Only in the last 5 years have microplastics been identified in the deep and abyssal oceans; the largest marine habitat on the planet (Woodall et al., 2014) (**Figure 2**). This new identification may in part be explained by advances in analytical approaches that enable microplastic identification, coupled with a growing societal concern to understand the global significance of plastic pollution; however, it is highly likely that the deep-sea is now experiencing the legacy of the exponential increase in microplastic production over the past five decades (Thompson et al., 2004).

Microplastics documented on the seafloor are dominated by fibers. The main source of microplastic particles is thought to be the breakdown of primary plastics (e.g., Andrady, 2011; Cole et al., 2011; ter Halle et al., 2016). These primary plastics are typically those which are not recycled and undergo breakdown in the terrestrial realm, e.g., on land and in rivers, and are transported to the marine realm either as microplastics or larger pieces which may degrade on the sea surface or seafloor (e.g., Willis et al., 2017; Hurley et al., 2018; Pierdomenico et al., 2019) (see section "Enhanced Suspension Fall-Out due to Reversing Buoyancy and Biological Modifications" on reversing buoyancy), as well those from fishing boats and shipping (Pham et al., 2014). Microfibers are derived from synthetic textiles and are typically derived from sewage plants where they are not retained, and from fishing gear (e.g., Browne et al., 2011; Dubaish and Liebezeit, 2013). The distribution and dynamic behavior of microplastics in the water column is poorly constrained but is known to be affected by dredging, trawling, tidal currents, and other processes which affect turbulence in the water column (e.g., Browne et al., 2010, 2011; Claessens et al., 2011; Van Cauwenberghe et al., 2015; Alomar et al., 2016; Moreira et al., 2016).

HOW MIGHT TERRESTRIAL MICROPLASTICS BE INTRODUCED TO DEEP-SEA ENVIRONMENTS?

Sediment, including macroplastic and microplastic, is transported to coastal zones by rivers, wind and ice. Rivers, in particular, are key agents in the transport of microplastics to the coast (e.g., Moore et al., 2011; Klein et al., 2015; Mani et al., 2015; Horton et al., 2017; Lebreton et al., 2017; Willis et al., 2017; Hurley et al., 2018; Pierdomenico et al., 2019). Other contributors of microplastics to the coastal zone include wastewater from treatment plants, shipyards, harbors, and other industries (e.g., Stolte et al., 2015), and urban run-off (e.g., Patters and Bratton, 2016) (**Figure 3**). When rivers reach the coast, the sediment within them is either sequestered into shallow marine sediment deposits, where it is prone to reworking by coastal processes including longshore drift, or it is fed into a submarine canyon head (e.g., Zalasiewicz et al., 2016; Blum et al., 2018; Pierdomenico et al., 2019) (**Figure 4**). Recent studies have shown that microplastics in beach sands can also be derived from oceanic waste transported by landward-directed surface currents and that this in some cases can dominate over delivery of river-derived microplastics (Chubarenko et al., 2018).

The duration of sediment storage in the onshore realm generally depends on the relief of the margin, which is related to the tectonic regime. Steep, tectonically active margins tend to have minimal onshore storage (e.g., Romans et al., 2016), and hence sediment and microplastics have a short residence time onshore; the opposite being true for mature, passive margins

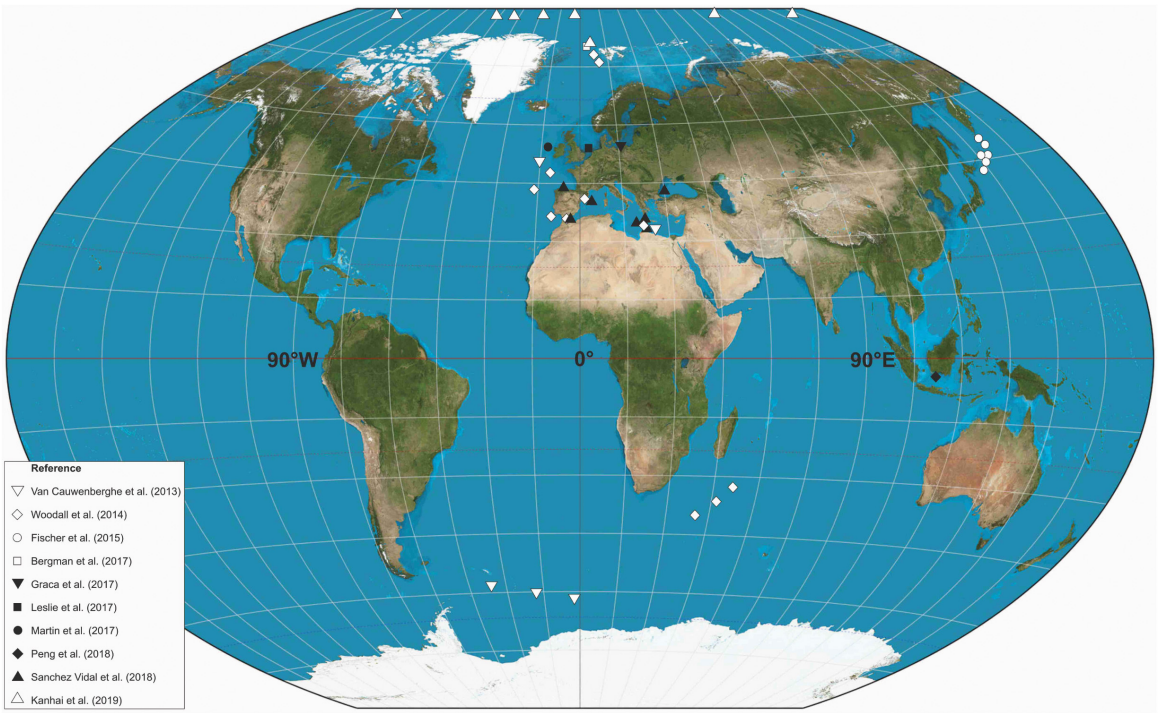


FIGURE 2 | Global distribution of studies which have identified microplastics in deep-marine sediment samples. Positions marked are approximate.

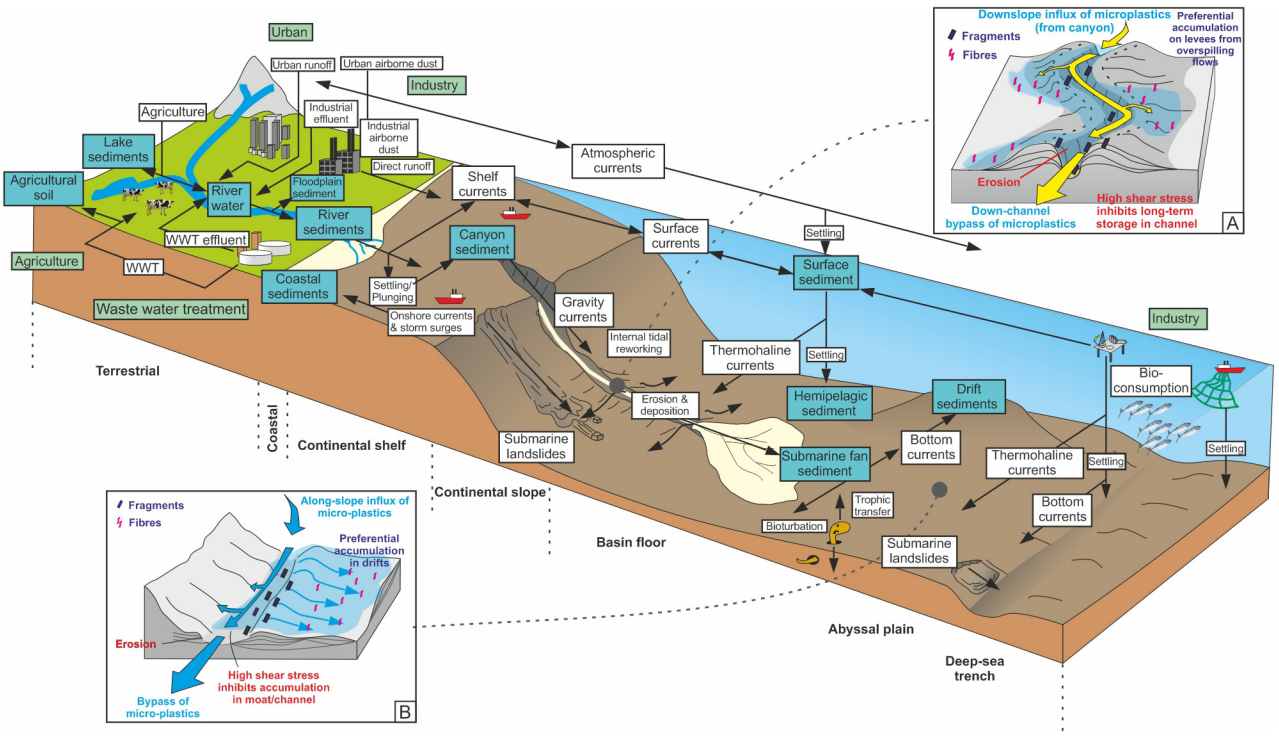


FIGURE 3 | Microplastic input, transport vectors, and sinks. Green boxes represent primary input, blue boxes range boxes represent temporary and permanent sinks, white boxes represent transport mechanisms and arrows represent transport vectors. Insets show the potential distribution and transport vectors of microplastics in **(A)** a channel-levee system and **(B)** a bottom current moat and drift system, respectively. Modified and extended (to include marine realm) from Horton and Dixon (2017). WWT, waste water treatment.

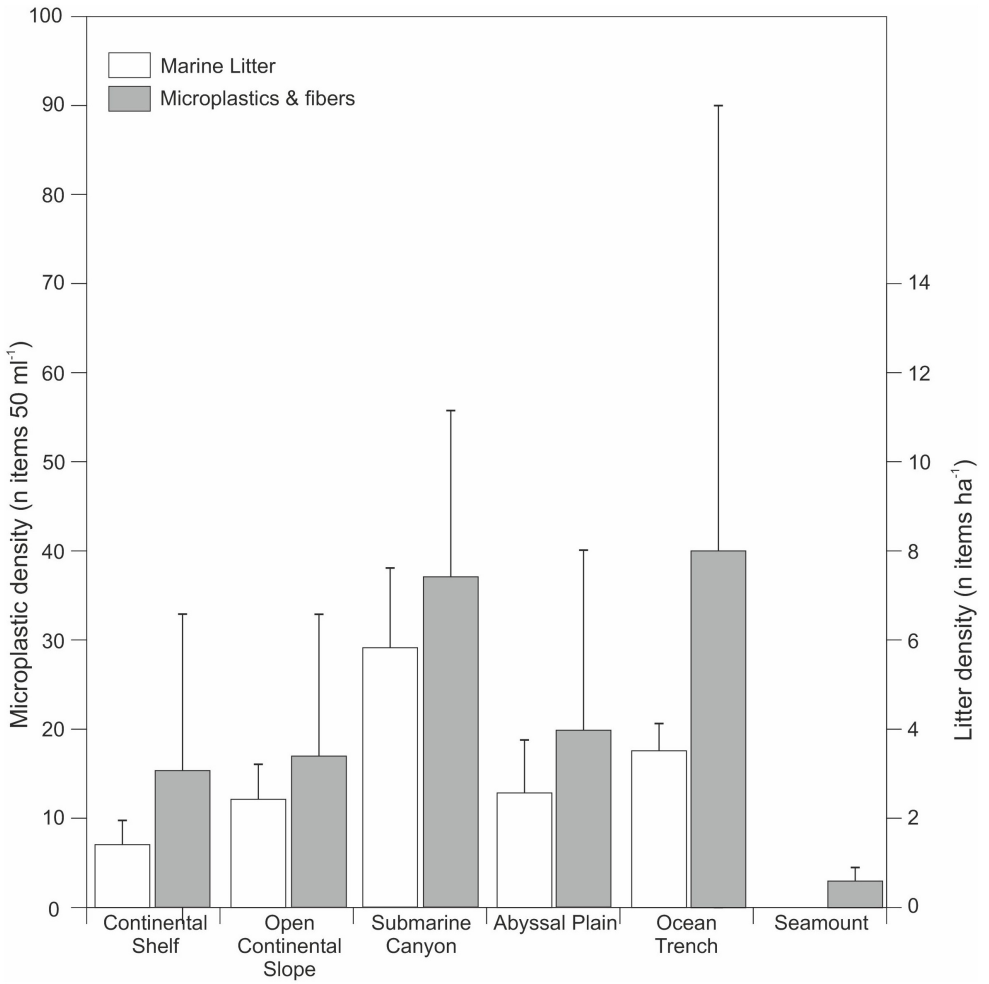


FIGURE 4 | Compilation of microplastic and microfiber distribution in deep-marine sediments and their gross depositional environments (data compiled from: Van Cauwenberghe et al., 2013; Woodall et al., 2014; Fischer et al., 2015; Bergmann et al., 2017; Graca et al., 2017; Leslie et al., 2017; Martin et al., 2017; Peng et al., 2018; Sanchez-Vidal et al., 2018; Kanhai et al., 2019). As a comparison data from marine litter distributions collected by Pham et al. (2014) are shown.

(e.g., the Mississippi River feeding into the Gulf of Mexico – Galloway et al., 2013). Longer duration of onshore storage will allow more time for macroplastics to degrade and for larger fragments to break into smaller fragments (**Figure 3**). The downstream transfer of sediment and microplastics in many systems may be staggered, particularly on passive margins with extensive drainage systems. Plastics may undergo temporary storage during periods of relatively low discharge, but be re-exhumed during flood events wherein they are flushed seawards (Hurley et al., 2018). The tectonic configuration of the continental margin also controls the transfer pathways of sediment and microplastics from rivers to deep-sea sediment routing systems, such as submarine canyons. As well as featuring steep and short onshore catchments, active margins are characterized by narrow continental shelves, and steep continental slopes, typically incised by submarine canyons (e.g., Cascadia and California margins, NW United States). Passive margins are characterized by long and relatively lower relief catchments with gentler slopes and wider shelves; hence there is often a much greater distance between rivers and the continental slope (with the exception of infrequent instances where submarine canyons cut back into the continental shelf; e.g., Congo Canyon, West Africa; Babonneau et al., 2002). The role of the continental shelf as both a filter and a conveyor of sediment is critical and especially so in today's highstand sea-level conditions where slope conduits may be isolated from a feeder system (e.g., Cosgrove et al., 2018). In such detached scenarios, areas of broad continental shelf may provide loci for long-term storage or along-contour redistribution of microplastics (as is also the case for organic carbon), depending on the vigor of along-shelf currents and other oceanographic perturbations, such as storm waves and surges (e.g., Aller and Blair, 2006).

We now consider a range of shelf and slope configurations that may explain variability in the efficiency of microplastics transfer from onshore to the deep-sea (**Figure 4**). At one end of the spectrum are situations where a river debouches directly into an offshore canyon head, in which the efficiency of

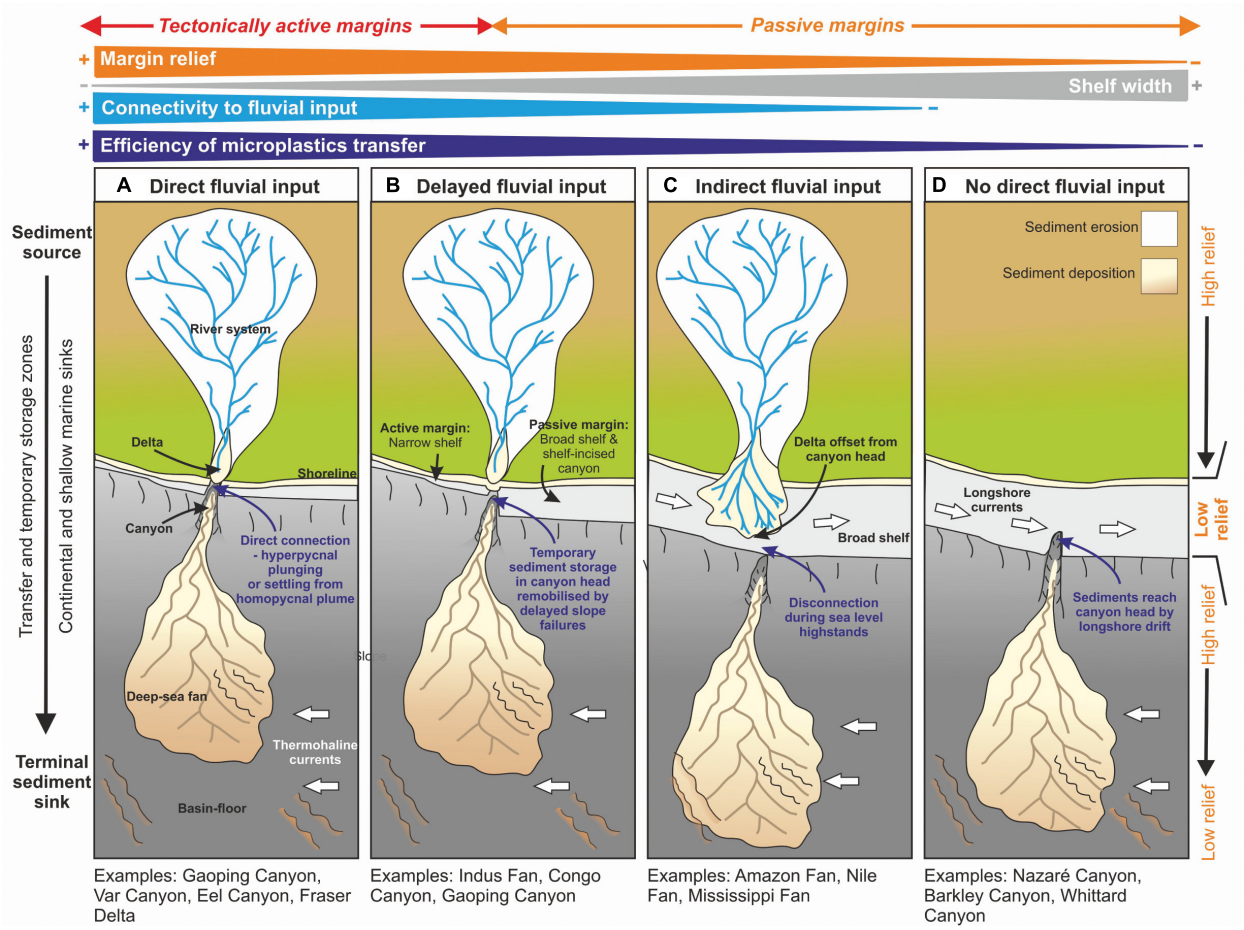


FIGURE 5 | The efficiency of transfer of microplastics and larger primary plastic items from the terrestrial to deep-marine realm is dependent on the duration of onshore sediment storage and the proximity of the canyon head to the principal terrestrial sources of sediment, e.g., river mouths, which is influenced primarily by the tectonic style of the margin. **(A)** Direct fluvial input to the canyon head, **(B)** delayed fluvial input as sediment is temporarily stored in the canyon head, **(C)** indirect fluvial input due to the canyon being offset from the river mouth, and **(D)** no direct fluvial feeder, sediment is sourced by longshore drift. Longshore currents as well as the volume and density of fluvial outflow will also have a strong influence on the likelihood of plastics reaching the canyon head. Modified from Sømme et al. (2009).

transfer for denser microplastics is likely to be high (**Figure 5A**). This is particularly the case where rivers with sufficiently high concentrations enter the sea, and lead to plunging of dense sediment-laden water (termed 'hyperpycnal flow') that initiates a turbidity current (e.g., Gaoping Canyon, Taiwan; Var Canyon, NW Mediterranean; Mulder et al., 2003; Khripounoff et al., 2009; Carter et al., 2012) (**Figure 5**). High outflows in such settings may also lead to rapid sediment accumulation in the canyon head, setting up slope failures, or settling from homopycnal river plumes, that can also trigger turbidity currents (Carter et al., 2012; Pope et al., 2017; Hizzett et al., 2018). The Messina Strait canyons of the Mediterranean are subject to flash-flood induced hyperpycnal flows, and these have been shown to transport huge volumes of anthropogenic waste to over 1,000 m water depth (Pierdomenico et al., 2019). These systems are termed 'reactive' with the source sediment supply conditions being relatively well-recorded in the deposits of the sink (**Figure 6**); an example is the La Jolla canyon-channel system (Romans et al., 2016). In such high efficiency transfer zones, the direct connection between terrestrial outflow and submarine canyon would be expected to result in a concentration of microplastics; in particular the larger size fractions but potentially also microfibers. If a river lacks a direct connection to a submarine canyon (**Figures 5B–D**), then along-shelf currents and wave action can redistribute and disperse sediments, thus reducing the efficiency of the river to slope connectivity (Mulder et al., 2012; Eidam et al., 2019). These systems may be termed 'buffered,' with the input conditions being less faithfully recorded in the sink (**Figure 6**); an example being the Indus River – Indus Submarine Fan (Romans et al., 2016). It has been demonstrated that longshore drift acts as a grain size segregator, with the finer and/or hydrodynamically lighter grains being more-readily transported along the shelf (Aller and Blair, 2006). Sediment will be transported along the shelf, until the load is diminished through wave and storm action, or until it meets an intersecting canyon head (e.g., La Jolla or Monterey Canyons, California;

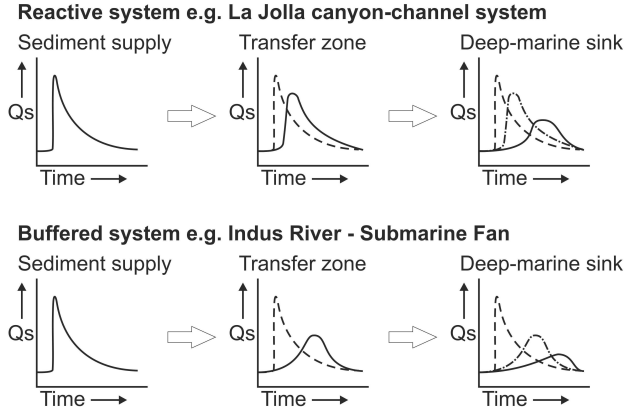


FIGURE 6 | Reactive versus buffered sediment delivery systems. Longer residence periods for sediment in the buffered systems suggests that plastics may be more degraded, both physically and chemically, suggesting that plastics delivered in these systems will be more degraded and smaller. In the buffered example, the seafloor expression of surges in plastic production may significantly lag behind their introduction to the sedimentary environment. Modified from Romans et al. (2016).

Xu et al., 2002; Covault et al., 2007) (**Figures 5C,D**). Thus, microfibers and the lightest microplastic particles will be more-readily dispersed in low-efficiency and buffered margin transfer zones (e.g., disconnection between river and canyon/continental slope, wide shelf dominated by currents), becoming preferentially transported along the coast and shelf. The general advection of fine grained particles over the shelf edge during longshore drift is anticipated to be widespread away from zones of fluvial input, both due to shelfal processes and hydrodynamic aspects, some of which are unique to microplastics. We now discuss some of the key properties of microplastics, and how they compare to sand and mud particles that are more routinely characterized and modeled in sediment transport studies.

IN WHICH PHYSIOGRAPHIC DOMAINS HAVE MICROPLASTICS BEEN DOCUMENTED TO ACCUMULATE AT SEAFLOOR?

Despite the relative infancy of marine microplastics research, a considerable, and steadily growing, number of publications now provide compelling evidence of the pervasive nature of microplastics across the seafloor worldwide. Many studies show that deep-sea microplastics occur in similar (or even higher) concentrations as in intertidal and shallow sub-tidal sediments, with microplastic particles being distributed primarily, but not solely, around input points such as submarine canyons (e.g., Woodall et al., 2014; Taylor et al., 2016; Bergmann et al., 2017; Hurley et al., 2018) (**Figures 2**, **3** and **Table 1**). Analysis of previous deep-sea studies that sampled seafloor sediments reveals that submarine canyons and ocean trenches are the physiographic domains with the highest density of microplastics (**Table 1** and **Figure 4**). These two environments feature almost double the microplastic density at seafloor compared to other deep-sea settings, such as continental shelves, open continental slopes, abyssal plains and seamounts (**Figure 4**). While a relatively wide range of settings have been sampled, it should be noted that there is some geographic bias to the existing sampling for microplastics (e.g., Atlantic, Mediterranean, and Pacific focus). Future efforts should ensure a wider geographic, as well as physiographic coverage.

Submarine canyons have previously been shown to be marine litter hotspots, especially where they occur in close proximity to industrial and densely populated coastal areas (Mordecai et al., 2011; Pham et al., 2014; Tubau et al., 2015; Buhl-Mortensen and Buhl-Mortensen, 2017). Sites offshore from popular tourism centers can be inundated with large quantities of litter that is transported offshore and to deeper water (over 1,000 m water depth) following storms or during seasonal cascades of dense water (Tubau et al., 2015; Pierdomenico et al., 2019). A study of the Lisbon, Blanes, Guilvinec, and Setubal canyons (NE Atlantic) found litter at all sites and all water depths (from 35 to 4,500 m), with a higher density than from all other physiographic settings; reaching an average of 9.3 ± 2.9 items ha^{-1} (Pham et al., 2014). Perhaps unsurprisingly, there is a close match between the recorded distribution of marine litter and microplastic fragments in the ocean (**Figure 4**).

Levels of microfiber contamination in bottom waters have been shown to be considerably higher than in surface waters, for example, 11 microfibers per liter of water were sampled in the Mariana trench, western Pacific Ocean, compared to a few pieces per liter in surface waters and 200–2,200 per liter of sediment (Peng et al., 2018). This may partially explain the relative abundance of microplastics in ocean trenches, with the presence of larger plastics and marine litter in that setting being attributed mostly to fishing and shipping activities (Peng et al., 2018).

While previous studies have provided valuable information on the type and abundance of microplastics in seafloor sediments, they have not yet included any detailed sedimentological data that can explain these physiographic biases for microplastic distribution, nor to enable prediction of how microplastics may be distributed within different system types (e.g., across the full extent of a deep-sea submarine channel system). As an example, the lack of microplastic particles identified at the deep-sea Congo Fan was viewed as anomalous due to the presence of major industrial cities on the Congo River (Van Cauwenberghe et al., 2013), but no information is provided about whether the part of the fan sampled was active (i.e., subject to recent turbidity current activity or near-bed oceanographic currents), nor regarding the grain size of the host sediment. Previous studies have demonstrated that, while much of the Congo canyon, deep-sea channel and fan system is a highly active conduit for sediment and organic carbon transport in the present day (Khripounoff et al., 2003; Azpiroz-Zabala et al., 2017), not all of the deep sea distributary networks are active (Picot et al., 2019). Thus, without any detailed information on the seafloor sediments and specific location within the submarine channel-fan system, it is challenging to determine how representative one core location is for an entire system. Recent studies in

TABLE 1 | Compilation of published studies documenting microplastics in deep-marine seafloor sediments.

Location	Depth	Depositional environment	Specific sub-environment	Sediment grain size	Microplastic size range	Microplastic type	Concentration	References
Irish Sea	Below MLD	Distal continental shelf	Not specified	Sandy	5–250 μm	Fibers (85%) fragments (15%)	1–7/25 ml	Martin et al., 2017
Mariana Trench	5,108–10,908	Deep ocean trench	Not specified	Not specified	0.1–0.5 mm	Mostly fibers	200–2,200/l	Peng et al., 2018
Subpolar N Atlantic	1,000–2,000	Open slope	Not specified	Not specified	<0.1 × 2–3 mm	Fibers	10–15/50 ml	Woodall et al., 2014
NE Atlantic	1,400	Continental margin	Canyon	Not specified	<0.1 × 2–3 mm	Fibers	40/50 ml	Woodall et al., 2014
NE Atlantic	2,200	Open slope	Not specified	Not specified	<0.1 × 2–3 mm	Fibers	10/50 ml	Woodall et al., 2014
Mediterranean	300–1,300	Continental margin	Canyon	Not specified	<0.1 × 2–3 mm	Fibers	10–35/ml	Woodall et al., 2014
Mediterranean	900	Open slope	Not specified	Not specified	<0.1 × 2–3 mm	Fibers	10/50 ml	Woodall et al., 2014
Mediterranean	3,500	Basin	Not specified	Not specified	<0.1 × 2–3 mm	Fibers	10/50 ml	Woodall et al., 2014
SW Indian Ocean	900–1,000	Seamount	Not specified	Not specified	<0.1 × 2–3 mm	Fibers	1.4–4/50 ml	Woodall et al., 2014
Atlantic, Southern Ocean	2,749	Polar front	Not specified	Not specified	60 × 118 μm	Fragments (no test for fibers)	1/25 cm^2	Van Cauwenberghe et al., 2013
N Atlantic, Porcupine Abyssal Plain	4,842–4,843	Abyssal plain	Not specified	Not specified	44 × 83–137 × 161 μm	Fragments (no test for fibers)	3/cm^2	Van Cauwenberghe et al., 2013
Gulf of Guinea, Congo Fan	4,785	Deep marine fan system	Distal lobe	Not specified	None present		0	Van Cauwenberghe et al., 2013
Mediterranean, Nile Fan	1,176	Deep marine fan system	Not specified	Not specified	53 × 75 μm	Fragments (no test for fibers)	1/25 cm^2	Van Cauwenberghe et al., 2013
SW Pacific Kuril–Kamchatka Trench	4,869–5,766	Deep ocean trench	Not specified	Not specified	<1 mm	Fibers (75%) fragments (25%)	2,020/m^2	Fischer et al., 2015
S. Baltic Sea, Gdansk deep	106	Slope	Not specified	Clay-silt	0.1–2 mm long	Fibers	3/kg	Graca et al., 2017
Cantabrian Sea	1,207–2,000	Canyon	Not specified	Clay-silt	3–8 mm long	Fibers	40–70/50 ml	Sanchez-Vidal et al., 2018
Alboran Sea	42	Continental shelf	Not specified	Clay-silt	3–8 mm long	Fibers	45/50 ml	Sanchez-Vidal et al., 2018
Alboran Sea	248–770	Open continental slope	Not specified	Clay	3–8 mm long	Fibers	25–60/50 ml	Sanchez-Vidal et al., 2018
Alboran Sea	389–1,857	Canyon	Not specified	Clay-silt	3–8 mm long	Fibers	25–50/50 ml	Sanchez-Vidal et al., 2018
Catalan Sea	67	Continental shelf	Not specified	Clay-silt	3–8 mm long	Fibers	45/50 ml	Sanchez-Vidal et al., 2018
Catalan Sea	281–2,196	Canyon	Not specified	Clay-silt	3–8 mm long	Fibers	25–75/50 ml	Sanchez-Vidal et al., 2018
Catalan Sea	2,117–2,222	Deep margin and basin (floor)	Not specified	Clay	3–8 mm long	Fibers	20–40/50 ml	Sanchez-Vidal et al., 2018
Cretan Sea	991–1,018	Open continental slope	Not specified	Clay	3–8 mm long	Fibers	10/50 ml	Sanchez-Vidal et al., 2018
Levantine Sea	1,615–2,015	Open continental slope	Not specified	Clay	3–8 mm long	Fibers	15/50 ml	Sanchez-Vidal et al., 2018
Levantine Sea	2,720–3,500	Deep margin and basin (floor)	Not specified	Clay	3–8 mm long	Fibers	10–60/50 ml	Sanchez-Vidal et al., 2018
Black Sea	840	Canyon	Not specified	Clay-silt	3–8 mm long	Fibers	20/50 ml	Sanchez-Vidal et al., 2018
Arctic Sea, Fram Strait	2,342	Trench	Not specified	Not specified	>11–150 μm	Fibers	2,303.98/l	Bergmann et al., 2017

(Continued)

TABLE 1 | Continued

Location	Depth	Depositional environment	Specific sub-environment	Sediment grain size	Microplastic size range	Microplastic type	Concentration	References
Arctic Sea, Fram Strait	2,460	Trench	Not specified	Not specified	>11–100 μm	Fibers	1,404.95/l	Bergmann et al., 2017
Arctic Sea, Fram Strait	3,127	Trench	Not specified	Not specified	>11–125 μm	Fibers	2,088.91/l	Bergmann et al., 2017
Arctic Sea, Fram Strait	3,430	Trench	Not specified	Not specified	>11–150 μm	Fibers	1,222.9/l	Bergmann et al., 2017
Arctic Sea, Fram Strait	4,092	Trench	Not specified	Not specified	>11–175 μm	Fibers	3,394.63/l	Bergmann et al., 2017
Arctic Sea, Fram Strait	5,108	Trench	Not specified	Not specified	>11–200 μm	Fibers	3,392.98/l	Bergmann et al., 2017
Arctic Sea, Fram Strait	5,570	Trench	Not specified	Not specified	>11–100 μm	Fibers	44.43/l	Bergmann et al., 2017
Arctic Sea, Fram Strait	2,783	Trench	Not specified	Not specified	>11–100 μm	Fibers	3,463.71/l	Bergmann et al., 2017
Arctic Sea, Fram Strait	2,549	Trench	Not specified	Not specified	>11–125 μm	Fibers	3,051.6/l	Bergmann et al., 2017
North Sea	Not specified	Continental shelf	Not specified	Not specified	10–5,000 μm	Particles, foils, and fibers	440/kg dw	Leslie et al., 2017
North Sea	Not specified	Continental shelf	Not specified	Not specified	10–5,000 μm	Particles, foils, and fibers	470/kg dw	Leslie et al., 2017
North Sea	Not specified	Continental shelf	Not specified	Not specified	10–5,000 μm	Particles, foils, and fibers	520/kg dw	Leslie et al., 2017
Arctic Central Basin – Yermak Plateau	855	Abyssal plain plateau	Not specified	Clay-silt	None present	(Test for >100 microns)	0	Kanhai et al., 2019
Arctic Central Basin – Amundsen Basin	4,353	Abyssal plain	Not specified	Clay-silt	1.38, 1.84 mm	Fibers (test for >100 microns)	2/10 g	Kanhai et al., 2019
Arctic Central Basin – Foot of Lomonosov Ridge	3,777	Abyssal plain	Not specified	Clay-silt	0.47 mm	Fiber (test for >100 microns)	1/10 g	Kanhai et al., 2019
Arctic Central Basin – Marvin Spur	3,936	Abyssal plain - ridge	Not specified	Clay-silt	0.91	Fragment (test for >100 microns)	1/10 g	Kanhai et al., 2019
Arctic Central Basin – Crest of Lomonosov Ridge	1,253	Abyssal plain - ridge	Not specified	Clay-silt	3.58 mm	Fiber (test for >100 microns)	1/10 g	Kanhai et al., 2019
Arctic Central Basin – Marvin Spur	3,941	Abyssal plain - ridge	Not specified	Clay-silt	None present	(Test for >100 microns)	0	Kanhai et al., 2019
Arctic Central Basin – Alpha Ridge	2,620	Abyssal plain - ridge	Not specified	Clay-silt	0.54, 0.88 mm	Fragments (test for >100 microns)	2/10 g	Kanhai et al., 2019
Arctic Central Basin – Alpha Ridge	2,212	Abyssal plain - ridge	Not specified	Clay-silt	0.45	Fragment (test for >100 microns)	1/10 g	Kanhai et al., 2019
Arctic Central Basin – Nautilus Basin	2,872	Abyssal plain	Not specified	Clay-silt	None present	(Test for >100 microns)	0	Kanhai et al., 2019
Arctic Central Basin – Makarov Basin	3,066	Abyssal plain	Not specified	Clay-silt	None present	(Test for >100 microns)	0	Kanhai et al., 2019
Arctic Central Basin – Crest of Lomonosov Ridge	1,269	Abyssal plain – ridge	Not specified	Clay-silt	1.03	Fragment (test for >100 microns)	1/10 g	Kanhai et al., 2019

Results are included where microplastics were tested for but were not present.

fluvial and shallow marine/tidal environments have started to address these issues, including the spatial, sedimentological, and temporal controls on microplastic distributions (e.g., Van Cauwenberghe et al., 2015; Hurley et al., 2018). We suggest that there is a pressing need to provide more detailed contextual information to link microplastics with the transport processes responsible for their accumulations in order to explain their distributions across different deep-sea depositional environments (**Table 1** and **Figure 4**). If we ever hope to link microplastics to the processes that control their distribution in the deep-sea, we must first understand how they are introduced to marine environments. The following section therefore first outlines the processes that transfer microplastics to the ocean, and then discusses how different tectonic, physiographic and oceanographic configurations may result in the wider dispersal or localized concentrations of microplastics.

PROPERTIES OF MICROPLASTICS AND PHYSICAL CONTROLS ON THEIR SUSPENSION, TRANSPORT AND DEPOSITION

Microplastics span a wide range of densities; from very low density, such as polystyrene (40 kgm^{-3}) to the densest, e.g., polytetrafluoroethylene (2,020 kgm^{-3}). In contrast, mineral sediment with a grain size larger than clay, i.e., silt and sand, delivered by rivers is dominated by quartz (2,650 kgm^{-3}), feldspar (2,560 kgm^{-3}), and mica (2,750 kgm^{-3}). Therefore, most of our understanding of sediment gravity flows on the seafloor is dominated by sand and mud transport, with less known about the behavior of lighter particles including microplastics, organic material such as plants, leaves and woody material (e.g., Zavala et al., 2012; Yamada et al., 2013). It is known that plant material can reach the distal parts of submarine fans, e.g., in Permian strata of Tanqua Karoo, Hodgson (2009) reported that plant material had been transported at least 150 km from the contemporaneous shoreline (where it was likely sourced). As well as particle density, grain shape plays an important role in the settling of grains from suspension, with platy particles, such as leaf fragments and mica (despite its high density), or those with intricate shapes, e.g., shells, typically settling more slowly than spherical particles (e.g., McNown and Malaika, 1950; Dietrich, 1982; Oehmig, 1993). Previous work has suggested the hydraulic 'equivalence' of organic material with 'platy' grains such as mica (Stanley, 1982), such that these particles often settle at lower velocities than slightly finer-grained siliciclastic sand and develop micaceous and organic rich caps to turbidite sand beds (e.g., Hodgson, 2009; Zavala et al., 2012) (**Figure 7**). Microplastics may exhibit a similar distribution and this would mean they are prone to erosion from subsequent flows, gradual down-system reworking, as well as erosion and resuspension

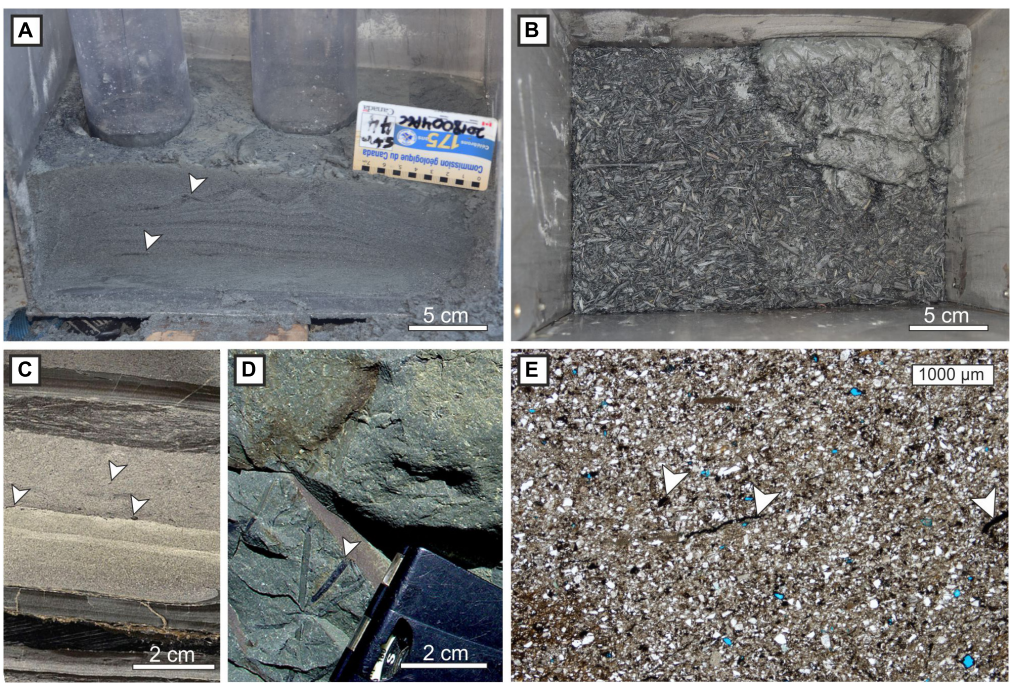


FIGURE 7 | (A) Organic-rich material incorporated within turbidite laminae, and **(B)** concentrated on the bed top; both from Bute Inlet, British Columbia (courtesy of Maarten Heijnen). **(C)** Organic material distributed within a hybrid bed and in the uppermost dark-colored division (cored interval, Palaeogene, Gulf of Mexico; Kane and Pontén, 2012). **(D)** Plant fragments in the upper part of a hybrid bed (Permian, Tanqua Karoo; Hodgson, 2009). **(E)** Thin-section photomicrograph showing small plant fragments within a hybrid bed (Permian, Tanqua Karoo; Kane et al., 2017). Microplastic fragments and fibers might be anticipated to have similar distributions in deep-water deposits.

by bottom-currents which may flow obliquely to the 'primary' depositional system (**Figure 3**).

The principal candidates for the transport of microplastics to and across the deep seafloor are: (i) settling, or conveyance through biological processes, of material that was formerly floating on the surface or suspended in the water column; (ii) gravity-driven transport in sediment-laden flows, such as turbidity currents; (iii) reworking and transport by thermohaline currents; and (iv) internal tides (i.e., topographically steered internal waves that exhibit tidal frequencies; Shepard, 1975). We will now discuss the settling velocity of particles, and then consider the implications of these transport processes.

Settling Velocities of Microplastic Particles

The paucity of contextual sedimentological data in existing microplastics studies (**Table 1**) inhibits a detailed investigation of transport processes at present. Information on the specific depositional environment (e.g., a canyon axis that features regular turbidity currents versus an adjacent flank elevated above the zone of flow interaction) and critically the grain size of the host sediments are omitted in most of the existing studies. One of the few studies to provide grain size information (Maes et al., 2017) does not provide water depths or other environmental information for the samples collected. Despite the lack of observational data to link microplastics to transport process, a number of recent laboratory studies have made measurements of the settling velocities of microplastics such that we can investigate the anticipated range of processes and environments that control their transport, dispersal and/or concentration. Laboratory experiments to measure settling velocities for a range of plastic particles (Kowalski et al., 2016; Khatmullina and Isachenko, 2017) have demonstrated the expected deviation from theoretical values (e.g., following Dietrich, 1982). Settling velocities (w_s) for spherical particles within a turbulent flow can be estimated, following Ferguson and Church (2004), using $w_s = \frac{RgD^2}{C_1\nu + \sqrt{0.75C_2RgD^3}}$ where R is the relative submerged density of the particles, g is gravity, D is the particle diameter, C_1 and C_2 are constants, 18 and 1, respectively. Relative submerged density (R) is given by $(\rho s - \rho f)/\rho f$ where ρs is the density of sediment and ρf is the density of fluid, in this case seawater, at 1,026.2 kg m^{-3}. Settling velocities estimated for various microplastic particles are lower than the main 'sand-forming' minerals, which indicates that for a given size, plastic particles will be deposited later than sand grains (**Figure 8**). This means, for example, that a 0.5 mm diameter spherical polyurethane pellet would settle at approximately the same rate as a 0.15 mm diameter quartz grain (fine sand), or a 5 mm diameter pellet at the same rate as a 0.75 mm diameter quartz grain (coarse sand). Both natural and plastic particles have a range of shapes and surface roughness so these theoretical values (for spheres) typically over-estimate settling velocity.

Sediment particle size sorting occurs during deposition and resuspension according to the relationship of w_s to the fluid shear stress (τ) (either turbidity current or bottom current). In general the fluid shear stress for non-cohesive sediment deposition (τ_d), is lower than that required for erosion (τ_e), which is lower still than that required for suspension (τ_s), such that $\tau_d < \tau_e < \tau_s$ (e.g., McCave et al., 2017). Plastic particle flocculation is poorly understood but it is assumed that most microplastics behave in a non-cohesive manner, however, they may be incorporated into larger aggregates when mixed with clay (Galgani et al., 2015) or when surfaces have accumulated biofilms (e.g., Lobelle and Cunliffe, 2011). Owing to their wide range of shapes, microfibers are anticipated to behave substantially differently to spherical (e.g., microbeads) or fragmented microplastics (e.g., Högberg et al., 2010). While there may be analogs with plankton fallout (Ptacnik et al., 2003; Peterson et al., 2005), plastic microfiber settling remains an area for future research (Kowalski et al., 2016; Khatmullina and Isachenko, 2017).

We now discuss some of the ways in which the preceding estimates of settling velocity may be modified, due to interactions of microplastics with the ambient marine environment.

Enhanced Suspension Fall-Out Due to Reversing Buoyancy and Biological Modifications

While many plastic particles start out with a given low density (and hence slow settling velocity), this can change over time as particles can: (i) accumulate biofilms (biofouling; e.g., Lobelle and Cunliffe, 2011; Muthukumar et al., 2011; Long et al., 2015; Cole et al., 2016; Fazey and Ryan, 2016; Kaiser et al., 2017); (ii) break down through UV light degradation (photodegradation; Shah et al., 2008); (iii) act as focal points for precipitation of chemicals and minerals on particle surfaces (Mato et al., 2001; Corcoran et al., 2015); (iv) undergo leaching of additives (Van Cauwenberghe et al., 2013, 2014 and (v) form aggregates of marine sediments (Galgani et al., 2015). Biofouling may explain the apparent lack of plastics on the sea surface; recorded levels of plastic at the surface are at least two orders of magnitude lower than anticipated (Cózar et al., 2014). Consumption of microplastic particles by organisms, such as polychaete worms, mysid shrimps and copepods can lead to the expulsion of microplastic-bearing fecal pellets with a greater density than initial microplastic densities (Kuo and Bolton, 2013; Setälä et al., 2014; Courtene-Jones et al., 2017), such that particles are prone to gravity driven settling in the water column. This mechanism has been demonstrated for enhanced settling flux of organic carbon in the Southern Ocean, due to its incorporation into the fecal pellets of krill (Belcher et al., 2019). Biological redistribution of microplastics may also occur through burial within sediment layers, by the burrowing action of organisms, or re-exhumation of previously buried microplastics at seafloor following its consumption and egestion (Urlaub et al., 2013; Näkki et al., 2017).

Inhibited Settling Due to Thermohaline Stratification and Influence of Near-Bed Ocean Currents

Little is known of the residence time of plastics on the sea surface, but it may be significant (>tens of years in some cases; Chubarenko et al., 2016). It has largely been presumed that the

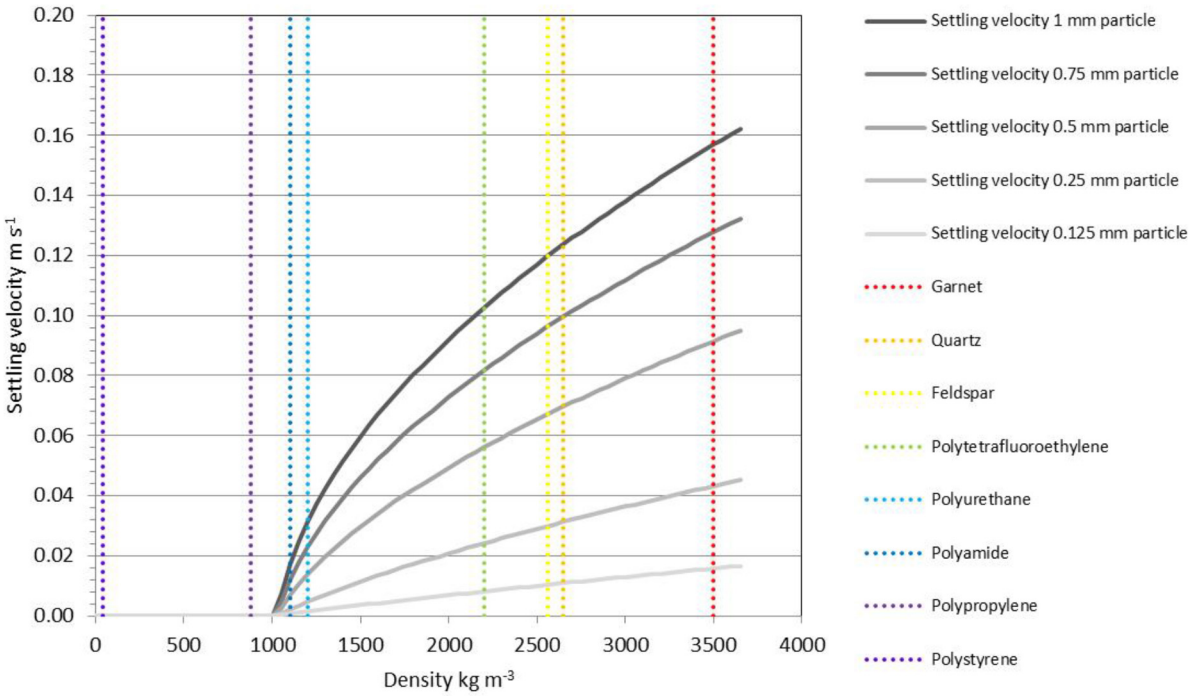


FIGURE 8 | Settling velocities estimated for a range of spherical particles in a turbulent flow; as an example a 1 mm polyurethane sphere would settle at similar velocity to a 0.25 mm quartz grain. Natural particles have a wide range of shapes and surface roughness which will affect their settling, and microfibers will diverge significantly from this model.

fallout of plastic from suspension will be concentrated in those areas prone to surface collection of particles as 'marine snow' (Wright et al., 2013); however, the influence of thermohaline circulation in the ocean must not be ignored. Thermohaline stratification can create nepheloid layers that inhibit fall-out and promote the lateral advection of fine sediments, while bottom-hugging contour currents can be agents of sediment deposition, bypass and reworking, and can develop very large accumulations of fine-grained sediment, known collectively as drift deposits (e.g., Stow and Lovell, 1979; Rebesco et al., 2014).

Settling of microplastics to the seabed will only occur when the shear stress at the base of a flow is lower than the settling velocity, thus leading to inhibited settling and advection of microplastics. Given the typical velocities of near-bed thermohaline currents in many deep-sea locations worldwide (∼0.1–0.4 m/s; McCave et al., 2017), it is not surprising that thermohaline currents have been implicated as a control on microplastic transport in several locations in the deep-ocean (Fischer et al., 2015; Bergmann et al., 2017; Peng et al., 2018). Microplastics and fibers in the Kuril–Kamchatka Trench (**Table 1**) have no immediately adjacent source area, and it has been suggested that northwards-flowing bottom currents in the trench could have brought material from Japan and from as far afield as Russia (Peng et al., 2018). Thermohaline currents have also been invoked for the transport of microplastic particles into the deep Fram Strait (Arctic Sea) owing to its distance from an obvious source (Bergmann et al., 2017) (**Table 1**). Where a stratified water column interacts with pronounced seafloor topography, internal tides often develop in response to surface tides. Internal tides can exert pronounced shear stresses at seafloor and play an important role in the modulation of downslope sediment transport processes; often acting to re-suspend and transport sediment within canyons and other areas of enhanced relief such as seamounts (e.g., Inman et al., 1976; Paull et al., 2005; Lee et al., 2009; Zhao et al., 2012). In a numerical modeling study of microplastic transport within the Nazaré Canyon (NE Atlantic), internal tides were found to resuspend and move microplastics both up and down canyon, with only a minor net-downstream movement (Ballent et al., 2013). It might be anticipated that one of the main effects of internal tides is to continuously re-suspend the lightest particles deposited on the seafloor priming them for entrainment by large gravity currents moving down the canyon (see Section "Modified Settling in Sediment-Laden Fluids and the Importance of Sediment Gravity Flows"). Current-related deposits, in particular contourite drifts, may account for large quantities of microplastics, however, this cannot yet be discerned from existing published studies (**Table 1**).

Modified Settling in Sediment-Laden Fluids and the Importance of Sediment Gravity Flows

Analysis of microplastic settling has so far been determined within clear fluids (Kowalski et al., 2016; Khatmullina and Isachenko, 2017). Given the global importance of gravity-driven flows in the transport of sediment and other hydrodynamically

light particles in the deep-sea (Galy et al., 2007; Talling et al., 2012a; Gwiazda et al., 2015; McArthur et al., 2017), further work is needed to understand the behavior of microplastic particles in sediment and fluid flows. Such work has been performed for mud and sand mixtures (e.g., Amy et al., 2006) but not yet for mixtures including microplastics, and will need to incorporate the spectrum of gravity flows; from turbidity currents (Talling et al., 2012a), to debris flows (e.g., Mohrig et al., 1998; Ilstad et al., 2004; Talling et al., 2012a,b; Baker et al., 2017), and slumps and slides which feature a lower degree of internal disaggregation than debris flows (e.g., Nardin et al., 1979; Booth et al., 1993; Masson et al., 2006; Talling et al., 2012b). This work will be important for the consideration of microplastic distribution within sediment gravity flow deposits (i.e., distributed throughout the bed versus on top of the bed), as this will impact the likelihood of long-term burial rather than erosion by the next gravity flow event.

Sediment gravity flows (in particular turbidity currents) may be significant agents for transporting and distributing microplastics in the deep sea. The first reason is that such flows will entrain and transport microplastics whose density is greater than that of seawater, or that are incorporated in a dense sediment suspension (Ballent et al., 2013; Schlining et al., 2013; Tubau et al., 2015; Zalasiewicz et al., 2016). Thus in a deep-sea system, such as a submarine canyon where gravity-driven flows typically decrease in energy both spatially and temporally, lower density/finer grains can be transported further than higher density/coarser grains, and tend to be deposited later at a given point, as has been shown for low density particulate organic carbon (e.g., Zavala et al., 2012; McArthur et al., 2017; Paull et al., 2018). The second reason relates to how and where sediment gravity flows initiate (i.e., often close to sites of significant terrestrial sediment dispersal such as rivers and/or are foci for the trapping along-shelf sediment transport). Turbidity currents are generated in two principal ways: firstly, by direct fluvial input of sediment-laden river water outflow, which either plunges as it debouches from the river mouth as a hyperpycnal flow (Mulder and Svytski, 1995; Mulder et al., 2003) or settles out from a lower density surface plume (Kineke et al., 2000; Ayranci et al., 2012; Hizzett et al., 2018) to trigger a turbidity current. Such flows have been shown to be significant for transferring organic carbon to deep-water, due to the direct connection of river outflow, and hence are also likely to be important for microplastics transfer (see section "In Which Physiographic Domains Have Microplastics Been Documented to Accumulate at Seafloor?"; Galy et al., 2007; Zavala et al., 2012; Sparkes et al., 2015). Secondly, turbidity currents may form due to externally or autogenically triggered collapse of sediment accumulations, such as at submarine canyon heads that trap littoral sediment transport (e.g., Xu et al., 2002; Paull et al., 2018; Smith et al., 2018), rapidly prograding delta fronts (e.g., Clare et al., 2016; Obelcz et al., 2017) or on open continental slopes (e.g., Nisbet and Piper, 1998; Talling et al., 2014; Soutter et al., 2018). Such failure-generated flows may be highly concentrated, contain a heterogeneous sediment mixture, and have the potential to run-out significant distances, eroding and entraining seafloor deposits from open slopes, or within a canyon or channel along their path (e.g., Piper and Savoye, 1993; Stevenson et al., 2015; Allin et al., 2016; Hunt, 2017; Mountjoy et al., 2018).

Where Should We Expect Microplastics to Be Deposited Within Individual Deep-Sea Deposits?

To date, there has been little to no work done on the vertical distribution of plastics within depositional units. Most samples collected have been from the top few centimeters of sediment and, presumably (although the information is generally not given), from relatively fine grained (clay-silt) deposits. Despite these limitations, our understanding of particulate density fractionation during transport and deposition provides a basis for an initial predictive assessment of their distribution within individual deposits. From the ancient record (e.g., Kneller and Branney, 1995; Talling et al., 2012b) and from observations in modern environments (e.g., Smith et al., 2007; Biscara et al., 2012; Clare et al., 2017; Hage et al., 2018; Mountjoy et al., 2018; Stevenson et al., 2018) we know that some individual event deposits (e.g., by gravity flows) can be many meters thick; hence, the assertion that plastics are only present in the first few centimeters of sediment below the seafloor is unlikely to hold (c.f. Martin et al., 2017). In the following section, we discuss how initial depositional processes may govern the depth below seafloor at which different types of microplastics accumulate, first focusing on episodic gravity flows and then on longer duration, more persistent ocean currents.

Gravity Flow Deposits

It has been suggested that turbidites will show sorting of plastic fragments based on their density, size and shape, with plastic fragments concentrated in the upper divisions (C–E) of 'Bouma (1962) type' turbidites (Zalasiewicz et al., 2016). Zalasiewicz et al. (2016) also suggest that plastic fragments may behave in a similar way to other non-spherical particles within sandy deposits (e.g., robust shell fragments, which typically end up in the bottom parts of beds while less dense shells are typically concentrated a little higher, in the ripple-laminated Bouma C division; Davies et al., 1997). In a turbidity current, particles settle according to their density and shape, such that particles with high settling velocities (e.g., dense, spherical particles) will tend to settle faster than those with low settling velocities (e.g., low density, platy particles or fibers). Accordingly, grains with higher settling velocities will tend to concentrate at the base of the flow, whilst those with lower settling velocities will be distributed throughout the flow, due to turbulent mixing (**Figure 9**). Flows that are forced to decelerate rapidly, either due to being overloaded with sediment or due to topography, will tend toward having high sediment fallout rates as the turbulent energy dissipates, and the deposit will reflect the stratification of the flow at that point. Where flows decelerate less rapidly (e.g., less concentrated flows running out over gradually decreasing slopes), the turbulent kinetic energy dissipates more slowly, such that particles with progressively lower settling velocity drop out of the flow (e.g., Kneller, 1995). The former case leads to the development of thick, poorly sorted, massive to crudely stratified

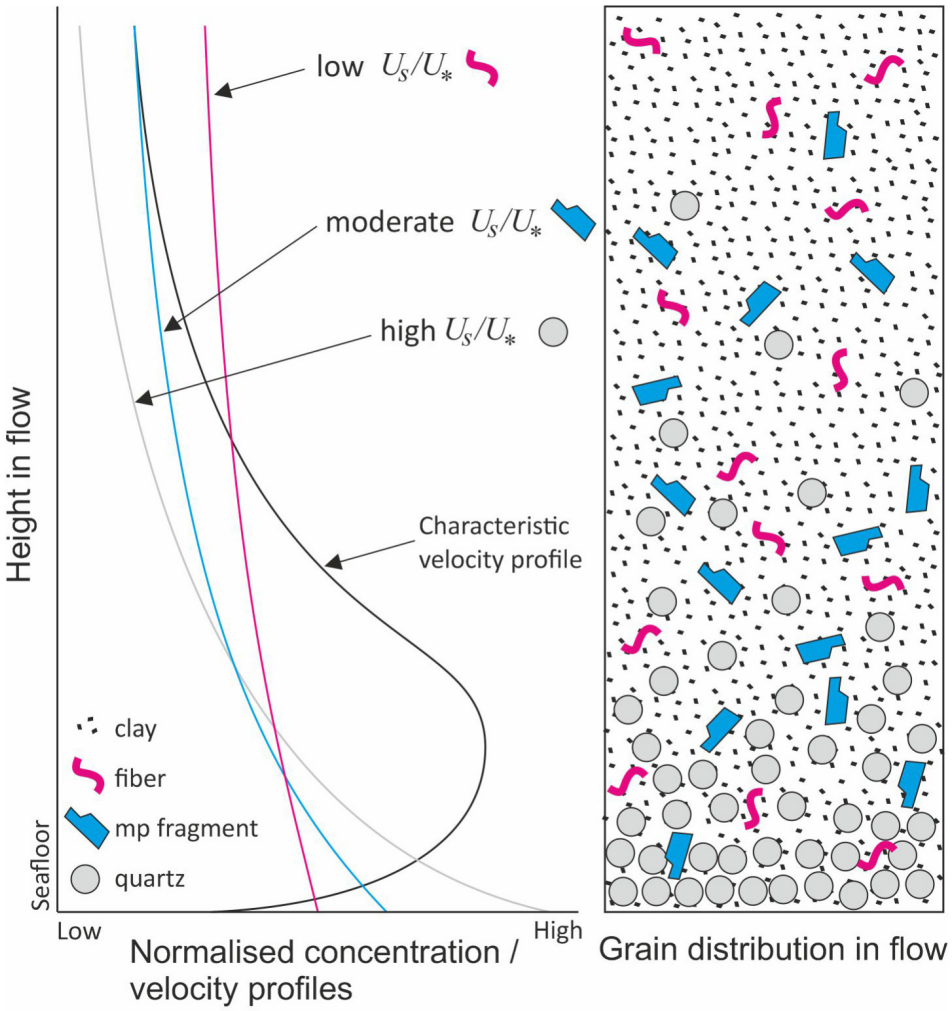


FIGURE 9 | Sediment distribution in a turbidity current. Particles with a relatively low settling velocity (U_S), in comparison to the shear velocity (U_*), e.g., microplastics, will tend to be more homogenously distributed throughout the flow than those with a high settling velocity, e.g., quartz and feldspar. U_S, settling velocity; U_*, shear velocity. Where microplastics end up in the flow deposits depends on the rate of flow deceleration, e.g., they might be distributed throughout high-density turbidites, but concentrated at bed tops in low-density turbidites. Modified from Hansen et al. (2015).

turbidites (i.e., 'high density turbidites'; Lowe, 1982; Kneller, 1995; Kneller and Branney, 1995; Baas and Best, 2002), while the latter produces a well-developed normal-grading grain-size trend and parallel- to ripple-laminated deposits (i.e., 'low density turbidites'). Consequently, microplastics in these flows will be distributed throughout beds according to these factors. In high density turbidites, microplastics may be distributed throughout the bed, which may be several meters (or more) thick. In low density turbidites, microplastics may be concentrated at the bed tops (**Figure 9**). This has a consequence for the likelihood of microplastic remobilization by subsequent turbidity currents, for sampling methodology (as most studies sample only the uppermost few centimeters of beds), as well as the availability of microplastics to ingestion by seafloor and/or burrowing fauna (Wright et al., 2013). In situations where a flow is constrained by topography (e.g., within a channel), the upper part of the overspilling flow will tend to concentrate particles that have a low settling velocity (e.g., Kane et al., 2007; Hansen et al., 2015, 2017; McArthur et al., 2017), making depositional areas such as levees more likely sites for microplastics accumulation. A summary of deep-marine gravity flow deposit types and likely microplastic distribution is presented in **Figure 10**.

Ocean Current-Related Deposits

Deposits related to ocean currents interacting with the seafloor (i.e., 'bottom currents'), form a wide range of morphologies grouped together into 'drifts.' The large drift deposits observed globally are built from sediment that was initially delivered by gravity flow systems, but subsequently reworked by bottom currents. This suggests that microplastics delivered to the basin floor by gravity currents may be prone to erosion and transport by bottom currents, and eventually be sequestered within drift deposits (Rebesco et al., 2014). Drift deposits are generally fine grained, clay-silt, and may reflect current strength

	Process / flow type	Bed type	Bed type description	Interpretation	Microplastics
Background	Hemipelagic settling	Hemipelagite	Grain size: clay, minor silt. Sedimentary structures: structureless or laminated.	Suspension settling from water column.	Fine fragments and fibres throughout, randomly distributed, larger particles deposited by reversing buoyancy and distributed randomly.
Individual sediment gravity flow deposits	Low-density turbidity current	Low-density turbidite	Grain size: silt-lower medium sand. Sedimentary structures: plane-parallel and ripple-cross lamination throughout, normally-graded.	Competence-related deposition and tractional working by low density turbidity current (Lowe, 1982; Hiscott, 1994).	Microplastics at bed top and vulnerable to erosion in channelized settings.
	High-density turbidity current	High-density turbidite	Grain size: medium to very coarse and granular. Sedimentary structures: dominantly structureless.	Deposition from a high density turbidity current (sensu Lowe, 1982).	Microplastics distributed throughout bed and prone to erosion at bed tops.
	Hybrid flow	Hybrid bed	Grain size: fine to medium sand. Sedimentary structures: banding, dewatering structures.	Deposition from flows with characteristics of turbidity currents and debris flows (Haughton et al., 2003; Talling, 2004; Haughton et al., 2009).	Microplastics concentrated at bed tops and within mud-rich internal divisions (transitional/debritic flow components). Typical in distal environments and less prone to erosion.
	Debris flow	Debrite	May include grains of all sizes. Sedimentary structures: diamictic, plastic deformation – fold and shear structures.	Deposition from debris flows where matrix strength is the main particle support mechanism (Lowe, 1982; Sohn, 1997).	Little if any density stratification of particles, so microplastics distributed throughout bed. tend to be deposited in topographic lows
	Slump	Slump deposit	Structures include evidence of plastic deformation, including folding and overturned beds.	Gravitational instability of un-lithified sediments which move downslope for a limited distance and begin to disintegrate but retain original structures.	Slumps and slides contain the material they begin with but are more typical in areas of higher topographic relief, e.g. slopes, canyons. Remobilisation may allow microplastics to be released from the host sediment where they may mix with seawater and disperse.
	Slide	Slide deposit	Structures include coherent bedding with thrust planes, sheared bedding contacts, extensional and compressional features.	Gravitational instability of sediments which move downslope initially as a coherent mass and may retain internal structures.	
Reworked deposits	Tractional lag	Tractional lag deposit	Grain size: silt-granular. Sedimentary structures: weak irregular stratification, erosional remnants, lenticular, clean but with mud-clasts, anomalously coarse, sharp base and top.	Winnowed tractional deposit formed at the base of a channel, scour or bedform trough typically by the passage of multiple flows leaving their coarsest material behind.	Larger microplastics may be trapped within basal lag deposits and would be prone to erosion and downslope reworking.
	Bottom current reworked	Bottom-current reworked sst	Grain size: silt to fine sand. Sedimentary structures: plane-parallel and ripple-cross lamination, mud draped foresets and laminae, variable grading, internal erosion surfaces, bioturbated.	Deep water sediment gravity flow silts and sands reworked by tractional currents attributed to bottom currents (thermohaline flows).	May act to concentrate fine microplastics and in particular microfibers, but as present very poorly-understood.
	Bottom current reworked	Drift deposit	Grain size: clay to silt. Sedimentary structures: plane-parallel and low angle dipping lamination, may be entirely bioturbated, or lack bioturbation.	Deep water sediment gravity flow clays and silts, and hemipelagite, reworked by quasi continuous thermohaline circulation (bottom currents) (e.g. Stow & Faugères, 2008).	May act to concentrate or remove fine microplastics (especially fibers) in certain areas and redistribute across the global seafloor.

FIGURE 10 | Range of sediment gravity flow types, their deposits, and the anticipated distribution of microplastics. This is important as specific benthic ecosystems develop in depositional sites prone to particular sediment gravity flow types; the deposit type then has a bearing on the likelihood of remobilization of microplastic and its availability for ingestion by benthic fauna.

variability through time (e.g., Stow, 1991) (**Figures 9**, **10**). The persistent nature of bottom currents, although they may show seasonal variation, means that their deposits are often relatively homogeneous with less well-defined beds than typical gravity current deposits, which tend to be related to episodic events. The velocities of bottom currents (0.06–0.5 ms^{-1}; e.g., Ridderinkhof et al., 2010; McCave et al., 2017; Miramontes et al., 2019) could easily provide enough shear stress to transport microplastics, in particular fibers. Drift deposits are often sites of intense bioturbation and this could be a pathway for microplastics into the deeper sediment (as well as preferentially ingested by benthic organisms). The exceedingly thick and stratigraphically continuous drift deposits preserved offshore east and west Africa, east of South America (e.g., Faugères et al., 1993; Rebesco et al., 2014), and elsewhere, demonstrate the high preservation potential of these features. We anticipate drift deposits to be

significant sites for microfiber concentration and storage in the sedimentary record (**Figures 3**, **9**).

IMPLICATIONS FOR THE LONG-TERM DISTRIBUTION OF MICROPLASTICS WITHIN DEPOSITIONAL SETTINGS AND THEIR ULTIMATE FATE

The arrival and storage of microplastics in the Earth's stratigraphic record has been suggested to mark the onset of the Anthropocene as a new geological epoch (e.g., Waters et al., 2016; Zalasiewicz et al., 2016). In the longer (geological) term, plastics will not be preserved but the breakdown of various types of plastics in seawater, at varying depths, salinities and levels of UV penetration, is poorly understood. However, it is considered that microplastics deposited in the benthic realm may breakdown more slowly than at the land surface, due to the lack of UV-radiation, colder temperatures and lower oxygenation (Woodall et al., 2014). We now revisit the global deep-sea distribution based on understanding of initial influxes, and processes that govern their transport. We integrate recent findings from repeat surveys and direct monitoring of sediment transport to try and understand how future microplastic distribution may change.

Open Continental Slopes

Open continental slopes are here described as the inter-canyon, predominantly non-channelized parts of the clinothems which form the slope between the continental shelf and the base of slope/basin floor. The nature of the tectonic setting will determine the size and the angle of the slope, and the width of the continental shelf, and hence the delivery of sediment to the shelf edge. Continental slopes are generally sites of steady sediment accumulation; microplastic accumulation may be pervasive where sediment is fed along the continental shelf by longshore currents. Submarine landslides may deliver very large volumes ($>>1$ km^3) of sediment to the base of the slope, some of which may transform into turbidity currents (Nisbet and Piper, 1998; Urlaub et al., 2013). These events may be a way of exhuming large volumes of microplastics which have accumulated over many years, and delivering them to the base of slope and beyond. Factors influencing the development and size of submarine landslides include the sedimentation rate, and the tectonic regime, for example small regular earthquakes may continuously shed sediment from the slope, whereas large infrequent events may remove much larger volumes. Slope reworking may occur during periods of enhanced bottom current activity, and open continental slopes are often sites of large drift mounds. Dense water cascades from the shelf, due to trawling and seafloor mining activity, are also common (Palanques et al., 2001; Shapiro et al., 2003). Submarine landslides and debris flow deposits are not restricted to active margins, they can also be common in passive margin settings, for example Eastern United States, NW African, and Norwegian margins (e.g., Masson et al., 2010; Hodgson et al., 2018b). Open slopes are thus generally considered to be sites for accumulation of fine microplastics, in particular fibers, and advection from the coast is dependent on the shelf width, location of canyons, and prevalence of longshore currents. Reworking by ocean currents may result in along-slope redistributions in drifts that reflect the trend and intensity of near-bed bottom currents. Submarine landslides may be relatively infrequent, but can serve to re-exhume large areas of previously sequestered microplastics and redistribute them further down-slope.

Submarine Canyon-Channel-Lobe Systems

Submarine Canyons

Submarine canyons are common features along continental margins, usually occurring seaward of major rivers (e.g., Shepard, 1955). They are large-scale erosional features incised into the shelf and slope that commonly have a V-shaped cross section, particularly in the upper reaches (e.g., Pickering et al., 1989). Toward the continental rise (at the base of the slope), canyons flare out and become less steep. Canyons occur across a wide range of scales, from tens to hundreds of kilometers wide, extending downslope for distances of tens to hundreds of kilometers (Pickering et al., 1989). The canyon head may lie within a couple of hundred meters off the coastline (e.g., Monterey Canyon, Paull et al., 2005) or may not extend onto the shelf at all (e.g., Orange et al., 1997), while the canyon mouth may feed one or more submarine channel-levee systems or fed directly into a submarine fan.

Studies of modern canyon systems and linked deep-water fans, such as the Congo canyon, have shown that sustained turbidity currents are very efficient transporters of organic material into deep-water, with organic material often reaching the most-distal parts of the fan (Khripounoff et al., 2003; Azpiroz-Zabala et al., 2017). Turbidity currents in the Congo canyon are estimated to contribute 2% of terrestrial organic carbon buried globally in the oceans, with individual flows delivering up to 0.19 Megatons of organic carbon. Such flows could therefore be highly capable of transporting microplastics, being of similar densities to organic material, to the distal parts of the fan. This organic material, together with relatively oxygenated water, is important for benthic ecosystems at extremely deep water depths (Rabouille et al., 2017). Similar distributions of organic material are recorded in ancient submarine fan systems (e.g., Stanley, 1982; McArthur et al., 2017). Other anthropogenic pollutants such as DDT pesticide have been demonstrated to preferentially flow down canyons. In the Monterey Canyon, Paull et al. (2002) documented levels of 10 ± 3 to 18 ± 8 ppb in the canyon, but only 2 ± 2 ppb in the intra-canyon flanks and background slope.

Large magnitude flows within canyons, e.g., due to large earthquakes, can result in 'flushing' of sediment that has accumulated within them (Piper and Savoye, 1993; Talling et al., 2013; Allin et al., 2016; Fildani, 2017; Mountjoy et al., 2018). This includes canyon muds and other deposits including levees, terrace and channel fill. If terrace deposits and levees are sites of preferential storage of deep-marine microplastics, as recent studies have suggested, then this flushing would potentially remobilize microplastics that are temporarily stored in these environments. Given the rates of decay cited for plastic

degradation, many of today's plastics may be around from 10s to upward of 1,000 years and consequently a large canyon flushing event could release a huge amount of non-degraded microplastic. Recent work on river transported microplastic has shown that flood events may flush river-bed microplastics; in the Mersey catchment (United Kingdom), winter flooding removed approximately 70% of the microplastic load stored in riverine sediments, and entirely removed microbeads at seven sites (Hurley et al., 2018). Whether all of this sediment was transported downstream or lighter particles were also delivered to the overbank, is unclear. Microplastics are anticipated to be equally prone to flushing in submarine environments. High-resolution seafloor surveys performed before and after a powerful (>7 ms^{-1}) turbidity current in the Monterey Canyon revealed that only the sandy axial channel (100–200 m width) was subjected to significant erosion (>3 m in places), while the more muddy canyon flanks showed no resolvable elevation difference (Paull et al., 2018). Thus, the influence of canyon flushing may be quite focused, ensuring more effective long-term microplastic sequestration in overbank areas.

Recent work focused on the distribution of different sediment gravity flow deposit types has shown that those with internal divisions of homogenous sediment deposited by transitional or laminar flow (e.g., hybrid beds), tend to occur in distal lobe settings that are less prone to erosion (e.g., Haughton et al., 2003), suggesting that plastics may be retained in the sedimentary deposit. In contrast, turbidites deposited within canyon or channel axes, that feature concentrations of lighter particles at the bed tops (e.g., low density turbidites), are prone to remobilization (e.g., Symons et al., 2016; Hage et al., 2018). The timescales of remobilization will depend upon the frequency and magnitude of successive seafloor flows.

Submarine Channels

Submarine channels are long-term conduits for sediment transport and extend from the canyon into the deeper basin, and terminate in lobe deposits beyond the channel mouth (Normark, 1970; Pickering et al., 1989; Mutti and Normark, 1991; Normark et al., 1997; Peakall et al., 2000; Jobe et al., 2015; Hansen et al., 2017). Channels may be bound at their margins by erosional surfaces or levees, or both (e.g., Clark and Pickering, 1996; Li P. et al., 2016). As much of their lifespan is dominated by bypass of turbidity currents, the deposits preserved at channel bases tend to be coarser particles and transient bedforms (e.g., Symons et al., 2016; Hunt, 2017; Hage et al., 2018). Microplastics will be both bypassed through the channel and spill over onto the internal levees and terraces, within a wider channel belt, and also onto the external levees bounding the channel system (Kane and Hodgson, 2011). Internal levees and terraces have moderate preservation potential but may still be prone to erosion by, and entrainment into large flows. External levees tend to have better preservation potential as overspilling flows tend to be relatively dilute (e.g., Piper and Normark, 1983). Vendettuoli et al. (2019) showed that over just 1 year, the average preservation of deposits across the active river-fed (fjord) Squamish submarine channel system was 11%, with much lower preservation in proximal parts of submarine channels, at the eroded flanks of channel bends, and at the channel-lobe transition zone (as low as 0% preservation). In thick turbidites of the same system, erosion by repeated turbidity currents tended to leave only the lowermost and coarsest fraction of individual beds in the channel axis, hence any other fines are reworked (Hage et al., 2018). On an even larger scale, intra-channel erosion by upstream-migrating knickpoints has been shown to result in poor preservation potential of deposits in the channel axis, while terraces and levees were sites of enhanced deposit preservation (Gales et al., 2018). In summary, channel axes are considered to be important conveyors of and temporary storage sites for microplastics, but it is levees and terraces that are the most likely hotspots for their long-term accumulation. To date there are no known studies of microplastics in this setting.

Submarine Lobes

Lobes represent the terminal parts of deep-water sediment routing systems and are repositories for the vast amount of mainly siliciclastic sediment transferred by channel systems (Normark, 1978; Walker, 1978; Nelson et al., 1992; Twichell et al., 1992; Gervais et al., 2006; Deptuck et al., 2008; Jegou et al., 2008; Saller et al., 2008; Prélat et al., 2009). Lobe bodies typically thin and become more fine-grained away from the feeder channel. The upper surfaces of lobes, in particular the distal parts, are commonly covered by mud and organic material transferred through the system (**Figure 7**). Repeated turbidity current activity on a lobe means that this lighter material will ultimately end up at the most distal parts of the lobe. Sedimentary facies broadly evolve from thick high density turbidites at the lobe axis, to thin low density turbidites at the lateral and distal fringes (e.g., Johnson et al., 2001; Hodgson et al., 2006). Transformation of turbidity currents into dense cohesive flows is common in these settings, as the fine cohesive material left on the seafloor is picked up and incorporated into incoming turbidity currents (Haughton et al., 2003; Hodgson, 2009; Talling et al., 2013; Kane et al., 2017; Southern et al., 2017; Spychala et al., 2017; Fildani et al., 2018). The deposits of these flows (hybrid beds) typically have an ungraded muddy-sand division which is rich in organic material; microplastics may be incorporated into these internal divisions and, being in a distal locality are less likely to be eroded by subsequent flows.

Repeated surveys of the submarine channel system in Lake Geneva indicate that, over a period of 125 years, channel-levees and the distal lobe account for 75% of stored sediment delivered to the system, but 52% of this was transported further toward more distal locations (16% of that was stored in the levees, and 37% on the lobe; Silva et al., 2018). Consequently, a significant proportion of sediment supplied by rivers ended up at the terminal lobe. This is similar to observations from the Squamish submarine channel system, where the lobes are generally sites of net accumulation (Hizzett et al., 2018; Vendettuoli et al., 2019). Overall, the distal fringes of lobes in major submarine sediment routing systems are considered to be likely hotspots for microplastic accumulation.

Abyssal Plains and Deep-Sea Trenches

The abyssal plain lies beyond the base of the continental slope, downslope of major submarine sediment routing systems.

Sedimentation rates are generally very low and dominated by pelagic settling, but in some cases influenced by the action of bottom currents (see section "Where Should We Expect Microplastics to Be Deposited Within Individual Deep-Sea Deposits?"), or interrupted infrequently by basin-wide emplacement of turbidites that initiated as submarine landslides (e.g., Rusnak and Nesteroff, 1963; Weaver and Rothwell, 1987; Clare et al., 2014). It has been suggested that bottom currents may transport plastics, particularly fibers, but the deposition of microplastics that have undergone biofouling or UV light degradation might be significant, as well as marine litter from shipping and fishing. Some of the samples analyzed by Van Cauwenberghe et al. (2013), Woodall et al. (2014), and Sanchez-Vidal et al. (2018) may be ascribed to the abyssal plain but the limited depositional context renders any further sedimentological analysis somewhat challenging.

The deepest reaches of the world's oceans, deep-sea trenches, occur along subduction plate boundaries and are sites of sediment accumulation. Deep-sea trench sediments have been shown to host disproportionately high quantities of microplastics (Fischer et al., 2015; Bergmann et al., 2017; Peng et al., 2018). Notably, Fischer et al. (2015) recorded plastic microfibers at depths of up to 5,766 m in the Kamchatka Trench and abyssal plain, with concentrations as high as 2,000 m^{-2}, and Peng et al. (2018) discovered microfiber levels as high as 1,600 pieces per liter of sediment at 10,903 m depth in the Mariana Trench. As these trenches are located large distances from any direct input, bottom currents and water column settling are considered to be the dominant processes for their transfer, but input arising from adjacent trench-slope failures may also make rare but significant contributions. Thin-skinned (cm-thick) but areally widespread slope failures have been shown to introduce large quantities of sediment (>0.1 km^3) and organic carbon (>1 Tg) to the Japan Trench (Kioka et al., 2019); hence might also be expected to remobilize previously buried microplastics.

Preservation Potential Summary

In general, proximal and high-energy environments, such as canyon and channel axes, are sites of sediment bypass rather than long-term storage (Stevenson et al., 2015). Microplastics in these settings will be transient and subject to downstream reworking. In areas where flows decelerate, and die out, such as on levees, terraces, and lobes, sediments and microplastics may be stored for longer time periods, or indefinitely. In the recent study of Martin et al. (2017), a depth of 4 cm was recommended to capture all of the microplastics in a deep-marine setting, however, in many deep-marine settings, microplastics may be much more deeply buried and the depositional environment needs consideration. No single rule fits all environments. For example, on the flanks of the upper Monterey Canyon, in their study of DDT pesticide distribution, Paull et al. (2002) recorded sedimentation rates of 0.6 cm/year; if no erosion took place since plastic production began, there may be areas where sediment thicknesses of 40 cm plus contain microplastics. In areas where large sandy turbidity currents are active, microplastic-bearing deposits may be tens of meters thick. Little is known regarding the transport of microplastics by bottom currents, but it seems highly likely that they are important agents for the redistribution of sediment gravity flow delivered microplastics across the global seafloor. Quiescent settings such as abyssal plains, and deep-sea trenches in particular, feature high preservation rates and are likely to be long-term deep-sea depositional sinks for microplastics.

Implications for Benthic Ecosystems

Despite their prevalence, the implications of the presence of microplastics on the seafloor are poorly understood – but it is thought that they are entering the food-chain via trophic transfer from benthic organisms (Ivar do Sul and Costa, 2007; Lusher, 2015; Rochman, 2015; GESAMP, 2016; Li W. C. et al., 2016; Taylor et al., 2016; United Nations Environment Programme [UNEP], 2016; Courtene-Jones et al., 2017; Fernandez-Arcaya et al., 2017; Näkki et al., 2017; Nelms et al., 2019). Microplastics may act as focal points for various toxins and hydrophobic compounds as demonstrated by Mato et al. (2001) who showed that PCB (polychlorinated biphenyls) concentration on polypropylene particles from offshore Japan was up to 10^6 higher than the surrounding seawater. These toxins may be concentrated in benthic organisms which consume them (Taylor et al., 2016; Courtene-Jones et al., 2017). Submarine canyons act to concentrate macrophyte and terrestrial organic matter, as well as other nutrients including those of an anthropogenic origin (e.g., Khripounoff et al., 2003; Pham et al., 2014). Oxygen and nutrient enrichment in modern channel and canyon environments has an influence on the benthic fauna that can be sustained. As an example, oxygen levels in La Jolla Canyon (offshore California) at 500 m depth are highly variable, averaging 1.37 ml/l but due to tidal oscillations range between 0.5 and 2.1 ml/l. In comparison, non-canyon areas at the same depth averaged 0.74 ml/l (Vetter and Dayton, 1998). Nutrient levels in the Congo fan are 100 times higher than the adjacent slope (Khripounoff et al., 2003). Seafloor sediment samples from Kaikoura Canyon, New Zealand, yielded an average of >500 individuals m^{-2} and a biomass of c. 1,300 g m^{-2}; adjacent slope environments yielded an average of <50 individuals m^{-2} and biomass of <100 g m^{-2} (Rex et al., 2006; De Leo et al., 2010). Similar scenarios have been reported from other canyons globally (e.g., Cunha et al., 2011). Due to this enrichment, submarine channels and canyons can contain a greater faunal density and/or biomass than adjacent non-channel/canyon regions of the slope or basin floor (Griggs et al., 1969; Vetter and Dayton, 1998; Gerino et al., 1999; De Leo et al., 2010; Duffy et al., 2013; Pham et al., 2014). As canyons are most likely repositories for microplastics (at least over decadal timescales), their critical role in marine ecosystems is potentially at risk.

The depth to which organisms burrow is also greater in more active parts of submarine sedimentary systems, as organisms burrow to find buried nutrients in the thicker deposits of these environments, and perhaps to evade evacuation by turbidity currents (Young et al., 1985; Wetzel, 1991; Gerino et al., 1999). It has recently been shown that bioturbation may extend into the subsurface by up to 8 m, which has implications for mixing of anthropogenic sediment with older sediment (Cobain et al., 2018). Many organisms have been shown to

consume microplastic particle and fibers, including polychaetes, molluscs including bivalves and brachiopods, echinoderms and copepods (e.g., Thompson et al., 2004; Ward and Shumway, 2004; Graham and Thompson, 2009; Cole et al., 2013). These particles can translocate into the tissue of organisms or be recycled in fecal pellets (Browne et al., 2008; von Moos et al., 2012). Taylor et al. (2016) shows evidence of microplastic (fiber) ingestion in the deep sea – from the mid-Atlantic and SW Indian Ocean. Various organisms showed accumulation of fibers within their tissues and hard parts. For example, a hermit crab from approximately 1,050 m depth in the SW Indian Ocean was found to yield five microfibers (Taylor et al., 2016). This is important as microplastics can concentrate organic pollutants and absorb metals which can then be consumed by marine organisms (Taylor et al., 2016). In a recent study of larger marine mammals washed up on United Kingdom beaches, all were found to have ingested microplastics; however, the pathways for trophic transfer remain unclear (Nelms et al., 2019). Some of this consumption could be accidental (e.g., by filter feeding), but some is likely transferred upward from benthic organisms which have been shown to ingest microplastics (e.g., Thompson et al., 2004; Ward and Shumway, 2004; Graham and Thompson, 2009; Claessens et al., 2013; Cole et al., 2013; Farrell and Nelson, 2013). In the Rockall Trough, of the 66 invertebrates identified, 48% had ingested microplastics in quantities comparable to coastal species (Courtene-Jones et al., 2017). Whilst it is clear that microplastics are entering the food chain, it is unclear how the depositional environments of microplastic accumulation are distributed, and how these relate to ecosystem variability. Therefore there is a pressing need to better integrate studies that address particulate transport, deep-sea microplastic sequestration and the resultant ecological implications.

SUMMARY AND CONCLUSION

The study of microplastics in deep-marine environments is in its infancy. While it has been shown that microplastics occur within seafloor sediments, the necessary sedimentological data to make meaningful predictions of the seafloor distribution of microplastics, such as grain size and mineralogy of the host sediment, specific depositional environment or seafloor current regimes, are currently lacking. Datasets which constrain microplastic input from the terrestrial realm, capture information on microplastics fed to deep-marine canyons and over the shelf edge by other means, and which document distributions in specific seafloor depositional environments, are essential in the development of process-product models for microplastic distribution. Experimental and physical models of microplastic behavior in sediment gravity flows are a vital step toward understanding the behavior in natural systems. The longevity of plastics in deep, cold, settings is poorly understood and an area requiring further research. Developing a basic understanding of the seafloor processes that control and modulate the distribution of microplastics is essential as we begin to understand their effect on benthic organisms and their passage into the trophic chain. The implications of ingested microplastics on fishing stocks as well as directly for human health are as-yet poorly understood, hence, a concerted research effort is required on multiple fronts. We hope some of the suggestions herein will contribute to addressing this global environmental crisis to address these and other societal and economic implications.

A Pressing Need to Understand the Processes by Which Microplastics Are Transported in the Deep-Sea

Microplastics pervade the modern day seafloor across the full range of marine environments. These light and highly mobile particles are delivered to the coast by rivers, wind and ice and to the sea surface from shipping and marine industries. The relative abundance of microplastics in submarine canyons and deep-sea trenches suggests that delivery of microplastics to the seafloor is strongly controlled by gravity currents (although this remains to be proven), and by settling from the surface through the water column, aided by densification processes such as mineral accretion and biofouling. Microplastic fragments, in particular, show an affinity with areas where macroplastics and marine litter are common (e.g., submarine canyons), while microfibers have a wider distribution and are likely to be transported easily by bottom currents. The role of redistribution by bottom currents is not well understood but we suggest that microplastics can be easily distributed far from direct input points such as major rivers.

Depositional and Post-depositional Processes Are Considered Strong Controls on the Ultimate Fate of Microplastics

Microplastics may be buried much deeper than is currently assumed. Sediment accumulation rates differ vastly according to depositional environment; hence in certain settings, microplastic-bearing sediments may be tens of meters thick and sampling the top few cm is therefore not always representative. Sediment preservation potential will dictate the storage time of microplastics at specific points within a submarine depositional system. Canyon and channel axes are prone to flushing and reworking, while levees, other overbank areas, and distal lobes are sites of lower disturbance, and hence enhanced preservation potential. The depth of microplastic burial as well as the density of those accumulations both influence bioavailability. While trophic transfer of these microplastics is highly likely, burrowing organisms are likely to mix the microplastic interface to deeper levels and the implications for the wider food web remain unclear. What is clear is that sites with high microplastic input are often foci for diverse and dense benthic communities. This is because the same seafloor flows flows that transfer the oxygen and nutrients that sustain them are also capable of transporting microplastics.

Future Recommendations

We have explained the important role different transport processes may play in the transport, accumulation density, and sequestration of microplastics in the deep-sea, yet few studies provide contextual information to enable detailed analysis nor to further develop predictive models. Future studies documenting microplastics on the seafloor should (at the very least) provide basic sedimentological information (grain size and mineralogy of the host sediment; depositional environment; water depth). These are all easily determined once a sample has been collected and should be provided alongside analytical information on microplastics (morphology, polymer type, size, shape, density, etc.). Better constraint on the sources (such as fluvial inputs) and the transfer route(s) of marine microplastics from shelf to deep sea is crucial in order to developed more robust global budgets for microplastics. Improved physical models to explain microplastic settling, and the behavior of fragments and fibers in thermohaline currents and gravity flows, will enable more effective microplastic transport models to be developed. These are required for global distribution models, to forecast future transport pathways, and potentially to inform mitigation strategies concerning their dispersal to critical offshore regions.

AUTHOR CONTRIBUTIONS

IK led on the review but both authors contributed equally to the writing and figure preparation.

FUNDING

MC was supported by the NERC National Capability CLASS Programme [Climate Linked Atlantic Sector Science Programme (No. NE/R015953/1)].

ACKNOWLEDGMENTS

This work was conducted as part of a joint Manchester University-NOC project – SCaMpI (Seafloor Currents and Micro-Plastics Investigation). We acknowledge the constructive reviews of the reviewers, RB and AG, and the useful summary and review by the editor DH. We also thank Thomas Bishop and John Moore (School of Geography, University of Manchester) for technical assistance with extraction of microplastics shown in **Figure 1**.

REFERENCES

Aller, R. C., and Blair, N. E. (2006). Carbon remineralization in the Amazon–Guianas tropical mobile mudbelt: a sedimentary incinerator. *Cont. Shelf Res.* 26, 2241–2259.

Allin, J. R., Hunt, J. E., Talling, P. J., Clare, M. A., Pope, E., and Masson, D. G. (2016). Different frequencies and triggers of canyon filling and flushing events in Nazaré Canyon, offshore Portugal. *Mar. Geol.* 371, 89–105.

Alomar, C., Estarellas, F., and Deudero, S. (2016). Microplastics in the Mediterranean Sea: deposition in coastal shallow sediments, spatial variation and preferential grain size. *Mar. Environ. Res.* 115, 1–10. doi: 10.1016/j.marenvres.2016.01.005

Amy, L. A., Talling, P. J., Edmonds, V. O., Sumner, E. J., and Lesueur, A. (2006). An experimental investigation of sand– mud suspension settling behaviour: implications for bimodal mud contents of submarine flow deposits. *Sedimentology* 53, 1411–1434.

Andrady, A. L. (2011). Microplastics in the marine environment. *Mar. Pollut. Bull.* 62, 1596–1605. doi: 10.1016/j.marpolbul.2011.05.030

Andrady, A. L., and Neal, M. A. (2009). Applications and societal benefits of plastics. *Philos. Trans. R. Soc. B Biol. Sci.* 364, 1977–1984. doi: 10.1098/rstb.2008.0304

Arthur, C., Baker, J. E., and Bamford, H. (eds) (2009). *Proceedings of the International Research Workshop on the Occurrence, Effects and Fate of Microplastic Marine Debris*, September 9–11, 2008. NOAA Technical Memorandum NOS-ORandR-30.

Ayranci, K., Lintern, D. G., Hill, P. R., and Dashtgard, S. E. (2012). Tide-supported gravity flows on the upper delta front, Fraser River delta, Canada. *Mar. Geol.* 326, 166–170.

Azpiroz-Zabala, M., Cartigny, M. J. B., Talling, P. J., Parsons, D. R., Sumner, E. J., Clare, M. A., et al. (2017). Newly recognized turbidity current structure can explain prolonged flushing of submarine canyons. *Sci. Adv.* 3:e1700200.

Baas, J. H., and Best, J. L. (2002). Turbulence modulation in clay-rich sediment-laden flows and some implications for sediment deposition. *J. Sediment. Res.* 72, 336–340.

Babonneau, N., Savoye, B., Cremer, M., and Klein, B. (2002). Morphology and architecture of the present canyon and channel system of the Zaire deep-sea fan. *Mar. Pet. Geol.* 19, 445–467.

Baker, M. L., Baas, J. H., Malarkey, J., Silva, R., Craig, M. J., Kane, I. A., et al. (2017). The effect of clay type on the properties of cohesive sediment gravity flows and their deposits. *J. Sediment. Res.* 87, 1176–1195. doi: 10.2110/jsr.2017.63

Ballent, A., Pando, S., Purser, A., Juliano, M. F., and Thomsen, L. (2013). Modelled transport of benthic marine microplastic pollution in Nazare Canyon. *Biogeosciences* 10, 7957–7970.

Barboza, L. G. A., Vethaak, A. D., Lavorante, B. R., Lundebye, A. K., and Guilhermino, L. (2018). Marine microplastic debris: an emerging issue for food security, food safety and human health. *Mar. Pollut. Bull.* 133, 336–348. doi: 10.1016/j.marpolbul.2018.05.047

Barnes, D. K. A., Galgani, F., Thompson, R. C., and Barlaz, M. (2009). Accumulation and fragmentation of plastic debris in global environments. *Philos. Trans. R. Soc. Lond. B Biol. Sci.* 364, 1985–1998. doi: 10.1098/rstb.2008.0205

Belcher, A., Henson, S. A., Manno, C., Hill, S. L., Atkinson, A., Thorpe, S. E., et al. (2019). Krill faecal pellets drive hidden pulses of particulate organic carbon in the marginal ice zone. *Nat. Commun.* 10:889. doi: 10.1038/s41467-019-08847-1

Bergmann, M., and Klages, M. (2012). Increase of litter at the Arctic deep-sea observatory HAUSGARTEN. *Mar. Pollut. Bull.* 64, 2734–2741. doi: 10.1016/j.marpolbul.2012.09.018

Bergmann, M., Wirzberger, V., Krumpen, T., Lorenz, C., Primpke, S., Tekman, M. B., et al. (2017). High Quantities of Microplastic in Arctic Deep-Sea Sediments from the HAUSGARTEN Observatory. *Environ. Sci. Technol.* 51, 11000–11010. doi: 10.1021/acs.est.7b03331

Biscara, L., Hanquiez, V., Leynaud, D., Marieu, V., Mulder, T., Gallissaires, J. M., et al. (2012). Submarine slide initiation and evolution offshore Pointe Odden, Gabon—Analysis from annual bathymetric data (2004–2009). *Mar. Geol.* 299, 43–50.

Blum, M., Rogers, K., Gleason, J., Najman, Y., Cruz, J., and Fox, L. (2018). Allogenic and autogenic singlans in the stratigraphic record of the deep-se Bengal Fan. *Sci. Rep.* 8:7973. doi: 10.1038/s41598-018-25819-5

Bouma, A. H. (1962). *Sedimentology of Some Flysch Deposits: A Graphic Approach to Facies Interpretation*. Amsterdam: Elsevier, 168.

Booth, J. S., O'Leary, D. W., Popenoe, P., and Danforth, W. W., (1993). "U.S. Atlantic continental slope landslides: their distribution, general attributes, and implications," in *Submarine landslides: Selected studies in the U.S. Exclusive*

Economic Zone: U.S. Geological Survey Bulletin no. 2002, eds W. C. Schwab, H. J. Lee, D. C. Twichell (Denver, CO: U.S Department of interior), 14–22.

Browne, M. A., Crump, P., Niven, S. J., Teuten, E., Tonkin, A., Galloway, T., et al. (2011). Accumulation of microplastic on shorelines woldwide: sources and sinks. *Environ. Sci. Technol.* 45, 9175–9179. doi: 10.1021/es201811s

Browne, M. A., Dissanayake, A., Galloway, T. S., Lowe, D. M., and Thompson, R. C. (2008). Ingested microscopic plastic translocates to the circulatory system of the mussel, *Mytilus edulis* (L.). *Environ. Sci. Technol.* 42, 5026–5031.

Browne, M. A., Galloway, T. S., and Thompson, R. C. (2010). Spatial patterns of plastic debris along estuarine shorelines. *Environ. Sci. Technol.* 44, 3404–3409. doi: 10.1021/es903784e

Buchanan, J. B. (1971). Pollution by synthetic fibres. *Mar. Pollut. Bull.* 2:23.

Buhl-Mortensen, L., and Buhl-Mortensen, P. (2017). Marine litter in the Nordic Seas: distribution composition and abundance. *Mar. Pollut. Bull.* 125, 260–270. doi: 10.1016/j.marpolbul.2017.08.048

Carpenter, E. J., Anderson, S. J., Harvey, G. R., Miklas, H. P., and Peck, B. B. (1972). Polystyrene spherules in coastal waters. *Science* 178, 749–750.

Carpenter, E. J., and Smith, K. L. (1972). Plastics on the Sargasso sea surface. *Science* 175, 1240–1241.

Carter, L., Milliman, J. D., Talling, P. J., Gavey, R., and Wynn, R. B. (2012). Near-synchronous and delayed initiation of long run-out submarine sediment flows from a record-breaking river flood, offshore Taiwan. *Geophys. Res. Lett.* 39:12.

Chiba, S., Saitoc, H., Fletcher, R., Yogid, T., Kayod, M., Miyagid, S., et al. (2018). Human footprint in the abyss: 30 year records of deep-sea plastic debris. *Mar. Policy* 96, 204–212.

Chubarenko, I., Bagaiev, A., Zobkov, M., and Esiukova, E. (2016). On some physical and dynamical properties of microplastic particles in marine environment. *Mar. Pollut. Bull.* 108, 105–112. doi: 10.1016/j.marpolbul.2016.04.048

Chubarenko, I. P., Esiukova, E. E., Bagaev, A. V., and Grave, A. N. (2018). Three-dimensional distribution of anthropogenic microparticles in the body of sandy beaches. *Sci. Total Environ.* 628, 1340–1351.

Claessens, M., De Meester, S., Van Landuyt, L., De Clerck, K., and Janssen, C. R. (2011). Occurrence and distribution of microplastics in marine sediments along the Belgian coast. *Mar. Pollut. Bull.* 62, 2199–2204. doi: 10.1016/j.marpolbul.2011.06.030

Claessens, M., Van Cauwenberghe, L., Vandegehuchte, M. B., and Janssen, C. R. (2013). New techniques for the detection of microplastics in sediments and field collected organisms. *Mar. Pollut. Bull.* 70, 227–233. doi: 10.1016/j.marpolbul.2013.03.009

Clare, M. A., Hughes Clarke, J. E., Talling, P. J., Cartigny, M. J., and Pratomo, D. G. (2016). Preconditioning and triggering of offshore slope failures and turbidity currents revealed by most detailed monitoring yet at a fjord-head delta. *Earth Planet. Sci. Lett.* 450, 208–220.

Clare, M. A., Talling, P. J., Challenor, P., Malgesini, G., and Hunt, J. (2014). Distal turbidites reveal a common distribution for large (0.1 km3) submarine landslide recurrence. *Geology* 42, 263–266.

Clare, M. A., Vardy, M. E., Cartigny, M. J., Talling, P. J., Himsworth, M. D., Dix, J. K., et al. (2017). Direct monitoring of active geohazards: emerging geophysical tools for deep-water assessments. *Near Surf. Geophys.* 15, 427–444.

Clark, J. D., and Pickering, K. T. (1996). Architectural elements and growth patterns of submarine channels: application to hydrocarbon exploration. *AAPG Bull.* 80, 194–220.

Cobain, S. L., Hodgson, D. M., Peakall, J., Wignall, P. B., and Cobain, M. R. D. (2018). A new macrofaunal limit in the deep biosphere revealed by extreme burrow depths in ancient sediments. *Sci. Rep.* 8:261. doi: 10.1038/s41598-017-18481-w

Cole, M., Lindeque, P., Fileman, E., Halsband, C., Goodhead, R., Moger, J., et al. (2013). 'Microplastic Ingestion by Zooplankton'. *Environ. Sci. Technol.* 47, 6646–6655. doi: 10.1021/es400663f

Cole, M., Lindeque, P., Halsband, C., and Galloway, T. S. (2011). Microplastics as contaminants in the marine environment: a review. *Mar. Pollut. Bull.* 62, 2588–2597. doi: 10.1016/j.marpolbul.2011.09.025

Cole, M., Lindeque, P. K., Fileman, E., Clark, J., Lewis, C., Halsband, C., et al. (2016). Microplastics alter the properties and sinking rates of zooplankton faecal pellets. *Environ. Sci. Technol.* 50, 3239–3246. doi: 10.1021/acs.est.5b05905

Colton, J. B. Jr., Knapp, F. D., and Burns, B. R. (1974). Plastic particles in surface waters of the northwestern Atlantic. *Science* 185, 491–497.

Corcoran, P. L., Jazvac, K., and Ballent, A. (2017). "Plastics and the anthropocene," in *Encyclopedia of the Anthropocene*, Vol. 2, eds D. A. DellaSala and M. I. Goldstein (Amsterdam: Elsevier).

Corcoran, P. L., Norris, T., Ceccanese, T., Walzak, M. J., Helm, P. A., and Marvin, C. H. (2015). Hidden plastics of Lake Ontario: Canada and their potential preservation in the sediment record. *Environ. Pollut.* 204, 17–25. doi: 10.1016/j.envpol.2015.04.009

Cosgrove, G. I. E., Hodgson, D. M., Poyatos-Moré, M., Mountney, N. P., and McCaffrey, W. D. (2018). Filter or conveyor? Establishing relationships between clinoform rollover trajectory, sedimentary process regime, and grain character within intrashelf clinothems, offshore New Jersey, U.S.A. *J. Sediment. Res.* 88, 917–941. doi: 10.2110/jsr.2018.44

Costa, M. F., and Barletta, M. (2015). Microplastics in coastal and marine environments of the western tropical and sub-tropical Atlantic Ocean Environ. *Sci. Process. Impacts* 17, 1868–1879. doi: 10.1039/c5em00158g

Courtene-Jones, W., Quinn, B., Gary, S. F., Mogg, A. O., and Narayanaswamy, B. E. (2017). Microplastic pollution identified in deep-sea water and ingested by benthic invertebrates in the Rockall Trough, North Atlantic Ocean. *Environ. Pollut.* 231, 271–280. doi: 10.1016/j.envpol.2017.08.026

Covault, J. A., Normark, W. R., Romans, B. W., and Graham, S. A. (2007). Highstand fans in the California borderland: the overlooked deep-water depositional systems. *Geology* 35, 783–786.

Cózar, A., Echevarria, F., Gonzalez-Gordillo, J. I., Irigoien, X., Úbeda, B., Hernandez-Leon, S., et al. (2014). Plastic debris in the open ocean. *Proc. Natl. Acad. Sci. U.S.A.* 111, 10239–10244. doi: 10.1073/pnas.1314705111

Cunha, M. R., Paterson, G. L., Amaro, T., Blackbird, S., de Stigter, H. C., Ferreira, C., et al. (2011). Biodiversity of macrofaunal assemblages from three Portuguese submarine canyons (NE Atlantic). *Deep Sea Res. Part 2 Top. Stud. Oceanogr.* 58, 2433–2447.

Davies, J. R., Fletcher, C. J. N., Waters, R. A., and Wilson, D. (1997). *Geology of the Country Around Llanilar and Rhayader. Memoir of the British Geological Survey, Sheets 178 & 179*. London: The Stationery Office.

De Leo, F. C., Smith, C. R., Rowden, A. A., Bowden, D. A., and Clark, M. R. (2010). Submarine canyons: hotspots of benthic biomass and productivity in the deep sea. *Proc. R. Soc. B Biol. Sci.* 277, 2783–2792. doi: 10.1098/rspb.2010.0462

Dekiff, J. H., Remy, D., Klasmeier, J., and Fries, E. (2014). Occurrence and spatial distribution of microplastics in sediments from Norderney. *Environ. Pollut.* 186, 248–256. doi: 10.1016/j.envpol.2013.11.019

Deptuck, M. E., Piper, D. J. W., Savoye, B., and Gervais, A. (2008). Dimensions and architecture of late Pleistocene submarine lobes off the northern margin of East Corsica. *Sedimentology* 55, 869–898.

Dietrich, W. E. (1982). Settling velocity of natural particles. *Water Resour. Res.* 18, 1615–1626.

Doyle, M. J., Watson, W., Bowlin, N. M., and Sheavly, S. B. (2011). Plastic particles in coastal pelagic ecosystems of the Northeast Pacific ocean. *Mar. Environ. Res.* 71, 41–52. doi: 10.1016/j.marenvres.2010.10.001

Dubaish, F., and Liebezeit, G. (2013). Suspended microplastics and black carbon particles in the Jade system, southern North Sea. *Water Air Soil Pollut.* 224:1352.

Duffy, G. A., Lundsten, L., Kuhnz, L. A., and Paull, C. K. (2013). A comparison of megafaunal communities in five submarine canyons off southern California, USA. *Deep-Sea Res. 2 Top. Stud.* Oceanogr. 104, 259–266. doi: 10.1016/j.dsr2.2013.06.002

Eidam, E. F., Ogston, A. S., and Nittrouer, C. A. (2019). Formation and removal of a coastal flood deposit. *J. Geophys. Res. Oceans* 124, 1045–1062.

Eriksen, M., Lebreton, L. C. M., Carson, H. S., Thief, M., Moore, C. J., Borerro, J. C., et al. (2014). Plastic pollution in the world's oceans: more than 5 trillion plastic pieces weighing over 250,000 tons afloat at Sea. *PLoS One* 9:e111913. doi: 10.1371/journal.pone.0111913

Farrell, P., and Nelson, K. (2013). Trophic level transfer of microplastic: *Mytilus edulis* (L.) to *Carcinus maenas* (L.). *Environ. Pollut.* 177, 1–3. doi: 10.1016/j.envpol.2013.01.046

Faugères, J.-C., Mézerais, M. L., and Stow, D. A. V. (1993). Contourite drift types and their distribution in the North and South Atlantic Ocean basins. *Sediment. Geol.* 82, 189–203.

Fazey, F. M., and Ryan, P. G. (2016). Biofouling on buoyant marine plastics: an experimental study into the effect of size on surface longevity. *Environ Pollut.* 210, 354–360. doi: 10.1016/j.envpol.2016.01.026

Fendall, L. S., and Sewell, M. A. (2009). Contributing to marine pollution by washing your face: microplastics in facial cleansers. *Mar. Pollut. Bull.* 58, 1225–1228. doi: 10.1016/j.marpolbul.2009.04.025

Ferguson, R. I., and Church, M. (2004). A simple universal equation for grain settling velocity. *J. Sediment. Res.* 74, 933–937. doi: 10.1306/051204740933

Fernandez-Arcaya, U., Ramirez-Llodra, E., Aguzzi, J., Allcock, A. L., Davies, J. S., Dissanayake, A., et al. (2017). Ecological role of submarine canyons and need for canyon conservation: a review. *Front. Mar. Sci.* 4:5. doi: 10.3389/fmars.2017.00005

Fildani, A. (2017). Submarine canyons: a brief review looking forward. *Geology* 45, 383–384.

Fildani, A., Clark, J., Covault, J. A., Power, B., Romans, B. W., and Aiello, I. W. (2018). Muddy sand and sandy mud on the distal Mississippi fan: Implications for lobe depositional processes. *Geosphere* 14, 1051–1066. doi: 10.1130/GES01580.1

Fischer, V., Elsner, N. O., Brenke, N., Schwabe, E., and Brandt, A. (2015). Plastic pollution of the Kuril–Kamchatka Trench area (NW pacific). *Deep Sea Res. Part 2 Top. Stud. Oceanogr.* 111, 399–405. doi: 10.1016/j.dsr2.2014.08.012

Gales, J. A., Talling, P. J., Cartigny, M. J., Hughes Clarke, J., Lintern, G., Stacey, C., et al. (2018). What controls submarine channel development and the morphology of deltas entering deep-water fjords? *Earth Surf. Process. Landf.* 44, 535–551.

Galgani, F., Hanke, G., and Maes, T. (2015). "Global distribution, composition and abundance of marine litter," in *Marine Anthropogenic Litter*, eds M. Bergmann, L. Gutow, and M. Klages (Cham: Springer), 29–56.

Gall, S. C., and Thompson, R. C. (2015). The impact of debris on marine life. *Mar. Pollut. Bull.* 92, 170–179. doi: 10.1016/j.marpolbul.2014.12.041

Galloway, T. S. (2015). "Micro-and nano-plastics and human health," in *Marine Anthropogenic Litter*, eds M. Bergmann, L. Gutow, and M. Klages (Cham: Springer), 343–366.

Galloway, W. E., Whiteaker, T. L., and Ganey-Curry, P. E. (2013). History of Cenozoic North American drainage basin evolution, sediment yield, and accumulation in the Gulf of Mexico basin. *Geosphere* 7, 938–973. doi: 10.1130/GES00647.1

Galy, V., France-Lanord, C., Beyssac, O., Faure, P., Kudrass, H., and Palhol, F. (2007). Efficient organic carbon burial in the Bengal fan sustained by the Himalayan erosional system. *Nature* 450:407.

Gerino, M., Stora, G., and Weber, O. (1999). Evidence of bioturbation in the Cap-Ferret Canyon in the deep northeastern Atlantic. *Deep Sea Res. Part 2 Top. Stud. Oceanogr.* 46, 2289–2307.

Gervais, A., Savoye, B., Mulder, T., and Gonthier, E. (2006). Sandy modern turbidite lobes: a new insight from high resolution seismic data. *Mar. Petrol. Geol* 23, 485–502.

GESAMP (2016). "Sources, fate and effects of microplastics in the marine environment: part two of a global assessment," in *(IMO/FAO/ UNESCO-IOC/UNIDO/WMO/IAEA/UN/UNEP/UNDP Joint Group of Experts on the Scientific Aspects of Marine Environmental Protection)*, (GESAMP Reports & Studies No 93, eds P. J. Kershaw and C. M. Rochman (London: GESAMP).

Geyer, R., Jambeck, J. R., and Law, K. L. (2017). Production, use, and fate of all plastics ever made. *Sci. Adv.* 3:e1700782. doi: 10.1126/sciadv.1700782

Goldberg, E. D. (1997). Plasticizing the seafloor: an overview. *Environ. Technol.* 18, 195–201.

Graca, B., Szewc, K., Zakrzewska, D., Dołęga, A., and Szczerbowska-Boruchowska, M. (2017). Sources and fate of microplastics in marine and beach sediments of the Southern Baltic Sea—a preliminary study. *Environ Sci Pollut Res.* 24, 7650–7661. doi: 10.1007/s11356-017-8419-5

Graham, E. R., and Thompson, J. T. (2009). Deposit- and suspension-feeding sea cucumbers (Echinodermata) ingest plastic fragments. *J. Exp. Mar. Biol. Ecol.* 368, 22–29.

Gregory, M. R. (1978). Accumulation and distribution of virgin plastic granules on New Zealand beaches. *N. Z. J. Mar. Freshw. Res.* 12, 399–414.

Gregory, M. R. (2009). Environmental implications of plastic debris in marine settings-entanglement, ingestion, smothering, hangers-on, hitch-hiking and alien invasions. *Philos. Trans. R. Soc. B Biol. Sci.* 364, 2013–2025. doi: 10.1098/rstb.2008.0265

Griggs, G. B., Carey, A. G. Jr., and Kulm, L. D. (1969). Deep-sea sedimentation and sediment-fauna interaction in Cascadia Channel and on Cascadia Abyssal Plain. *Deep Sea Res. Oceanogr.* Abstr. 16, 157–170.

Gwiazda, R., Paull, C. K., Ussler, W. III, and Alexander, C. R. (2015). Evidence of modern fine-grained sediment accumulation in the Monterey Fan from measurements of the pesticide DDT and its metabolites. *Mar. Geol.* 363, 125–133.

Hage, S., Cartigny, M. J., Clare, M. A., Sumner, E. J., Vendettuoli, D., Hughes Clarke, J. E., et al. (2018). How to recognize crescentic bedforms formed by supercritical turbidity currents in the geologic record: Insights from active submarine channels. *Geology* 46, 563–566.

Hansen, L., Janocko, M., Kane, I. A., and Kneller, B. C. (2017). Submarine channel evolution, terrace development, and preservation of intra-channel thin-bedded turbidites: Mahin and Avon channels, offshore Nigeria. *Mar. Geol.* 383, 146–167. doi: 10.1016/j.margeo.2016.11.011

Hansen, L. A., Callow, R. H., Kane, I. A., Gamberi, F., Rovere, M., Cronin, B. T., et al. (2015). Genesis and character of thin-bedded turbidites associated with submarine channels. *Mar. Pet. Geol.* 67, 852–879.

Hardesty, B. D., Harari, J., Isobe, A., Lebreton, L., Maximenko, N., Potemra, J., et al. (2017). Using Numerical Model Simulations to Improve the Understanding of Micro-plastic Distribution and Pathways in the Marine Environment. *Front. Mar. Sci.* 4:30. doi: 10.3389/fmars.2017.00030

Haughton, P. D. W., Barker, S. P., and McCaffrey, W. D. (2003). 'Linked' debrites in sand-rich turbidite systems – origin and significance. *Sedimentology* 50, 459–482.

Hiscott, R. N. (1994). Loss of capacity, not competence, as the fundamental process governing deposition from turbidity currents. *J. Sediment. Res.* 64, 209–214.

Hizzett, J. L., Hughes Clarke, J. E., Sumner, E. J., Cartigny, M. J. B., Talling, P. J., and Clare, M. A. (2018). Which triggers produce the most erosive, frequent, and longest runout turbidity currents on deltas? *Geophys. Res. Lett.* 45, 855–863.

Hodgson, D. M. (2009). Distribution and origin of hybrid beds in sand-rich submarine fans of the Tanqua depocentre, Karoo Basin, South Africa. *Mar. Pet. Geol.* 26, 1940–1956.

Hodgson, D. M., Browning, J. V., Miller, K. G., Hesselbo, S. P., Poyatos-Moré, M., Mountain, G. S., et al. (2018a). Sedimentology, stratigraphic context, and implications of Miocene intrashelf bottomset deposits, offshore New Jersey. *Geosphere* 141, 95–114.

Hodgson, D. M., Bernhardt, A., Clare, M., Silva, A., Fosdick, J., Mauz, B., et al. (2018b). Grand Challenges (and Great Opportunities) in Sedimentology, Stratigraphy, and Diagenesis Research. *Front. Earth Sci.* 6:173. doi: 10.3389/feart.2018.00173

Hodgson, D. M., Flint, S. S., Hodgetts, D., Drinkwater, N. J., Johannessen, E. P., and Luthi, S. M. (2006). Stratigraphic evolution of fine-grained submarine fan systems, Tanqua depocenter, Karoo Basin, South Africa. *J. Sediment. Res.* 76, 20–40. doi: 10.2110/jsr.2006.03

Högberg, S. M., Åkerstedt, H. O., Lundström, T. S., and Freund, J. B. (2010). Respiratory deposition of fibers in the non-inertial regime—development and application of a semi-analytical model. *Aerosol Sci. Technol.* 44, 847–860. doi: 10.1080/02786826.2010.498455

Horton, A. A., and Dixon, S. J. (2017). Microplastics: an introduction to environmental transport processes. *WIREs Water* 2018:e1268. doi: 10.1002/wat2.1268

Horton, A. A., Svendsen, C., Williams, R. J., Spurgeon, D. J., and Lahive, E. (2017). Large microplastic particles in sediments of tributaries of the River Thames, UK—abundance, sources and methods for effective quantification. *Mar. Pollut. Bull.* 114, 218–226. doi: 10.1016/j.marpolbul.2016.09.004

Hunt, J. E. (2017). Identifying and quantifying erosion beneath the deposits of long-runout turbidity currents along their pathway. *Mar. Geol.* 389, 32–51.

Hurley, R., Woodward, J., and Rothwell, J. R. (2018). Microplastic contamination of river beds significantly reduced by catchment-wide flooding. *Nat. Geosci.* 11, 251–257.

Ilstad, T., Elverhøi, A., Issler, D., and Marr, J. G. (2004). Subaqueous debris flow behaviour and its dependence on the sand/clay ratio: a laboratory study using particle tracking. *Mar. Geol.* 213, 415–438.

Inman, D. L., Nordstrom, C. E., and Flick, R. E. (1976). Currents in submarine canyons: an air-sea-land interaction. *Annu. Rev. Fluid Mech.* 8, 275–310.

Ivar do Sul, J. A., and Costa, M. F. (2007). Marine debris review for Latin America and the wider Caribbean region: from the 1970s until now, and where do we go from here? *Mar. Pollut. Bull.* 54, 1087–1104. doi: 10.1016/j.marpolbul.2007.05.004

Jambeck, J. R., Geyer, R., Wilcox, C., Siegler, T. R., Perryman, M., Andrady, A., et al. (2015). Plastic waste inputs from land into the ocean. *Science* 347, 768–771. doi: 10.1126/science.1260352

Jegou, I., Savoye, B., Pirmez, C., and Droz, L. (2008). Channel-mouth lobe complex of the recent Amazon Fan: the missing piece. *Mar. Geol.* 252, 62–77.

Jobe, Z., Sylvester, N., Parker, A. O., Howes, N., Slowey, N., and Pirmez, C. (2015). Rapid adjustment of submarine channel architecture to changes in sediment supply. *J. Sediment. Res.* 85, 729–753.

Johnson, S. D., Flint, S., Hinds, D., and Wickens, H. D. V. (2001). Anatomy, geometry and sequence stratigraphy of basin floor to slope turbidite systems, Tanqua Karoo, South Africa. *Sedimentology* 48, 987–1023.

Kaiser, D., Kowlaski, N., and Waniek, J. J. (2017). Effects of biofouling on the sinking behavior of microplastics. *Environ. Res. Lett.* 12:124003. doi: 10.1016/j.envpol.2018.07.131

Kane, I., and Hodgson, D. (2011). Sedimentological criteria to differentiate submarine channel levee sub-environments: exhumed examples from the Rosario Fm. (Upper Cretaceous) of Baja California, Mexico, and the Fort Brown Fm. (Permian), Karoo Basin. *S. Africa. Mar. Pet. Geol.* 28, 807–823.

Kane, I., Kneller, B., Dykstra, M., Kassem, A., and McCaffrey, W. D. (2007). Anatomy of a submarine channel–levee: an example from Upper Cretaceous slope sediments, Rosario Formation, Baja California, Mexico. *Mar. Pet. Geol.* 24, 540–563. doi: 10.1016/j.marpetgeo.2007.01.003

Kane, I. A., and Pontén, A. S. M. (2012). Submarine transitional flow deposits in the Paleogene Gulf of Mexico. *Geology* 40, 1119–1122.

Kane, I. A., Pontén, A. S. M., Vangdal, B., Eggenhuisen, J. T., Hodgson, D. M., and Spychala, Y. T. (2017). The stratigraphic record and processes of turbidity current transformation across deep-marine lobes. *Sedimentology* 64, 1236–1273. doi: 10.1111/sed.12346

Kanhai, L. D. K., Johansson, C., Frias, J. P. G. L., Gardfeldt, K., Thompson, R. C., and O'Connor, I. (2019). Deep sea sediments of the Arctic Central Basin: a potential sink for microplastics. *Deep Sea Res. Part I Oceanogr. Res. Pap.* 145, 137–142. doi: 10.1016/j.dsr.2019.03.003

Khatmullina, L., and Isachenko, I. (2017). Settling velocity of microplastic particles of irregular shapes. *Mar. Pollut. Bull.* 114, 871–880. doi: 10.1016/j.marpolbul.2016.11.024

Khripounoff, A., Vangriesheim, A., Babonneau, N., Crassous, P., Dennielou, B., and Savoye, B. (2003). Direct observation of intense turbidity current activity in the Zaire submarine valley at 4000 m water depth. *Mar. Geol.* 194, 151–158.

Khripounoff, A., Vangriesheim, A., Crassous, P., and Etoubleau, J. (2009). High frequency of sediment gravity flow events in the Var submarine canyon (Mediterranean Sea). *Mar. Geol.* 263, 1–6.

Kineke, G. C., Woolfe, K. J., Kuehl, S. A., Milliman, J. D., Dellapenna, T. M., and Purdon, R. G. (2000). Sediment export from the Sepik River, Papua New Guinea: evidence for a divergent sediment plume. *Cont. Shelf Res.* 20, 2239–2266.

Kioka, A., Schwestermann, T., Moernaut, J., Ikehara, K., Kanamatsu, T., McHugh, C. M., et al. (2019). Megathrust earthquake drives drastic organic carbon supply to the hadal trench. *Sci. Rep.* 9:1553. doi: 10.1038/s41598-019-38834-x

Klein, S., Worch, E., and Knepper, T. P. (2015). Occurrence and spatial distribution of microplastics in river shore sediments of the Rhine-Main area in Germany. *Environ. Sci. Technol.* 49, 6070–6076.

Kneller, B. C. (1995). "Beyond the turbidite paradigm; physical models for deposition of turbidites and their implications for reservoir prediction," in *Characterization of Deep Marine Clastic Systems. Geological Society*, eds A. Hartley and J. Prosser (London: Special Publications), 31–49.

Kneller, B. C., and Branney, M. J. (1995). Sustained high-density turbidity currents and the deposition of thick massive sands. *Sedimentology* 42, 607–616.

Kowalski, N., Reichardt, A. M., and Waniek, J. J. (2016). Sinking rates of microplastics and potential implications of their alteration by physical, biological, and chemical factors. *Mar. Pollut. Bull.* 109, 310–319. doi: 10.1016/j.marpolbul.2016.05.064

Kuo, M., and Bolton, M. (2013). The nature and origin of deep ocean clay crust from the Gulf of Guinea. *Géotechnique* 63, 500–509.

Lebreton, L. C., Van der Zwet, J., Damsteeg, J. W., Slat, B., Andrady, A., and Reisser, J. (2017). River plastic emissions to the world's oceans. *Nat. Commun.* 8:15611. doi: 10.1038/ncomms15611

Lee, I.-H., Lien, R.-C., Liu, J. T., and Chuang, W. S. (2009). Turbulent mixing and internal tides in Gaoping (Kaoping) Submarine Canyon, Taiwan. *J. Mar. Syst.* 76, 383–396.

Leslie, H. A., Brandsma, S. H., van Velzena, M. J. M., and Vethaak, A. D. (2017). Microplastics en route: Field measurements in the Dutch river delta and Amsterdam canals, wastewater treatment plants, North Sea sediments and biota. *Environ. Int.* 101, 133–142. doi: 10.1016/j.envint.2017.01.018

Li, P., Kneller, B. C., Hansen, L., and Kane, I. A. (2016). The classical turbidite outcrop at San Clemente, California, revisited: an example of sandy submarine channels with asymmetric facies architecture. *Sediment. Geol.* 346, 1–16.

Li, W. C., Tse, H. F., and Fok, L. (2016). Plastic waste in the marine environment: a review of sources, occurrence and effects. *Sci. Total Environ.* 566-567, 333–349. doi: 10.1016/j.scitotenv.2016.05.084

Lobelle, D., and Cunliffe, M. (2011). Early microbial biofilm formation on marine plastic debris. *Mar. Pollut. Bull.* 62, 197–200. doi: 10.1016/j.marpolbul.2010.10.013

Long, M., Moriceau, B., Gallinari, M., Lambert, C., Huvet, A., Raffray, J., et al. (2015). Interactions between microplastics and phytoplankton aggregates: impact on their respective fates. *Mar. Chem.* 175, 39–46.

Lowe, D. R. (1982). Sediment gravity flows: II. Depositional models with special reference to the deposits of high- density turbidity currents. *J. Sediment. Petrol.* 52, 279–297.

Lusher, A. L. (2015). "Microplastics in the marine environment: distribution, interactions and effects," in *Marine Anthropogenic Litter*, eds M. Bergmann, L. Gutow, and M. Klages (Berlin: Springer), 245–307.

Maes, T., Barry, J., Leslie, H. A., Vethaak, A. D., Nicolaus, E. E. M., Law, R. J., et al. (2018). Below the surface: Twenty-five years of seafloor litter monitoring in coastal seas of North West Europe (1992–2017). *Sci. Total Environ.* 630, 790–798. doi: 10.1016/j.scitotenv.2018.02.245

Maes, T., Van der Meulen, M. D., Devriese, L. I., Leslie, H. A., Huvet, A., Frère, L., et al. (2017). Microplastics baseline surveys at the water surface and in sediments of the North-East Atlantic. *Front. Mar. Sci.* 4:135. doi: 10.3389/fmars.2017.00135

Mani, T., Hauk, A., Walter, U., and Burkhardt-Holm, P. (2015). Microplastics profile along the Rhine River. *Sci. Rep.* 5:17988. doi: 10.1038/srep17988

Martin, J., Lusher, A., Thompson, R. C., and Morley, A. (2017). The deposition and accumulation of microplastics in marine sediments and bottom water from the Irish continental shelf. *Nat. Sci. Rep.* 7:10772. doi: 10.1038/s41598-017-11079-2

Mason, S. A., Garneau, D., Sutton, R., Chu, Y., Ehmann, K., Barnes, J., et al. (2016). Microplastic pollution is widely detected in US municipal wastewater treatment plant effluent. *Environ. Pollut.* 218, 1045–1054. doi: 10.1016/j.envpol.2016.08.056

Masson, D. G., Harbitz, C. B., Wynn, R. B., Pedersen, G., and Løvholt, F. (2006). Submarine landslides: processes, triggers and hazard prediction. *Philos. Trans. R. Soc. Lond.* 364, 2009–2039.

Masson, D. G., Wynn, R. B., and Talling, P. J. (2010). "Large landslides on passive continental margins: processes, hypotheses and outstanding questions," in *Submarine Mass Movements and their Consequences*, eds D. C. Mosher, R. C. Shipp, L. Moscardelli, J. D. Chaytor, C. D. P. Baxter, H. J. Lee et al. (Dordrecht: Springer), 153–165.

Mato, Y., Isobe, T., Takada, H., Kanehiro, H., Ohtake, C., and Kaminuma, T. (2001). Plastic resin pellets as a transport medium for toxic chemicals in the marine environment. *Environ. Sci. Technol.* 35, 318–324.

McArthur, A. D., Gamberi, F., Kneller, B. C., Wakefield, M. I., Souza, P. A., and Kuchle, J. (2017). Palynofacies classification of submarine fan depositional environments: outcrop examples from the Marnoso-Arenacea Formation, Italy. *Mar. Pet. Geol.* 88, 181–199.

McCave, I. N., Thornalley, D. J. R., and Hall, I. R. (2017). Relation of sortable silt grain-size to deep-sea current speeds: Calibration of the 'Mud Current Meter'. *Deep Sea Res. Part 1 Oceanogr. Res. Pap.* 127, 1–12.

McNown, J. S., and Malaika, J. (1950). Effects of particle shape on settling velocity at low Reynolds numbers. *Eos Trans. Am. Geophys. Union* 31, 74–82.

Miramontes, E., Garreau, P., Caillaud, M., Jouet, G., Hernandez-Molina, J., Clare, M., et al. (2019). Contourite distribution and bottom currents in the NW Mediterranean Sea: coupling seafloor geomorphology and hydrodynamic modelling. *Geomorphology*

Mohrig, D. G., Whipple, K., Ellis, C., and Parker, G. (1998). Hydroplaning of subaqueous debris flows. *Geol. Soc. Am. Bull.* 110, 387–394.

Moore, C. J., Lattin, G. L., and Zellers, A. F. (2011). Quantity and type of plastic debris flowing from two urban rivers to coastal waters and beaches of Southern California. *J. Integr. Coast. Zone Manag.* 11, 65–73.

Mordecai, G., Tyler, P. A., Masson, D. G., and Huvenne, V. A. I. (2011). Litter in submarine canyons off the west coast of Portugal. *Deep Sea Res. Part 2 Top. Stud. Oceanogr.* 58, 2489–2496. doi: 10.1016/j.dsr2.2011.08.009

Moreira, F. T., Balthazar-Silva, D., Barbosa, L., and Turra, A. (2016). Revealing accumulation zones of plastic pellets in sandy beaches. *Environ. Pollut.* 218, 313–321. doi: 10.1016/j.envpol.2016.07.006

Morét-Ferguson, S., Law, K. L., Proskurowski, G., Murphy, E. K., Peacock, E. E., and Reddy, C. M. (2010). The size, mass, and composition of plastic debris in the western North Atlantic Ocean. *Mar. Poll. Bull.* 60, 1873–1878. doi: 10.1016/j.marpolbul.2010.07.020

Mountjoy, J. J., Howarth, J. D., Orpin, A. R., Barnes, P. M., Bowden, D. A., Rowden, A. A., et al. (2018). Earthquakes drive large-scale submarine canyon development and sediment supply to deep-ocean basins. *Sci. Adv.* 4:eaar3748. doi: 10.1126/sciadv.aar3748

Mulder, T., and Svytski, J. P. M. (1995). Turbidity currents generated at river mouths during exceptional discharges to the world oceans. *J. Geol.* 103, 285–299.

Mulder, T., Syvitski, J. P. M., Migeon, S., Faugères, J.-C., and Savoye, B. (2003). Marine hyperpycnal flows: initiation, behavior and related deposits. A review. *Mar. Pet. Geol.* 20, 861–882.

Mulder, T., Zaragosi, S., Garlan, T., Mavel, J., Cremer, M., Sottolichio, A., et al. (2012). Present deep-submarine canyons activity in the Bay of Biscay (NE Atlantic). *Mar. Geol.* 295, 113–127.

Muthukumar, T., Aravinthan, A., Lakshimi, K., Venkatesan, R., Vedaprakash, L., and Doble, M. (2011). Fouling and stability of polymers and composites in marine environment. *Int. Biodeter. Biodegr.* 62, 276–284.

Mutti, E., and Normark, W. (1991). "An integrated approach to the study of turbidite systems," in *Seismic Facies and Sedimentary Processes of Submarine Fans and Turbidite Systems*, eds P. Weimer and M. Link (New York, NY: Springer-Verlag), 75–106.

Näkki, P., Setälä, O., and Lehtiniemi, M. (2017). Bioturbation transports secondary microplastics to deeper layers in soft marine sediments of the northern Baltic Sea. *Mar. Pollut. Bull.* 119, 255–261. doi: 10.1016/j.marpolbul.2017.03.065

Nardin, T. R., Hein, F. J., Gorsline, D. S., and Edwards, B. D. (1979). "A review of mass movement processes, sediment and acoustic characteristics, and contrasts in slope and base-of-slope systems versus canyon–fan-basin floor systems," in *Geology of Continental Slopes*, Vol. 27, eds L. H. Doyle and O. H. Pilkey (SEPM Special Publication), 61–73.

Nelms, S. E., Barnett, J., Brownlow, A., Davison, N. J., Deaville, R., Galloway, T. S., et al. (2019). Microplastics in marine mammals stranded around the British coast: ubiquitous but transitory? *Sci. Rep.* 9:1075. doi: 10.1038/s41598-018-37428-3

Nelson, C. H., Twichell, D. C., Schwab, W. C., Lee, H. J., and Kenyon, N. H. (1992). Upper Pleistocene turbidite sand beds and chaotic silt beds in the channelized, distal, outer-fan lobes of the Mississippi fan. *Geology* 20, 693–696.

Nisbet, E. G., and Piper, D. J. (1998). Giant submarine landslides. *Nature* 392, 329–330.

Normark, W. R. (1970). Growth patterns of deep-sea fans. *AAPG Bull.* 54, 2170–2195.

Normark, W. R. (1978). Fan valleys, channels, and depositional lobes on modern submarine fans: characters for recognition of sandy turbidite environments. *AAPG Bull.* 62, 912–931.

Normark, W. R., Damuth, J. E., and The Leg 155 Sedimentology Group (1997). "Sedimentary facies and associated depositional elements of the Amazon Fan," in *Proceedings of the Ocean Drilling Programme, Scientific Results, Leg 155*, eds R. D. Flood, D. J. W. Piper, A. Klaus, and L. C. Peterson (College Station, TX: Ocean Drilling Programme), 611–651.

Obelcz, J., Xu, K., Georgiou, I. Y., Maloney, J., Bentley, S. J., and Miner, M. D. (2017). Sub-decadal submarine landslides are important drivers of deltaic sediment flux: Insights from the Mississippi River Delta Front. *Geology* 45, 703–706.

Oehmig, R. (1993). Entrainment of planktonic foraminifera: effect of bulk density. *Sedimentology* 40, 869–877.

Orange, D. L., McAdoo, B. G., Moore, J. C., Tobin, H., Screaton, E., Chezar, H., et al. (1997). Headless submarine canyons and fluid flow on the toe of the Cascadia accretionary complex. *Basin Res.* 9, 303–312.

Palanques, A., Guillén, J., and Puig, P. (2001). Impact of bottom trawling on water turbidity and muddy sediment of an unfished continental shelf. *Limnol. Oceanogr.* 46, 1100–1110.

Patters, C. A., and Bratton, S. P. (2016). Urbanization is a major influence on microplastic ingestion by sunfish in the Brazos River Basin, Central Texas, USA. *Environ. Pollut.* 210, 380–387. doi: 10.1016/j.envpol.2016.01.018

Paull, C. K., Greene, H. G., Ussler, W., and Mitts, P. J. (2002). Pesticides as tracers of sediment transport through Monterey Canyon. *Geo Mar. Lett.* 22, 121–126. doi: 10.1007/s00367-002-0110-1

Paull, C. K., Mitts, P., Ussler, B., Keaten, R., and Greene, H. G. (2005). Trail of sand in upper Monterey Canyon: offshore California. *Geol. Soc. Am. Bull.* 117, 1134–1145. doi: 10.1130/B25390.1

Paull, C. K., Talling, P. J., Maier, K. L., Parsons, D., Xu, J., Caress, D. W., et al. (2018). Powerful turbidity currents driven by dense basal layers. *Nat. Commun.* 9:4114. doi: 10.1038/s41467-018-06254-6

Peakall, J., McCaffrey, W. D., and Kneller, B. C. (2000). A process model for the evolution, morphology and architecture of meandering submarine channels. *J. Sediment. Res.* 70, 434–448.

Peng, X., Chen, M., Chen, S., Dasgupta, S., Xu, H., Ta, K., et al. (2018). Microplastics contaminate the deepest part of the world's ocean. *Geochem. Perspect. Lett.* 9, 1–5. doi: 10.7185/geochemlet.1829

Peterson, M. L., Wakeham, S. G., Lee, C., Askea, M. A., and Miquel, J. C. (2005). Novel techniques for collection of sinking particles in the ocean and determining their settling rates. *Limnol. Oceanogr. Methods* 3, 520–532.

Pham, C. K., Ramirez-Llodra, E., Alt, C. H. S., Amaro, T., Bergmann, M., Canals, M., et al. (2014). Marine litter density and distribution in European seas, from shelves to deep basins. *PLoS One* 9:e95839. doi: 10.1371/journal.pone.0095839

Pickering, K. T., Hiscott, R. N., and Hein, F. J. (1989). *Deep-Marine Environments—Clastic Sedimentation and Tectonics*. Crows Nest: Allen & Unwin.

Picot, M., Marsset, T., Droz, L., Dennielou, B., Baudin, F., Hermoso, M., et al. (2019). Monsoon control on channel avulsions in the Late Quaternary Congo Fan. *Quat. Sci. Rev.* 204, 149–171.

Pierdomenico, M., Casalbore, D., and Latino Chiocci, F. (2019). Massive benthic litter funnelled to deep sea by flash-flood generated hyperpycnal flows. *Sci. Rep.* 9:5330. doi: 10.1038/s41598-019-41816-8

Piper, D. J. W., and Normark, W. R. (1983). Turbidite depositional patterns and flow characteristics, Navy submarine fan, California Borderland. *Sedimentology* 30, 681–694.

Piper, D. J. W., and Savoye, B. (1993). Processes of late Quaternary turbidity current flow and deposition on the Var Deep-sea fan, North-west Mediterranean Sea. *Sedimentology* 40, 557–582.

Plastics Europe (2013). *Plastics - the Facts an Analysis of European Latest Plastics Production, Demand and Waste Data.* Brussels: Plastics Europe, 40.

Pope, E. L., Talling, P. J., Carter, L., Clare, M. A., and Hunt, J. E. (2017). Damaging sediment density flows triggered by tropical cyclones. *Earth Planet. Sci. Lett.* 458, 161–169.

Prélat, A., Hodgson, D. M., and Flint, S. S. (2009). Evolution, architecture and hierarchy of distributary deep-water deposits: a high-resolution outcrop investigation from the Permian Karoo Basin, South Africa. *Sedimentology* 56, 241–270.

Ptacnik, R., Diehl, S., and Berger, S. (2003). Performance of sinking and nonsinking phytoplankton taxa in a gradient of mixing depth. *Limnol. Oceanogr.* 48, 1903–1912.

Rabouille, C., Olu, K., Baudin, F., Khripounoff, A., Dennielou, B., Arnaud-Haond, S., et al. (2017). The Congolobe project, a multidisciplinary study of Congo deep-sea fan lobe complex: overview of methods, strategies, observations and sampling. *Deep Sea Res. Part 2 Top. Stud. Oceanogr.* 142, 7–24.

Rebesco, M., Hernández-Molina, F. J., Van Rooij, D., and Wåhlin, A. (2014). Contourites and associated sediments controlled by deep-water circulation processes: state-of-the-art and future considerations. *Mar. Geol.* 352, 111–154.

Rex, M. A., Etter, R. J., Morris, J. S., Crouse, J., McClain, C. R., Johnson, N. A., et al. (2006). Global bathymetric patterns of standing stock diversity and body size in the deep-sea benthos. *Mar. Ecol. Prog. Ser.* 317, 1–8.

Ridderinkhof, H., Van der Werf, P. M., Ullgren, J. E., Van Aken, H. M., Van Leeuwen, P. J., and De Ruijter, W. P. M. (2010). Seasonal and interannual variability in the Mozambique Channel from moored current observations. *J. Geophys. Res.* 115:C06010

Rochman, C. M. (2015). "The complex mixture, fate and toxicity of chemicals associated with plastic debris in the marine environment," in *Marine Anthropogenic Litter*, eds M. Bergmann, L. Gutow, and M. Klages (Berlin: Springer), 117–140. doi: 10.1007/978-3-319-16510-3

Romans, B. W., Castelltort, S., Covault, J. A., Fildani, A., and Walsh, J. P. (2016). Environmental signal propagation in sedimentary systems across timescales. *Earth Sci. Rev.* 153, 7–29.

Rusnak, G. A., and Nesteroff, W. D. (1963). Modern turbidites: terrigenous abyssal plain versus bioclastic basin. *AAPG Bull.* 47, 368–368.

Ryan, P. G., Moore, C. J., vanFraneker, J. A., and Moloney, C. L. (2009). Monitoring the abundance of plastic debris in the marine environment. *Philos. Trans. R. Soc. B* 364, 1999–2012.

Saller, A., Werner, K., Sugiaman, F., Cebastiant, A., May, R., Glenn, D., et al. (2008). Characteristics of Pleistocene deep-water fan lobes and their application to an upper Miocene reservoir model, offshore East Kalimantan, Indonesia. *AAPG Bull.* 92, 919–949.

Sanchez-Vidal, A., Thompson, R. C., Canals, M., and de Haan, W. P. (2018). The imprint of microfibres in southern European deep seas. *PLoS One* 13:e0207033. doi: 10.1371/journal.pone.0207033

Schlining, K., von Thun, S., Kuhnz, L., Schlining, B., Lundsten, L., Stout, N. J., et al. (2013). Debris in the deep: using a 22-year video annotation database to survey marine litter in Monterey Canyon, central California, USA. *Deep Sea Res. Part 1 Oceanogr. Res. Pap.* 79, 96–105. doi: 10.1016/j.dsr.2013.05.006

Setälä, O., Fleming-Lehtinen, V., and Lehtiniemi, M. (2014). Ingestion and transfer of microplastics in the planktonic food web. *Environ. Pollut.* 185, 77–78. doi: 10.1016/j.envpol.2013.10.013

Shah, A. A., Hasan, F., Hameed, A., and Ahmed, S. (2008). Biological degradation of plastics: a comprehensive review. *Biotechnol. Adv.* 26, 246–265. doi: 10.1016/j.biotechadv.2007.12.005

Shapiro, G. I., Huthnance, J. M., and Ivanov, V. V. (2003). Dense water cascading off the continental shelf. *J. Geophys. Res.* 108:3390. doi: 10.1146/annurev-marine-010213-135037

Sharma, S., and Chatterjee, S. (2017). Microplastic pollution, a threat to marine ecosystem and human health: a short review. *Environ. Sci. Pollut. Res.* 24, 21530–21547. doi: 10.1007/s11356-017-9910-8

Shepard, F. P. (1955). Delta-front valleys bordering the Mississippi distributaries. *Geol. Soc. Am. Bull.* 66, 1489–1498.

Shepard, F. P. (1975). Progress of internal waves along submarine canyons. *Mar. Geol.* 19, 131–138.

Silva, T. A., Girardclos, S., Stutenbecker, L., Bakker, M., Costa, A., Schlunegger, F., et al. (2018). The sediment budget and dynamics of a delta-canyon-lobe system over the anthropocene timescale: the Rhone river delta, Lake Geneva (Switzerland/France). *Sedimentology* 66, 838–858.

Smith, D. P., Kvitek, R., Iampietro, P. J., and Wong, K. (2007). Twenty-nine months of geomorphic change in upper Monterey Canyon (2002–2005). *Mar. Geol.* 236, 79–94.

Smith, M. E., Werner, S. H., Buscombe, D., Finnegan, N. J., Sumner, E. J., and Mueller, E. R. (2018). Seeking the shore: Evidence for active submarine canyon head incision due to coarse sediment supply and focusing of wave energy. *Geophys. Res. Lett.* 45, 12403–12413.

Sømme, T. O., Helland-Hansen, W., Martinsen, O. J., and Thurmond, J. B. (2009). Relationships between morphological and sedimentological parameters in source-to-sink systems: a basis for predicting semi-quantitative characteristics in subsurface systems. *Basin Res.* 21, 361–387.

Southern, S. J., Kane, I. A., Warchoł, M. J., Porten, K. W., and McCaffrey, W. D. (2017). Hybrid event beds dominated by transitional-flow facies: character, distribution and significance in the Maastrichtian Springar Formation, north-west Vøring Basin, Norwegian Sea. *Sedimentology* 64, 747–776.

Soutter, E., Kane, I. A., and Huuse, M. (2018). Giant submarine landslide triggered by Paleocene mantle plume activity in the North Atlantic. *Geology* 46, 511–514.

Sparkes, R. B., Lin, I. T., Hovius, N., Galy, A., Liu, J. T., Xu, X., et al. (2015). Redistribution of multi-phase particulate organic carbon in a marine shelf and canyon system during an exceptional river flood: Effects of Typhoon Morakot on the Gaoping River–Canyon system. *Mar. Geol.* 363, 191–201.

Spychala, Y. T., Hodgson, D. M., Prélat, A., Kane, I. A., Flint, S. S., and Mountney, N. P. (2017). Frontal and lateral submarine lobe fringes: comparing sedimentary facies, architecture and flow processes. *J. Sediment. Res.* 87, 75–96.

Stanley, D. J. (1982). Welded slump-graded sand couplets: evidence for slide generated turbidity currents. *Geo Mar. Lett.* 2, 149–155.

Stevenson, C. J., Feldens, P., Georgiopoulou, A., Schönke, M., Krastel, S., Piper, D. J., et al. (2018). Reconstructing the sediment concentration of a giant submarine gravity flow. *Nat. Commun.* 9:2616. doi: 10.1038/s41467-018-05042-6

Stevenson, C. J., Jackson, C. A. L., Hodgson, D. M., Hubbard, S. M., and Eggenhuisen, J. T. (2015). Deep-water sediment bypass. *J. Sediment. Res.* 85, 1058–1081.

Stolte, A., Forster, S., Gerdts, G., and Schubert, H. (2015). Microplastic concentrations in beach sediments along the German Baltic coast. *Mar. Pollut. Bull.* 99, 216–229. doi: 10.1016/j.marpolbul.2015.07.022

Stow, D. A. (1991). Distinguishing between Fine-Grained Turbidites and Contourites on the Nova Scotian Deep-Water Margin. *Deep-Water Turbidite Syst.* 149–165.

Stow, D. A. V., and Faugères, J. C. (2008). "Contourite facies and the facies model," in *Contourites, Developments in Sedimentology*, Vol. 60, eds M. Rebesco and A. Camerlenghi (Amsterdam: Elsevier), 223–256.

Stow, D. A. V., and Lovell, J. P. B. (1979). Contourites: their recognition in modern and ancient sediments. *Earth Sci. Rev.* 14, 251–291.

Symons, W. O., Sumner, E. J., Cartigny, M. J. B., and Clare, M. A. (2016). Large-scale sediment waves and scours on the modern seafloor and their implications for the prevalence of supercritical flow. *Mar. Geol.* 371, 130–148. doi: 10.1016/j.margeo.2015.11.009

Talling, P. J., Clare, M. L., Urlaub, M., Pope, E., Hunt, J. E., and Watt, S. F. (2014). Large submarine landslides on continental slopes: geohazards, methane release, and climate change. *Oceanography* 27, 32–45.

Talling, P. J., Paull, C. K., and Piper, D. J. W. (2013). How are subaqueous sediment density flows triggered, what is their internal structure and how does it evolve? Direct observations from monitoring of active flows. *Earth Sci. Rev.* 125, 244–287.

Talling, P. J., Sumner, E. J., Masson, D. G., and Malgesini, G. (2012a). Subaqueous sediment density flows: depositional processes and deposit types. *Sedimentology* 59, 1937–2003. doi: 10.1111/j.1365-3091.2012.01353.x

Talling, P. J., Malgesini, G., and Felletti, F. (2012b). Can liquefied submarine debris flows deposit clean sandstone over large areas? Field evidence from the Marnoso–Arenacea Formation, Italian Apennines. *Sedimentology* 59, 1937–2003.

Taylor, M. L., Gwinnett, C., Robinson, L. F., and Woodall, L. C. (2016). Plastic microfibre ingestion by deep-sea organisms. *Sci. Rep.* 6:33997. doi: 10.1038/srep33997

ter Halle, A., Ladirat, L., Gendre, X., Goudouneche, D., Pusineri, C., Routaboul, C., et al. (2016). Understanding the fragmentation pattern of marine plastic debris. *Environ. Sci. Technol.* 50, 5668–5675. doi: 10.1021/acs.est.6b00594

Teuten, E. L., Saquing, J. M., Knappe, D. R., Barlaz, M. A., Jonsson, S., Björn, A., et al. (2009). 'Transport and release of chemicals from plastics to the environment and to wildlife'. *Philos. Trans. R. Soc. B Biol. Sci.* 364, 2027–2045. doi: 10.1098/rstb.2008.0284

Thompson, R. C., Olsen, Y., Mitchell, R. P., Davis, A., Rowland, S. J., John, A. W. G., et al. (2004). Lost at sea: Where is all the plastic? *Science* 304:838.

Tubau, X., Canals, M., Lastras, G., Rayo, X., Rivera, J., and Amblas, D. (2015). Marine litter on the floor of deep submarine canyons of the northwestern Mediterranean sea: the role of hydrodynamic processes. *Prog. Ocean* 134, 379–403.

Twichell, D. C., Schwab, W. C., Nelson, C. H., Kenyon, N. H., and Lee, H. J. (1992). Characteristics of a sandy depositional lobe on the outer Mississippi fan from DeaMARC IA sidescan sonar images. *Geology* 20, 689–692.

Underwood, A., Chapman, M., and Browne, M. A. (2017). Some problems and practicalities in design and interpretation of samples of microplastic waste. *Anal. Methods* 9, 1332–1345.

United Nations Environment Programme [UNEP] (2016). *Marine Plastic Debris and Microplastics – Global Lessons and Research to Inspire Action and Guide Policy Change*. Nairobi: United Nations Environment Programme.

United States Environmental Protection Agency [USEPA] (1992). *Plastic Pellets in the Aquatic Environment: Sources and Recommendations*. EPA Oceans and Coastal Protection Division Report 842-B-92-010. Washington, DC: EPA.

Urlaub, M., Talling, P. J., and Masson, D. G. (2013). Timing and frequency of large submarine landslides: implications for understanding triggers and future geohazard. *Quat. Sci. Rev.* 72, 63–82.

Van Cauwenberghe, L., Devriese, L., Galgani, F., Robbens, J., and Janssen, C. R. (2015). Microplastics in sediments: a review of techniques, occurrence and effects. *Mar. Environ. Res.* 111, 5–17. doi: 10.1016/j.marenvres.2015.06.007

Van Cauwenberghe, L., and Janssen, C. R. (2014). Microplastics in bivalves cultured for human consumption. *Environ. Pollut.* 193, 65–70. doi: 10.1016/j.envpol.2014.06.010

Van Cauwenberghe, L., Vanreusel, A., Mees, J., and Janssen, C. R. (2013). Microplastic pollution in deep-sea sediments. *Environ. Pollut.* 182, 495–499. doi: 10.1016/j.envpol.2013.08.013

Vendettuoli, D., Clare, M., Hughes Clarke, J., Talling, P., Cartigny, M., Hubbard, S., et al. (2019). Daily bathymetric surveys document how stratigraphy is built and its extreme incompleteness in submarine channels. *Earth Planet. Sci. Lett.* 515, 231–247.

Vetter, E. W., and Dayton, P. K. (1998). Macrofaunal communities within and adjacent to a detritus-rich submarine canyon system. *Deep Sea Res. Part 2 Top. Stud. Oceanogr.* 45, 25–54.

Vianello, A., Boldrin, A., Guerriero, P., Moschino, V., Rella, R., Sturaro, A., et al. (2013). Microplastic particles in sediments of Lagoon of Venice, Italy: first observations on occurrence, spatial patterns and identification'. *Estuar. Coast. Shelf Sci.* 130, 54–61.

von Moos, N., Burkhardt-Holm, P., and Koehler, A. (2012). Uptake and effects of microplastics on cells and tissues of the blue mussel *Mytilus edulis* L. after experimental exposure. *Environ. Sci. Technol.* 46, 11327–11335. doi: 10.1021/es302332w

Walker, R. G. (1978). Deep-water sandstone facies and ancient submarine fans: models for exploration and stratigraphic traps. *AAPG Bull.* 62, 932–966.

Ward, J. E., and Shumway, S. E. (2004). Separating the grain from the chaff: particle selection in suspension- and deposit-feeding bivalves. *J. Exp. Mar. Biol. Ecol.* 300, 83–130.

Waters, C. N., Zalasiewicz, J., Summerhayes, C., Barnosky, A. D., Poirier, C., Gałuszka, A., et al. (2016). The Anthropocene is functionally and stratigraphically distinct from the holocene. *Science* 351:aad2622. doi: 10.1126/science.aad2622

Weaver, P. P. E., and Rothwell, R. G. (1987). "Sedimentation on the madeira abyssal plain over the last 300 000 years," in *Geological Society of Abyssal Plains*, eds P. P. E. Weaver, and J. Thomson (London: Special Publications), 31, 71–86.

Wetzel, A. (1991). Ecologic interpretation of deep-sea trace fossil communities. *Palaeogeogr. Palaeoclimatol. Palaeoecol.* 85, 47–69.

Willis, K. A., Eriksen, R., Wilcox, C., and Hardesty, B. D. (2017). Microplastic Distribution at Different Sediment Depths in an Urban Estuary. *Front. Mar. Sci.* 4:419. doi: 10.3389/fmars.2017.00419

Woodall, L. C., Sanchez-Vidal, A., Canals, M., Paterson, G. L. J., Coppock, R., Sleight, V., et al. (2014). The deep sea is a major sink for microplastic debris. *R. Soc. Open Sci.* 1:140317. doi: 10.1098/rsos.140317

Wright, S. L., Thompson, R. C., and Galloway, T. S. (2013). The physical impacts of microplastics on marine organisms: a review. *Environ. Pollut.* 178, 483–492. doi: 10.1016/j.envpol.2013.02.031

Xu, J. P., Noble, M., Eittreim, S. L., Rosenfeld, L. K., Schwing, F. B., and Pilskaln, C. H. (2002). Distribution and transport of suspended particulate matter in Monterey Canyon, California. *Mar. Geol.* 181, 215–234.

Yamada, Y., Fukuda, H., Inoue, K., Kogure, K., and Nagata, T. (2013). Effects of attached bacteria on organic aggregate settling velocity in seawater. *Aquat. Microb. Ecol.* 70, 261–272. doi: 10.3354/ame01658

Young, D. K., Walter, W. H., Richardson, M. D., and Lohanwick, A. W. (1985). Photographs of deep-sea lebensspuren: a comparison of sedimentary processes in the Venezuela Basin, Caribbean Sea. *Mar. Geol.* 68, 269–301.

Zalasiewicz, J., Waters, C. N., Ivar do Sul, J. A., Corcoran, P. L., Barnosky, A. D., Cearreta, A., et al. (2016). The geological cycle of plastics and their use as a stratigraphic indicator of the Anthropocene. *Anthropocene* 13, 4–17. doi: 10.1016/j.ancene.2016.01.002

Zavala, C., Arcuri, M., and Blanco Valiente, L. (2012). The importance of plant remains as diagnostic criteria for the recognition of ancient hyperpycnites. *Rev. Paléobiol.* 11, 457–469.

Zhao, Z., Alford, M. H., Lien, R.-C., Gregg, M. C., and Carter, G. S. (2012). Internal tides and mixing in a submarine canyon with time-varying stratification. *J. Phys. Oceanogr.* 42, 2121–2142.

Zitko, V., and Hanlon, M. (1991). Another source of pollution by plastics: skin cleaners with plastic scrubbers. *Mar. Pollut. Bull.* 22, 41–42.

Conflict of Interest Statement: The authors declare that the research was conducted in the absence of any commercial or financial relationships that could be construed as a potential conflict of interest.

The reviewer AG declared a past co-authorship with one of the authors MC to the handling Editor.

Copyright © 2019 Kane and Clare. This is an open-access article distributed under the terms of the Creative Commons Attribution License (CC BY). The use, distribution or reproduction in other forums is permitted, provided the original author(s) and the copyright owner(s) are credited and that the original publication in this journal is cited, in accordance with accepted academic practice. No use, distribution or reproduction is permitted which does not comply with these terms.

frontiers in Earth Science

ORIGINAL RESEARCH
published: 17 May 2019
doi: 10.3389/feart.2019.00109

Modern to Ancient Barrier Island Dimensional Comparisons: Implications for Analog Selection and Paleomorphodynamics

Julia S. Mulhern[1]*, *Cari L. Johnson*[2] and *John M. Martin*[3]

[1] Shell International Exploration and Production, New Orleans, LA, United States, [2] Department of Geology and Geophysics, University of Utah, Salt Lake City, UT, United States, [3] Shell International Exploration and Production, Houston, TX, United States

OPEN ACCESS

Edited by:
Amanda Owen,
University of Glasgow,
United Kingdom

Reviewed by:
Andrew Green,
University of KwaZulu-Natal,
South Africa
Jorge Lorenzo-Trueba,
Montclair State University,
United States

***Correspondence:**
Julia S. Mulhern
juliamulhern5@gmail.com

Specialty section:
This article was submitted to Sedimentology, Stratigraphy and Diagenesis, a section of the journal Frontiers in Earth Science

Received: 23 January 2019
Accepted: 26 April 2019
Published: 17 May 2019

Citation:
Mulhern JS, Johnson CL and Martin JM (2019) Modern to Ancient Barrier Island Dimensional Comparisons: Implications for Analog Selection and Paleomorphodynamics. Front. Earth Sci. 7:109. doi: 10.3389/feart.2019.00109

Ancient barrier islands are poorly understood relative to other clastic depositional environments, despite being prominent features along modern coastlines and important for understanding transgressive shoreline deposits. A new dataset of ancient barrier island dimensions (n = 83 examples) addresses this knowledge gap with a quantitative analysis of barrier island sand body dimensions including thickness (vertical), length (shore-parallel direction), and width (shore-perpendicular direction). This dataset of barrier island deposits was compared to planform measurements made for modern islands (n = 274), to investigate possible scaling relationships and other aspects of modern to ancient linkages. These measurements are nuanced and challenging to perform, and first-pass comparisons show that modern barrier islands should not be used as direct analogs for ancient systems. Nevertheless, results emphasize key depositional and preservation processes, and the dimensional differences between deposits formed over geologic vs. modern time scales. Using the methods outlined herein, barrier island deposits appear to be 2-5x longer (p50 modern = 10.7 km; p50 ancient = 20.0 km), and 6–15x wider (p50 modern = 1.2 km; p50 ancient = 7.3 km) than modern barrier islands. We interpret the results to indicate that ancient barrier islands are time-transgressive deposits recording vertical amalgamation, and barrier island growth by lateral accretion, and progradation. When comparing single barrier islands, thickness measurements do not vary systemically between modern and ancient examples, suggesting that local accommodation dictates barrier island thickness as a preservation control. Gross length, width, and thickness measurements are too coarse for robust paleomorphodynamic calculations, therefore more detailed sub-environment analysis (e.g., upper shoreface delineation), with improved facies models, is required before rigorous quantifications can

be generated. However, these initial comparisons do show scaling trends between length and width which could be leveraged, with caution, in the interim. As sea levels continue to rise, understanding barrier island motion and preservation will be central to predicting coastal change.

Keywords: paleomorphodynamics, barrier island, scaling relationships, accommodation, shallow marine, dimension prediction, modern analog, transgressive

INTRODUCTION

Barrier islands are elongate coastal sand bodies which comprise 10% of the world's coastlines (Hoyt, 1967; Oertel, 1985; Stutz and Pilkey, 2011). Modern barrier islands have been thoroughly studied, largely due to their relevance to growing coastal populations and infrastructure (Fisher and Dolan, 1977; Davis, 1994b; Short, 1999; Dronkers, 2005; Dyke, 2007; Anthony, 2009; Moore et al., 2010; McBride et al., 2013). Well-known examples from the U.S. Atlantic and Gulf coasts as well as the Dutch Wadden Sea form the basis of facies models that are used to interpret ancient barrier island deposits (Davies, 1978; Barwis and Hayes, 1979; Reinson, 1979; McCubbin, 1982).

While barrier island deposits have been interpreted for over 80 years, their dimensions have not been rigorously quantified (c.f. Reynolds, 1999). The dimensions of preserved barrier island deposits lend insight into transgressive processes on siliciclastic coastlines (McCubbin, 1982; Cooper et al., 2018a; Jones et al., 2018). Barrier islands commonly form the thickest sandstone units within a transgressive succession, therefore quantifying the range of preserved barrier island dimensions could improve predictions for subsurface hydrocarbon reservoirs (Davies et al., 1971; Reinson, 1992; Reynolds, 1999). Barrier islands will become an increasingly important hydrocarbon reservoir type as exploration expands beyond regressive sequences (Hampson et al., 2004).

Modern coastlines provide a natural laboratory for understanding barrier island processes and dimensions, and therefore are commonly used as analogs to interpret both outcrops and subsurface data (Chiang, 1984; Reinson, 1992; Hubbard et al., 2002; Boyd, 2010). However, the accuracy and effectiveness of analog usage is limited by a lack of dimensional comparisons between modern and ancient barrier islands. Paleomorphodynamics is the broad term for the field of quantitative sedimentology that uses equations and empirical relationships to link and scale modern and ancient depositional systems (Syvitski and Milliman, 2007; Sømme et al., 2009; Blum et al., 2013). Although these relationships have been developed for fluvial (Mohrig et al., 2000; Parker, 2006; Hajek and Wolinsky, 2010; Milliken et al., 2012), deltaic (Edmonds and Slingerland, 2007; Jerolmack and Swenson, 2007; Martin et al., 2018), and deepwater (Pirmez and Imran, 2003; Covault et al., 2012) settings, comparable research in shallow marine settings, including barrier islands, lags behind (cf. Hudock et al., 2014; Lazarus, 2016). For barrier island systems specifically, the modern morphodynamics are a topic of ongoing research (Hayes, 1980; McBride et al., 2013; Short and Jackson, 2013; Cooper et al., 2018a; Mellett and Plater, 2018), however, comparisons to ancient barrier islands are lacking. In developing the dataset presented here, we explore the methods that can be used to measure and compare barrier islands, an initial step toward shallow marine paleomorphodynamics, and, in the process, enhanced understanding of barrier island deposits.

The new dataset helps constrain the range of ancient barrier island dimensions, and was used to assess the feasibility of measurement comparisons between modern and ancient systems. This first order comparison of modern and ancient barrier island systems is used to refine existing models of barrier island motion and preservation. Specifically, we compare the thickness, length, and width of modern and ancient barrier islands. This approach highlights some of the challenges of using modern barrier island measurement data, because truly analogous architectures are not necessarily preserved in the rock record due to processes like ravinement, reworking, and stacking through time (e.g., Hendricks, 1994; Sixsmith et al., 2008). These comparisons also reveal inherent measurement inconsistencies, and terminology problems in barrier island literature. Articulating and highlighting these challenges provides a cautionary message to those using direct analog comparisons, especially for predictive purposes. Although complicated, these results highlight the difference between barrier islands and other depositional settings in terms of paleomorphodynamic potential, and create a starting point for further analysis.

METHODS

Database Development

Ancient barrier island dimensions were collected from an extensive literature review ($n = 123$ publications; **Figure 1**; **Table 1**). The database includes studies that use the term "barrier," or that suggest the preservation of barrier island deposits (e.g., Heward, 1981; Rawn-Schatzinger and Schatzinger, 1993). To establish internal consistency, the depositional environment of each example was assessed and reclassified as needed (**Table 1**). In straightforward examples, the extent of barrier island deposits was measured or recorded directly from the publication (e.g., Bridges, 1976; Franks, 1980). For more ambiguous examples, however, the sedimentology and geologic context was considered in detail (e.g., Berg, 1976; Guscott et al., 2003). Deposits were interpreted as barrier islands if the preserved shoreface was directly associated with estuarine, lagoon (Davies, 1978), or back barrier deposits, as per widely-used definitions (Oertel, 1985; Otvos, 2012). This designation includes examples of recently drowned barriers on the present day shelf (Mellett et al., 2012; Green et al., 2013, 2018; Salzmann

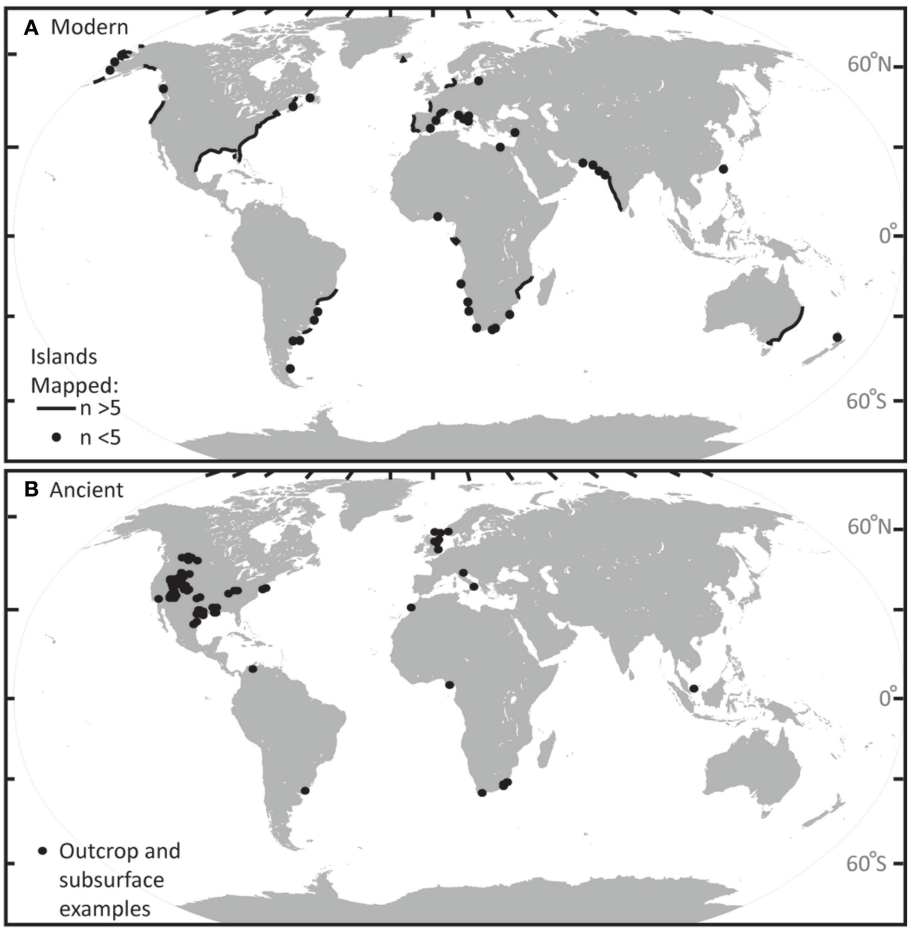


FIGURE 1 | Distribution of modern **(A)** and ancient **(B)** barrier islands used in the databases.

et al., 2013; Cooper et al., 2016, 2018b; Pretorius et al., 2016; Brooke et al., 2017; Mellett and Plater, 2018).

Of the 123 total ancient examples documented, 83 were determined to be barrier island deposits (**Table 1**). Other studies were interpreted as back barriers ($n = 1$), tidal inlets ($n = 3$), tidal bars ($n = 2$), spits ($n = 3$), strand plains ($n = 3$), and delta fronts ($n = 2$), or were designated as uncertain ($n = 4$), and not included in analysis. Duplicate studies of the same strata and locations ($n = 9$) were included in the database, but only one value for each unique island deposit was used in this analysis. Barrier islands closely associated with deltas ($n = 13$) are not included in this analysis because the proximity to deltaic processes likely influences the growth, shape, and preservation statistics of this subset of barrier island systems relative to those developed away from direct fluvial input (Hoyt, 1969; Penland et al., 1988; Penland and Suter, 1989; Van Maren, 2005). Although this is clearly an oversimplification of the processes controlling the interaction between deltaic and barrier island deposits (amalgamation, reworking, etc.), these examples were excluded in this first pass analysis.

Measurements from ancient examples were estimated using scaled figures (e.g., measured sections and maps), or pulled from the text of each publication. Key dimensions (length, width, and thickness) available from each study vary: the majority of examples (56%) have all spatial dimensions measured, whereas 24% have thickness and width, and 14% have only thickness (**Figure 2**). Maps and cross-sections are stored as images within the database, as are key contextual metadata, including age, location, and nomenclature used to describe the deposits. Each study was given a confidence designation (1-high to 3-low), which indicates the quality of the available data and the confidence in the measurements, high (1) indicates clear and well-supported data, whereas low (3) indicates poorly-supported data or vague figures (**Table 1**).

These ancient barrier island dimensions were compared to a previously generated dataset of planform dimensions of modern barrier islands ($n = 274$) mapped using Google Earth aerial imagery (**Figure 1A**; Mulhern et al., 2017). Barrier islands (visibly separated by water on all sides) and spits (partially attached; Oertel, 1985) were mapped by tracing each individual object at the water line along roughly 29,000 km of global coastlines (**Figure 1A**; Mulhern et al., 2017). The spatial data were combined with thickness values gathered from the literature and measured from core, seismic, and ground penetrating radar

TABLE 1 | Barrier Island dimensions from ancient literature.

Publication, Year, and Formation (Fm.)	Field, Basin, Location	Study type	Thickness-SP	Thickness-MP	Width	Length
Allen and Johnson, 2011; Cretaceous Straight Cliffs Fm.	Kaiparowits Basin, Utah, U.S.	(1, RF, NA)	20, 27.8, 31.1 m		> 4.8 km	> 6.7 km
Ambrose and Ayers, 2007; Cretaceous Fruitland Fm.	Carbon Junction, San Juan Basin, New Mexico, U.S.	(1, RF, ASP)	12–36 m	45.45 m	8 km	
Ambrose and Ferrer, 1997; Eocene Misoa Fm.	Langunillas Field, Maracaibo Basin, Venezuela	(2, F, NA)	3.66 m		4.08 km	8.12 km
Antia et al., 2011; Cretaceous Muddy Fm.	Various, Denver-Julesburg Basin, Nebraska, U.S.	(1, RF, NA)	18 m	46 m	9.71 km	34.95 km
Barwis and Horne, 1979; Carboniferous Carter Caves Ss.	Appalachian Basin, Kentucky, U.S.	(3, RF, NA)	14 m			3–8 km
Bass, 1934; Carboniferous Cherokee	Various, Anadarko Basin, Kansas, U.S.	(3, A, NA)	50–100 ft		0.5–1.5 mi	2–6 mi
Berg, 1976; Cretaceous Muddy Fm.	Hilight Muddy Field, Powder River Basin, Wyoming, U.S.	(1, RF, NA)	6 m		4–13 km	25 km
Berg, 1970; Cretaceous Muddy Fm.	Recluse Field, Powder River Basin, Wyoming, U.S.	(1, RF, NA)	44 ft		1.75 mi	11 mi
Berg and Davies, 1968; Cretaceous Muddy Fm.	Bell Creek Field, Powder River Basin, Montana, U.S.	(1, RF, NA)	9 m/27 ft		7.5 km	20 km/11 mi
Bergman and Walker, 1987; Cretaceous Cardium Fm.	Carrot Creek Field, Alberta, Canada	(3, RF, NA)	100 ft		27.2 km	
Bibler and Schmitt, 1986; Cretaceous Horsethief Fm.	Central Montana, Montana, U.S.	(1, RF, ASP)	20, 10, 80, 25 m	140 m		
Boyd and Dyer, 1964; Oligocene Frio Fm.	Texas Gulf Coast Basin, Texas, U.S.	(2, PM, ASP)	400 ft	894 m	9 km	220 km
Bridges, 1976; Silurian Skomer Volcanic Group	Welsh Basin, Wales, United Kingdom	(1, R, NA)	5–28 m		0.2–2 km, 2–4 km	
Buatois et al., 1999; Carboniferous Kearney Fm.	Gentzler and Arroyo Fields, Anadarko Basin, Kansas, U.S.	(3, A, UC)				
Campbell, 1979; Cretaceous Gallup Sandstone*	San Juan Basin, New Mexico, U.S.	(4, RF, AMP)				
Campbell, 1971; Cretaceous Gallup Sandstone	San Juan Basin, New Mexico, U.S.	(2, RF, AMP)		100 m	160 km	320 km
Cant, 1984; Cretaceous Spirit River Fm.	Alberta, Canada	(3, RF, NA)	12–30 m			
Caplan and Moslow, 1999; Triassic Halfway; Doig Fm.	Peejay Field, British Columbia, Canada	(1, PM, NA)	8 m		4.3 km	6 km
Carter, 1978; Miocene Cohansey Sand	NJ Coastal Plain, New Jersey, U.S.	(2, PM, NA)	12 m/6 m		45 km	80 km
Cavaroc et al., 1976; Carboniferous Tindouf Basin	Tindouf Basin, Morocco	(1, R, ASP)	6–10 m	200 m	6 km	12 km
Chiang, 1984; Cretaceous Mannville Group-Glauconitic Fm.	Hoadley Gas Field, Alberta, Canada	(1, RF, AMP)	10 m/80 ft	24	24 km	209 km
Davies, 1969; Jurassic Lias Sand Fm.	Mendip Basin, England, United Kingdom	(3, R, AMP)		150 ft/ 300 ft		
Davies and Berg, 1969; Cretaceous Muddy Fm.*	Bell Creek Field, Powder River Basin, Montana, U.S.	(4, RF, UC)				
Davies and Ethridge, 1971; Eocene Cailborne Group	Texas Gulf Coast Basin, Texas, U.S.	(2, PM, NA)	40–80 ft			
Davies et al., 2006; Cretaceous Blackhawk Fm.	Book Cliffs, Utah, U.S.	(1, RF, ASP)	4–20 m	48 m	5–25 km/40 km	
Davies et al., 1971; Cretaceous Muddy Fm.*	Bell Creek Field, Powder River Basin, Montana, U.S.	(4, RF, UC)	22 ft			
Devine, 1991; Cretaceous Point Lookout Sandstone	San Juan Basin, New Mexico, U.S.	(2, RF, AMP)	9 m	18 m	10.4 mi	
Dickinson, 1976; Eocene Jackson Group	Texas Gulf Coast Basin, Texas, U.S.	(3, PM, AMP)	9–12 m		8–24 km	

(Continued)

TABLE 1 | Continued

Publication, Year, and Formation (Fm.)	Field, Basin, Location	Study type	Thickness-SP	Thickness-MP	Width	Length
Elliott, 1975; Carboniferous Great Limestone	Pennie Basin, England, United Kingdom	(3, R, AMP)	5 m/7.5–16 m	16 m	15.3 /20 km	40.7/40 km
Exum and Harms, 1968; Cretaceous Muddy Fm.	Various, Denver Basin, Nebraska, U.S.	(1, RF, NA)	25 ft		0.5–1.5 mi	2–5 mi
Finkelstein, 1992; Pleistocene Mockhorn Island	Atlantic Coast, Virginia, U.S.	(1, PM, NA)	2–4 m		0.82 km	10.38 km
Fisher et al., 1970; Eocene Jackson Group	Texas Gulf Coast Basin, Texas, U.S.	(1, PM, ASP)	50–500 ft	152 m	28 mi	100–150 mi
Flores, 1978; Cretaceous Almond Fm.*	Rock Springs Embayment, Wyoming, U.S.	(2, RF, UC)	5–18 m			8 km
Franks, 1980; Cretaceous Kiowa Fm.	Anadarko Basin, Kansas, U.S.	(1, RF, NA)	18 m		2 km	6 km
Galloway, 1986; Eocene Jackson—Tegua Fm and Frio Fm	Greta, West Ranch Field, Texas Gulf Coast Basin, Texas, U.S.	(2, PM, NA)	100 ft (30 m)			
Galloway, 1986; Eocene Jackson—Tegua Fm and Frio Fm	Glasscock, West Ranch Field, Texas Gulf Coast Basin, Texas, U.S.	(2, PM, NA)	20 ft		7.33 km	
Galloway, 1986; Eocene Jackson—Tegua Fm and Frio Fm	41-A, West Ranch Field, Texas Gulf Coast Basin, Texas, U.S.	(2, PM, NA)	10–100 ft, 3–30 m		5 mi (8 km)	
Guscott et al., 2003; Jurassic Sgiath Fm.	Scott Field, Moray Firth Basin, Scotland, United Kingdom	(1, R, U)	100–150 ft			
Hamilton, 1995; Eocene Jackson—Tegua Fm.	Seventy Six West Field, Texas Gulf Coast Basin, Texas, U.S.	(1, PM, NA)	3.2–10 m		0.6–1.2 km	~4.8 km
Hamilton, 1995; Eocene Jackson—Tegua Fm.	Seventy Six West Field, Texas Gulf Coast Basin, Texas, U.S.	(1, PM, NA)	4.5–7.3 m		0.48–1.3 km	
Harms et al., 1965; Cretaceous Fox Hills Sandstone	Rock Springs Embayment, Wyoming, U.S.	(1, RF, ASP)	50 ft	29 m	4.5 mi	13.5 mi
Hawkins, 1980; Cretaceous Frontier Fm.	Fontenelle, Storm Shelter, Whiskey Buttes, Wyoming, U.S.	(2, RF, UC)				
Hendricks, 1994; Cretaceous Almond Fm.	Green River Basin, Wyoming, U.S.	(2, RF, NA)	25–150 ft	45	~2 mi	
Hobday and Horne, 1977; Carboniferous Pennsylvanian	Pocahontas Basin, West Virginia, U.S.	(1, RF, AMP)	10–25 m	25	1.6–8 km	16 km
Hobday and Jackson, 1979; Pleistocene Port Durnford Fm.	KwaZulu Margin, KwaZulu Natal, South Africa	(3, PM, NA)	5.5 m			
Hobday and Orme, 1974; Pleistocene Port Durnford Fm.*	KwaZulu Margin, KwaZulu Natal, South Africa	(4, PM, NA)				
Hobday and Tankard, 1978; Ordovician Peninsula Fm.	Karoo Basin, Cape Peninsula, South Africa	(3, R, AMP)		100 m	75–100 km	
Hollenshead and Pritchard, 1960; Cretaceous Cliffhouse Fm.*	San Juan Basin, New Mexico, U.S.	(3, RF, AMP)	15–45/5–70 m	82 m	75 km	150 km
Holmes and Rivard, 1976; Cretaceous Glauconitic Fm.	Jenner Field, Alberta, Canada	(2, RF, NA)	13.62 m		3.22 km	28.9 km
Holz et al., 2002; Permian Rio Bonito Fm.	Candiota Coal Field, Parana Basin, Rio Grande do Sul, Brazil	(2,I, ASP)	3–12 m		< 14 km	
Horne and Ferm, 1976; Carboniferous Pennsylvanian*	Pocahontas Basin, Virginia, U.S.	(4, RF, UC)	4.3 m		1.5 km	
Horne and Ferm, 1976; Carboniferous Pennsylvanian*	Pocahontas Basin, West Virginia, U.S.	(4, RF, UC)	11–26 m		1.6–8 km	max 64 km
Hubbard et al., 2002; Cretaceous Bluesky Fm.	Various Fields, Alberta, Canada	(1, RF, NA)	17.5 m/30 m		8 km	23 km
Johannessen and Nielsen, 2010; Jurassic Heno Fm.	Freja Oil Field, Danish Central Graben, North Sea, Denmark	(1, R, AMP)		71–88 m	30.7 km	13.8 km
Johnston and Johnson, 1987; Eocene Wilcox Fm.	Livingston Field, Texas Gulf Coast Basin, Louisiana, U.S.	(2, PM, NA)	40–50 ft/12–16 m		4.8 km	14.4 km
Kamola and Howard, 1985; Cretaceous Blackhawk Fm.	Book Cliffs Basin, Utah, U.S.	(2, RF, UC)				

(Continued)

TABLE 1 | Continued

Publication, Year, and Formation (Fm.)	Field, Basin, Location	Study type	Thickness-SP	Thickness-MP	Width	Length
Kieft et al., 2011; Cretaceous Almond Fm.	Rock Springs Embayment, Wyoming, U.S.	(1, RF, ASP)	5–22 m	28 m		26 km
deVries Klein, 1974; Pennsylvanian Atoka Fm.	Arkoma Basin, Arkansas, U.S.	(3, RF, ASP)	5.48, 7.17, 9.68, 12.14 m			
Land, 1972; Cretaceous Fox Hills Sandstone	Rock Springs Embayment, Wyoming, U.S.	(3, RF, NA)	18–75 m, 21–63 m/ 46–90 ft		10–30 m/6–12 mi	30 km
Leckie, 1985; Cretaceous Fort St. John Group	Deep Basin, British Columbia, Canada	(2, RF, NA)	22-35 m			
Løseth et al., 2009; Jurassic Tarbert Fm.	Various, North Sea Basin, Oseberg South, Norway	(1, R, AMP)		30–50 m	30 km	40 km
McCubbin and Brady, 1969; Cretaceous Almond Fm.	Patrick Draw Area, Rock Springs Embayment, Wyoming, U.S.	(3, RF, NA)	30 m max, 6 m		10 km/6 mi/ 6.4 km	10 miN /16 km
Mellere et al., 2005; Pliocene Spartizzo-Scandale	Crotone Basin, Italy	(2, R, NA)	10–60 m	67 m	0.5–2 km	
Miller Jr., 1962; Cretaceous Fall River Fm.	Various Fields, Powder River Basin, Wyoming, U.S.	(3, RF, NA)	40–90 ft			
Mulhern and Johnson, 2016; Cretaceous Straight Cliffs Fm.	Kaiparowits Basin, Utah, U.S.	(1, RF, NA)	10–30 m		<10 km	> 7 km
Navilova and Kurniawan, 2013; Miocene Upper Arang Fm.	Belanak Field, Malay Basin, Indonesia	(2, I, NA)	0–28 m		0.57 km	5.42 km
Olsen et al., 1999; Cretaceous Cliffhouse Fm.	San Juan Basin, Colorado, U.S.	(2, RF, AMP)	12 m	55 m	10–20 km	
Painter et al., 2013; Cretaceous Mesa Verde Group	Book Cliffs Basin, Colorado, U.S.	(1, RF, ASP)	8.9 m	19.41 m	3.811 km	
Percival, 1992; Carboniferous Harthope Ganister	Pennie Basin, England, United Kingdom	(1, R, NA)	9 m		2.5 km	4.5 km
Rautman, 1978; Jurassic Sundance Fm.	Black Hills Region, South Dakota, U.S.	(3, RF, AMP)		30 m	100 km	
Roehler, 1988; Cretaceous Almond Fm.	Rock Springs Embayment, Wyoming, U.S.	(1, RF, NA)	9 m	29 m	3.5 mi	60 mi
Sabins, 1963; Cretaceous Gallup Sandstone	Bisti Field, San Juan Basin, New Mexico, U.S.	(1, RF, NA)	12.2 m		1.6–3.2 km	50 km
Salzmann et al., 2013; Holocene KwaZulu-Natal	South African Coast, KwaZulu-Natal, South Africa	(1, PM, NA)	10–12 m		80 m	1.5 km
Sanders and Kumar, 1975; Holocene Fire Island	Atlantic Coast, New York, U.S.	(1, PM, NA)	8.3, 17.08, 19.2		363–850 m	
Schultz and Stewart, 1991; Eocene Reklaw Fm.	Atkinson Field, Texas Gulf Coast Basin, Texas, U.S.	(3, PM, NA)	31 ft		5,333 ft	16,000 ft
Self et al., 1986; Eocene Wilcox Fm.	Lockhart Crossing Field, Louisiana, U.S.	(1, PM, NA)	40–45 ft/12–14 m		4–6 mi/7–10 km	tens of mi
Sharma et al., 1990; Cretaceous Muddy Fm.*	Bell Creek Field, Powder River Basin, Montana, U.S.	(4, RF, UC)				
Shelton, 1967; Cretaceous Eagle Sandstone	Lake Basin, Montana, U.S.	(1, RF, AMP)	30–70 ft/50–100 ft	30 m	20–30 mi	40 mi
Sixsmith et al., 2008; Cretaceous Point Lookout Sandstone	San Juan Basin, New Mexico, U.S.	(1, RF, AMP)	8–16 m	22 m	3,500–5,500 m	2,700–15,000
Snedden and Kersey, 1981; Eocene Jackson Yegua Fm.*	Texas Gulf Coast Basin, Texas, U.S.	(4, PM, UC)				
Storms et al., 2008; Holocene Adriatic Shelf Quaternary	Adriatic Basin, Italy	(3, RF, NA)				
Sturm et al., 2001; Cretaceous Almond Fm.	Siberia Ridge Field, Washakie Basin, Wyoming, U.S.	(3, RF, ASP)	40 ft	137 m	2–5 mi	5–40 mi
Tavener-Smith, 1982; Permian Vryheid Fm.	Karoo Basin, South Africa	(2, R, NA)	19.65 m			
Thomas and Mann, 1966; Jurassic Terryville Sandstone	Texas Gulf Coast Basin, Louisiana, U.S.	(2, PM, AMP)	3–5 m	426 m	40–85 km/115 km	135 km /22 km

(Continued)

TABLE 1 | Continued

Publication, Year, and Formation (Fm.)	Field, Basin, Location	Study type	Thickness-SP	Thickness-MP	Width	Length
Tizzard and Lerbekmo, 1975; Cretaceous Viking Fm.	Suffield Area, Alberta, Canada	(3, RF, AMP)	10 m	38 m	104–128 km	
Tye et al., 1994; Oligocene Freeman Fm.	Vedder Fields, San Joaquin Basin, California, U.S.	(2, F, AMP)		23-30 m	8.7–15 km	28 km
Valasek, 1995; Cretaceous Tocito Sandstone	San Juan Basin, New Mexico, U.S.	(1, RF, NA)	4–20 m		1.5–3 km	6.9, 7.1,8.4, 15.9 km
Weidie, 1968; Cretaceous Difunta Group	Parras Basin, Mexico	(3, PM, NA)				3.5 mi
Weimer, 1966; Cretaceous Almond Fm.	Patrick Draw Field, Rock Springs Embayment, Wyoming, U.S.	(2, RF, ASP)	9 m	96 m	6.4 km	14 km
Williams et al., 1975; Jurassic Sgiath Fm.	Piper Field, Moray Firth Basin, Scotland, United Kingdom	(1, R, NA)	9–15 m	110 m	1.6–160 km	16-160 mi
Willis and Moslow, 1994; Triassic Halfway-Doig Fm.	Wembley Field, Alberta, Canada	(1, PM, NA)	2–6 m		2 km	> 30 km
Yang, 1999; Eocene Jackson Group	Texas Gulf Coast Basin, Texas, U.S.	(3, PM, NA)	80 ft			

**indicates repeat study not included in analysis.*
Data separated by/indicate two different sources (i.e., text vs. image). Data are reported in the units of the literature cited and converted for plotting.
Study Type (confidence, basin type, amalgamation).
Confidence: 1, high; 2, medium; 3, low; 4, repeat study.
Basin types: PM, Passive Margin; RF, Retroarc Foreland; F, Forearc; R, Rift; I, Intracratonic; A, Aulacogen.
Amalgamation: ASP, Amalgamated-Single Parasequence; AMP, Amalgamated–Multiple Parasequences; NA, not amalgamated; UC, unclear.
Fm, Formation; Ss, Sandstone; SP, Single Parasequence; MP, Multiple Parasequences.

studies of Holocene deposits as described below (e.g., Davis, 1994b; Salzmann et al., 2013; Fruergaard et al., 2015).

A key challenge in this approach is that modern examples consist of a single island, whereas ancient examples can have multiple barrier island parasequences preserved, either stacked vertically or *en echelon* (**Figure 3**). Here the term parasequence is used to describe a single preserved barrier island shoreface succession, indicating the preservation of a distinct barrier island (Van Wagoner et al., 1988; cf. Arnott, 1995; Catuneanu et al., 2010). More specifically, for this study a parasequence is considered a single, genetically related, stacked successions of depositional enviroments bound by either flooding or ravinement surfaces. To investigate the importance of vertical amalgamation and barrier island stacking, examples with multiple barrier island parasequences were designated as amalgamated if the parasequences are in vertical contact with one another (**Figure 3A**). When possible, the dimensions of individual island deposits within these amalgamated deposits were measured. If the individual parasequences are not clearly separated, the entire amalgamated succession was measured, and designated as a separate subset. Ancient examples were considered not amalgamated (**Figure 3B**) if they contain only a single parasequence, or if they contain multiple parasequences which are not in sand-on-sand contact with one another and thus were measured individually.

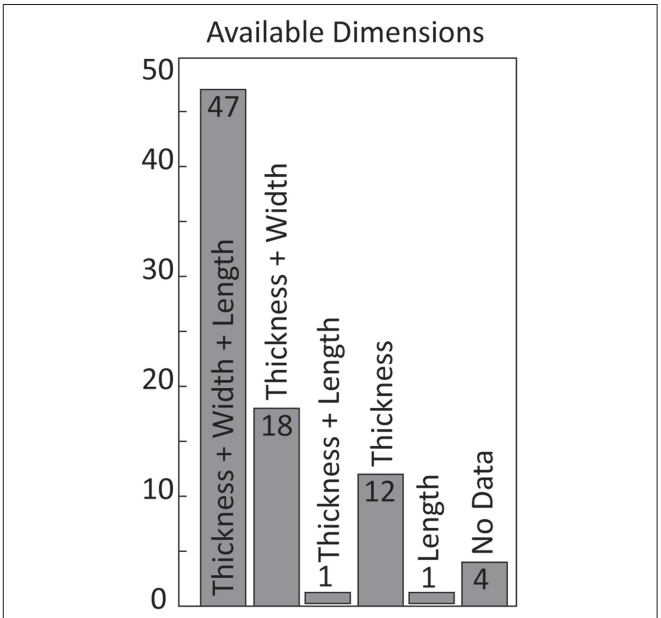


FIGURE 2 | Histogram showing the dimension data available (length, width, and thickness) for the 83 ancient barrier island examples used in analysis.

Measurement Comparisons

Modern and ancient barrier islands were measured using the most straightforward methods and the most readily available data (**Figure 4**), but clearly these data are not directly analogous. Subaerial exposure of modern barrier islands is most conducive to measuring through global imagery (e.g., Google Earth). In contrast, the entire shoreface, rather than just the sub-aerial foreshore and dune, is most conducive to measuring ancient examples (**Figure 4**), because the shoreface is commonly preserved, forms large outcrops (Allen and Johnson, 2011; Kieft et al., 2011), and creates distinct well-log patterns (Tizzard and Lerbekmo, 1975; Willis and Moslow, 1994). Our procedures for

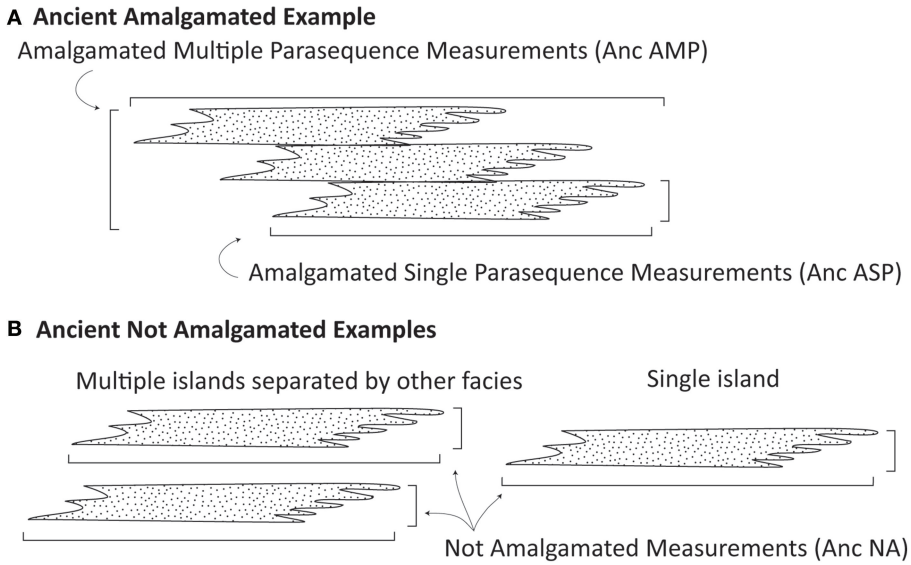


FIGURE 3 | Diagram showing how ancient barrier island examples were separated by amalgamation. The classic coarsening upwards model for a shoreface profile was used to determine and define paraseqeunces. Examples with multiple coarsening upwards progressions stacked vertically were considered amalgamated **(A)**. Examples were designated as amalgamated multiple parasequence (Anc AMP) examples if the boundary between the parasequences was not marked clearly enough for them to be differentiated. Examples that showed amalgamation but single, clear, individual parasequences could be measured were designated as amalgamated single parasequence measurement (Anc ASP). Not amalgamated examples do not have sand-on-sand contact between each coarsening upwards succession **(B)**. These were individually measured and designated as not amalgamated (Anc NA).

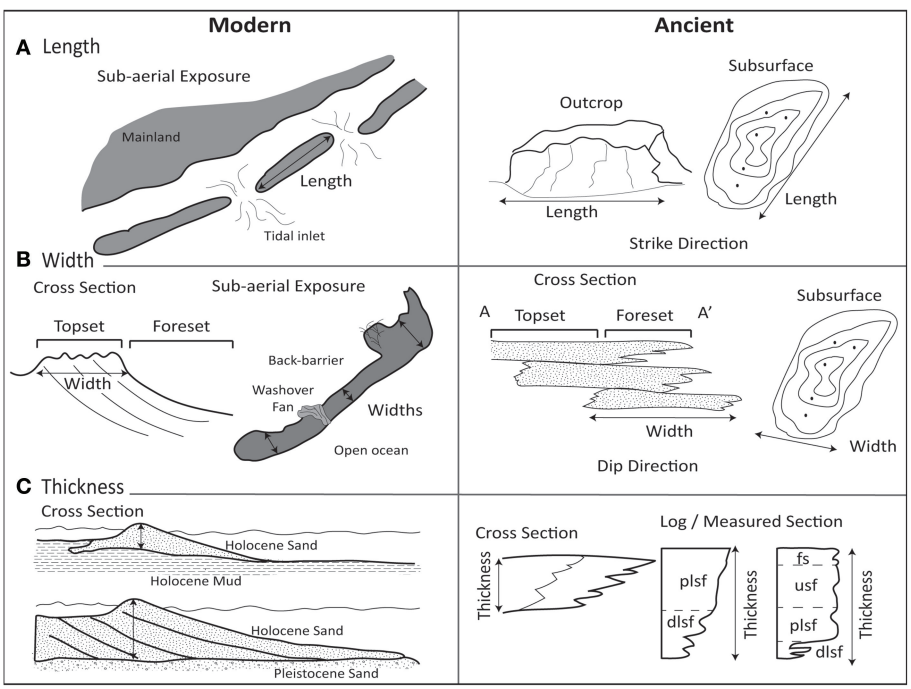


FIGURE 4 | Modern and ancient barrier island measurement methods. Modern lengths **(A)** are measured along the island centerline parallel to the shoreline from inlet to inlet. Ancient lengths were measured in the strike direction while width are measured in the dip direction. Modern widths **(B)** are measured in across the island in the shore-perpendicular direction in three locations and averaged. Modern widths represent only the island topset. Ancient width measurements include both the topset and foreset width. Modern thickness **(C)** measurements were made to the underlying substrate. Ancient thicknesses are measured vertically through the preserved shoreface.

collecting database measurements are outlined here (**Figure 4**), the limitations and implications of which are explored in the discussion.

Modern lengths were measured along each island centerline in the shore-parallel direction from one tidal inlet to the next (**Figure 4A**). While tidal inlet location may be transient, sub-aerial exposure provides a consistent way to measure islands globally and the shore-parallel length of modern islands is used extensively in the morphodynamic literature (McBride et al., 2013; Short and Jackson, 2013). Ancient lengths were measured from one end of the preserved shoreface to the other in the strike (shore-parallel) direction, potentially including or crossing the tidal inlet (**Figure 5**). If a range of values was evident from the text or figures of a particular example, the range was recorded in the database and a representative value is used for analysis. Examples with tidal channel or tidal inlet deposits associated with the barrier island were included because these facies are often contiguous with the barrier island shoreface facies and thus form part of preserved barrier islands successions (Davies and Ethridge, 1971; Davies, 1978; Flores, 1978; Self et al., 1986). Easily measurable modern planform extent allows us to consider whether or not the sub-aerial expression of the barrier island carries any scaling capability relative to outcrop and subsurface measurements to potentially develop dimensional scaling proxies for the subsurface.

Modern widths were measured in the shore-perpendicular direction in three locations along the length of the island, and averaged. These measurements document the subaerial extent of the island for a single snapshot in time, thus recording the topset width (**Figure 4B**). In ancient examples, the extent of the preserved shoreface in the dip-direction was measured, documenting both topset and foreset widths (**Figure 4B**). As such, these measurements reflect the width of the whole barrier island deposit, rather than just the subaerial portion. It is not feasible to measure strictly the subaerial portion of ancient barrier island deposits because the water line moves through time and deposits are potentially subject to removal during ravinement. Additionally, the foreshore is rarely specifically designated in literature examples (Allen and Johnson, 2011; Kieft et al., 2011; Painter et al., 2013). Inversely, subaqueous width measurements for the modern are not feasible at a global scale because they are inhibited by the scarcity of available data and the difficulty in defining, constraining, and documenting the subsurface back-barrier and shoreface boundary without ground penetrating radar or seismic data (Jol et al., 1996; Daly et al., 2002; Wernette et al., 2018). Again, while these measurements are not analogous, their comparison will determine whether the sub-aerial extent can be scaled and used as a proxy for ancient width.

Modern thicknesses were measured vertically from the dune crest to the underlying substrate based on published images and figures (**Figure 4C**). These values reflect the thickness of multiple shoreface sub-environments (i.e., dune, foreshore, upper shoreface, etc.) depending on the slope of the shoreface and the underlying shelf (**Figure 6**; Roy et al., 1994). Cores through some modern islands contain a range of depositional environments (e.g., Bernard et al., 1962), while others contain only thin upper shoreface deposits above underlying lagoonal facies (e.g., Belknap and Kraft, 1981).

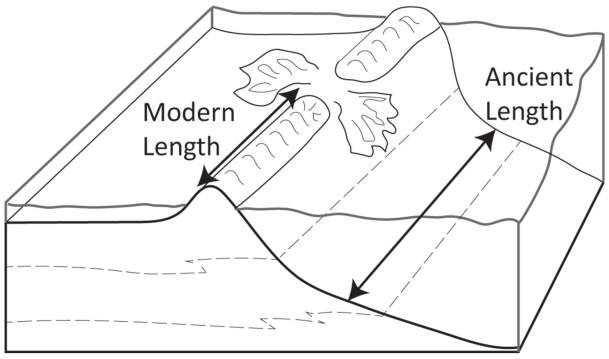


FIGURE 5 | Block diagram showing the conceptual difference between modern and ancient length measurements. Modern lengths are limited by short-term inlet location, whereas ancient lengths can span inlets, recording shore-perpendicular motion through time.

Ancient thicknesses were measured vertically through the sandstone portion of preserved barrier island deposits. These thickness measurements also represent variable sub-environments, depending on which portions of the barrier island are preserved (**Figure 4C**). For example, some outcrops preserve only the upper shoreface (e.g., Mulhern and Johnson, 2016) while others record stacked offshore, lower shoreface, and middle shoreface successions (e.g., Løseth et al., 2009). For examples with multiple barrier island parasequences, the thickness of each individual sequence was measured when possible. In some cases, only the thickness of the entire interval was available, so these examples were given different amalgamation designations (**Figure 3**) to distinguish the type of measurements recorded.

Although different portions of the barrier island are being measured in modern and ancient settings, the expression of progradation via either topset width (modern) or a dip-oriented shoreface width (ancient) represents a similar process, which is the underlying morphodynamic link between modern and ancient systems. Modern examples with the full island (topset and forest) documented bolster comparisons. This attempt to quantify and compare barrier island features provides an initial focus on the feasibility of such comparisons, as well as insight into barrier island processes and preservation. Direct 1:1 relationships between modern and ancient examples are not expected precisely because of non-stationality. If offsets between the two databases are systematic, however, then there could be predictive scaling relationships between the two. The modern planform expression of barrier islands could be scaled and used to predict ancient dimensions once preservation processes are better understood.

RESULTS

A total of 123 ancient examples were documented and 83 were determined to be barrier island deposits (as described above; **Table 1**). Gathering and quantifying preserved barrier island

dimensions was more difficult than anticipated, highlighting trends and problems with nomenclature as well as potential literature bias. Barrier island studies vary in frequency over time, with 39 studies between 1970 and 1979 compared to 20 studies between 1980 and 1989 (**Figure 7**). Authors describe the deposits using 29 different terms (**Figure 8**). Reported barrier island deposits occur mainly in passive margin (n = 42) and retroarc foreland basin (n = 58) settings, relative to other basins [forearc (n = 2), rift (n = 13), intracratonic (n = 3), and aulacogen (n = 4); **Figure 9**]. The majority of ancient barrier island examples are Mesozoic Western Interior Seaway deposits from the U.S. (n = 32) and Canada (n = 8; **Figure 9**). A large number are also Tertiary Gulf of Mexico passive margin deposits (n = 14; **Figure 9**).

Kernel distributions (**Figure 10**) of dimensional data show that, using these measurement methods, modern and ancient barrier islands are quantitatively different. Ancient barrier islands are 2–5 times longer (p50 modern = 10.7 km; p50 ancient = 20.0 km), and 6–15 times wider (p50 modern = 1.2 km; p50 ancient = 7.3 km) than modern barrier islands. The median thickness values of the two datasets are similar (p50 modern = 11.0; p50 ancient = 15.2), however, the range of ancient thicknesses is three times greater than the modern range (**Figure 10A**).

Because of these distinct size differences, modern examples were compared to ancient examples separated by vertical amalgamation. Ancient examples were split into three groups (**Figure 3**): vertically amalgamated ancient examples with multiple parasequence measurements (Anc AMP), vertically amalgamated ancient examples with single parasequence measurements (Anc ASP), and non-amalgamated ancient examples (Anc NA). Box-and-whisker plots (**Figure 11**) show that vertically amalgamated ancient examples with multiple sequences (Anc AMP) are significantly thicker (5–10x) and wider (4–20x) than the other groups. Both types of amalgamated ancient examples, i.e., both multiple (Anc AMP; p50 = 40.70 km) and single (Anc ASP; p50 = 26.00 km) parasequence measurements, are longer than non-amalgamated ancient examples (Anc NA; p50 = 14.7) and modern examples (p50 = 10.69; **Figure 11B**).

Cross-plots (**Figure 12**) were used to compare modern dimensions to non-amalgamated and single parasequence amalgamated ancient examples. Cross-plotting thickness vs. length (**Figure 12A**) shows direct overlap between the modern and ancient with a single outlier. Cross-plotting thickness vs. width (**Figure 12B**) shows some overlap between modern and ancient datasets, with the ancient examples skewed toward larger width values. Cross-plotting length vs. width shows a distinct separation between modern and ancient values (**Figure 12C**). The datasets have unique lines of best fit (**Figure 12C**) with some overlap of their 90% confidence intervals. Scaling relationships exist between length and width for both modern (R^2 = 0.30) and the combined ancient single parasequence data (R^2 = 0.51), however, these lines of best fit do not intersect, indicating

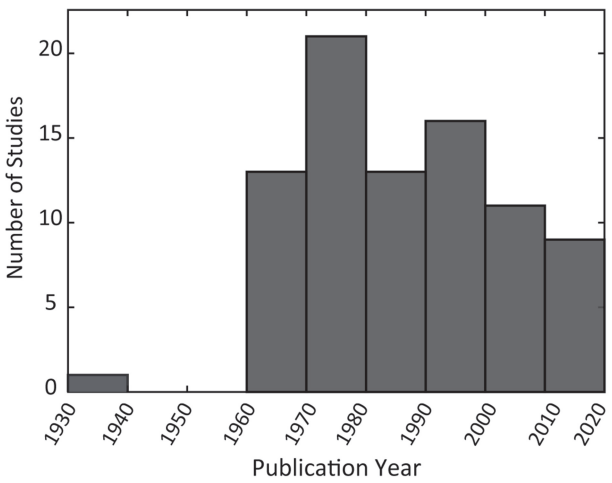


FIGURE 7 | Plot of barrier island studies by publication year showing variable usage over time. All ancient studies determined to be barrier islands (n = 83) included.

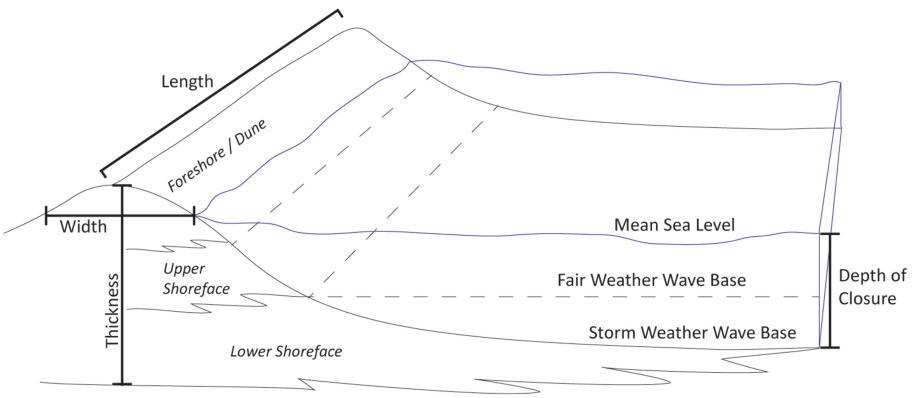


FIGURE 6 | Schematic diagram of a barrier island showing the relationship between the inner and outer depth of closure and fair and storm weather wave base.

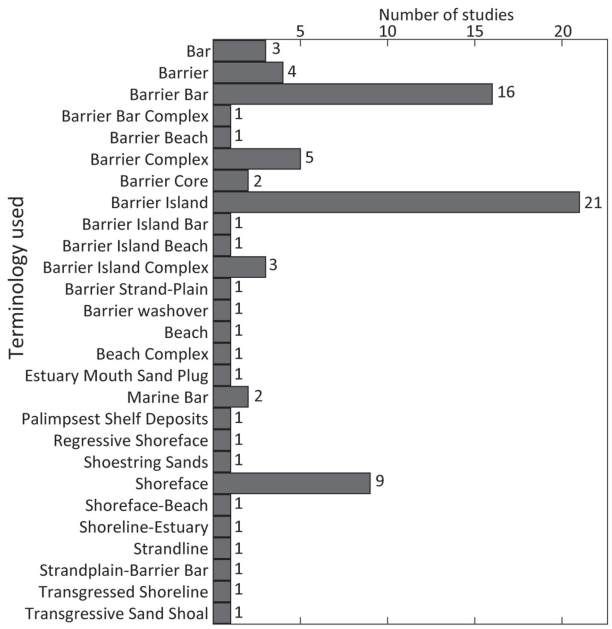


FIGURE 8 | A variety of terminology is used to describe barrier islands. This bar graph shows the prevalence of each term within the database. All ancient studies determined to be barrier islands ($n = 83$) included.

scaling between the modern and ancient using the offset between these trends.

DISCUSSION

Dimensional Comparisons

Initial comparisons using the dataset presented here show that ancient barrier island dimensions are systematically longer, thicker, and wider than modern barrier islands (**Figure 10**). These results suggest that barrier islands are time-transgressive, underscoring that for barrier islands, the modern is only indirectly the key to the past. At a first order, it is clear that modern barrier island dimensions should not be directly extrapolated to predict subsurface or outcrop dimensions, nor should such interpretations from the rock record be used exclusively to choose modern analogs. Instead, modern to modern and ancient to ancient comparisons are more appropriate and can be informed by the new datasets compiled for this analysis (**Table 1**; Mulhern et al., 2017). When evaluated from a process-based perspective, this database highlights the challenges associated with making comparable measurements as short time-scale processes are overprinted by geologic time-scale processes. These results reveal the importance of factors such as parasequence stacking, accretion through motion, and post depositional processes like ravinement in ancient barrier island deposits.

The ancient systems documented here are overwhelmingly from the Cretaceous of North America (48%; **Figure 9**). Many of these ancient barrier island examples were deposited in the high accommodation, high sediment supply setting of the Cordilleran foredeep (DeCelles, 2004) during a monsoonal greenhouse climate (Kauffman, 1977; Dennis et al., 2013). These temperate and high sediment supply conditions are thought to be ideal for modern barrier island development (Hoyt, 1967; Weidie, 1968; Hayes, 1979; Otvos, 2012) which, along with excellent outcrop exposures, accessibility, and subsurface data, could explain the abundance of Western Interior Seaway examples. The prevalence of these examples might suggest that climate should be considered during analog selection, and in developing systematic paleomorphodynamic relationships. A component of the scaling difference described here is likely resulting from the non-ideal comparison between these ancient islands, dominated by examples deposited in Cretaceous greenhouse conditions, and modern examples, formed during current interglacial conditions.

Another factor impacting the ancient database is the historical context of barrier island interpretations, which were most common in the 1960's and 1970's, following a detailed characterization of Galveston Island by Bernard et al. (1962). Interestingly, the database presented here shows that Galveston Island, one of the most heavily cited analogs for ancient barrier island deposits (e.g., Miller, 1962; Shelton, 1967; Davies and Berg, 1969; deVries Klein, 1974; Tizzard and Lerbekmo, 1975; Chiang, 1984; Yoshida et al., 2004; Ambrose and Ayers, 2007) is unusually large compared to the modern global dataset (**Figure 12C**), and therefore may be a very poor choice as a modern analog for many ancient systems, at least based on scaling relationships.

Barrier island interpretations declined slightly in the 1980's (**Figure 7**) relative to the previous two decades, which may reflect the proliferation of sequence stratigraphic models during this time. Simple sequence stratigraphic models predict a condensed interval or lag deposits during transgression (Vail et al., 1977; Galloway and Hobday, 1983; Posamentier et al., 1988; Van Wagoner et al., 1988; Cattaneo and Steel, 2003; Coe et al., 2003). Although the processes favoring preservation of transgressive deposits including barrier island-lagoon systems are now recognized, and sequence stratigraphic models are expanding (Jones et al., 2018; Pattison, 2018), a lack of updated facies models likely compounds the terminology problem in barrier island literature (**Figure 8**). Consequently, barrier island interpretations remain controversial because barrier island motion and preservation are poorly understood (Reinson, 1992; Cooper et al., 2018a). These challenges may explain why some interpretations avoid barrier island terminology and use descriptive but less environmentally-specific "shoreface" nomenclature (**Figure 8**) to describe shallow marine sandstones deposited during transgression (Allen and Johnson, 2011; Kieft et al., 2011; Olsen et al., 2017). As a result, barrier island deposits are likely under-represented in the last 30 years of geologic literature (**Figure 7**).

Compiling and comparing modern and ancient barrier islands sheds light on the role of time and preservation in controlling barrier island dimensions, increasing understanding to improve comparisons, interpretations, and predictions. Ancient barrier islands preserve motion at the 10^5-10^7 year timescales while modern barrier island motion takes place over 10^1-10^3 year timescales (Cooper et al., 2018a). Given that modern barrier islands build landward, seaward, laterally, and vertically

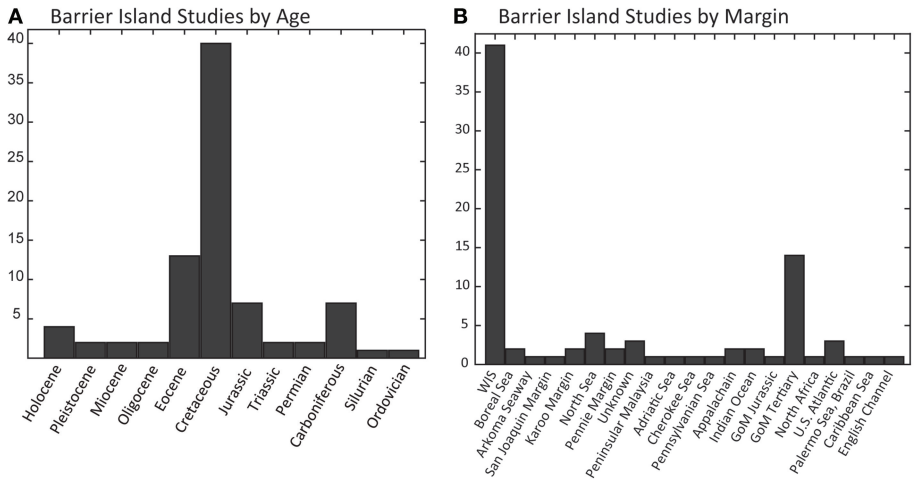
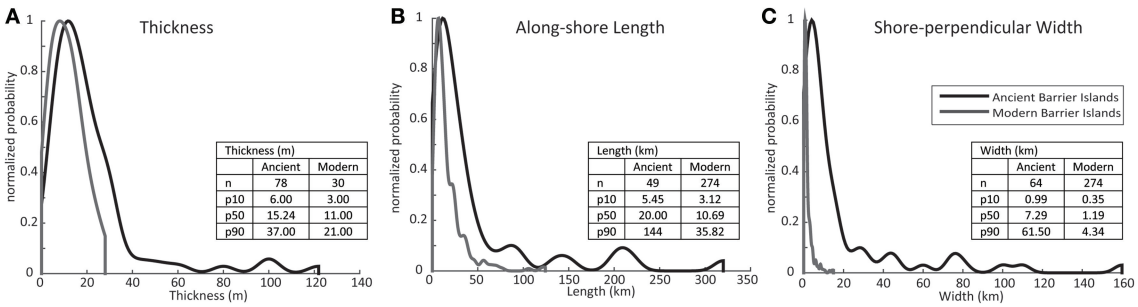


FIGURE 9 | Age **(A)** and paleo-margin **(B)** distribution of ancient barrier island studies.

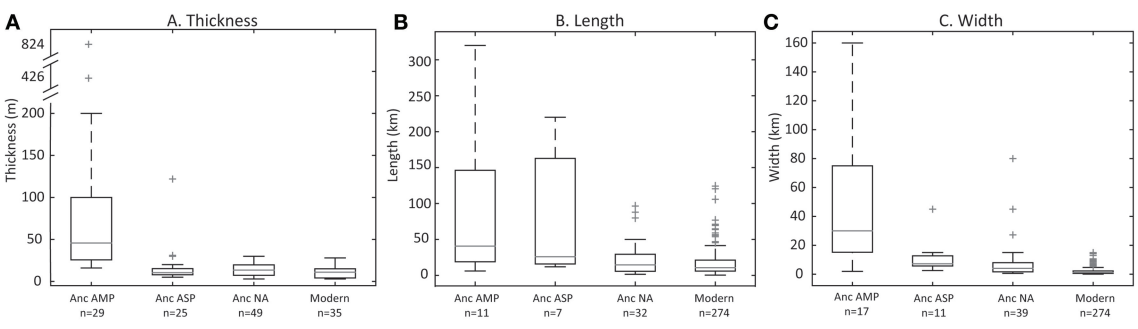


Thickness (m)	Ancient	Modern
n	78	30
p10	6.00	3.00
p50	15.24	11.00
p90	37.00	21.00

Length (km)	Ancient	Modern
n	49	274
p10	5.45	3.12
p50	20.00	10.69
p90	144	35.82

Width (km)	Ancient	Modern
n	64	274
p10	0.99	0.35
p50	7.29	1.19
p90	61.50	4.34

FIGURE 10 | Normalized kernel distributions (non-parametric representations of the probability density function) showing the range of thickness **(A)**, length **(B)**, and width **(C)** values of modern barrier islands (gray) and ancient barrier islands (black). The lower ten percent (p10), median (p50), and upper ten percent (p90) values are listed for each dimension.



	Anc AMP	Anc ASP	Anc NA	Mod
n	29	25	49	35
p10	19.73	7.50	4.46	3.00
p50	45.72	10.50	13.50	11.00
Mean	102.90	17.29	14.04	10.96
p90	180.80	30.00	24.75	21.00

	Anc AMP	Anc ASP	Anc NA	Mod
n	11	7	32	274
p10	10.74	12.40	4.86	3.12
p50	40.70	26.00	14.7	10.69
Mean	93.00	77.53	22.28	16.18
p90	253.40	216.20	59.00	35.82

	Anc AMP	Anc ASP	Anc NA	Mod
n	17	11	39	274
p10	6.34	3.31	0.85	0.35
p50	30.00	7.24	4.08	1.19
Mean	46.36	11.15	8.01	1.90
p90	108.00	27.00	12.88	4.34

FIGURE 11 | Box-and-whisker plots the ancient data separated as ancient amalgamated multiple parasequence (Anc AMP), ancient amalgamated single parasequence (Anc ASP), ancient not amalgamated (Anc NA) compared to the modern (Mod). While amalgamated ancient examples with multiple parasequences measured (Anc AMP) are larger than the other categories, comparisons between the single parasequence examples (Anc ASP and Anc NA) lend insight into barrier island preservation. Gray lines mark the median. Plus signs mark outliers. The lower ten percent (p10), median (p50), and upper ten percent (p90) values are listed for each dimension.

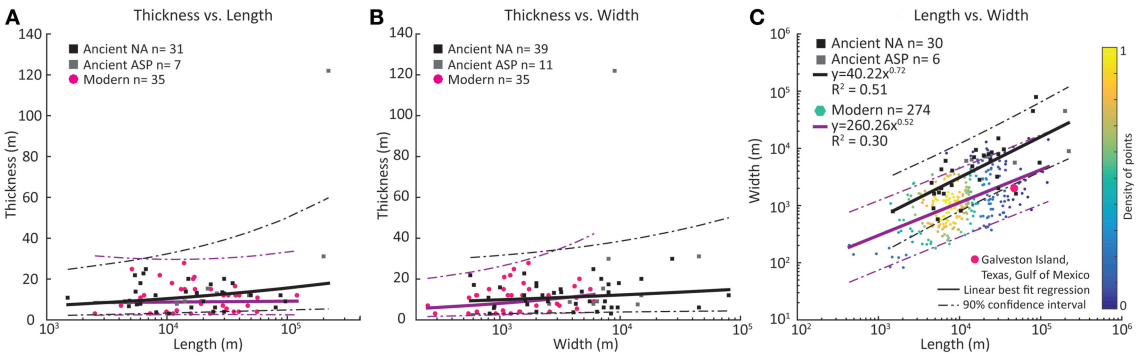


FIGURE 12 | Cross plots of thickness vs. length **(A)** and thickness vs. width **(B)** for modern (pink), ancient not amalgamated (NA-black), and ancient amalgamated single parasequences (ASP-gray) barrier island dimensions. Length vs. width **(C)** cross-plot showing ancient not amalgamated (NA-black), ancient amalgamated single parasequences (ASP-gray), and modern thickness data are colored by density (color bar on right), ranging from more dense data (yellow) to less dense (blue). On all three plots, the solid lines (modern: purple, ancient: black) show the best-fit trend through the data, while the dashed lines show the 10 and 90% confidence limits on the dataset. Galveston Island (pink circle) is large relative to the modern global dataset.

(**Figure 13**), larger dimensions from ancient examples can likely be attributed to motion-driven accretion and/or the stacking of individual islands through time (Ambrose and Ayers, 2007). The stacking and erosional processes that occur at geologic timescales are more complex than the accretion and washover processes dictating barrier island motion at modern time scales. A more detailed look the initial comparisons presented here (**Figure 10**) sheds light on the processes of barrier island preservation and areas of further study required for the development of robust paleomorphodynamic relationships.

To investigate the impact of amalgamation and stacking over geologic time, ancient barrier island examples that contain multiple stacked parasequences were separated from those interpreted as a single island (**Figure 3**). While determining vertical amalgamation is not always straightforward (**Figure 14**), these comparisons (**Figure 11**) show that ancient barrier island examples with multiple parasequences are larger (longer, wider, and thicker) than all other examples. This is a logical result given that multiple barrier islands can be stacked and preserved in conjunction with one another as the shoreline shifts over geologic timescales. Nevertheless, the prevalence of not amalgamated (n = 51) relative to amalgamated barrier island examples (n = 32) suggests that both island motion and stacking take place, emphasizing that barrier island accretion and preservation are key considerations for barrier island system evolution (Dickinson et al., 1972; Barwis and Hayes, 1979; Reinson, 1992).

Here we discuss both the full dataset results and the results separated by vertical amalgamation for each dimensional measurement (length, width, thickness) to consider the processes dictating those dimensions and the impact of barrier island motion and preservation dynamics.

Thickness

Ancient barrier island examples are thicker than modern examples (**Figure 10A**). The median thickness values of the two datasets are similar (p50 modern = 11.0 m; p50 ancient =15.2 m; **Figure 10A**), however the range of ancient barrier island thicknesses is three times greater than the modern range. The range in ancient barrier island thicknesses could partly reflect measurement uncertainty, given that thickness can vary laterally along strike and that the measurement requires an interpretation of the base of the island deposits (**Figure 4**). Nevertheless, a logical result is that vertically amalgamated islands with multiple parasequences (Anc AMP; p50 = 45.72 m) are significantly thicker than individual (single) ancient (~6x; Anc ASP; p50 = 10.50 m) and modern (~10x; p50 = 11.00 m) barrier islands (**Figure 11A**). The thickness of ancient multiple parasequence examples (Anc AMP; p50 = 45.72 m) is likely a function of the available accommodation through time, assuming sufficient sediment supply. In contrast, the other two groups of ancient examples (amalgamated single parasequence (Anc ASP; p50 = 10.50 m) and non-amalgamated (Anc NA; p50 = 13.50 m), are both similar to modern thicknesses (Mod; p50 = 11.00 m), a result that increases confidence in thickness measurements for individual modern and ancient barrier islands. The values likely reflect local accommodation and variability in the depth of closure, which could potentially be used to quantitatively link modern and ancient systems.

Length

Ancient barrier island lengths (p50 ancient = 20 km) are 2–5 times modern lengths (p50 modern = 10.69 km; **Figure 10B**) demonstrating that, as a whole, ancient islands preserve lateral migration at geologic timescales. When separated by vertical amalgamation (**Figure 11B**), comparisons show that both multiple (Anc AMP; p50 = 40.70 km) and single (Anc ASP; p50 = 26.00 km) parasequence amalgamated ancient examples are longer than ancient non-amalgamated (Anc NA; p50 = 14.7 km) and modern examples (p50 = 10.69 km).

In addition to the parasequence stacking preserved by the ancient amalgamated multiple parasequence examples, the long lengths of single parasequence amalgamated examples (relative to the modern) demonstrates that barrier island systems can preserve lateral, shore-parallel, accretion, and amalgamation over

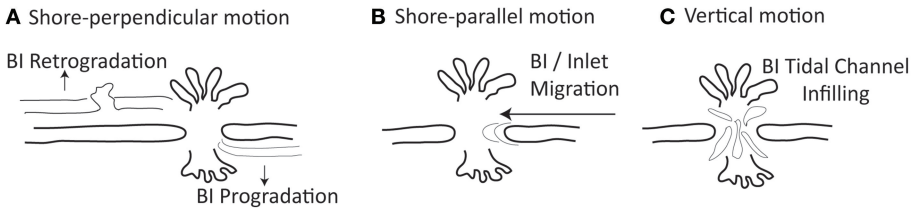


FIGURE 13 | Modern barrier islands are highly ephemeral and display multiple directions of localized motion. Schematic plan-form maps show that **(A)** barrier islands move in the shore-perpendicular direction through basinward progradation or landward washover processes (Davis, 1994a; Cooper et al., 2018a). **(B)** Barrier islands move in the shore-parallel direction through tidal inlet migration and accretion driven by long-shore drift (Moslow and Tye, 1985; Hayes and FitzGerald, 2013). **(C)** Barrier islands build and accrete vertically with sufficient sediment supply and accommodation (Simms et al., 2006).

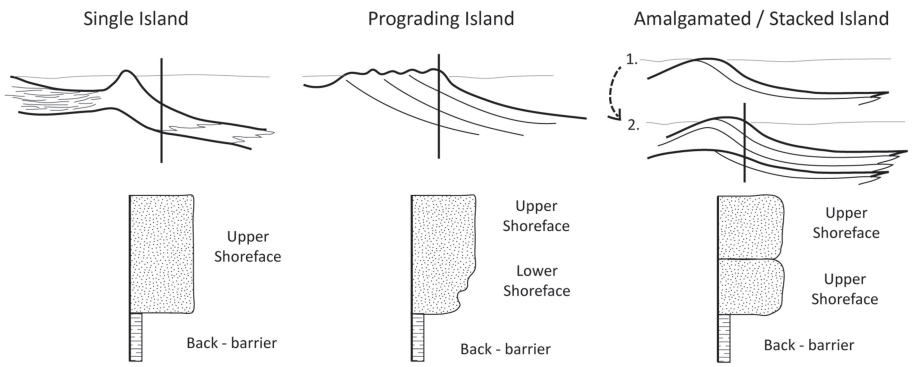


FIGURE 14 | Schematic cross-sections and measured sections through barrier islands at three different stages of amalgamation. These sections illustrate that barrier island amalgamation and reworking likely increases as a function of time, therefore, most preserved barrier islands contain some degree of amalgamation. Additionally, the degree of amalgamation may be difficult to determine due to the similarity in the preserved facies.

geologic time. Modern barrier islands move in the shore-parallel direction through tidal inlet migration and island accretion driven by long-shore transport (e.g., recurved spit migration; FitzGerald, 1988; Seminack and McBride, 2015). Evidence of barrier island reworking through inlet generation, migration, and healing, is commonly observed in preserved deposits (Davies and Ethridge, 1971; Davies, 1978; Galloway, 1986; Self et al., 1986; Hendricks, 1994; Mulhern and Johnson, 2016) and these processes likely increase the length of single parasequence amalgamated examples. In addition to lateral migration, if an inlet infills with sand vertically, it can link two separate barrier islands into a single larger one. In some cases, migrating tidal inlet deposits comprise the primary barrier island succession, recording lateral motion of the island across the inlet channel through time (Moslow and Tye, 1985). Alternatively, in some modern examples, the shoreface can extend across the inlet mouth, uninterrupted by inlet process, particularly on wave-dominated coasts where ebb-tidal deltas tend to be smaller and sand is readily reworked across the inlet mouth (**Figure 5**; Hayes, 1979; FitzGerald et al., 2012). The increased length of ancient examples suggests that barrier island deposits are inherently time-transgressive, recording lateral island motion via tidal inlet migration (lateral accretion) and amalgamation on a different time scale than modern barrier island migration.

Modern (p50 = 10.69 km) and non-amalgamated ancient (Anc NA; p50 = 14.70 km) examples have similar lengths (**Figure 11B**), however the processes limiting island length in the modern and ancient are different. In modern systems, tidal inlets can limit barrier island length (**Figure 4A**; Hayes, 1979), and inlet location and frequency can depend on a variety of factors including the tidal range, tidal prism, the location of storm scours or paleovalleys, longshore transport, and spit migration (Phleger, 1969; Hayes and FitzGerald, 2013; Mulhern et al., 2017). These limiting factors are less clear in the rock record, where measurements are derived from the preserved shoreface, which commonly grades laterally from shoreface to tidal facies along the length (strike-direction) of a single island (**Figure 5**; Davies and Ethridge, 1971; Davies, 1978; Galloway, 1986; Self et al., 1986; Hendricks, 1994; Mulhern and Johnson, 2016). Thus a given inlet location may not be discernable in ancient barrier island systems, and certainly cannot be recognized without very detailed facies analysis (e.g., Reddering, 1983; Caplan and Moslow, 1999). Non-amalgamated ancient examples are more likely limited by the outcrop exposure or type and spacing of available subsurface data. Therefore, while modern and ancient non-amalgamated length values are similar, the large range of values (both modern and ancient) could reflect database limitations rather than an inherent sedimentary process.

Width

Ancient barrier islands are 6–15 times wider (p50 modern = 1.2 km; p50 ancient = 7.3 km) than modern barrier islands

(**Figure 10C**). This large width difference is likely due to both measurement techniques and amalgamation processes. Comparisons separated by amalgamation (**Figure 11C**) show that ancient amalgamated examples with multiple parasequences (Anc AMP; p50 = 30.00 km) are significantly wider than other ancient examples (4–5x) and modern examples (23x). Similarly, the remaining ancient examples, ancient amalgamated single parasequence (Anc ASP; p50 = 7.24 km) and ancient non-amalgamated examples (Anc NA; p50 = 4.08 km), are both wider than modern examples (Mod; p50 = 1.19 km). The topset vs. foreset widths of some modern examples were measured to understand whether the systematically greater ancient widths are a function of how the width measurements were made, or whether they are geologically significant. In modern settings, the subaerial topset defines the width; in ancient examples, both the topset width and the final foreset width combine to define the preserved width (**Figure 4B**). In order to better mirror the ancient width scale in the modern, both subaerial topset width and foreset length would need to be measured. Foreset data are quite rare from modern barrier systems, because core studies and data constraining modern barrier island clinothems are sparse. The few complete examples in the modern barrier island database (n = 5) have foresets that are 1.2–4.0 times the topset width (Rampino and Sanders, 1980; Chiang, 1984; Davis and Hayes, 1984; Moslow and Heron, 1994). Ancient examples are 3.4–6.1 times wider than modern examples (based on their mean values). This large difference, compared to the 1.2–4.0 topset vs. foreset difference, suggests that there is more variability than can be explained by measurement differences, indicating that ancient barrier island deposits preserve some shore-perpendicular motion through time.

Further evidence for ancient barrier island motion is manifest in the internal facies patterns of preserved barrier island deposits. Some preserved examples show coarsening and shallowing upwards successions (Sabins, 1963; Land, 1972; Bridges, 1976; Roehler, 1988; Roy et al., 1994; Sixsmith et al., 2008), indicating progradation of the shoreface via Walther's law (Middleton, 1973). Other examples show internal washover processes, suggesting retrogradation ((Hobday and Orme, 1974; Hobday and Jackson, 1979; Willis and Moslow, 1994)a). Because similar processes occur in both modern and ancient systems, the increased relative width of ancient examples suggests that ancient barrier islands are time-transgressive and that the deposit widths record motion at longer time scales than modern barrier island widths. In summary, these comparisons show that the processes occurring at geologic time scales alter the dimensions of ancient barrier islands. Comparisons by amalgamation (**Figure 11**) emphasize the complexity of barrier island motion and reworking, highlighting the need for an improved understanding of barrier island preservation. Amalgamation and reworking of barrier islands likely increases through time. Barrier islands can be deposited rapidly (Stutz and Pilkey, 2011) resulting in massive and undifferentiated sandbodies lacking internal differentiation. This homogeneity may mask internal sedimentological evidence or trends in grainsize which can be used to interpret parasequence boundaries. Reworking of units through tidal ravinement or lateral motion can complicate the depositional history and overwrite sedimentological evidence of parasequence boundaries within a single deposit. Depending on how islands stack and the degree of ravinement, the preserved vertical sequence of an amalgamated system may look similar to that of a single island or a prograding system. Considering the possible complexities preserved in barrier island deposits highlights the additional research needed to fully understand barrier island preservation, enable modern to ancient analog selection, and develop paleomorphodynamic relationships. As coastlines continue to change in response to the warming climate, a detailed understanding of the role of accommodation, sediment supply, and preservation timescales will be helpful in predicting future coastal morphology and creating effective environmental policy, development plans, and coastal remediation strategies.

While this analysis starts to investigate modern and preserved barrier island dimensions, it does not include a full analysis of the multitude of factors thought to play a role in determining barrier island morphology, which, in addition to those discussed above, include sediment supply, sediment composition, basement slope, and substrate geology (Cooper et al., 2018a). Both datasets, modern and ancient, are comprised of examples from a wide range of sediment supply regimes, therefore the interpretations discussed here can be applied to a variety of settings. Sediment supply in barrier islands is complicated by the intermingling of direct fluvial inputs to the coast line, reworking, long shore transport, and sediment storage offshore, therefore quantifying sediment supply fluctuations and links barrier island motion may be difficult.

Paleomorphodynamic Implications

Cross-plots of length vs. thickness and width vs. thickness (**Figures 12A,B**) do not show systematic scaling relationships between modern and ancient examples, and therefore are not helpful in developing predictive modern to ancient relationships. This is unsurprising given the various time-based factors influencing the thickness of ancient examples (accretion, stacking, and ravinement) in addition local accommodation and post-depositional erosion. However, thickness similarities between ancient and modern examples could potentially be linked to a process-based control, such as depth of closure.

The depth of closure is vertical height between the mean sea level and storm weather wave base (**Figure 6**) calculated using wave height, wave period and sediment grain size (Brutsché et al., 2014) and is the depth below which there is no significant net sediment transport (Birkemeier, 1985; Kraus, 1988; Nicholls et al., 1998; Wallace et al., 2010). A variety of time-dependent equations estimate depth of closure for use in modern morphodynamics and hydrodynamics (Hallermeier and Nauman, 1978; Hallermeier, 1981; Birkemeier, 1985; Brutsché et al., 2014), empirically quantifying the limit of storm and wave processes on near shore sediments. Because the depth of closure relates to levels of wave base, it could be used to precisely compare specific portions of modern and ancient barrier island shorefaces. For example, ancient upper and lower shoreface thicknesses could be compared to inner and outer depth of closure values, respectively (**Figure 6**).

While conceptually straightforward, these comparisons would be difficult to execute because of limited data availability, ambiguity in the rock record, and difficulty in measuring and/or modeling the depth of closure in modern settings (Bernabeu et al., 2003a; Kana et al., 2011). Utilizing depth of closure would require careful consideration because depth of closure is highly variable (both along strike on a given barrier island and through time) and is dependent on the timescale over which it is measured (Bernabeu et al., 2003b; Phillips and Williams, 2007; Wallace et al., 2010). These complexities in determining the depth of closure in the modern would likely be magnified when extrapolating between modern and ancient.

More broadly, the fields of nearshore hydrodynamics and numerical modeling can help to quantify and predict modern barrier island geometries, generating relationships that could be used in paleomorphodynamics. Although imperfect (Cooper and Pilkey, 2004; Cooper et al., 2018a), equilibrium beach profile equations (Bruun, 1962) could be adapted and modified to account for variable erosion rates, impact of storms, and multiple modes of barrier island motion (roll over, erosion, over-stepping) to better estimate shelf morphology and slope to predict available accommodation (Loureiro et al., 2012; Mellett et al., 2012; Cooper et al., 2018a; Mellett and Plater, 2018). Tidal inlet depth (de Swart and Zimmerman, 2009), cross-sectional area (Gao and Collins, 1994; van de Kreeke, 2004), or symmetry (Hoyt and Henry, 1965) calculations could be linked to island characteristics and morphology. Direct comparisons between specific modern and ancient sub-environments (i.e., upper shoreface) could also potentially aid in understanding scaling. Recently drowned barrier island examples on modern shelves may provide clues to understanding the link between the modern and the ancient. Drowned barrier islands have been the focus of ongoing research (Mellett et al., 2012; Green et al., 2013, 2018; Salzmann et al., 2013; Cooper et al., 2016, 2018b; Pretorius et al., 2016; Brooke et al., 2017; Mellett and Plater, 2018). Measurements show that drowned islands are smaller than equivalent modern barriers (Green et al., 2013), emphasizing the importance of understanding timescale and motion processes in linking modern and ancient barrier islands.

Although crossplots using thickness values are not currently insightful, length, and width differences between the modern and ancient realms are significant and persist once multiple amalgamated parasequence examples are removed (**Figures 11B,C**). Increased lengths and widths of ancient barrier islands suggest that preserved deposits are time-transgressive. Cross-plotting length vs. width highlights the dimensional difference between modern and ancient barrier islands (single parasequence measurements only; **Figure 12C**). The ancient barrier islands are skewed to longer and wider values relative to the modern examples. There is some overlap in the 90% confidence intervals, however, modern dimensions do not directly predict ancient dimensions because the trend lines of both datasets are offset. These trend lines are predictive (modern $R^2 = 0.30$, ancient $R^2 = 0.51$) meaning that length predicts width and vice versa for both systems for the two datasets independently, but not together. The offset between the lines implies that modern dimensions need to be scaled to be used in subsurface predictions, and vice versa.

In summary, future development of paleomorphodynamic relationships for barrier islands cannot escape the fundamental complication that ancient barrier islands preserve motion through time and post-depositional processes, which dictate their dimensions. In contrast to channelized systems, which are self-organized and display dynamic scaling (Sapozhnikov and Foufoula-Georgiou, 1997; Paola and Foufoula-Georgiou, 2001; Lane, 2006; Martin et al., 2018), the barrier island dynamics are time-scale dependent: processes occurring at short time scales (accretion and washover) vary from those occurring at geologic time scales (amalgamation, stacking, back-stepping, ravinement, reworking). Consequently, ancient barrier island deposits cannot be linked to a single modern snapshot in time. This complexity will influence the way paleomorphodynamics can be developed for the shallow marine realm. This dataset outlines a workflow for quantifying ancient barrier islands and begins quantitative comparison of modern and ancient systems. The significant scaling relationships between length and width (**Figure 12C**) suggest that rotation and translation could potentially be used to relate the two datasets, pending more data. Although more examples are needed, gathering and measuring ancient barrier island dimensions constrains the range and distribution of dimensional values (**Table 1**; **Figures 11**, **12**). These examples could be leveraged as analogs for modeling and subsurface predictions and combined with other shallow marine datasets (Colombera et al., 2016; Brooke et al., 2017) to refine paleomorphodynamic comparisons.

CONCLUSIONS

Ancient barrier island dimensions are highly variable, ranging widely by age and tectonic and climatic settings. Simple measurement methods are not directly analogous for modern and ancient datasets, therefore unsurprisingly, first pass comparisons show that modern and ancient barrier island dimensions do not scale 1:1. Consequently, modern analog dimensions should not be directly applied to ancient interpretations and predictions, and caution should be used when comparing between ancient examples. First-order comparison of modern and ancient barrier island dimensions shows that ancient barrier island deposits are wider and longer than modern barrier islands, recording lateral and shore-perpendicular motion through time. Thickness differences suggest that ancient barrier island deposits can record vertical stacking of multiple barrier islands through time, emphasizing the role of accommodation in determining barrier island preservation potential. Available accommodation determines the thickness of ancient deposits, rather than the size of the paleo-island. There appear to be systematic shifts in modern vs. ancient barrier island dimensions (length and width), suggesting that ancient barrier island deposits are time-transgressive. These results are a first step toward understanding and quantifying the paleomorphodynamic relationships between modern and ancient barrier islands. The dataset also highlights inconsistencies in barrier island terminology and facies models based on depositional trends, underscoring the need for updated barrier island facies models. Additional research into barrier

island facies and preservation processes may provide key insight to predicting how coast lines respond to climate change.

AUTHOR CONTRIBUTIONS

JSM was the primary author of this paper as it was original research conducted as part of her Ph.D., advised by CLJ. JMM helped with database construction, coding, and analysis. All authors provided input to the methods, interpretation, and writing process.

FUNDING

A variety of sources funded this original research as part of JSM Ph.D. Her work was supported by the Rocks2Models research consortium with funding from Chevron, ConocoPhillips, Hess Corporation, Shell, and Statoil. Support was also received from University of Utah Graduate Research Fellowship, ConocoPhillips Graduate Research Fellowship, Rocky Mountain Association of Geologists Foundation Babock Scholarship and SEPM Rocky Mountain section Donald Smith Research Grant.

REFERENCES

Allen, J. L., and Johnson, C. L. (2011). Architecture and formation of transgressive-regressive cycles in marginal marine strata of the John Henry Member, straight cliffs formation, Upper Cretaceous of southern Utah, USA. *Sedimentology* 58, 1486–1513. doi: 10.1111/j.1365-3091.2010.01223.x

Ambrose, W. A., and Ayers, W. B. (2007). Geologic controls on transgressive-regressive cyles in the upper pictured cliffs sandstone and coal geometry in the lower fruitland formation, northern San Juan Basin, New Mexico and Colorado. *Am. Assoc. Pet. Geol. Bull.* 91, 1099–1122. doi: 10.1306/03080706040

Ambrose, W. A., and Ferrer, E. R. (1997). Seismic stratigraphy and oil recovery potential of tide-dominated depositional sequences in the Lower Misoa Formation (Lower Eocene), LL-652 Area, Lagunillas Field, Lake Maracaibo, Venezuela. *Geophysics* 62, 1483–1495. doi: 10.1190/1.1444252

Anthony, E. J. (2009). *Shore Processes and Their Palaeoenvironmental Applications, 1st Edn*. Amsterdam: Elsevier.

Antia, J., Fielding, C. R., and Joeckel, R. M. (2011). Multiple cycles of wave-dominated estuarine deposits in low-accommodation settings, Cretaceous J sandstone, northwestern Nebraska. *Am. Assoc. Pet. Geol. Bull.* 95, 1227–1256. doi: 10.1306/11051009105

Arnott, R. W. C. (1995). The parasequence definition-are transgressive deposits inadequately addressed? *J. Sediment. Res.* 65, 1–6. doi: 10.1306/D42681D0-2B26-11D7-8648000102C1865D

Barwis, J. H., and Hayes, M. O. (1979). "Regional patterns of modern barrier island and tidal inlet deposits as applied to paleoenvironmental studies," in *Carboniferous Depositional Environments in the Appalachian Region*, eds J. C. Ferm and J. C. Horne (Columbia, SC: University of South Carolina Geology Department), 472–498.

Barwis, J. H., and Horne, J. C. (1979). "Paleotidal range indicators in the carboniferous barriers of northeastern kentucky," in *Carboniferous Depositional Environments in the Appalachian Region*, eds J. C. Ferm, J. C. Horne, G. A. Weisenfluh, and J. R. Staub Columbia (Columbia, SC: United States: Univ. S.C., Dep. Geol).

Bass, N. W. (1934). Origin of Bartlesville shoestring sands, Greenwood and Butler Counties, Kansas. *Am. Assocation Pet. Geol. Bull.* 18, 1313–1345. doi: 10.1306/3D932C7A-16B1-11D7-8645000102C1865D

Belknap, D. F., and Kraft, J. C. (1981). Preservation potential of transgressive coastal lithosomes on the U.S. *Atlant. Shelf. Mar. Geol.* 42, 429–442. doi: 10.1016/S0070-4571(08)70309-1

Berg, R. R. (1970). Identification of sedimentary environments in reservoir sandstones. *Trans. Gulf Coast Assicat. Geol. Soc.* 20, 137–143.

Berg, R. R. (1976). Hilight muddy field-lower cretaceous transgressive deposits in the powder river basin, Wyoming. *Mt. Geol.* 13, 33–45.

Berg, R. R., and Davies, D. (1968). Origin of lower cretaceous muddy sandstone at bell creek field, Montana. *Am. Assoc. Pet. Geol. Bull.* 52, 1888–1898. doi: 10.1306/5D25C53B-16C1-11D7-8645000102C1865D

Bergman, K. M., and Walker, R. G. (1987). The importance of sea-level fluctuations in the formation of linear conglomerate bodies; carrot creek member of cardium formation, cretaceous western interior seaway, Alberta, Canada. *J. Sediment. Res.* 57, 651–665. doi: 10.1306/212F8BCA-2B24-11D7-8648000102C1865D

Bernabeu, A. M., Medina, R., and Vidal, C. (2003a). A morphological model of the beach profile integrating wave and tidal influences. *Mar. Geol.* 197, 95–116. doi: 10.1016/S0025-3227(03)00087-2

Bernabeu, A. M., Medina, R., and Vidal, C. (2003b). Wave reflection on natural beaches: an equilibrium beach profile model. *Estuar. Coast. Shelf Sci.* 57, 577–585. doi: 10.1016/S0272-7714(02)00393-1

Bernard, H. A., LeBlanc, R. J., and Major, C. F. (1962). "Recent and Pleistocene geology of southeast Texas, Field excursion no. 3," in *Geology of the Gulf Coast and Central Texas and Guidebook of Excursions*, eds E. H. Rainwater and R. P. Zingula (Houston, TX: Houston Geological Society), 175–224.

Bibler, C. J., and Schmitt, J. G. (1986). Barrier-island coastline deposition and paleogeographic implications of the upper cretaceous horsethief formation, Northern Disturbed Belt, Montana. *Mt. Geol.* 23, 113–127.

Birkemeier, W. A. (1985). Field data on seaward limit of profile change. *J. Waterw. Port Coast. Ocean Eng.* 111, 598–602. doi: 10.1061/(ASCE)0733-950X(1985)111:3(598)

Blum, M., Martin, J., Milliken, K., and Garvin, M. (2013). Paleovalley systems: insights from quaternary analogs and experiments. *Earth Sci. Rev.* 116, 128–169. doi: 10.1016/j.earscirev.2012.09.003

Boyd, D. R., and Dyer, B. F. (1964). Frio barrier bar system of south Texas. *Trans. Gulf Coast. Assoc. Geol. Soc.* 14, 309–322.

Boyd, R. (2010). "Transgressive wave-dominated coasts," in *Facies Models 4*, eds N. P. James and R. W. Dalrymple (St. John's, NL: Geological Association of Canada), 265–294.

Bridges, P. H. (1976). Lower Silurian transgressive barrier islands, southwest Wales. *Sedimentology* 23, 347–362. doi: 10.1111/j.1365-3091.1976.tb00054.x

Brooke, B. P., Nichol, S. L., Huang, Z., and Beaman, R. J. (2017). Palaeoshorelines on the Australian continental shelf: morphology, sea-level relationship and applications to environmental management and archaeology. *Cont. Shelf Res.* 134, 26–38. doi: 10.1016/j.csr.2016.12.012

Brutsché, K. E., Rosati, J., Pollock, C. E., McFall, B. C., Iii, J. R., and Cheryl, E. (2014). *Calculating Depth of Closure Using WIS Hindcast Data*. US Army Corps Eng. ERDC/CHL C, 1–10.

Bruun, P. (1962). Sea-level rise as a cause of shore erosion. *Proc. Am. Soc. Civ. Eng.* 88, 117–130.

Buatois, L. A., Mángano, M. G., and Carr, T. R. (1999). Sedimentology and ichnology of Paleozoic estuarine and shoreface reservoirs, Morrow Sandstone, Lower Pennsylvanian of southwest Kansas, USA. *Geol. Soc. Bull.* 243, 1–35.

Campbell, C. V. (1971). Depositional model: upper cretaceous Gallup beach shoreline, Ship Rock area, northwestern New Mexico. *J. Sediment. Res.* 41, 395–409. doi: 10.1306/74D7227F-2B21-11D7-8648000102C1865D

Campbell, C. V. (1979). *Model for Beach Shoreline in Gallup Sandstone (Upper Cretaceous) of Northwestern New Mexico*. Socorro, NM: NM Bur Mines Min. Resour Circ.

Cant, D. J. (1984). Development of shoreline-shelf sand bodies in a Cretaceous epeiric sea deposit. *J. Sediment. Petrol.* 54, 541–556. doi: 10.1306/212F8463-2B24-11D7-8648000102C1865D

Caplan, M. L., and Moslow, T. F. (1999). Depositional origin and facies variability of a middle triassic barrier island complex, peejay field, northeastern British Columbia. *Am. Assoc. Pet. Geol. Bull.* 83, 128–154.

Carter, C. H. (1978). A regressive barrier and barrier-protected deposit: depositional environments and geographic setting of the late tertiary cohansey sand. *J. Sediment. Res.* 48, 933–949. doi: 10.1306/212F75AE-2B24-11D7-8648000102C1865D

Cattaneo, A., and Steel, R. J. (2003). Transgressive deposits: a review of their variability. *Earth Sci. Rev.* 62, 187–228. doi: 10.1016/S0012-8252(02)00134-4

Catuneanu, O., Bhattacharya, J. P., Blum, M. D., Dalrymple, R. W., Eriksson, P. G., Fielding, C. R., et al. (2010). Sequence stratigraphy: common ground after three decades of development. *First Break* 28, 21–34. doi: 10.3997/1365-2397.2010002

Cavaroc, V. V., Padgett, G., Stephens, D. G., Kanes, W. H., Boudda, A., and Woolen, I. D. (1976). Late Paleozoic of the Tindouf Basin-North Africa. *J. Sediment. Res.* 46, 77–88. doi: 10.1306/212F6EC4-2B24-11D7-8648000102C1865D

Chiang, K. K. (1984). "The giant Hoadley gas field, south-central Alberta," in *Elmworth: Case Study of a Deep Basin Gas Field*, ed J. A. Masters (Tulsa, OK: American Association of Petroleum Geologists Memior, 38), 297–313.

Coe, A. L., Bosence, D. W., Church, K. D., Flint, S. S., Howell, J. A., and Wilson, R. C. L. (eds). (2003). *The Sedimentary Record of Sea-Level Change*. Cambridge: Cambridge University Press.

Colombera, L., Mountney, N. P., Hodgson, D. M., and McCaffrey, W. D. (2016). The shallow-marine architecture knowledge store: a database for the characterization of shallow-marine and paralic depositional systems. *Mar. Pet. Geol.* 75, 83–99. doi: 10.1016/j.marpetgeo.2016.03.027

Cooper, J. A. G., Green, A. N., and Loureiro, C. (2018a). Geological constraints on mesoscale coastal barrier behaviour. *Glob. Planet. Change* 168, 15–34. doi: 10.1016/j.gloplacha.2018.06.006

Cooper, J. A. G., Green, A. N., Meireles, R. P., Klein, A. H. F., Souza, J., and Toldo, E. E. (2016). Sandy barrier overstepping and preservation linked to rapid sea level rise and geological setting. *Mar. Geol.* 382, 80–91. doi: 10.1016/j.margeo.2016.10.003

Cooper, J. A. G., Meireles, R. P., Green, A. N., Klein, A. H. F., and Toldo, E. E. (2018b). Late quaternary stratigraphic evolution of the inner continental shelf in response to sea-level change, Santa Catarina, Brazil. *Mar. Geol.* 397, 1–14. doi: 10.1016/j.margeo.2017.11.011

Cooper, J. A. G., and Pilkey, O. H. (2004). Sea-level rise and shoreline retreat: time to abandon the Bruun Rule. *Glob. Planet. Change* 43, 157–171. doi: 10.1016/j.gloplacha.2004.07.001

Covault, J. A., Shelef, E., Traer, M., Hubbard, S. M., Romans, B. W., and Fildani, A. (2012). Deep-water channel run-out length: insights from seafloor geomorphology. *J. Sediment. Res.* 82, 21–36. doi: 10.2110/jsr.2012.2

Daly, J., McGeary, S., and Krantz, D. E. (2002). Ground-penetrating radar investigation of a late Holocene spit complex: cape Henlopen, Delaware. *J. Coast. Res.* 18, 274–286.

Davies, D. K. (1969). Shelf sedimentation: an example from the Jurassic of Britain. *J. Sediment. Res.* 39, 1344–1370. doi: 10.1306/74D71E29-2B21-11D7-8648000102C1865D

Davies, D. K. (1978). "Models and concepts for exploration in barrier islands," in *Sedimentary Environments and Hydrocarbons*, ed R. S. Saxena (New Orleans, LA: Gulf Coast Association of Geological Societies), 79–115.

Davies, D. K., and Berg, R. R. (1969). "Sedimentary characteristics of Muddy barrier-bar reservoir and lagoonal trap at Bell Creek Field," in *The Economic Geology of Eastern Montana and Adjacent Areas 20th Annual Conference 1969 Eastern Montana Symposium Oct 19-22, 1969* (Billings, MT: Montana Geological Society), 97–105.

Davies, D. K., and Ethridge, F. G. (1971). The Claiborne group of central Texas. *Trans. Gulf Coast Assoc. Geol. Soc.* 21, 115–124.

Davies, D. K., Ethridge, F. G., and Berg, R. R. (1971). Recognition of barrier environments. *Am. Assoc. Pet. Geol. Bull.* 4, 550–565.

Davies, R., Howell, J., Boyd, R., Flint, S., and Diessel, C. (2006). High-resolution sequence-stratigraphic correlation between shallow-marine and terrestrial strata: examples from the sunnyside member of the cretaceous blackhawk formation, book cliffs, eastern Utah. *Am. Assoc. Pet. Geol. Bull.* 90, 1121–1140. doi: 10.1306/02210604077

Davis, R. A. Jr. (1994a). "Barrier island systems- a geologic overview," in *Geology of Holocene Barrier Island Systems*, ed R. A. Davis Jr. (Berlin: Springer-Verlag), 1–46. doi: 10.1007/978-3-642-78360-9_1

Davis, R. A. Jr. (ed.) (1994b). *Geology of Holocene Barrier Island Systems*. Berlin: Springer.

Davis, R. A. Jr., and Hayes, M. O. (1984). What is a wave-dominated coast? *Mar. Geol.* 60, 313–329. doi: 10.1016/S0070-4571(08)70152-3

de Swart, H. E., and Zimmerman, J. T. F. (2009). Morphodynamics of tidal inlet systems. *Annu. Rev. Fluid Mech.* 41, 203–229. doi: 10.1146/annurev.fluid.010908.165159

DeCelles, P. G. (2004). Late jurassic to eocene evolution of the Cordilleran thrust belt and foreland basin system, western, U.S.A. *Am. J. Sci.* 304, 105–168. doi: 10.2475/ajs.304.2.105

Dennis, K. J., Cochran, J. K., Landman, N. H., and Schrag, D. P. (2013). The climate of the late cretaceous: new insights from the application of the carbonate clumped isotope thermometer to Western Interior Seaway macrofossil. *Earth Planet. Sci. Lett.* 362, 51–65. doi: 10.1016/j.epsl.2012.11.036

Devine, P. E. (1991). Transgressive origin of channeled estuarine deposits in the Point Lookout Sandstone, northwestern New Mexico: a model for Upper Cretaceous, cyclic regressive parasequences of the U.S. Western Interior. *Am. Assoc. Pet. Geol. Bull.* 75, 1039–1063. doi: 10.1306/0C9B28C1-1710-11D7-8645000102C1865D

deVries Klein, G. (1974). Estimating water depths from analysis of barrier island and deltaic sedimentary sequences. *Geology* 2:409. doi: 10.1130/0091-7613(1974)2<409:EWDFAO>2.0.CO;2

Dickinson, K. A. (1976). Sedimentary depositional environments of uranium and petroleum host rocks of the Jackson Group, south Texas. *J. Res. US Geol. Surv.* 4, 615–629.

Dickinson, K. A., Berryhill, H. L., and Holmes, C. W. (1972). "Criteria for recognizing ancient barrier coastlines," in *Recognition of Ancient Sedimentary Environments*, eds J. K. Rigby and W. K. Hamblin (Tulsa, OK: SEPM, Special Publication 16), 108–145. doi: 10.2110/pec.72.02.0192

Dronkers, J. J. (2005). *Dynamics of Coastal Systems*. Singapore: World Scientific.

Dyke, P. G. (2007). *Modeling Coastal and Offshore Processes*. London: Imperial College Press.

Edmonds, D. A., and Slingerland, R. L. (2007). Mechanics of river mouth bar formation: implications for the morphodynamics of delta distributary networks. *J. Geophys. Res. Earth Surf.* 112, 1–14. doi: 10.1029/2006JF000574

Elliott, T. (1975). The sedimentary history of a delta lobe from a Yoredale (Carboniferous) cyclothem. *Proc. Yorksh. Geol. Soc.* 40, 505–536. doi: 10.1144/pygs.40.4.505

Exum, F. A., and Harms, J. C. (1968). Comparison of marine-bar with valley-fill stratigraphic traps, western Nebraska. *Am. Assoc. Pet. Geol. Bull.* 52, 1851–1868. doi: 10.1306/5D25C537-16C1-11D7-8645000102C1865D

Finkelstein, K. (1992). "Stratigraphy and preservation potential of sediments from adjacent Holocene and Pleistocene barrier-island systems, Cape Charles, Virginia," in *Quaternary Coasts of the United States: Marine and Lacustrine Systems*, eds C. H. Fletcher III and J. F. Wehmiller (Tulsa, OK: SEPM Special Publication, 48), 129–140. doi: 10.2110/pec.92.48.0129

Fisher, J. S., and Dolan, R. (eds) (1977). *Beach Processes and Coastal Hydrodynamics*. Stroudsburg, PA: Dowden, Hutchinson & Ross.

Fisher, W. L., Proctor, C. V. Jr.,Galloway, W. E., and Nagle, J. S. (1970). Depositional systems in the jackson group of Texas– their relationship to oil, gas, and uranium. *Geol. Circ.* 70–74, 234–261.

FitzGerald, D. M. (1988). "Shoreline erosional-depositional processes associated with tidal inlets," in *Hydrodynamics and Sediment Dynamics of Tidal Inlets* (Washington, DC: AGU), 186–225. doi: 10.1007/978-1-4757-4057-8_11

FitzGerald, D. M., Buynevich, I., and Hein, C. (2012). "Morphodynamics and facies architecture of tidal inlets and tidal deltas," in *Principles of Tidal Sedimentology*, eds R. A. Davis, Jr., and R. W. Dalrymple (Dordrecht: Springer Netherlands), 301–333. doi: 10.1007/978-94-007-0123-6_12

Flores, R. M. (1978). Barrier and back-barrier environments of deposition of the upper cretaceous almond formation, Rock Springs Uplift, Wyoming. *Mt. Geol.* 15, 57–65.

Franks, P. C. (1980). Models of marine transgression - example from Lower Cretaceous fluvial and paralic deposits, north-central Kansas. *Geology* 8, 56–61. doi: 10.1130/0091-7613(1980)8<56:MOMTEF>2.0.CO;2

Fruergaard, M., Møller, I., Johannessen, P. N., Nielsen, L. H., Andersen, T. J., Nielsen, L., et al. (2015). Stratigraphy, evolution, and controls of a holocene transgressive – regressive barrier island under changing sea level: danish North Sea coast. *J. Sediment. Res.* 85, 820–844. doi: 10.2110/jsr.2015.53

Galloway, W. E. (1986). Reservoir facies architecture of microtidal barrier systems. *Am. Assoc. Pet. Geol. Bull.* 70, 787–808. doi: 10.1306/9488634E-1704-11D7-8645000102C1865D

Galloway, W. E., and Hobday, D. K. (eds) (1983). *Terrigenous Clastic Depositional Systems: Applications to Petroleum, Coal, and Uranium Exploration*. New York, NY: Springer-Verlag. doi: 10.1007/978-1-4684-0170-7

Gao, S., and Collins, M. (1994). Tidal inlet equilibrium, in relation to cross-sectional area and sediment transport patterns. *Estuar. Coast. Shelf Sci.* 38, 157–172. doi: 10.1006/ecss.1994.1010

Green, A. N., Cooper, J. A. G., Leuci, R., and Thackeray, Z. (2013). Formation and preservation of an overstepped segmented lagoon complex on a high-energy continental shelf. *Sedimentology* 60, 1755–1768. doi: 10.1111/sed.12054

Green, A. N., Cooper, J. A. G., and Salzmann, L. (2018). The role of shelf morphology and antecedent setting in the preservation of palaeo-shoreline (beachrock and aeolianite) sequences: the SE African shelf. *Geo-Marine Lett.* 38, 5–18. doi: 10.1007/s00367-017-0512-8

Guscott, S., Russell, K., Thickpenny, A., and Poddubiuk, R. (2003). "The Scott Field, Blocks 15/21a, 15/22, UK North Sea," in *United Kingdom Oil and Gas Fields Commemorative Millennium Volume*, eds J. G. Gluyas and H. M. Hichens (Geological Society, London, Memoirs, 20), 467–482. doi: 10.1144/GSL.MEM.2003.020.01.38

Hajek, E. A., and Wolinsky, M. A. (2010). Simplified process modeling of river avulsion and alluvial architecture: connecting models and field data. 2.

Hallermeier, R. J. (1981). A profile zonation for seasonal sand beaches from wave climate. *Coast. Eng.* 4, 253–277. doi: 10.1016/0378-3839(80)90022-8

Hallermeier, R. J., and Nauman, K. E. (1978). "Uses for a calculated limit depth to beach erosion," in *Proceedings of the Coastal Engineering Conference* (New York, NY: American Society of Civil Engineers), 1493–1512. doi: 10.1061/9780872621909.090

Hamilton, D. S. (1995). Approaches to identifying reservoir heterogeneity in barrier/strandplain reservoirs and the opportunities for increased oil recovery: an example from the prolific oil-producing Jackson-Yegua trend, south Texas. *Mar. Pet. Geol.* 12, 273–290. doi: 10.1016/0264-8172(95)98380-N

Hampson, G. J., Sixsmith, P. J., and Johnson, H. D. (2004). A sedimentological approach to refining reservoir architecture in a mature hydrocarbon province: the Brent Province, UK North Sea. *Mar. Pet. Geol.* 21, 457–484. doi: 10.1016/S0264-8172(03)00094-1

Harms, J. C., MacKenzie, D. B., and McCubbin, D. G. (1965). *Depositional Environment of the Fox Hills Sandstone, Near Rock Springs Wyoming*. Sediment. Late Cretac. Tert. Outcrops Rock Springs Uplift, 113–130.

Hawkins, C. M. (1980). *Barrier bar Sands in the Second Frontier Formation, Green River basin, Wyoming*. Guideb. Wyoming Geol. Assoc., 155–161.

Hayes, M. O. (1979). "Barrier island morphology as a function of tidal and wave regime," in *Barrier Islands from the Gulf of Mexico to the Gulf of St. Lawrence*, ed S. P. Leatherman (New York, NY: Academic Press), 1–28.

Hayes, M. O. (1980). General morphology and sediment patterns in tidal inlets. *Sediment. Geol.* 26, 139–156. doi: 10.1016/0037-0738(80)90009-3

Hayes, M. O., and FitzGerald, D. M. (2013). Origin, evolution, and classification of tidal inlets. *J. Coast. Res.* 69, 14–33. doi: 10.2112/SI_69_3

Hendricks, M. L. (1994). "Ravinement surface control on hydrocarbon accumulation in transgressive systems tracts: Almond Formation, Green River Basin, Wyoming," in *Unconformity Related Hydrocarbons in Sedimentary Sequences*, eds J. C. Dolson, M. Hendricks, and W. Westcott (Denver, CO: Rocky Mountain Association of Geologists), 209–218.

Heward, A. P. (1981). A review of wave-dominated clastic shoreline deposits. *Earth Sci. Rev.* 17, 223–276. doi: 10.1016/0012-8252(81)90022-2

Hobday, D. K., and Horne, J. C. (1977). Tidally influenced barrier island and estuarine sedimentation in the Upper Carboniferous of southern West Virginia. *Sediment. Geol.* 18, 97–122. doi: 10.1016/0037-0738(77)90007-0

Hobday, D. K., and Jackson, M. P. A. (1979). Transgressive shore zone sedimentation and syndepositional deformation in the Pleistocene of Zululand, South Africa. *J. Sediment. Res.* 49, 145–158. doi: 10.1306/212F76DA-2B24-11D7-8648000102C1865D

Hobday, D. K., and Orme, A. R. (1974). The port durnford formation. *Verh. van die Geol. Ver. van Suid Afrika* 77, 141–149.

Hobday, D. K., and Tankard, A. J. (1978). Transgressive-barrier and shallow-shelf interpretation of the lower paleozoic peninsula formation, South Africa. *Bull. Geol. Soc. Am.* 89, 1733–1744. doi: 10.1130/0016-7606(1978)89<1733:TASIOT>2.0.CO;2

Hollenshead, C. T., and Pritchard, R. I. (1960). "Geometry of producing Mesaverde sandstones, San Juan Basin," in *Geometry of Sandstone Bodies*, eds J. A. Peterson and J. C. Osmond (Tulsa, OK: American Association of Petroleum Geologists Special Publication, 22), 98–118.

Holmes, I. G., and Rivard, Y. A. (1976). "A marine barrier island bar, Jenner Field, southeastern Alberta," in *The Sedimentology of Selected Clastic Oil and Gas Reservoirs in Alberta*, ed M. M. Lerand (Calgary, AB: Canadian Society of Petroleum Geology), 44–61.

Holz, M., Kalkreuth, W., and Banerjee, I. (2002). Sequence stratigraphy of paralic coal-bearing strata: an overview. *Int. J. Coal Geol.* 48, 147–179. doi: 10.1016/S0166-5162(01)00056-8

Horne, J. C., and Ferm, J. C. (1976). *Carboniferous Depositional Environments in the Pocahontas Basin, eastern Kentucky and southern West Virginia*. Columbia, SC: University of South Carolina.

Hoyt, J., and Henry, J.r., V. J. (1965). "Significance of inlet sedimentation in the recognition of ancient barrier islands," in *Sedimentation of Late Cretaceous and Tertiary Outcrops, Rock Springs Uplift*, eds R. H. DeVoto and R. K. Bitter (Casper, WY: Ninteenth Annual Field Conference Guidebook, Wyoming Geological Association), 190–194.

Hoyt, J. H. (1967). Barrier island formation. *Geol. Soc. Am. Bull.* 78, 1125–1136. doi: 10.1130/0016-7606(1967)78[1125:BIF]2.0.CO;2

Hoyt, J. H. (1969). Chenier versus barrier, genetic and stratigraphic distinction. *Am. Assoc. Pet. Geol. Bull.* 53, 299–306. doi: 10.1306/5D25C60D-16C1-11D7-8645000102C1865D

Hubbard, S. M., Gingras, M. K., Pemberton, S. G., and Thomas, M. B. (2002). Variability in wave-dominated estuary sandstones: implications on subsurface reservoir development. *Bull. Can. Pet. Geol.* 50, 118–137. doi: 10.2113/50.1.118

Hudock, J. W., Flaig, P. P., and Wood, L. J. (2014). Washover fans: a modern geomorphologic analysis and proposed classification scheme to improve reservoir models. *J. Sediment. Res.* 84, 854–865. doi: 10.2110/jsr.2014.64

Jerolmack, D. J., and Swenson, J. B. (2007). Scaling relationships and evolution of distributary networks on wave-influenced deltas. *Geophys. Res. Lett.* 34:L23402. doi: 10.1029/2007GL031823

Johannessen, P. N., and Nielsen, L. H. (2010). Architecture of an upper jurassic barrier island sandstone reservoir, Danish Central Graben: implications of a holocene-recent analogue from the Wadden Sea. *Pet. Geol. Conf. Ser.* 7, 145–155. doi: 10.1144/0070145

Johnston, D. D., and Johnson, R. J. (1987). Depositional and diagenetic controls on reservoir quality in first wilcox Sandstone, Livingston Field, Louisiana. *Am. Assoc. Pet. Geol. Bull.* 71, 1152–1161. doi: 10.1306/703C8038-1707-11D7-8645000102C1865D

Jol, H. M., Smith, D. G., Meyers, R., Jol, H. M., Smith, D. G., and Meyers, R., a (1996). Digital ground penetrating radar (GPR): a new geophysical tool for coastal barrier research (examples from the Atlantic, Gulf and Pacific Coasts, U.S.A.). *J. Coast. Res.* 12, 960–968.

Jones, M. T., Dashtgard, S. E., and MacEachern, J. A. (2018). A conceptual model for the preservation of thick, transgressive shoreline successions: examples from the forearc Nanaimo Basin, British Columbia, Canada. *J. Sediment. Res.* 88, 811–826. doi: 10.2110/jsr.2018.40

Kamola, D. L., and Howard, J. D. (1985). *Back Barrier and Shallow Marine Depositional Facies Spring Canyon Member*, Blackhawk Formation.

Kana, T. W., Rosati, J. D., and Traynum, S. B. (2011). Lack of evidence for onshore sediment transport from deep water at decadal time scales: Fire Island, New York. *J. Coast. Res.* 59, 61–75. doi: 10.2112/SI59-007.1

Kauffman, E. G. (1977). Geological and biological overview: western interior cretaceous basin. *Mt. Geol.* 14, 75–99.

Kieft, R. L., Hampson, G. J., Jackson, C. A. L., and Larsen, E. (2011). Stratigraphic architecture of a net-transgressive marginal- to shallow-marine succession: upper almond formation, rock springs uplift, Wyoming, U.S.A. *J. Sediment. Res.* 81, 513–533. doi: 10.2110/jsr.2011.44

Kraus, N. C. (1988). "Inlet cross-sectional area calculated by process-based model," in *26th International Conference on Coastal Engineering* (Copenhagen: American Society of Civil Engineers), 3265–3278.

Land, C. B. (1972). Stratigraphy of fox hills sandstone and associated formations, rock springs uplift and Wamsutter Arch area, Sweetwater County, Wyoming: a shoreline-estuary sandstone model for the Late Cretaceous. *Q. Color. Sch. Mines* 67, 1–69.

Lane, S. N. (2006). "Approaching the system-scale understanding of braided river behaviour," in *Braided Rivers: Processes, Deposits, Ecology, and Management*, eds G. H. Sambrook Smith, J. L. Best, C. S. Bristow, and G. E. Petts (Oxford: Special Publication of the International Association of Sedimentologists), 107–135. doi: 10.1002/9781444304374.ch5

Lazarus, E. D. (2016). Scaling laws for coastal overwash morphology. *Geophys. Res. Lett.* 43, 12,113-12,119. doi: 10.1002/2016GL071213

Leckie, D. (1985). The lower cretaceous notikewin member (Fort St. John Group), northeastern British Columbia: a progradational barrier island system. *Bull. Can. Pet. Geol.* 33, 39–51.

Løseth, T. M., Ryseth, A. E., Young, M., and Asa, S. (2009). Sedimentology and sequence stratigraphy of the middle Jurassic Tarbert Formation, Oseberg South area (northern North Sea). *Basin Res.* 21, 597–619. doi: 10.1111/j.1365-2117.2009.00421.x

Loureiro, C., Ferreira, Ó., and Cooper, J. A. G. (2012). Extreme erosion on high-energy embayed beaches: influence of megarips and storm grouping. *Geomorphology* 139–140, 155–171. doi: 10.1016/j.geomorph.2011.10.013

Martin, J., Fernandes, A. M., Pickering, J., Howes, N., Mann, S., Neil, K. M. C., et al. (2018). The stratigraphically preserved signature of persistent backwater dynamics in a large paleodelta system: the Mungaroo Formation, northwest shelf, Australia. *J. Sediment. Res.* 88, 850–872. doi: 10.2110/jsr.2018.38

McBride, R. A., Anderson, J. B., Buynevich, I. V., Cleary, W., Fenster, M. S., FitzGerald, D. M., et al. (2013). "Morphodynamics of barrier systems: a synthesis," in *Treatise on Geomorphology: Volume 10 Coastal Geomorphology*, ed D. J. Sherman (San Diego, CA: Academic Press), 166–244. doi: 10.1016/B978-0-12-374739-6.00279-7

McCubbin, D. G. (1982). "Barrier-island and strand plain facies," in *Sandstone Depositional Environments,* eds P. A. Scholle and D. Spearing (Tulsa, OK: American Association of Petroleum Geologists Memior, 31), 247–279.

McCubbin, D. G., and Brady, M. J. (1969). Depositional environment of the almond reservoirs, Patrick Draw field, Wyoming. *Mt. Geol.* 6, 3–23.

Mellere, D., Zecchin, M., and Perale, C. (2005). Stratigraphy and sedimentology of fault-controlled backstepping shorefaces, middle pliocene of crotone basin, Southern Italy. *Sediment. Geol.* 176, 281–303. doi: 10.1016/j.sedgeo.2005.01.010

Mellett, C. L., Hodgson, D. M., Lang, A., Mauz, B., Selby, I., and Plater, A. J. (2012). Preservation of a drowned gravel barrier complex: a landscape evolution study from the north-eastern English Channel. *Mar. Geol.* 315–318, 115–131. doi: 10.1016/j.margeo.2012.04.008

Mellett, C. L., and Plater, A. J. (2018). "Drowned barriers as archives of coastal-response to sea-leve rise," in *Barrier Dynamics and Response to Changing Climate*, eds L. J. Moore and A. B. Murray (Cham: Springer International Publishing), 57–89. doi: 10.1007/978-3-319-68086-6_2

Middleton, G. V. (1973). Johannes Walther's Law of the correlation of facies. *Geol. Soc. Am. Bull.* 84, 979. doi: 10.1130/0016-7606(1973)84<979:JWLOTC>2.0.CO;2

Miller Jr., D. N. (1962). "Patterns of barrier bar sedimentation and its similarity to Lower Cretaceous Fall River Stratigraphy," in *Symposium of Early Cretaceous Rocks of Wyoming and Adjacent Areas 17th Annual Field Conference Guidebook*, eds R. L. Enyert and W. H. Curry III (Casper, WY: Wyoming Geological Association), 232–247.

Milliken, K., Blum, M., and Martin, J. (2012). "Scaling relationships in fluvial depostional systems. in Search and Discovery Article #30245," in *American Association of Petroleum Geologists Annual Conference and Exhibition* (Long Beach, CA, April 22–25).

Mohrig, D., Heller, P. L., Paola, C., and Lyons, W. J. (2000). Interpreting avulsion process from ancient alluvial sequences: guadalope-matarranya system (northern Spain) and Wasatch Formation (western Colorado). *Geol. Soc. Am. Bull.* 112, 1787–1803. doi: 10.1130/0016-7606(2000)112<1787:IAPFAA>2.0.CO;2

Moore, L. J., List, J. H., Williams, S. J., and Stolper, D. (2010). Complexities in barrier island response to sea level rise: Insights from numerical model experiments, North Carolina Outer Banks. *J. Geophys. Res. Earth Surf.* 115, 1–27. doi: 10.1029/2009JF001299

Moslow, T. F., and Heron, S. D. (1994). "The Outer Banks of North Carolina," in *Geology of Holocene Barrier Island Systems*, ed R. A. Davis Jr. (Berlin: Springer-Verlag), 47–76. doi: 10.1007/978-3-642-78360-9_2

Moslow, T. F., and Tye, R. S. (1985). Recognition and characterization of Holocene tidal inlet sequences. *Mar. Geol.* 63, 129–151. doi: 10.1016/0025-3227(85)90081-7

Mulhern, J. S., and Johnson, C. L. (2016). "Time–space variability of paralic strata deposited in a high accommodation, high sediment supply setting: example from the Cretaceous of Utah," in *Geological Society, London, Special Publications*, eds G. J. Hampson, A. D. Reynolds, B. Kostic, and M. R. Wells (London, UK: Geological Society, London, Special Publication, 444). doi: 10.1144/SP444.7

Mulhern, J. S., Johnson, C. L., and Martin, J. M. (2017). Is barrier island morphology a function of tidal and wave regime? *Mar. Geol.* 387, 74–84. doi: 10.1016/j.margeo.2017.02.016

Navilova, H., and Kurniawan, B. A. (2013). "Comparing and contrasting a meandering point bar sequence and barrier island system within the Upper Arang Formation, Belanak Field, West Natuna Basin," in *Proceedings, Indonesian Petroleum Association Thirty-Seventh Annual Convention & Exhibition* (Jakarta).

Nicholls, R. J., Larson, M., Capobianco, M., and Birkemeier, W. A. (1998). Depth of closure: improving understanding and prediction. *Proc. Coast. Eng. Conf.* 3, 2888–2901.

Oertel, G. F. (1985). The barrier island system. *Mar. Geol.* 63, 1–18. doi: 10.1016/0025-3227(85)90077-5

Olsen, H., Briedis, N. A., and Renshaw, D. (2017). Sedimentological analysis and reservoir characterization of a multi-darcy, billion barrel oil field – The Upper Jurassic shallow marine sandstones of the Johan Sverdrup field, North Sea, Norway. *Mar. Pet. Geol.* 84, 102–134. doi: 10.1016/j.marpetgeo.2017.03.029

Olsen, T. R., Mellere, D., and Olsen, T. (1999). Facies architecture and geometry of landward-stepping shoreface tongues: the Upper Cretaceous Cliff House Sandstone (Mancos Canyon, south-west Colorado). *Sedimentology* 46, 603–625. doi: 10.1046/j.1365-3091.1999.00234.x

Otvos, E. G. (2012). Coastal barriers - nomenclature, processes, and classification issues. *Geomorphology* 139–140, 39–52. doi: 10.1016/j.geomorph.2011.10.037

Painter, C. S., York-Sowecke, C. C., and Carrapa, B. (2013). Sequence stratigraphy of the upper cretaceous sego sandstone member reveals spatio-temporal changes in depositional processes, northwest Colorado, U.S.A. *J. Sediment. Res.* 83, 323–338. doi: 10.2110/jsr.2013.21

Paola, C., and Foufoula-Georgiou, E. (2001). "Statistical geometry and dynamics of braided rivers," in *Gravel Bed Rivers V*, ed M. P. Mosley (Wellington: New Zealand Hydrological Society), 47–69.

Parker, G. (2006). *1D Sediment Transport Morphodynamics With Applications to Rivers And Turbidity Currents*. University of Illinois Available online at: http://hydrolab.illinois.edu/people/parkerg//morphodynamics_e-book.htm?q=people/parkerg/morphodynamics_e-book.htm

Pattison, S. A. J. (2018). Using classic outcrops to revise sequence stratigraphic models: reevaluating the Campanian Desert Member (Blackhawk Formation) to lower Castlegate Sandstone interval, Book Cliffs, Utah and Colorado, USA. *Geology* 46, 1–4. doi: 10.1130/G45592.1

Penland, S., Boyd, R., and Suter, J. R. (1988). Transgressive depositional systems of the Mississippi Delta plain. *J. Sediment. Petrol.* 58, 932–949.

Penland, S., and Suter, J. R. (1989). The geomorphology of the Mississippi River chenier plain. *Mar. Geol.* 90, 231–258. doi: 10.1016/0025-3227(89)90127-8

Percival, C. J. (1992). The Harthope Ganister; a transgressive barrier island to shallow-marine sand-ridge from the Namurian of northern England. *J. Sediment. Res.* 62, 442–454. doi: 10.1306/D426791F-2B26-11D7-8648000102C1865D

Phillips, M. R., and Williams, A. T. (2007). Depth of closure and shoreline indicators: empirical formulae for beach management. *J. Coast. Res.* 232, 487–500. doi: 10.2112/05-0593.1

Phleger, F. B. (1969). "Some general features of coastal lagoons," in *Coastal Lagoons, A Symposium: Memoir of the International Symposium on Coastal Lagoons*, eds F. B. Phleger and A. A. Castañares (Mexico City: Universidad nacional autónoma de México), 5–26.

Pirmez, C., and Imran, J. (2003). Reconstruction of turbidity currents in Amazon Channel. *Mar. Pet. Geol.* 20, 823–849. doi: 10.1016/j.marpetgeo.2003.03.005

Posamentier, H. W., Jervey, M. T., and Vail, P. R. (1988). "Eustatic controls on clastic deposition I - conceptual framework," in *Sea-Level Changes: An Integrated Approach*, eds C. K. Wilgus, B. S. Hastings, H. W. Posamentier, J. C. Van Wagoner, C. A. Ross, and C. G. S. C. Kendall (Tulsa, OK: SEPM Special Publication, 42), 109–124. doi: 10.2110/pec.88.01.0109

Pretorius, L., Green, A., and Cooper, A. (2016). Submerged shoreline preservation and ravinement during rapid postglacial sea-level rise and subsequent "slowstand." *Geol. Soc. Am. Bull.* 128, 1059–1069. doi: 10.1130/B31381.1

Rampino, M. R., and Sanders, J. E. (1980). Evolution of the barrier: islands of southern Long Island, New York. *Sedimentology* 28, 37–47. doi: 10.1111/j.1365-3091.1981.tb01661.x

Rautman, C. A. (1978). Sedimentology of late Jurassic barrier-island complex; lower sundance formation of black hills. *Am. Assoc. Pet. Geol. Bull.* 62, 2275–2289. doi: 10.1306/C1EA53D2-16C9-11D7-8645000102C1865D

Rawn-Schatzinger, V., and Schatzinger, R. A. (1993). *Annotated Bibliography of Selected References on Shoreline Barrier Island Deposits With Emphasis on Patrick Draw Field*, Sweetwater County, Wyoming. Bartlesville, OK: ITT Research Institute, U.S. Department of Energy, Technical Report, NIPER-622.

Reddering, J. S. V. (1983). An inlet sequence produced by migration of a small microtidal inlet against longshore drift: the Keurbooms Inlet, South Africa. *Sedimentology* 30, 201–218. doi: 10.1111/j.1365-3091.1983.tb00665.x

Reinson, G. E. (1979). "Barrier island systems," in *Facies Models*, ed R. G. Walker (Toronto, ON: Geosciences Canada), 57–74.

Reinson, G. E. (1992). "Transgressive barrier island and estuarine systems," in *Facies Models: Response to Sea-Level Changes*, eds R. G. Walker and N. P. James (St. John's, NL: Geological Association of Canada), 179–194.

Reynolds, A. D. (1999). Dimensions of paralic sandstone bodies. *Am. Assoc. Pet. Geol. Bull.* 83, 211–229. doi: 10.1306/00AA9A48-1730-11D7-8645000102C1865D

Roehler, H. W. (1988). *The Pintail Coal Bed and Barrier Bar G - a Model for Coal of Barrier Bar - Lagoon Origin, Upper Cretaceous Almond Formation, Rock Springs Coal Field, Wyoming*. U.S. Geol. Surv. Prof. Pap. 1398. doi: 10.3133/pp1398

Roy, P. S., Cowell, P. J., Fernland, M. A., and Thom, B. G. (1994). "Wave-dominated coasts," in *Coastal Evolution: Late Quaternary Shoreline Morphodynamics*, eds R. W. G. Carter and C. D. Woodroffe (Cambridge: Cambridge University Press), 121–186. doi: 10.1017/CBO9780511564420.006

Sabins Jr, F. F. (1963). Anatomy of stratigraphic trap, Bisti field, New Mexico. *Am. Assocation Pet. Geol. Bull.* 47, 193–228. doi: 10.1306/BC74397F-16BE-11D7-8645000102C1865D

Salzmann, L., Green, A., and Cooper, J. A. G. (2013). Submerged barrier shoreline sequences on a high energy, steep and narrow shelf. *Mar. Geol.* 346, 366–374. doi: 10.1016/j.margeo.2013.10.003

Sanders, J. E., and Kumar, N. (1975). Evidence of shoreface retreat and in-place "drowning" during Holocene submergence of barriers, shelf off Fire Island, New York. *Geol. Soc. Am. Bull.* 86, 65–76. doi: 10.1130/0016-7606(1975)86<65:EOSRAI>2.0.CO;2

Sapozhnikov, V., and Foufoula-Georgiou, E. (1997). Experimental evidence of dynamic scaling and indications of self organized criticality in braided rivers. *Water Resour. Res.* 33, 1983–1991. doi: 10.1029/97WR01233

Schultz, A. L., and Stewart, G. F. (1991). Atkinson field: barrier bar or channel-fill sandstone? Evidence from geologic well-log analysis. *Bull. South Texas Geol. Soc.* 31, 11–36.

Self, G. A., Breard, S. Q., Rael, H. P., Stein, J. A., Thayer, P. A., Traugott, M. O., et al. (1986). Lockhart crossing field: new Wilcox Trend in Southeastern Louisiana. *Am. Assoc. Pet. Geol. Bull.* 70, 501–515.

Seminack, C. T., and McBride, R. A. (2015). Geomorphic history and diagnostic features of former tidal inlets along Assateague Island, Maryland-Virginia: a life-cycle model for inlets along wave-dominated barrier islands. *Shore Beach* 83, 3–24.

Sharma, B., Honarpo, J. S. R., Schatzinger, R. A., and Tomutsa, L. (1990). Determining the productivity of a barrier island sandstone deposit from integrated facies analysis based on log and core data and fluid production. *SPE Formation Eval.* 133–148. doi: 10.2118/19584-PA

Shelton, J. W. (1967). Stratigraphic models and general criteria for recognition of alluvial, barrier-bar, and turbidity-current sand deposits. *Am. Assoc. Pet. Geol. Bull.* 51, 2441–2461. doi: 10.1306/5D25C27F-16C1-11D7-8645000102C1865D

Short, A. D. (ed.) (1999). *Handbook of Beach and Shoreface Morphodynamics*. Chichester: John Wiley & Sons.

Short, A. D., and Jackson, D. W. T. (2013). "10.5 Beach Morphodynamics," in *Coastal Geomorphology*, ed J. F. Shroder (San Diego, CA: Academic Press), 106–129. doi: 10.1016/B978-0-12-374739-6.00275-X

Simms, A. R., Anderson, J. B., and Blum, M. (2006). Barrier-island aggradation via inlet migration: Mustang Island, Texas. *Sediment. Geol.* 187, 105–125. doi: 10.1016/j.sedgeo.2005.12.023

Sixsmith, P. J., Hampson, G. J., Gupta, S., Johnson, H. D., and Fofana, J. F. (2008). Facies architecture of a net transgressive sandstone reservoir analog: the Cretaceous Hosta Tongue, New Mexico. *Am. Assoc. Pet. Geol. Bull.* 92, 513–547. doi: 10.1306/01020807017

Snedden, J. W., and Kersey, D. G. (1981). Origin of the San Miguel lignite deposit and associated lithofacies, Jackson Group, south Texas. *Am. Assoc. Pet. Geol. Bull.* 65, 1099–1109. doi: 10.1306/03B59602-16D1-11D7-8645000102C1865D

Sømme, T. O., Helland-hansen, W., Martinsen, O. J., Thurmond, J. B., Sømme, T. O., Helland-hansen, W., et al. (2009). Relationships between morphological and sedimentological parameters in source-to-sink systems: a basis for predicting semi-quantitative characteristics in subsurface systems. *Basin Res.* 21, 361–387. doi: 10.1111/j.1365-2117.2009.00397.x

Storms, J. E. A., Weltje, G. J., Terra, G. J., Cattaneo, A., and Trincardi, F. (2008). Coastal dynamics under conditions of rapid sea-level rise: Late Pleistocene to Early Holocene evolution of barrier-lagoon systems on the northern Adriatic shelf (Italy). *Quat. Sci. Rev.* 27, 1107–1123. doi: 10.1016/j.quascirev.2008.02.009

Sturm, S., Evans, L., Keusch, B., and Clark, W. (2001). "Almond Formation reservoir characterization and sweet spot analysis in Siberia Ridge field, Wyoming," in *Gas in the Rockies*, ed D. Anderson (Denver, CO: Rocky Mountain Association of Geologists), 145–170.

Stutz, M. L., and Pilkey, O. H. (2011). Open-ocean barrier islands: global influence of climatic, oceanographic, and depositional settings. *J. Coast. Res.* 27, 207–222. doi: 10.2112/09-1190.1

Syvitski, J. P. M., and Milliman, J. D. (2007). Geology, geography, and humans battle for dominance over the delivery of fluvial sediment to the coastal ocean. *J. Geol.* 115, 1–19. doi: 10.1086/509246

Tavener-Smith, R. (1982). Prograding coastal facies associations in the Vryheid formation (Permian) at Effingham quarries near Durban, South Africa. *Sediment. Geol.* 32, 111–140. doi: 10.1016/0037-0738(82)90017-3

Thomas, W. A., and Mann, C. J. (1966). Late Jurassic depositional environments, Louisiana and Arkansas. *Am. Assoc. Pet. Geol. Bull.* 50, 178–182. doi: 10.1306/5D25B47B-16C1-11D7-8645000102C1865D

Tizzard, P. G., and Lerbekmo, J. F. (1975). Depositional history of the Viking Formation, Suffield area, Alberta, Canada. *Bull. Can. Pet. Geol.* 22, 715–752.

Tye, R. S., Hewlett, J. S., Thompson, P. R., and Goodman, D. K. (1994). "Integrated stratigraphic and depositional-facies analysis of parasequences in a transgressive systems tract, San Joaquin Basin, California," in *Siliciclastic Sequence Stratigraphy: Recent Developments and Applications*, eds P. Weimer and H. W. Posamentier (Tulsa, OK: American Association of Petroleum Geologists, Memior, 58), 99–133.

Vail, P. R., Mitchum, J.r,., R. M., and Thompson III, S. (1977). "Seismic stratigraphy and global changes of sea level, part 3: relative changes of sea level from coastal onlap," in *Seismic Stratigraphy: Applications to Hydrocarbon Exploration*, ed. *C. E. Payton (American Association of Petroleum Geologists Memior*, 26), 63–81.

Valasek, D. (1995). "The Tocito Sandstone in a sequence stratigraphic framework: an example of landward-stepping small-scale genetic sequences," in *Sequence Stratigraphy of Foreland Basin Deposits*, eds J. C. Van Wagoner and G. T. Bertram (Tulsa, OK: American Association of Petroleum Geologists Memior, 64), 349–369.

van de Kreeke, J. (2004). Equilibrium and cross-sectional stability of tidal inlets: Application to the Frisian Inlet before and after basin reduction. *Coast. Eng.* 51, 337–350. doi: 10.1016/j.coastaleng.2004.05.002

Van Maren, D. S. (2005). Barrier formation on an actively prograding delta system: the Red River Delta, Vietnam. *Mar. Geol.* 224, 123–143. doi: 10.1016/j.margeo.2005.07.008

Van Wagoner, J. C., Posamentier, H. W., Mitchum, R. M., Vail, P. R., Sarg, J. F., Loutit, T. S., et al. (1988). "An overview of the fundamentals of sequence stratigraphy and key definitions," in *Sea-level Changes: An integrated approach*, eds C. K. Wilgus, H. W. Posamentier, C. K. Ross, and C. G. Kendall (Tulsa, OK: SEPM Special Publication, 42), 39–45. doi: 10.2110/pec.88.01.0039

Wallace, D. J., Anderson, J. B., and Fernández, R. A. (2010). Transgressive ravinement versus depth of closure: a geological perspective from the upper Texas coast. *J. Coast. Res.* 26, 1057–1067. doi: 10.2112/JCOASTRES-D-10-00034.1

Weidie, A. E. (1968). Bar and barrier island sands. *Trans. Gulf Coast Assoc. Geol. Soc.* 18, 405–415.

Weimer, R. J. (1966). Time-stratigraphic analysis and petroleum accumulations, Patrick Draw Field, Sweetwater County, Wyoming. *Am. Assoc. Pet. Geol. Bull.* 50, 2150–2175. doi: 10.1306/5D25B713-16C1-11D7-8645000102C1865D

Wernette, P. A., Houser, C., Weymer, B. A., Everett, M. E., Bishop, M. P., and Reece, B. (2018). Directional dependency and coastal framework geology: implications for barrier island resilience. *Earth Surf. Dynam.* 6, 1139–1153. doi: 10.5194/esurf-6-1139-2018

Williams, J. J., Conner, D. C., and Peterson, K. E. (1975). Piper Oil Field, North Sea: fault-block structure with Upper Jurassic beach/bar reservoir sands. *Am. Assoc. Pet. Geol. Bull.* 59, 1585–1601. doi: 10.1306/83D9200A-16C7-11D7-8645000102C1865D

Willis, A. J., and Moslow, T. F. (1994). Stratigraphic setting of transgressive barrier-island reservoirs with an example from the Triassic Halfway Formation, Wembley Field, Alberta, Canada. *Am. Assoc. Pet. Geol. Bull.* 78, 775–791. doi: 10.1306/A25FE3B5-171B-11D7-8645000102C1865D

Yang, W. (1999). *Stratigraphic Architecture and Dynamic Evolution of Barrier Bar-Lagoon Depositional Systems, Eocene Jackson Group, Duval County, South Texas*. Gulf Coast Assoc. Geol. Soc. Trans. XLIX.

Yoshida, S., Johnson, H. D., Pye, K., and Dixon, R. J. (2004). Transgressive changes from tidal estuarine to marine embayment depositional systems: the Lower Cretaceous Woburn Sands of southern England and comparison with Holocene analogs. *Am. Assoc. Pet. Geol. Bull.* 88, 1433–1460. doi: 10.1306/05140403075

Conflict of Interest Statement: This research was completed while JSM was at the University of Utah. After completing this work JSM became, and is currently, employed by Shell Exploration and Production Company (United States). JMM is employed by Shell Exploration and Production Company (United States).

The remaining author declares that the research was conducted in the absence of any commercial or financial relationships that could be construed as a potential conflict of interest.

Copyright © 2019 Mulhern, Johnson and Martin. This is an open-access article distributed under the terms of the Creative Commons Attribution License (CC BY). The use, distribution or reproduction in other forums is permitted, provided the original author(s) and the copyright owner(s) are credited and that the original publication in this journal is cited, in accordance with accepted academic practice. No use, distribution or reproduction is permitted which does not comply with these terms.

frontiers in Earth Science

ORIGINAL RESEARCH
published: 12 September 2019
doi: 10.3389/feart.2019.00234

Left High and Dry: Deglaciation of Dogger Bank, North Sea, Recorded in Proglacial Lake Evolution

Andy R. Emery[1], David M. Hodgson[1], Natasha L. M. Barlow[1], Jonathan L. Carrivick[2], Carol J. Cotterill[3] and Emrys Phillips[3]*

[1] School of Earth and Environment, University of Leeds, Leeds, United Kingdom, [2] School of Geography, University of Leeds, Leeds, United Kingdom, [3] British Geological Survey, The Lyell Centre, Edinburgh, United Kingdom

Reconstructions of palaeo-ice sheet retreat in response to climate warming using offshore archives can provide vital analogs for future ice-sheet behavior. At the Last Glacial Maximum, Dogger Bank, in the southern North Sea, was covered by the Eurasian Ice Sheet. However, the maximum extent and behavior of the ice sheet in the North Sea basin is poorly constrained. We reveal ice-marginal dynamics and maximum ice extent at Dogger Bank through sedimentological and stratigraphic investigation of glacial and proglacial lake sediments. We use a large, integrated subsurface dataset of shallow seismic reflection and geotechnical data collected during windfarm site investigation. For the first time, an ice stream is identified at Dogger Bank, based on preserved subglacial bedforms, eskers and meltwater channels. During ice-sheet advance, a terminal thrust-block moraine complex formed, whose crest runs approximately north-northeast to south-southwest. Subsequent ice stream shutdown caused stagnation of ice, and rapid retreat of the ice-sheet margin. The moraine complex, and outwash head from an adjacent ice-sheet lobe to the west, dammed a large (approximately 750 km^2) proglacial lake. Subsequent sedimentation infilled the lake with 30 m of glacial outwash sediments. A lobate subaqueous fan formed at the ice-sheet margin, which thins toward the southeast with iceberg scours and ice-rafted debris at the base, and is onlapped by lake sediments calibrated to core as alternating clay and silt laminae, interpreted to be varves. The lake became isolated from the retreating ice-sheet margin, and ice-sheet retreat slowed. Sediment-laden meltwater was supplied to the ice-distal proglacial lake for c. 1500–2000 years. Subsequent ice-sheet retreat off Dogger Bank was more rapid due to the negative subglacial slope. The stepped retreat of rapid downwasting, slow retreat, and a final rapid phase off Dogger Bank occurred after the LGM at around 27 ka and before formation of a ribbon lake, dated previously to 23 ka and approximately 60 m lower in elevation, formed to the north of Dogger Bank. The complicated stratigraphic architecture revealed through these data improves forecasting of ground conditions for turbine footings at Dogger Bank, an important step in the provision of clean, sustainable energy.

Keywords: North Sea, ice stream, proglacial lake, British-Irish Ice Sheet, glacial geomorphology, glacial stratigraphy, shallow seismic, Quaternary

OPEN ACCESS

Edited by:
Barbara Mauz,
University of Salzburg, Austria

Reviewed by:
Aggeliki Georgiopoulou,
University of Brighton,
United Kingdom
Nicholas Perez,
Texas A&M University, United States

****Correspondence:***
Andy R. Emery
ee06ae@leeds.ac.uk

Specialty section:
This article was submitted to Sedimentology, Stratigraphy and Diagenesis, a section of the journal Frontiers in Earth Science

Received: *03 June 2019*
Accepted: *27 August 2019*
Published: *12 September 2019*

Citation:
Emery AR, Hodgson DM, Barlow NLM, Carrivick JL, Cotterill CJ and Phillips E (2019) Left High and Dry: Deglaciation of Dogger Bank, North Sea, Recorded in Proglacial Lake Evolution. Front. Earth Sci. 7:234. doi: 10.3389/feart.2019.00234

INTRODUCTION

Reconstructing palaeo-ice sheet dynamics from offshore sedimentological and stratigraphic archives around the world has become an important topic of focus in the last decade (e.g., Dowdeswell and Ottesen, 2013; Stewart et al., 2013; Jakobsson et al., 2014; Sejrup et al., 2015; Hogan et al., 2016; Lamb et al., 2016; Dove et al., 2017; Greenwood et al., 2017; Streuff et al., 2017; Callard et al., 2018; Lockhart et al., 2018). Understanding how past ice sheets retreated in response to climate warming provides a vital analog for the projection of ice sheet behavior during future climate change (IPCC, 2013). As the projection of future sea-level rise depends on accurate modeling of ice-sheet retreat, sedimentology and stratigraphy plays a key role in addressing one of society's grand challenges (Hodgson et al., 2018).

Particular focus has been on understanding the dynamics of the British-Irish Ice Sheet during Marine Isotope Stage (MIS) 2 (∼30 – 11.7 ka BP) and, as such, it has become one of the best constrained palaeo-ice sheets (Clark et al., 2004, 2012, 2018). The extent and dynamics of northern and western sectors of the ice sheet has become well understood through both data and modeling approaches (Bradwell et al., 2007; Boston et al., 2010; Davies et al., 2011; Bradwell and Stoker, 2015; Peters et al., 2016; Smedley et al., 2017; Callard et al., 2018; Chiverrell et al., 2018; Gandy et al., 2018; Scourse et al., 2019). Confluence and interaction of the British-Irish and Scandinavian ice sheets in the North Sea Basin is unclear, and the maximum extent and dynamics of the ice sheet in the North Sea are still poorly constrained (Phillips et al., 2017b), with few studies into the controls of ice sheet advance and retreat (Cotterill et al., 2017a; Phillips et al., 2018; Roberts et al., 2018). Models imply a key, regional-scale influence of the British-Irish Ice Sheet in the North Sea Basin (Boulton and Hagdorn, 2006; Hubbard et al., 2009; Patton et al., 2016). At a local scale, the role of palaeo-ice streams and glacial hydrology in controlling ice-marginal dynamics has long been recognized (Stokes and Clark, 1999, 2001, 2003; Evans et al., 2008, 2014; Stewart et al., 2013; Margold et al., 2015; Stokes et al., 2015; Greenwood et al., 2016a,b; Stokes, 2018) but these processes have yet to be identified and described in the southern North Sea.

Proglacial lakes are a common feature of ice-sheet margins during deglaciation, with several lake-fills preserved in the Quaternary geological record (Carrivick and Tweed, 2013), and have been identified in many locations around the margin of the British-Irish Ice Sheet (Livingstone et al., 2010; Clark et al., 2012; Murton and Murton, 2012; Evans et al., 2016a, 2018). A large proglacial lake has been previously interpreted at Dogger Bank, with three phases of infill (Cotterill et al., 2017a). However, the detailed lake stratigraphy and environments of deposition, and the implications for landscape evolution and ice-sheet retreat, have not been documented previously.

In this study, we deduce the behavior of the ice sheet through investigation of an integrated, high resolution dataset from Dogger Bank, North Sea. Our aim is to describe the role of ice streaming and subglacial conditions on the advance, maximum extent and retreat of the ice sheet during MIS 2. Through investigation of the sedimentology and stratigraphy of glacial landforms and proglacial lake-fills, we identify for the first time a palaeo-ice stream and the controls on its subsequent retreat. We review the role of basal conditions on forming differing landsystems along the margin of the ice sheet at Dogger Bank. By combining local and regional geomorphic interpretation, we constrain the timing and maximum extent of the ice sheet in the southern North Sea.

SETTING

Dogger Bank is a large (approximately 15,000 km^2), flat-topped bank of sediment in the southern North Sea (**Figure 1**) that forms a present-day bathymetric high, between 18 and 63 m below mean sea level (MSL). Recent acquisition of high-resolution seismic reflection data and geotechnical boreholes up to 50 m deep collected in support of windfarm site investigations have revealed the stratigraphic complexity of the Dogger Bank (Cotterill et al., 2017a,b; Phillips et al., 2018; Emery et al., 2019). A glacial origin was first suggested by Belt (1874), proposing it to be a bank of moraine sediment, later observed to be similar in scale to the Main Stationary Line of Denmark (Carr et al., 2006). Early investigations into the extent of the Last Glacial Maximum in the North Sea proposed small ice sheets terminating onshore or nearshore (Jansen et al., 1979; Sejrup et al., 1987; Long et al., 1988; Hall and Bent, 1990; Ehlers and Wingfield, 1991; Cameron et al., 1992; Phillips et al., 2017b). However, the presence of a large ice-sheet confluence in the North Sea was confirmed when the examination of cores and boreholes containing tills that were dated to the MIS 3-2 boundary (Sejrup et al., 2000) and contained evidence of significant subglacial deformation on Dogger Bank (Carr et al., 2006). Subsequent investigation of high-resolution seismic reflection data revealed a complex of large moraines (Cotterill et al., 2017a; Phillips et al., 2018), ground-truthed in vibrocores on the south-eastern flank of Dogger Bank (Emery et al., 2019), indicating ice sheet advance to at least the edge of Dogger Bank (**Figure 1**).

For the purposes of this study, the Late Pleistocene and Holocene stratigraphy of Dogger Bank can be simplified into four main formations (**Table 1**), which are applied to lithostratigraphic units in this study. The oldest of these formations is the Dogger Bank Formation that comprises massive clays, sands and diamicts of glacial origin (Cotterill et al., 2017a), subdivided informally in this study into the Lower and Upper Dogger Bank sub-units. On top of this, Botney Cut Formation proglacial lake sediments are observed (Cotterill et al., 2017a), informally subdivided in this study to the Upper, Lower and Basal Lake Dogger sub-units. The overlying three formations, one unnamed, the Elbow and the Nieuw-Zeeland Gronden formations (**Table 1**) are a mixture of clays, peats, silts, sands and gravels from terrestrial, fluvial, estuarine, coastal and shallow marine sedimentary environments (Cotterill et al., 2017a; Emery et al., 2019).

Onset of glaciation around the Dogger Bank area occurred via confluence of the British-Irish (or Celtic) and Scandinavian (or Fennoscandian) ice sheets around 30-29 ka BP, reaching its maximum extent by around 27 ka BP (Sejrup et al., 2000; Carr et al., 2006; Clark et al., 2012; Hughes et al., 2016;

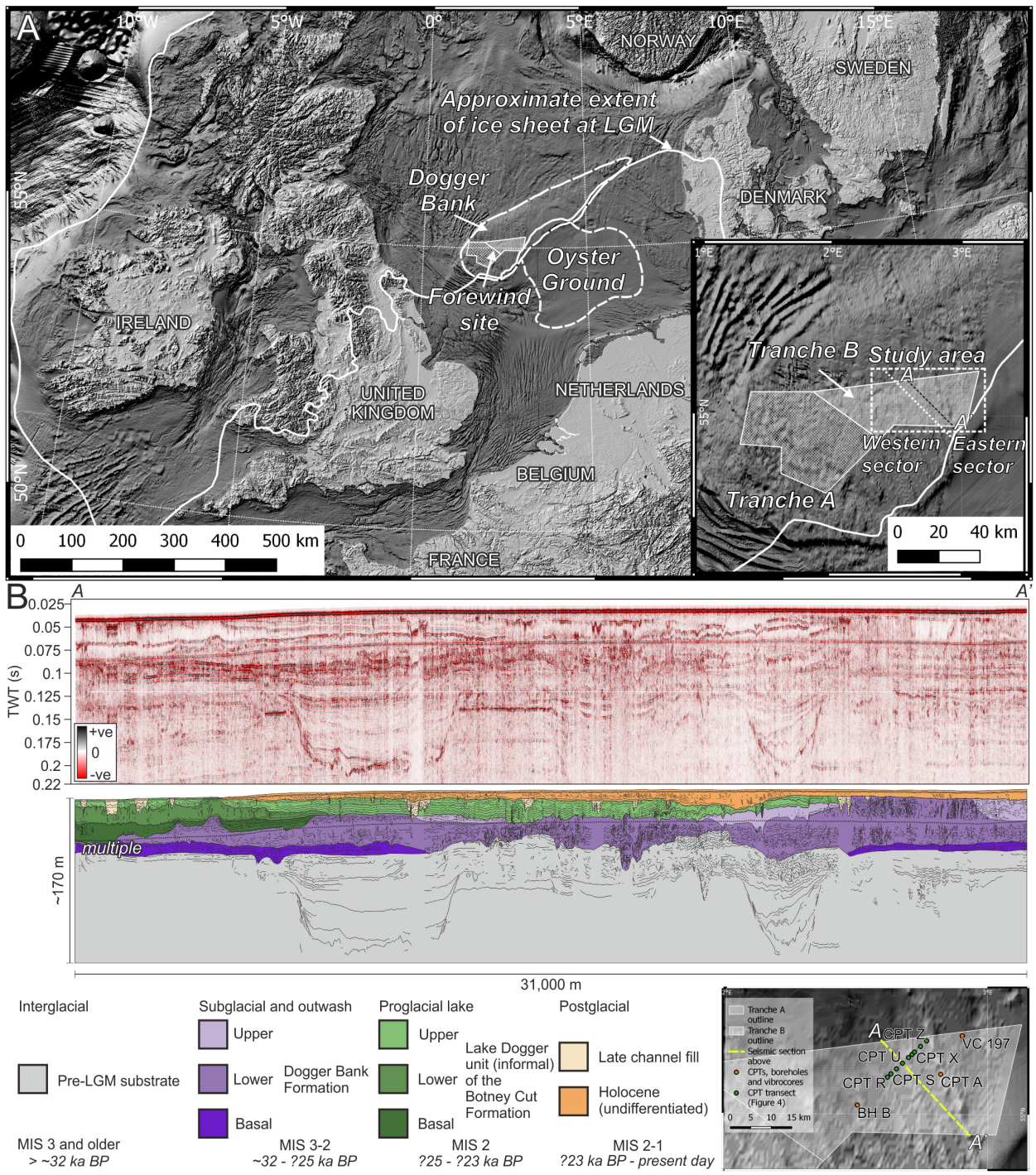


FIGURE 1 | (A) Location of Dogger Bank in the southern North Sea showing the location of the Forewind offshore wind project. Inset shows Tranches **(A,B)** of the Forewind project, and the area of focus for this study. Ice sheet extent combined from this study and Sejrup et al. (2005), Bradwell et al. (2008), and Ballantyne (2010). Bathymetry data: GEBCO (https://www.gebco.net). **(B)** Stratigraphic section through Dogger Bank showing the relationship between the pre-MIS 2 stratigraphy, Dogger Bank Formation glacial sediments, Botney Cut Formation proglacial lake sediments, and subsequent Late Pleistocene and Holocene sediments. Stratigraphy compiled from Cotterill et al. (2017a).

Roberts et al., 2018), although the exact timing and extent is poorly constrained. Ice retreated from Dogger Bank prior to 23 ka BP, shown by Optically Stimulated Luminescence (OSL) dating of proglacial ribbon lake deposits north of Dogger Bank (Roberts et al., 2018), rather than a late phase of rapid retreat caused by debuttressing at 18.5 ka BP (Clark et al., 2012;

TABLE 1 | Formations encountered within the study area, compiled from Stoker et al. (2011) and Cotterill et al. (2017a,b).

Group Stoker et al., 2011; Cotterill et al., 2017a	Formation	Age	Subdivisions Cotterill et al., 2017a	Sedimentary environment	Description in Tranche B Cotterill et al., 2017a	Seismic velocity Cotterill et al., 2017b
California Glaciogenic Group	Nieuw Zeeland Gronden Formation	Holocene, MIS 1 Present day - ~ 6000 BP	Terschellinger Bank Member	Shallow marine	Bioturbated marine sands, transgressive gravel deposits Emery et al., 2019	1600 m/s
	Elbow Formation	Holocene, MIS 1 ~11000 BP – ~6000 BP		Estuarine, intertidal	Tidal mudflats, barrier sands, peats and silts Emery et al., 2019	1600 m/s
	Unnamed	Late Pleistocene, MIS 2 ~17500 BP to ~11000 BP		Periglacial, sandur and glaciofluvial outwash	Not formally recorded within other Formations. Well sorted sands, evidence for cryoturbation. Extensive channel networks exist in seismic reflection data.	1600 m/s
	Botney Cut Formation	Late Pleistocene, MIS 2 ?deglacial stage, ~21000 BP to ~17500 BP	Informally subdivided in this study to Upper, Lower and Basal Lake Dogger sub-units.	Proglacial	Found in an intra-moraine basin as rhythmically laminated silts and very fine sands with rare dropstones, interpreted to be proglacial lake deposits.	1650 m/s
	Dogger Bank Formation	Late Pleistocene, MIS 2–4 ~70000 BP - ~17500 BP	Upper sub-unit Lower sub-unit	Glacial and periglacial	Upper Dogger Bank: Interbedded sands and silty clays with some clast-supported gravels. Lower Dogger Bank: Massive clays with some sand, silt and gravel, clays with shell fragments, clays with chalk clasts, and matrix-supported diamict with chalk and flint, sand pods and intraclasts. Micromorphology suggesting subglacial deformation Carr et al., 2006, and often glaciotectonised into arcuate ridges interpreted to be moraines related to ice margin oscillation Cotterill et al., 2017a; Phillips et al., 2018	1650 m/s

Sejrup et al., 2016). On the western side of Dogger Bank (Tranche A of the Forewind windfarm site, **Figure 1**), ice-sheet retreat is characterized by multiple readvances forming thrust-block moraine complexes and glaciotectonic deformation of the Lower and Basal Dogger Bank sub-unit sediments (**Table 1**), implying an active, oscillating ice margin during deglaciation (Phillips et al., 2018). On the eastern side of Dogger Bank (Tranche B of the Forewind windfarm site, **Figure 1**), a large, proglacial lake has been identified (Cotterill et al., 2017a), hereafter named Lake Dogger, covering approximately 750 km^2 with a sedimentary lake-fill sequence reaching up to 30 m thick. Stratigraphically, the lake basin occupies a depression between, and onlapping onto, moraine ridges (**Figure 1**). Cotterill et al. (2017a) suggested that these lake sediments form part of the Botney Cut Formation (BCF), although there is a marked difference in depositional environment between the proglacial lake-fill and the tunnel valley-fill of the rest of the BCF. The lake sediments overlie the Upper and Lower sub-units of the Dogger Bank Formation, and are incised by younger channels (Cotterill et al., 2017a), and truncated by wave ravinement surfaces (Emery et al., 2019).

The area covered in this study is shown in **Figure 1**. The study area covers the eastern side of Tranche B of the Forewind site. Due to differing observations of stratigraphic thicknesses of interpreted seismic units, the study area is subdivided into two sectors, east and west (**Figure 1**).

MATERIALS AND METHODS

A large, integrated sub-surface dataset of 2D seismic reflection profiles, geotechnical logs and sediment samples from boreholes and vibrocores were used in this study.

Borehole, Geotechnical and Vibrocore Data

Vibrocore Data

Twenty-five vibrocores were available throughout Tranche B, acquired by the British Geological Survey (BGS) between 1981 and 1994 as part of regional mapping programs. Vibrocores vary in length but can give continuous sediment recovery up to 6 m below seabed. Generally, the vibrocores are in good condition, although some desiccation has occurred in clay-rich sediments (**Figure 2**).

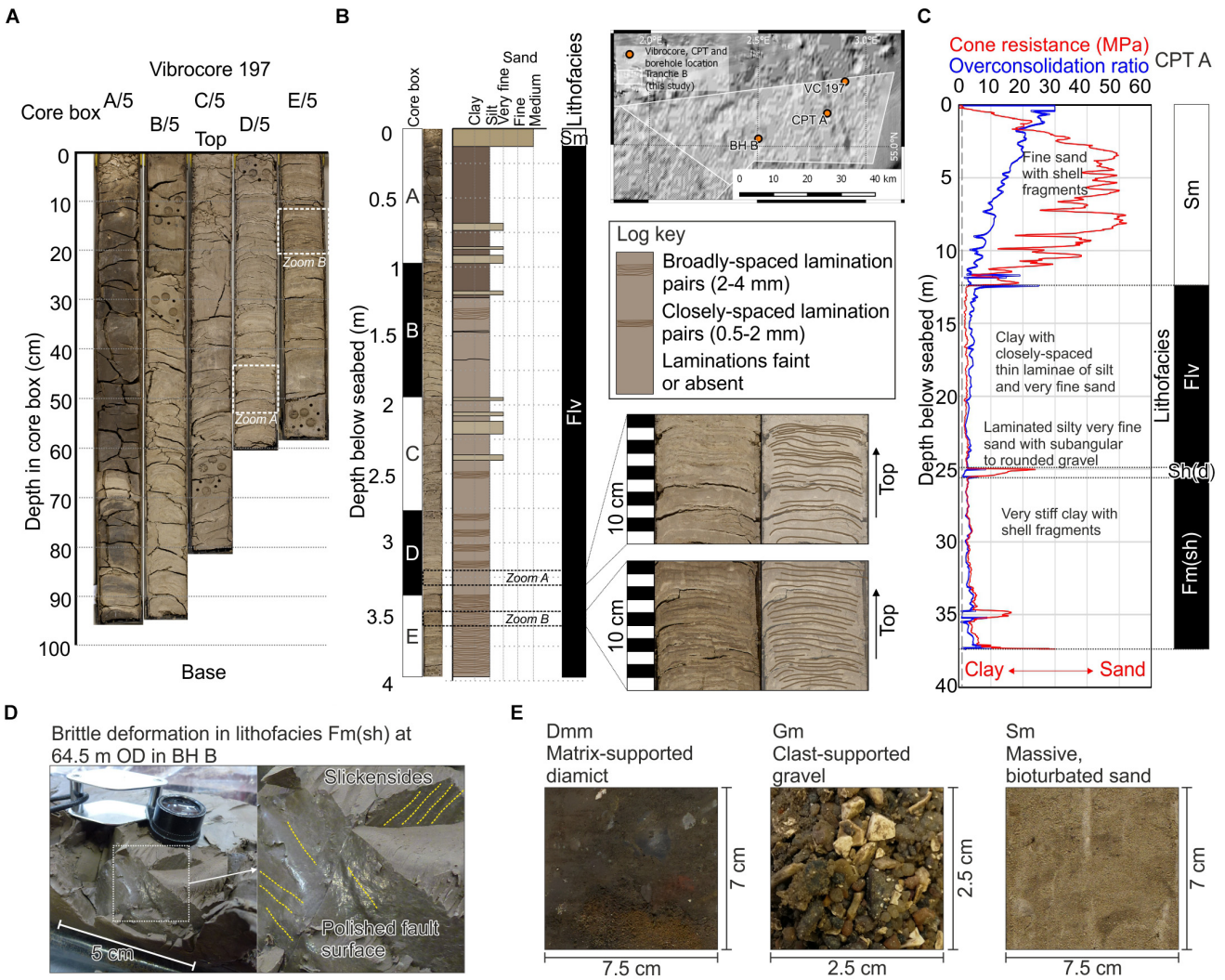


FIGURE 2 | (A) Photograph of vibrocore 197 and **(B)** its sedimentary log with interpreted lithofacies, showing proglacial lake clay and silt rhythmites interpreted to be varves. Vibrocore 197 acquired June 1983, photograph date August 2017. **(C)** Log of Cone Penetration Test (CPT) A showing cone resistance plotted against depth. Low cone resistance represents clay (generally low friction) and high cone resistance represents sand (generally high friction). **(D)** Photograph of a short core section of borehole BH B showing brittle deformation in lithofacies Fm(sh). **(E)** Representative photographs of lithofacies Dmm (matrix-supported diamict), Gm (clast-supported gravel), and Sm (massive, bioturbated sand). For lithofacies descriptions see **Table 4**.

Sedimentary facies were identified from vibrocores and borehole samples based on visual grain size distribution, Munsell color, composition, texture and gradation, as well as use of sedimentary structures. Sedimentary facies were assigned lithofacies codes based on Evans and Benn (2004). Centimeter-scale sediment logs were used to calibrate seismic facies and key seismic stratigraphic surfaces. Vibrocore depths were converted to seismic Two-Way Travel time (TWT) using the average velocities given in **Table 1**.

Borehole and Geotechnical Logs

Boreholes and Cone Penetration Tests (CPTs) up to 50 m deep were acquired as part of the Forewind site investigation dataset. Boreholes provide spot samples and short core sections (usually <6 cm, occasional 60 cm core lengths), spaced intermittently at intervals of 0.1–6 m, for geotechnical investigation. Twenty boreholes were drilled, each with a CPT, allowing for correlation of CPT response to each encountered sedimentary facies. A further 63 CPTs were acquired throughout Tranche B. An example CPT log is shown in **Figure 2**. Borehole spot sample and CPT depths were converted to TWT using the average velocities given in **Table 1**.

Seismic Reflection Data Interpretation

Seismic Data

A dense grid of 2D shallow seismic reflection data were acquired as part of the site investigation for the Forewind project. A total of 17,000 line km were available in Tranche B, along with an additional 6,000 line km of regional lines (Cotterill et al., 2017b).

In Tranche B, 629 2D lines are spaced every 100 m in the NE-SW orientation, and 75 lines every 500–1000 m in the NW-SE orientation. Regional lines are spaced at 2,500 m intervals in both the NW-SE and NE-SW orientations. Seismic data were handled using IHS Kingdom Suite. The profiles were acquired using a Sparker seismic source, with the Tranche B grid acquired at a higher resolution than the regional grid. The regional lines have a maximum vertical resolution of approximately 2–3 m, and a maximum depth of investigation of approximately 180 ms below the seabed, equivalent to approximately 150 m. The Tranche B grid has a similar depth of investigation, but a vertical resolution of 1 m. Seismic reflection data are minimum phase. Data were interpreted using a black-red color scheme, with black for peaks and red for troughs (**Figure 1**). Horizons were interpreted on the peaks or troughs depending on the maximum amplitude observed, and interpreted consistently on the maximum amplitude.

Maps generated from interpreting seismic reflection data in two-way time were converted to depth using the P-wave velocities derived from local geotechnical data as well as the velocity of similar sediments recorded regionally in the North Sea, as given by Cotterill et al. (2017a). The sea water velocity was taken to be 1505 m/s (Cotterill et al., 2017b). The velocity used to depth convert each formation is shown on **Table 1**. Individual interpreted seismic horizons were gridded in Kingdom Suite using the flex gridding algorithm, which provides geologically reasonable surfaces.

Seismic Facies

Seismic facies were used to distinguish stratigraphic units and correlate major surfaces and sedimentary environments. The terminology described by Mitchum et al. (1977) has been used. Closer investigation of seismic facies, which may traditionally have been described as reflection-free (or acoustically transparent) or chaotic using the Mitchum et al. (1977) terminology, has revealed seismic facies that provide a more detailed interpretation of glacial processes. Terminology to describe these seismic facies is presented and described in **Table 2**. These new seismic facies have been used in conjunction with the accepted terminology as described by Mitchum et al. (1977).

RESULTS

Seismic Units

Seismic facies and stratigraphic relationships were used to define seven main seismic units, described in **Table 3**. The stratigraphically oldest (SU-Basement) and youngest (SU-Postglacial) units comprise multiple stratigraphic units, but remain undifferentiated in this study for the purposes of brevity. Stratigraphic relationships between each seismic unit are shown in **Figure 3**. Units are described from the stratigraphically oldest (SU-A) to youngest (SU-E).

SU-Basement

The lowest stratigraphic unit forms the basement to the study area (**Figure 3**). It comprises horizontal, low frequency, moderate to high amplitude reflectors. Large, up to 5 km wide, channel forms filled with low-frequency, medium amplitude, parallel reflectors are observed (**Figure 1**). The top of the seismic unit is defined by a continuous, high-amplitude reflector that separates SU-A from different seismic facies above.

SU-A

Seismic unit A is present throughout the study area, although its thickness is irregular. SU-A seismic facies are generally high amplitude, but inconsistent, and its geometry is also highly variable, forming mounds and ridges, as well as channel-fills that truncate the underlying SU-Basement. The ridges are 20 to 40 m high, 10 to >27 km long, and generally orientated northeast-southwest. Mounds are 5 to 20 m high, 300 m wide, and 500 to 1000 m long. The channel-fills are generally 3–6 m deep, but can be up to 100 m deep. Seismic facies vary depending on geometry of the seismic unit. Seismic facies within the ridges of SU-A can be separated into distinct zones within the broader seismic unit (**Figure 4**). Two sets of inclined, asymmetric serrate reflectors have differing senses of vergence; one set verges to the northwest and the other verges to the southeast. These two sets surround a zone of symmetric serrate reflectors. These distinct structural domains occur within a long (at least 27 km within the study area), 5 km wide, 40 m high ridge. Internally, the mound forms are transparent to patchy. Where SU-A is thin, in areas between ridges and mounds, reflectors are high-amplitude, and can be continuous or inclined. Despite the variable geometries and seismic facies, SU-A is one seismic unit because of its stratigraphic position, bounded below by SU-Basement and above by a continuous, high-amplitude reflector marking an unconformity.

SU-B

Seismic unit B is present throughout the study area and downlaps onto the underlying seismic unit. In the eastern sector of the study area, its geometry is generally sheet-like and its thickness varies from absent to 10 m. In the western sector of the study area, its thickness varies from 5 to 40 m (**Figure 3**). Seismic facies are generally low amplitude, with variable to transparent reflectors and high frequency, low amplitude, sigmoidal reflectors (**Figure 3**).

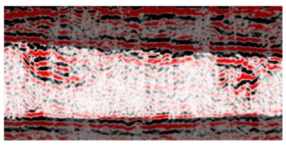
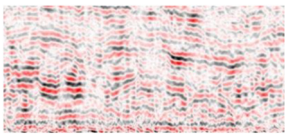
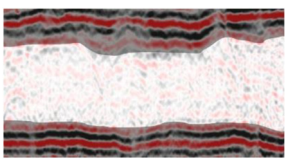
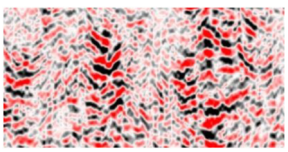
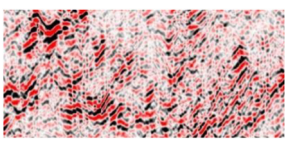
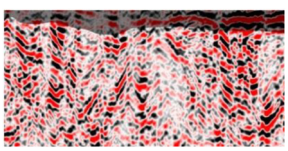
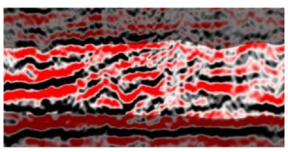
SU-C

Seismic unit C is present infilling a small basin in the north of the eastern sector of the study area. Its seismic facies are generally transparent. Reflectors onlap the underlying seismic units. The top of the unit is marked by a horizontal, high-amplitude reflector (**Figure 5**). SU-C is up to a maximum of 10 m thick.

SU-D

A lobate seismic unit D is present in the north of the study area. It thins toward the southeast and downlaps onto SU-C (where present) and SU-B (**Figure 5**). It is mainly transparent but also some patchy, inclined reflectors and asymmetrical serrate reflectors. It is a maximum of 10 m thick (**Figure 5**).

TABLE 2 | Description of new seismic facies expanded from the terms "reflection-free" and "chaotic" Mitchum et al. (1977).

Former description Mitchum et al., 1977	New description	Image	Character	Interpretations	Glacial stratigraphy interpretation	Reason for clarification
Reflection free	Sporadic		Less than 30% of the seismic facies has reflectors of some form separated by areas with no reflectors	Homogeneous sediment with occasional deformation	Subaerial or subaqueous, with some evidence of subsequent mass movement of outwash	Seismic facies termed reflection free often contain useful, low-amplitude events, above background noise, often overlooked
	Variable		Occasional, discontinuous low amplitude reflectors with some dip and curvature	Stacking of broadly homogeneous sediment	Subaerial outwash with bedding inclined due to draping and progradation	
	Transparent		Nothing distinguishable above background noise.	Highly homogeneous sediment with little internal structure	Outwash, subaerial or subaqueous, with highly homogeneous sediment supply	
Chaotic	Patchy		Greater than 30% of the seismic facies has reflectors of some form separated by areas with no reflectors	Intense deformation	Glaciotectonics implying repeated or prolonged phases of deformation and/or intense brittle deformation	Chaotic implies no order or a degree of randomness, which cannot be used to describe a geological system
	Asymmetric serrate		Inclined or flat reflectors with sudden, sharp angle changes to shorter-length reflectors, with another sharp angle change to longer reflectors	Folding with differing limb length showing vergence. Also fault-propagation folding and thrust sheet stacking.	Glaciotectonics with vergence on a larger-scale antiform/synform limb. Vergence direction is generally the same as thrusting direction	
	Symmetric serrate		Reflectors with opposing dip directions separated by sharp angle changes.	Chevron folding	Glaciotectonics with no distinct vergence direction implying centre of antiform/synform. Usually upright fold axes.	
	Inclined		Stacked, inclined reflectors	Imbricated thrust stacks	Continuous shear along a plane due to subglacial deformation	

The glacial interpretations are not the only possible interpretation of formational process; other processes in differing sedimentary and tectonic environments may form similar geometries. These new seismic facies are therefore able to be applied to different geological settings.

SU-E

Seismic unit E is characterized by high-frequency, medium-amplitude, continuous, parallel reflectors that are draped over the underlying stratigraphy, filling a large (750 km^2) basin in the eastern sector of the study area formed by SU-A, SU-B and SU-D. SU-E drapes and onlaps the edges of its basin (**Figure 5**). SU-E reaches a maximum thickness of 30 m in the center of its basin (**Figure 1**).

SU-Postglacial

The stratigraphically youngest seismic unit truncates or incises into previous units throughout the study area, except in the

TABLE 3 | Descriptions of seismic facies, stratigraphic relationships and geometry used to define the seismic units (SUs) in this study.

Seismic unit	Seismic facies Table 2; Mitchum et al., 1977	Geometry	Stratigraphic relationship	Other notes
SU-Postglacial	Low frequency, low amplitude continuous parallel to sigmoidal reflectors and medium to high frequency, high amplitude, continuous parallel reflectors	Sheet (low amplitude), channel (high amplitude)	Truncation of, or incision into, previous seismic units	Channel forms always appear below the sheet forms. Channel forms often cause acoustic blanking below.
SU-E	High frequency, medium amplitude, continuous, parallel, draped reflectors	Sheet	Onlaps onto SU-D and SU-A. Draped over SU-D, D and E.	Occasionally discontinuous and inclined.
SU-D	Mainly transparent with some patchy, inclined reflectors and asymmetric serrate reflectors.	Lobate, thinning toward southeast	Downlaps onto SU-C (where present) and SU-B	No distinct, continuous top reflector.
SU-C	Transparent	Basin fill	Onlaps SU-B and E.	High amplitude top reflector
SU-B	High frequency, low amplitude sigmoidal reflectors and variable reflectors	Varying. Lobate, sheet, channel, mound, basin fill.	Downlaps and onlaps onto SU-A depending on morphology	Complex occurrence and relationship with SU-A. Can be difficult to differentiate from SU-A.
SU-A	Many differing facies. Asymmetric serrate, symmetric serrate, and inclined reflectors, and patchy and sporadic reflectors. High amplitude, continuous inclined reflectors also present.	Mounds, ridges, sheet, channels of varying scale. Ridges up to 40 m high and 30 km long. Mounds up to 20 m high and 1 km long. Channels up to 100 m deep, 200 m wide and 50 km long.	Concordant with, or incises into, basement	Complex morphology and arrangement of multiple seismic facies
SU-Basement	Low frequency, high amplitude parallel reflectors	Sheet and large channels (5 km wide in places)	Basal	Often below the maximum depth of investigation.

*Seismic facies terminology is from Mitchum et al. (1977) and **Table 2**.*

southeastern corner of the study area, where it is concordant with underlying stratigraphy (**Figure 1**). It comprises low-amplitude, low-frequency, discontinuous parallel to sigmoidal reflectors in a sheet geometry, and high-amplitude continuous reflectors within channel forms. The channel forms are stratigraphically lower than the sheet forms (**Figure 3**).

Sedimentary Facies

Nine main lithofacies were identified from vibrocores, CPT logs and borehole samples. Full descriptions of these lithofacies are given in **Table 4**. Images of the lithofacies, where available, are shown in **Figure 2**. Colors given in the descriptions below refer to Munsell color names; full color details are given in **Table 4**.

Dmm – Matrix-Supported Diamict

A brown diamict was recovered from vibrocores in the southeast of the study area. Grain size varies from silty clay to very large pebbles (**Figure 2**). The clasts are predominantly subangular and striated. Rip-up clasts and sand inclusions are also found within lithofacies Dmm.

Flv – Finely Laminated Silts and Clays

A grayish-brown silt and a dark brown clay in alternating laminae were recovered from vibrocores and boreholes, and calibrate to a distinct low cone resistance in CPT logs as seen in CPT A (**Figure 2**). Pairs of laminae vary in thickness from 0.5 to 4 cm. Lithofacies Flv is shown in vibrocore 197 in **Figure 2**.

Fm – Clay

Lithofacies Fm was not recovered in vibrocores or boreholes, but is penetrated by CPTs such as CPT V (**Figure 3**). The very low cone resistance implies it is a massive clay.

Fm(sh) – Massive Silty Clay With Shell Fragments

A very dark grayish brown silty clay was recovered in borehole samples. The short core segments (0.6 m) show the clay to be massive and contain shell fragments, chalk clasts and fine gravel. Slickensides are present along polished planes that are present within the core segment (**Figure 2**). The clay is very stiff and overconsolidated.

Gm – Clast-Supported Gravel

A very dark grayish brown clast-supported gravel was recovered from a borehole spot sample. The matrix comprises silty clay. Clasts are small to medium pebbles in size. The gravel is stiff and overconsolidated. Clasts are of mixed lithology and occasional shell fragments are present. No sedimentary structures are evident. Lithofacies Gm is shown in **Figure 2**.

Sh(d) – Laminated Silty Fine Sand With Dropstones

A dark grayish-brown sand was logged in CPT A (**Figure 2**). Borehole samples show the sand to be laminated and containing occasional subangular to rounded gravel and pockets of clay.

Sl(o)/Fl(o) – Interbedded Sands and Clays With Organic Matter

The interbedded lithofacies Sl(o)/Fl(o) was not recovered in continuous cores. Isolated spot samples show the sand to be grayish-brown fine sand interbedded with very dark grayish-brown clays. Both sand and clay interbeds contain abundant peat fragments and organic material. Lithofacies Sl(o)/Fl(o) has a highly variable CPT log response in CPTs V and W (**Figure 3**) responding to the interbedding of sand and clay.

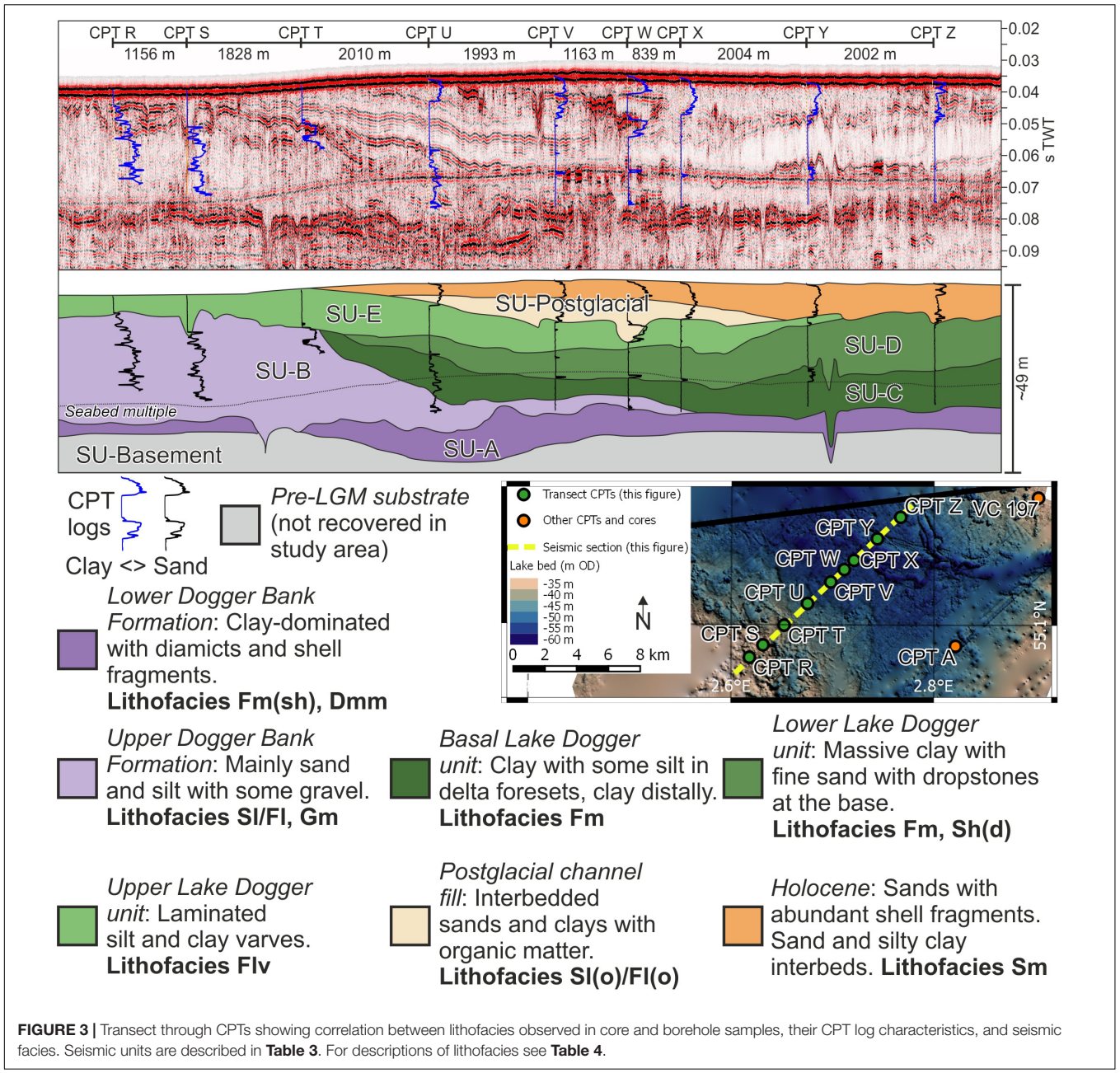


FIGURE 3 | Transect through CPTs showing correlation between lithofacies observed in core and borehole samples, their CPT log characteristics, and seismic facies. Seismic units are described in **Table 3**. For descriptions of lithofacies see **Table 4**.

Sl/Fl – Interbedded Sand and Sandy Clay

A further lithofacies of interbedded sand and clay was recovered in isolated borehole spot samples. This lithofacies varies from Sl(o)/Fl(o) by its lack of organic material. The medium to fine sand is dark grayish brown and the sandy clay is very dark grayish brown. The highly variable CPT log response in CPTs R and S implies it is interbedded (**Figure 3**). The sand is moderately to poorly sorted and occasionally contains fine to coarse gravel and small shell fragments. Some clasts are striated.

Sm – Massive, Bioturbated Sand

A massive, very fine to fine, dark grayish brown sand was recovered at and immediately below the seabed in vibrocores and boreholes. The sand is well sorted and contains abundant whole shells and large (1–2.5 cm) shell fragments. Its mottled appearance suggests it could be bioturbated. Lithofacies Sm is shown in **Figure 2**.

INTERPRETATION OF RESULTS

Stratigraphic Architecture and Geomorphology

In map view, key surfaces between each seismic unit reveal buried geomorphology that provide further evidence of ice-sheet retreat behavior in the study area (cf. Cotterill et al., 2017a,b;

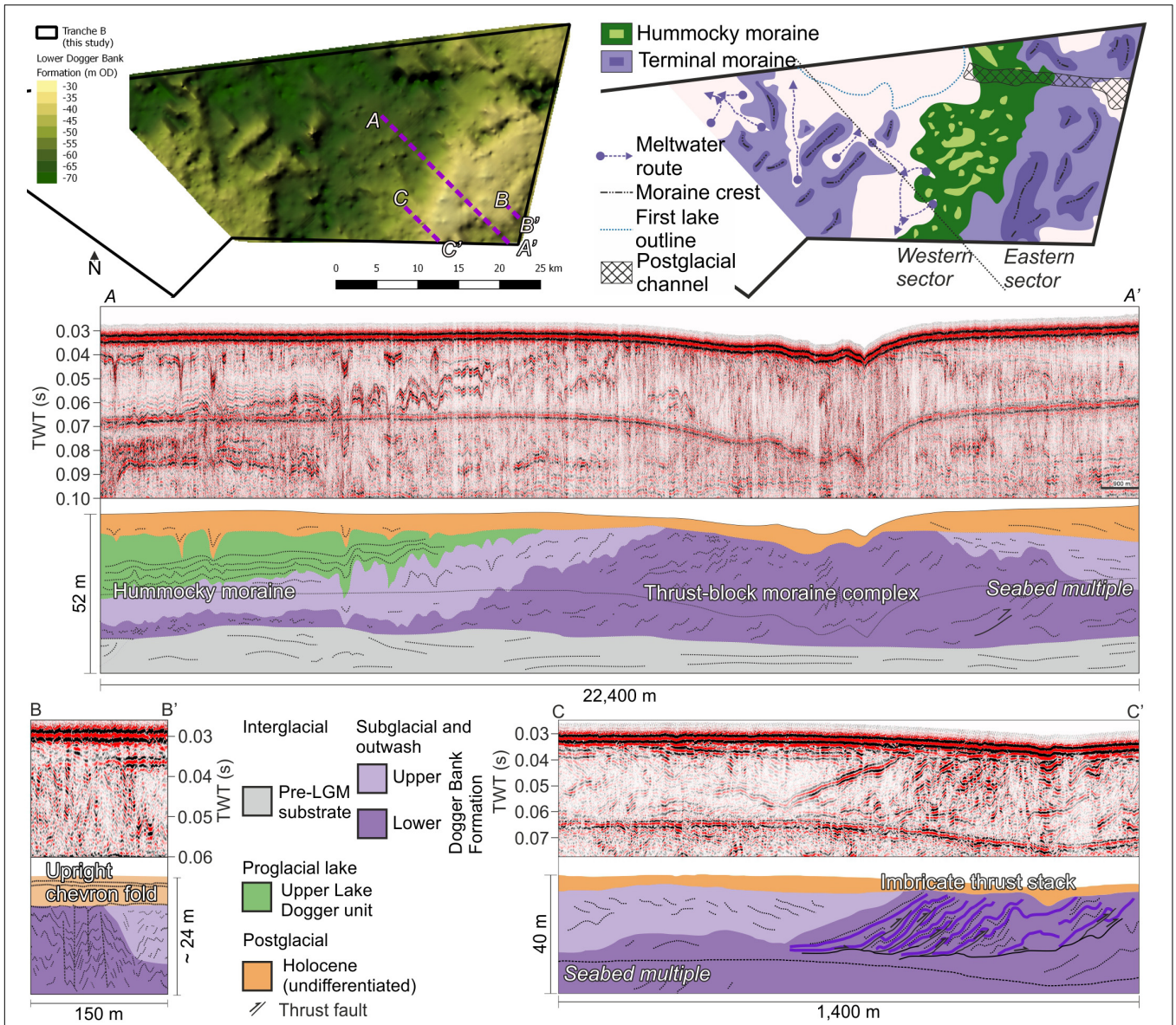


FIGURE 4 | Map of the top Lower sub-unit of the Dogger Bank Formation, revealing the large terminal thrust-block moraine complex, an area of hummocky moraine, and smaller moraines to the west. Seismic section **(A,A')**, through the thrust-block moraine complex, shows the internal deformation, with thrust faults and asymmetric serrate reflectors implying a southeast vergence direction. Seismic section **(B,B')** shows symmetric serrate reflectors that show chevron folding in a different section of the thrust-block moraine complex. Seismic section **(C,C')** shows extensive imbrication and thrust faulting of sediments.

Phillips et al., 2018). These geomorphological features are described in stratigraphic order, from oldest to youngest.

Subglacial Bedforms

A series of elongate mounds are present at the top of seismic unit A. The mounds are rounded, and generally up to 16 m high, 300 m wide, and 1000 m long (**Figure 6**). Seismic facies within the mounds are characterized by patchy, inclined, asymmetric serrate reflectors that imply a degree of deformation. The elongate mounds mainly occur in the eastern sector of the study area, although a single mound that is over 10 km long exists in the western sector. On the basis of their morphology, stratigraphic position and seismic facies, the mounds are interpreted as subglacially streamlined bedforms. Their dimensions conform to many subglacially streamlined bedforms observed globally (Spagnolo et al., 2014; Ely et al., 2016; Jamieson et al., 2016), and are similar in dimension to many drumlins and mega-scale glacial lineations observed elsewhere in the former British-Irish and Scandinavian ice sheets, and in areas with low topographic relief (e.g., Hughes et al., 2010; Evans et al., 2014; Greenwood et al., 2016b; Chiverrell et al., 2018; Delaney et al., 2018; Hermanowski et al., 2019). Two distinct sets of elongation direction are observed within these postulated subglacial bedforms. In the eastern sector of the study area, the bedforms are generally

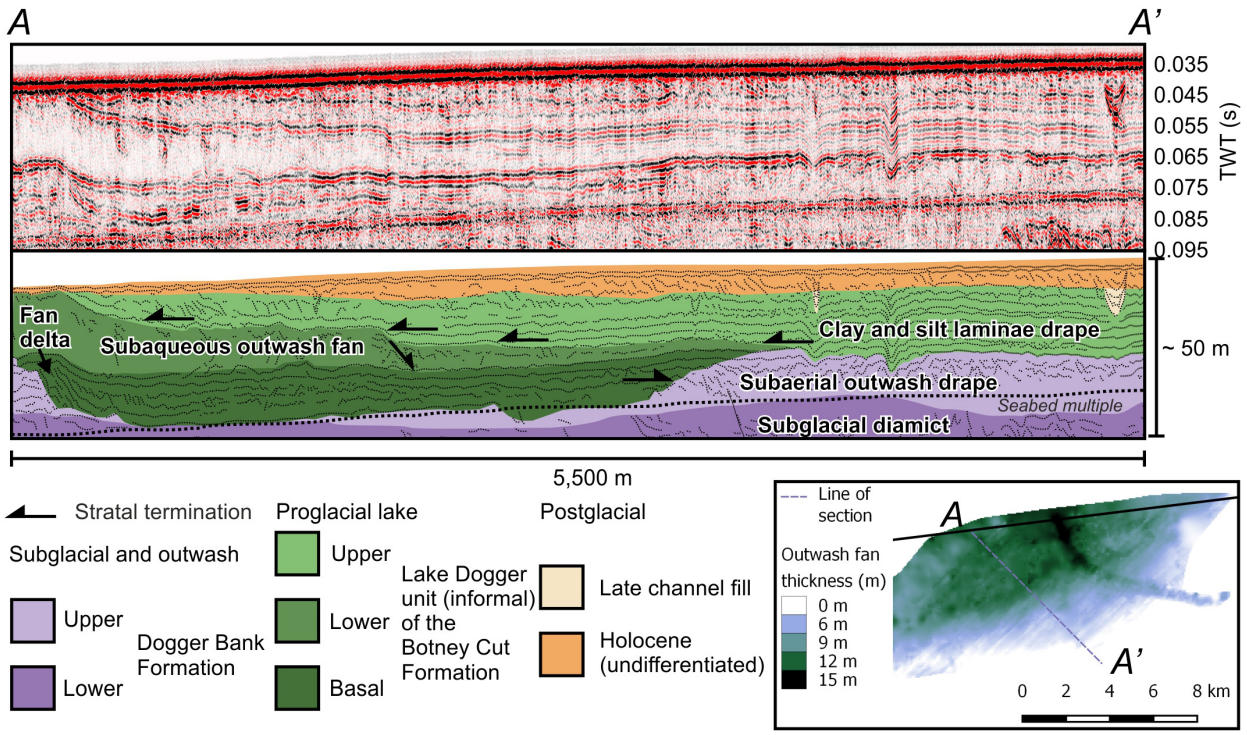


FIGURE 5 | Stratigraphic section showing the proglacial lake stratigraphic relationships. Inset: Isopach map of the Lower Lake Dogger sub-unit showing its lobate geometry, thinning toward the east and south.

elongate about a northeast-southwest axis. In the western sector of the study area, the mound is elongate about a north-south axis (**Figure 6**).

At the same stratigraphic level as the streamlined bedforms, in the eastern sector of the study area, are four northwest-southeast-trending sinuous ridges, up to 15 m high, but generally 5–10 m high, 100 m wide and greater than 4000 m long, extending beyond the study area (**Figure 6**). Internally, medium amplitude, low frequency, subhorizontal, parallel reflectors imply bedding. At the southeastern tip of the ridge, a broad, flat-topped mound is observed, with evidence of stratification. Because of their sinuous ridge morphology with internal bedding, these ridges are interpreted as eskers (Banerjee and McDonald, 1975; Aylsworth and Shilts, 1989; Storrar et al., 2014a,b), which drained sediment-laden meltwater into an outwash fan or small subglacial lake at its southeastern tip. The eskers form a connected network of ridges, interpreted to be a braided esker network in the basis of the channel relationships (Auton, 1992).

Numerous channel forms incise into the subglacial Lower sub-unit of the Dogger Bank Formation and the underlying pre-LGM substrate (**Figure 6**). The channels are 25 to 75 m wide, 3 to 8 m deep, and vary in length from 0.9 to 5 km. One large channel exists on the border between the eastern and western sectors of the study area, and is an order of magnitude larger than the other channels, being 500 m wide, up to 25 m deep and over 10 km long, extending out of the study area. This channel has an undulating thalweg and is slightly sinuous, running northwest to southeast. Networks of the smaller channels vary between the eastern and western sectors. In the east, channels are dendritic and are orientated northwest-southeast. Their orientations are approximately the same as the orientations of the subglacially streamlined bedforms and eskers. There is a change from esker- to channel-dominated landforms associated with a thickening of the till to the southeast (**Figure 6**). In the western side of the study area, there are fewer channels, and the networks are non-dendritic, anastomosing, orientated north-south, and show abrupt terminations at both ends of the channel (**Figure 6**). Both channel networks erode into the substrate. Despite the differences in networks between the eastern and western sectors, the channels have been interpreted as subglacial meltwater channels on the basis of their network, termination style, erosion into the substrate, and morphology (Greenwood et al., 2007; Pearce et al., 2017).

Moraines

The large composite ridge formed by SU-A in the eastern sector of the study area (**Figure 4**) comprises multiple smaller ridge crests within one main ridge, orientated from north-northeast to south-southwest that is up to 40 m high, 10 km wide and extends at least 27 km. The ridge is slightly arcuate. The southeast-verging internal deformation within the ridges, combined with their morphology, imply that these ridges form a thrust-block moraine complex (Benn and Evans, 2010 and references therein) as ice moved from northwest to southeast.

To the northwest of the thrust-block moraine complex, and to the southeast of the subglacial landforms described above, is an

TABLE 4 | Lithofacies descriptions as observed in vibrocores and borehole samples.

Lithofacies code (based on Evans and Benn, 2004)	Short description	Munsell color	Grain size	Sedimentary structures	Other notes
Gm	Clast-supported gravel	Very dark grayish brown 10YR 3/2 (clay matrix)	Silty clay to medium pebbles (Φ −3).	Massive	Very stiff, consolidated, clast-supported gravel with shell fragments and clasts of mixed lithology.
Dmm	Matrix-supported diamict	Brown 10YR 4/3	Silty clay to very large pebbles (Φ −6)	Massive	Clasts angular to subrounded, predominantly subangular, consisting of mixed lithologies. Some striations preserved on clasts. Rip-up clasts and inclusions of sand.
Flv	Finely laminated silts and clays	Grayish brown 10YR 5/2, light brownish gray 2.5Y 6/2 (silt), dark brown 7.5YR 3/2 (clay), light yellowish brown 2.5Y 6/3 (very fine sand)	Silt (Φ 6 to 8) and clay (Φ 10) with some very fine sand (up to Φ 4)	Alternating laminae of clay and silt. Laminae pairs 0.5 to 4 cm thick. Some occasional ball-and-pillow structures and convolute bedding. Patches of very fine sand may occur, with clay-silt laminae draped over.	Very fine sand appears in thin laminations, 1–2 cm, fining upward, of differing frequency, but remains rare (every 25–50 cm)
Fm(sh)	Massive silty clay	Very dark grayish brown 10YR 3/2	Clay (Φ 10) with some silt (Φ 8)	Massive	Occasional shell fragments, chalk clasts and fine gravel. Some planes with slickensides preserved.
Fm	Clay	Not recovered	Clay (Φ 10) with some silt (Φ 8)	Not observed in continuous cores	Overconsolidated. Not recovered.
Sh(d)	Laminated silty fine sand with dropstones	Dark grayish brown 2.5Y 4/2 (sand)	Very silty (Φ 6 to 8) fine sand (Φ 3 to 4) with fine gravel (Φ −2 to −3)	Sand laminated (0.5 to 2 cm).	Gravel is subangular to rounded and of mixed lithology. Pockets of clay present. Poorly sorted.
Sl(o)/Fl(o)	Interbedded sands and clays with organic matter	Grayish brown 2.5Y 5/2 (sand), very dark grayish brown 10YR 3/2 (clay)	Fine sand (Φ 2 to 3) with sandy clay (Φ 10)	Not observed in continuous cores	Mica-rich. Abundant organic material, peat fragments.
Sl/Fl	Interbedded sand and sandy clay	Dark grayish brown 2.5Y 4/2 (sand), very dark grayish brown 10YR 3/2 (clay)	Medium to fine sand (Φ 1 to 3) and clay (Φ 10) with very fine sand (Φ 4) and silt (Φ 6 to 8).	Not observed in continuous cores	Moderately to poorly sorted sand, occasionally with fine to coarse gravel, frequent granule-sized chalk. Some striations preserved on clasts. Small shell fragments frequent. Interbed thickness varies greatly.
Sm	Massive very fine to fine sand	Dark grayish brown 2.5Y 4/2, olive brown 2.5Y 4/3	Very fine to fine sand (Φ 2 to 4)	Some bioturbation.	Well sorted. Contains whole shells and abundant shell fragments. Mottled texture.

area of irregular, hummocky topography that internally show evidence for deformation within the seismic facies (**Figure 4**). The thin unit of deformed seismic facies with a hummocky top surface implies subglacial deformation of fine-grained tills. This is consistent with hummocky moraines, similar to those observed close to the margin of the former Laurentide ice sheet (Evans and Rea, 1999; Eyles et al., 1999; Boone and Eyles, 2001; Evans et al., 2014).

Smaller moraine ridges also exist in the western sector of the study area (**Figure 4**). The moraines are up to 10 km long, 2 km wide, and 15 m high, and are narrower and single-crested, implying a different formational process to the large thrust-block moraine complex. Furthermore, these moraine ridges trend northeast to southwest, and are generally more arcuate than the thrust-block moraine complex. The relative scale and geometry of these buried glacial landforms are comparable to those described by Phillips et al. (2018), 50 km to the southwest, as having formed during the active retreat of the ice sheet northward across Dogger Bank.

Lake Basin Morphology

The stratigraphically lowest lake-fill sediments of the Basal Lake Dogger sub-unit occur in the north of the eastern sector of the study area (**Figure 4**), whilst the Lower and Upper Lake Dogger sub-units are laterally more extensive and can be traced across most of the eastern sector of the study area (**Figure 7**). The initial lake basin, represented by the Basal Lake Dogger sub-unit sediments, has been mapped over an area of at least 90 km^2 within the study area (**Figure 4**), but extends further north outside of the data coverage. Typically, this basal sedimentary unit is 10 to 12 m thick, but reaches a maximum thickness of 20 m. The subsequent, more areally extensive lake is represented by the Lower and Upper Lake Dogger sub-units and forms an elongate north-south trending basin, which is over 43 km in length (extending beyond data coverage) and up to 17 km wide, and covers an area of over 700 km^2 (**Figure 7**). The sediments (combined Lower and Upper Lake Dogger sub-units) within this lake basin reach a maximum thickness of 30 m (**Figure 1**).

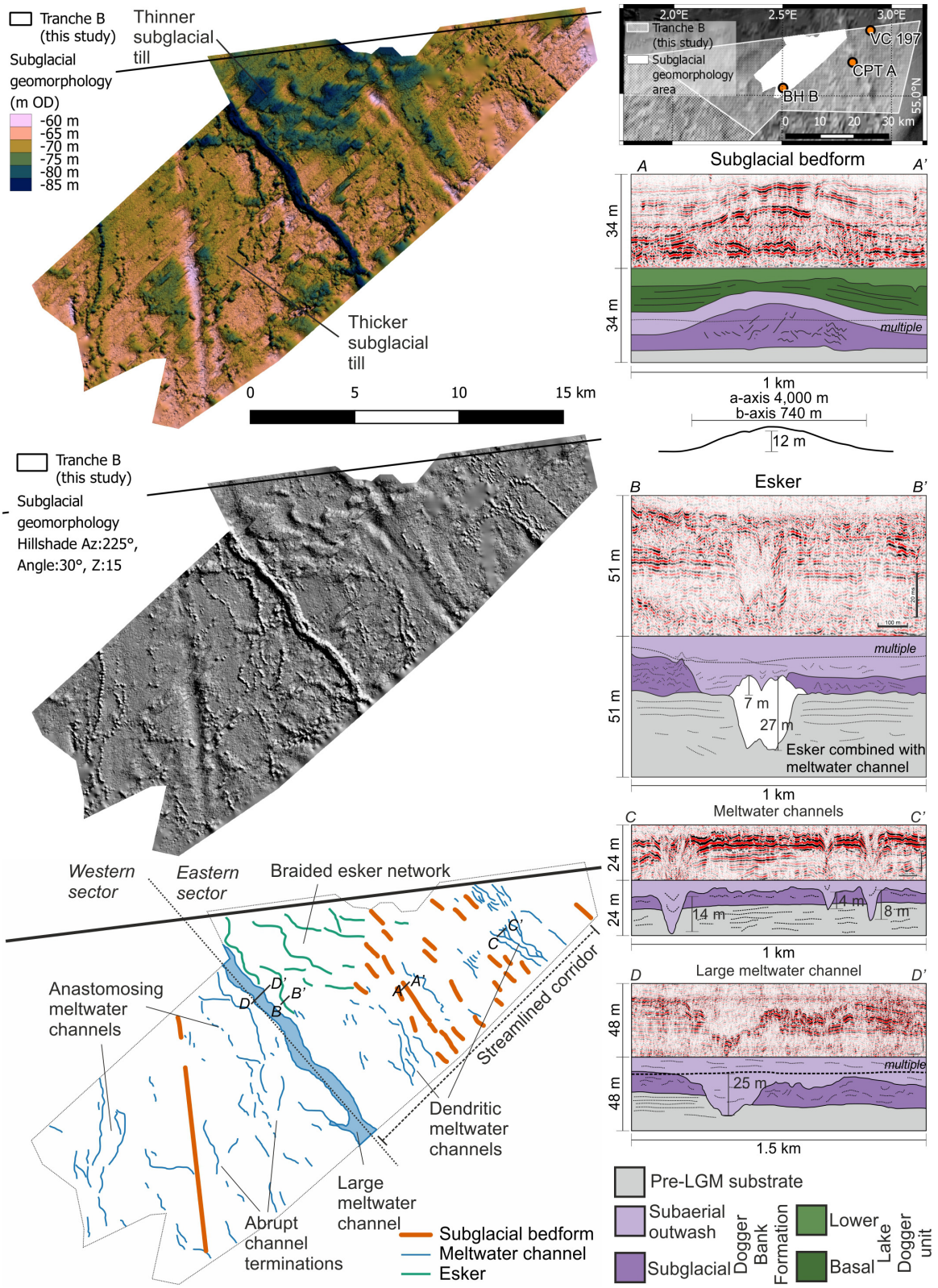


FIGURE 6 | Elevation-colored and hillshaded maps of the Lower sub-unit of the Dogger Bank Formation with a detailed interpretation showing subglacial bedforms, meltwater channels and eskers. Cross-sectional morphology of a subglacial bedform **(A,A')**, an esker **(B,B')**, the smaller meltwater channels **(C,C')**, and the large meltwater channel **(D,D')** are shown in the seismic sections. Color bar "Batlow" from Crameri (2018).

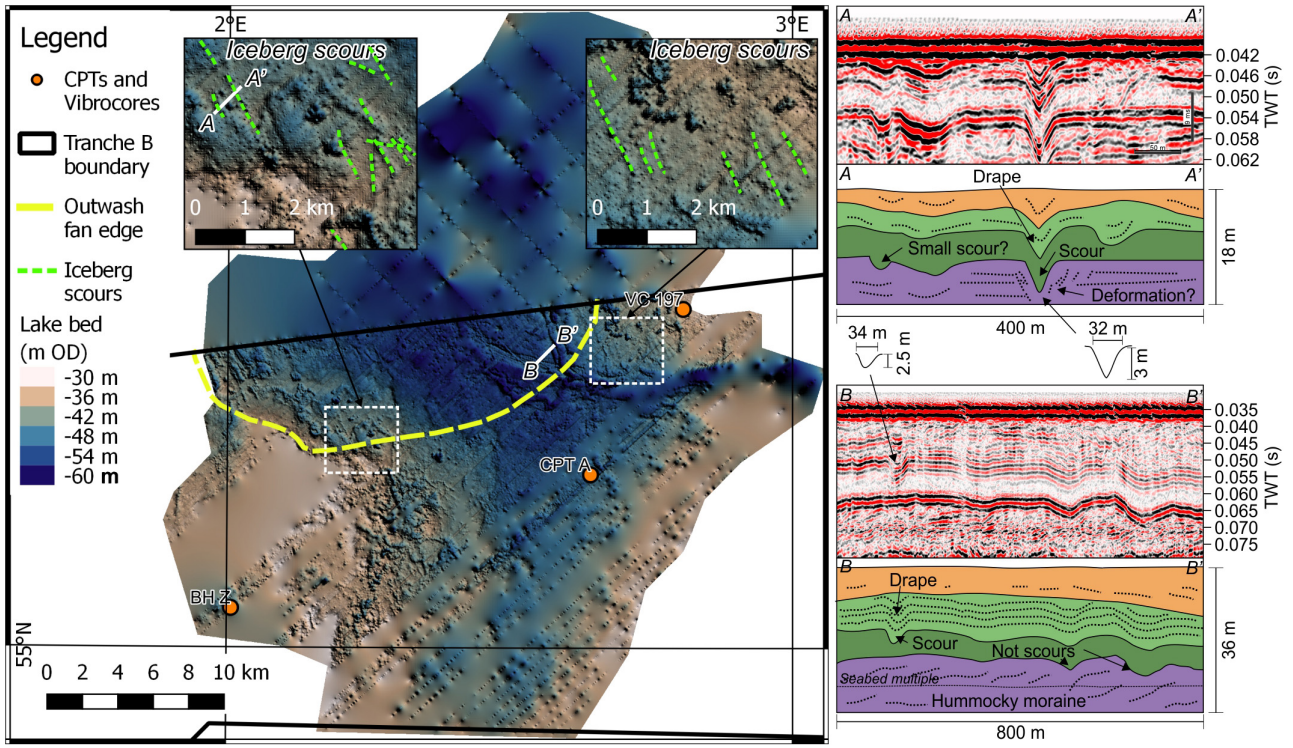


FIGURE 7 | Map of the proglacial lake bed showing its morphology and the presence of iceberg scours. Seismic sections show morphology of iceberg scours as well as lake-bed topography that may appear to be scours in map form. The location of ice-rafted debris found in CPT A is shown. Color bar "La Paz" from Crameri (2018).

The lake bed surface onto which the Lower and Upper Lake Dogger sub-units were deposited shows a series of concave-up lineations (**Figure 7**). These features generally strike NNW-SSE and range in length from 400 to 1000 m. They are generally less than 100 m wide, with most being 10 to 30 m. Their depth varies from 1 to 3 m (**Figure 7**). The lineations occur at elevations below −38 m OD. Seismic sections through the lineations confirm they truncate the substrate, and also show some evidence for deformation of the substrate such as faulting immediately adjacent to the lineations (**Figure 7**). These features are interpreted to be iceberg scours. The iceberg scours are similar in dimension to many of those collated by Eden and Eyles (2001), especially those with similar water depths to those expected in Lake Dogger (e.g., Wahlgren, 1979; Dredge, 1982; Thomas and Connell, 1985; Eyles and Clark, 1988; Longva and Bakkejord, 1990). Deformation of soft sediments surrounding the lineations due to the iceberg keel pushing fine-grained sediments is also diagnostic of iceberg scouring (Woodworth-Lynas and Guigné, 1990; Linch et al., 2012; Linch and van der Meer, 2015).

Depositional Environments

Depositional environments are interpreted from correlation of sedimentary facies to the seismic units. Borehole samples were calibrated to CPT logs and seismic reflection data (**Figure 3**). Further correlation of sedimentary facies to seismic facies was provided by continuous vibrocores.

Pre-LGM Substrate

Few boreholes in the study area reach the pre-LGM substrate (**Figure 3**). A layer of clean very fine sand with large shell fragments at ∼50 m depth in a borehole at the south of Tranche B may represent a pre-LGM shelly lag in shallow marine sand (Cotterill et al., 2017a). Seismic reflections show very large (>5 km in width, and up to 200 m deep) channel-fills incised into previous deposits. The top of these channel-fills lie below the sand, and are interpreted to be either tunnel-valley fills or a proglacial drainage network, most likely formed by the thick, extensive Elsterian (MIS 12) ice sheet (Cotterill et al., 2017a). The sequence underlying the Dogger Bank Formation throughout Tranche B is therefore likely to comprise marine interglacial deposits of sands and gravelly sands with some silt and clay, all with abundant shells, belonging to the Eem, Cleaver Bank and Egmond Ground formations (Cotterill et al., 2017a).

Subglacial and Glaciotectonised Sediments (Lower Sub-Unit of the Dogger Bank Formation)

Seismic unit SU-A calibrates to two lithofacies observed in vibrocores and boreholes, a matrix-supported diamict (Dmm) and a massive silty clay (Fm). Both lithofacies are dense and overconsolidated (**Figure 2**). The diamict contains shell fragments and gravel of mixed lithology as well as sand inclusions that indicate incorporation of frozen sediments. Because of

the incorporation of sand inclusions, the diamict is interpreted to be a glaciotectonite. The massive clay also contains shell fragments and occasional fine gravel of mixed lithology. Planes with slickensides within the massive clay observed in the western sector of the study area imply brittle deformation, probably due to glaciotectonics. The massive clay is interpreted to be a subglacial till (Evans et al., 2006).

Internally, the ridge morphology of SU-A contains evidence for deformation of the sediment. Serrate reflectors are interpreted to be chevron folds (**Figure 4**). Thrust faulting is also observed within the ridge morphology (**Figure 4**). The structural domains are similar to those observed in Dogger Bank moraines to the west of the study area (Phillips et al., 2018). The chevron folds belong to structural domain 3 and the inclined, verging reflectors belong to structural domain 5 of Phillips et al. (2018). Because of its lithology, depositional environment and deformation, as well as its proximity and similar stratigraphic context to those moraines observed by Phillips et al. (2018), this seismic unit and correlated subglacial till and glaciotectonite is assigned to of the Lower Dogger Bank sub-unit of the Dogger Bank Formation.

Subaerial Glacial Outwash (Upper Sub-Unit of the Dogger Bank Formation)

Seismic unit-B unconformably overlies and downlaps onto SU-A, and comprises mainly variable and transparent (see **Table 2** for description) seismic facies (**Figures 3**, **4**). When calibrated to borehole samples and CPTs (**Figure 4**), these seismic units comprise the clast-supported gravel (Gm) and the interbedded sands, silts and silty clay (Sl/Fl) lithofacies (**Figure 2**). The grain sizes are generally coarser than those observed in the Lower Dogger Bank sub-unit, as shown on CPT logs (**Figure 4**). Both lithofacies are overconsolidated on CPT logs (**Figure 2**). The mixed grain sizes and interbedded nature of the sediments implies that these sediments were deposited in a mixed-energy environment. Overconsolidation of the lithofacies implies the sediments were overridden by ice or exposed subaerially, allowing for desiccation. Because of their stratigraphic position above subglacial and glaciotectonised sediments, and their lithofacies differences, desiccation is inferred to be the process responsible for the overconsolidation. The presence of shell fragments and clasts of mixed lithology imply reworking of marine sediments as well as clastic input from a varied catchment, as observed in similar formations by Cotterill et al. (2017a). This depositional environment is interpreted to be glacial outwash, deposited subaerially from sediment-laden sub- and englacial meltwater at the retreating ice-sheet margin. The thickness of the Upper sub-unit of the Dogger Bank Formation varies across the study area. In the eastern sector, its thickness varies from absent, up to a maximum of 10 m. In the western sector of the study area, it is much thicker, between 15 and 30 m thick (**Figure 3**).

Proglacial Lake Sediments (Botney Cut Formation)

In the eastern sector of the study area, three seismic units (SU-C, SU-D, and SU-E) fill a large basin formed between the elongate ridges of glaciotectonised sediments of SU-A, and large accumulations of outwash of SU-B (**Figure 4**).

Basal proglacial lake fill (Basal Lake Dogger sub-unit)

The first unit deposited in the basin fill, seismic unit SU-C, onlaps onto previous deposits and comprises a mixture of oblique tangential and transparent seismic facies (**Figure 5**). No vibrocores or boreholes penetrate SU-C, but a generally low cone resistance from CPT logs implies interbedded clay and silt (**Figure 3**). The oblique tangential reflectors imply a fan delta prograding into the lake basin. At least three packages of oblique tangential reflectors exist, with delta topsets at different elevations, implying a relative, stepped lake level rise. The top reflector of SU-C is high amplitude and horizontal (**Figure 5**), possibly suggesting that lake basin accommodation was filled, or that meltwater and sediment supply to the lake stopped. Downlapping and draping of the overlying seismic units onto the top surface imply a gap in the depositional record (**Figure 5**). The high amplitude reflector is interpreted to represent overconsolidation, either through ice margin readvance or desiccation. As no deformation related to ice-marginal oscillation is observed, subaerial exposure likely led to desiccation of the initial lake fill, as observed in other subaerially exposed units on Dogger Bank (Cotterill et al., 2017a,b) and in other lake-fills observed in seismic data in the geological record (D'Agostino et al., 2002).

Ice-contact proglacial lake fill (Lower Lake Dogger sub-unit)

The lobate, downlapping, southwest-thinning transparent SU-D corresponds to clay-rich responses from CPTs, but are not penetrated by vibrocores or borehole samples (**Figure 3**). Patchy, inclined, and locally folded reflectors imply small-scale, localized deformation that is interpreted as slumping due to gravitational instability (**Figure 5**). Due to its lobate shape (**Figure 5**), fine-grained sediments and slumping, SU-D is interpreted to be an ice-contact subaqueous outwash fan, with finer-grained sediments in the distal part of the fan. Commonly, the base of SU-D and the onlapping seismic unit of SU-E contains a laminated silt to fine sand layer with subangular to rounded gravel of lithofacies Sh(d) and clasts of clay (**Figures 2**, **3**). This thin (<50 cm) layer of coarser sediments is interpreted to be ice-rafted debris (IRD) on the basis of the presence of oversized clasts of mixed lithology and clay till pellets within laminated lake sediments (Thomas and Connell, 1985; Cowan et al., 2012). These sediments were carried out to the distal parts of the lake by floating icebergs calved from the glacier margin, as opposed to transport within the lake water.

Ice-distal proglacial lake fill (Upper Lake Dogger sub-unit)

The youngest proglacial lake unit comprises characteristic high frequency, medium-amplitude, continuous seismic reflectors (SU-E) that are draped above, and are parallel to, the lake bed. Laterally, the reflectors onlap onto the ice-contact lake fill and the subglacial and glacial outwash (**Figure 5**). In vibrocore and borehole, this seismic unit corresponds to the finely laminated silts and clays (lithofacies Flv). The laminae pairs alternate between pale silt and dark clay with sharp contacts. Where very fine sand is present, it occurs at the base of the pale silty unit and is normally graded. Because of the silt-clay pairs and the normally graded silt laminae (**Figure 2**), the lithofacies is interpreted to be a siliciclastic varve sequence (Zolitschka, 2007). The fine-grained

deposits imply quiet-water conditions during their deposition. The low-energy rhythmites that are draped parallel with the lake bed could be interpreted as overflow-interflow dispersal of sediments within the lake that is typical of proglacial lakes distal to the ice margin (Smith and Ashley, 1985; Carrivick and Tweed, 2013). Therefore, it is interpreted that this uppermost unit of the Lake Dogger sub-unit was deposited at a time when the ice margin was further to the northwest, not in contact.

Postglacial

Two depositional environments are grouped together. Channel forms with high-amplitude fill calibrate to interbedded sands and clays with organic matter [lithofacies Sl(o)/Fl(o)]. The interbedded nature of sands and clays of the channel-fills imply a fluvial depositional environment, with accumulation of organic matter washed in from the surrounding tundra plain (Cotterill et al., 2017a). One large, east-west orientated channel (**Figure 3**) with a high-amplitude fill may be related to an earlier channel that allowed lake drainage. However, the high-amplitude fill destroys any signal from below the channel, and its stratigraphic relationship to the proglacial lake sediments cannot be determined.

On top of, and in places partially filling, the channel network is clean, well sorted, bioturbated sand (lithofacies Sm) with abundant shells and shell fragments (**Figure 2**). This represents the transition to a fully marine depositional environment as documented by Emery et al. (2019). The shallow marine sand cover varies in thickness throughout the study area from absent to up to 13 m in the southeast of the study area (see Figure 3 in Cotterill et al., 2017a). Sigmoidal reflectors within the shallow marine sand are interpreted to show progradation of the sand from west to east (**Figure 3**).

DISCUSSION

Paleogeographic Evolution of Southeastern Dogger Bank

The sedimentological, seismic stratigraphic and geomorphic observations are combined to present a conceptual, six-stage model of ice sheet advance and retreat, and landscape evolution on the southeastern edge of Dogger Bank (**Figure 8**).

Stage One: Ice Sheet Advance to Maximum Extent

The preserved landform assemblage in the eastern sector of the study area comprises a complex network of subglacial bedforms, meltwater channels, eskers, hummocky moraines, and a single thrust-block moraine complex at the same stratigraphic level (**Figures 4**, **6**). The subglacial landforms are located to the northwest of the hummocky moraines, which in turn are located to the northwest of the thrust-block moraine complex (**Figure 4**). Streamlined subglacial bedforms of this scale imply warm-based ice and fast ice flow with low bed shear stresses (Stokes and Clark, 1999; Jamieson et al., 2016). The subglacial landforms and streamlined bedforms form a corridor, orientated northwest-southeast, which is at least 15 km wide (**Figure 6**) that occupies the eastern sector of the study area. Because of the warm-based, fast ice flow with a streamlined corridor of subglacial landforms, the eastern sector of the study area is interpreted to have been formed by an ice stream (Stokes and Clark, 1999, 2001; Evans et al., 2008). Furthermore, this landform assemblage conforms to a surging ice-stream landsystem (Evans and Rea, 1999; Evans et al., 2014). In this situation, ice flows rapidly to its maximum extent, forms a thrust-block moraine complex, then shuts down and stagnates, resulting in an isochronous (or near-synchronous) imprint of an ice stream in the sedimentary archive (Stokes and Clark, 1999; Stokes, 2018).

The main control invoked on ice-stream location is topographic focusing (Winsborrow et al., 2010). However, in the North Sea Basin, relief is low, therefore topography is not inferred to be the only influence. Subglacial meltwater routing can control the location of an ice stream (Winsborrow et al., 2010). Dendritic meltwater channels and a braided esker network imply efficient, channelized drainage of large volumes of meltwater (Röthlisberger, 1972; Auton, 1992; Greenwood et al., 2007, 2016a; Storrar et al., 2014b). The implication of this well-ordered drainage is that meltwater was at low pressure during the formation of this drainage network (Greenwood et al., 2016a), which may imply high basal shear stress due to high effective stress at the base of the ice sheet. This is at odds with high-pressure fluids usually inferred to be associated with fast ice flow (Engelhardt et al., 1990; Wellner et al., 2006; Peters et al., 2007; Greenwood et al., 2016a; Stearns and van der Veen, 2018). It is therefore likely that a time-transgressive subglacial hydrological imprint was left on the subglacial bed, and we suggest low-pressure, dendritic channels formed close to the ice-sheet margin during ice advance, which then controlled the location of ice streaming with higher meltwater pressures and bed shear stress.

In the western sector of the study area, a different landform assemblage is observed (**Figures 4**, **6**). No streamlined subglacial bedforms, eskers or hummocky moraine are present, and the relatively sparse subglacial meltwater channel network is strongly non-dendritic and anastomosing, with abrupt channel terminations (**Figure 6**). This implies an inefficient drainage of high-pressure fluid in a canal network (Greenwood et al., 2016a), often observed with deformable beds (Walder and Fowler, 1994). The relative lack of meltwater influence at the bed implies englacial meltwater transport, with fluid pressures near that of ice pressure. This allowed cold-based ice to dominate, resulting in higher shear stresses within the deforming sediment and the formation of brittle deformation features, such as shear planes and faults (Szuman et al., 2013) as observed from subglacial diamicts in borehole BH B (**Figure 2**). The lack of bedforms suggests a slower ice flow (Punkari, 1997b; Szuman et al., 2013; Stokes, 2018), or that bedforms have been reworked during active ice-margin retreat. However, the subglacial meltwater channels have been preserved, favoring the interpretations of slower, interstream ice-sheet flow.

The southern limit of ice in the North Sea at the LGM is poorly constrained due to a lack of data, leading to several competing hypotheses (Phillips et al., 2017b). Previous authors have interpreted that the ice sheet stopped to the north and west of Dogger Bank (e.g., Cameron et al., 1992), or overrode

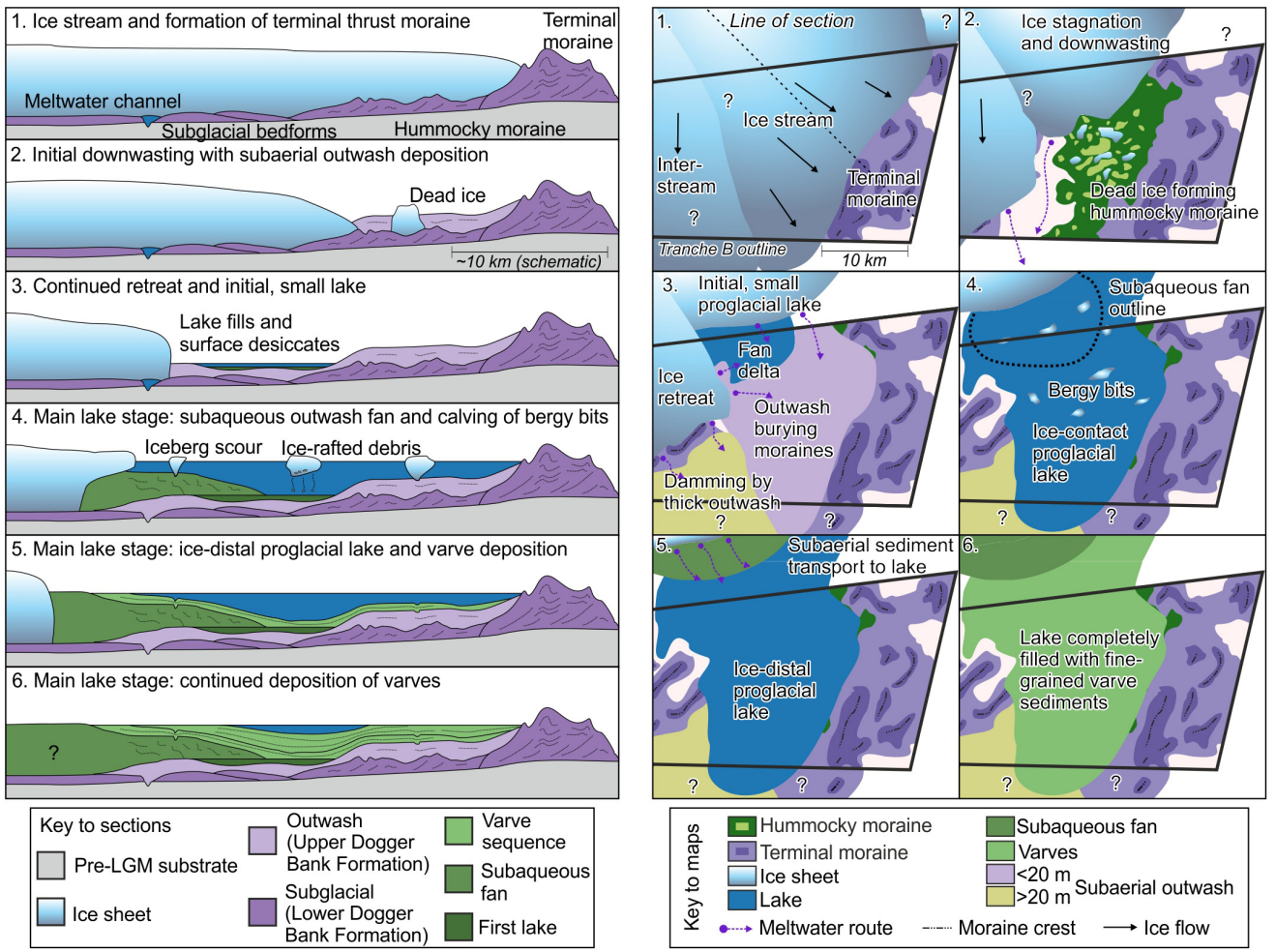
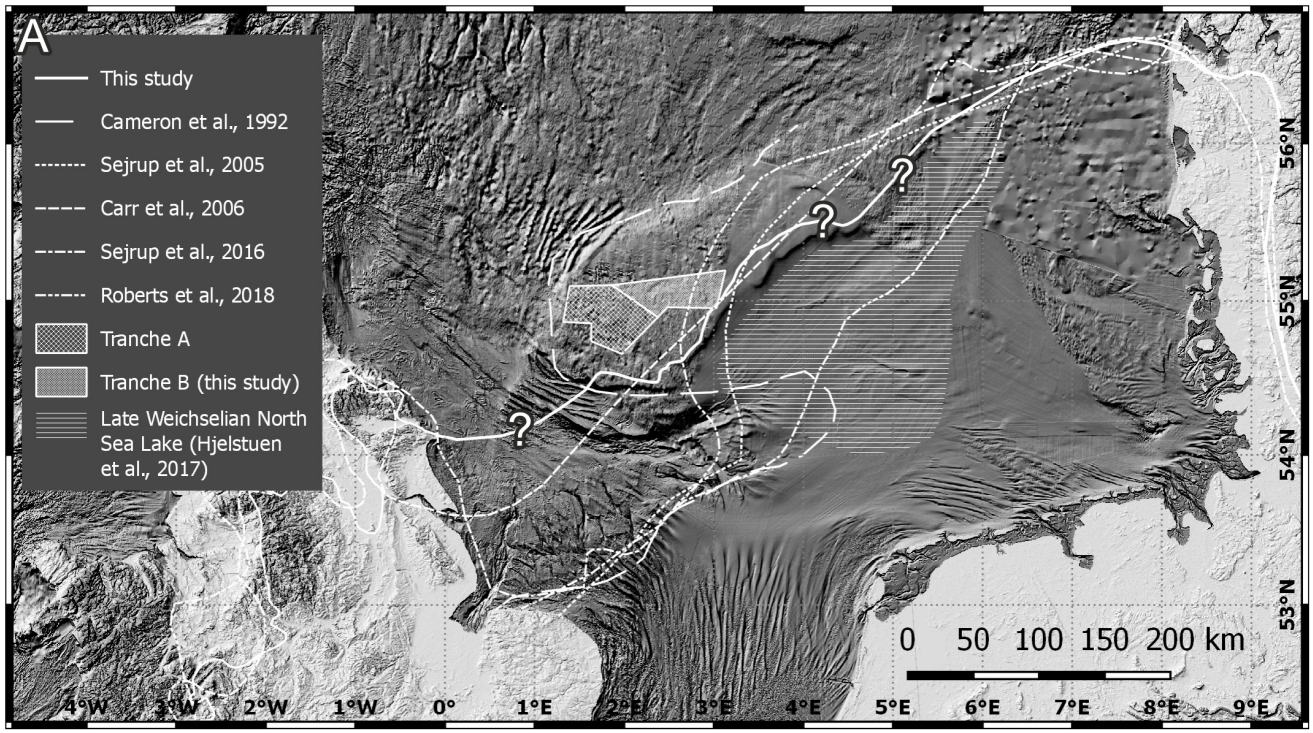


FIGURE 8 | Conceptual landscape evolution model during ice-sheet retreat in the study area. Schematic cross-section stages show stratigraphic evolution of the ice stream and proglacial lake. Paleogeographic maps show the spatial landscape evolution and lateral changes in ice sheet margin. Numbers correspond to stages described in section "Paleogeographic Evolution of Southeastern Dogger Bank."

Dogger Bank entirely, varying by up to 200 km in places (e.g., Sejrup et al., 2005, 2016; Carr et al., 2006; Phillips et al., 2018; Roberts et al., 2018). No precise limit can be seen within the study area as the terminal moraines extend to the south and west (**Figure 4**). However, an inference can be made based on the Dogger Bank Formation abruptly thinning toward the southeastern corner of the study area (**Figure 4**) which suggests that this was the terminal position of the ice sheet during the Last Glacial Maximum. An alternative interpretation that the thinning is due to erosion can be ruled out because the reflectors within the Upper and Lower sub-units of the Dogger Bank Formation are not truncated at their top surfaces (**Figure 4**). The flat bathymetry of Oyster Ground, to the southeast of Dogger Bank (**Figure 1**), lacks any evidence for glacial advance such as terminal moraines. The thickening Late Holocene sand wedge on the southern edge of Dogger Bank imply that this shallowest point of Dogger Bank is a more recent feature than an MIS 2 ice sheet extent (**Figure 1**; Emery et al., 2019). Because of these constraints, it is inferred that the ice sheet did not extend beyond the southern margin of Dogger Bank, in contrast to previous estimates (Hughes et al., 2016; Sejrup et al., 2016; Cotterill et al., 2017a; Phillips et al., 2018), but reached a limit just to the north of the break in the southern slope of today's Dogger Bank (**Figure 9**). The juxtaposition of different ice flow velocities is interpreted in many lobate-margined, lowland-terminating ice sheets in the geological record (Punkari, 1995, 1997a,b; Evans and Rea, 1999; Evans et al., 2008, 2014, 2016b; Szuman et al., 2013; Darvill et al., 2014; Margold et al., 2015, 2018; Stokes et al., 2015; Larsen et al., 2016; Phillips et al., 2017a). The ice stream and interstream areas identified in this study may have resulted in a more lobate margin than presented in **Figure 9**. Further constraint on the actual character of the ice-sheet margin in the North Sea is limited due to a lack of high-resolution seismic reflection data.

Subglacial topography revealed through interpretation of regional BGS seismic surveys (**Figure 10**) shows that Dogger Bank was a topographic high prior to the LGM, formed due



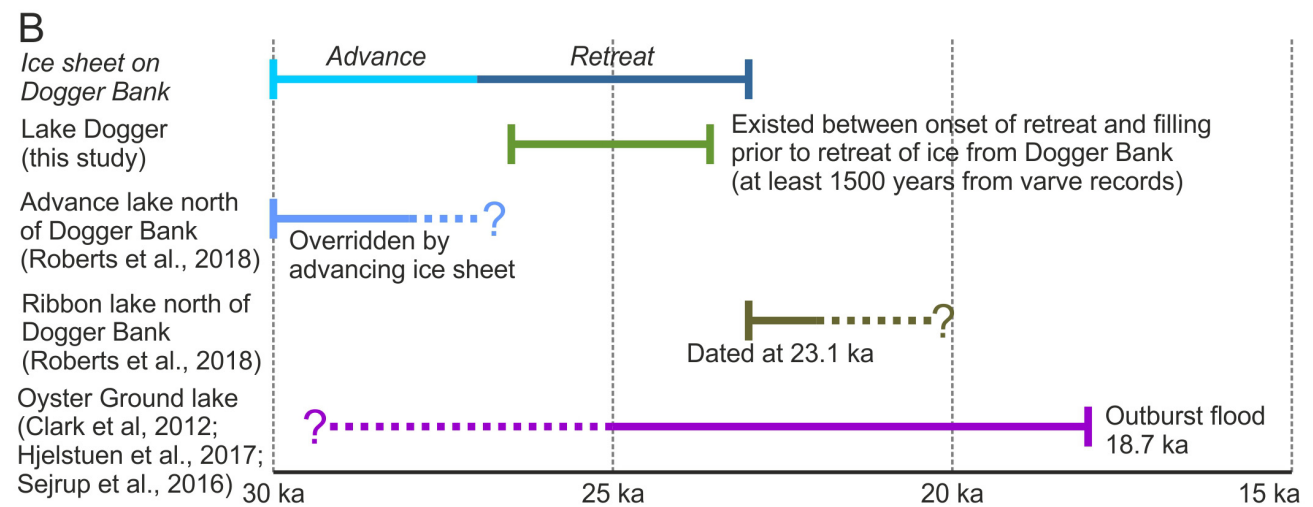


FIGURE 9 | (A) Comparison between previous inferred maximum LGM ice sheet extents (Cameron et al., 1992; Sejrup et al., 2005, 2016; Carr et al., 2006; Roberts et al., 2018) and the new extent proposed in this study. The North Sea Lobe is a later feature of the ice sheet (Dove et al., 2017; Roberts et al., 2018) and has been left off our LGM reconstruction. **(B)** Timeline of the existence of different proglacial lakes in the North Sea basin during and after the LGM. Compiled from this study Clark et al. (2012), Sejrup et al. (2016), Hjelstuen et al. (2017), and Roberts et al. (2018). Bathymetry data: GEBCO (https://www.gebco.net).

to the northward progradation of shallow marine sands into open waters (Cameron et al., 1992; Cotterill et al., 2017a). This would have provided an inverse, north-dipping gradient for the advancing, thin ice sheet to climb, potentially explaining why the ice sheet did not reach any further than the southern margin of Dogger Bank. Geothermal heat-flow density at Dogger Bank is also low, potentially causing a sticking point and arresting any further southerly progress of the rapidly advancing ice sheet (Hurtig, 1995; Hurter and Haenel, 2002; Doornenbal and Stevenson, 2010). This opposite geothermal effect is observed at the southern margin of the Scandinavian Ice Sheet in the Wielkopolska Lowlands, where a higher geothermal heat flux than the surrounding area increased ice velocity and flow (Szuman et al., 2013, 2018).

The presence of a large proglacial lake, distinct from that identified in this study, which occupied Oyster Ground (**Figure 1**) during MIS 2 has been debated (**Figure 9**; Toucanne et al., 2010; Clark et al., 2012; Murton and Murton, 2012; Sejrup et al., 2016;

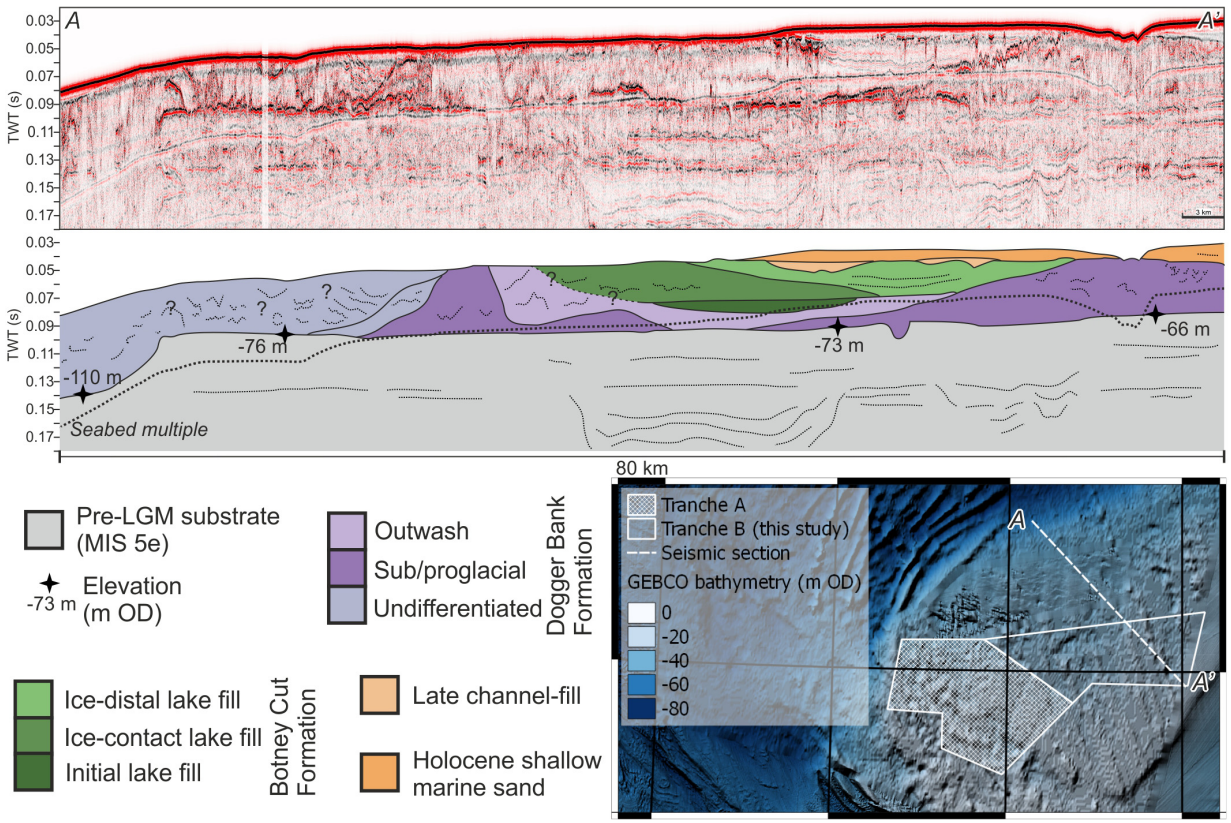


FIGURE 10 | British Geological Survey regional seismic section through Dogger Bank showing the subglacial topography toward the northern slope of Dogger Bank. Elevation of the subglacial surface deepens to the northwest and is echoed in the present-day bathymetry. No detailed seismic investigation of the northern slopes of Dogger Bank has yet been undertaken. Bathymetry data: GEBCO (https://www.gebco.net).

Hjelstuen et al., 2017; Roberts et al., 2018). If the ice stream terminated in a lake, a narrow terminal zone would result in calving and no moraine (Boyce and Eyles, 1991; Stokes and Clark, 2001), and the presence of geomorphologically distinct grounding zone wedges (Powell, 1984; McCabe and Eyles, 1988; Powell and Alley, 1997; Dowdeswell and Fugelli, 2012). However, the ice stream in the study area conforms to a land-terminating terrestrial ice-stream because of the presence of the large terminal thrust-block moraine complex (Patterson, 1997; Stokes and Clark, 2001). It is possible that ice advanced into a lake beyond the interpreted terminal thrust-block moraine complex, but no suitable data exist to the southwest of the study area to test this. It seems unlikely that this particular ice stream was lake-terminating when considering the preserved landforms and the lack of evidence for further southward advance beyond Dogger Bank from bathymetry data.

Stage Two: Ice Stream Shutdown and Ice Margin Retreat

Hummocky moraine observed in the study area formed as the ice stream shut down and began to stagnate, with dead ice pressing and deforming the clay-rich Lower sub-unit of the Dogger Bank Formation subglacial till (Evans and Rea, 1999; Eyles et al., 1999; Boone and Eyles, 2001). An alternative explanation for the hummocky topography is meltwater runoff and mass-wasting events from the side of larger landforms. However, the hummocky topography shows no evidence for meltwater channels, and the relief underneath the hummocky moraine is close to horizontal, implying no mass wasting could occur (**Figure 4**). Ice stagnation preserved the subglacial bedforms, meltwater channels, and eskers, as the ice downwasted and retreated rapidly without reworking. In addition to the preservation of the subglacial landforms, no evidence of ice sheet readvance, such as overriding or reworking of landforms and subglacial till deposition, is seen in the east of the study area, implying the formation of the thrust-block moraine complex and subsequent retreat was a single advance and retreat event, at least in this location. A single, rapid phase of retreat of the ice stream contrasts with observations from Tranche A of the Forewind area (Cotterill et al., 2017b; Phillips et al., 2018), where intense reworking and multiple moraine ridges are a time-transgressive imprint of the ice margin (Stokes and Clark, 1999), formed under active retreat (**Figure 11**). A stepped ice-sheet retreat in Tranche A, with reworking of previous deposits is shown by at least four retreat moraine ridges. The ice margin in Tranche A is interpreted to represent a cold-based interstream, between ice streams, that deglaciated more slowly. Basal conditions in the ice sheet appear to be the main control of the style

and rate of ice sheet retreat. Due to the high fluid pressures and coupling between the ice sheet bed and the substrate, intense, brittle-dominated glaciotectonic deformation resulted from oscillations of the ice sheet margin (Phillips et al., 2017a, 2018). Therefore, each fluctuation of mass balance during ice-sheet retreat may have resulted in formation of retreat moraines.

In the eastern sector of the study area, only a thin (typically <5 m) layer of Upper sub-unit of the Dogger Bank Formation outwash sediments are present between the Lower sub-unit of the Dogger Bank Formation and the lake bed (**Figures 3**, **5**), which drapes inherited subglacial topography (**Figure 8**). A source of the outwash drape is englacial sediment entrained within the ice sheet during advance over soft substrate (Alley et al., 1997). However, the abundance of meltwater under the ice stream resulted in reduced ability to entrain subglacial sediment. The relatively thin outwash in the eastern sector of the study area contrasts with the thick outwash in the interstream area. The cold-based interstream ice allowed greater amounts of sediment entrainment through adfreezing and supercooling (Alley et al., 1997; Christoffersen and Tulaczyk, 2003), which was then transported englacially to the ice sheet margin. This explains the significant accumulations of outwash in the interstream lobe area (**Figure 3**).

Stage Three: Initial Lake Formation

During this stage of retreat, a relatively small proglacial lake (∼90 km^2) formed in a shallow basin within the outwash sediments (**Figure 8**). Proglacial deposition of the Basal Lake Dogger sub-unit is recorded in three levels of fan deltas prograding and backstepping toward the northwest. The first of these deltas is in the southeast of the initial lake basin, and delta transgression occurred in a northwesterly direction. The flat, high-amplitude reflector at the top of this depositional unit (**Figure 5**) implies a period of subaerial exposure and desiccation, either due to accommodation filling, or due to a lake drainage event. This period of subaerial exposure implies that during this stage, no large lake formed (**Figure 8**), which implies that there was either not sufficient damming of meltwater or an insufficient supply of meltwater to the basin. Inferred ice stagnation, combined with continued supply from the margin inferred from the presence of eskers, implies that meltwater supply was plentiful during this stage, therefore it seems more likely the dam must have been incomplete to allow drainage. The thrust-block moraine complex forms a continuous dam to the south and east, implying that the meltwater was able to drain through a gap to the west.

Stage Four: Large Ice-Contact Proglacial Lake

A larger dam must have formed to allow the formation of a larger proglacial lake with a higher lake level, up to at least −26 m OD (**Figure 5**). The gap in the west was plugged, either by a separate ice lobe readvance, or by accumulation of a thick sequence of outwash sediments from an adjacent ice lobe (**Figure 8**). In the western sector of the study area, subaerial outwash is up to 30 m thick (**Figure 3**), implying a significant accumulation of these sediments during retreat of the interstream ice-sheet margin. The presence of the lake for an extended period of time, along with the drape of proglacial lake sediments on top of subaerial outwash, suggests that the accumulation of outwash sediment is responsible for completing the dam. These outwash sediments onlap onto the side of the thrust-block moraine complex in the south of the study area (**Figure 4**), forming a combined subaerial outwash and thrust-block moraine dam. This combined outwash-head and terminal moraine dam is commonly observed in New Zealand and Icelandic proglacial lakes (e.g., Lake Pukaki and Lake Oahu, Sutherland et al., 2019; Heinabergsjökull, Evans and Orton, 2015). In these lakes, the outwash heads are a sign of sediment-laden meltwater exiting across the ice-sheet margin at many points, allowing outwash fans to build. This supports the interpretation of outwash sediments deposited from an adjacent lobe of the ice sheet that was still in the process of retreating (**Figure 8**).

Ice-rafted debris is found in borehole samples and iceberg scours are present on the lake bed (**Figure 7**), and the presence of floating ice in the lake is diagnostic of a calving ice-sheet margin (Smith and Ashley, 1985; Thomas and Connell, 1985; Carrivick and Tweed, 2013; Sutherland et al., 2019). The lobate geometry and downlapping stratal terminations of the Lower Lake Dogger sub-unit (**Figure 5**) imply a subaqueous outwash fan, with sediment-laden subglacial meltwater plumes fed from subglacial conduits flowing into the lake and depositing the fan, which has then been subject to localized gravitational collapse. The lobate shape of the Lower Lake Dogger sub-unit suggests that sediment was supplied at a velocity or concentration that it settled out of suspension close to the meltwater source, as opposed to being distributed by overflows or interflows (Smith and Ashley, 1985; Carrivick and Tweed, 2013). Increases in stress at the margin due to contact with the lake would have driven an increase in ablation due to iceberg calving, leading to rapid ice-sheet retreat (Benn et al., 2007).

Stage Five: Large Ice-Distal Proglacial Lake

Continued ice-sheet retreat caused the isolation of the proglacial lake from the ice-sheet margin (**Figure 8**). There is no direct evidence within the study area for why the lake became cut off from the ice sheet, but may have been due to lake-level fall or increase in outwash deposition. The rhythmic distribution of fine-grained sediments draped over lake-bed topography implies deposition of sediments in a low-energy, quiet-water lake (**Figure 5**). The draping of sediments implies the development of a strong thermocline within the lake, distributing sediments within the water column via overflows and interflows (Smith and Ashley, 1985; Carrivick and Tweed, 2013). The development of a strong thermocline suggests that the ice-sheet margin was not in contact with the lake as high sediment and cold meltwater supply associated with ice-margin contact prevent density stratification in proglacial lakes (Smith and Ashley, 1985; Carrivick and Tweed, 2013). Up to 30 m of varves accumulated during this time (**Figure 1**) implying a constant supply of sediment from the ice sheet to the lake for an extended period of time.

Combining varve thickness (15 – 20 mm) with the thickness of the succession (30 m) gives an estimate of 1500 to 2000 years of lake sedimentation. The lake must have received sediment-laden meltwater from a distal ice sheet for at least this period

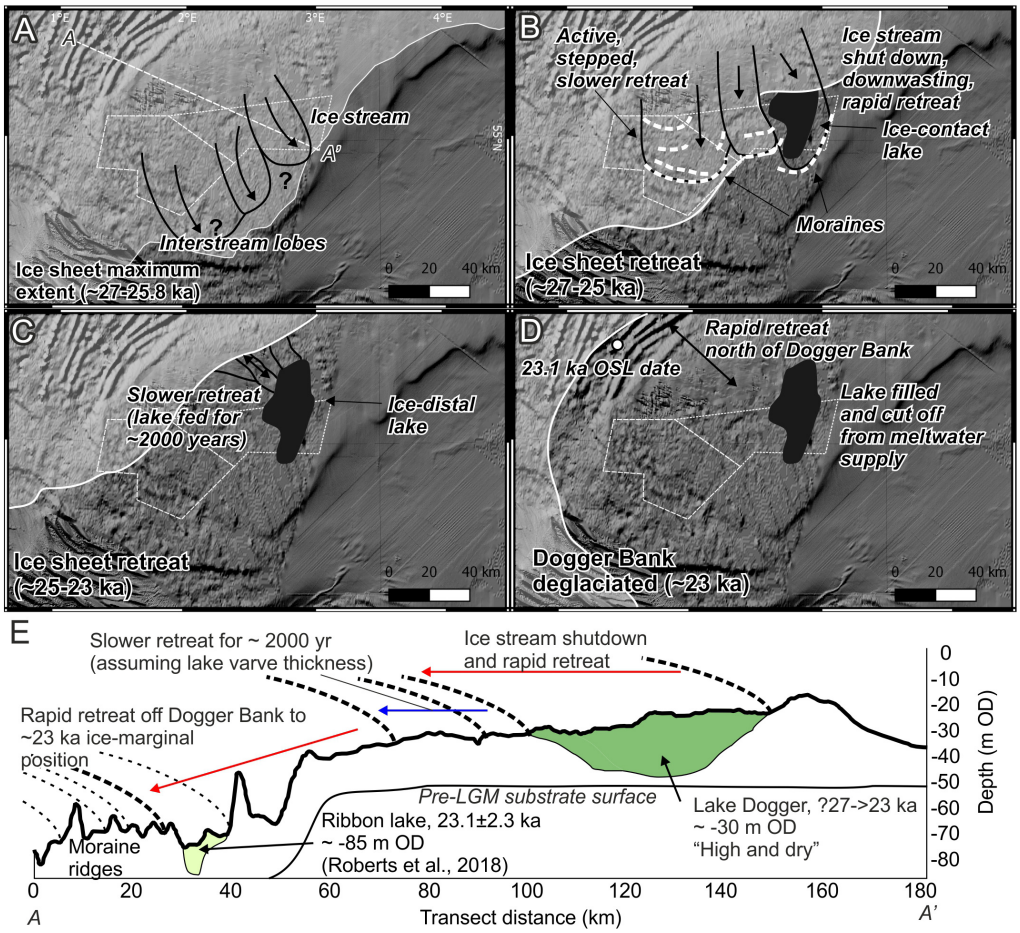


FIGURE 11 | Wider implications and approximate timing of observed ice-sheet retreat in the study area. **(A)** Ice at its maximum extent, showing the locations of possible ice streams and interstream lobes. The inferred lobate nature of the margin is shown schematically. **(B)** Initial ice-sheet retreat and ice-contact proglacial lake stage. Moraines in Tranche A are from Phillips et al. (2018). **(C)** Continued retreat and ice-distal proglacial lake stage, with postulated channels draining from the ice sheet into the lake. **(D)** Final rapid retreat off the northward-dipping inverse slope and isolation of the proglacial lake. The 23.1 ka OSL date is from Roberts et al. (2018). **(E)** Bathymetry profile through Dogger Bank to the ribbon lake of Roberts et al. (2018) highlighting approximate ice-sheet retreat rates and the higher, older lake on top of Dogger Bank. Bathymetry data: GEBCO (https://www.gebco.net).

of time, implying a reduction in the rate of ice retreat prior to complete retreat off Dogger Bank. Ice reached its maximum extent at Dogger Bank between 27–25.8 ka BP (Clark et al., 2012; Hughes et al., 2016; Roberts et al., 2018) and had retreated north of Dogger Bank by 23.1 ka BP (**Figure 11**; Roberts et al., 2018). The intervening period of approximately 2.6 to 3.8 k year is the duration of ice retreat over a distance of approximately 50 km. An initial phase of rapid retreat due to ice stream stagnation and downwasting, with the margin retreating approximately 30–40 km during this phase, was followed by a slower phase of retreat, around 30 km in 1,500 to 2000 yr, before another rapid phase of retreat by around 20 km off Dogger Bank (**Figure 11**).

Subglacial topography was likely a control on the rate of retreat. As the ice sheet retreated northward, it encountered a southward-dipping topography, slowing the retreat rate and allowing subsequent varve deposition (**Figure 11**). A steeper and larger inverse (northward-dipping) slope at the northern margin of Dogger Bank resulted in a second rapid retreat phase (**Figure 11**). The magnitude of variability of subglacial topography beneath the retreating ice sheet is on the order of tens of meters. This relatively subtle topographic variability appears to have been sufficient to control the rate of retreat when combined with proglacial lake calving. The apparent control of subtle subglacial topography on rate of retreat suggests a thin ice sheet at its margin that was sensitive to subtle topographic changes.

Stage Six: Lake Filling, Desiccation, and Subsequent Marine Transgression

Overconsolidation of the lake sediments (Cotterill et al., 2017a) implies they were able to desiccate. Lake sediments reach elevations close to seabed of approximately −26 m OD (**Figure 3**), implying that these significant accumulations of sediment filled the lake basin accommodation, forcing a change in sediment and meltwater routing to a channelized network flowing southward and eastward. Another option is that lake water was able to drain via a large channel that may exist

running eastward from the lake. However, it is difficult to ascertain whether this was a single drainage event (e.g., Glacial Lake Outburst Flood, GLOF; Cotterill et al., 2017a), or whether draining was more protracted. It may also be possible that the channel is unrelated to the proglacial lake, as the acoustic blanking due to the high-amplitude fill within the channel makes it difficult to determine the stratigraphic relationship between the channel and lake sediments.

Subsequent erosion of channel forms seen in SU-Postglacial was followed by marine transgression and wave ravinement of some of the previous moraine and lake deposits (Emery et al., 2019). This was followed by deposition of shallow marine sands during the Holocene. The accumulation of glacial, outwash, proglacial lake, and shallow marine sediments at Dogger Bank result in a very different present-day bathymetry to the pre-glacial topography that the ice sheet advanced over. The discrepancy in pre- and post-glacial topographic surfaces may go some way to explain why models of ice sheet extent in the North Sea basin have currently been unable to recreate the extent interpreted from geomorphic evidence (e.g., Boulton and Hagdorn, 2006; Hubbard et al., 2009; Clason et al., 2014; Patton et al., 2016). The use of modern-day bathymetry as an input to previous models will inhibit a modeled ice stream initiating and flowing southward to the interpreted maximum extent. Future modeling of ice sheets in the North Sea basin should employ a reconstruction of subglacial topography based on seismic interpretation to rectify this situation.

Implications for Offshore Engineering and Ground Models

The detailed seismic interpretation undertaken in this study emphasizes the stratigraphic complexity, with many smaller seismic units, such as the subaqueous outwash fan, not being penetrated by boreholes, so no geotechnical information can be determined for these deposits. This highlights potential issues when identifying sites for wind turbines whose monopile footings may be up to 40 m deep with a diameter up to 7.5 or 10 m, such as other offshore windfarms within the North Sea (Lesny and Wiemann, 2005; Cuéllar et al., 2012; Kallehave et al., 2015). The Horns Rev windfarm, offshore Denmark, for example, has monopile foundations 4 m wide and between 30 and 32.7 m deep (Augustesen et al., 2009). This depth at Dogger Bank may encounter many different sedimentary environments, with vibrocores showing up to seven depositional environments in less than 6 m of core in the southwest of the study area (Emery et al., 2019). Detailed seismic and stratigraphic mapping, and interpretation of sedimentary process and environments of deposition, integrated with geotechnical and lithological information, are therefore recommended to be an essential step in building a ground model during site investigation for offshore infrastructure. Cost-effective wind turbine placement relies on the detailed level of understanding of landscape evolution undertaken in this study.

The study highlights the unusual juxtaposition of a lake-fill preserved perched on a topographic high (**Figure 11**). This phenomenon is recognized in hard-bedrock substrate settings in Greenland and Antarctica (Björck et al., 1996; Briner et al., 2010; Nedbalová et al., 2013; Carrivick et al., 2018), but not in soft sediment settings. Previous studies of proglacial lakes in the palaeo-record have identified lakes that are partially preserved in the stratigraphy in a present-day terrestrial setting, such as Glacial Lake Agassiz (Teller et al., 2002) or ice-marginal lakes of the Scandinavian Ice Sheet in northwest Russia (Lyså et al., 2011). Due to the unique location of Dogger Bank and its Holocene marine transgression, the lake sediments are well-preserved and their desiccated, overconsolidated nature has contributed toward their continued preservation. Such a lake being left "high and dry" on top of Dogger Bank raises the important point of superposition and elevation, whereby an older lake-fill is at a higher elevation than a younger lake-fill to the north (**Figure 11**; Roberts et al., 2018). This has implications for geotechnical properties due to the amount of time a lake bed may have been exposed subaerially and become desiccated and overconsolidated, prior to marine transgression, with further implications for cost-effective wind turbine placement.

The transition to clean, renewable energy as a necessity for society is hugely dependent on cost-effective delivery of infrastructure such as offshore wind. It is therefore recommended that all offshore infrastructure would benefit from project development in conjunction with geologists seeking to understand the recent landscape evolution of our offshore areas. The added benefit of the insights gained into ice-sheet behavior, and its implications for projection of future sea-level rise, make such studies of great benefit to society.

CONCLUSION

Detailed investigation of a large, integrated dataset of vibrocores, geotechnical logs and a dense grid of 2D seismic reflection data has revealed a complicated glacial and proglacial stratigraphy at Dogger Bank. Above a pre-LGM substrate, a deformed subglacial and glaciotectonic unit is observed. After this, a subaerial outwash succession was deposited, followed by three stages of proglacial lake stratigraphy, before marine transgression during the Holocene.

Mapping of the subglacial and glaciotectonic surfaces has revealed a typical surging ice stream landsystem, which flowed from northwest to southeast. This ice stream shut down, stagnated and downwasted, causing rapid deglaciation. This left a basin for the proglacial lake to form, and allowed accumulation of proglacial lake sediments. The initial, small lake had limited accommodation, and so filled with sediment and desiccated before a much larger proglacial lake formed after damming by outwash sediments to the southwest. At first, this large lake was ice-contact, with deposition of a subaqueous outwash fan and iceberg calving resulting in scouring of the lake bed and distal deposition of ice-rafted debris. Continued rapid retreat, aided by iceberg calving, eventually separated the ice sheet margin from the proglacial lake. This allowed varve deposition in the quiet-water, ice-distal lake. Approximately 1500–2000 years of varve deposition are recorded. This implies a slower rate of retreat

whilst the ice sheet was still on Dogger Bank and able to feed sediment-laden meltwater to the lake. Final, rapid retreat of the ice sheet off Dogger Bank was aided by the inverse, north-dipping subglacial slope.

A refined maximum ice-sheet extent has been proposed for the North Sea during this time based on the geomorphological evidence presented. The large thrust-block moraine complex observed in the southeast corner of the study area is assumed to be terminal based on its scale and the lack of evidence for advance or readvance any further southeast of the moraine complex. Retreat from this maximum extent was controlled by basal conditions of the ice sheet. In the study area, initial ice sheet retreat was rapid due to the collapse of the warm-based ice stream. Because of the downwasting, little reworking of the previously deposited landforms and sediment occurred. This contrasts with observations from Tranche A to the west, where cold-based ice, associated with high-pressure fluids, record a slower, active ice sheet retreat. The rapid retreat in the study area is recorded in the proglacial lake stratigraphy and highlights the lobate nature of ice sheet margins and complexity of ice sheet retreat in the palaeo-record.

DATA AVAILABILITY

The datasets generated for this study will not be made publicly available because they belong to a confidential industry dataset. Requests to access the datasets should be directed to the corresponding author.

AUTHOR CONTRIBUTIONS

AE conducted the data analysis and interpretation, and wrote the manuscript, with significant support, contributions and improvements from all other authors.

FUNDING

This study was undertaken as part of a studentship funded by the Leeds Anniversary Research Scholarships. AE acknowledges the support of the Institute of Applied Geosciences at the University of Leeds, the Leeds for Life Foundation, the Quaternary Research Association INQUA Travel Fund, and the International Union for Quaternary Research INQUA Congress travel bursary for supporting earlier presentations of this work.

ACKNOWLEDGMENTS

The Forewind consortium and the British Geological Survey are thanked for provision of the data and permission to publish. CC and EP publish with permission of the Executive Director of the British Geological Survey. Professor David Roberts, Dr. Louise Callard, Dr. Claire Mellett, and Professor Brice Rea are thanked for their helpful discussions on the stratigraphy and palaeoglaciology of Dogger Bank. The reviewers, AG and NP, and the editor, BM, are thanked for their valuable input, which greatly improved the quality and clarity of this manuscript.

REFERENCES

Alley, R. B., Cuffey, K. M., Evenson, E. B., Strasser, J. C., Lawson, D. E., and Larson, G. J. (1997). How glaciers entrain and transport basal sediment: physical constraints. *Quat. Sci. Rev.* 16, 1017–1038. doi: 10.1016/S0277-3791(97)00034-6

Augustesen, A. H., Brødbaek, K. T., Møller, M., Sørensen, S. P. H., Ibsen, L. B., Pedersen, T. S., et al. (2009). "Numerical modelling of large-diameter steel piles at horns rev," in *Proceedings of the Twelfth International Conference on Civil, Structural and Environmental Engineering Computing*, eds B. H. V. Topping, L. F. Costa Neves, and R. C. Barros, (Stirlingshire: Civil-Comp Press), 239. doi: 10.4203/ccp.91.239

Auton, C. A. (1992). Scottish landform examples — 6: the Flemington eskers. *Scott. Geogr. Mag.* 108, 190–196. doi: 10.1080/00369229218736865

Aylsworth, J. M., and Shilts, W. W. (1989). Bedforms of the Keewatin Ice Sheet. Canada. *Sediment. Geol.* 62, 407–428. doi: 10.1016/0037-0738(89)90129-2

Ballantyne, C. K. (2010). Extent and deglacial chronology of the last British-Irish Ice Sheet: implications of exposure dating using cosmogenic isotopes. *J. Quat. Sci.* 25, 515–534. doi: 10.1002/jqs.1310

Banerjee, I., and McDonald, B. C. (1975). "Nature of Esker sedimentation," in *Glaciofluvial and Glaciolacustrine Sedimentation*, eds A. V. Jopling, and B. C. McDonald, (Tulsa, OK: Society for Sedimentary Geology), 132–154. doi: 10.2110/pec.75.23.0132

Belt, T. (1874). An examination of the theories that have been proposed to account for the climate of the glacial period. *Q. J. Sci.* 4, 421–464.

Benn, D. I., and Evans, D. J. A. (2010). *Glaciers & Glaciation*, 2nd Edn. London: Hodder Education.

Benn, D. I., Warren, C. R., and Mottram, R. H. (2007). Calving processes and the dynamics of calving glaciers. *Earth Sci. Rev.* 82, 143–179. doi: 10.1016/j.earscirev.2007.02.002

Björck, S., Olsson, S., Ellis-Evans, C., Håkansson, H., Humlum, O., and de Lirio, J. M. (1996). Late Holocene palaeoclimatic records from lake sediments on James Ross Island, Antarctica. *Palaeogeogr. Palaeoclimatol. Palaeoecol.* 121, 195–220. doi: 10.1016/0031-0182(95)00086-0

Boone, S. J., and Eyles, N. (2001). Geotechnical model for great plains hummocky moraine formed by till deformation below stagnant ice. *Geomorphology* 38, 109–124. doi: 10.1016/S0169-555X(00)00072-6

Boston, C. M., Evans, D. J. A., and Cofaigh, C. Ó (2010). Styles of till deposition at the margin of the Last Glacial Maximum North Sea lobe of the British-Irish Ice Sheet: an assessment based on geochemical properties of glacigenic deposits in eastern England. *Quat. Sci. Rev.* 29, 3184–3211. doi: 10.1016/j.quascirev.2010.05.028

Boulton, G., and Hagdorn, M. (2006). Glaciology of the British Isles Ice Sheet during the last glacial cycle: form, flow, streams and lobes. *Quat. Sci. Rev.* 25, 3359–3390. doi: 10.1016/j.quascirev.2006.10.013

Boyce, J. I., and Eyles, N. (1991). Drumlins carved by deforming till streams below the Laurentide Ice Sheet. *Geology* 19, 787–790. doi: 10.1130/0091-76131991019<0787:DCBDTS<2.3.CO;2

Bradwell, T., and Stoker, M. S. (2015). Asymmetric ice-sheet retreat pattern around northern Scotland revealed by marine geophysical surveys. *Earth Environ. Sci. Trans. R. Soc. Edinburgh* 105, 297–322. doi: 10.1017/S1755691015000109

Bradwell, T., Stoker, M. S., Golledge, N. R., Wilson, C. K., Merritt, J. W., Long, D., et al. (2008). The northern sector of the last British Ice Sheet: maximum extent and demise. *Earth Sci. Rev.* 88, 207–226. doi: 10.1016/j.earscirev.2008.01.008

Bradwell, T., Stoker, M. S., and Larter, R. (2007). Geomorphological signature and flow dynamics of The Minch palaeo-ice stream, northwest Scotland. *J. Quat. Sci.* 22, 609–617. doi: 10.1002/jqs.1080

Briner, J. P., Stewart, H. A. M., Young, N. E., Philipps, W., and Losee, S. (2010). Using proglacial-threshold lakes to constrain fluctuations of the Jakobshavn Isbrae ice margin, western Greenland, during the Holocene. *Quat. Sci. Rev.* 29, 3861–3874. doi: 10.1016/j.quascirev.2010.09.005

Callard, S. L., Cofaigh, C. Ó, Benetti, S., Chiverrell, R. C., Van Landeghem, K. J. J., Saher, M. H., et al. (2018). Extent and retreat history of the Barra Fan Ice Stream offshore western Scotland and northern Ireland during the last glaciation. *Quat. Sci. Rev.* 201, 280–302. doi: 10.1016/j.quascirev.2018.10.002

Cameron, T., Crosby, A., Balson, P., Jeffery, D. H., Lott, G. K., Bulat, J., et al. (1992). *United Kingdom Offshore Regional Report: The Geology of the Southern North Sea*. London: HMSO.

Carr, S. J., Holmes, R., van der Meer, J. J. M., and Rose, J. (2006). The Last Glacial Maximum in the North Sea Basin: micromorphological evidence of extensive glaciation. *J. Quat. Sci.* 21, 131–153. doi: 10.1002/jqs.950

Carrivick, J. L., and Tweed, F. S. (2013). Proglacial Lakes: character, behaviour and geological importance. *Quat. Sci. Rev.* 78, 34–52. doi: 10.1016/j.quascirev.2013.07.028

Carrivick, J. L., Yde, J. C., Knudsen, N. T., and Kronborg, C. (2018). Ice-dammed lake and ice-margin evolution during the Holocene in the Kangerlussuaq area of west Greenland. *Arctic Antarct. Alp. Res.* 50:S100005. doi: 10.1080/15230430.2017.1420854

Chiverrell, R. C., Smedley, R., Small, D., Ballantyne, C. K., Burke, M., Callard, S. L., et al. (2018). Ice margin oscillations during deglaciation of the northern Irish Sea basin. *J. Quat. Sci.* 33, 739–762. doi: 10.1002/jqs.3057

Christoffersen, P., and Tulaczyk, S. (2003). Response of subglacial sediments to basal freeze-on 1. Theory and comparison to observations from beneath the West Antarctic Ice Sheet. *J. Geophys. Res. Solid Earth* 108, 1–16. doi: 10.1029/2002jb001935

Clark, C. D., Ely, J. C., Greenwood, S. L., Hughes, A. L. C., Meehan, R., Barr, I. D., et al. (2018). BRITICE Glacial Map, version 2: a map and GIS database of glacial landforms of the last British-Irish Ice Sheet. *Boreas* 47:11-e8. doi: 10.1111/bor.12273

Clark, C. D., Evans, D. J. A., Khatwa, A., Bradwell, T., Jordan, C. J., Marsh, S. H., et al. (2004). Map and GIS database of glacial landforms and features related to the last British Ice Sheet. *Boreas* 33, 359–375. doi: 10.1111/j.1502-3885.2004.tb01246.x

Clark, C. D., Hughes, A. L. C., Greenwood, S. L., Jordan, C., and Sejrup, H. P. (2012). Pattern and timing of retreat of the last British-Irish Ice Sheet. *Quat. Sci. Rev.* 44, 112–146. doi: 10.1016/j.quascirev.2010.07.019

Clason, C. C., Applegate, P. J., and Holmlund, P. (2014). Modelling Late Weichselian evolution of the Eurasian ice sheets forced by surface meltwater-enhanced basal sliding. *J. Glaciol.* 60, 29–40. doi: 10.3189/2014JoG13J037

Cotterill, C. J., Phillips, E. R., James, L., Forsberg, C. F., Tjelta, T. I., Carter, G., et al. (2017a). The evolution of the Dogger Bank, North Sea: a complex history of terrestrial, glacial and marine environmental change. *Quat. Sci. Rev.* 171, 136–153. doi: 10.1016/j.quascirev.2017.07.006

Cotterill, C. J., Phillips, E. R., James, L., Forsberg, C. F., and Tjelta, T. I. (2017b). How understanding past landscapes might inform present-day site investigations: a case study from Dogger Bank, southern central North Sea. *Near Surf. Geophys.* 15, 403–413. doi: 10.3997/1873-0604.2017032

Cowan, E. A., Christoffersen, P., and Powell, R. D. (2012). Sedimentological signature of a deformable bed preserved beneath an ice stream in a late pleistocene glacial sequence, Ross Sea, Antarctica. *J. Sediment. Res.* 82, 270–282. doi: 10.2110/jsr.2012.25

Crameri, F. (2018). Geodynamic diagnostics, scientific visualisation and StagLab 3.0. *Geosci. Model Dev.* 11, 2541–2562. doi: 10.5194/gmd-11-2541-018

Cuéllar, P., Georgi, S., Baeßler, M., and Rücker, W. (2012). On the quasi-static granular convective flow and sand densification around pile foundations under cyclic lateral loading. *Granul. Matter* 14, 11–25. doi: 10.1007/s10035-011-0305-0

D'Agostino, K., Seltzer, G., Baker, P., Fritz, S., and Dunbar, R. (2002). Late-quaternary lowstands of Lake Titicaca: evidence from high-resolution seismic data. *Palaeogeogr. Palaeoclimatol. Palaeoecol.* 179, 97–111. doi: 10.1016/S0031-0182(01)00411-4

Darvill, C. M., Stokes, C. R., Bentley, M. J., and Lovell, H. (2014). A glacial geomorphological map of the southernmost ice lobes of Patagonia: the Bahía Inútil – San Sebastián, Magellan, Otway, Skyring and Río Gallegos lobes. *J. Maps* 10, 500–520. doi: 10.1080/17445647.2014.890134

Davies, B. J., Roberts, D. H., Bridgland, D. R., Cofaigh, C. Ó, and Riding, J. B. (2011). Provenance and depositional environments of quaternary sediments from the western North Sea Basin. *J. Quat. Sci.* 26, 59–75. doi: 10.1002/jqs.1426

Delaney, C. A., McCarron, S., and Davis, S. (2018). Irish Ice Sheet dynamics during deglaciation of the central Irish Midlands: evidence of ice streaming and surging from airborne LiDAR. *Geomorphology* 306, 235–253. doi: 10.1016/j.geomorph.2018.01.011

Doornenbal, H., and Stevenson, A. (2010). *Petroleum Geological Atlas of the Southern Permian Basin*. Houten: EAGE.

Dove, D., Evans, D. J. A., Lee, J. R., Roberts, D. H., Tappin, D. R., Mellett, C. L., et al. (2017). Phased occupation and retreat of the last British–Irish Ice Sheet in the southern North Sea; geomorphic and seismostratigraphic evidence of a dynamic ice lobe. *Quat. Sci. Rev.* 163, 114–134. doi: 10.1016/j.quascirev.2017.03.006

Dowdeswell, J. A., and Fugelli, E. M. G. (2012). The seismic architecture and geometry of grounding-zone wedges formed at the marine margins of past ice sheets. *Bull. Geol. Soc. Am.* 124, 1750–1761. doi: 10.1130/B30628.1

Dowdeswell, J. A., and Ottesen, D. (2013). Buried iceberg ploughmarks in the early quaternary sediments of the central North Sea: a two-million year record of glacial influence from 3D seismic data. *Mar. Geol.* 344, 1–9. doi: 10.1016/j.margeo.2013.06.019

Dredge, L. A. (1982). Relict ice-scour marks and late phases of Lake Agassiz in Northernmost Manitoba. *Can. J. Earth Sci.* 19, 1079–1087. doi: 10.1139/e82-089

Eden, D. J., and Eyles, N. (2001). Description and numerical model of Pleistocene iceberg scours and ice-keel turbated facies at Toronto, Canada. *Sedimentology* 48, 1079–1102. doi: 10.1046/j.1365-3091.2001.00409.x

Ehlers, J., and Wingfield, R. (1991). The extension of the Late Weichselian/Late Devensian ice sheets in the North Sea Basin. *J. Quat. Sci.* 6, 313–326. doi: 10.1002/jqs.3390060406

Ely, J. C., Clark, C. D., Spagnolo, M., Stokes, C. R., Greenwood, S. L., Hughes, A. L. C., et al. (2016). Do subglacial bedforms comprise a size and shape continuum? *Geomorphology* 257, 108–119. doi: 10.1016/j.geomorph.2016.01.001

Emery, A. R., Hodgson, D. M., Barlow, N. L. M., Carrivick, J. L., Cotterill, C. J., Mellett, C. L., et al. (2019). Topographic and hydrodynamic controls on barrier retreat and preservation: an example from Dogger Bank, North Sea. *Mar. Geol.* 416:105981. doi: 10.1016/j.margeo.2019.105981

Engelhardt, H., Humphrey, N., Kamb, B., and Fahnestock, M. (1990). Physical conditions at the base of a fast moving glacier. *Science* 248, 57–59. doi: 10.1126/science.248.4951.57

Evans, D. J. A., Bateman, M. D., Roberts, D. H., Medialdea, A., Hayes, L., Duller, G. A. T., et al. (2016a). Glacial Lake Pickering: stratigraphy and chronology of a proglacial lake dammed by the North Sea Lobe of the British-Irish Ice Sheet. *J. Quat. Sci.* 32, 295–310. doi: 10.1002/jqs.2833

Evans, D. J. A., Phillips, E. R., Hiemstra, J. F., and Auton, C. A. (2006). Subglacial till: Formation, sedimentary characteristics and classification. *Earth-Science Rev.* 78, 115–176. doi: 10.1016/j.earscirev.2006.04.001

Evans, D. J. A., Storrar, R. D., and Rea, B. R. (2016b). Crevasse-squeeze ridge corridors: diagnostic features of late-stage palaeo-ice stream activity. *Geomorphology* 258, 40–50. doi: 10.1016/j.geomorph.2016.01.017

Evans, D. J. A., and Benn, D. I. (2004). *A Practical Guide to the Study of Glacial Sediments*. London: Arnold.

Evans, D. J. A., Clark, C. D., and Rea, B. R. (2008). Landform and sediment imprints of fast glacier flow in the southwest Laurentide Ice Sheet. *J. Quat. Sci.* 23, 249–272. doi: 10.1002/jqs.1141

Evans, D. J. A., and Orton, C. (2015). Heinabergsjökull and Skalafellsjökull, Iceland: active temperate piedmont lobe and outwash head glacial landsystem. *J. Maps* 11, 415–431. doi: 10.1080/17445647.2014.919617

Evans, D. J. A., and Rea, B. R. (1999). Geomorphology and sedimentology of surging glaciers: a land-systems approach. *Ann. Glaciol.* 28, 75–82. doi: 10.3189/172756499781821823

Evans, D. J. A., Roberts, D. H., Bateman, M. D., Medialdea, A., Ely, J., Moreton, S. G., et al. (2018). Sedimentation during marine isotope stage 3 at the eastern margins of the Glacial Lake Humber basin, England. *J. Quat. Sci.* 33, 1–21. doi: 10.1002/jqs.3066

Evans, D. J. A., Young, N. J. P., and Cofaigh, C. O. (2014). Glacial geomorphology of terrestrial-terminating fast flow lobes/ice stream margins in the southwest Laurentide Ice Sheet. *Geomorphology* 204, 86–113. doi: 10.1016/j.geomorph.2013.07.031

Eyles, N., Boyce, J. I., and Barendregt, R. W. (1999). Hummocky moraine: sedimentary record of stagnant Laurentide Ice Sheet lobes resting on soft beds. *Sediment. Geol.* 123, 163–174. doi: 10.1016/S0037-0738(98)00129-8

Eyles, N., and Clark, B. M. (1988). Storm-influenced deltas and ice scouring in a late Pleistocene glacial lake. *Bull. Geol. Soc. Am.* 100, 793–809. doi: 10.1130/0016-76061988100<0793:SIDAIS<2.3.CO;2

Gandy, N., Gregoire, L. J., Ely, J. C., Clark, C. D., Hodgson, D. M., Lee, V., et al. (2018). Marine Ice sheet instability and ice shelf buttressing influenced deglaciation of the minch ice stream, Northwest Scotland. *Cryosph. Discuss.* 12, 3635–3651. doi: 10.5194/tc-2018-116

Greenwood, S. L., Clark, C. D., and Hughes, A. L. C. (2007). Formalising an inversion methodology for reconstructing ice-sheet retreat patterns from meltwater channels: application to the British Ice Sheet. *J. Quat. Sci.* 22, 637–645. doi: 10.1002/jqs.1083

Greenwood, S. L., Clason, C. C., Helanow, C., and Margold, M. (2016a). Theoretical, contemporary observational and palaeo-perspectives on ice sheet hydrology: processes and products. *Earth Sci. Rev.* 155, 1–27. doi: 10.1016/j.earscirev.2016.01.010

Greenwood, S. L., Clason, C. C., and Jakobsson, M. (2016b). Ice-flow and meltwater landform assemblages in the Gulf of Bothnia. *Geol. Soc. Lond. Mem.* 46, 321–324. doi: 10.1144/M46.163

Greenwood, S. L., Clason, C. C., Nyberg, J., Jakobsson, M., and Holmlund, P. (2017). The Bothnian Sea ice stream: early Holocene retreat dynamics of the south-central Fennoscandian Ice Sheet. *Boreas* 46, 346–362. doi: 10.1111/bor.12217

Hall, A. M., and Bent, A. J. A. (1990). The limits of the last British ice sheet in northern Scotland and the adjacent shelf. *Quat. Newsl.* 61, 2–12.

Hermanowski, P., Piotrowski, J. A., and Szuman, I. (2019). An erosional origin for drumlins of NW Poland. *Earth Surf. Process. Landforms* 44:4630. doi: 10.1002/esp.4630

Hjelstuen, B. O., Sejrup, H. P., Valvik, E., and Becker, L. W. M. (2017). Evidence of an ice-dammed lake outburst in the North Sea during the last deglaciation. *Mar. Geol.* 402, 118–130. doi: 10.1016/j.margeo.2017.11.021

Hodgson, D. M., Bernhardt, A., Clare, M. A., Da Silva, A.-C., Fosdick, J. C., Mauz, B., et al. (2018). Grand challenges (and Great Opportunities) in sedimentology, stratigraphy, and diagenesis research. *Front. Earth Sci.* 6:173. doi: 10.3389/feart.2018.00173

Hogan, K. A., Cofaigh, ÓC., Jennings, A. E., Dowdeswell, J. A., and Hiemstra, J. F. (2016). Deglaciation of a major palaeo-ice stream in Disko Trough, West Greenland. *Quat. Sci. Rev.* 147, 5–26. doi: 10.1016/j.quascirev.2016.01.018

Hubbard, A., Bradwell, T., Golledge, N., Hall, A., Patton, H., Sugden, D., et al. (2009). Dynamic cycles, ice streams and their impact on the extent, chronology and deglaciation of the British-Irish ice sheet. *Quat. Sci. Rev.* 28, 758–776. doi: 10.1016/j.quascirev.2008.12.026

Hughes, A. L. C., Clark, C. D., and Jordan, C. J. (2010). Subglacial bedforms of the last British Ice Sheet. *J. Maps* 6, 543–563. doi: 10.4113/jom.2010.1111

Hughes, A. L. C., Gyllencreutz, R., Lohne, ØS., Mangerud, J., and Svendsen, J. I. (2016). The last Eurasian ice sheets - a chronological database and time-slice reconstruction, DATED-1. *Boreas* 45, 1–45. doi: 10.1111/bor.12142

Hurter, S., and Haenel, R. (2002). *Heat-Flow Density in Atlas of Geothermal Resources in Europe*. Luxemburg: Office for Official Publications of the European Communities, 611–612.

Hurtig, E. (1995). Temperature and heat-flow density along European transcontinental profiles. *Tectonophysics* 244, 75–83. doi: 10.1016/0040-1951(94)00218-X

IPCC, (2013). *IPCC Fifth Assessment Report*. Geneva: IPCC.

Jakobsson, M., Andreassen, K., Bjarnadóttir, L. R., Dove, D., Dowdeswell, J. A., England, J. H., et al. (2014). Arctic ocean glacial history. *Quat. Sci. Rev.* 92, 40–67. doi: 10.1016/j.quascirev.2013.07.033

Jamieson, S. S. R., Stokes, C. R., Livingstone, S. J., Vieli, A., Cofaigh, C., Hillenbrand, C. D., et al. (2016). Subglacial processes on an Antarctic ice stream bed. 2: can modelled ice dynamics explain the morphology of mega-scale glacial lineations? *J. Glaciol.* 62, 285–298. doi: 10.1017/jog.2016.19

Jansen, J. H. F., Van Weering, T. C., and Eisma, D. (1979). "Late quaternary sedimentation in the North Sea," in *The Quaternary History of the North Sea*, eds E. Oele, R. T. E. Schiittenhelm, and A. J. Wiggers, (Uppsala: University of Uppsala), 175–187.

Kallehave, D., Byrne, B. W., LeBlanc Thilsted, C., and Mikkelsen, K. K. (2015). Optimization of monopiles for offshore wind turbines. *Philos. Trans. R. Soc. A Math. Phys. Eng. Sci.* 373:20140100. doi: 10.1098/rsta.2014.0100

Lamb, R. M., Huuse, M., and Stewart, M. A. (2016). Early quaternary sedimentary processes and palaeoenvironments in the central North Sea. *J. Quat. Sci.* 32, 127–144. doi: 10.1002/jqs.2894

Larsen, E., Fredin, O., Lyså, A., Amantov, A., Fjeldskaar, W., and Ottesen, D. (2016). Causes of time-transgressive glacial maxima positions of the last Scandinavian Ice Sheet. *Nor. Geol. Tidsskr.* 96, 1–12. doi: 10.17850/njg96-2-06

Lesny, K., and Wiemann, J. (2005). "Design aspects of monopiles in German offshore wind farms," in *Proceedings of the International Symposium on Frontiers in Offshore Geotechnics*, (Perth), 383–389.

Linch, L. D., and van der Meer, J. J. M. (2015). Micromorphology of ice keel scour in pebbly sandy mud and fine-grained sands: Scarborough Bluffs, Ontario, Canada. *Sedimentology* 62, 110–129. doi: 10.1111/sed.12142

Linch, L. D., van der Meer, J. J. M., and Menzies, J. (2012). Micromorphology of iceberg scour in clays: glacial Lake Agassiz, Manitoba, Canada. *Quat. Sci. Rev.* 55, 125–144. doi: 10.1016/j.quascirev.2012.07.008

Livingstone, S. J., Ócofaigh, C., Evans, D. J. A., and Palmer, A. (2010). Sedimentary evidence for a major glacial oscillation and proglacial lake formation in the Solway Lowlands (Cumbria, UK) during Late Devensian deglaciation. *Boreas* 39, 505–527. doi: 10.1111/j.1502-3885.2010.00149.x

Lockhart, E. A., Scourse, J. D., Praeg, D., Van Landeghem, K. J. J., Mellett, C., Saher, M., et al. (2018). A stratigraphic investigation of the Celtic Sea megaridges based on seismic and core data from the Irish-UK sectors. *Quat. Sci. Rev.* 198, 156–170. doi: 10.1016/j.quascirev.2018.08.029

Long, D., Laban, C., Streif, H., Cameron, T. D. J., and Schüttenhelm, R. T. E. (1988). The sedimentary record of climatic variation in the southern North Sea. *Philos. Trans. R. Soc. Lond.* 318, 523–537. doi: 10.1098/rstb.1988.0022

Longva, O., and Bakkejord, K. J. (1990). Iceberg deformation and erosion in soft sediments, southeast Norway. *Mar. Geol.* 92, 87–104. doi: 10.1016/0025-3227(90)90028-I

Lyså, A., Jensen, M. A., Larsen, E., Fredin, O., and Demidov, I. N. (2011). Ice-distal landscape and sediment signatures evidencing damming and drainage of large pro-glacial lakes, northwest Russia. *Boreas* 40, 481–497. doi: 10.1111/j.1502-3885.2010.00197.x

Margold, M., Stokes, C. R., and Clark, C. D. (2015). Ice streams in the Laurentide Ice Sheet: identification, characteristics and comparison to modern ice sheets. *Earth Sci. Rev.* 143, 117–146. doi: 10.1016/j.earscirev.2015.01.011

Margold, M., Stokes, C. R., and Clark, C. D. (2018). Reconciling records of ice streaming and ice margin retreat to produce a palaeogeographic reconstruction of the deglaciation of the Laurentide Ice Sheet. *Quat. Sci. Rev.* 189, 1–30. doi: 10.1016/j.quascirev.2018.03.013

McCabe, A. M., and Eyles, N. (1988). Sedimentology of an ice-contact glaciomarine delta, Carey Valley, Northern Ireland. *Sediment. Geol.* 59, 1–14. doi: 10.1016/0037-0738(88)90097-8

Mitchum, R. M., Vail, P. R., and Sangree, J. B. (1977). "Seismic stratigraphy and global changes of sea level, Part six: stratigraphic interpretation of seismic reflection patterns in depositional sequences," in *Seismic Stratigraphy–Applications to Hydrocarbon Exploration*, ed. C. E. Payton, (Tulsa, OK: AAPG), 117–134. doi: 10.1038/272400a0

Murton, D. K., and Murton, J. B. (2012). Middle and Late Pleistocene glacial lakes of lowland Britain and the southern North Sea Basin. *Quat. Int.* 260, 115–142. doi: 10.1016/j.quaint.2011.07.034

Nedbalová, L., Nývlt, D., Kopáèek, J., Šobr, M., and Elster, J. (2013). Freshwater lakes of Ulu Peninsula, James Ross Island, north-east Antarctic Peninsula: origin, geomorphology and physical and chemical limnology. *Antarct. Sci.* 25, 358–372. doi: 10.1017/S0954102012000934

Patterson, C. J. (1997). Southern Laurentide ice lobes were created by ice streams: Des Moines Lobe in Minnesota, USA. *Sediment. Geol.* 111, 249–261. doi: 10.1016/S0037-0738(97)00018-3

Patton, H., Hubbard, A., Andreassen, K., Winsborrow, M. C. M., and Stroeven, A. P. (2016). The build-up, configuration, and dynamical sensitivity of the Eurasian ice-sheet complex to Late Weichselian climatic and oceanic forcing. *Quat. Sci. Rev.* 153, 97–121. doi: 10.1016/j.quascirev.2016.10.009

Pearce, D. M., Ely, J. C., Barr, L. D., and Boston, C. M. (2017). "Glacier reconstruction," in *Geomorphological Techniques*, 1st Edn, ed. A. Goudie, (Abingdon: Routledge), 16.

Peters, J. L., Benetti, S., Dunlop, P., Cofaigh, ÓC., Moreton, S. G., Wheeler, A. J., et al. (2016). Sedimentology and chronology of the advance and retreat of the last British-Irish Ice Sheet on the continental shelf west of Ireland. *Quat. Sci. Rev.* 140, 101–124. doi: 10.1016/j.quascirev.2016.03.012

Peters, L. E., Anandakrishnan, S., Alley, R. B., and Smith, A. M. (2007). Extensive storage of basal meltwater in the onset region of a major West Antarctic ice stream. *Geology* 35, 251–254. doi: 10.1130/G23222A.1

Phillips, E., Cotterill, C., Johnson, K., Crombie, K., James, L., Carr, S., et al. (2018). Large-scale glacitectonic deformation in response to active ice sheet retreat across Dogger Bank (southern central North Sea) during the Last Glacial Maximum. *Quat. Sci. Rev.* 179, 24–47. doi: 10.1016/j.quascirev.2017.11.001

Phillips, E. R., Evans, D. J. A., Atkinson, N., and Kendall, A. (2017a). Structural architecture and glacitectonic evolution of the Mud Buttes cupola hill complex, southern Alberta. *Canada Quat. Sci. Rev.* 164, 110–139. doi: 10.1016/j.quascirev.2017.03.027

Phillips, E. R., Hodgson, D. M., and Emery, A. R. (2017b). The quaternary geology of the North Sea basin. *J. Quat. Sci.* 32, 117–126. doi: 10.1002/jqs.2932

Powell, R. D. (1984). Glacimarine processes and inductive lithofacies modelling of ice shelf and tidewater glacier sediments based on quaternary examples. *Mar. Geol.* 57, 1–52. doi: 10.1016/0025-3227(84)90194-4

Powell, R. D., and Alley, R. B. (1997). "Grounding-line systems: processes, glaciological inferences and the stratigraphic record," in *Geology and Seismic Stratigraphy of the Antarctic Margin*, eds A. K. Cooper, P. F. Barker, G. Brancolini, (Hoboken, NJ: Wiley) 2, 169–187. doi: 10.1029/ar071p0169

Punkari, M. (1995). Glacial flow systems in the zone of confluence between the Scandinavian and Novaja Zemlya Ice Sheets. *Quat. Sci. Rev.* 14, 589–603. doi: 10.1016/0277-3791(95)00026-L

Punkari, M. (1997a). Glacial and glaciofluvial deposits in the interlobate areas of the Scandinavian ice sheet. *Quat. Sci. Rev.* 16, 741–753. doi: 10.1016/S0277-3791(97)00020-6

Punkari, M. (1997b). Subglacial processes of the Scandinavian ice sheet in Fennoscandia inferred from flow-parallel features and lithostratigraphy. *Sediment. Geol.* 111, 263–283. doi: 10.1016/S0037-0738(97)00019-5

Roberts, D. H., Evans, D. J. A., Callard, S. L., Clark, C. D., Bateman, M. D., Medialdea, A., et al. (2018). Ice marginal dynamics of the last British-Irish Ice Sheet in the southern North Sea: ice limits, timing and the influence of the Dogger Bank. *Quat. Sci. Rev.* 198, 181–207. doi: 10.1016/j.quascirev.2018.08.010

Röthlisberger, H. (1972). Water pressure in intra- and subglacial channels. *J. Glaciol.* 11, 177–203. doi: 10.3189/S0022143000022188

Scourse, J., Saher, M., Van Landeghem, K. J. J., Lockhart, E. A., Purcell, C., Callard, S. L., et al. (2019). Advance and retreat of the marine-terminating Irish Sea Ice Stream into the Celtic Sea during the last glacial: timing and maximum extent. *Mar. Geol.* 412, 53–68. doi: 10.1016/j.margeo.2019.03.003

Sejrup, H. P., Aarseth, I., Ellingsen, K. L., Reither, E., Jansen, E., Lovlie, R., et al. (1987). Quaternary stratigraphy of the Fladen area, central North Sea: a multidisciplinary study. *J. Quat. Sci.* 2, 35–58. doi: 10.1002/jqs.3390020105

Sejrup, H. P., Clark, C. D., and Hjelstuen, B. O. (2016). Rapid ice sheet retreat triggered by ice stream debuttressing: evidence from the North Sea. *Geology* 44, 355–358. doi: 10.1130/G37652.1

Sejrup, H. P., Hjelstuen, B. O., Dahlgren, K. I. T., Haflidason, H., Kuijpers, A., Nygård, A., et al. (2005). Pleistocene glacial history of the NW European continental margin. *Mar. Pet. Geol.* 22, 1111–1129. doi: 10.1016/j.marpetgeo.2004.09.007

Sejrup, H. P., Hjelstuen, B. O., Nygård, A., Haflidason, H., and Mardal, I. (2015). Late Devensian ice-marginal features in the central North Sea - processes and chronology. *Boreas* 44, 1–13. doi: 10.1111/bor.12090

Sejrup, H. P., Larsen, E., Landvik, J., King, E. L., Haflidason, H., and Nesje, A. (2000). Quaternary glaciations in southern Fennoscandia: evidence from southwestern Norway and the northern North Sea region. *Quat. Sci. Rev.* 19, 667–685. doi: 10.1016/S0277-3791(99)00016-5

Smedley, R. K., Chiverrell, R. C., Ballantyne, C. K., Burke, M. J., Clark, C. D., Duller, G. A. T., et al. (2017). Internal dynamics condition centennial-scale oscillations in marine-based ice-stream retreat. *Geology* 45, 787–790. doi: 10.1130/G38991.1

Smith, N. D., and Ashley, G. (1985). "Proglacial Lacustrine environment," in *Glacial Sedimentary Environments*, eds G. M. Ashley, J. Shaw, and N. D. Smith, (Tulsa, OK: Society of Economic Paleontologists and Mineralogists), 135–216. doi: 10.2110/scn.85.02.0135

Spagnolo, M., Clark, C. D., Ely, J. C., Stokes, C. R., Anderson, J. B., Andreassen, K., et al. (2014). Size, shape and spatial arrangement of mega-scale glacial lineations from a large and diverse dataset. *Earth Surf. Process. Landforms* 39, 1432–1448. doi: 10.1002/esp.3532

Stearns, L. A., and van der Veen, C. J. (2018). Friction at the bed does not control fast glacier flow. *Science* 2217:eaat2217. doi: 10.1126/science.aat2217

Stewart, M. A., Lonergan, L., and Hampson, G. (2013). 3D seismic analysis of buried tunnel valleys in the central North Sea: morphology, cross-cutting generations and glacial history. *Quat. Sci. Rev.* 72, 1–17. doi: 10.1016/j.quascirev.2013.03.016

Stoker, M. S., Balson, P. S., Long, D., and Tappin, D. R. (2011). *An Overview of the Lithostratigraphical Framework for the Quaternary Deposits on the United Kingdom Continental Shelf*. Nottingham: British Geological Survey, 48.

Stokes, C. R. (2018). Geomorphology under ice streams: moving from form to process. *Earth Surf. Process. Landforms* 43, 85–123. doi: 10.1002/esp.4259

Stokes, C. R., and Clark, C. D. (1999). Geomorphological criteria for identifying Pleistocene ice streams. *Ann. Glaciol.* 28, 67–74. doi: 10.3189/172756499781821625

Stokes, C. R., and Clark, C. D. (2001). Palaeo-ice streams. *Quat. Sci. Rev.* 20, 1437–1457. doi: 10.1016/S0277-3791(01)00003-8

Stokes, C. R., and Clark, C. D. (2003). The Dubawnt Lake palaeo-ice stream: evidence for dynamic ice sheet behaviour on the Canadian Shield and insights regarding the controls on ice-stream location and vigour. *Boreas* 32, 263–279. doi: 10.1111/j.1502-3885.2003.tb01442.x

Stokes, C. R., Tarasov, L., Blomdin, R., Cronin, T. M., Fisher, T. G., Gyllencreutz, R., et al. (2015). On the reconstruction of palaeo-ice sheets: recent advances and future challenges. *Quat. Sci. Rev.* 125, 15–49. doi: 10.1016/j.quascirev.2015.07.016

Storrar, R. D., Stokes, C. R., and Evans, D. J. A. (2014a). Increased channelization of subglacial drainage during deglaciation of the laurentide ice sheet. *Geology* 42, 239–242. doi: 10.1130/G35092.1

Storrar, R. D., Stokes, C. R., and Evans, D. J. A. (2014b). Morphometry and pattern of a large sample (>20,000) of Canadian eskers and implications for subglacial drainage beneath ice sheets. *Quat. Sci. Rev.* 105, 1–25. doi: 10.1016/j.quascirev.2014.09.013

Streuff, K., Cofaigh, ÓC., Hogan, K., Jennings, A., Lloyd, J. M., Noormets, R., et al. (2017). Seafloor geomorphology and glacimarine sedimentation associated with fast-flowing ice sheet outlet glaciers in Disko Bay, West Greenland. *Quat. Sci. Rev.* 169, 206–230. doi: 10.1016/j.quascirev.2017.05.021

Sutherland, J. L., Carrivick, J. L., Shulmeister, J., Quincey, D. J., and James, W. H. M. (2019). Ice-contact proglacial lakes associated with the last glacial maximum across the Southern Alps, New Zealand. *Quat. Sci. Rev.* 213, 67–92. doi: 10.1016/j.quascirev.2019.03.035

Szuman, I., Ewertowski, M., and Kasprzak, L. (2013). Thermo-mechanical facies representative of fast and slow flowing ice sheets: the Weichselian ice sheet, a central west Poland case study. *Proc. Geol. Assoc.* 124, 818–833. doi: 10.1016/j.pgeola.2012.09.003

Szuman, I., Kalita, J. Z., and Ewertowski, M. W. (2018). The impact of geothermal heat flux on the last Scandinavian ice sheet over W Poland and E Germany. *Geogr. Ann. Ser. A Phys. Geogr.* 100, 388–403. doi: 10.1080/04353676.2018.1524711

Teller, J. T., Leverington, D. W., and Mann, J. D. (2002). Freshwater outbursts to the oceans from glacial Lake Agassiz and their role in climate change during the last deglaciation. *Quat. Sci. Rev.* 21, 879–887. doi: 10.1016/S0277-3791(01)00145-7

Thomas, G. S. P., and Connell, R. J. (1985). Iceberg drop, dump, and grounding structures from Pleistocene Glacio-Lacustrine Sediments, Scotland. *SEPM J. Sediment. Res.* 55, 243–249. doi: 10.1306/212F8689-2B24-11D7-8648000102C1865D

Toucanne, S., Zaragosi, S., Bourillet, J.-F., Marieu, V., Cremer, M., Kageyama, M., et al. (2010). The first estimation of Fleuve Manche palaeoriver discharge during the last deglaciation: evidence for Fennoscandian ice sheet meltwater flow in the English Channel ca 20–18ka ago. *Earth Planet. Sci. Lett.* 290, 459–473. doi: 10.1016/j.epsl.2009.12.050

Wahlgren, R. V. (1979). Ice-scour tracks in eastern Mackenzie Bay and north of Pullen Island, Beaufort Sea. *Curr. Res. Part B Geol. Surv. Canada* 7, 51–62.

Walder, J. S., and Fowler, A. (1994). Channelized subglacial drainage over a deformable bed. *J. Glaciol.* 40, 3–15. doi: 10.3189/S002214300000 3750

Wellner, J. S., Heroy, D. C., and Anderson, J. B. (2006). The death mask of the antarctic ice sheet: comparison of glacial geomorphic features across the continental shelf. *Geomorphology* 75, 157–171. doi: 10.1016/j.geomorph.2005. 05.015

Winsborrow, M. C. M., Clark, C. D., and Stokes, C. R. (2010). What controls the location of ice streams? *Earth Sci. Rev.* 103, 45–59. doi: 10.1016/j.earscirev.2010. 07.003

Woodworth-Lynas, C. M. T., and Guigné, J. Y. (1990). Iceberg scours in the geological record: examples from glacial Lake Agassiz. *Geol. Soc. Lond. Spec. Publ.* 53, 217–233. doi: 10.1144/GSL.SP.1990.053.01.12

Zolitschka, B. (2007). "Varved lake sediments," in *Encyclopedia of Quaternary Science*, ed. S. A. Elias, (Amsterdam: Elsevier), 3105–3114. doi: 10.1016/B0-44-452747-8/00065-X

Conflict of Interest Statement: The authors declare that the research was conducted in the absence of any commercial or financial relationships that could be construed as a potential conflict of interest.

Copyright © 2019 Emery, Hodgson, Barlow, Carrivick, Cotterill and Phillips. This is an open-access article distributed under the terms of the Creative Commons Attribution License (CC BY). The use, distribution or reproduction in other forums is permitted, provided the original author(s) and the copyright owner(s) are credited and that the original publication in this journal is cited, in accordance with accepted academic practice. No use, distribution or reproduction is permitted which does not comply with these terms.

frontiers in Earth Science

ORIGINAL RESEARCH
published: 24 October 2019
doi: 10.3389/feart.2019.00269

Where's the Carbon: Exploring the Spatial Heterogeneity of Sedimentary Carbon in Mid-Latitude Fjords

Craig Smeaton[1]* *and William E. N. Austin*[1,2]

[1] School of Geography and Sustainable Development, University of St Andrews, St Andrews, United Kingdom, [2] Scottish Association for Marine Science, Scottish Marine Institute, Oban, United Kingdom

Fjords are recognized as globally significant hotspots for the burial and long-term storage of marine and terrestrially derived organic carbon (OC). By trapping and locking away OC over geological timescales, fjord sediments provide a potentially important yet largely overlooked climate regulation service. Currently, our understanding of the spatial distribution of OC within the surficial sediments of fjords is limited and this potentially implies an overestimation in the global estimates of OC buried in fjords as current calculation methods assume a homogenous seabed. Using the mid-latitude fjords of Scotland and Ireland as a natural laboratory, we have developed a multi-tiered methodological approach utilizing a spectrum of data ranging from freely available chart data to the latest multibeam geophysics to determine and map the seabed sediment type. Targeted sampling of fjord sediments was undertaken to establish a calibration of sediment type against OC content. The results show that fjord sediments are highly heterogeneous both in sediment type and OC content. Utilizing the tiered mapping outputs, first order estimates of the surficial (top 10 cm) sediment OC stock within Scottish fjords (4.16 ± 0.5 Mt OC) and Irish systems (2.09 ± 0.26 Mt OC), when normalized for area the surficial sediments of Scottish and Irish fjords hold 2027 ± 367 and 1844 ± 94 tonnes OC km^{-2} respectively far exceed estimates for the continental shelf, again highlighting fjord sediments as hotspots for the capture of OC. This tiered approach to mapping sediment type is ideally suited to areas of the marine environment where data availability and quality is a limiting issue. Further understanding of the spatial heterogeneity of these sediments provides a foundation to reevaluate global fjord OC burial rates and to better understand the role of fjord sediments in regulating the global climate.

Keywords: fjord, carbon, sediment, spatial, Scotland, mid-latitude, organic carbon, mapping

OPEN ACCESS

Edited by:
Michael Andrew Clare, University of Southampton, United Kingdom

Reviewed by:
Zhixiong Shen, Coastal Carolina University, United States
Valier Galy, Woods Hole Oceanographic Institution, United States

***Correspondence:**
Craig Smeaton
cs244@st-andrews.ac.uk

Specialty section:
This article was submitted to Sedimentology, Stratigraphy and Diagenesis, a section of the journal Frontiers in Earth Science

Received: *08 May 2019*
Accepted: *30 September 2019*
Published: *24 October 2019*

Citation:
Smeaton C and Austin WEN (2019) Where's the Carbon: Exploring the Spatial Heterogeneity of Sedimentary Carbon in Mid-Latitude Fjords. Front. Earth Sci. 7:269. doi: 10.3389/feart.2019.00269

INTRODUCTION

Sediments at the land-ocean interface have been identified as key components in the global carbon (C) cycle (Berner, 1982; Bauer et al., 2013), with fjord sediments being highlighted as hotspots for high organic carbon (OC) burial (Smith et al., 2015; Cui et al., 2016) and storage (Smeaton et al., 2016, 2017). Globally, fjords are estimated to bury 21–31 Tg OC yr^{-1} (Smith et al., 2015; Cui et al., 2016), which equates to approximately 11% of annual marine OC burial. Further it is estimated

that 55–62% of the OC buried in fjords is terrestrial in origin (Cui et al., 2016). The trapping and storage of both marine and terrestrial OC in these systems may provide an important and largely overlooked climate regulation service.

While the importance of fjords as sedimentary OC stores is becoming clearer, our limited understanding of the spatial distribution and heterogeneity of OC on the seabed may result in the over-estimation of the quantity of OC buried and in turn the amount of OC stored annually. Current OC burial estimates (Smith et al., 2015; Cui et al., 2016) assume that the seabed sediments within fjords are homogenous and that the burial rates calculated from a sediment core is applicable across a fjord or even an entire geographical region. However, it is well known that the seabed of both fjords and other coastal sedimentary systems are spatially highly variable and that this heterogeneity impacts the sedimentary OC content of the sediments. This issue can be further confounded by the choice of coring sites; the best coring sites for paleo- and geochemical studies tend to be the OC rich muddy sediments. The coarser and OC poor sediments are often under-sampled as they are poor sites for coring. As well as the uncertainty arising in net OC burial rates, there is also uncertainty as to where the OC is buried and stored, which hinders potential policy or management actions aimed to protect these globally significant C stores.

The first steps toward reducing uncertainty in the global OC burial estimates within fjords are to improve our understanding of the sediment heterogeneity at the seabed. Fjords, and coastal systems in general, are less well studied than the continental shelf where there is a generally good understanding of the spatial distribution of sediment types (Lark et al., 2012; Bockelmann et al., 2018; Wilson et al., 2018; Kaskela et al., 2019). In turn, such data provide insights into the potential spatial heterogeneity of OC on the continental shelf (Diesing et al., 2017). The approaches to mapping sediment type on the shelf are largely statistically based (Lark et al., 2012; Bockelmann et al., 2018; Wilson et al., 2018) and require large datasets (sediment descriptions, grain size etc.) to allow reliable predictions. Scottish and Irish fjords largely lack these data, a pattern observed in coastal systems globally. Other approaches to map the seabed and sediment type utilize multibeam and backscatter geophysical techniques (Serpetti et al., 2012; Lark et al., 2015; Audsley et al., 2016; Brown et al., 2019) where changes in acoustic responses are used to characterize seabed type. These methods provide an understanding of the spatial distribution of sediment types but have largely not been applied to fjord systems. The lack of data alongside the complex geomorphological and oceanographic conditions within fjords hinders the application of the statistical approaches which are currently available. High resolution sampling and geophysical techniques require significant financial and time investments to collect and process the data required, commonly restricting their use to single fjords or small areas of the coast.

While there are several approaches to mapping sediment type, only a few studies consider how this relates to the distribution of surficial OC and none of these are from fjords (Serpetti et al., 2012; Diesing et al., 2017). A common thread through much of this research is the link between OC and the physical properties of the seabed, in particular the sediment type and particle size (Mayer, 1994; Keil et al., 1997; McBreen et al., 2008; Serpetti et al., 2012; Diesing et al., 2017; Bao et al., 2019). If a relationship between sediment type and OC can be established for fjords there is potential for wide scale mapping and quantification of OC within surficial fjord sediments as significant volumes of legacy and "non-traditional" sediment type data are available globally (Mitchell et al., 2019).

Using the mid-latitude fjords of Scotland and Ireland as an example, we developed a tiered approach to mapping which acknowledges data gaps and limitations yet provides a robust technique to map the sediment type and surficial (top 10 cm) OC content across fjords with differing levels of existing data coverage. This research will provide a new template for both fjordic and other marine systems globally, delivering a strong foundation to re-evaluate global sedimentary OC burial rates in fjords and a tool to allow for targeted management and eventually protection of these globally significant C stores from future disturbance.

STUDY AREA

The west coast and islands of Scotland are dominated by sea lochs (fjords) (**Figure 1**). In total, there are 226 fjords which can be subdivided into 111 large fjords (over 2 km long, with fjord length twice fjord width) (Edwards and Sharples, 1986) and 115 smaller systems. This study focuses on 133 systems spanning both groups (**Supplementary Table 1**). Recently, the 111 large fjords have been shown to be significant long-term store of OC with an estimated 252.4 ± 62 Mt OC being held within their postglacial sediments (Smeaton et al., 2017). Further research showed that a significant proportion of the OC stored in Loch Sunart (42 ± 10%) and Loch Teacuis (64.8 ± 5.2%) was terrestrial in origin (Smeaton and Austin, 2017) which are comparable to other fjords systems globally (Cui et al., 2016). Smeaton et al. (2017) highlighted that the Scottish fjords can be subdivided into different types both geographically (Mainland, Inner Hebrides, Outer Hebrides and the Shetland islands) and based on physical characteristics; for example, the fjords of the mainland and Inner Hebrides are classic fjords characterized by heavily glaciated geomorphology (Syvitski et al., 1987; Syvitski and Shaw, 1995; Howe et al., 2002). By contrast, the systems that dominate the coastline of the Outer Hebrides and the Shetland Islands differ significantly and tend to be shallower with a more subdued submarine geomorphology and could be referred to a fjards. Fjards are long and narrow and a products of glacial processes but unlike classical fjords they are relatively shallow and flat-bottomed and lack the geomorphological characteristics observed within glacially over-deepened fjords (Syvitski et al., 1987; Syvitski and Shaw, 1995; Howe et al., 2010). The differing geomorphological characteristics of these systems has resulted in different OC contents within the postglacial sediments, with the mainland fjords storing the majority of the estimated 252.4 ± 62 Mt of OC (Smeaton et al., 2017).

Ireland's glacial history (Ehlers et al., 1991; Peters et al., 2015; O'Cofaigh et al., 2019) shares similarities with Scotland and this has resulted in a coastline with comparable geomorphology

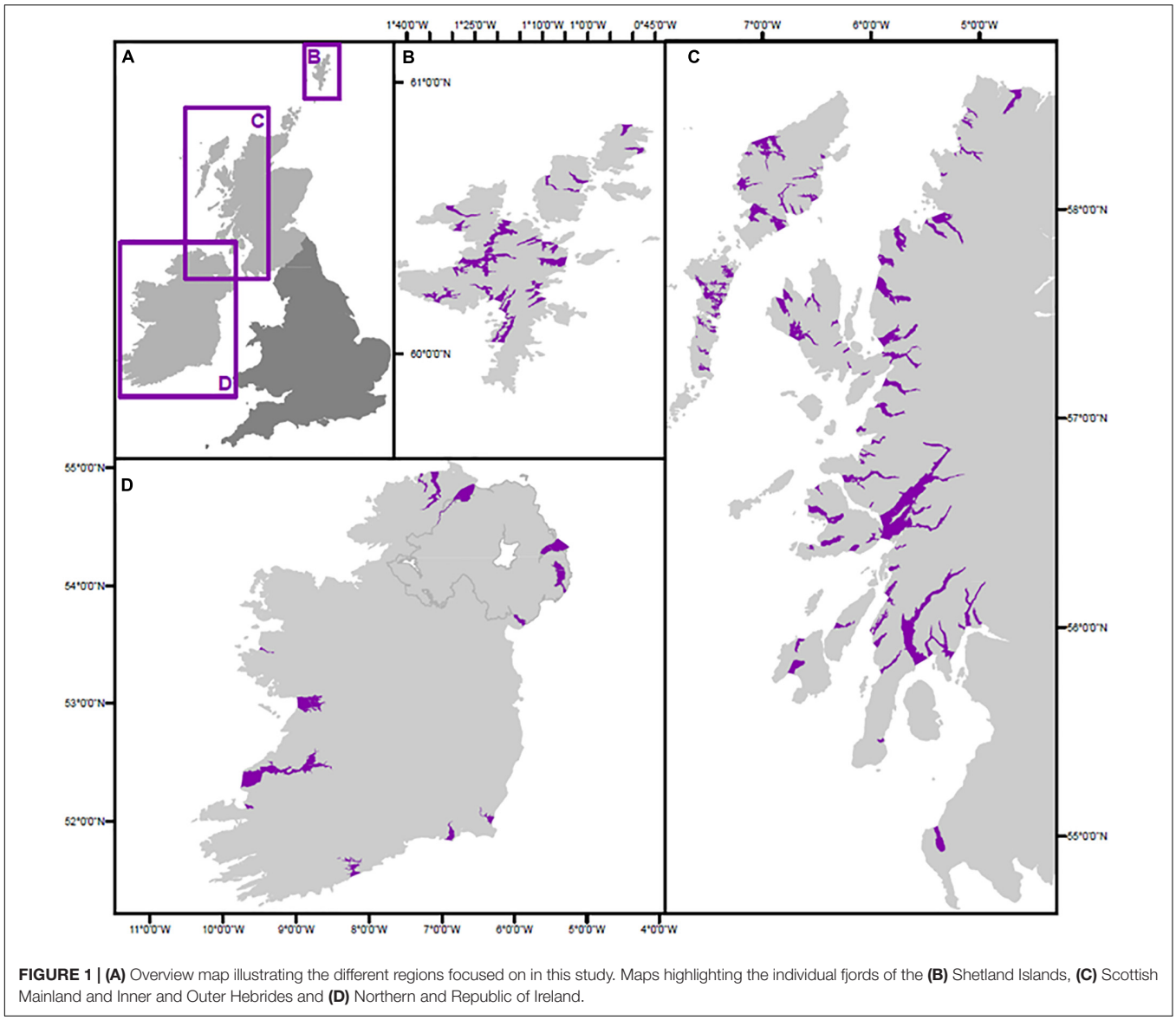


FIGURE 1 | (A) Overview map illustrating the different regions focused on in this study. Maps highlighting the individual fjords of the **(B)** Shetland Islands, **(C)** Scottish Mainland and Inner and Outer Hebrides and **(D)** Northern and Republic of Ireland.

(Sinnot and Devoy, 1992) to that of Western Scotland. The Irish coast is dominated by bays and sea loughs (**Figure 1**); of these numerous systems, only Carlingford Lough, Killary Harbour and Lough Swilly are considered fjords (Nairn, 2005). The other sea loughs can be classified as fjards similar to the systems found on the islands of Scotland. These sea loughs are similar to the sea lochs of Shetland and the Outer Hebrides of Scotland. This study includes the three Irish fjords, in addition to 12 sea loughs (**Figure 1D**).

MATERIALS AND METHODS

Primary Data Collection

Sampling

Surficial sediment samples were collected from 20 fjords around Scotland (**Supplementary Figure 1**). Between 2004 and 2017, sampling was conducted in Lochs Sunart, Etive, Creran, Ewe and Melfort from the RV *Seòl Mara*, RV *Calanus,* MV *Walrus* and RV *Morwena*. In 2015, samples were collected from the Shetland Islands from six fjords onboard the MV *Moder Dy* (Lo Giudice Cappelli et al., 2019 in review). The final phase of sampling took place in July 2017 aboard the MRV *Alba na Mara,* where 74 samples were collected from across eight Northern Scottish fjords (Lochs Eriboll, a Chairn Bhain, Glencoul, Glendhu, Gairloch, Torridon, Carron, Kishorn). A number of sampling techniques were employed during these cruises. The majority of the samples were collected using grab samplers (both Van Veen and Day) with corers (Gilson, Craib, Sholkovitch and Mega) also being employed at various times and locations. Cores were subsampled at 1 cm intervals. Full details of these samples and sampling techniques can be found in the **Supplementary Data**.

In addition, further samples were collected from the British Geological Survey (BGS) and British Ocean Sediment Core

Research Facility (BOSCROF) sample repository to augment the sample collection. The repository provided sediments from across 15 fjords, bringing the number of samples for this study to 356 covering 35 fjords.

Physical Properties

On collection, the surficial samples were described using the modified Folk classification (Folk, 1954) scheme using five standard classes: gravel, sand, coarse sediment, mixed sediment and mud and muddy sand (Lark et al., 2012; Kaskela et al., 2019). The scheme was further supplemented with rock and biogenic/carbonate classes. Wet (WBD) and dry bulk density (DBD) were calculated from the sediment cores following the methodology set out by Dadey et al. (1992). These data were further supplemented by DBD data from Loch Sunart, Creran, Broom and Little Loch Broom and Etive (Smeaton et al., 2016, 2017). Additionally, DBD values for the coarser sediments (gravel, sand, etc.) were derived from the literature (Flemming and Delafontaine, 2000; Diesing et al., 2017).

Geochemical Analysis

The 356 surface sediment samples were analyzed to determine bulk elemental composition (OC and N). Each sample was freeze dried, homogenized, and approximately 10 mg of processed sediment was weighed out into silver capsules. The encapsulated samples underwent acid fumigation (Harris et al., 2001) to remove the carbonate, this entailed placing the samples in a desiccator with a beaker of 37% HCl acid for 48 h. Upon removal from the desiccator the samples were dried for 24 h at 40°C, OC was measured using an Elementar Vario EL elemental analyzer. The standard deviation of triplicate measurements (n = 30) were OC: 0.18% and N: 0.06%, respectively. Further quality control was assured by the repeat analysis of standard reference material B2178 (Medium Organic content standard from Elemental Microanalysis, United Kingdom) these samples deviated from the reference value by: OC = 0.07% and N = 0.02% (n = 20).

Secondary Data Collection

Sediment Type (Point Observations)

Point observations on sediment type (i.e., descriptions) for Scottish and Irish fjords were compiled from numerous sources (**Supplementary Table 2**). The main sources of these data were from habitat surveys which require substrate type to be recorded for each individual habitat; these data were accessed through the Joint Nature Conservation Committee (JNCC) Marine Recorder database. These data is largely collected by scuba divers and/or camera drops, and as a consequence tends to be from the shallower, marginal regions (i.e., edges, sill) of the fjords and therefore underrepresent a significant portion of the seabed.

Nautical charts also provide an important resource of bottom type data. The United Kingdom Hydrographic Office (UKHO) have been compiling a database of seabed bottom type for over 100 years to help characterize potential anchoring locations. This record of sediment type data is readily available but has been largely overlooked as a resource for seabed mapping. While this data may be considered "non-traditional," it is quality controlled by UKHO under its statutory responsibilities to provide accurate information on charts for anchoring. The chart data has excellent spatial coverage across both Scottish and Irish fjords (**Supplementary Figure 2**), although the data does not extend to the shallower areas of the fjords. The habitat and chart datasets complement one another and together they provide observations from across the shallow and deeper regions of the fjords.

The dataset was further augmented with seabed descriptions from the BGS and Infomar. In total 60,405 point observations describing seabed sediment type were compiled for fjords across both Scotland and Ireland (**Supplementary Figure 2**). **Supplementary Table 1** provides information on the location of the original data used within this study.

Unifying the Data

The secondary datasets differ in the classification schemes used to describe the seabed sediment types. The UKHO, BGS, Infomar and the data extracted from the nautical charts use the classical Folk scheme (Folk, 1954) which consists of 12 different classes. Furthermore, the sediment type data associated with the habitat descriptions accessed through the JNCC marine recorder do not utilize a standardized classification scheme and descriptions differ between surveys. To unify the data to the modified Folk classification scheme outlined in Section "Physical Properties," a hierarchical classification tree similar to that used in Kaskela et al. (2019) was developed (**Supplementary Figure 3**).

Organic Carbon and Grain Size Data

Grain size and OC data for the fjords of Scotland and Ireland is limited (**Supplementary Figures 4, 5**) and is mainly associated with monitoring activities, particularly for the detection of polycyclic aromatic hydrocarbons (Webster et al., 2000, 2001, 2003, 2004; Guinan et al., 2001; Russell et al., 2008, 2011; McIntosh et al., 2012). The data from these studies was extracted and further supplemented by data from the International Council for the Exploration of the Sea (ICES) which stores all marine monitoring data for North Atlantic nations required under the OSPAR convention (Oslo Paris Convention). The grain size data included in these datasets are largely reported in the % < 63 μm (i.e., clay and silt content) which has been shown to correlate to OC content in some environments (Serpetti et al., 2012).

Unlike the other secondary data, the OC data collected from these sources will not be used to map the surficial OC content. Rather it will be used as a ground-truthing and validation dataset to test the accuracy of the outputs by directly comparing to the OC values from the predictive mapping to that of known OC values. Quality control measures were taken to assure these data are comparable to the primary OC data collect as part of this research. This involves only using OC data collected from bulk samples, and discarding OC data measured from specific size fractions (i.e., <63 and 20 μm).

Backscatter Data

Backscatter data was accessed through the BGS offshore index and Infomar's data portal from 24 Scottish fjords and 5 Irish systems (**Supplementary Figure 2**). The data was assessed to determine the areal coverage and the quality of the backscatter

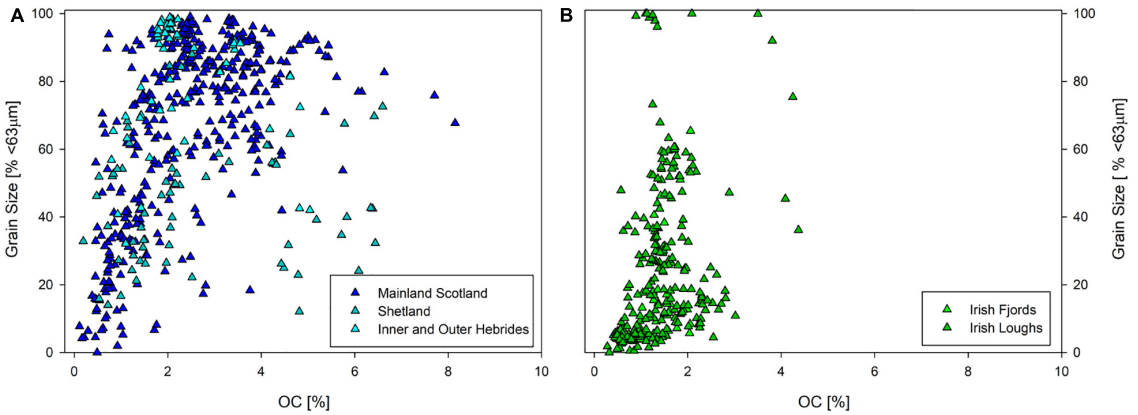


FIGURE 2 | The relationship between grain size (% < 63 μm) and OC content explored using secondary data **(A)** Scotland (*n* = 670) and **(B)** Ireland (*n* = 274).

signal (**Supplementary Table 3**). Geophysical techniques such as multibeam and backscatter often struggles to map the full extent of the seabed in fjords because of the geomorphological nature of these systems. The shallower areas (i.e., edges, sills) within fjords and coastal regions are difficult to survey because the water depth does not allow access to the vessels carrying the geophysical instruments.

Mapping the Seabed

Tier 1 Point Observations

Each of the modified Folk classes and the point observations within each class (**Supplementary Figure 6**) were assigned a numerical value from 0 for biogenic/carbonate to 7 for mud and muddy sand. The compiled data were statistically tested to determine the gridding technique best suited to the interpolation of the data. Twelve gridding techniques were subjected to cross validation (Chiles and Delfiner, 2009), where the residual Z mean value and standard deviation were examined. The technique with the lowest residual Z mean and standard deviation was chosen as the gridding technique best suited for this study. Kriging, with linear interpolation (Cressie, 1990), performed best with the interpolation because of the irregularly spaced nature of the data used in this study. This technique was twinned with a 1000 by 10000 node structure to create computationally efficient mapping of the different sediment types. Finally, the areal coverage of each sediment type was calculated for the 133 Scottish and 15 Irish systems (**Supplementary Data**). In addition to mapping the sediment type, this approach allows for the kriging standard error (KSE) to be calculated by taking the square root of the kriging variance. This allows the KSE to be mapped and used as a measure of uncertainty related to the predicted values (i.e., as a proxy for confidence in our predictions).

Tier 2 Backscatter

Backscatter classification was undertaken utilizing an unsupervised classification technique which has been widely used for benthic habitat mapping (Brown et al., 2011; Calvert et al., 2014). Unsupervised classification was performed using the ISO Cluster algorithm in ArcGIS (Brown and Collier, 2008; Ierodiaconou et al., 2011). This method organizes the backscatter raster into a number of groups using the maximum likelihood supervised classification approach. We undertook 250 iterations of the clustering procedure and found increasing the number of iterations beyond 250 had negligible impact on the outputs but increased computational strain similar to that observed by Calvert et al. (2014). The ISO Cluster outputs were ground-truthed using the independent sediment type dataset produced from the samples collected from the research cruises (see Section Physical Properties) and those reported in the ICES database (see Section Organic Carbon and Grain Size Data).

Chi-squared (χ^2) tests for independence where carried out on contingency tables created from ISO Cluster analysis. As χ^2 is sensitive to the sample size n, with large n producing significant χ^2, we were able to calculate Cramer's *V* statistics (Cramér, 1946). Cramer's *V* values range from 0 (no relationship) to 1 (relationship) and are not sensitive to sample size; results from these statistical analyses are reported in the **Supplementary Data**.

Tier 3 Composite Mapping

Composite sediment type maps (Tier 3) were created through the merger of the Tier 1 and 2 maps. This approach was applied to the 29 fjords which have both Tier 1 and 2 maps available. As with the previous tiered approaches, the areal coverage of each sediment type was calculated (**Supplementary Data**).

Surficial Carbon Mapping

The spatial distribution of the surficial OC was mapped utilizing the OC data collected from the 356 samples collected from fjords around Scotland. The minimum and maximum values were calculated for each of the Folk classes and corrected to exclude outliers (i.e., lower and upper whiskers on a boxplot). These values were utilized to create a ramped scale increasing in 0.5% OC increments, the ramped scale was applied to the best available sediment type map (i.e., Tier 1 to 3) for each of the Scottish and Irish fjords. The surficial OC maps were ground-truthed using the OC data produced from the data reported in the literature and in the ICES database (see Section Organic Carbon and Grain Size Data).

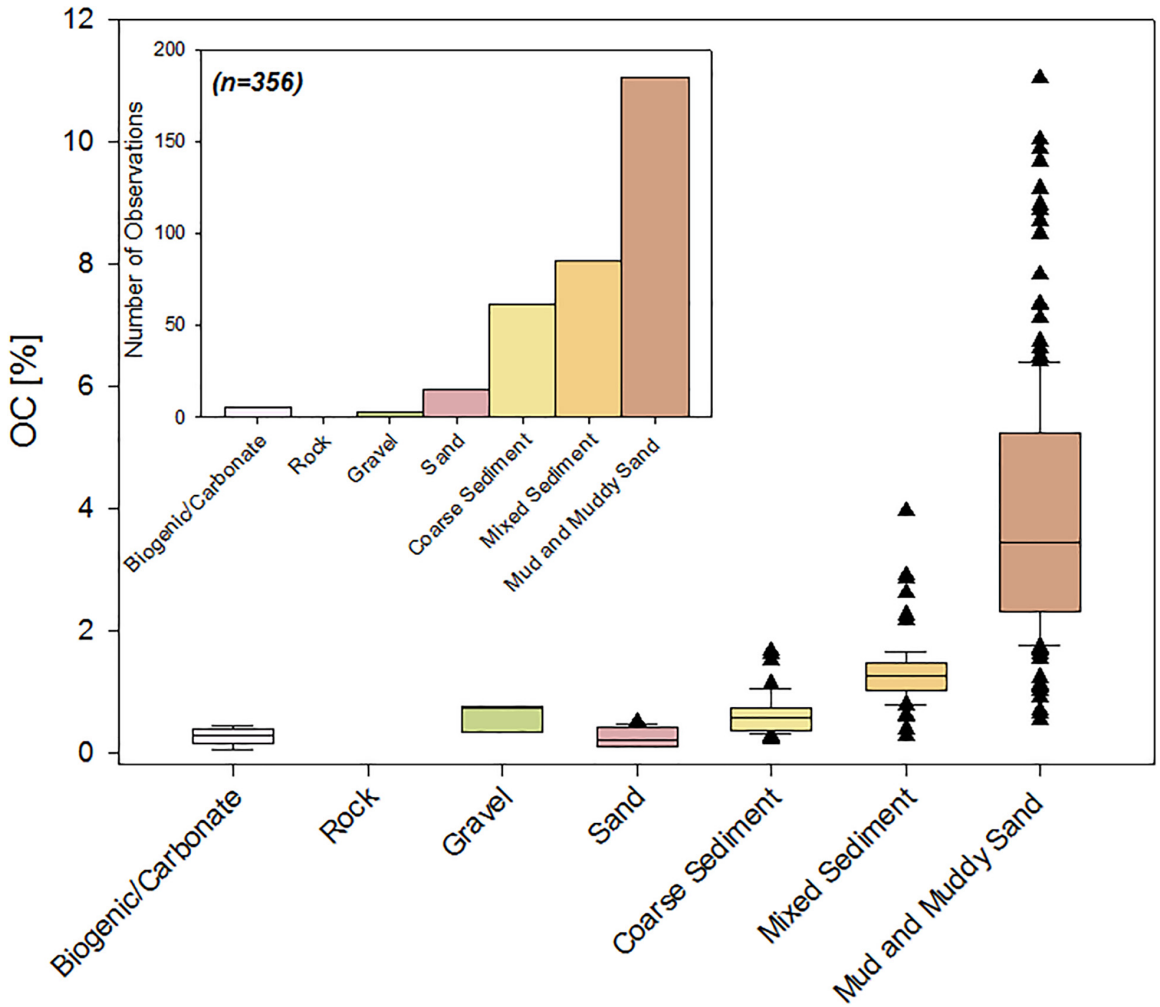


FIGURE 3 | OC content of samples (n = 356) across the modified Folk classification scheme collected from 35 fjords around Scotland. **Inset:** Number of samples in each of the Folk classes.

The surficial OC stocks (top 10 cm) were calculated for each fjord to allow comparison to other surficial sediment stock estimates (Burrows et al., 2014, 2017; Diesing et al., 2017; Luisetti et al., 2019). The surficial OC stock was calculated using the sediment coverage (m^2) combined with the sediment depth (0.1 m), bulk density data (kg m^{-3}) and the available OC data (%). The bulk density and mean OC contents used in the calculations are reported in **Supplementary Table 4**.

RESULTS AND INTERPRETATION

Exploring the Relationship Between Sediment Type and OC

Using the secondary data (**Supplementary Figures 3, 4**), the relationship between grain size (% < 63 μm and OC was explored to determine if it could be exploited as a tool to map surficial OC (**Figure 2**) across both Scotland and Ireland. The results indicate that the clay and silt component of the sediment and OC content in Scottish and Irish fjords are poorly correlated (especially as OC increases), although there is be a degree of covariance between the variables.

This is counter to the previous findings on continental shelves (McBreen et al., 2008; Serpetti et al., 2012; Diesing et al., 2017) where there is normally a strong correlation between mud content (i.e., % < 63 μm) and OC. Fjords, are significantly influenced by local factors (hydrology, run-off, bathymetry, etc.) this in conjunction with the greater heterogeneity in both bottom water temperature and dissolved oxygen concentrations, both of which are known to influence sediment OC (Woulds et al., 2007, 2016; Middelburg and Levin, 2009), may explain why the universal relationship between sediment grain size and OC content is not as strong as some studies from open-shelf regions suggest. However, when this relationship is explored within individual systems (**Supplementary Figures 7–9**) strong correlations are observed between grain size and OC but this relationship is not universal across all 33 fjords where data are available.

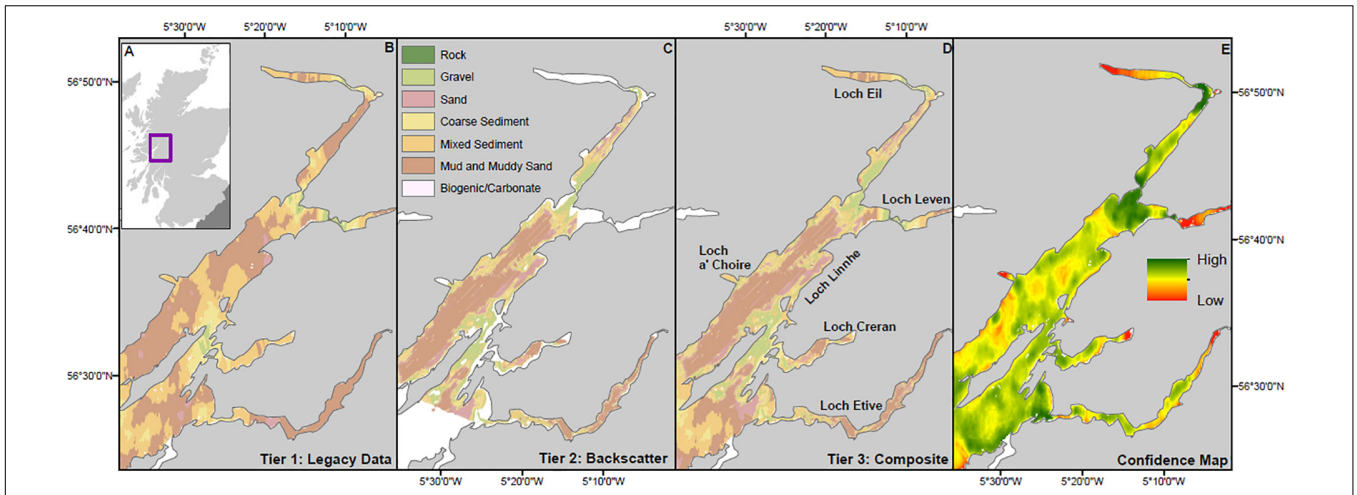


FIGURE 4 | Sediment type mapped across the Loch Linnhe fjord complex. **(A)** Loch Linnhe in context of the United Kingdom, **(B)** Tier 1, point observations, **(C)** Tier 2, backscatter, **(D)** Tier 3 Composite approaches, and **(E)** Confidence map produced from the Kriging Standard Error.

TABLE 1 | Difference in seabed coverage (%) for each of modified Folk classes (Kaskela et al., 2019) across the Loch Linnhe fjord complex calculated using the different mapping techniques, Green indicates that the Tier 1 map underestimates seabed coverage while Red is indicative of an overestimation in comparison to the Tier 3 approach.

	Estimated Seabed Coverage [%]							
	Unmapped	**Biogenic/ Carbonate**	**Rock**	**Gravel**	**Sand**	**Coarse Sediment**	**Mixed Sediment**	**Mud and Muddy Sand**
Tier 1		0	0	10.79	8.74	17.28	24.98	38.22
Tier 2	26.2	0	0	9.34	6.17	17.21	15.74	24.92
Tier 3		0	0	11.82	9.64	11.82	25.75	40.97
Tier 3 – Tier 1		0	0	1.02	0.91	−5.46	0.78	2.75

In contrast, when the sediments are classified using the modified Folk scale there is a clear link between OC and sediment type (**Figure 3**). The OC content in these sediment types increase significantly as we transition from coarser grained to the muddier substrates. This pattern is consistent over all the sediment classes apart from gravel where the OC content is equivalent to that of the coarse sediment class. This is due to the small number of samples ($n = 3$) in comparison to the other classes; additionally, gravels can trap fine particles (and OC) within their coarse sedimentary matrix.

Mapping Sediment Type

The sediment type of the 133 Scottish fjords and 15 Irish systems were successfully mapped using the three-tiered approach described above (high resolution maps included in the **Supplementary Material**) which also allowed the aerial coverage of each sediment type to be calculated (**Supplementary Data**). To determine the differences between the different mapping techniques and their relative performance, we initially used the Loch Linnhe complex of fjords which consist of six fjords with differing data availability (**Figure 4**).

When we compare the outputs from Tier 1 and Tier 3 mapping for the Loch Linnhe complex, Tier 1 underestimates the areal coverage of all the sediment classes when compared to the Tier 3 map, with the exception of the coarse sediment (**Table 1**). Most of the classes show an underestimation of between 0.78 and 2.75%, while the coarse sediment was overestimated by 5.46%. The relatively small difference between the Tier 1 and 3 mapping approaches provides confidence that if high quality backscatter is not available, robust maps of sediment type can be produced from available point observations.

The quality of the different mapping techniques was further tested using the data from the 29 systems where backscatter data were available (**Figure 5**). When the estimated seabed coverage for the 24 Scottish fjords are compared, the Tier 1 mapping underestimated the rock (0.52%), gravel (4.41%) and sand (5.07%) and overestimated the coarse sediment (4.70%), mixed sediment (4.70%) and the mud and muddy sands (0.59%) when compared to the Tier 3 estimate of seabed coverage. The five Irish systems exhibit greater variation between Tier 1 and 3 mapping approaches. The Tier 1 maps underestimated the coverage of rock (0.61%), mixed sediment (5.07%) and the mud and muddy sands (0.48%) and overestimated the coverage of gravel (0.2%) in comparison to the Tier 3 maps. These values are broadly similar but the two mapping techniques differ significantly, overestimating sand by 25% and underestimating coarse sediments by 19%. The largest differences between these two mapping techniques is between the sand and the coarse sediment, probably because sand is a significant component of coarse sediments. The broad similarity in these sediments is

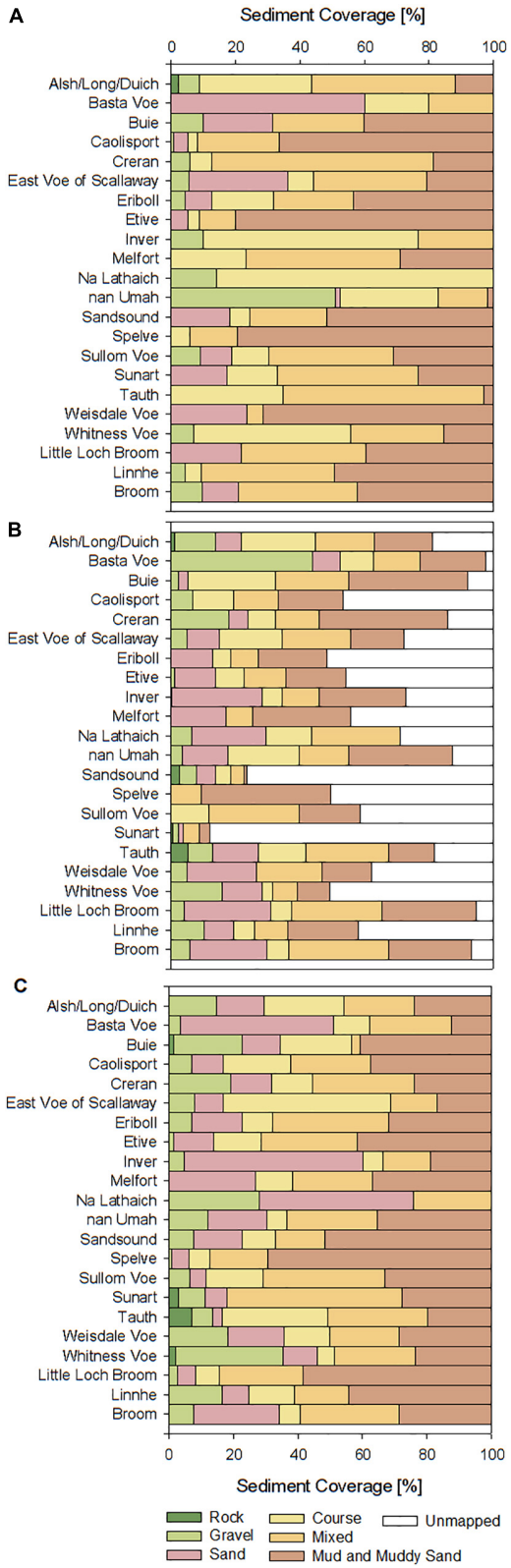


FIGURE 5 | Visualization of the difference between the three-tiered mapping approach across the Scottish fjords with all data types. **(A)** Tier 1, point observations, **(B)** Tier 2, backscatter, and **(C)** Tier 3 Composite.

potentially the result of misidentification of these sediment types that leads to differing estimates of sediment coverage between the mapping approaches. However, as the mud and muddy sands hold the greatest quantity of OC (**Figure 3**), the fact that we only see between −0.59 and 0.48% variation in coverage between the different mapping approaches is encouraging. A final test was undertaken using samples collected from the research cruises to ground-truth the sediment maps. The test used the sediment description from these samples and compared them to the Tier 1 and, where available, the Tier 3 maps. In total 84% of the 356 samples had matching sediment descriptions. The remaining 16% of these samples were mismatches exclusively between the coarser sediments (sand and coarse sediments). This multifaceted analysis indicates that for the OC rich sediments, all mapping approaches perform well and allow sediment type to be mapped across data poor and rich systems; however, caution should be applied when interpreting the coarser sedimentary types, especially in areas where sand and coarse sediment are collocated.

The mean errors calculated through these comparisons were applied to calculate the areal coverage (km^2) of the different sediment types allowing the surficial OC stocks and their uncertainties to be estimated. The full results from the comparison between mapping approaches can be found in **Supplementary Tables 5, 6**.

A National Overview (Sediment Coverage)

The results of the mapping reveal distinct difference in the regional sedimentary composition of fjords in both Scotland and Ireland (**Figure 6**). The mean composition of the fjords of mainland Scotland are dominated by mixed and muddy sediments, with the fjord sediments elsewhere tending to be coarser in nature. This pattern is most apparent in the fjards of the Outer Hebrides where gravels and coarse sediments significantly overshadow other sediment types. This may reflect both a diminished sediment supply and the shallow, flat bottomed nature of these fjards, where coarse material is retained within the fjord and finer-grained sediments are flushed out to sea. The sediments from the fjords of the Inner Hebrides and the Shetland Islands are distributed over the different classes more equally than the mainland fjords, where mixed and muddy sediments dominate. The only mapped occurrence of biogenic/carbonate rich sediments were in the fjords of Shetland; samples collected from the MV *Moder Dy* confirm the presence of large quantities of broken shell material (Lo Giudice Cappelli et al., 2019 *in review*). The sediment coverage of the seabed of both the Irish fjords and sea loughs is far more diverse than that observed in Scotland's fjords (**Figure 6**). The sediment in these systems contain a far larger sand component as well as generally coarser particles than their Scottish counterparts. There are similarities between the Irish systems and those of the Scottish Islands. The shallow nature of these systems may be conducive to the capture of coarser material that also hinders the accumulation of the finer OC rich sediments. In addition, the coastal and shelf sediments surrounding Ireland are dominated by sand and coarse sediments (Kaskela et al., 2019),

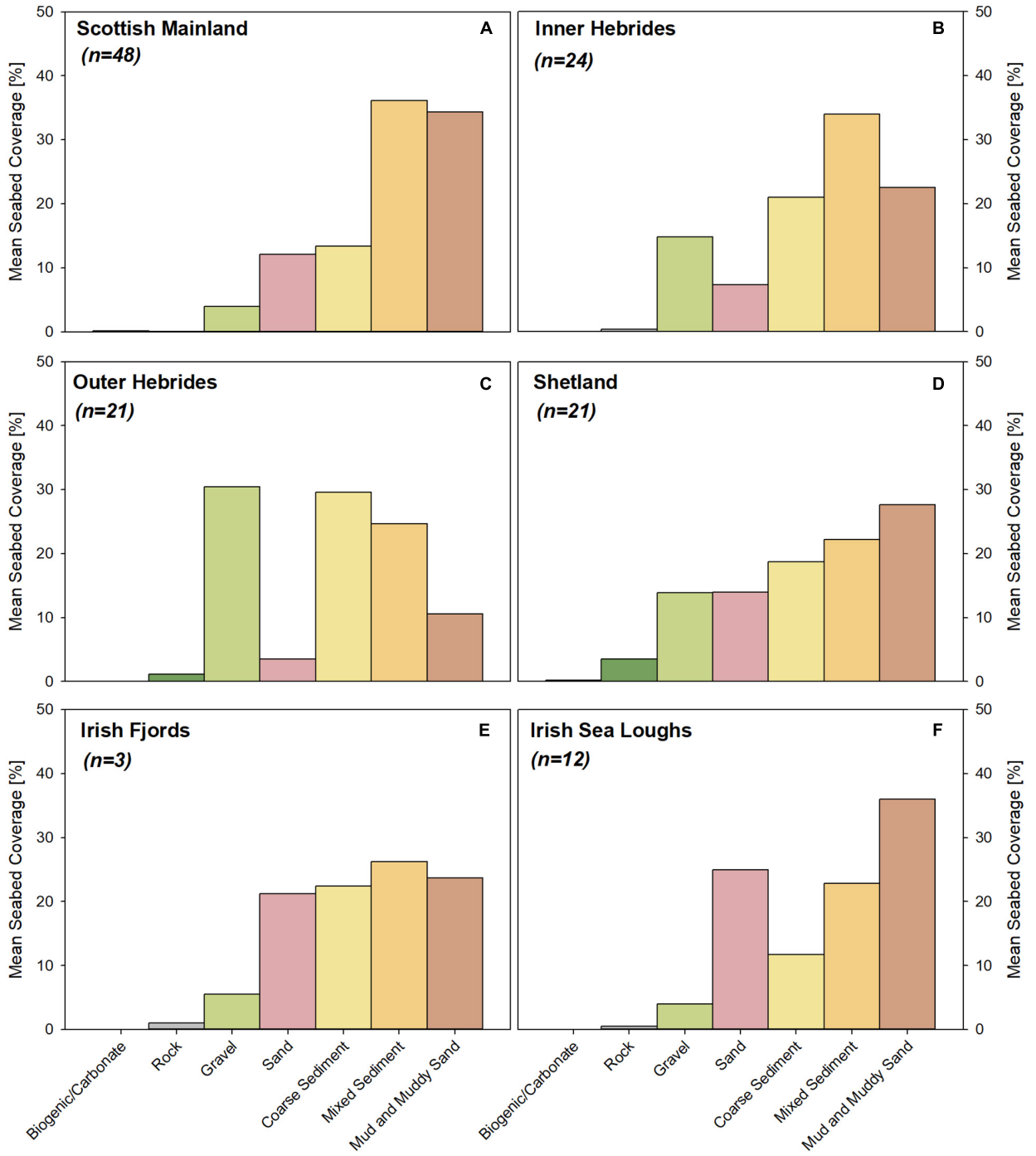


FIGURE 6 | Regional differences in mean seabed coverage (%) of the seven different sediment types across the fjords of **(A)** Mainland Scotland, **(B)** the Inner Hebrides, **(C)** the Outer Hebrides, **(D)** the Shetland Islands, **(E)** the fjords, and **(F)** sea loughs of Ireland.

the transport of this material to the fjords and sea loughs may be a secondary cause for the sediment composition in these systems.

When the sediment type coverage of the seabed is converted to areal extent (km^2), the mud and muddy sand class is estimated to cover the greatest area in both Scotland and Ireland (**Figure 7**). The extent of the different sediment classes in Ireland mirror the pattern observed in the calculated% seabed coverage estimates, but the Scottish fjords differ. In Scotland (mainland and island systems), the average fjord sediment composition is dominated by mixed sediments (**Figure 6**); and when areal extent is calculated, the mud and muddy sands are the dominate class. This

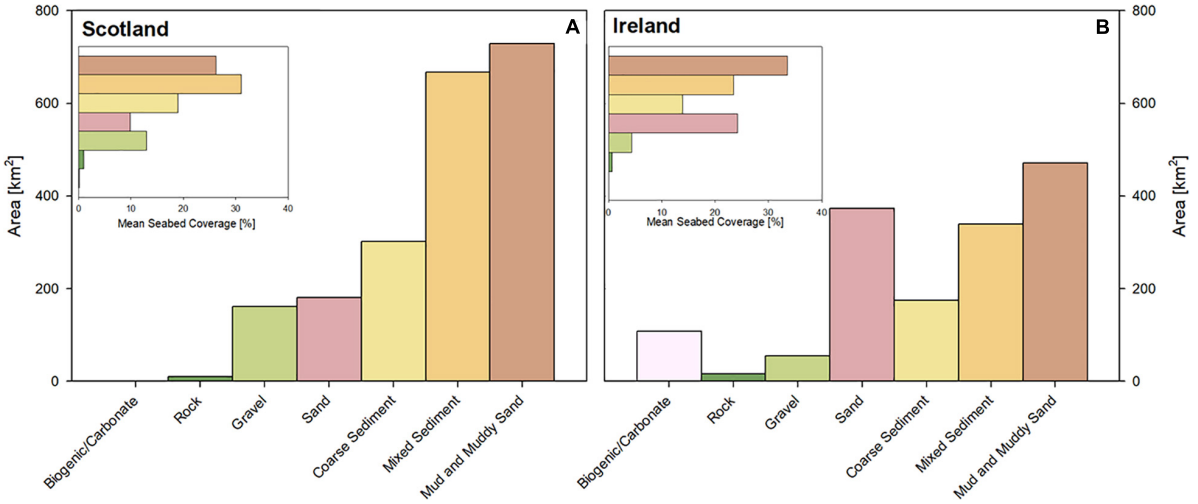


FIGURE 7 | Areal extent of the different sediment types across **(A)** Scotland and **(B)** Ireland. **Inset:** Mean seabed coverage for Scotland and Ireland.

difference is driven by the larger systems such as Loch Linnhe's seabed being dominate by mud and muddy sands (**Table 1**).

The regional differences in sediment coverage within these systems emphasizes the importance of understanding the seabed conditions within fjords, and in the marine environment more generally, highlighting that not all mid-latitude fjord systems are equivalent depositional environments.

Sedimentary OC Heterogeneity

The best available sediment map (i.e., Tier 1 or 3) for each fjord was combined with the OC data (**Figure 3**) to map the spatial distribution of the OC at 0.5% OC increments (high resolution maps included in the **Supplementary Material**). Using the Loch Linnhe complex as a case study (**Figure 8**), the greatest concentrations of OC is observed in the muddy sediments, typically occupying the upper portions and the deep central basins of the fjords. The fjord edges and sill regions, in contrast, are low in OC due to the coarse/rocky nature of the seabed in these locations. It is important to highlight that the muddy sediments are mapped as having an OC content of >2% and that the actual OC content of these sediments can be lower and also far exceed these values (**Figure 3**). Therefore, the maps outlining the spatial distribution of sediment OC are indicative, highlighting the location of OC "hotspots" rather than definitive measures of OC content.

The accuracy of these OC maps was tested by comparing them to the independent OC data (see Section Organic Carbon and Grain Size Data). Within the Loch Linnhe complex, there were 20 independent samples (**Figure 8**), 80% of these fell within the mapped OC unit appropriate for the measured OC concentration. The remaining 20% were samples associated with the sand and coarse sediments, where the measured OC content of the samples did not match the predicted values, of these sample only one overestimated the %OC. The error between the measured OC concentration and the mapped value rarely exceeds the mapped OC increments (i.e., 0.5% OC). These error is likely due to the co-location of multiple sediment types and the influx of multiple sources of OC. The pattern observed in Loch Linnhe is mirrored throughout Scotland and Ireland when the mapped OC predictions are compared to the ground-truthing samples (**Supplementary Figure 4**). In Scotland as a whole, 72% of the ground-truthing samples correspond to the mapped OC values while 64% of the Irish samples match the mapped OC concentration data. It should be noted that the low OC values around the sills and edges of the fjords are difficult to ground-truth as there is a general lack of samples from these areas. However, these low OC zones are probably appropriate because we would expect coarse materials, such as gravel, to accumulate in these high energy areas (Inall et al., 2004; Stigebrandt, 2012; Staalstrøm and Røed, 2016). The larger errors of OC prediction observed within the Irish systems is most likely due to the fact that the calibrated sediment type and associated OC content originate solely from Scottish fjords.

Surficial OC Stocks

OC stocks were calculated for the top 10 cm of sediment in both the Irish and Scottish systems to allow comparisons to other studies but it is important to highlight that the organic matter at this depth is still actively degrading. Therefore, the OC held within the top 10 cm can only be considered a stock rather than a store of OC and caution should be applied when using such shallow depths to estimate OC stocks of fjord and continental shelf sediments.

Nevertheless, it was estimated that in the top 10 cm of sediment in Scotland's fjords contain 4.16 ± 0.5 Mt OC with the muddy sediments holding 63% of that OC (**Table 2**). Of the 4.16 ± 0.5 Mt OC 72% is held in the sediments of mainland Scotland. The systems of Northern Ireland and the Republic of Ireland hold 0.94 ± 0.12 Mt OC and 1.15 ± 0.14 Mt OC respectively, again with the greatest proportion of this total held within the muddy sediments. Previous assessments of surficial sediment of Scottish fjords estimated the OC stock to be 0.33Mt

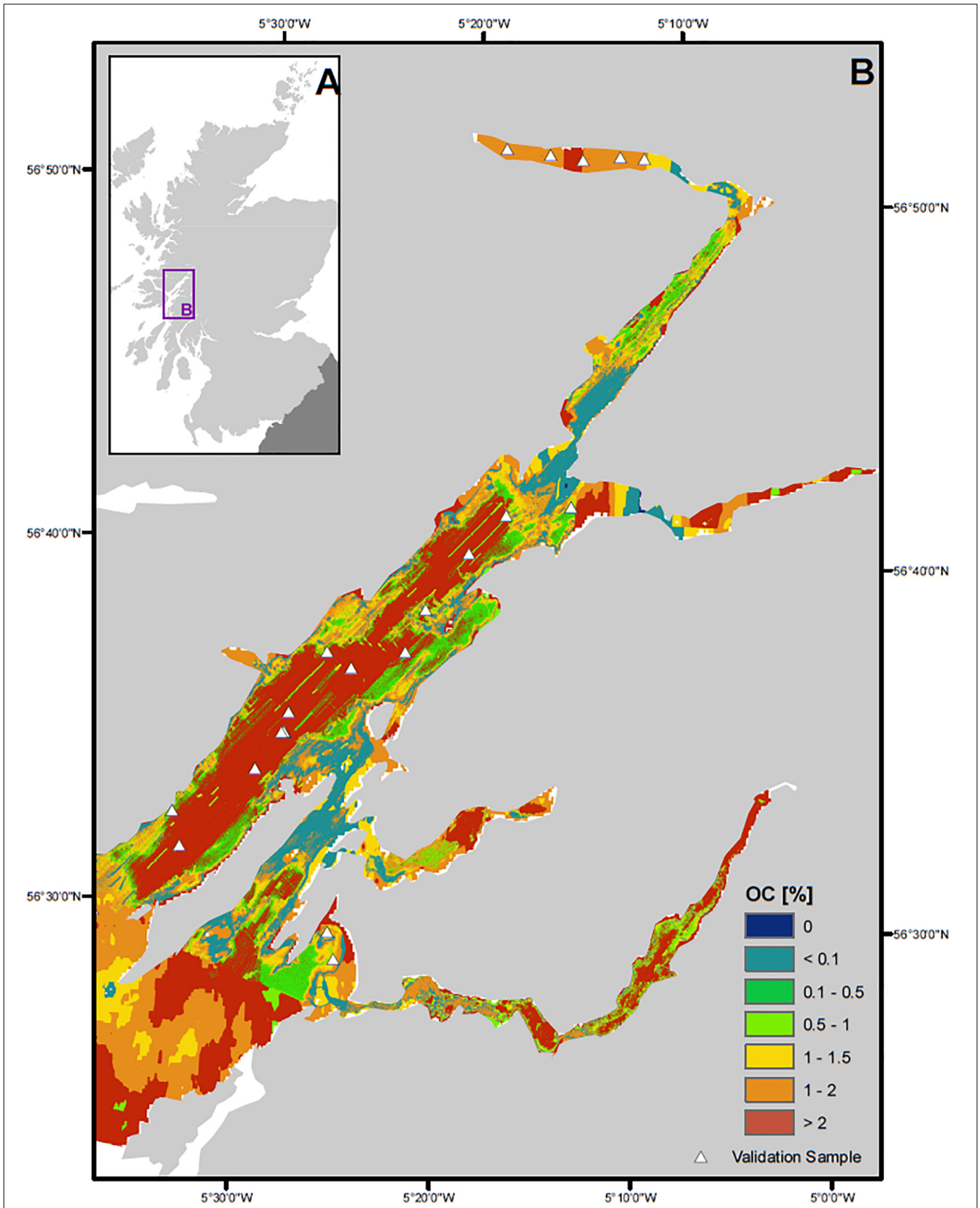


FIGURE 8 | Spatial distribution of OC in surficial sediments (top 10cm). **(A)** The Loch Linnhe fjord complex in context of the United Kingdom and **(B)** surficial sediment OC content (%).

TABLE 2 | Surficial (top 10 cm) OC stocks for fjords for Scotland and Ireland broken down to regions.

	Top 10 cm OC Stock [Mt]							
Location	**Biogenic/ Carbonate**	**Rock**	**Gravel**	**Sand**	**Coarse Sediment**	**Mixed Sediment**	**Mud and Muddy Sand**	**Total**
Mainland Scotland	0.00	0.00	0.06	0.05	0.13	0.67	2.07	3.00
Inner Hebrides	0.00	0.00	0.04	0.00	0.08	0.29	0.38	0.80
Outer Hebrides	0.00	0.00	0.04	0.00	0.03	0.06	0.06	0.20
Shetland	0.00	0.00	0.01	0.01	0.02	0.04	0.10	0.17
Scotland	**0.00**	**0.00**	**0.15**	**0.07**	**0.26**	**1.06**	**2.62**	**4.16**
Irish Fjords	0.00	0.00	0.02	0.02	0.07	0.11	0.23	0.45
Irish Sea Lough	0.00	0.00	0.04	0.05	0.24	0.69	1.08	2.10
Northern Ireland	**0.00**	**0.00**	**0.01**	**0.00**	**0.04**	**0.23**	**0.65**	**0.94**
Republic of Ireland	**0.00**	**0.00**	**0.05**	**0.07**	**0.26**	**0.57**	**0.65**	**1.60**

National surficial OC stocks are highlighted in bold.

(Burrows et al., 2014). The results presented in **Table 1** suggest these previous estimates significantly underestimated the OC held within the top 10 cm of sediment in these systems. The United Kingdom/North sea continental shelf surficial sediments (top 10 cm) are estimated to hold 205 – 592 Mt OC (Burrows et al., 2014, 2017; Diesing et al., 2017; Luisetti et al., 2019) in comparison the fjord OC stocks are relatively small in magnitude but it must be remembered that there is a significant difference in areal coverage.

The top 10 cm of sediment in fjords hold a relatively small amount of OC in comparison to shelf sediments; yet when normalized for area the fjords are a significantly more effective at trapping OC in the surficial sediments. The Scottish and Irish fjords have an OC density of 2027 ± 367 and 1844 ± 94 tonnes OC km^{-2} respectively (**Figure 9**), which far exceeds that observed on the continental shelf with estimates ranging between 428 and 1259 tonnes OC km^{-2} (Burrows et al., 2014, 2017; Diesing et al., 2017; Luisetti et al., 2019). The fjords of mainland Scotland have the highest OC density followed by the fjords of the Inner Hebrides and the Shetland Islands with the Outer Hebrides having the lowest OC density in Scotland (**Figure 9**). This pattern is likely due to the submarine geomorphology and supply of OC to the fjords. The mainland systems are deeply glaciated and tend to have larger catchment thus supplying greater quantities of OC.

TABLE 3 | Surficial (top 10 cm) OC stocks ranked in magnitude (Mt) compared to fully depth-integrated postglacial OC stocks (Smeaton et al., 2017).

Ranking	Top 10 cm OC Stock [Mt] *(This Study)*		Depth integrated OC Stock [Mt] (Smeaton et al., 2017)	
1	Loch Linnhe	0.59	Loch Linnhe	52.61
2	Loch Fyne	0.55	Loch Fyne	47.76
3	Loch Torridon	0.27	Loch Torridon	14.20
4	Loch Sunart	0.10	Loch Sunart	12.52
5	Loch Ryan	0.09	Loch Ewe	11.47
6	Loch Long (Clyde)	0.09	Loch Etive	10.22
7	Loch Ewe	0.08	Loch Long (Clyde)	7.77
8	Loch Scridian	0.07	Loch Hourn	7.12
9	Loch Hourn	0.07	Loch Ryan	6.78
10	Loch Na Keal	0.07	Loch na Keal	6.63

In contrast, the Outer Hebrides systems are shallow and have small catchments resulting terrestrial OC likely being flushed out to sea. This pattern was observed by Smeaton et al. (2017) where the postglacial sedimentary OC stocks of the mainland fjords of Scotland far exceeded that of other Scottish locations. The Irish fjords and loughs are comparable to that the fjards found on the Scottish Islands (**Figure 9**). The Republic and Northern Irish sea loughs have the highest OC density, due to these systems having a more "fjord like" geomorphology (i.e., restricted exchange) compared to the more estuarine like loughs of the Republic of Ireland.

When the surficial OC stocks are ranked (**Table 3**) it is clear that a small number of systems hold much of the 4.16 ± 0.5 Mt OC (**Table 2**). This pattern is also observed in the postglacial OC stocks where the 14 largest fjords hold 65% of the sedimentary OC (Smeaton et al., 2017). When the top 10 rankings of both datasets are compared the same fjords appear on the list though in a slightly different order, with the exception of Loch Etive which is replaced by Loch Scridian. Loch Etive holds the sixth largest postglacial OC store but only ranks 17th when considering the 10 cm stock, in comparison Loch Scridian is ranked 8th (Surficial OC Stock) and 11th (Postglacial OC Stock). The cause of this discrepancy is due to the bottom waters in the upper basin of Loch Etive which are semi-permanently hypoxic (Friedrich et al., 2014). Low oxygen conditions are recognized as an important factor in governing the burial and preservation of OC (Woulds et al., 2007; Middelburg and Levin, 2009), these conditions preserve a greater quantity of OC in-turn increasing the magnitude of the postglacial OC store and allowing Loch Etive to rank higher.

Beyond regional differences in OC density, the sediment classes differ significantly with the muddy surficial sediments in Scottish and Irish systems holding 3596 ± 172 tonnes of OC km^{-2} respectively. These results highlight that fjords are "hotspots" for the burial and potential storage of OC; more so the results highlight that the muddy sediments themselves are OC hotspots within the fjords. By mapping the OC content of the surficial sediments (10 cm) we provide a tool for policy makers to potentially target areas for protection and or management of these important OC resources. For example, **Figure 9** highlights that the mud and muddy sands within Scotland's mainland fjords

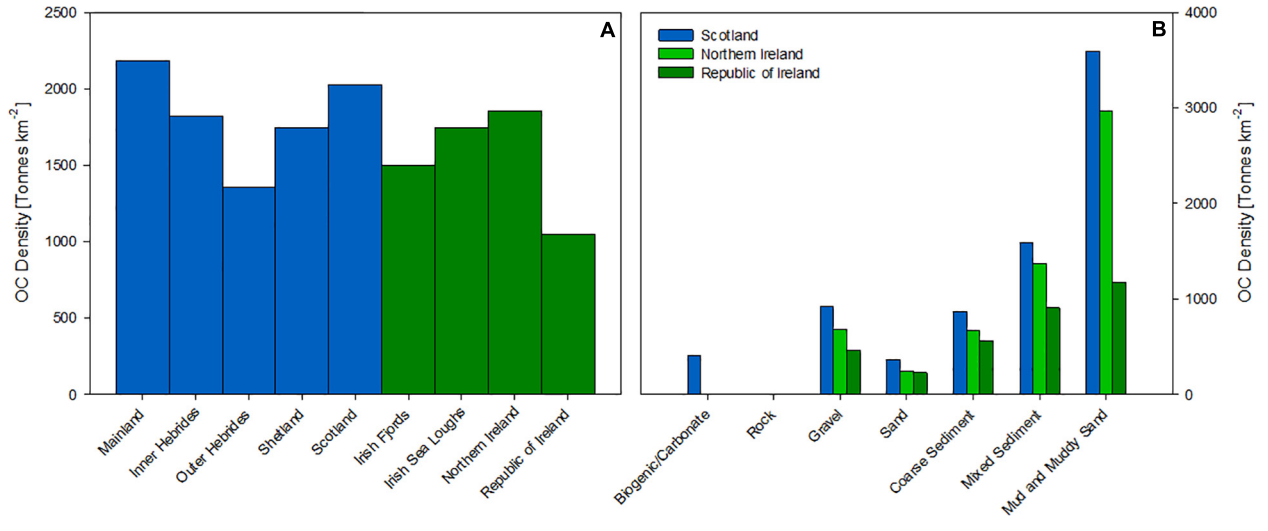


FIGURE 9 | OC density (tonnes km^{-2}) across **(A)** regions and nations **(B)** the seven Folk classes.

are where the greatest surficial OC stock are held and would be the areas where targeted management (i.e., protection from benthic disturbance) would have the most C benefits.

Revisiting Global OC Burial

While a focus on OC burial is not the purpose of this work, the results from the sediment and OC mapping highlight the need to revisit the current estimates of OC burial in fjords globally, particularly in light of our improved understanding of seabed heterogeneity. It is currently estimated that 21–31 Mt OC is buried in fjords sediments each year (Smith et al., 2015; Cui et al., 2016). But as previously stated, these calculations are based on the assumption that the seabed of these fjords are homogenous and covered in muddy sediments; an issue which impacts many marine OC stock estimates (Berner, 1982; Hedges et al., 1997). The mapping undertaken in this study estimates that 26–33% of the seabed of Scotland's and Ireland's fjords are dominated by muddy sediments (i.e., mud and muddy sands) which cover an area of 1,159 km^2. Using these systems as a proxy for fjords globally we can calculate the muddy sediments within fjords potentially bury between 5.46 and 10.23 Mt OC yr^{-1}. Globally fjords are estimated to cover an area of 455000 km^2 (Dürr et al., 2011) if we assume that the areal coverage of the muddy sediments matches that of the Scottish systems it is estimated that globally the muddy sediments bury between 57 and 107 tonnes OC km^{-2} yr^{-1} which far exceeds all other marine environments (Berner, 1982; Hedges et al., 1997; Smith et al., 2015) with the upper range being similar to the OC rich intertidal environments (Duarte et al., 2013).

These estimates are highly speculative as there are significant differences between fjord systems around the world. Yet the results do emphasize that the muddy sediments within fjords are globally significant habitats for the capture and potential storage of OC. Perhaps more significantly, these results highlight that we know very little about the non-muddy sediments which potentially represent up to 74% of the seabed area within fjords. To better understand OC burial in these coarser sediments will require a concerted effort by the research community to sample the coarser sediments; these sediments have traditionally been overlooked in favor of finer grain sediments better suited to geochemical and paleo study.

This research outlines an approach to better understand the spatial heterogeneity of the type and OC content of fjordic and marine sediments more generally. If this methodological approach can be applied to fjord systems globally, it will provide a robust foundation from which to revisit and better constrain the current estimates of OC burial rates in these environments.

CONCLUSION

Understanding the spatial heterogeneity of seabed sediments in fjords is a crucial step toward quantifying OC stocks, the formation of long-term OC stores and any associated rates of change in these globally significant OC burial hotspots. There is now a growing international awareness that natural climate solutions exist which can deliver negative emissions potential for managing our atmospheric greenhouse gases. A fundamental opportunity therefore presents itself to society, namely to manage and protect these significant OC hotspots because of their potentially significant role in regulating global climate. We have demonstrated that when combined with the tiered mapping approach, both readily available point observation and backscatter data can produce equally robust predictions of sediment type and surficial sediment OC content. The results highlight that the seafloor of fjords are highly heterogeneous which is reflected in the distribution of the surficial OC within these systems. In addition, by improving our understanding of the seabed sediment, it has been possible to refine sedimentary OC stock (top 10 cm) estimates. Scotland's fjord sediments are estimated to hold 4.16 ± 0.5 Mt OC; this is an order of

magnitude higher than previous estimates (Burrows et al., 2014). The maps depicting the spatial distribution of sediment type and OC content are potentially powerful tools for policy makers and in support of coastal management decision making, allowing a future targeted approach to the protection of these important OC hotspots. Analysis of the mapped outputs highlight that the muddy sediments within the fjords of mainland Scotland hold the majority of this sedimentary OC stock and might therefore benefit most from targeted management measures to protect and preserve these long-term OC stores from anthropogenic disturbance.

DATA AVAILABILITY STATEMENT

All datasets generated/analyzed for this study are included in the manuscript/**Supplementary Files**.

AUTHOR CONTRIBUTIONS

CS led the conception and design of the study in conjunction with WA. CS undertook the research and wrote the first draft of the manuscript. Both authors contributed to the manuscript revision, and approved the submitted version.

FUNDING

This work was jointly supported by the Natural Environment Research Council (Grant Number NE/L501852/1) and Marine Scotland. Additional support from NERC/BBSRC (BB/M026620/1) and NERC Life Sciences Mass Spectrometry Facility (CEH_L_115_05_2018) allowed additional field and analytical work to be undertaken. BGS provided access to samples through there In-kind sample loan scheme (Loan: 237389).

ACKNOWLEDGMENTS

The authors would like to thank the captains, crews, and fellow scientists from the many research vessels used to collect the samples utilized in this study. The British Ocean Sediment Core Research Facility (BOSCORF) is thanked for supplying sediment samples. In addition, the authors would like to thank the staff of the BGS Core Store for their assistance in gaining access to samples. The authors would also like to thank the data managers at both BGS and UKHO for their help in gaining access to backscatter data and survey reports. Finally, the authors thank John Baxter and Ian Davies for comments on an early draft of the manuscript and the two reviewers for providing useful comments and guidance to improve the manuscript.

SUPPLEMENTARY MATERIAL

The Supplementary Material for this article can be found online at: https://www.frontiersin.org/articles/10.3389/feart.2019.00269/full#supplementary-material

REFERENCES

Audsley, A., Arosio, R., and Howe, J. A. (2016). A geomorphological reconstruction of the deglaciation of loch etive during the loch lomond stadial. *Scott. J. Geol.* 52, 55–63. doi: 10.1144/sjg2015-004

Bao, R., Zhao, M., McNichol, A., Galy, V., McIntyre, C., Haghipour, N., et al. (2019). Temporal constraints on lateral organic matter transport along a coastal mud belt. *Organ. Geochem.* 128, 86–93. doi: 10.1016/j.orggeochem.2019.01.007

Bauer, J. E., Cai, W. J., Raymond, P. A., Bianchi, T. S., Hopkinson, C. S., and Regnier, P. A. (2013). The changing carbon cycle of the coastal ocean. *Nature* 504:61. doi: 10.1038/nature12857

Berner, R. A. (1982). Burial of organic carbon and pyrite sulfur in the modern ocean: its geochemical and environmental significance. *Am. J. Sci.* 282, 451–473. doi: 10.2475/ajs.282.4.451

Bockelmann, F. D., Puls, W., Kleeberg, U., Müller, D., and Emeis, K. C. (2018). Mapping mud content and median grain-size of North Sea sediments–A geostatistical approach. *Mar. Geol.* 397, 60–71. doi: 10.1016/j.margeo.2017.11.003

Brown, C. J., Beaudoin, J., Brissette, M., and Gazzola, V. (2019). Multispectral multibeam echo sounder backscatter as a tool for improved seafloor characterization. *Geosciences* 9:126. doi: 10.3390/geosciences9030126

Brown, C. J., and Collier, J. S. (2008). Mapping benthic habitat in regions of gradational substrata: an automated approach utilising geophysical, geological, and biological relationships. *Estuar. Coast. Shelf Sci.* 78, 203–214. doi: 10.1016/j.ecss.2007.11.026

Brown, C. J., Todd, B. J., Kostylev, V. E., and Pickrill, R. A. (2011). Image-based classification of multibeam sonar backscatter data for objective surficial sediment mapping of Georges Bank, Canada. *Cont. Shelf Res.* 31, S110–S119.

Burrows, M. T., Hughes, D. J., Austin, W. E. N., Smeaton, C., Hicks, N., Howe, J. A., et al. (2017). *Assessment of Blue Carbon Resources in Scotland's Inshore Marine Protected Area Network Scottish Natural Heritage Commissioned*. Report. No. 957. St Andrews: University of St Andrews.

Burrows, M. T., Kamenos, N. A., Hughes, D. J., Stahl, H., Howe, J. A., and Tett, P. (2014). *Assessment of Carbon Budgets and Potential Blue Carbon Stores in Scotland's Coastal and Marine Environment Scottish Natural Heritage Commissioned*. Report. No. 761. Scotland: Scottish Natural Heritage.

Calvert, J., Strong, J. A., Service, M., McGonigle, C., and Quinn, R. (2014). An evaluation of supervised and unsupervised classification techniques for marine benthic habitat mapping using multibeam echosounder data. *ICES J. Mar. Sci.* 72, 1498–1513. doi: 10.1093/icesjms/fsu223

Chiles, J. P., and Delfiner, P. (2009). *Geostatistics: Modeling Spatial Uncertainty*. Hoboken, NJ: John Wiley & Sons.

Cramér, H. (1946). *Mathematical Methods of Statistics*. Princeton: Princeton University Press.

Cressie, N. (1990). The origins of kriging. *Math. Geol.* 22, 239–252. doi: 10.1007/bf00889887

Cui, X., Bianchi, T. S., Savage, C., and Smith, R. W. (2016). Organic carbon burial in fjords: terrestrial versus marine inputs. *Earth Planet. Sci. Lett.* 451, 41–50. doi: 10.1016/j.scitotenv.2018.04.242

Dadey, K. A., Janecek, T., and Klaus, A. (1992). "Dry-bulk density: its use and determination," in *Proceedings of the Ocean Drilling Program, Scientific Results*, College Station, TX.

Diesing, M., Kröger, S., Parker, R., Jenkins, C., Mason, C., and Weston, K. (2017). Predicting the standing stock of organic carbon in surface sediments of the North–West European continental shelf. *Biogeochemistry* 135, 183–200. doi: 10.1007/s10533-017-0310-4

Duarte, C. M., Losada, I. J., Hendriks, I. E., Mazarrasa, I., and Marbà, N. (2013). The role of coastal plant communities for climate change mitigation and adaptation. *Nat. Clim. Chang.* 3:961. doi: 10.1371/journal.pone.0044727

Dürr, H. H., Laruelle, G. G., van Kempen, C. M., Slomp, C. P., Meybeck, M., and Middelkoop, H. (2011). Worldwide typology of nearshore coastal systems: defining the estuarine filter of river inputs to the oceans. *Estuar. Coast.* 34, 441–458. doi: 10.1007/s12237-011-9381-y

Edwards, A., and Sharples, F. (1986). *Scottish Sea Lochs: A Catalogue. Scottish Marine Biological Association*. Peterborough: Nature Conservancy Council.

Ehlers, J., Gibbard, P. L., and Rose, J. (1991). *Glacial Deposits in Great Britain and Ireland*. Rotterdam: Balkema.

Flemming, B. W., and Delafontaine, M. T. (2000). Mass physical properties of muddy intertidal sediments: some applications, misapplications and non-applications. *Cont. Shelf Res.* 20, 1179–1197. doi: 10.1016/s0278-4343(00)00018-2

Folk, R. L. (1954). The distinction between grain size and mineral composition in sedimentary-rock nomenclature. *J. Geol.* 62, 344–359. doi: 10.1086/626171

Friedrich, J., Janssen, F., Aleynik, D., Bange, H. W., Boltacheva, N. A., Çağatay, M. N., et al. (2014). Investigating hypoxia in aquatic environments: diverse approaches to addressing a complex phenomenon. *Biogeosciences* 11, 1215–1259. doi: 10.5194/bg-11-1215-2014

Guinan, J., Charlesworth, M., Service, M., and Oliver, T. (2001). Sources and geochemical constraints of polycyclic aromatic hydrocarbons (PAHs) in sediments and mussels of two Northern Irish Sea-loughs. *Mar. Pollut. Bull.* 42, 1073–1081. doi: 10.1016/s0025-326x(01)00077-7

Harris, D., Horwáth, W. R., and Van Kessel, C. (2001). Acid fumigation of soils to remove carbonates prior to total organic carbon or carbon-13 isotopic analysis. *Soil Sci. Soc. Am. J.* 65, 1853–1856.

Hedges, J. I., Keil, R. G., and Benner, R. (1997). What happens to terrestrial organic matter in the ocean? *Organ. Geochem.* 27, 195–212. doi: 10.1016/s0146-6380(97)00066-1

Howe, J. A., Austin, W. E., Forwick, M., Paetzel, M., Harland, R., and Cage, A. G. (2010). Fjord systems and archives: a review. *Geol. Soc. Spec. Publ.* 344, 5–15. doi: 10.1144/sp344.2

Howe, J. A., Shimmield, T., Austin, W. E., and Longva, O. (2002). Post-glacial depositional environments in a mid-high latitude glacially-overdeepened sea loch, inner Loch Etive, western Scotland. *Mar. Geol.* 185, 417–433. doi: 10.1016/s0025-3227(01)00299-7

Ierodiaconou, D., Monk, J., Rattray, A., Laurenson, L., and Versace, V. L. (2011). Comparison of automated classification techniques for predicting benthic biological communities using hydroacoustics and video observations. *Cont. Shelf Res.* 31, S28–S38.

Inall, M., Cottier, F., Griffiths, C., and Rippeth, T. (2004). Sill dynamics and energy transformation in a jet fjord. *Ocean Dyn.* 54, 307–314.

Kaskela, A. M., Kotilainen, A. T., Alanen, U., Cooper, R., Green, S., Guinan, J., et al. (2019). Picking up the pieces–Harmonising and collating seabed substrate data for European maritime areas. *Geosciences* 9:84. doi: 10.3390/geosciences9020084

Keil, R. G., Mayer, L. M., Quay, P. D., Richey, J. E., and Hedges, J. I. (1997). Loss of organic matter from riverine particles in deltas. *Geochim. Cosmochim. Acta* 61, 1507–1511. doi: 10.1016/s0016-7037(97)00044-6

Lark, R. M., Dove, D., Green, S. L., Richardson, A. E., Stewart, H., and Stevenson, A. (2012). Spatial prediction of seabed sediment texture classes by cokriging from a legacy database of point observations. *Sediment. Geol.* 281, 35–49. doi: 10.1016/j.sedgeo.2012.07.009

Lark, R. M., Marchant, B. P., Dove, D., Green, S. L., Stewart, H., and Diesing, M. (2015). Combining observations with acoustic swath bathymetry and backscatter to map seabed sediment texture classes: the empirical best linear unbiased predictor. *Sediment. Geol.* 328, 17–32. doi: 10.1016/j.sedgeo.2015.07.012

Lo Giudice Cappelli, E., Clarke, J. L., Smeaton, C., and Davidson, K. (2019). Organic carbon rich sediments: benthic foraminifera as bio-indicators of depositional environments. *Biogeosciences* 16, 3725–3746. doi: 10.5194/bg-2019-2125

Luisetti, T., Turner, R. K., Andrews, J. E., Jickells, T. D., Kröger, S., Diesing, M., et al. (2019). Quantifying and valuing carbon flows and stores in coastal and shelf ecosystems in the UK. *Ecosyst. Serv.* 35, 67–76. doi: 10.1016/j.ecoser.2018.10.013

Mayer, L. M. (1994). Relationships between mineral surfaces and organic carbon concentrations in soils and sediments. *Chem. Geol.* 114, 347–363. doi: 10.1016/0009-2541(94)90063-9

McBreen, F., Wilson, J. G., Mackie, A. S., and Aonghusa, C. N. (2008). Seabed mapping in the southern Irish Sea: predicting benthic biological communities based on sediment characteristics. *Chall. Mar. Ecosyst.* 606, 93–103. doi: 10.1007/978-1-4020-8808-7_9

McIntosh, A. D., Fryer, R. J., Webster, L., and Cundy, A. B. (2012). Long-term fate of polycyclic aromatic hydrocarbons (PAH) in sediments from loch leven after closure of an aluminium smelter. *J. Environ. Monit.* 14, 1335–1344. doi: 10.1039/c2em11006g

Middelburg, J. J., and Levin, L. A. (2009). Coastal hypoxia and sediment biogeochemistry. *Biogeosciences* 6, 1273–1293. doi: 10.5194/bg-6-1273-2009

Mitchell, P. J., Aldridge, J., and Diesing, M. (2019). Legacy data: how decades of seabed sampling can produce robust predictions and versatile products. *Geosciences* 9:182. doi: 10.3390/geosciences9040182

Nairn, R. (2005). *Ireland's Coastline: Exploring its Nature and Heritage*. West Link Park: Collins Press.

O'Cofaigh, C., Weilbach, K., Lloyd, J. M., Benetti, S., Callard, S. L., Purcell, C., et al. (2019). Early deglaciation of the British-Irish ice sheet on the Atlantic shelf northwest of Ireland driven by glacioisostatic depression and high relative sea level. *Quat. Sci. Rev.* 208, 76–96. doi: 10.1016/j.quascirev.2018.12.022

Peters, J. L., Benetti, S., Dunlop, P., and Cofaigh, C. O. (2015). Maximum extent and dynamic behaviour of the last British–Irish ice sheet west of Ireland. *Quat. Sci. Rev.* 128, 48–68. doi: 10.1016/j.quascirev.2015.09.015

Russell, M., Robinson, C. D., Walsham, P., Webster, L., and Moffat, C. F. (2011). Persistent organic pollutants and trace metals in sediments close to scottish marine fish farms. *Aquaculture* 319, 262–271. doi: 10.1016/j.aquaculture.2011.06.030

Russell, M., Webster, L., Walsham, P., Packer, G., Dalgarno, E. J., McIntosh, A. D., et al. (2008). Composition and concentration of hydrocarbons in sediment samples from the oil producing area of the East Shetland Basin, Scotland. *J. Environ. Monit.* 10, 559–569. doi: 10.1039/b715765g

Serpetti, N., Heath, M., Rose, M., and Witte, U. (2012). High resolution mapping of sediment organic matter from acoustic reflectance data. *Hydrobiologia* 680, 265–284. doi: 10.1007/s10750-011-0937-4

Sinnot, A. M., and Devoy, R. J. N. (1992). The geomorphology of Ireland's coastline: patterns, processes and future prospects. *Hommes Terres Nord* 3, 145–153. doi: 10.3406/htn.1992.2370

Smeaton, C., Austin, W., Davies, A., Baltzar, A., Abell, R. E., and Howe, J. A. (2016). Substantial stores of sedimentary carbon held in mid-latitude fjords. *Biogeosciences* 13, 5771–5787. doi: 10.5194/bg-13-5771-2016

Smeaton, C., and Austin, W. E. (2017). Sources, sinks, and subsidies: terrestrial carbon storage in mid-latitude fjords. *J. Geophys. Res. Biogeosci.* 122, 2754–2768. doi: 10.1002/2017jg003952

Smeaton, C., Austin, W. E., Davies, A., Baltzer, A., Howe, J. A., and Baxter, J. M. (2017). Scotland's forgotten carbon: a national assessment of mid-latitude fjord sedimentary stocks. *Biogeosciences* 14, 5663–5674. doi: 10.5194/bg-14-5663-2017

Smith, R. W., Bianchi, T. S., Allison, M., Savage, C., and Galy, V. (2015). High rates of organic carbon burial in fjord sediments globally. *Nat. Geosci.* 8, 450–453. doi: 10.1038/ngeo2421

Staalstrøm, A., and Røed, L. P. (2016). Vertical mixing and internal wave energy fluxes in a sill fjord. *J. Mar. Syst.* 159, 15–32. doi: 10.1016/j.jmarsys.2016.02.005

Stigebrandt, A. (2012). "Hydrodynamics and circulation of fjords," in *Encyclopedia of Lakes and Reservoirs. Encyclopedia of Earth Sciences Series*, eds L. Bengtsson, R. W. Herschy, and R. W. Fairbridge, (Dordrecht: Springer), 327–344. doi: 10.1007/978-1-4020-4410-6_247

Syvitski, J. P., Burrell, D. C., and Skei, J. M. (1987). *Fjords: Processes and Products*. Berlin: Springer Science & Business Media.

Syvitski, J. P., and Shaw, J. (1995). Sedimentology and geomorphology of fjords. *Dev. Sedimentol.* 53, 113–178. doi: 10.1016/s0070-4571(05)80025-1

Webster, L., Fryer, R. J., Dalgarno, E. J., Megginson, C., and Moffat, C. F. (2001). The polycyclic aromatic hydrocarbon and geochemical biomarker composition of sediments from voes and coastal areas in the Shetland and Orkney Islands. *J. Environ. Monit.* 3, 591–601. doi: 10.1039/B106408H

Webster, L., Fryer, R. J., Megginson, C., Dalgarno, E. J., McIntosh, A. D., and Moffat, C. F. (2004). The polycyclic aromatic hydrocarbon and geochemical biomarker composition of sediments from sea lochs on the west coast of Scotland. *J. Environ. Monit.* 6, 219–228.

Webster, L., McIntosh, A. D., Dalgarno, E. J., Megginson, C., Shepherd, N. J., and Moffat, C. F. (2003). The polycyclic aromatic hydrocarbon composition of mussels (*Mytilus edulis*) from Scottish coastal waters. *J. Environ. Monit.* 5, 150–159. doi: 10.1039/b208691n

Webster, L., McIntosh, A. D., Moffat, C. F., Dalgarno, E. J., Brown, N. A., and Fryer, R. J. (2000). Analysis of sediments from Shetland Island voes for polycyclic aromatic hydrocarbons, steranes and triterpanes. *J. Environ. Monit.* 2, 29–38. doi: 10.1039/a907556i

Wilson, R. J., Speirs, D. C., Sabatino, A., and Heath, M. R. (2018). A synthetic map of the north-west European shelf sedimentary environment for applications in marine science. *Earth Syst. Sci. Data* 10, 109–130. doi: 10.5194/essd-10-109-2018

Woulds, C., Bouillon, S., Cowie, G. L., Drake, E., Middelburg, J. J., and Witte, U. (2016). Patterns of carbon processing at the seafloor: the role of faunal and microbial communities in moderating carbon flows. *Biogeosciences* 13, 4343–4357. doi: 10.5194/bg-13-4343-2016

Woulds, C., Cowie, G. L., Levin, L. A., Andersson, J. H., Middelburg, J. J., Vandewiele, S., et al. (2007). Oxygen as a control on sea floor biological communities and their roles in sedimentary carbon cycling. *Limnol. Oceanogr.* 52, 1698–1709. doi: 10.4319/lo.2007.52.4.1698

Conflict of Interest: The authors declare that the research was conducted in the absence of any commercial or financial relationships that could be construed as a potential conflict of interest.

Copyright © 2019 Smeaton and Austin. This is an open-access article distributed under the terms of the Creative Commons Attribution License (CC BY). The use, distribution or reproduction in other forums is permitted, provided the original author(s) and the copyright owner(s) are credited and that the original publication in this journal is cited, in accordance with accepted academic practice. No use, distribution or reproduction is permitted which does not comply with these terms.

frontiers in Earth Science

ORIGINAL RESEARCH
published: 05 November 2019
doi: 10.3389/feart.2019.00277

Muddying the Picture? Forecasting Particulate Sources and Dispersal Patterns in Managed Catchments

Janet Cristine Richardson[1], David Mark Hodgson[1], Paul Kay[2], Benjamin J. Aston[3] and Andrew C. Walker[3]*

[1] Stratigraphy Group, School of Earth and Environment, University of Leeds, Leeds, United Kingdom, [2] School of Geography, University of Leeds, Leeds, United Kingdom, [3] Yorkshire Water, Clean Water and Catchment Strategy, Bradford, United Kingdom

Satellite imagery and climate change projections improve our ability to map and forecast sediment sources and transport pathways at high resolution, which is vital for catchment management. Detailed assessment of temporal and spatial changes in erosion risk are key to forecasting pollutant dispersal, which affects water treatment costs and ecology. Outputs from scenario modeling of the River Derwent catchment, Yorkshire, indicate clear spatial and temporal trends in erosion risk. These trends are not picked up by using traditional methods, which rely on static land use maps. Using satellite-derived maps show that lower resolution traditional land-use maps relatively underestimate erosion risk in terms of location of source areas and seasonal variation in erosion risk. Seasonal variation in agricultural practices can be assessed by incorporating bare land variation into models, which show that erosion risk is relatively overestimated if all agricultural land is assumed to have the same character. Producing seasonal land use maps also allows the assessment of temporal variation in rainfall, which in combination with climate change projections allows for adaptable management plans. The bias in gradient in modeling, which assumes that high gradients result in greater sediment erosion risk, show that traditional models underestimate the contribution of erosion risk in lowland areas. This is compounded by the absence of artificial drainages in topographic rasters, which increases connectivity in lowland areas. By producing end member scenarios, model outputs help to inform where catchment management should be targeted, and whether seasonal interventions should be implemented. This information is vital to communicate with landowners when they implement catchment management practices, such as sediment traps and earth bunds. Adaption of erosion risk modeling practices is urgently needed in order to quantify the impact of artificial interference in which human activity disrupts 'natural' sediment source-to sink configurations, such as integrating new pathways and stores due to land use change and management. Furthermore, integrating higher resolution catchment modeling and improved seasonal forecasts of pollutant flux to oceans will permit more effective interventions. This paper highlights single output erosion risk maps are not effective to inform catchment management.

Keywords: erosion risk, satellite imagery, seasonality, land use, sediment budget, diffuse pollution

OPEN ACCESS

Edited by:
Barbara Mauz,
University of Salzburg, Austria

Reviewed by:
Jorge Lorenzo-Trueba,
Montclair State University, United States
Michael Andrew Clare,
University of Southampton, United Kingdom
Valerio Acocella,
Roma Tre University, Italy

****Correspondence:***
Janet Cristine Richardson
J.C.Richardson@leeds.ac.uk

Specialty section:
This article was submitted to Sedimentology, Stratigraphy and Diagenesis, a section of the journal Frontiers in Earth Science

Received: *07 May 2019*
Accepted: *11 October 2019*
Published: *05 November 2019*

Citation:
Richardson JC, Hodgson DM, Kay P, Aston BJ and Walker AC (2019) Muddying the Picture? Forecasting Particulate Sources and Dispersal Patterns in Managed Catchments. Front. Earth Sci. 7:277. doi: 10.3389/feart.2019.00277

INTRODUCTION

One of the major uncertainties facing several global industries is forecasting the distribution and impact of particulates and pollutants in the water supply system (Owens et al., 2005; Syvitski et al., 2005; Collins et al., 2011; Syvitski and Kettner, 2011; Zalasiewicz et al., 2016; Hodgson et al., 2018). A holistic approach is needed to improve the forecast of particulate source areas and their entrainment, transport, and deposition over different temporal and spatial scales (Dietrich and Dunne, 1978; Slaymaker, 1982; Köthe, 2003; Bracken et al., 2015). Recent advances in high resolution satellite imagery, digital elevation models (DEM) and open-source GIS software have made it possible to constrain the flux (source areas and pathways) of particulates (e.g., Mertes, 2002; Coulthard et al., 2012), thus reducing the need for extensive fieldwork. The erosion, transport and deposition (source, storage and sinks) of fine-grained sediment (and associated particulates) is complicated, and can change temporally and spatially due to variations in hillslope processes and the supply of sediment (e.g., Bryan, 2000; Walling et al., 2000; Huang et al., 2002), hydrology (e.g., Mossa, 1996) and human intervention (e.g., Walling and Fang, 2003). Typically, sediment transport is not a single event, with particles moving through the catchment as a sediment cascade (Fryirs, 2013). Long-term sediment transport patterns are complicated by changing boundary conditions, such as tectonics and climate (e.g., Tucker, 2004). However, humans are the main geomorphic agent globally (Wilkinson and McElroy, 2007) due to artificial drainage and land use changes impacting sediment supply (Lane, 2003; Orr and Carling, 2006; Walling, 2006; Milledge et al., 2012). For example, Farnsworth and Milliman (2003) estimated that between 80–90% of fluvial sediment delivered to oceans is directly or indirectly the result of human activity.

Fine grained particles are a natural part of a river's sediment budget and desktop based modeling offers a rapid and repeatable way to assess source-to-sink relationships under changing conditions. Too much fine grained sediment in the river channel system have been shown to cause multiple impacts, such as increased flood risk (due to deposition in the channel reducing capacity), decreased ecological quality and associated impacts on water quality (Holmes, 1988; Dampney et al., 2002; Covich et al., 2004; Greig et al., 2005; Owens et al., 2005; Bilotta and Brazier, 2008; Collins et al., 2011; Reaney et al., 2011; Rickson, 2014). Furthermore, due to the adsorptive properties of fine grained sediment, it is a multiple stressor in terms of water quality (Rickson, 2014) because of the increased potential of adsorption of nutrients (e.g., phosphorous; Collins et al., 2005; Ballantine et al., 2009), pesticides, medicines (e.g., Kronvang et al., 2003; Zhou et al., 2011) and heavy metals. Too much sediment in the channel causes increased water extraction costs (e.g., Holmes, 1988), changes in channel morphology (Owens et al., 2005), undermines river restoration efforts (Reaney et al., 2011), forces dredging of waterways/reservoirs for flood defense, and causes loss of recreational areas (Owens et al., 2005; Kondolf et al., 2014). Soil erosion also reduces soil productivity by removing top-soil (Vrieling et al., 2008), and was identified as a key priority for the protection of soil by the European Union, who estimated soil loss costs to be €7 billion/year within Europe (Panagos et al., 2014). Nonetheless, too little fine grained sediment in the channel can lead to erosion and 'hungry water,' which is often associated with impoundment (e.g., Heckmann et al., 2017). A balance between the natural regime suspended sediment load, and when this becomes too much, is needed in sediment management as the impacts are complicated and multidimensional (Collins et al., 2011). Understanding where to place interventions to reduce sediment loads within river networks has multiple benefits to catchment users, with control of the source areas seen as the preferred approach before different areas of the catchment can join up (Heathwaite et al., 2005; Lane et al., 2006; Wilkinson et al., 2009; Rickson, 2014). Catchment management refers to any intervention that is put in place within a river catchment, and ranges from 'natural flood management' such as earth bunds and woody debris dams, through land management practices employed by farmers, to hard engineering such as embankments.

Fine-grained sediment is often referred to as a diffuse pollutant, which cannot be attributed to a single identifiable source ('non-point source' pollution; Munafo et al., 2005). Understanding the sources of fine grained sediment is vital for land management due to the reasons above. In recent years, there has been an increasing dominance of mathematical models using a risk based approach to assess erosion risk (e.g., Van Sickle and Paulsen, 2008). In a risk-based model, sources of risk, such as the source areas of fine grained sediment, are distributed across a catchment (Reaney et al., 2011). The main assumption for risk-based modeling is that the amount of erosion in a piece of land can be traced to the properties of the landscape including how it is managed. In this sense, erosion risk relates to the likelihood of erosion occurring at a specific location, in relation to diffuse pollution (Heathwaite, 2003; Heathwaite et al., 2003a,b; Jordan and Smith, 2005; Munafo et al., 2005).

A range of approaches, equations and models exist to assess erosion risk and to identify critical source areas within a catchment, including the revised universal soil loss equation (RUSLE; e.g., Boggs et al., 2001; Lu et al., 2004; Gitas et al., 2009), the index of connectivity (Cavalli et al., 2013), and Sensitive Catchment Integrated Modeling and Analysis Platform (SCIMAP; Lane et al., 2006, 2009; Reaney et al., 2011; Milledge et al., 2012). Many erosion risk models, which can be used in GIS software, require at a minimum data on land use, rainfall and slope (DEM), but can be used in the absence of spatially distributed in-river data. A risk-based model associates erosion risk with the availability of soil to erode (e.g., resistance, land-use etc.) and the ability to transport this to the channel network (gradient, connectivity etc.).

Studies investigating erosion risk rarely account for seasonal variation in sediment production. This is because the land-use cover data used, such as land cover maps from the Centre of Ecology and Hydrology (CEH) or the European Union's 'coordination of information on the environment' program land use maps (CORINE) produce a yearly averaged erosion risk output map (e.g., Reaney et al., 2011; Horton et al., 2015). Reaney et al. (2011) highlight that the CEH land use map from 2000 used in their study of the River Eden, Cumbria is probably misinterpreted as it is synoptic and dated. Erosion

risk outputs, therefore, relate to yearly averages, and land use maps do not capture the seasonal presence of bare land (Reaney et al., 2011; Horton et al., 2015). This is especially apparent in catchments from temperate climates, where agricultural practices are characterized by marked variation in crop densities and types between seasons.

Erosion risk, and the associated impact on suspended sediment loads, varies due to changes in erosive forces, such as changes in precipitation and land use (Mossa, 1996; Bryan, 2000; Walling et al., 2000; Huang et al., 2002; Walling and Fang, 2003). The changes in erosive forces are also exacerbated by land-use management and may be compounded by future climate change. For example, the impact of agricultural land on sediment supply is highest when the soil is left bare and during management activities (e.g., Le Bissonnais et al., 2002; Heathwaite et al., 2005; Cerdan et al., 2010). The increasing availability of data, including rainfall variation, satellite imagery and open source GIS software, has allowed some seasonal assessments of erosion risk to be carried out in Europe (e.g., Crete, Panagos et al., 2014; Greece, Gitas et al., 2009) and South America (e.g., Brazil, Vrieling et al., 2008) in a timely manner without extensive fieldwork. However, the temporal variation in erosion risk vulnerability (related to erosive forces and soil erosion) is often not incorporated into erosion risk modeling, which is a key component of diffuse pollution catchment management, especially in light of climate change and the longevity of catchment interventions. Furthermore, the human influence on the drainage network, through construction of artificial pathways, is rarely included in models. These additional pathways can increase rates of transport in areas of lowland, increasing connectivity to the river channels (e.g., through tramlines) (Heathwaite et al., 2005) and increasing erosion risk. This challenges the dogma that erosion risk is highest in steeper areas of a catchment due to the water flowing faster downslope and reducing infiltration rates (e.g., Liu and Singh, 2004).

We aim to assess end member erosion risk model outputs, based on different scenarios, in a single catchment, the River Derwent in northern United Kingdom, which has both upland and lowland areas. The catchment is in a temperate climate that sees marked seasonal land use changes, and therefore represents a suitable case study catchment to assess erosion risk modeling. We address the following objectives: (i) to compare seasonal variation in erosion risk using high resolution satellite imagery and traditional static land use maps (e.g., CEH or CORINE); (ii) to assess the use of erosion risk models in catchments dominated by agriculture and artificial drainage; (iii) to assess how source areas may change under climate change projections; (iv) to assess the causes of erosion risk within the River Derwent catchment; and (v) to discuss concepts of source-to-sink in terms of a modern catchment dominated by agriculture.

MATERIALS AND METHODS

Study Area

The River Derwent, Yorkshire, United Kingdom, is a tributary of the River Ouse drainage system. The Derwent catchment (2,057 km^2), comprises the River Rye, River Hertford, River Derwent and The Beck (**Figure 1A**). The catchment has extensive upland areas in the north, and around the chalk escarpment in the north east. However, much of the catchment comprises lowland areas (51% < 57 m; **Figure 1B**). The lowland catchment is dominated by agriculture due to the fertile soil. Rainfall varies slightly across the catchment, from 1,100 $mmyr^{-1}$ at the source in the North York Moors to 600 $mmyr^{-1}$ in the lowland area of Barmby Barrage (**Figure 1A**). The bedrock substrate of the Derwent catchment predominantly comprises mudstones, siltstones and sandstones (e.g., Ancholme Group, Corallion Group; Mercia Mudstone Group, Ravenscar Group and Sherwood Sandstone Group), and limestones (Great Oolite Group) and chalk (Chalk Group) (**Figure 1C**). The superficial geology (**Figure 1D**) is dominated by glaciolacustrine, glacigenic, glaciofluvial and fluvial deposits, and a lake-fill near Pickering. The River Derwent has a recognized fine grained sediment problem (Royal Haskoning, 2010; Natural England, 2015). Thirteen waterbodies within the catchment have failed to reach an ecological good standard under the Water Framework Directive (River Basin Management Plan Cycle 2) with sediment as a primary reason, whilst water treatment costs at Elvington Treatment Works are escalating, and ∼11,000 tons of sediment per year is removed during water treatment (Sustainable Futures, 2018).

Erosion Risk Modeling

Erosion risk was modeled using the open-source plugin SCIMAP developed by the University of Durham (Lane et al., 2006, 2009; Reaney et al., 2011; Milledge et al., 2012) in 'System for Automated Geoscientific Analyses' (SAGA) GIS (Conrad et al., 2015). We modify the input data to SCIMAP in order to assess seasonality (in terms of rainfall and land use) and the impact of human influence on the catchment. Seasonality was tested in the year 2016 by assessing erosion risk for 1 month of the hydrological year; winter – February 2016; spring – April 2016; summer – July 2016; and autumn – November 2016. The months chosen were dictated by satellite imagery quality in relation to cloud coverage and are deemed representative of each season. SCIMAP requires the following datasets as inputs: DEM, precipitation data and land-use data. The DEM was downloaded from the Ordnance Survey (OS), in British National Grid co-ordinates and has a grid size of 5 m, and a vertical root mean square error of 1.5 m in urban areas and 2.5 m in rural, mountainous and moorland areas. The DEM was clipped to the study area, but no other processing was carried out, such as infilling the data gaps, as the SCIMAP plugin has this option. Rainfall data for the selected months were downloaded from the Met Office via the Centre for Environmental Data Analysis. The data grids, used in the UK Climate Projections 2009 (UKCP09) have a spatial resolution of 5 km. The monthly averages (total, mm) and long term averages (mm) data sets were downloaded, resampled to 5 m, and clipped to the study catchment.

SCIMAP produces a relative assessment of erosion risk across the catchment (a comparison of the riskiness of one location in a catchment compared to another location in a catchment), and does not produce absolute values (e.g., erosion in terms

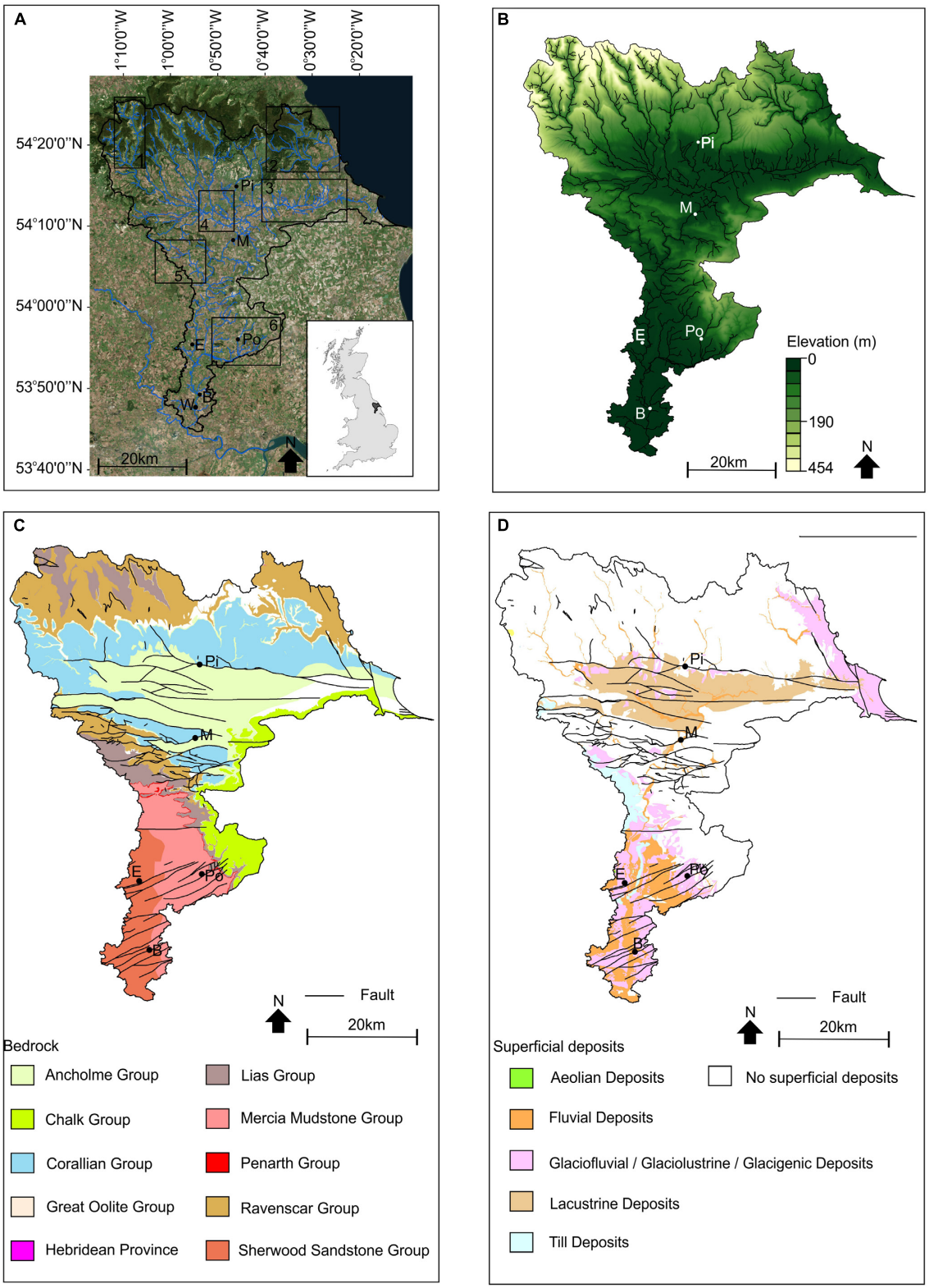


FIGURE 1 | Locations and geological setting of the River Derwent Catchment; **(A)** Location of catchment. Including the sub-catchment locations for assessing macroinvertebrate data. Locations are shown; Pi, Pickering; M, Malton; Po, Pocklington; E, Elvington; B, Bubwith; and W, Wressel; **(B)** elevation variation within the catchment, locations shown; **(C)** bedrock geology and **(D)** superficial geology. Locations shown for **B–D**; Pi, Pickering; M, Malton; Po, Pocklington; E, Elvington; and B, Bubwith.

of tons ha^{-1}); this is because the primary aim of erosion risk modeling is to identify the sources areas of sediment for management purposes. SCIMAP models erosion risk related to soil erosion, and associated in-channel risk, the methodology of this is explained below.

SCIMAP calculates erosion risk based on the energy available for erosion (hydrological risk) and the resistance to erosion (related to the potential for soil erosion), which is used to weight the hydrological risk (Reaney et al., 2011). The risk generation parameter in SCIMAP is a combination of these two parameters:

$$Pi^g = Pi^h \cdot Pi^e$$

Where Pi^g is the risk generation parameter, Pi^h is the energy available to erode the material, and Pi^e is the risk of that material being eroded.

The energy available to erode the material (Pi^h) is represented as a stream power index related to the upstream contributing area, which determines the depth of water and soil erosion potential, and the local slope (Reaney et al., 2011), which is stored in the topographic data:

$$\Omega i = Ai \tan \beta i$$

Where Ωi is the stream power index, Ai is the upstream contributing area and βi is the local slope.

The risk of the material being eroded (Pi^e) is a function of the land-cover, in which each land-cover category is assigned an erosion risk value. SCIMAP uses the following values: Agricultural land – 1; grasslands – 0.03 peat bogs – 0.05; Woodland – 0.05, Heathland – 0.05; urban/sub-urban – 0. The land use map is reclassified to these values in order to run the model. This part of the risk framework assumes that the erodibility of the material, as conditioned by the land cover, is the most important (rather than integrating soil or geological data) (Reaney et al., 2011).

Once the risk generation parameter has been assigned, SCIMAP assesses the likelihood of the eroded material reaching the channel network looking at the hydrological connection of the landscape as defined by the topographic wetness index:

$$k = ln(\alpha / tan\, \beta)$$

Where k is the topographic wetness index, β represents the local slope and α represents the rainfall weighted upslope contributing area. The local slope data are determined by the topographic data, whilst the rainfall data are input in a raster format.

SCIMAP modifies the topographic wetness index, resulting in the network index (Reaney et al., 2011) as Walling et al. (2002) found only very small amounts of the total sediment mobilized are likely to reach the river channel. Therefore, less continuous hydrological flow pathways will result in more on-slope deposition. Therefore, the network index is based on the lowest value of topographic wetness index along a given flow path from the point of interest (source areas) to the drainage network (Lane et al., 2004). The network index combines topographic information (e.g., DEM) with rainfall data. Points with higher values of network index are more likely to be connected to the drainage net for a longer period of time. Only when there is a clear pathway for the sediment to enter the river network is risk considered. If there is erosion in part of the catchment that is not hydrologically connected to the river network, there will be no impact from the sediment production (Reaney et al., 2011).

SCIMAP finally routes and accumulates the risk through the channel network, and it is assumed the risk at a point is the sum of all location risk upstream of that point; this risk loading (the sum of the upstream risk) results in the in-channel risk concentration. The final stage of the SCIMAP framework does not take into account the loss of risk due to deposition or chemical transformations (Reaney et al., 2011). SCIMAP's approach has been validated in a range of studies (e.g., Lane et al., 2006, 2009; Reaney et al., 2011) and is currently the main erosion risk tool used by stakeholders in the United Kingdom, such as the Environment Agency.

The erosion risk data presented here, which are related to the risk generation parameter and hydrological connectivity, range from 0 to 100%, and are shown where there is >50% erosion risk (e.g., the landscape unit has >50% likeliness to be contributing to diffuse pollution in the catchment). In order to compare the different model scenario outputs, the relative in-channel concentration (the risk loading) data were classified as: high risk >1.5 standard deviation; medium risk 0.83 – 1.5 standard deviation, low risk 0.17 – 0.83 standard deviation; and very low risk <0.17 standard deviation. **Table 1** presents the datasets used within the erosion risk modeling undertaken in this paper.

Land Use Data

Commonly, freely available datasets, such as the CORINE land use map or CEH (2015) land use maps, are used in erosion risk mapping. Although these are based on satellite imagery they do not show seasonal variation. Therefore, Sentinel 2 data, freely available from the European Space Agency (spatial resolution of 10 m) were downloaded (bands 2, 3, 4, and 8) and processed in SAGA GIS using image processing tools. Object-based image segmentation creates shapefile segments depending on the colors of the underlying image (e.g., similar greens will form a polygon). Once the image has segments, 50 segments for each land use type are 'trained' by assigning a land use classification. For this project, the following land-use classes were used, based on the CEH land use map: urban/sub-urban; peat bog; pastures; forest; agriculture; moors/heathland; and bare land. As this land use map was employed for erosion risk, the differentiation of different habitats, for example broadleaved forest versus conifer forest, was not required. Supervised classification for shapes is based on the information provided in training cells combined with the color combination of the underlying image. This tool produces a classified land use map for the whole catchment to which the SCIMAP landscape erosion values can be assigned.

Artificial Drainage

SCIMAP, like all GIS software, extracts the drainage network using the upstream contributing area. However, artificial drains/pathways are small features that are not picked up using the normal DEM and extracting processes. Due to the agricultural history of the Derwent Catchment, artificial drains

TABLE 1 | Modeling scenarios and data used.

Scenario	Land use data	Rainfall data	DEM manipulation	End members
CEH land use/Monthly rainfall scenario	CEH land use map (static land use map)	Monthly	n/a	CEH land use model run vs. Satellite land use derived maps
Satellite land use/monthly rainfall scenario	Satellite land use map (based on erosion risk values of 1 for agriculture and bare land)	Monthly	n/a	
Long term rainfall average	Satellite land use map (based on erosion risk values of 1 for agriculture and bare land)	Long term average	n/a (e.g., natural drainage network)	Monthly rainfall vs. long term average rainfall
Artificial drainage network	Satellite land use map (based on erosion risk values of 1 for agriculture and bare land)	Long term average	Artificial network burned into DEM by 1m	Long term rainfall average model run vs. artificial drainage network
Bare land vs. Agriculture land	Satellite land use map (based on erosion risk values of 0.9 for agriculture and 1 bare land)	Monthly	n/a	Satellite land map model run vs. manipulating bare land and agricultural erosion risk values.
Climate change	Satellite land use map (based on erosion risk values of 1 for agriculture and bare land)	Long term averages + climate change scenarios	n/a	Tested for February 2016

(trellised drainage around field boundaries, Radcliffe et al., 2015) are common. Artificial drains, especially during high intensity rainfall events, can provide additional pathways for sediment to enter the drainage network, and therefore need to be incorporated into the modeling. Artificial drainage lines were downloaded as shapefiles from OS maps. These drainage lines were 'burned' into the DEM by 1 m using the 'burn stream network into DEM' tool in SAGA GIS (Conrad et al., 2015); this tool allows the DEM to be artificially deepened in these locations to ensure a flow path is created when the DEM is used in hydrological processing. The depth of the artificial drains is unknown, as they have not been surveyed, and higher resolution topographic information is not available; the 1 m depth is considered a conservative estimate in the absence of depth information.

Climate Change Data

Climate change data were downloaded from the Met Office, via the United Kingdom Climate projects website. The United Kingdom Climate Projections 2009 (UKCP09) cumulative distribution function (CDF) plots were used to change the long term average rainfall raster files downloaded from Centre for Environmental Data Analysis (CEDA), under different climate change forecasts. The month of February was chosen as a test, as climate predictions show wetter winters, until higher resolution UKCP18 data are released (which will be able to look at high intensity rainfall events in more detail). CDF plots for high, medium and low scenarios were looked at with the percent change in rainfall in the following quartiles recorded: Q10, Q50 and Q90; this provides a range of different climate scenarios that can be used to assess future sediment risk changes. Climate change scenarios were run for the years 2020–2049. CDF plots are split into 25 km^2 squares. Therefore, the long term rainfall raster for February was clipped into the squares. Once a square of the raster was clipped, the percent change in rainfall due to a scenario (e.g., high emissions, Q10) was applied to the raster using the raster calculator. For example, if there was a 5.5% increase in rainfall, the raster calculator was used to increase the raster cell values by 5.5% (e.g., cell/100 * 105.5). The new climate change rasters were then used in erosion risk mapping.

Model Runs and Assumptions

Erosion risk scenarios were run using the following assumptions and data (**Table 1**): (1) CEH land use maps (2015 version); (2) 'seasonal' satellite land use; (3) natural drainage; (4) artificial drainage; (5) current rainfall; (6) long term average rainfall; (7) land use risk between bare land and agriculture; and (8) projected climate change (for the month of February only). Running the model with different scenarios produces end members of erosion risk. This allows a range of outputs to be created to help understand the variation of erosion risk within the catchment.

Modifying the DEM by 'burning' the artificial drainage assumes: (1) that the field drains are hydrologically connected to the drainage network and will have flowing water during high flow conditions; (2) that the drains are not dredged by land owners; and (3) that the drains are roughly 1 m in depth (a value used in the absence of field data to verify drain depth). In previous studies of the Derwent catchment, field drains in the River Rye catchment were shown to be an important pathway for the transfer of sediment to the main river network (Sear, 1992). However, Newson (2006) concluded that the level of connectivity needs further investigation. Therefore, using the artificial network forms one end member of model runs. In order to understand variation between different scenario outputs, a DEM of difference was produced, which calculates the difference between two rasters by using the 'minus' tool in ArcGIS.

Morphometry

Morphometry is the quantification of catchments via indices such as river network analysis and stream profile analysis (Horton, 1932; Miller, 1953; Schumm, 1956; Chorley, 1957; Strahler, 1964). Morphometry can provide information on the history of a

catchment, and current system dynamics, such as stream power. The normalized steepness index (K_{SN}) quantifies the stream gradient, and is expected to be relatively consistent along a river course. Variation in the index is typically due to variation in tectonics or climate or lithology (Hack, 1973). The normalized steepness index was calculated using the topotoolbox plugin for Matlab (Schwanghart and Kuhn, 2010; Schwanghart and Scherler, 2014) and the equation is detailed below:

$$K_{SN} = S/A^{-\theta}$$

Where, K_{SN} is the normalized steepness index, S is slope and θ is channel concavity.

Slope was extracted from the DEM using the slope toolbox in GIS. The slope tool calculates the maximum rate of change in value from that original cell to neighboring cells.

Sediment Sensitive Species

Understanding the impact of temporal variation in sediment concentration requires repeated sampling across the entire catchment, with samples taken across the entire range of hydrological flow conditions (Reaney et al., 2011). However, routine water quality sampling is rarely undertaken in catchments. In previous studies assessing erosion risk within catchments, results have been displayed in terms of impacts on salmonids (Reaney et al., 2011) and pearl mussels (Horton et al., 2015). Macroinvertebrates are reliable indicators of environmental conditions (Extence et al., 2013), and have been used to assess water quality in a range of locations (Armitage et al., 1983). One indicator is the Proportion of Sediment Sensitive Invertebrates (PSI; see Extence et al., 2013, for calculation), which looks at the invertebrate communities present to assess the influence of sediment (silt) on the channel bed. Briefly, the different species taxa present are assigned to one of four fine sediment-sensitivity ratings, due to their habitat preference (after extensive literature reviews and assessment of anatomical, physiological and behavioral traits of the species). The overall value is abundance weighted, showing the sensitivity of the whole population sample. PSI varies based on the species present, therefore it can be used to interpret the presence or absence of silt. PSI ranges from 0 (entirely silted bed) to 100 (unsilted bed) (Extence et al., 2013). Macroinvertebrate assemblages are routinely monitored under the Water Framework Directive (WFD) in the United Kingdom, within the Derwent catchment six sub-catchments (**Figure 1A**) were used to assess how helpful PSI is when trying to understand seasonal erosion risk using SCIMAP model outputs. Sediment sensitive invertebrate data were provided by the Environment Agency, who have processed the species present during the Spring and Autumn of 2016 through the PSI method (Extence et al., 2013) and provided a score between 0 and 100 for each site. These datasets combine the data collected during the routine WFD monitoring to produce an average value for the season for each site within the study areas. Within the six sub-catchments, a maximum of 22 sites and minimum of 1 site have fed into the PSI analysis (the spatial coverage of sites is related to WFD pressures in each sub-catchment).

RESULTS

Catchment Morphometry

Figure 2A shows the slope of the River Derwent Catchment. Overall, the catchment has low slopes (<2°). Higher angled slopes can be found in the upland areas and North East areas of the catchment around Pocklington (>8°), and the upland headwater regions in the north of the catchment, north of Pickering (>25°). Normalized steepness index values (**Figure 2B**) are >18 in the upland areas, reflecting the higher slope values. The highest values (>50) can be found along the River Derwent and River Rye, upstream of their confluences. The middle reaches of the River Derwent are characterized by low slopes (<2°) and K_{SN} values below 13, which are dominated by agricultural land use (**Figures 2A,B**).

Erosion Risk Modeling: Scenario Outputs

Seasonal Variation

Erosion risk mapping scenarios for each season (**Figures 3–6**) show: (A) CEH land use map; (B) Satellite-derived land use map; (C) the DEM of difference between the two land use maps; (D) long term rainfall average; (E) monthly rainfall totals; (F) the DEM of difference between the two rainfall scenarios; and (G) the artificial drainage network.

Overall, source areas of sediment are dominated by the agricultural lowland areas. The upland areas that comprise moorland and peatland had a relatively low risk of erosion through all of the modeling scenarios. **Table 2** highlights the percentage of catchment coverage for each risk category between the scenarios tested, and offers a way to semi-quantify the modeling output as SCIMAP produces a relative assessment of erosion risk.

There are clear spatial trends in the yearly 2016 rainfall data (**Figure 7**). Maximum rainfall in February 2016 centered on the escarpment areas to the north east of the catchment and toward the mouth of the catchment. During July, rainfall rates are highest in the east of the catchment. However, in the upland area of the catchment there is not an associated increase in risk due to the land use cover (primarily peat/moorland). In November and April 2016, rainfall rates were lowest in the upland areas of the catchment and highest across the lowland areas. Overall, when using monthly rainfall values, April had more areas of high and medium risk within the catchment (52% coverage of the catchment area, **Table 2**), and February had more areas of low and very low risk (55% coverage of the catchment area, **Table 2**). When using the long term average rainfall data, April had more high and medium risk areas (53% coverage of the catchment area, **Table 2**), and February had more areas of low and very low risk (50% coverage of the catchment area, **Table 2**). In April, there is higher risk of erosion in the upland areas of the catchment, which is not seen during the other months modeled. Overall, when using the long term rainfall values, the DEM of difference highlights that the 2016 monthly values underestimate erosion risk, with the largest difference in February (**Table 2**).

When modeling the difference in land use maps, the main critical source areas (high risk areas) have limited

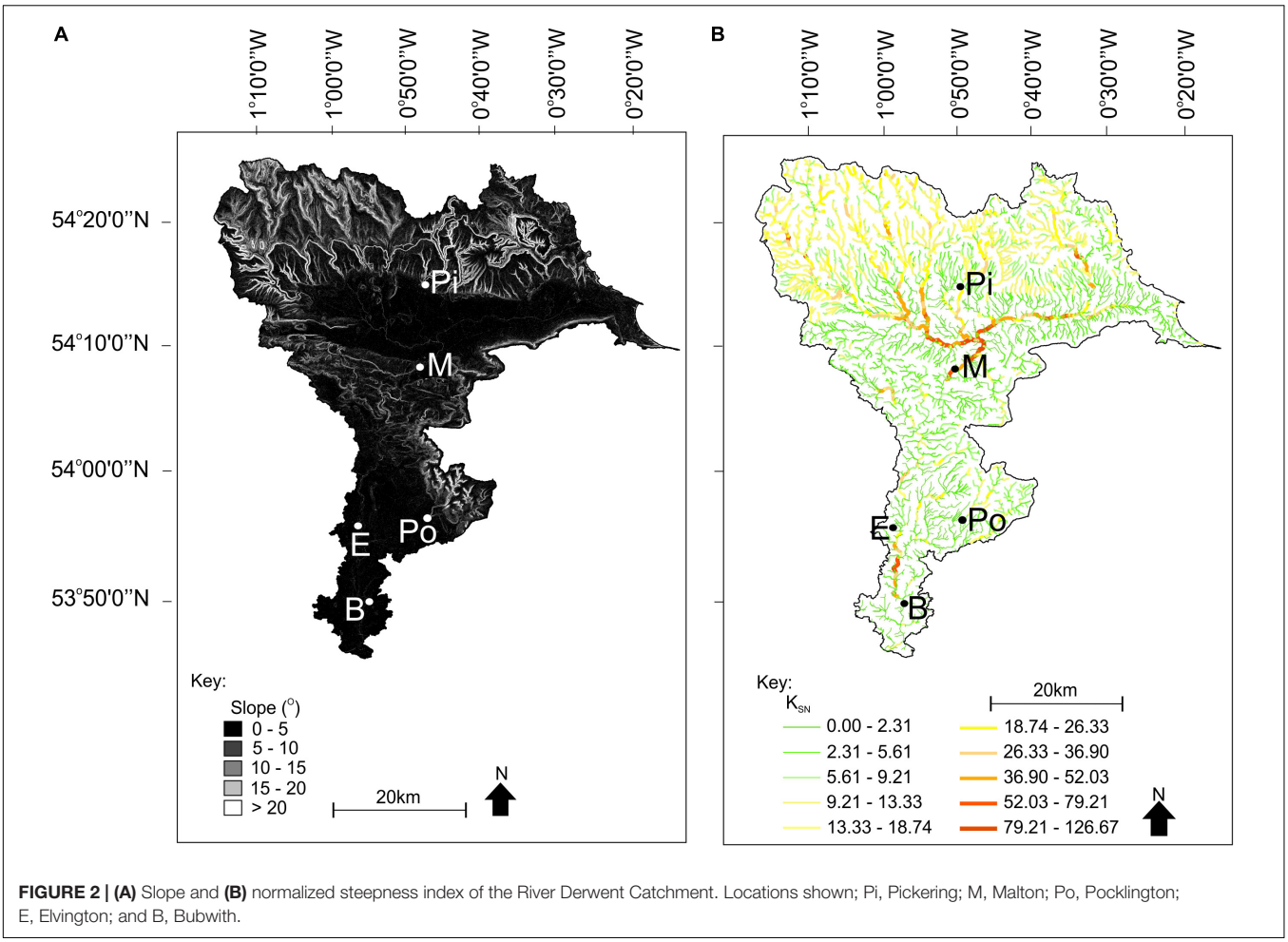


FIGURE 2 | (A) Slope and **(B)** normalized steepness index of the River Derwent Catchment. Locations shown; Pi, Pickering; M, Malton; Po, Pocklington; E, Elvington; and B, Bubwith.

variation between the CEH- and satellite-derived land use maps (**Figures 3–6**), and are reasonably consistent seasonally, in which the lowland areas show greater levels of risk. When using both the CEH- and satellite-derived land use maps, erosion risk was highest in April. However, the satellite-derived land use maps had a greater coverage of high and medium risk areas (53% coverage of the catchment area, **Table 2**) compared to the CEH maps (46% coverage of the catchment area, **Table 2**). There is slightly less risk in the area around Pocklington in November compared to the other months modeled (**Figure 6**). Within each month modeled there are subtle differences between the CEH- and satellite-derived land use maps (when using the monthly rainfall values); as shown by the DEMs of difference (**Figures 3C–6C**). Typically, the CEH land use maps relatively underestimate the coverage of medium erosion risk across the catchment (by up to 6%, **Table 2**) and relatively overestimate areas of very low risk (by up to 7%, **Table 2**) when compared to the satellite-derived land use maps.

Erosion Modeling in Agriculture Dominated Catchments

Integrating the artificial drainage network only has an influence in the agricultural intensive areas, and no changes are seen in the upland areas of the catchment in erosion risk (**Figures 3G–6G**). By increasing the number of pathways there are more medium risk areas in the lowland regions of the Derwent catchment in July (45% coverage of the catchment area, **Table 2**). Overall, incorporating the artificial drainage increases the relative coverage of low risk areas in the lowland areas, across 3 of the 4 seasons modeled compared to the other scenarios modeled (**Table 2**).

Bare land changes seasonally within the Derwent Catchment due to cropping practices. The maximum bare land recorded is 18% (363 km^2) of the catchment in February, reducing to 15% in April and February (314 km^2) with the lowest coverage of bare land being 10% recorded in July (216 km^2). When comparing agricultural land and bare land by manipulating the erosion risk values assigned to the land uses in SCIMAP there is a clear difference in erosion risk between each scenario (**Figure 8**). By integrating differences in erosion risk between bare land and agricultural land with crops visible on the satellite imagery, traditional erosion risk mapping that use the same value for all agricultural land regardless of cropping stage relatively overestimate high and medium risk areas by up to 5%, with the greatest variation in the

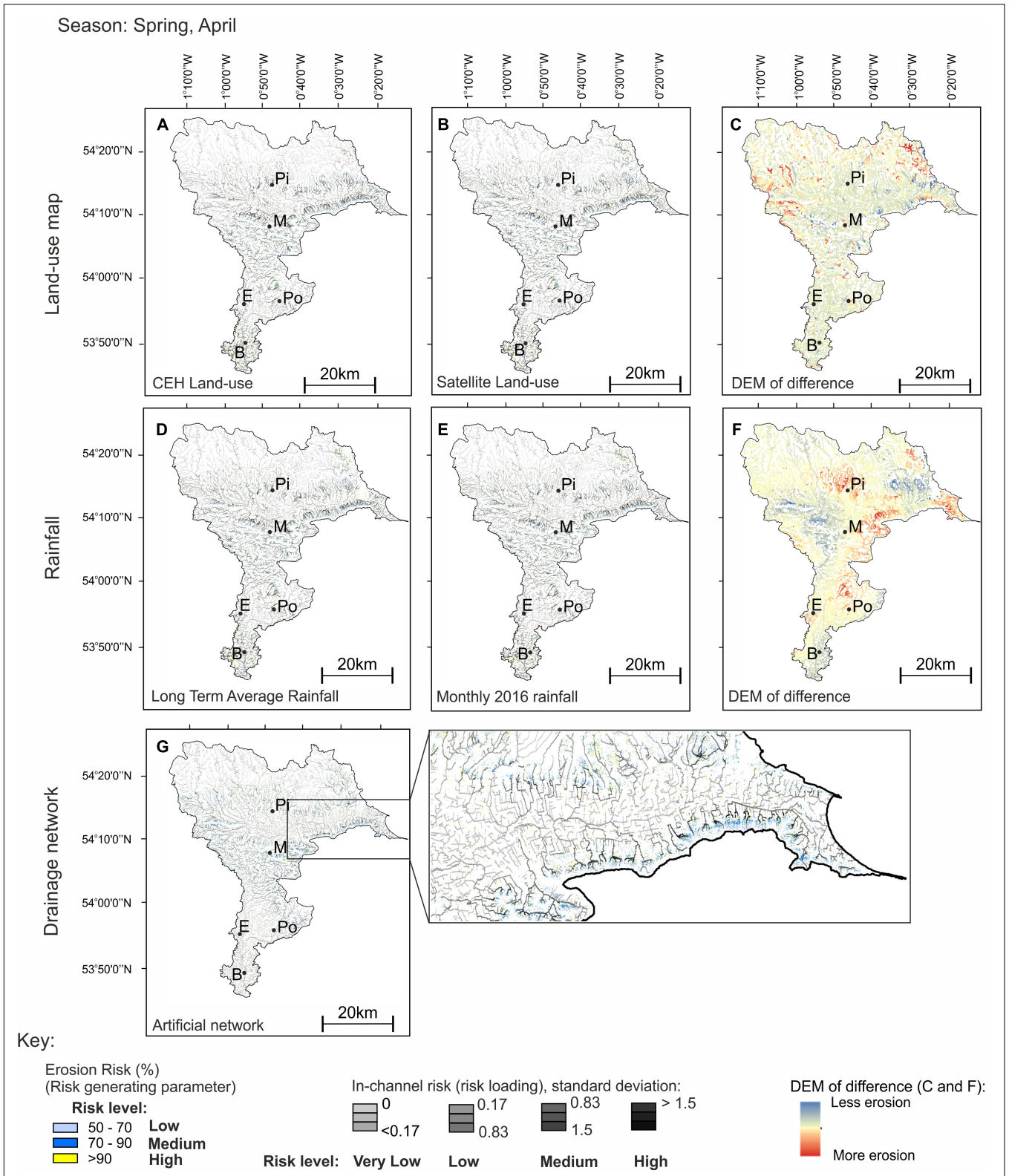


FIGURE 3 | Model scenario outputs for April, **(A)** CEH land use map; **(B)** Satellite derived land use map; **(C)** the DEM of difference between the two land use maps; **(D)** Long term rainfall average; **(E)** monthly rainfall totals; **(F)** the DEM of difference between the two rainfall scenarios; and **(G)** the artificial drainage network. Locations are shown on each map; Pi, Pickering; M, Malton; Po, Pocklington; E, Elvington; B, Bubwith.

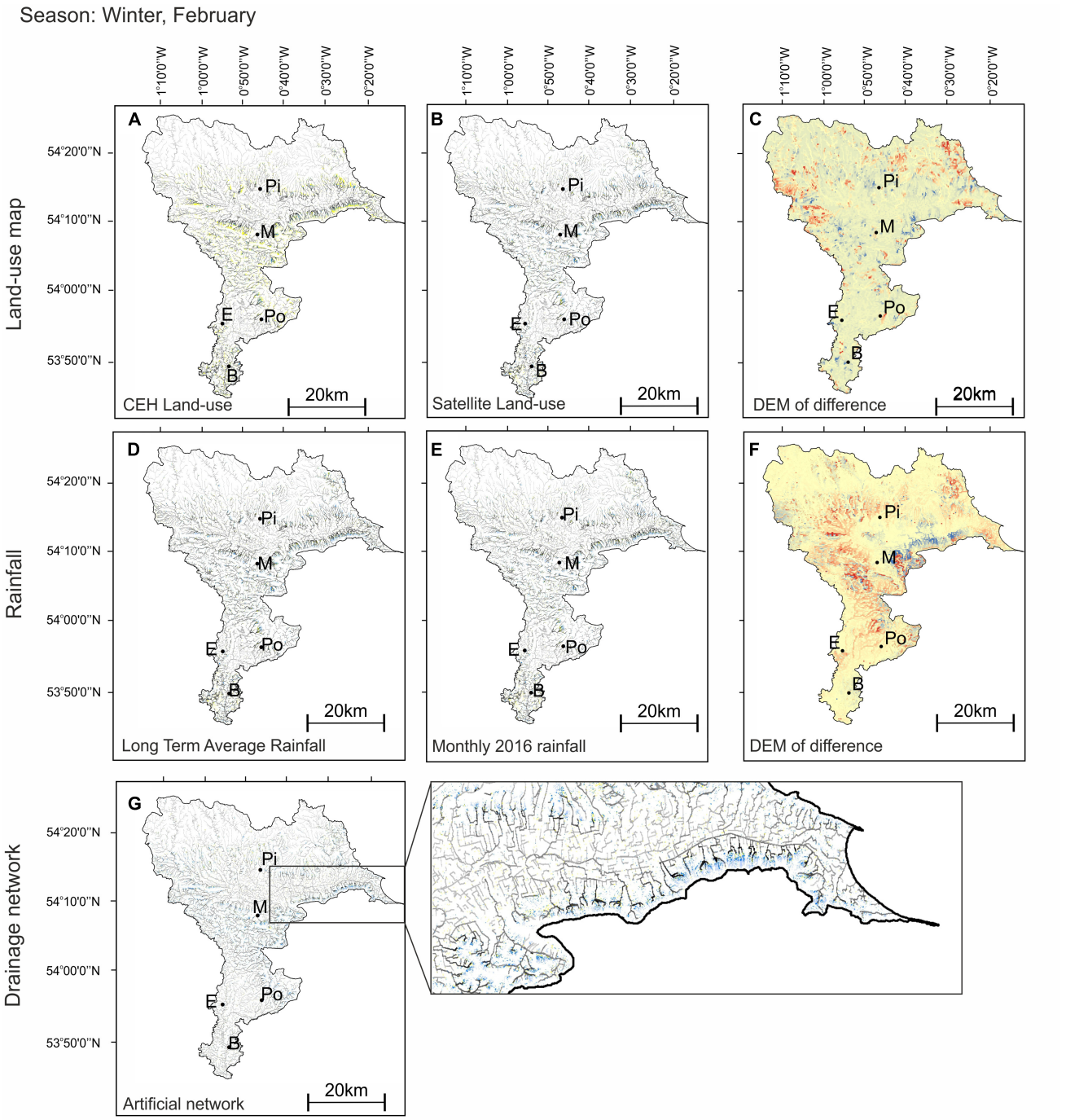


FIGURE 4 | Model scenario outputs for February, **(A)** CEH land use map; **(B)** satellite-derived land use map; **(C)** the DEM of difference between the two land use maps; **(D)** long-term rainfall average; **(E)** monthly rainfall totals; **(F)** the DEM of difference between the two rainfall scenarios; and **(G)** the artificial drainage network. Locations are shown on each map; Pi, Pickering; M, Malton; Po, Pocklington; E, Elvington; B, Bubwith.

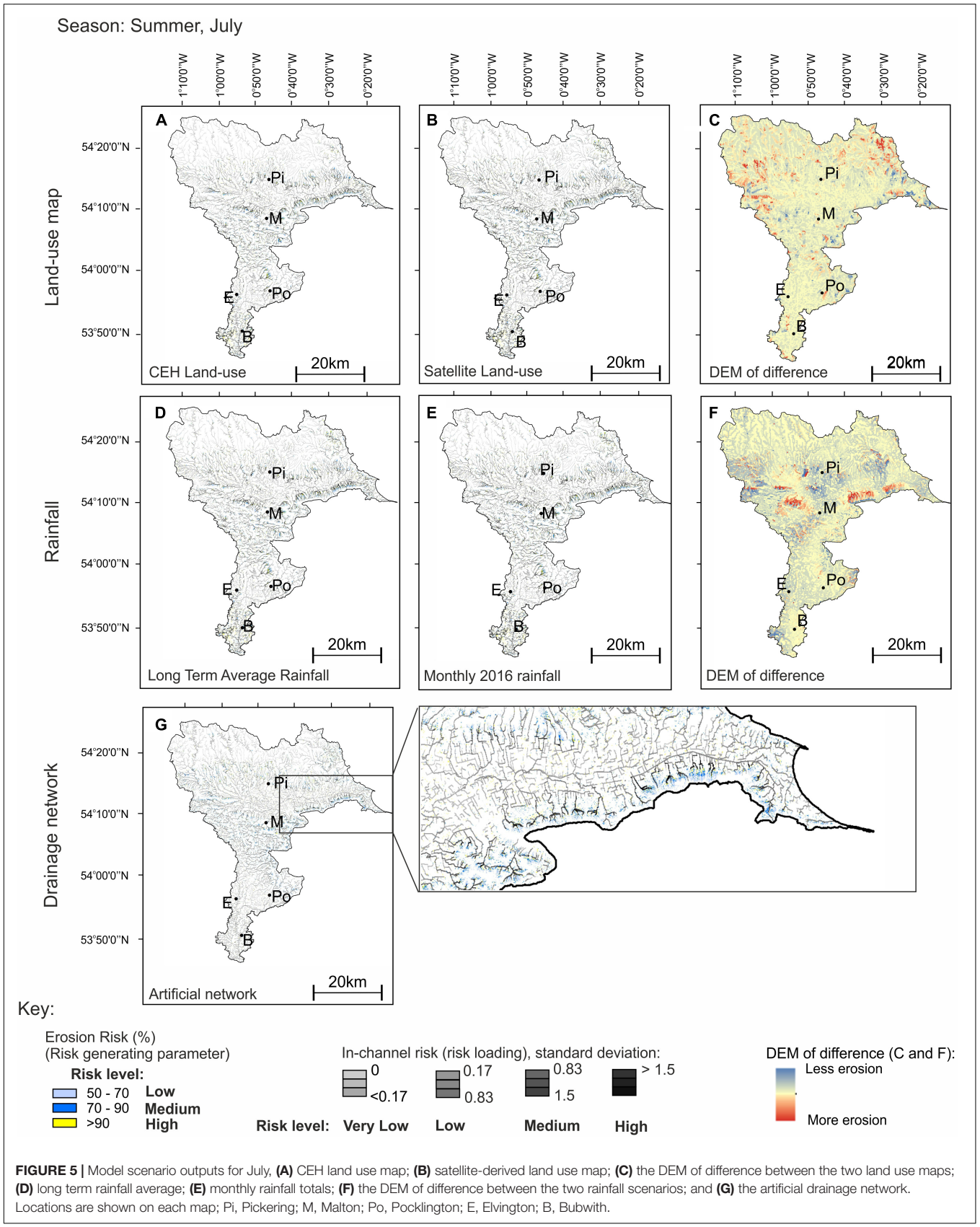


FIGURE 5 | Model scenario outputs for July, **(A)** CEH land use map; **(B)** satellite-derived land use map; **(C)** the DEM of difference between the two land use maps; **(D)** long term rainfall average; **(E)** monthly rainfall totals; **(F)** the DEM of difference between the two rainfall scenarios; and **(G)** the artificial drainage network. Locations are shown on each map; Pi, Pickering; M, Malton; Po, Pocklington; E, Elvington; B, Bubwith.

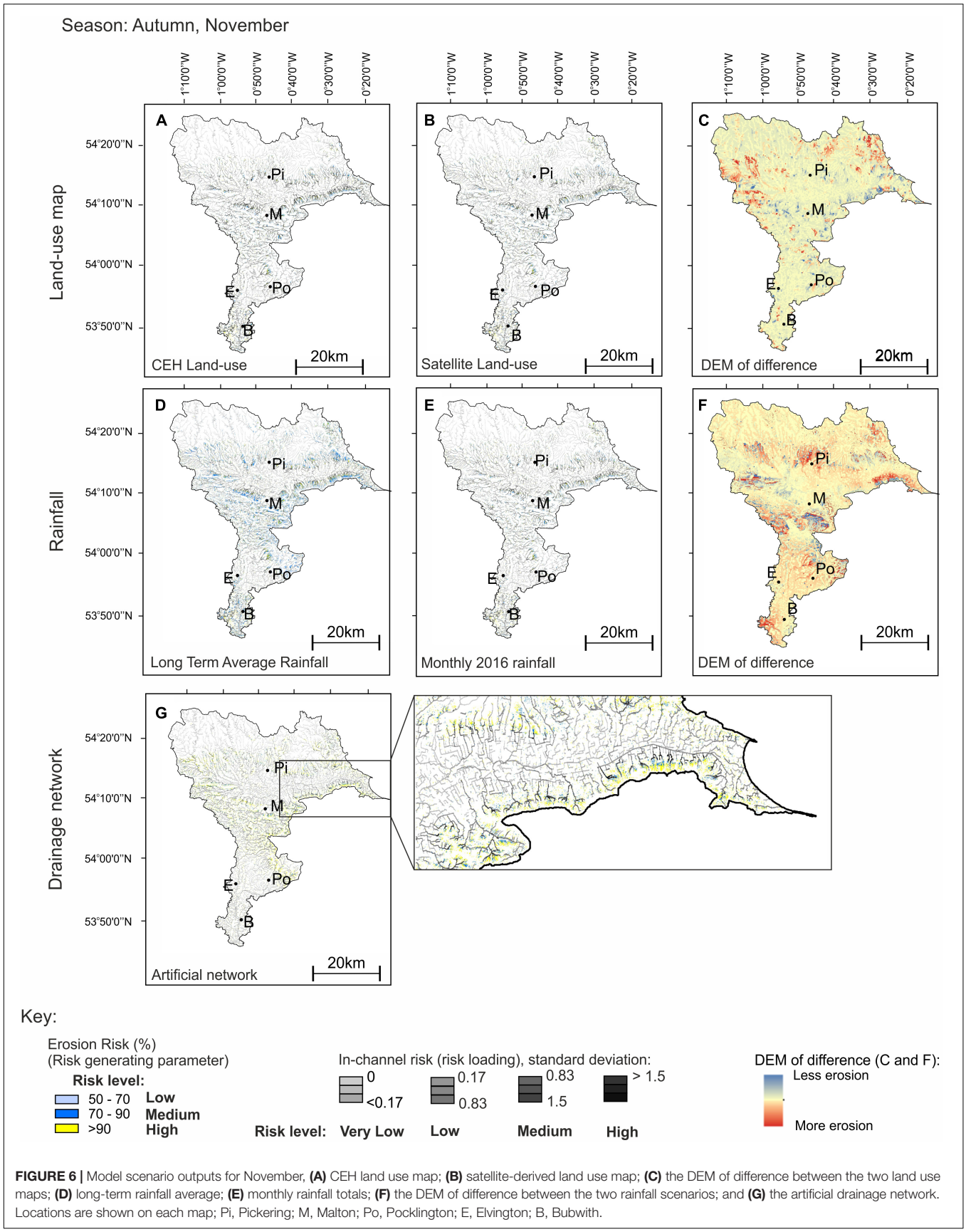


FIGURE 6 | Model scenario outputs for November, **(A)** CEH land use map; **(B)** satellite-derived land use map; **(C)** the DEM of difference between the two land use maps; **(D)** long-term rainfall average; **(E)** monthly rainfall totals; **(F)** the DEM of difference between the two rainfall scenarios; and **(G)** the artificial drainage network. Locations are shown on each map; Pi, Pickering; M, Malton; Po, Pocklington; E, Elvington; B, Bubwith.

TABLE 2 | Variation in categories of erosion risk (%) in different scenarios modeled (see **Table 1** for end member comparisons and data used).

	High Risk (%)				Medium Risk (%)				Low Risk (%)				Very Low Risk (%)			
	February	**April**	**July**	**November**	**February**	**April**	**July**	**November**	**February**	**April**	**July**	**November**	**February**	**April**	**July**	**November**
Static land use maps	12.06	12.05	11.22	12.08	33.69	34.02	34.70	34.17	37.59	36.98	36.85	36.87	16.65	16.94	17.23	16.88
Satellite-land use map	11.83	11.68	11.29	11.40	36.88	41.40	39.11	39.61	38.38	37.02	39.11	36.72	12.89	9.89	10.48	12.27
Rainfall – Long term average	12.08	11.93	12.13	11.46	37.00	41.11	37.93	39.65	37.91	37.31	39.53	36.64	13.00	9.63	10.41	12.26
Artificial drainage network	4.56	5.65	4.95	4.14	28.60	30.97	44.83	30.62	49.83	50.82	36.75	49.00	16.99	12.55	13.47	16.25
Land-use agricultural risk	9.43	9.04	7.91	8.80	35.23	39.65	37.67	38.23	41.63	40.74	43.22	40.07	13.71	10.56	11.21	12.90

month of July, with the highest risk in April in the River Derwent catchment.

Future Climate Change

Figure 9 shows the impact of climate change under different climate projections (Low, Medium, and High); the source areas of sediment do not change regardless of the climate change scenario used. Under different climate change scenarios, source areas continue to be dominated by the lowland agricultural areas in the River Derwent catchment (assuming land use does not change).

Sediment Sensitive Species

Figure 10 shows the portion of sediment sensitive species (%) within the Derwent catchment. Values vary seasonally within the catchment. The upper reaches of the catchment show high values of PSI (70+) within both spring (**Figure 10A**) and autumn (**Figure 10B**) indicating the bed is not affected by silt. However, PSI decreases downstream in the lowland area (0–50), which indicates there is increased silt deposition. Spring has more PSI values below 30 within the lowland areas of the catchment, which suggests higher levels of silt deposition (**Figure 10A**).

DISCUSSION

Seasonal Variation

The purpose of this work is to show the importance of seasonal data when assessing erosion risk. The output modeling of SCIMAP requires validation in future work; results presented here therefore represent a relative assessment of different erosion models. **Figures 3A-C–6A-C** illustrate the importance of using seasonal land use maps, as the yearly averaged CEH maps relatively estimate 6% less erosion risk (**Table 2** and **Figures 3C–6C**), although many of the critical source areas (high and medium risk) stay the same. Management may be targeted in the wrong areas and misuse limited resources due to the difference between yearly and seasonal estimations. Management based on the CEH land-use maps may not be in the most effective places or may prioritize the wrong areas. The variation is due to the data resolution (CEH is 1 km compared to 10 m for the satellite data). If smaller pockets of different land use can be identified using high resolution imagery, then more realistic land use maps can be produced that will improve modeling outputs. The variation in land use maps is exacerbated by the dominance of agriculture in the Derwent catchment, which is discussed in Section "Erosion Risk in Agricultural Dominated Catchments." Land use types that can be modeled to reflect variations in plant coverage could also include areas of tree plantation, or areas affected by moorland fires. However, areas with relatively continuous cover, such as grasslands or peatlands, may not benefit from high risk modeling as there is limited seasonal variation. Nonetheless, by using high resolution satellite images the temporal and spatial variation in risk can be assessed more robustly as more detailed rainfall information can be used.

The spatial variation in rainfall across the catchment is compared to the seasonal bare land cover and erosion risk output

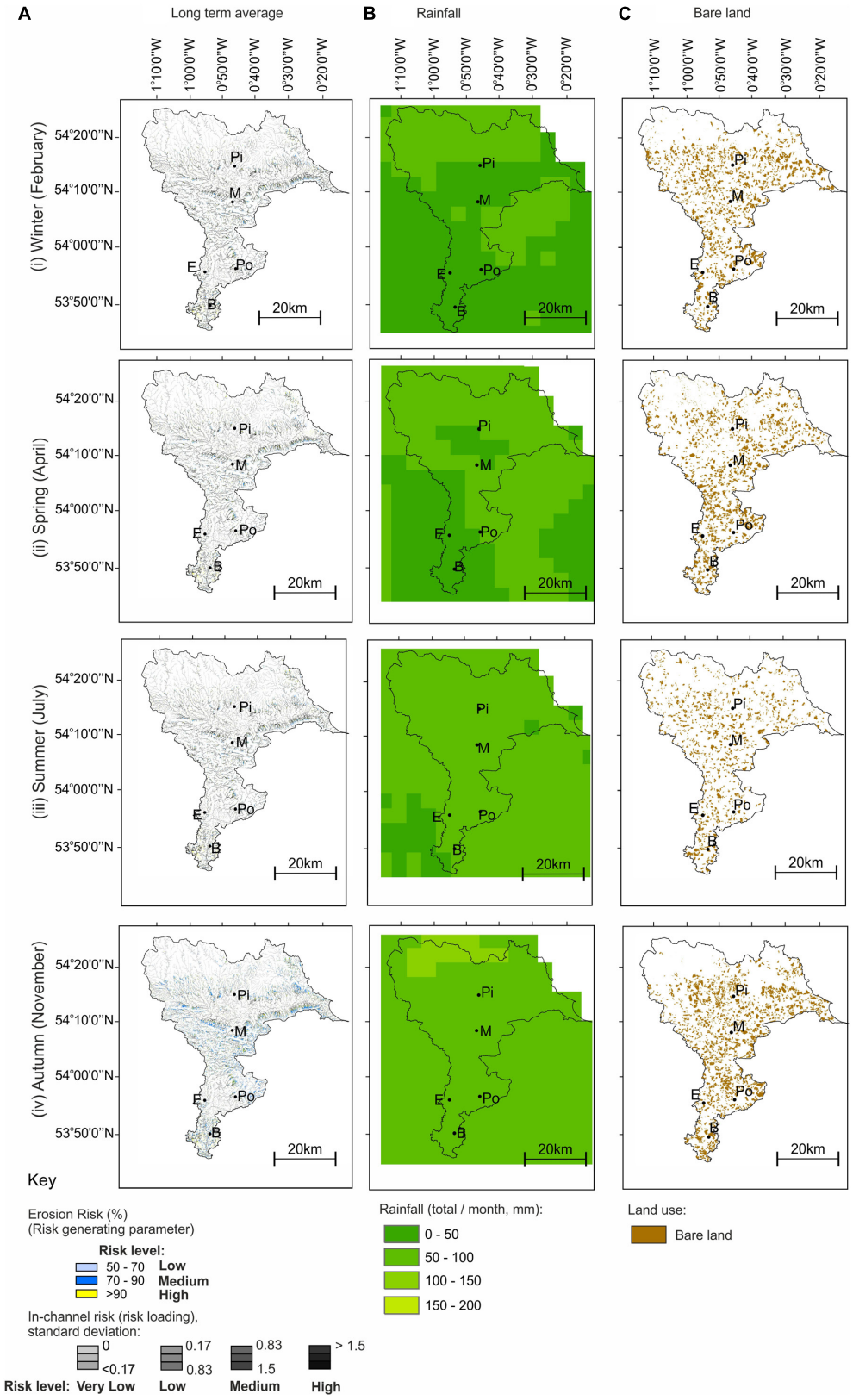


FIGURE 7 | Seasonal variation in **(A)** erosion risk; **(B)** rainfall data and **(C)** bare land for 2016, for (i) winter; (ii) Spring; (iii) Summer; and (iv) Autumn. Location are shown on each map; Pi, Pickering; M , Malton; Po, Pocklington; E, Elvington; and B, Bubwith.

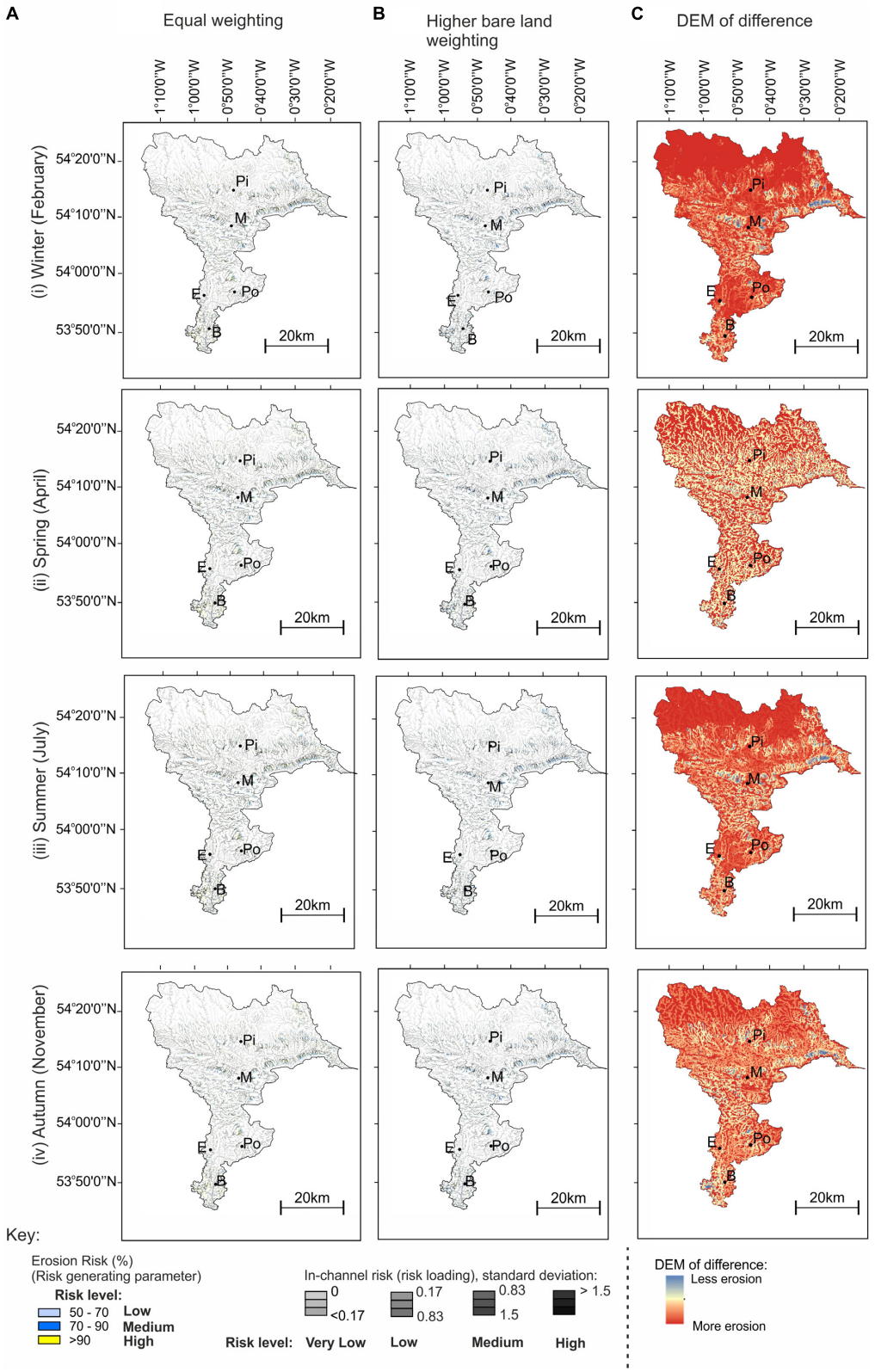


FIGURE 8 | Model scenario showing change in erosion risk across the seasons: (i) Winter; (ii) Spring; (iii) summer; (iv) Autumn, when **(A)** agricultural land and bare land have the same erosion risk assigned; **(B)** when erosion risk in bare land is higher and **(C)** the DEM of difference. Locations are shown on each map; Pi, Pickering; M, Malton; Po, Pocklington; E, Elvington; B, Bubwith.

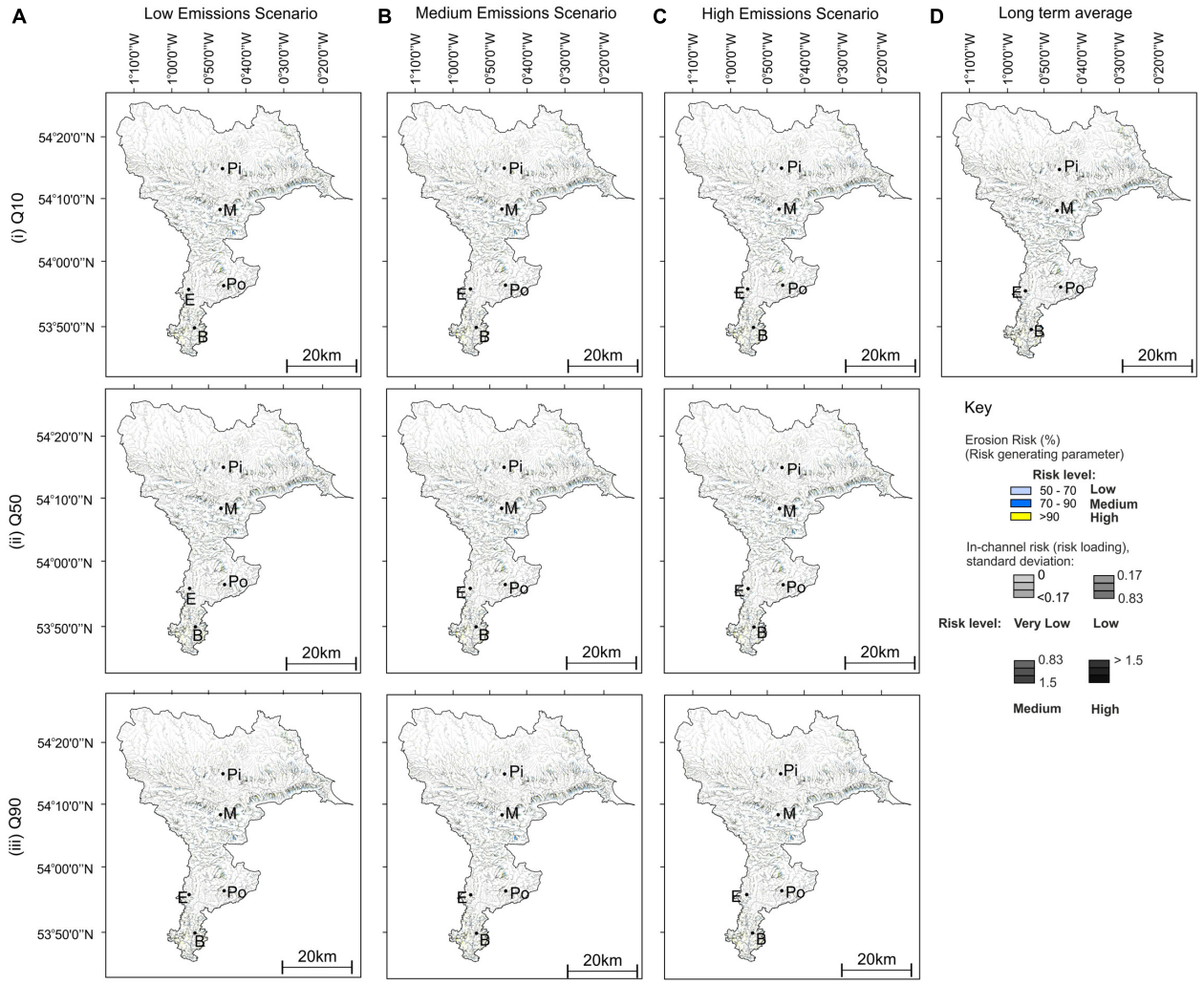


FIGURE 9 | Model scenario outputs for climate change scenarios in February, depicting **(A)** Low, **(B)** medium and **(C)** high emission scenarios, for the following quartiles: (i) Q10; (ii) Q50 and (iii) Q90 using UCKCP09 data **(D)** the long term average. Locations are shown on each map; Pi, Pickering; M, Malton; Po, Pocklington; E, Elvington; B, Bubwith.

(**Figure 7**). SCIMAP depicts relative risk within the catchment, and although the source areas are consistent, the volumes of sediment eroded and transported are expected to change due to variation in rainfall quantity and intensity. In 2016, November was the wettest month and had the largest percentage of bare land (18%), which would result in more sediment production. However, in November source areas around Pocklington have slightly less risk than the other months. This is possibly due to the spatial coverage of rainfall, resulting in a different configuration of connectivity between the source cells (land units), as defined by the network index. In alternative rainfall scenarios, different parts of the catchment may become activated, allowing seasonal variation in different flow pathways. April 2016 was also expected to produce high volumes of sediment due to the rainfall amounts and the second highest percentage of bare land. **Figures 3D-F–6D-F** show the variation in modeling when using the monthly and long term average rainfall values. Overall, the monthly 2016 rainfall values relatively underestimate erosion risk compared to the long term average rainfall, which is especially evident in February.

The modeling we present has compared the use of long term rainfall rates and monthly values, and seasonal land use maps, resulting in a range of scenarios. Erosion risk is an interlinked process, and risk based models relate this to land use and rainfall. Land use variation, especially in agricultural settings, is important to integrate. The percentage and location of bare land change seasonally; this could affect the pattern of source area cells and change connectivity. Seasonal variation in the intensity and location of rainfall will affect soil erosion, connectivity, and transport processes within the fluvial network. Producing a yearly average risk does not adequately show the complexity in risk that is experienced across the year. A scenario-based approach for erosion risk, using open access satellite imagery and rainfall data, allows multiple datasets and outcomes to be interrogated, and

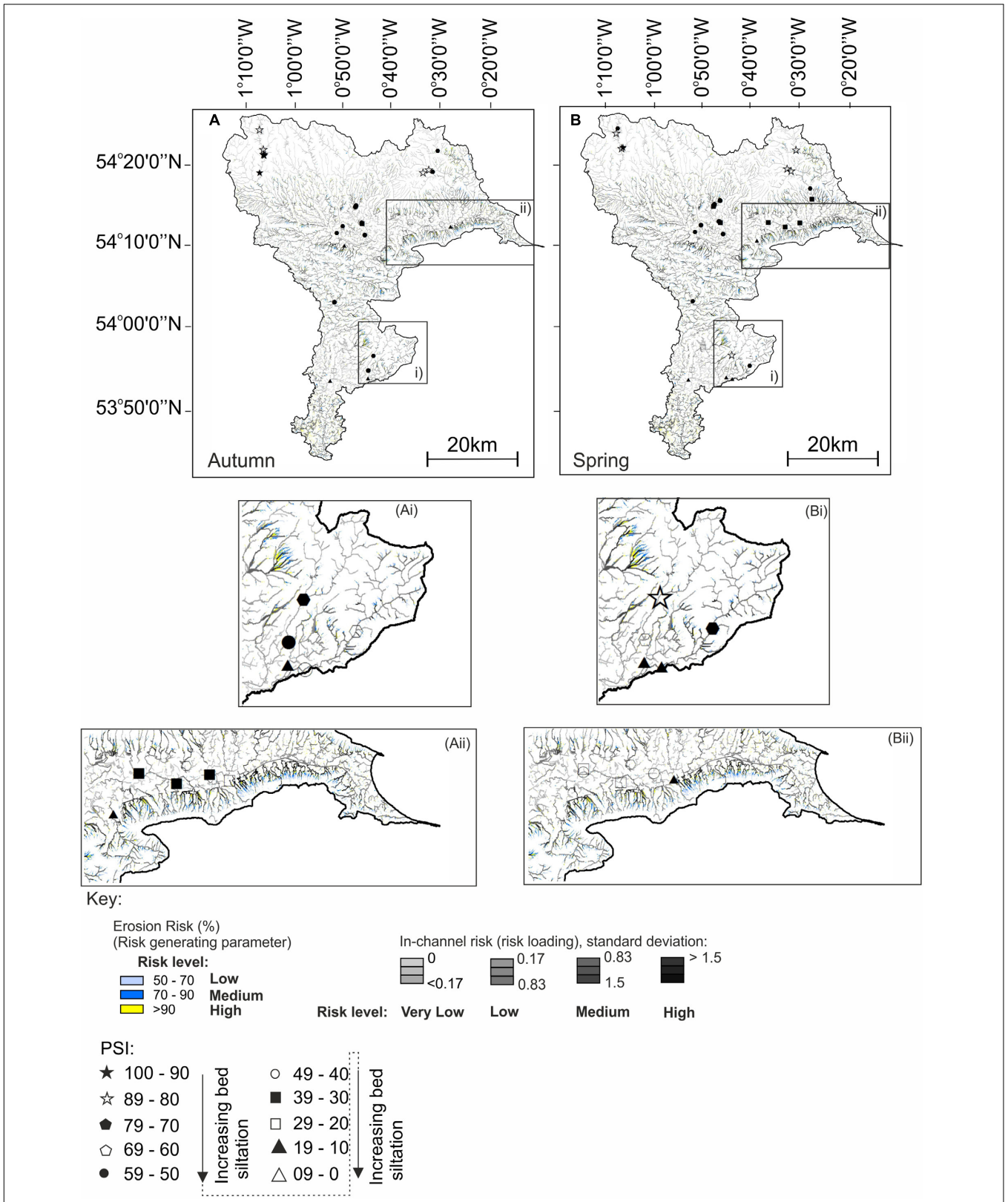


FIGURE 10 | Variation in sediment sensitive species in **(A)** autumn and **(B)** spring across the year, the base maps show the erosion risk when using the long term average rainfall scenario (**Table 2**). Inserts show higher resolution study areas from **(A,B)**. Locations are shown on each map; Pi, Pickering; M, Malton; Po, Pocklington; E, Elvington; B, Bubwith.

by integrating in seasonal variation help sediment management to become more strategic and resistant to future climate change. Catchments with clear variations in seasonal land coverage are particularly susceptible to poor management decisions using yearly average datasets. However, when mapping seasonality, caution must be taken to integrate both the monthly and long term averages of rainfall for each month. Management decisions based on an extreme monthly average (either high – a flood-prone year, or low – a drought year), could be flawed by placing management in areas that are not source areas each year. This would result in waste of resources, and could also negatively affect relationships with landowners who have set aside land.

Erosion Risk in Agricultural Dominated Catchments

Figures 3G–6G show the influence of using the artificial drainage network within the catchment. The sub-catchments dominated by agriculture and a higher coverage of field drains, such as the large lowland areas of the catchment, have increased area coverage of medium risk when incorporating the artificial network. Artificial networks should be incorporated in sub-catchments where there is a high coverage of field drains. Further investigation is required to assess if and when all drains are hydrologically connected, and these results represent one end member (fully connected 1 m deep field drains). Within erosion risk modeling, there is often an emphasis on gradient; high gradient areas cause greater risk and there is a greater coupling between source areas and the river channels (Hooke, 2003). However, within low gradient agricultural areas, sediment transport and overland flow has been recorded in tramlines that have increased connectivity within the catchment regardless of the low gradients. Recorded values of runoff have increased during a storm event from 0.4 to 8.4 mm due to creation of tramlines, resulting in increased sediment loads from 21 kg ha^{-1} to 400 kg ha^{-1} (Silgram et al., 2006).

By integrating the artificial drainage, the modeling is forced to recognize the additional pathways, and therefore represents the agricultural areas better. This work integrated artificial channels that were trellised around field boundaries. However, under-field drains also represent a key pathway (Radcliffe et al., 2015; Smith et al., 2015) that is often unmapped, whilst other water management practices such as irrigation can also increase erosion rates (Koluvek et al., 1993; García-Ruiz, 2010; Sojka, 2018).

The greatest seasonal variation in agricultural land is related to cropping cycles. Using satellite imagery not only increases the resolution of the data to 10 m, but seasonal maps are especially important in agriculturally dominated catchments where fields may be left bare seasonally (due to crop seeding or field rotation etc.), which increases erosion risk (Le Bissonnais et al., 2002). When assessing the erosion risk values assigned for SCIMAP, agricultural land is assumed to have the highest risk (of 1) regardless of the stage of cropping. However, the erosion risk associated with agricultural land can vary spatially and temporally due to multiple factors, such as the direction of contouring, crop types, crop growth stage, and management practices such as crop rotation (Heathwaite et al., 2005). When the crops are visible on satellite imagery, the erosion risk would be less than for bare land. By integrating land use maps developed from satellite imagery, bare land can be mapped and adequately included. **Figure 8** shows the difference assigning bare land the highest erosion risk (1) and agricultural land, when the crop is visible (0.9), which more realistically represents erosion risk than assuming all agricultural land has the highest risk. By modeling the change in erosion risk due to the stage of agriculture development, satellite imagery can produce a more detailed assessment of erosion risk within a given year. In an agricultural setting, this is important as farmers may have to give up part of their land for sediment management, and by assessing when there is greatest risk, temporary measures could be implemented so that the land could be used for farming the rest of the year.

How Will Climate Change Affect Source Areas?

The source areas with the highest erosion risk (critical source areas) within the catchment do not change with different climate scenarios (**Figure 9**). This indicates that even with a maximum increase in rainfall using the high emission scenario, the areas of erosion risk will not change and there will be no new areas of sediment production. However, SCIMAP does not show erosion volumes, and the fact the source areas are the same does not indicate the amount of sediment produced will stay the same as erosion volumes are likely to increase due to higher quantities of rain providing more energy for geomorphic work (Burt et al., 2016). We used long term average rainfall data. However, geomorphic work is often carried out during high rainfall events, which have been shown to mobilize large volumes of sediment and cause increased risk (e.g., Mohamadi and Kavian, 2015; Marzen et al., 2017). Climate change scenarios suggest that high magnitude rainfall events are likely to become more frequent (e.g., Sarhadi and Soulis, 2017), and therefore mapping storm tracks and intensities could enable land managers to understand both the average and extreme events that contribute to the production and transport of sediment within a catchment. Incorporating climate change data into erosion risk studies is an essential future step to assess the longevity of management that can be proposed as well as future proofing the reduction in diffuse pollution.

Comparison of Data Output With Ecological Data

PSI, based on observed macroinvertebrate species data, has been shown to have a statistical relationship with sediment deposition (e.g., Glendell et al., 2014). Comparing PSI and erosion risk shows that the PSI is a good indicator of where sediment is deposited within the channel network (**Figure 10**). When assessing deposition from a geomorphological perspective, the PSI values can be used to infer geomorphological processes related to stream power variation which affect deposition, erosion and transportation within the network, which can be shown by K_{SN} and surrounding slope values. When PSI values do not correspond to surrounding high levels of erosion risk in the Derwent as produced by SCIMAP, it shows that the channel

in that location is efficient enough to transport sediment due to higher stream power. In some areas of low PSI scores (**Figure 10Ai**), the surrounding risk area is low. This indicates that sediment is sourced from upstream and that the river in the reach is not able to transport the sediment, either due to low stream power or the volume of sediment within the channel. Therefore, it is important to look upstream of the PSI location, as intervention in the immediate reach will not solve the local issues.

The upland areas of the catchment generally have low erosion risk and corresponding high PSI values (**Figure 10**). In these locations, the river is able to transport any suspended sediment that enters the drainage network. In agricultural areas, PSI decreases downstream indicating the buildup of sediment within the channel network (**Figures 10Aii**,**Bii**). In these locations, K_{SN} and slope is low, indicating low rates of stream power. Some seasonal variation was shown in the PSI values in the agricultural areas, indicating that in spring the drainage network is not able to transport the sediment within the channel network. When looking at the long-term average rainfall rates, the highest erosion risk occurred within spring. However, the increase in discharge is balanced by the increase in erosion risk and therefore the overall channel capacity is reduced.

Incorporating further evidence, such as ecological data, is important in order to ground truth the erosion risk maps where detailed hydrological or hydraulic modeling cannot be carried out. Macroinvertebrate data can also focus where management should be placed. When incorporating these data it can be shown that the source areas for low PSI values are much further upstream and it would be more efficient to target those areas than the immediate surrounding area.

Causes of Erosion Risk

The Derwent catchment has a long history of natural and anthropogenic modification. In recent years, the channel has been straightened and deepened in several locations. The catchment is agriculturally intensive, and the seasonal variation in bare land and crops does impact the erosion risk within the catchment, as shown by using seasonal satellite imagery. The network of artificial field drains also increases connectivity by producing a complicated network of pathways.

The K_{SN} shows that the main trunk of the River Derwent has a generally high capacity to transport sediment. However, fine grained sediment (clays, silts and fine grained sand) is stored in the system because of the volumes of sediment in the river, the lack of natural areas for the sediment to be deposited, the levees that keep flood waters contained, and the singular flow regime related to channel modification. This has caused high volumes of sediment to be processed at Elvington Treatment Works and has affected the designated sites in the lower Derwent.

The intensive agriculture, erodible soils due to geological history (**Figure 1D**) and management history has exacerbated the erosion regime within the River Derwent catchment. However, there is a lack of information on the catchment with regards to bank erosion that would be able to close the sediment budget. Due to the superficial deposits (**Figure 1D**), especially around Pickering, bank erosion is expected to be high. Bank erosion represents a key source of sediment within drainage networks, which is often exacerbated by animals entering the river course via the banks (poaching). A bank erosion study on the Rivers Swale, Ure and Ouse (the Derwent is a tributary of the River Ouse), Yorkshire, found average bank erosion between March 1996 and May 1997 to range from 77 to 440 mm (Lawler et al., 1999). Currently, there are no sediment budgets for the River Ouse that quantify the amount of sediment sourced from bank erosion relative to land use. Due to the erodible nature of the bedrock and superficial geology, bank erosion could represent a key sediment source in the Derwent catchment that needs to be monitored and integrated into further modeling.

Future Work and Wider Implications

Sediment concentrations naturally vary both spatially and temporally within river channels (e.g., Chakrapani, 2005). However, in the Derwent catchment as well as many other catchments modeled, there is no long term assessment of sediment concentrations. This is needed to assess how much of the present sediment problem is due to human modification in land use and channel management, or if a large portion is due to the erodible nature of the substrate that causes a 'high' natural base level. In order to inform policy and management of a catchment, the modern background sediment delivery needs to be understood, as well as historic rates which will give a more holistic approach to sediment management (Collins et al., 2011). Further, new climate change projections need to be integrated into modeling to forecast the future change in order to future proof any management or policies that are put in place. Additional data are needed to verify the model outputs, including identification of source areas in the field.

This paper has started to integrate seasonal variation in land-use and rainfall information into SCIMAP (Reaney et al., 2011) by varying the input data (land use maps and rainfall data). However, more in-depth seasonal modeling to look at different environmental scenarios needs to be undertaken using satellite imagery. Antecedent conditions such as the impact of a prolonged drought which could affect land-use (e.g., percent of bare land) or a high intensity localized storm event, which could increase hydrological connectivity, will impact and change diffuse pollution risk across the catchment. However, SCIMAP does not have a function to vary antecedent conditions for each model run. Because SCIMAP produces an erosion risk map for the length of data entered (e.g., monthly in this case), in order to understand the impact of a drought, preferably a daily time series (which will be affected by the satellite imagery temporal resolution related to the orbit of the satellites) would be needed to compare the output of a drought year to a 'normal' or wet year.

Future modeling should include bedrock/superficial geology and soil information (e.g., using RUSLE) in order to understand how much of the erosion is due to the erodible nature of the underlying geology. Land-use maps are a good proxy; incorporating additional information will give a greater confidence to erosion risk maps. Future modeling efforts should also incorporate high resolution information at field level, such as crop types and crop practices. Finally, in order to close the sediment budget the location and rate of bank erosion is vital to understand, as bank management as well as management

of the landscape may be needed to reduce sediment loads within the river.

Additional information is required on the smaller pathways, which cannot be picked up using the 5 m DEM. High resolution reach-scale mapping should be used to investigate smaller pathways (e.g., rills within woodland areas). For the Derwent Catchment, these small pathways should be investigated on farmland and woodland areas. Furthermore, the depth and connectivity of the artificial channels need to be mapped during fieldwork, to allow correct manipulation of the DEM, rather than using a standard depth across the study area. Although a standard depth has been integrated for these model runs, it is not assumed that other depth values will significantly change the source areas; this is because when artificially modifying the DEM, flow is routed down these new channels. Nonetheless, deeper artificial channels will have the capacity to route higher sediment quantities and the areas of in-channel risk may vary; however, further work is needed to confirm this by collecting representative depths and re-running the models.

As well as impacting sediment volumes, anthropogenic activity impacts the 'natural' source to sink configuration (**Figure 11**) by accelerating pathways (e.g., artificial drainage), which is likely to be exacerbated by climate change increasing the volume of sediment produced (Burt et al., 2016). Although the delivery rate of sediment to the channel network has increased, additional stores, such as impoundments or natural flood management (e.g., earth bunds, buffer strips), may increase transport time to the sink (**Figure 11**). The movement of sediment through the channel network needs to be assessed to investigate lag times.

Rivers are a key transport route for pollutants and particulates, such as microplastics (e.g., Cole et al., 2011; Van Cauwenberghe et al., 2013; Lusher et al., 2015). However, there have been few studies linking source areas to the marine realm (e.g., Klein et al., 2015; Horton et al., 2017; Kane and Clare, 2019). Integrating high resolution modeling of source area erosion risk will allow a more holistic approach to be taken when assessing the dispersal of pollutants. This work has shown that seasonal variations in erosion risk is often relatively under-represented by modeling approaches. The seasonal variation in risk will translate to the flux of pollutants and particulates to the marine realm, which is an important aspect that needs to be integrated.

CONCLUSION

The Derwent catchment, Yorkshire, United Kingdom, illustrates how a scenario approach to erosion risk mapping can inform catchment management plans. By using seasonal land-use maps derived from open source satellite images and seasonal rainfall data, there is a clear variation in erosion risk both spatially and temporally. Typically, CEH land-use maps relatively underestimate erosion risk due to resolution issues and the static nature of the land-use map. Furthermore, in an agriculturally dominated catchment, artificial drainage should be incorporated, as this will overcome the natural bias to gradient in erosion risk mapping (e.g., steeper areas are of greater risk), as farming practices produce additional pathways that need to be considered. When using rainfall information, using the long term average for each month is recommended in order to remove the 'extremes.' However, future work should focus on using high resolution climate projections to assess the impact of localized high intensity rainfall events on erosion risk. For the Derwent catchment, this

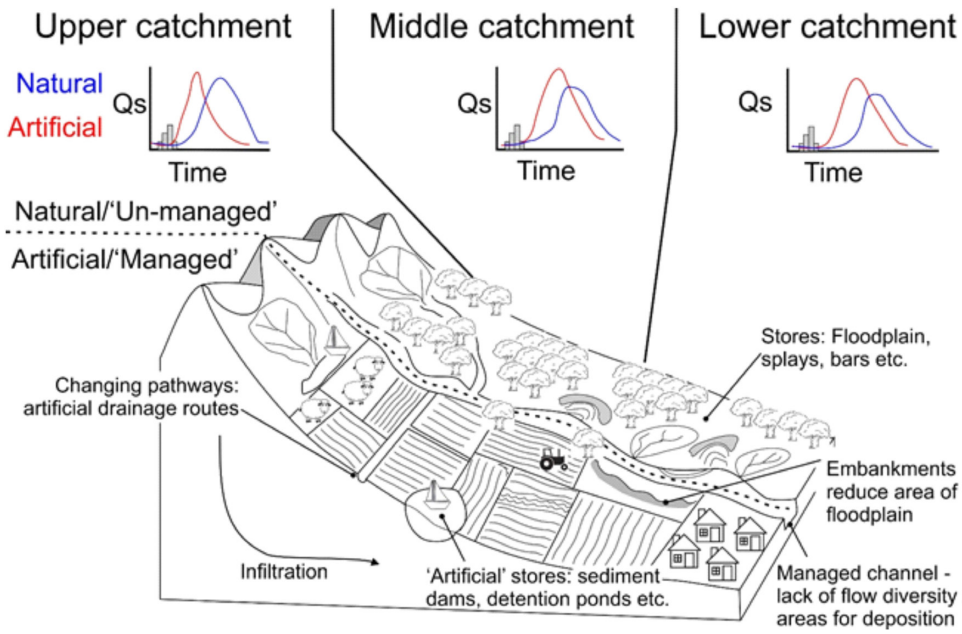


FIGURE 11 | Synthesis figure showing the influence of anthropogenic (a 'managed catchment') activity on source to sink.

can be carried out when UKCP18 data are fully released. Further, the impact of drought or variation in other environmental conditions need to be integrated, and SCIMAP should be updated to integrate antecedent conditions.

In catchments dominated by agriculture, with large changes in seasonal land cover, a range of scenarios in erosion risk mapping is critical to improve management practices. Anthropogenic activity has changed the source-to-sink system. A holistic approach is needed to understand the new pathways and stores being created across the landscape to ensure that the 'natural' amount of particulates is transported through the system to reduce the risk of hungry water, and to forecast the flux of pollutants to the marine realm.

DATA AVAILABILITY STATEMENT

The datasets generated for this study are available on request to the corresponding author.

AUTHOR CONTRIBUTIONS

JR collected and analyzed the data, led the writing and drafting of figures, with major contributions on the text from DH and PK. DH helped to improve **Figure 11**. BA and AW supported JR throughout JRs NERC Industrial Mobility Fellowship and provided comments on the manuscript.

FUNDING

This work was funded under a NERC Industrial Mobility Fellowship to JR entitled 'An Integrated Approach to Assessing Catchment Resilience: Combining GIS and Field Data in Relation To Climate Change Projections in the River Derwent' (NERC Ref: NE/R013012/1). DH is funded under NERC Grant 'Yorkshire iCASP – Yorkshire Integrated Catchment Solutions Programme' (NERC Ref: NE/P011160/1).

ACKNOWLEDGMENTS

The Environment Agency Analysis and Reporting team for the Yorkshire Area and the Environment Agency catchment co-ordinator are thanked for their help during JRs NERC Industrial Mobility Fellowship and for providing ecological data on sediment sensitive species. We acknowledge the reviews by the three reviewers who helped to improve this manuscript.

REFERENCES

Armitage, P. D., Moss, D., Wright, J. F., and Furse, M. T. (1983). The performance of a new biological water quality score system based on macroinvertebrates over a wide range of unpolluted running-water sites. *Water Res.* 17, 333–347. doi: 10.1016/0043-1354(83)90188-4

Ballantine, D. J., Walling, D. E., Collins, A. L., and Leeks, G. J. L. (2009). The content and storage of phosphorus in fine-grained channel bed sediment in contrasting lowland agricultural catchments in the UK. *Geoderma* 151, 141–149. doi: 10.1016/j.geoderma.2009.03.021

Bilotta, G. S., and Brazier, R. E. (2008). Understanding the influence of suspended solids on water quality and aquatic biota. *Water Res.* 42, 2849–2861. doi: 10.1016/j.watres.2008.03.018

Boggs, G., Devonport, C., Evans, K., and Puig, P. (2001). GIS-based rapid assessment of erosion risk in a small catchment in the wet/dry tropics of Australia. *Land Degrad. Dev.* 12, 417–434. doi: 10.1002/ldr.457

Bracken, L. J., Turnbull, L., Wainwright, J., and Bogaart, P. (2015). Sediment connectivity: a framework for understanding sediment transfer at multiple scales. *Earth Surf. Process. Landf.* 40, 177–188. doi: 10.1002/esp.3635

Bryan, R. B. (2000). Soil erodibility and processes of water erosion on hillslope. *Geomorphology* 32, 385–415. doi: 10.1016/S0169-555X(99)00105-1

Burt, T., Boardman, J., Foster, I., and Howden, N. (2016). More rain, less soil: long-term changes in rainfall intensity with climate change. *Earth Surf. Process. Landf.* 41, 563–566. doi: 10.1002/esp.3868

Cavalli, M., Trevisani, S., Comiti, F., and Marchi, L. (2013). Geomorphometric assessment of spatial sediment connectivity in small Alpine catchments. *Geomorphology* 188, 31–41. doi: 10.1016/j.geomorph.2012.05.007

Cerdan, O., Govers, G., Le Bissonnais, Y., Van Oost, K., Poesen, J., Saby, N., et al. (2010). Rates and spatial variations of soil erosion in Europe: a study based on erosion plot data. *Geomorphology* 122, 167–177. doi: 10.1016/j.geomorph.2010.06.011

Chakrapani, G. J. (2005). Factors controlling variations in river sediment loads. *Curr. Sci.* 88, 569–575.

Chorley, R. J. (1957). Climate and morphometry. *J. Geol.* 65, 628–638.

Cole, M., Lindeque, P., Halsband, C., and Galloway, T. S. (2011). Microplastics as contaminants in the marine environment: a review. *Mar. Pollut. Bull.* 62, 2588–2597. doi: 10.1016/j.marpolbul.2011.09.025

Collins, A. L., Naden, P. S., Sear, D. A., Jones, J. I., Foster, I. D., and Morrow, K. (2011). Sediment targets for informing river catchment management: international experience and prospects. *Hydrol. Process.* 25, 2112–2129. doi: 10.1002/hyp.7965

Collins, A. L., Walling, D. E., and Leeks, G. J. L. (2005). "Storage of fine-grained sediment and associated contaminants within the channels of lowland permeable catchments in the UK," in *Proceedings of the Sediment Budgets 1 Symposium S1 Held During the Seventh IAHS Scientific Assembly at Foz do Iguaçu*, (Wallingford, UK: IAHS Press), 259–268.

Conrad, O., Bechtel, B., Bock, M., Dietrich, H., Fischer, E., Gerlitz, L., et al. (2015). System for automated geoscientific analyses (SAGA) v. 2.1.4. *Geosci. Model Dev.* 8, 1991–2007. doi: 10.5194/gmd-8-1991-2015

Coulthard, T. J., Ramirez, J., Fowler, H. J., and Glenis, V. (2012). Using the UKCP09 probabilistc scenarios to model the amplified impact of climate change on drainage basin sediment yield. *Hydrol. Earth Syst. Sci.* 16, 4401–4416. doi: 10.5194/hess-16-4401-2012

Covich, A. P., Austen, M. C., Bärlocher, F., Chauvet, E., Cardinale, B. J., Biles, C. L., et al. (2004). The role of biodiversity in the functioning of freshwater and marine benthic ecosystems. *Bioscience* 54, 767–775.

Dampney, P., Mason, P., Goodlass, G., and Hillman, J. (2002). *Methods and Measures To Minimise the Diffuse Pollution of Water From Agriculture–a Critical Appraisal*. Report for Defra project NT2507. London.

Dietrich, W. E., and Dunne, T. (1978). Sediment budget for a small catchment in a mountainous terrain. *Z. Geomorphol. Suppl.* 29, 191–206.

Extence, C. A., Chadd, R. P., England, J., Dunbar, M. J., Wood, P. J., and Taylor, E. D. (2013). The assessment of fine sediment accumulation in rivers using macro-invertebrate community response. *River Res. Appl.* 29, 17–55. doi: 10.1002/rra.1569

Farnsworth, K. L., and Milliman, J. D. (2003). Effects of climatic and anthropogenic change on small mountainous rivers: the Salinas River example. *Glob. Planet. Chang.* 39, 53–64. doi: 10.1016/S0921-8181(03)00017-1

Fryirs, K. (2013). (Dis) Connectivity in catchment sediment cascades: a fresh look at the sediment delivery problem. *Earth Surf. Process. Landf.* 38, 30–46. doi: 10.1002/esp.3242

García-Ruiz, J. M. (2010). The effects of land uses on soil erosion in Spain: a review. *Catena* 81, 1–11. doi: 10.1016/j.catena.2010.01.001

Gitas, I. Z., Douros, K., Minakou, C., Silleos, G. N., and Karydas, C. G. (2009). Multi-temporal soil erosion risk assessment in N. Chalkidiki using a modified USLE raster model. *EARSeL eProceedings* 8, 40–52.

Glendell, M., Extence, C., Chadd, R., and Brazier, R. E. (2014). Testing the pressure-specific invertebrate index (PSI) as a tool for determining ecologically relevant targets for reducing sedimentation in streams. *Freshwater Biol.* 59, 353–367. doi: 10.1111/fwb.12269

Greig, S. M., Sear, D. A., Carling, P. A., and Whitcombe, L. (2005). Fine sediment accumulation in salmon spawning gravels and the survival of incubating salmon progeny: implications for spawning habitat management. *Sci. Total Environ.* 344, 241–258.

Hack, J. T. (1973). Stream-profile analysis and stream-gradient index. *J. Res. U.S. Geol. Sur.* 1, 421–429.

Heathwaite, A. L. (2003). Making process-based knowledge useable at the operational level: a framework for modelling diffuse pollution from agricultural land. *Environ. Modell. Soft.* 18, 753–760.

Heathwaite, A. L., Fraser, A. I., Johnes, P. J., Hutchins, M., Lord, E., and Butterfield, D. (2003a). The phosphorus indicators tool: a simple model of diffuse P loss from agricultural land to water. *Soil Use Manage.* 19, 1–11.

Heathwaite, A. L., Sharpley, A. N., Beckmann, M., and Rekolainen, S. (2003b). "Assessing the risk of agricultural nonpoint source phosphorus pollution," in *Phosphorus: Agriculture and the Environment*, eds J. T. Sims, and A. N. Sharpley (United Kingdom: ASA).

Heathwaite, A. L., Quinn, P. F., and Hewett, C. J. M. (2005). Modelling and managing critical source areas of diffuse pollution from agricultural land using flow connectivity simulation. *J. Hydrol.* 304, 446–461. doi: 10.1016/j.jhydrol.2004.07.043

Heckmann, T., Haas, F., Abel, J., Rimböck, A., and Becht, M. (2017). Feeding the hungry river: fluvial morphodynamics and the entrainment of artificially inserted sediment at the dammed river Isar, Eastern Alps, Germany. *Geomorphology* 291, 128–142. doi: 10.1016/j.geomorph.2017.01.025

Hodgson, D. M., Bernhardt, A., Clare, M. A., Da Silva, A. C., Fosdick, J., Mauz, B., et al. (2018). Grand challenges (and great opportunities) in sedimentology, stratigraphy, and diagenesis research. *Front. Earth Sci.* 6:173. doi: 10.3389/feart.2018.00173

Holmes, T. P. (1988). The offsite impact of soil erosion on the water treatment industry. *Land Econ.* 64, 356–366.

Hooke, J. M. (2003). Coarse sediment connectivity in river channel systems: a conceptual framework and methodology. *Geomorphology* 56, 79–94. doi: 10.1016/s0169-555x(03)00047-3

Horton, A. A., Svendsen, C., Williams, R. J., Spurgeon, D. J., and Lahive, E. (2017). Large microplastic particles in sediments of tributaries of the River Thames, UK–Abundance, sources and methods for effective quantification. *Mar. Pollut. Bull.* 114, 218–226. doi: 10.1016/j.marpolbul.2016.09.004

Horton, M., Keys, A., Kirkwood, L., Mitchell, F., Kyle, R., and Roberts, D. (2015). Sustainable catchment restoration for reintroduction of captive bred freshwater pearl mussels Margaritifera margaritifera. *Limnologica* 50, 21–28. doi: 10.1016/j.limno.2014.11.003

Horton, R. E. (1932). Drainage-basin characteristics. *Trans. Am. Geophys. Union* 13, 350–361.

Huang, C., Gascuel-Odoux, C., and Cros-Cayot, S. (2002). Hillslope topographic and hydrologic effects on overland flow and erosion. *Catena* 46, 177–188. doi: 10.1016/S0341-8162(01)00165-5

Jordan, C., and Smith, R. V. (2005). Methods to predict the agricultural contribution to catchment nitrate loads: designation of nitrate vulnerable zones in Northern Ireland. *J. Hydrol.* 304, 316–329.

Kane, I. A., and Clare, M. (2019). Dispersion, accumulation and the ultimate fate of microplastics in deep-marine environments: a review and future directions. *Front. Earth. Sci.* 7:80. doi: 10.3389/feart.2019.00080

Klein, S., Worch, E., and Knepper, T. P. (2015). Occurrence and spatial distribution of microplastics in river shore sediments of the Rhine-Main area in Germany. *Environ. Sci. Tech.* 49, 6070–6076. doi: 10.1021/acs.est.5b00492

Koluvek, P. K., Tanji, K. K., and Trout, T. J. (1993). Overview of soil erosion from irrigation. *J. Irrig. Drain. Eng.* 119, 929–946. doi: 10.1061/(ASCE)0733-94371993119:6(929)

Kondolf, G. M., Gao, Y., Annandale, G. W., Morris, G. L., Jiang, E., Zhang, J., et al. (2014). Sustainable sediment management in reservoirs and regulated rivers: experiences from five continents. *Earth's Future* 2, 256–280.

Köthe, H. (2003). Existing sediment management guidelines: an overview. *J. Soils Sediments* 3, 139–143.

Kronvang, B., Laubel, A., Larsen, S. E., and Friberg, N. (2003). Pesticides and heavy metals in Danish streambed sediment. *Hydrobiologia* 494, 93–101.

Lane, S. N. (2003). "More floods, less rain: changing hydrology in a Yorkshire context," in *Global Warming in a Yorkshire Context*, ed. M. Atherden (York: Place Research Centre), 18–19.

Lane, S. N., Brookes, C. J., Kirkby, M. J., and Holden, J. (2004). A network-index-based version of TOPMODEL for use with high-resolution digital topographic data. *Hydrol. Proc.* 18, 191–201. doi: 10.1002/hyp.5208

Lane, S. N., Brookes, C. J., Louise Heathwaite, A., and Reaney, S. (2006). Surveillant science: challenges for the management of rural environments emerging from the new generation diffuse pollution models. *J. Agric. Econ.* 57, 239–257. doi: 10.1111/j.1477-9552.2006.00050.x

Lane, S. N., Reaney, S. M., and Heathwaite, A. L. (2009). Representation of landscape hydrological connectivity using a topographically driven surface flow index. *Water Resour. Res.* 45, doi: 10.1029/2008WR007336

Lawler, D. M., Grove, J. R., Couperthwaite, J. S., and Leeks, G. J. L. (1999). Downstream change in river bank erosion rates in the Swale–Ouse system, northern England. *Hydrol. Proc.* 13, 977–992. doi: 10.1002/(sici)1099-1085(199905)13:7<977::aid-hyp785>3.3.co;2-x

Le Bissonnais, Y., Montier, C., Jamagne, M., Daroussin, J., and King, D. (2002). Mapping erosion risk for cultivated soil in France. *Catena* 46, 207–220. doi: 10.1016/S0341-8162(01)00167-9

Liu, Q. Q., and Singh, V. P. (2004). Effect of microtopography, slope length and gradient, and vegetative cover on overland flow through simulation. *J. Hydrol. En.* 9, 375–382. doi: 10.1061/(ASCE)1084-069920049:5(375)

Lu, D., Li, G., Valladares, G. S., and Batistella, M. (2004). Mapping soil erosion risk in Rondonia, Brazilian Amazonia: using RUSLE, remote sensing and GIS. *Land Degrad. Dev.* 15, 499–512. doi: 10.1002/ldr.634

Lusher, A. L., Tirelli, V., O'Connor, I., and Officer, R. (2015). Microplastics in Arctic polar waters: the first reported values of particles in surface and sub-surface samples. *Sci. Rep.* 5:14947. doi: 10.1038/srep14947

Marzen, M., Iserloh, T., de Lima, J. L., Fister, W., and Ries, J. B. (2017). Impact of severe rain storms on soil erosion: experimental evaluation of wind-driven rain and its implications for natural hazard management. *Sci. Total Environ.* 590, 502–513. doi: 10.1016/j.scitotenv.2017.02.190

Mertes, L. A. (2002). Remote sensing of riverine landscapes. *Freshwater Biol.* 47, 799–816. doi: 10.1046/j.1365-2427.2002.00909.x

Milledge, D. G., Lane, S. N., Heathwaite, A. L., and Reaney, S. M. (2012). A Monte Carlo approach to the inverse problem of diffuse pollution risk in agricultural catchments. *Sci. Total Environ.* 433, 434–449. doi: 10.1016/j.scitotenv.2012.06.047

Miller, V. C. (1953). *A Quantitative Geomorphic Study of Drainage Basin Characteristics in the Clinch Mountain Area*. Virginia and Tennessee, Project. NR, Technical Report, Columbia University, New York, NY 389–402.

Mohamadi, M. A., and Kavian, A. (2015). Effects of rainfall patterns on runoff and soil erosion in field plots. *Int. Soil Water Conserv. Res.* 3, 273–281. doi: 10.1016/j.iswcr.2015.10.001

Mossa, J. (1996). Sediment dynamics in the lowermost Mississippi River. *Eng. Geol.* 45, 457–479. doi: 10.1016/S0013-7952(96)00026-9

Munafo, M., Cecchi, G., Baiocco, F., and Mancini, L. (2005). River pollution from nonpoint sources: a new simplified method of assessment. *J. Environ. Manage.* 77, 93–98.

Natural England, (2015). *Pollution Risk Assessment and Source Apportionment: River Derwent Catchment*. York: Natural England.

Newson, M. D. (2006). *Desk-based Targeting for a Fluvial Audit of the Yorkshire River Derwent*. Report on Contract 13691, Environment Agency North-east Region, York.

Orr, H. G., and Carling, P. A. (2006). Hydro-climatic and land use changes in the River Lune catchment, North West England, implications for catchment management. *River Res. Appl.* 22, 239–255. doi: 10.1002/rra.908

Owens, P. N., Batalla, R. J., Collins, A. J., Gomez, B., Hicks, D. M., Horowitz, A. J., et al. (2005). Fine-grained sediment in river systems: environmental significance and management issues. *River Res. Appl.* 21, 693–717. doi: 10.1002/rra.878

Panagos, P., Christos, K., Cristiano, B., and Ioannis, G. (2014). Seasonal monitoring of soil erosion at regional scale: an application of the G2 model in Crete focusing on agricultural land uses. *Int. J. Appl. Earth Obs. Geoinfo.* 27, 147–155. doi: 10.1016/j.jag.2013.09.012

Radcliffe, D. E., Reid, D. K., Blombäck, K., Bolster, C. H., Collick, A. S., Easton, Z. M., et al. (2015). Applicability of models to predict phosphorus losses in drained fields: a review. *J. Environ. Qual.* 44, 614–628. doi: 10.2134/jeq2014.05.0220

Reaney, S. M., Lane, S. N., Heathwaite, A. L., and Dugdale, L. J. (2011). Risk-based modelling of diffuse land use impacts from rural landscapes upon salmonid fry abundance. *Ecol. Model.* 222, 1016–1029. doi: 10.1016/j.ecolmodel.2010.08.022

Rickson, R. J. (2014). Can control of soil erosion mitigate water pollution by sediments? *Sci. Total Environ.* 468, 1187–1197. doi: 10.1016/j.scitotenv.2013.05.057

Royal Haskoning, (2010). *Restoring the Yorkshire Derwent: River Restoration Plan*. Amersfoort: Royal Haskoning.

Sarhadi, A., and Soulis, E. D. (2017). Time-varying extreme rainfall intensity-duration-frequency curves in a changing climate. *Geophy. Res. Lett.* 44, 2454–2463. doi: 10.1002/2016GL072201

Schumm, S. A. (1956). Evolution of drainage systems and slopes in badlands at Perth Amboy. *New Jersey. Geol. Soc. Am. Bull.* 67, 597–646.

Schwanghart, W., and Kuhn, N. J. (2010). TopoToolbox: a set of Matlab functions for topographic analysis. *Environ. Model. Softw.* 25, 770–781. doi: 10.1016/j.envsoft.2009.12.002

Schwanghart, W., and Scherler, D. (2014). TopoToolbox 2 – MATLAB-based software for topographic analysis and modeling in Earth surface sciences. *Earth Surf. Dyn.* 2, 1–7. doi: 10.5194/esurf-2-1-2014

Sear, D. A. (1992). *Siltation at the confluence of the River Derwent and River Rye, North Yorkshire*. Report to Yorkshire NRA Flood Defence Function, University of Newcastleupon-Tyne.

Silgram, M., Jackson, B., Quinton, J., and Stevens, C. (2006). "Practical mitigation options for controlling phosphorus and sediment loss at hillslope scale," in *Proceedings of the British Hydrological Society, 9th National Hydrology Symposium*, (Durham).

Slaymaker, O. (1982). Land use effects on sediment yield and quality. *Hydrobiologia* 9, 93–109.

Smith, D. R., King, K. W., Johnson, L., Francesconi, W., Richards, P., Baker, D., et al. (2015). Surface runoff and tile drainage transport of phosphorus in the midwestern United States. *J. Environ. Qual.* 44, 495–502. doi: 10.2134/jeq2014.04.0176

Sojka, R. E. (2018). "Understanding and managing irrigation-induced erosion," in *Advances in Soil and Water Conservation*, ed. F. J. Pierce (Abingdon: Routledge), 21–37.

Strahler, A. N. (1964). "Quantitative geomorphology of drainage basins and channel networks," in *Handbook of Applied Hydrology*, ed. V. T. Chow (New York, NY: McGraw Hill Book Company), 39–76.

Sustainable Futures (2018). *Walk The Supply Chain, Yorkshire Water at Elvington Water Treatment Works*. Available at: https://www.sustainablefutures.uk.com/walk-the-supply-chain/walk-supply-chain-yorkshire-water-elvington-water-treatment-works/ (accessed January 2019).

Syvitski, J. P., and Kettner, A. (2011). Sediment flux and the anthropocene. *Philosophi. Transac. Royal Soc. A.* 369, 957–975. doi: 10.1098/rsta.2010.0329

Syvitski, J. P., Vörösmarty, C. J., Kettner, A. J., and Green, P. (2005). Impact of humans on the flux of terrestrial sediment to the global coastal ocean. *Science* 308, 376–380. doi: 10.1126/science.1109454

Tucker, G. E. (2004). Drainage basin sensitivity to tectonic and climatic forcing: implications of a stochastic model for the role of entrainment and erosion thresholds. *Earth Surf. Process. Landf.* 29, 185–205. doi: 10.1002/esp.1020

Van Cauwenberghe, L., Vanreusel, A., Mees, J., and Janssen, C. R. (2013). Microplastic pollution in deep-sea sediments. *Environ. Pollut.* 182, 495–499. doi: 10.1016/j.envpol.2013.08.013

Van Sickle, J., and Paulsen, S. G. (2008). Assessing the attributable risks, relative risks, and regional extents of aquatic stressors. *J. N. Am. Benthol. Soc.* 27, 920–931. doi: 10.1899/07-152.1

Vrieling, A., De Jong, S. M., Sterk, G., and Rodrigues, S. C. (2008). Timing of erosion and satellite data: a multi-resolution approach to soil erosion risk mapping. *Int. J. Appl. Earth Obs. Geoinf.* 10, 267–281. doi: 10.1016/j.jag.2007.10.009

Walling, D. E. (2006). Human impact on land–ocean sediment transfer by the world's rivers. *Geomorphology* 79, 192–216. doi: 10.1016/j.geomorph.2006.06.019

Walling, D. E., and Fang, D. (2003). Recent trends in the suspended sediment loads of the world's rivers. *Glob. Planet. Chang.* 39, 111–126. doi: 10.1016/S0921-8181(03)00020-1

Walling, D. E., Owens, P. N., Waterfall, B. D., Leeks, G. J., and Wass, P. D. (2000). The particle size characteristics of fluvial suspended sediment in the Humber and Tweed catchments, UK. *Sci. Total Environ.* 251, 205–222. doi: 10.1016/S0048-9697(00)00384-3

Walling, D., Russell, M., and Hodkinson, R. (2002). Establishing sediment budgets for two small lowland agricultural catchments in the UK. *Catena* 47, 323–353. doi: 10.1016/s0341-8162(01)00187-4

Wilkinson, B. H., and McElroy, B. J. (2007). The impact of humans on continental erosion and sedimentation. *Geol. Soc. Am. Bull.* 119, 140–156. doi: 10.1130/B25899.1

Wilkinson, S. N., Prosser, I. P., Rustomji, P., and Read, A. M. (2009). Modelling and testing spatially distributed sediment budgets to relate erosion processes to sediment yields. *Environ. Model. Softw.* 24, 489–501. doi: 10.1016/j.envsoft.2008.09.006

Zalasiewicz, J., Waters, C. N., do Sul, J. A. I., Corcoran, P. L., Barnosky, A. D., Cearreta, A., et al. (2016). The geological cycle of plastics and their use as a stratigraphic indicator of the anthropocene. *Anthropocene* 13, 4–17. doi: 10.1016/j.ancene.2016.01.002

Zhou, L. J., Ying, G. G., Zhao, J. L., Yang, J. F., Wang, L., Yang, B., et al. (2011). Trends in the occurrence of human and veterinary antibiotics in the sediments of the Yellow River, Hai River and Liao River in northern China. *Environ. Pollut.* 159, 1877–1885. doi: 10.1016/j.envpol.2011.03.034

Conflict of Interest: AW and BA are employed by Yorkshire Water.

The remaining authors declare that the research was conducted in the absence of any commercial or financial relationships that could be construed as a potential conflict of interest.

Copyright © 2019 Richardson, Hodgson, Kay, Aston and Walker. This is an open-access article distributed under the terms of the Creative Commons Attribution License (CC BY). The use, distribution or reproduction in other forums is permitted, provided the original author(s) and the copyright owner(s) are credited and that the original publication in this journal is cited, in accordance with accepted academic practice. No use, distribution or reproduction is permitted which does not comply with these terms.

frontiers in Earth Science

ORIGINAL RESEARCH
published: 05 December 2019
doi: 10.3389/feart.2019.00319

Event Stratigraphy in a Hadal Oceanic Trench: The Japan Trench as Sedimentary Archive Recording Recurrent Giant Subduction Zone Earthquakes and Their Role in Organic Carbon Export to the Deep Sea

Arata Kioka[1,2], Tobias Schwestermann[1], Jasper Moernaut[1], Ken Ikehara[3], Toshiya Kanamatsu[4], Timothy I. Eglinton[5] and Michael Strasser[1,6]*

[1] Institute of Geology, University of Innsbruck, Innsbruck, Austria, [2] Department of Earth Resources Engineering, Kyushu University, Fukuoka, Japan, [3] Geological Survey of Japan, National Institute of Advanced Industrial Science and Technology (AIST), Tsukuba, Japan, [4] Research Institute for Marine Geodynamics, Japan Agency for Marine-Earth Science and Technology (JAMSTEC), Yokohama, Japan, [5] Geological Institute, ETH Zürich, Zurich, Switzerland, [6] MARUM – Center for Marine Environmental Sciences, University of Bremen, Bremen, Germany

OPEN ACCESS

Edited by:
Michael Andrew Clare, University of Southampton, United Kingdom

Reviewed by:
Patrick Lajeunesse, Laval University, Canada
Yvonne Therese Spychala, Utrecht University, Netherlands

***Correspondence:**
Arata Kioka
kioka@mine.kyushu-u.ac.jp

Specialty section:
This article was submitted to Sedimentology, Stratigraphy and Diagenesis, a section of the journal Frontiers in Earth Science

Received: *15 June 2019*
Accepted: *18 November 2019*
Published: *05 December 2019*

Citation:
Kioka A, Schwestermann T, Moernaut J, Ikehara K, Kanamatsu T, Eglinton TI and Strasser M (2019) Event Stratigraphy in a Hadal Oceanic Trench: The Japan Trench as Sedimentary Archive Recording Recurrent Giant Subduction Zone Earthquakes and Their Role in Organic Carbon Export to the Deep Sea. Front. Earth Sci. 7:319. doi: 10.3389/feart.2019.00319

Hadal trenches are the deepest places on Earth and are important foci for natural carbon sequestration. Much of the sedimentary sequences that accumulate within hadal trenches have been linked to widespread slope sediment remobilization events, triggered by subduction zone earthquakes. Therefore, hadal trench deposits may provide valuable insights into the hazards posed by large earthquakes and their implications for the carbon cycle. Despite this strong societal relevance, no studies to date have provided the necessary coverage to understand the spatial and temporal variations of earthquake-triggered deposition along a hadal trench axis. We address these issues by integrating high-resolution bathymetry and subbottom profiler data, and sediment cores acquired over the entire hadal trench axis of the Japan Trench. We identify around 40 isolated trench-fill basins along the trench axis of the Japan Trench that document 115 sediment remobilization event deposits. We map the spatio-temporal distribution of the acoustically transparent event deposit bodies imaged in subbottom profiler data from the trench-fill basins. Using radiocarbon dating, slope failure deposits identified from subbotom profiles and sediment coring were shown to be co-eval with major historic earthquake (e.g., AD2011 M_w9.0–9.1 Tohoku-oki, AD1454 $M_w \geq$8.4 Kyotoku, and AD869 $M_w \geq$8.6 Jogan events). Furthermore, the lower part of the acoustically imaged stratigraphic succession in isolated basins along the Japan Trench also documents several thick acoustically transparent bodies that relate to older events. These identifications of event deposits allow quantitative constraints of along-strike variation of sediment volumes redistributed by episodic events along the entire trench axis, revealing that the total volumes of event deposits triggered by different

historic large earthquakes are highly variable. We conclude that at least 7 Tg (10^{12} g) of organic carbon remobilized from surficial slope sediments is exported to the hadal axis of Japan Trench in the last 2,000 years by giant earthquakes. These findings highlight the significance of seismo-tectonic events for the long-term carbon cycle in hadal trenches and societal implications.

Keywords: hadal zone, event deposit, organic carbon, paleoseismology, Japan Trench

INTRODUCTION

Hadal trenches are formed by the downward bending of oceanic crust in the plate subduction zone at 6–11 km water depths. As a result of the challenges in surveying and sampling in such great water depths, hadal trenches remain largely unexplored, yet they act as terminal sinks for sediment, organic carbon (OC) and even pollutants (Kioka et al., 2019; Peng et al., in press). The study of hadal trenches may allow to (i) unravel the history of subduction zone processes, including the world's largest earthquakes that occur in such subduction margin settings, and (ii) to investigate the deep-marine carbon cycle. In hadal trenches, the steep slopes and isolated nature of the deep-water basins act as potential depocenters for organic matter (Jamieson et al., 2010). Sediment mass-wasting events and the resulting high supply of organic matter influence the benthic communities in the hadal environments (Danovaro et al., 2003; Glud et al., 2013; Leduc et al., 2016), as the hadal microbial system is distinct relative to shallower water depths and retained by internal recycling of organic matter (Nunoura et al., 2015). Short-term biogeochemistry models predict global decreases in ocean benthic mass particularly at the hadal zone, in response to reduced supply of organic material due to climate change during the 21st century (e.g., Jones et al., 2014). Moreover, on longer geological time scales, the deposition, burial and subduction of OC within marine sediment in plate subduction margins can play a pivotal role in the long-term carbon cycle, influencing atmospheric CO_2 amounts over millions of years (Berner, 1982; Burdige, 2007; Clift, 2017). Nevertheless, quantitative studies in hadal trenches have been hindered due to the limited availability of high quality data, in contrast to other continental margins. However, the recent improvement in data acquisition and observation in the hadal trenches has greatly benefited these studies. Therefore, unraveling sedimentary sequences in hadal trenches represents new frontiers in sedimentology, allowing a better understanding of sediment mass and carbon transport and storage from shallow waters to the ultimate deepest sinks of the world's oceans and their societal implications.

Megathrust earthquakes and associated tsunami have resulted in major societal and economic impacts. Globally, there have been five magnitude-9 class earthquakes instrumentally recorded during the last century, including AD 1952 moment magnitude (M_w) ∼9.0 Severo-Kurilsk earthquake offshore Kamchatka Peninsula (e.g., MacInnes et al., 2010), AD 1960 M_w9.4–9.6 Valdivia earthquake in Chile (e.g., Satake and Atwater, 2007), AD 1964 M_w∼9.2 Alaskan earthquake (e.g., Kanamori, 1977), AD 2004 M_w9.1–9.3 Indian Ocean earthquake offshore Sumatra (Lay et al., 2005; Stein and Okal, 2005), and AD 2011 M_w9.0–9.1 Tohoku-oki earthquake offshore northeast Japan. Four of these megathrust earthquakes occurred near hadal trenches. Notably, the AD 2011 Tohoku-oki earthquake, which occurred along the hadal Japan Trench, generated the largest-ever-recorded coseismic slip (Ide et al., 2011), horizontal displacement and vertical uplift (Fujiwara et al., 2011; Kodaira et al., 2012; Chester et al., 2013), and a powerful tsunami with coastal run-up heights up to 40 m (Mori et al., 2011). Our knowledge of large magnitude earthquakes can be extended prior to the window of instrumental records (around 100 years) using historical documents (Satake and Atwater, 2007). Depositional archives from coasts, lakes, and marine sediments have been used to look further back in time (Goldfinger, 2011; Satake, 2015; Moernaut et al., 2018). Yet, there remain significant uncertainties with respect to the locations, magnitudes, and mechanisms of historical large earthquakes, and their societal impacts. Hence, investigating sedimentary sequences in hadal trenches also helps reconstructing past subduction zone earthquake magnitude-frequency relations, allowing a better assessment of hazard and risk for coastal populations and infrastructure along the active margins.

In the hadal Japan Trench, the AD 2011 Tohoku-oki earthquake remobilized young fine-grained surficial slope sediments enriched in organic matter, which was eventually deposited in the more than 7 km deep trench (Arai et al., 2013; Oguri et al., 2013; Strasser et al., 2013; Ikehara et al., 2016; McHugh et al., 2016; Kanamatsu et al., 2017; Bao et al., 2018; Kioka et al., 2019; Molenaar et al., 2019). Remarkably, the 2011 earthquake delivered >1 Tg (10^{12} g) of OC to the Japan Trench between 36.0° and 39.5°N through the resedimentation of spatially widespread remobilization of surficial sediment with a total volume of ∼0.2 km^3 (Kioka et al., 2019). Moreover, several cores from the central part of the Japan Trench document evidence for event deposits related to surficial sediment remobilization triggered by older large earthquakes in the last few thousands of years, including the well-known AD 1454 Kyotoku and AD 869 Jogan earthquakes (Ikehara et al., 2016, 2018; Usami et al., 2018). Yet, little is understood about (1) the temporal and spatial extent of the earthquake-triggered event deposits along the plate subduction zone, (2) whether older deposits may indicate prehistoric large earthquakes, and (3) the importance of recurrent large earthquakes for the carbon cycle at subduction margins.

Here, we aim to address these issues by integrating high-resolution bathymetry and dm-scale vertical resolution subbottom profiler (SBP) data, and sediment cores acquired by many research cruises during 2012–2018 over 530 km along

strike the hadal trench axis of the Japan Trench (36.0°–40.5°N). These data allow a detailed study of event stratigraphy in an entire hadal trench for the first time to our knowledge. First, we identify isolated trench-fill basins along the trench axis of Japan Trench that document sediment remobilization event deposits. Second, at the identified trench-fill basins, we map the event-stratigraphic distribution of the acoustically transparent bodies imaged in SBP data. Third, we correlate the acoustically transparent bodies that represent the event deposits triggered by major historic earthquakes. Fourth, we quantify along-strike variation of sediment volumes and OC contents of the event deposits related to past large earthquakes along the entire trench axis. By integrating and discussing the results, we also examine (i) the submarine paleoseismology approach of linking the spatio-temporal inventory of major sediment remobilization event deposits to the history of giant earthquakes, and (ii) the hypothesis that sediment remobilization induced by recurring giant earthquakes supplies large quantities of OC to the hadal trench over geological time scales.

JAPAN TRENCH

Geological Setting

The Japan Trench occurs at the plate boundary where the Pacific Plate is subducting beneath the Okhotsk Plate (Bird, 2003) or its separated microplate (e.g., Seno et al., 1996), extending from the triple junction between the Pacific, Philippine Sea and Okhotsk plates in the south to the intersection with the Kuril Trench in the north. A relatively moderate to rapid convergence rate of 7–9 cm/yr (e.g., Loveless and Meade, 2010) and relatively thin sediment cover at the trench (0.4–1 km: Lallemand et al., 1994; Nakamura et al., 2013) control development of the Japan Trench, which may favor the occurrence of subduction erosion producing tectonic subsidence (von Huene and Lallemand, 1990; Clift and Vannucchi, 2004). Although there is no typical forearc basin, isolated basins occur on the upper slope terrace (Arai et al., 2014; Boston et al., 2017). The lower slope is steeper with an average gradient of ∼5° (Kodaira et al., 2012; Koge et al., 2014). Active faulting along the subduction margin (Tsuru et al., 2002; Tsuji et al., 2013; Boston et al., 2017; Kodaira et al., 2017) forms a narrow mid-slope terrace at water depths of 4,000–6,000 m. The Japan Trench is characterized by the N-S to NNE-SSW trending horst-and-graben structures formed by flexural bending of the subducting Pacific plate, resulting in rough trench-floor morphology with isolated trench-fill and graben-fill basins (Nakamura et al., 2013; Kioka et al., 2019). Our study area of the deep Japan Trench is bounded by the subducting Erimo and Daiichi-Kashima seamounts in the north and south, respectively (Cadet et al., 1987), constraining the trench to around 530 km long (**Figure 1**). The floor of the trench-axis is relatively shallower at the northern and central trench basins ranging between around 7,400 and 7,700 m, while the southern trench basin north of Daiichi-Kashima Seamount reaches a water depth of 8,030 m (Kioka et al., 2019). While no major canyon system is present along most parts of the Japan Trench, the Ogawara and Nakaminato submarine canyon systems connect the continental margin and trench axis in the northernmost and southernmost Japan Trench (**Figure 1**). In this study, we divided the Japan Trench into the three segments, southern, central, and northern Japan Trench, based on water depths at the trench axis and structural complexities along the trench.

Historically Documented Large Earthquakes

The AD 2011 M_w9.0–9.1 Tohoku-oki earthquake is one of the largest earthquakes instrumentally recorded. Other than the 2011 earthquake, several large earthquakes with magnitude of >8 are historically well known along the Japan Trench that have been identified from tsunami deposits along the coast of Fukushima, Miyagi, Iwate, and Aomori Prefectures (**Figure 1**). For example, the AD 1968 M_w8.2–8.3 Tokachi-oki (Northern Sanriku-oki) megathrust earthquake (Kanamori, 1971) occurred offshore Aomori and Iwate Prefectures, and AD 1933 M_w∼8.4 Showa-Sanriku (Kanamori, 1977) and AD 1896 M_w8.0–8.4 Sanriku-oki Tsunami earthquakes (e.g., Kanamori, 1972; Tanioka and Satake, 1996) occurred immediately to the west of the trench and the trench-outer rise offshore Iwate Prefecture, respectively. Along the southern Japan Trench, the AD 1677 Empo Boso-oki Tsunami earthquake is thought to have occurred offshore Boso Peninsula (Takeuchi et al., 2007; Sawai et al., 2012) with M_w8.3–8.6 based on a tsunami inversion model (Yanagisawa et al., 2016). The AD 1454 M_w≥8.4 Kyotoku (Sawai et al., 2015) and AD 869 M_w≥8.6 Jogan earthquakes (Sawai et al., 2012; Namegaya and Satake, 2014) are modeled to occur offshore Miyagi Prefecture. Ikehara et al. (2016, 2018) and Bao et al. (2018) reported thick event deposits from sediment cores along the central Japan Trench that are linked to the AD 2011 Tohoku-oki, AD 1454 Kyotoku, and AD 869 Jogan earthquakes. Similarly large earthquakes older than these events have also been documented from widespread tsunami deposits (Satake, 2015) and marine sediments on the mid-slope terrace (Usami et al., 2018).

Another potentially large earthquake, the AD 1611 Keicho event, is discussed in the literature to be of possible similar size as the AD 1454 earthquake, as inferred from tsunami reported along the coast of Iwate and Miyagi Prefectures (Tsuji and Ueda, 1995; Ishimura and Miyauchi, 2015; Goto et al., 2019). However, the inferred seismic source is still debated, because the Keicho tsunami was reported to have reached the coast a few hours after a major earthquake. This historical report is very different from the other known large events like the AD 2011 and AD 869 Tsunamis (Sawai et al., 2015) that hit the coast within far less than 1 h after earthquake shaking. The AD 1611 Keicho Tsunami, therefore, is attributed to either submarine landslide (Tsuji and Ueda, 1995) or a remote rupture along the Kuril Trench (Okamura and Namegaya, 2011), and most likely does not link to a megathrust rupture along the Japan Trench. The occurrence of only one large earthquake that ruptured the Japan Trench megathrust between the mid-14th and early-17th century is also supported by the fact that only one event deposit is identified in the Japan Trench during this time window. While early studies lacked the dating resolution to pin point the specific triggering event (e.g.,

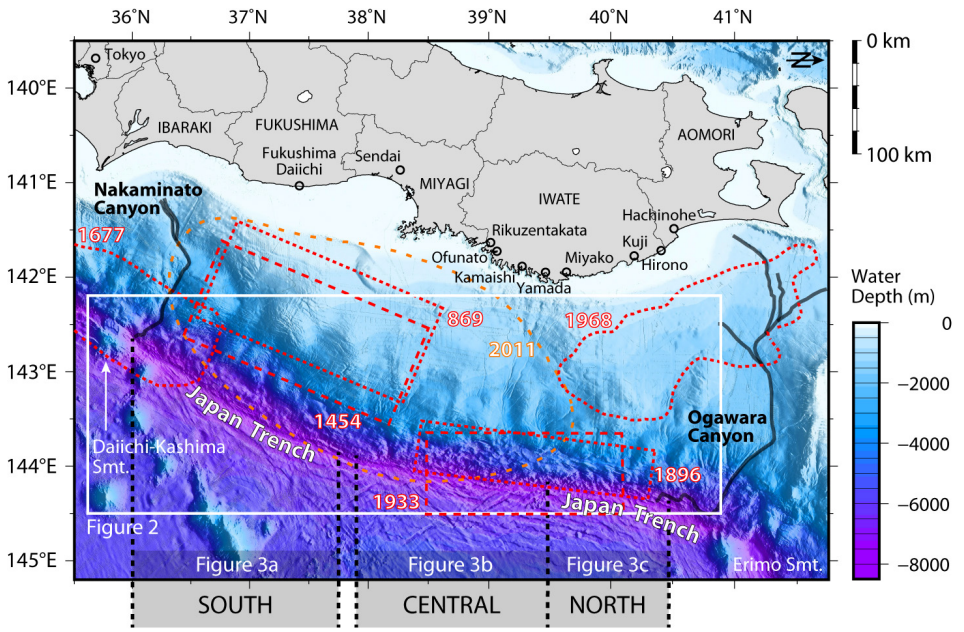


FIGURE 1 | Map of Japan Trench with historically known large earthquakes. Source areas of the earthquakes (red dash lines) are derived from literature: AD 1968 M_w8.2–8.3 Tokachi-oki (Sanriku-oki Hokubu) earthquake (Nagai et al., 2001); AD M_w~8.4 1933 Showa Sanriku earthquake (Kanamori, 1971); AD 1896 M_w8.0–8.4 Meiji Sanriku earthquake (Tanioka and Satake, 1996); AD 1677 M_w8.3–8.6 Enpo Boso-oki earthquake (Takeuchi et al., 2007; Sawai et al., 2012); AD 1454 M_w>=8.4 Kyotoku earthquake (Sawai et al., 2015); AD 869 M_w>=8.6 Jogan earthquake (Sawai et al., 2012). The orange dashed line represents an interred 2 m-coseismic slip of the 2011 Tohoku-oki mainshock (Sun et al., 2017). A white rectangular is a domain showing the result of flow accumulation (**Figure 2**). Water depths and SBP images along the trench axis in the southern, central, and northern Japan Trench are shown in **Figure 3**.

Ikehara et al., 2016), recent high-resolution radiocarbon dating constrains the age of the event deposit to the 15th century and thus corroborates the correlation to the AD 1454 Kyotoku earthquake (Bao et al., 2018).

DATA AND METHODS

Bathymetry Data

We acquired high-resolution bathymetry data along the entire trench axis during the R/V Sonne SO251-1 cruise in October 2016 (Fujiwara et al., 2017; Strasser et al., 2017; Kioka et al., 2019). The data were acquired by a 12 kHz frequency KONGSBERG EM122 system equipped on R/V Sonne, which has 432 beams with a transducer of 0.5 (transmission) by 1 (receiving) degrees, and a dual swath (multiping) function. Such a small transducer configuration, together with higher beam counts and dual ping system results in high lateral resolution (footprint of 60–70 m along-track by 130–140 m across-track in water depths of 7–8 km) and optimized signal-to-noise ratio of the bathymetric data. The theoretical vertical resolution is a function of the water depth (a few to tens of meters in water depths of 7–8 km). This high spatial resolution results in being uniquely capable of identifying even small depositional basins within the structurally complex and hadal trench-floor system (Kioka et al., 2019).

We combined a modern digital evaluation model (DEM) calculated from bathymetry data at the water depths of <~6,000 m acquired before 2011 by the Japanese research cruises (Hydrographic and Oceanographic Department Japan Coast Guard and JAMSTEC, 2011) with our post 2011 earthquake data (>5500 m depth) acquired during the R/V Sonne SO251-1 cruise (Fujiwara et al., 2017; Strasser et al., 2017; Kioka et al., 2019). This allows analyzing the flow network of potential sediment pathways across the margin into the trench and estimating relative contribution of sediment volume that can be routed into individual terminal trench basins. The use of the SO251-1 cruise data enables an approximate determination of sediment transport pathways and depocentres using a simple flow network model at the hadal depths of the trench. We approximated the flow path by using the single neighboring algorithm (D8 algorithm) that passes the flow from a given cell to its lowest adjacent cell (e.g., O'Callaghan and Mark, 1984). With the produced flow network, flow accumulation along the Japan Trench was calculated following the method of Schwanghart and Scherler (2014) on the combined DEM of 70 × 70 m cell size. The flow accumulation (m^2) was computed as product of the number of upstream cells and the square of the cell size, representing the accumulated weight of each grid cells flowing into the deepest cells of the terminal trench basins. We did not define spatially variable weights and runoff ratios. This approach is originally developed for rivers, and submarine sediment density flows can have much higher runups and may respond very differently to topography than rivers. Despite such a limitation, this relatively simplistic approach provides first-order insights into likely flow pathways given the scale of the study area.

High-Resolution Subbottom Profiler (SBP) Data

In this study, we combine SBP data that were obtained during eight research cruises with two different acquisition systems: SO251-1 (October 2016) and SO219A-2 cruises (March–April 2012) by *R/V Sonne* equipped with ATLAS PARASOUND P70 echosounder and KS-18-10 (August 2018), KS-17-13 (October 2017), KS-16-14 (September 2016), KS-15-16 (November 2015), KS-15-3 (May 2015), and KS-14-16 cruises (September 2014) by *R/V Shinsei-maru* with KONGSBERG TOPAS PS18. The PARASOUND echosounder emits two high frequencies of 18 kHz and 22 kHz, and non-linear interference of the high frequencies produces a secondary frequency of about 4 kHz. The TOPAS system uses a primary frequency of 15–21 kHz, and a secondary frequency of 0.5–6.0 kHz. Frequency filtering was done through low-pass bandpass at 6 kHz for PARASOUND data (Strasser et al., 2017) and high- and low-pass filters at 2 and 7 kHz for TOPAS data. Theoretical vertical resolutions is in the order of ∼10–20 cm for bandwidths of 4–7 kHz. The SBP taken by Parasound system records mostly at 30–70 m per shot point (SP), while that taken by Topas system at 5–40 m/SP. All the studied SBP lines were carefully determined in light of high-resolution bathymetry data acquired by the SO251-1 cruise and acquired extensively throughout the entire Japan Trench.

The studied SBP data acquired by both systems often contain noisy traces that are caused by either interference of the ship's multibeam system or bad weather conditions (i.e., swell). Thus, following supplementary material of Kioka et al. (2019), we post-processed the noisy SBP data by removing bad traces and interpolation of the resultant irregularly populated trace data, to ensure identification of acoustically transparent bodies with ponding geometries and reliable signal analyses for basin-to-basin correlation (see section "Correlation of Acoustically Transparent Bodies Between Neighboring Basins"). Interpolation of the killed traces in a given seismic data was solved as a sparse inverse problem using the projection-onto-convex sets algorithm (Abma and Kabir, 2006; Chen et al., 2015). We used the method of soft thresholding by the iterative shrinkage-thresholding algorithm (Daubechies et al., 2004) with a sufficiently high thresholding level, and applied 1,000–5,000 iterations to assure the convergence (the number of iterations depends on trace samples and number of noisy traces). These processes benefit from preventing losses of spatial information of SBP data because most of data were acquired with a constant ship's speed.

Sediment Cores and Radiocarbon Dating of Background Sediment

Previous studies reported many sediment cores taken along the trench axis of the Japan Trench. Several of these cores have been used previously to establish detailed understanding of sedimentation processes, including the deposition of thick event deposits correlated to historical earthquakes (Ikehara et al., 2016; Bao et al., 2018). We use the event-stratigraphic information from these studies to validate and constrain age information for our interpretation of SBP data (see section "Identification of the Event Deposits Within Individual Trench-Fill Basins and Areal Extent and Volume of the Identified Event Deposits"). However, available data from cores are mostly from the central Japan Trench with fewer cores located in the southern and northern Japan Trench. To fill the gaps, we acquired and analyzed cores GeoB21804 and GeoB21817 taken during *R/V Sonne* SO251-1 cruise, KS-15-16 PC01, KS-17-13 PC01, and KS-18-10 PC01 taken during *R/V Shinsei-Maru* KS-15-16, KS-17-13 and KS-18-10 cruises, respectively (see **Supplementary Figure S1** for the core locations). The core locations were carefully determined with the help of bathymetry and onboard initial SBP data interpretation during these cruises. Core processing and analyses followed the same core description and investigation methods (including visual core description, radiograph image analyses, and multi-sensor core logging) to identify thick sedimentary events deposits as used by previous studies (Ikehara et al., 2016, 2018; Strasser et al., 2017; Bao et al., 2018; Kioka et al., 2019).

Following the same concept of age determination and relative dating of event-deposits as applied for cores from the central Japan Trench (Ikehara et al., 2016; Bao et al., 2018), we also made radiocarbon (^{14}C) dating of bulk OC separated from background sediments from the cores GeoB21804 and GeoB21817. The samples were freeze-dried in pre-combusted vials, and aliquots were weighed into Ag capsules for fumigation with ∼30 ml of concentrated HCl (37%, metal-trace purity) for 72 h at 60 °C to remove inorganic carbon. The acidified samples were subsequently neutralized with ∼20 g NaOH under the same conditions (72 h). The bulk organic ^{14}C ages were measured using a coupled EA/IRMS/AMS online system at ETH Zurich (McIntyre et al., 2017). Errors of the ^{14}C measurement were within ± 80 years (one standard deviation) in our samples. As revealed by previous studies by Bao et al. (2018) and Ikehara et al. (2016), bulk organic ^{14}C ages do not represent the actual depositional age of the sediment (age offset in the order of ∼1,600 years), however, background sedimentation at the trench-fill basin of the Japan Trench yields a strong linear relationship between bulk OC ^{14}C age and sediment depth (Bao et al., 2018; see section "RESULTS"). Thus, we can calculate a linear regression for ^{14}C ages of background sediments to obtain a linear sedimentation rate of background sediments through re-sorting sediment depths after removing all the identified turbidite columns. Here, we obtain the linear sedimentation rate using a linear errors-in-variables model (measurement error model) to take into account errors arisen from ^{14}C analyses (**Supplementary Figure S2**).

Identification of the Event Deposits Within Individual Trench-Fill Basins and Areal Extent and Volume of the Identified Event Deposits

As reported in previous studies, high-resolution SBP data along and across the flat trench basins image distinct bodies with acoustically transparent seismic facies, a basal higher amplitude reflection and ponded geometries. Acoustically transparent bodies in SBP data represent event deposition of thick homogenous, fine-grained relatively young sediments, in part overlying comparably thin basal sand beds

(Ikehara et al., 2016, 2018; Kioka et al., 2019). The acoustic facies of these depositional bodies are distinct from chaotic reflection patterns and irregular top morphology in the areas where local deep-seated slumps have transported older sedimentary units to trench basins (Kawamura et al., 2012; Strasser et al., 2013) or where shallow co-seismic slip propagation has deformed trench sediment (Kodaira et al., 2012). Here we systematically analyzed the newly compiled SBP data set of the entire Japan Trench for identification and spatio-temporal mapping of such acoustically transparent bodies with ponded geometries throughout the entire data set. We applied the same methodological principles as Kioka et al. (2019) used for mapping the 2011 Tohoku-oki event deposit to the deeper subsurface data. Following conventional seismic-stratigraphic interpretation methods, we picked the top and bottom horizon of uniquely identifiable acoustically transparent body. We only picked the acoustic bodies that are thicker than 0.4 m (more than twice the vertical resolution of SBP data) at their potential depocentres to reveal clear lateral pinch-out geometries of the acoustically transparent facies against the acoustically laminated facies of "background" strata. We did not map the event deposits where seismic interpretation is non-unique. For the uppermost 5–10 m subsurface depth, the interpretation of the recent deposition of fine-grained remobilized sediment in SBP data is validated by the studied cores that document homogenous diatomaceous mud deposits (see section "RESULTS"). We identified trench-fill basins where we could detect such acoustically transparent bodies in SBP and cores. For convenience, we labeled the identified trench-fill basins from south to north as JTS01, JTS02, ..., JTC01, JTC02, ..., and JTN01, JTN02, ..., in the southern, central, and northern Japan Trench, respectively. In addition, we also labeled acoustically transparent bodies, from shallow to deep, such as U1-S01, U2-S01, U3-S01, ... in the identified trench-fill basin JTS01. We then estimated areal extent and volume of identified acoustically transparent bodies (i.e., event deposits) in individual trench-fill basins, as constrained through integrating SBP and bathymetry data following the method of Kioka et al. (2019). Uncertainties in areal extent and volume of given event deposit at a given trench-fill basin are calculated, taking into account lateral resolution of bathymetry (∼100 m), vertical resolution of SBP (±0.1 m), and variable thicknesses of event deposits upon the choice of internal velocity (1,500–1,700 m/s).

Correlation of Acoustically Transparent Bodies Between Neighboring Basins

Only in rare cases can picked horizons be confidently tracked across individual trench-fill basins. Therefore, stratigraphic correlation of acoustically transparent bodies of interest between neighboring trench-fill basins (i.e., testing for the respective deposits in a given trench-basin to correspond to the same event in its neighboring basins), relies on visual correlation and comparative pattern recognition. To objectively validate the visual correlation, we also applied computational signal analysis for SBP data. We performed the automatic correlation for the SBP traces of interest using the conventional dynamic time warping (DTW; Sakoe and Chiba, 1978; Müller, 2007). The DTW is a commonly used algorithm to find an optimal alignment between two given time-dependent signals. Let us consider two different representative traces of SBP data at different trench-fill basins:

$$\mathbf{a} = \begin{bmatrix} t_1 & a_1 \\ \vdots & \vdots \\ t_m & a_m \end{bmatrix}, \mathbf{b} = \begin{bmatrix} t_1 & b_1 \\ \vdots & \vdots \\ t_n & b_n \end{bmatrix},$$

where $m \in \mathbb{N}$ and $n \in \mathbb{N}$ are the lengths of the two SBP traces, t_i $(i = 1, 2, \ldots)$ is the TWT, and a_i and b_i are the envelope values of the two SBP traces. We obtained an alignment between the two SBP traces **a** and **b** having minimal overall cost through computing the Euclidian distances between the ith $(i \in [1, m])$ sample of **a** and jth $(j \in [1, n])$ sample of **b**. Event deposits are generally homogenous and thus characterized by low-amplitude wiggles in SBP data. Event deposits from cores are in parts accompanied with basal sand beds (Ikehara et al., 2016), showing high amplitudes of reflection in SBP data. Therefore, the presence of sand beds ensures DTW for correlating acoustically transparent bodies of interest between two basins (e.g., **Supplementary Figure S3**).

RESULTS

Inferred Flow Pathways and Accumulation Along the Trench

Using a DEM made through combining the bathymetry data shallower than hadal depths and high-resolution bathymetry deeper than >5500 m, we calculated flow accumulation along the Japan Trench (**Figure 2**). The trench floor of the northernmost Japan Trench, where it connects to the Ogawara canyon, has the largest flow accumulation in the entire Japan Trench (trench-floor basin JTN08: 5.3×10^{10} m^2). Similarly, the southernmost Japan Trench also can experience large flow accumulation as it connects to the Nakaminato canyon (trench-floor basin JTS01: 1.4×10^{10} m^2). It is also fed by a smaller sediment routing system from the north (indicated by gray arrows in **Figure 2**) connecting trench-floor basins JTS04, JTS03, and JTS02 (see section "Identification, Dating, and Correlation of the Event Deposits Along the Trench" for these identified basins). On the other hand, the trench axis floors between 36.8°N and 36.9°N, 38.1°N and 38.3°N, 39.0°N and 39.3°N, 39.7°N and 40.0°N, and 40.1°N and 40.2°N, are fed by individual smaller sediment routing systems yield low flow accumulation values ranging between 1×10^7–1×10^8 m^2. This suggests smaller catchment areas for sediment remobilization and/or less along-trench connectivity between these areas. The flow accumulation analysis also reveals that the different lateral sediment transport systems from the upper slope into the trench are funneled and can be reflected to form flow path systems along the trench axis for several tens of kilometers, connecting individual trench-slope basins. These systems are separated by bathymetric highs formed by the interconnection of different

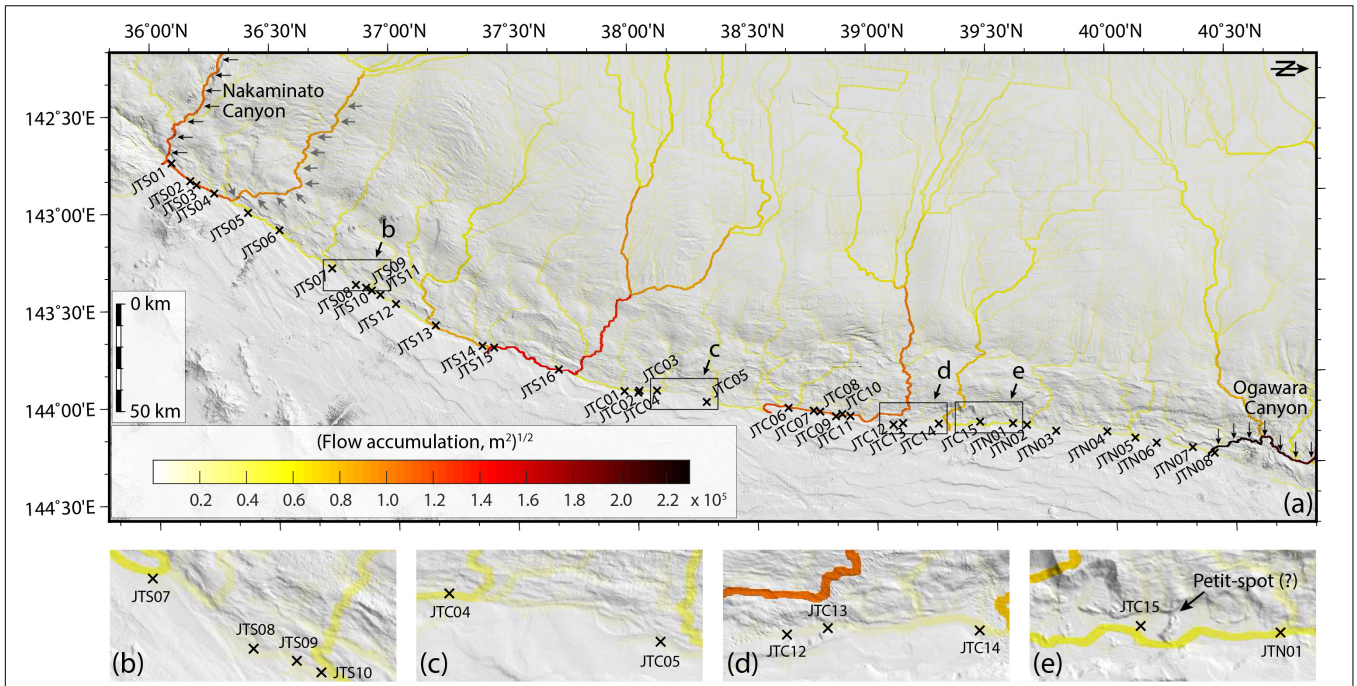


FIGURE 2 | Flow accumulation in **(a)** the entire Japan Trench, **(b)** the southern Japan Trench, **(c,d)** the central Japan Trench, and **(e)** petit-spot area. The square root of flow accumulation (m^2) is shown for the presentation purpose. The identified isolated fill-basins are also shown (see **Figure 3**).

structural elements of the flexural-bended Pacific plate entering the subduction zone system.

Identification, Dating, and Correlation of the Event Deposits Along the Trench

Southern Japan Trench

The seafloor of the trench axis in the southern Japan Trench is up to 8,030 m deep in the southernmost segment (36.08°N), while it becomes shallower (7,560 m) in the northernmost segment at 37.7°N (**Figure 3A**). The overall quality of along-trench SBP data was relatively good even for deep and narrow trench-fill basins. The SBP data imaged laterally continuous reflection signals down to ∼40–100 millisecond two-way travel time (ms TWT) below the seafloor in the trench-fill basins (i.e., ∼30–80 m below the seafloor (mbsf) assuming *P*-wave velocities of 1,500–1,700 m/s). The SBP data at several basins had less signal penetration, partly due to complex subsurface structures with chaotic acoustic facies that strongly attenuated the acoustic signals. For example, deeper acoustic facies at the basins JTS05 and JTS13 might be interpreted as local mass-transport deposits (Strasser et al., 2013) or trench-sediment deformation structures (Kodaira et al., 2012). These structures are not further considered here for mapping the inferred deposits of fine-grained surficial slope remobilization events. Several acoustically transparent bodies of ∼1 to ∼8 ms TWT in thickness were interbedded in the laterally continuous, parallel reflection pattern within the trench-fill basins (**Figure 4**). With these data, we identified sixteen isolated trench-fill basins (JTS01–JTS16) in the southern Japan Trench (**Table 1** and **Figure 3A**), that each comprises 1–7 event deposits clearly imaged in SBP data. The uppermost acoustically transparent body in SBP images that is related to recent remobilization events linked to the AD 2011 earthquake (Kioka et al., 2019) was recognized in most of identified basins.

At the southernmost basin (JTS01), the largest trench-fill basin located at the deepest water depth, seven acoustically transparent bodies (U1-S01, U2-S01, . . ., U7-S01) were identified in the ∼50 m thick stratigraphic succession imaged by the SBP data (**Figures 3A**, **4A,B**). The core GeoB21804 taken from the depocentre of JTS01 basin exhibits olive-gray diatomaceous mud interbedded with silt laminae, sand beds with sharp upper and lower contacts, and intervals of mixed mud (**Figure 5**; Strasser et al., 2017). The visual core description, magnetic susceptibility data (Strasser et al., 2017) and detailed analyses of radiograph images (this study; **Figure 5**) of core GeoB21804 document four stratigraphic levels of (50–140 cm) thick homogenous-to-mixed diatomaceous mud with thin (few cm thick) basal fine-sand bed intercalated within bioturbated diatomaceous mud with silt laminae in the upper 7.5 mbsf (**Figures 5**, **6**). Core-to-SBP correlation (**Figures 4**, **6**) reveals very good correlation between event-deposits inferred from SBP interpretation and the four intervals of thick homogenous-to-mixed sediments, which thus are interpreted as event-deposits representing major sediment-remobilization events. The uppermost acoustically transparent body U1-S01 is the event deposit linked to the 2011 earthquake (Kioka et al., 2019). Bulk OC ^{14}C ages of background sediment interbedded between the event deposits within the core GeoB21804 revealed a linear sedimentation rate of 5.44 (+0.13/-0.09) m/kyr for background sediment in the basin JTS01 (**Figure 6** and

Supplementary Figure S2). By extrapolating such inter-event linear sedimentation rates to the entire depth range covered by SBP data, the ages of the lower six acoustically transparent bodies (U2-S01, U3-S01, . . ., U7-S01) were estimated to be AD 1846 (+22/−25), AD 1671 (+44/−52), AD 980 (+78/−157), 3.39 (+0.52/−0.15) ka, 5.46 (+0.83/−0.22) ka, and 6.91 (+1.06/−0.27) ka, respectively. The U4-S01 [AD 980 (+78/−157)] showed the second largest volume of deposit in the basin S01 [0.040 (+0.010/−0.004) km^3; **Table 1**].

At the basin JTS15, where flow accumulation is highest in the southern Japan Trench (**Figure 2**), six acoustically transparent bodies (U1-S15, U2-S15, . . ., U6-S15) were identified in SBP data (**Figures 3A**, **4**). The core KS-15-3 PC08 (Ikehara et al., 2018) taken near the depocenter documented three homogenous deposits in the upper 7 mbsf that indicate that the upper acoustically transparent deposits (U1-S15, U2-S15, and U3-S15) correlate to the AD 2011 Tohoku-oki, AD 1454, and AD 869 Jogan earthquakes (**Figures 4**, **6**). Assuming constant linear sedimentation rate inferred from inter-event background sedimentation, the lower three bodies U4-S15, U5-S15, and U6-S15 date back to 2.3 (+0.4/-0.2) ka, 4.0 (+1.0/-0.5) ka, and 8.0 (+ 2.5/-1.1) ka, respectively.

At the basin JTS16, located at shallowest water depth in the southern Japan Trench, we could identify only one very thin (∼5 ms TWT below the seafloor) and one deep (60–65 ms TWT below the seafloor) acoustically transparent body. Correlation between SBP data and core GeoB16444-1 (Ikehara et al., 2016) indicates that the upper very thin event deposit links to the event deposit of the AD 869 earthquake, and that the younger events (AD 1454 and 2011 earthquakes) positively identified in core data by Ikehara et al. (2016) are below the vertical resolution of the SBP data (and thus not considered in the SBP-data based event-stratigraphy mapping of this study). The deeper stratigraphic succession may also contain several events below SBP data resolution, but only one deeper (larger) SBP-resolved event deposit is clearly identified that dates back to 25–40 ka, when extrapolating a constant sedimentation rate as revealed from inter-event background sedimentation estimated from core GeoB16444-1.

Core-to-SBP data correlation is also relatively good in trench-basins JTS09 and JTS10, where acoustically transparent bodies in SBP data correlate with intervals of homogenous diatomaceous mud in cores KS-14-16 PC01 (Ikehara et al., 2018) and KS-17-13 PC01 (**Figure 6**). Although no age information on events

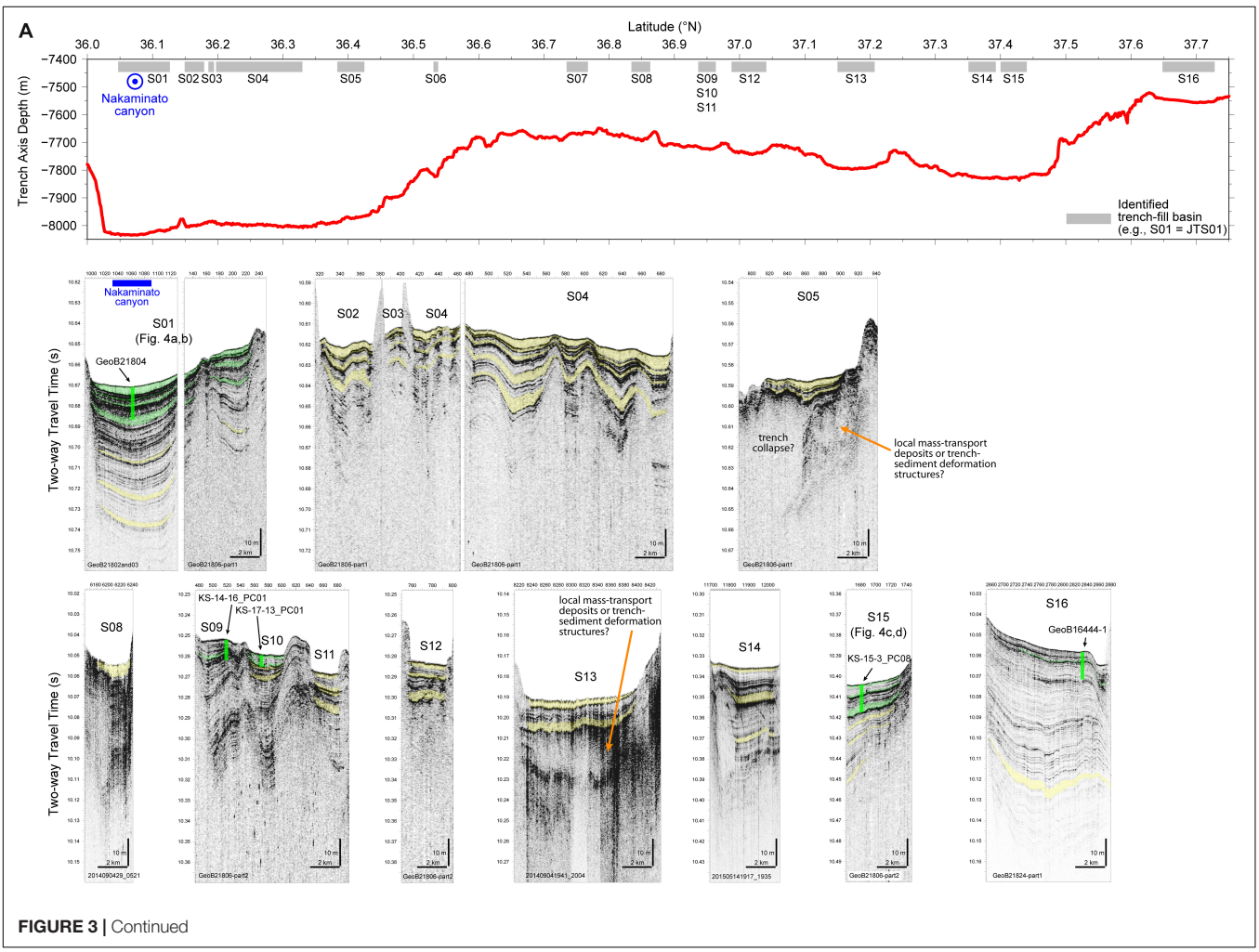


FIGURE 3 | Continued

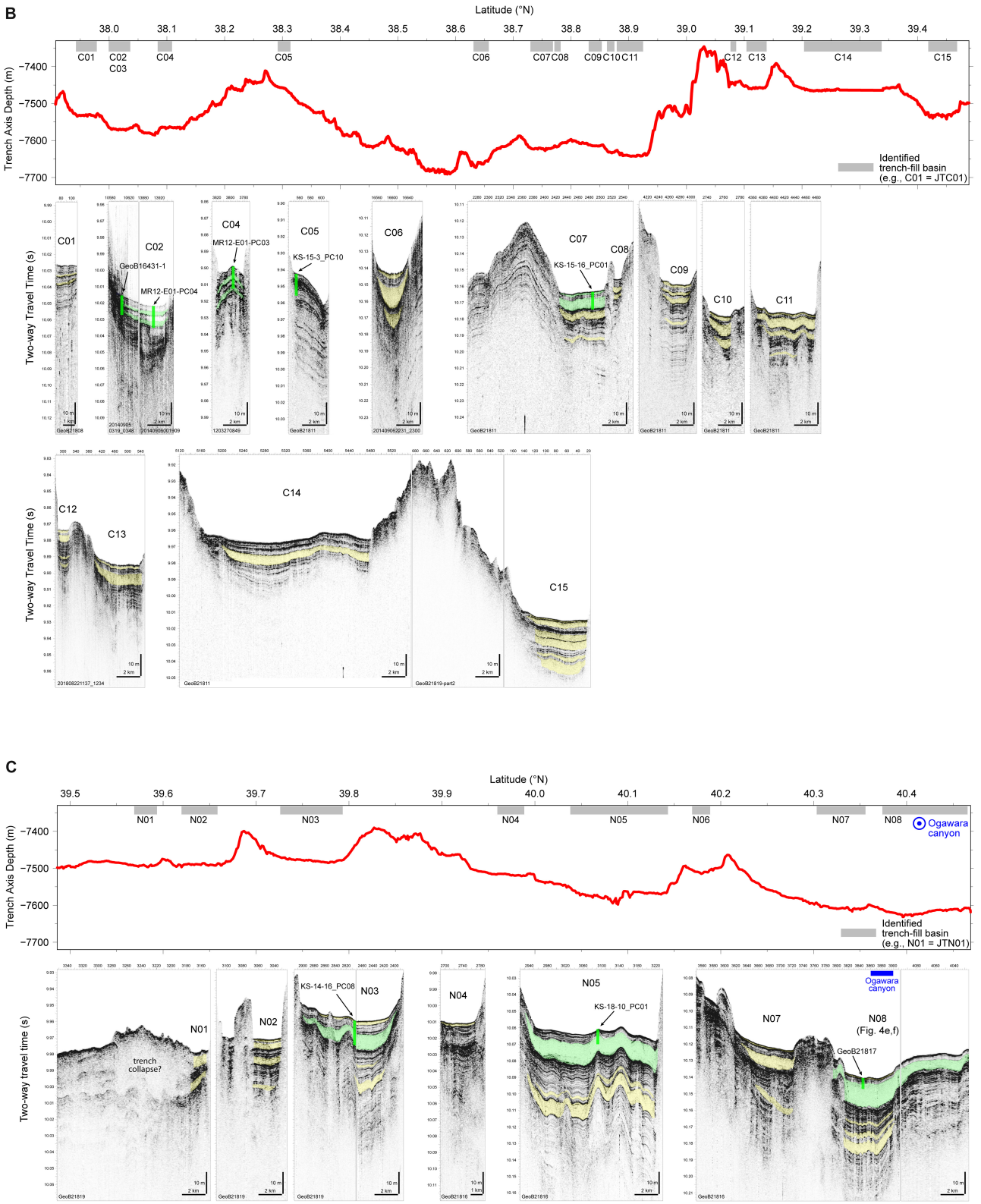


FIGURE 3 | Water depth, identified trench-fill basins, and their SBP images along the trench axis of **(A)** southernJapan Trench, **(B)** central Japan Trench, and **(C)** northern Japan Trench. Yellow fills are identified acoustically transparent event bodies based solely on SBP data, whereas green fills are the acoustically transparent event bodies validated by sediment cores.

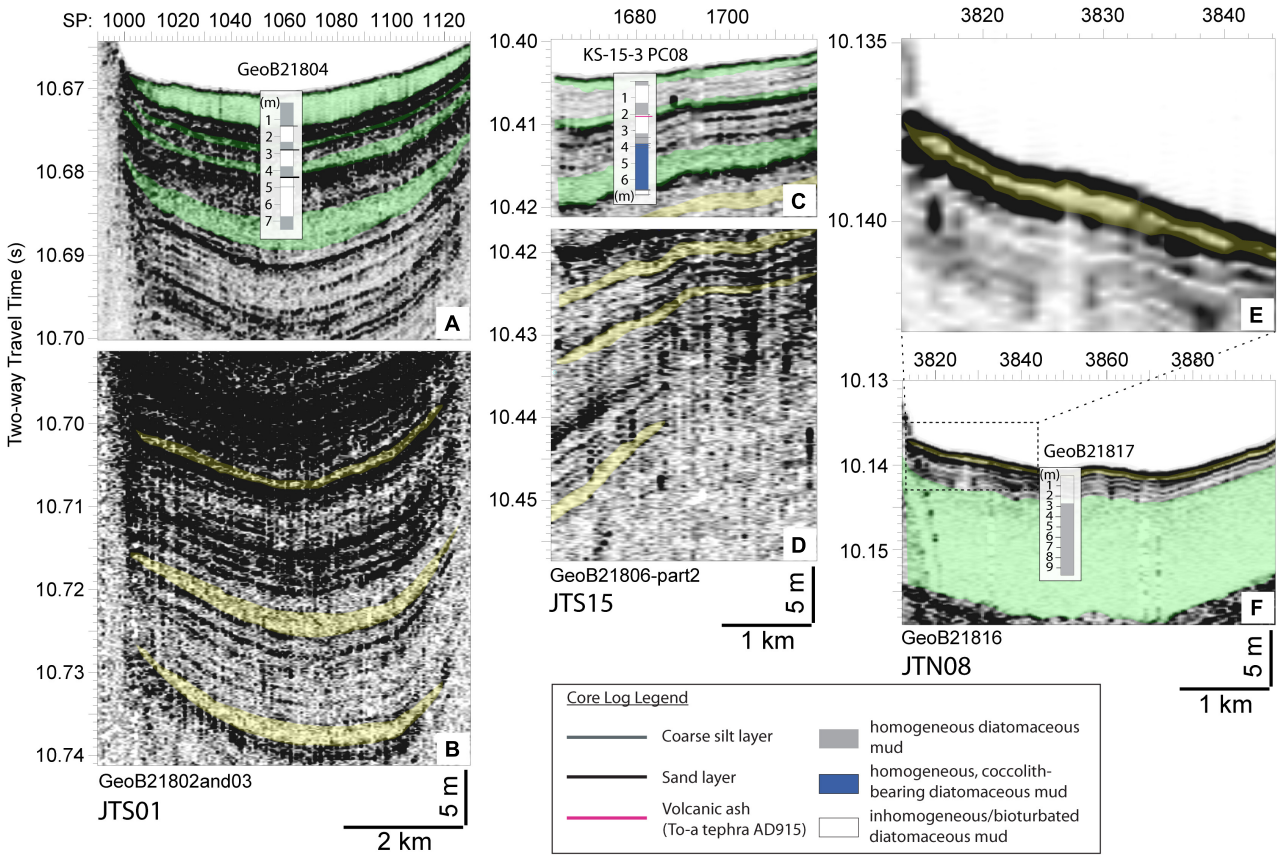


FIGURE 4 | Close-up examples of acoustically transparent bodies and SBP-to-core correlation. Note that the deeper intervals of SBP images **(B,D)** are gained as compared with the shallower intervals **(A,C)**. The deeper interval of SBP image **(F)** is presented at a reduced vertical exaggeration as compared with the shallower interval **(E)**.

deposits in these basins is available from core data, basin-to-basin correlation suggests that several acoustically transparent deposits, where imaged in neighboring trench-fill basins, can reliably be correlated across basins throughout the entire southern Japan Trench (**Figure 7**). Other than the 2011 event deposit (Kioka et al., 2019), for example, the acoustically transparent body U4-S01 [AD 980 (+78/-157)] in the basin JTS01 can be correlated widely to the acoustically transparent bodies at different basins and the 869 event deposit (U3-S15) in the basin JTS15. This indicated that the 869 Jogan event deposit was distributed mostly throughout the southern Japan Trench.

Central Japan Trench

The water depth of the trench floor in the central Japan Trench is generally shallower than the southern Japan Trench, ranging between 7,350 and 7,690 m (**Figure 3B**). Most of SBP penetration in the central Japan Trench was limited to 35 ms TWT (26–30 m) below the seafloor. Nevertheless, we identified several acoustically transparent bodies of ∼1 to ∼13 ms TWT in thickness within the basins. We consequently identified fifteen isolated trench-fill basins (JTC01–JTC15) in the central Japan Trench (**Table 2** and **Figure 3B**). The basins JTC01–JTC13 identified between 37.9° and 39.1°N are narrow and limited to 5 km long along the trench, because of local slumps and trench-floor deformation by coseismic slip-to-the trench (Kodaira et al., 2012; Strasser et al., 2013). Less connectivity along the trench axis was found between basins JTC04 and JTC05, JTC05 and JTC06, and JTC11 and JTC12.

At the basins JTC02 and JTC04, two acoustically transparent bodies (U1-C02 and U2-C02; U1-C04 and U2-C04) were identified in SBP data (**Figure 3B**). The sediment core GeoB16431-1 from the basin JTC02 documents thick (up to 1.5 m) fining-upward turbidite units exhibiting cross- and parallel-laminated sand-to-silt layer and a tephra layer (To-a tephra; AD 915) interbedded within bioturbated diatomaceous mud with a distinct erosional basal contact (**Figures 5**, **6**; Ikehara et al., 2016; Bao et al., 2018). The cores GeoB16431-1 and MR12-E01 PC04 from the basin JTC02 and MR12-E01 PC03 from the basin JTC04 document three homogeneous deposits in the upper 7.5–9.7 mbsf that were identified and dated as sediment remobilization event deposits linked to the AD 2011, AD 1454, and AD 869 earthquakes (Ikehara et al., 2016; Bao et al., 2018). Core-to-SBP correlation links the acoustically transparent bodies in SBP images to the 1454 Kyotoku and 869 Jogan events, while the 2011 event deposit is too thin (<∼30 cm) for distinct imaging in limited vertical resolution of SBP data (Kioka et al., 2019).

TABLE 1 | Longitude, latitude and water depth (WD) of modern depocenter, acoustically transparent SBP body units, correlation to neighboring SBP units inferred by DTW, maximum thicknesses, areal extents, and volumes of identified event deposits, estimated ages from cores, and possible links to historically known large earthquakes at a given trench fill-basin in the southern Japan Trench.

Basin	SBP Unit	Correlation inferred by DTW	Maximum thickness (m)	Area (km^2)	Volume ($\times 10^6$ m^3)	Age estimated from cores	Possible link to known large earthquakes
Southern Japan Trench							
JTS01 (142.727°E, 36.076°N, WD: −8034 m)							
	U1-S01	U1-S02	3.7 (+ 0.6/−0.1)	29.4 (±0.5)	54 (+11/−3)	AD 2011	AD 2011
	U2-S01		1.0 (+0.2/−0.1)	27.9 (±1.1)	14 (+6/−3)	AD 1846 (+22/−25)	AD 1793/1896/1897 (?)
	U3-S01	U3-S02	2.6 (+0.4/−0.1)	28.3 (±1.1)	31 (+9/−4)	AD 1671 (+44/−52)	AD1677
	U4-S01	U4-S02	3.4 (+0.6/−0.1)	27.1 (±1.1)	40 (+10/−4)	AD 980 (+78/−157)	AD 869
	U5-S01		1.4 (+0.3/−0.1)	23.0 (±1.0)	15 (+5/−3)	3.39 (+0.52/−0.15) ka	
	U6-S01		2.2 (+0.4/−0.1)	23.0 (±1.0)	32 (+8/−4)	5.46 (+0.83/−0.22) ka	
	U7-S01		2.0 (+0.4/−0.1)	23.0 (±1.0)	30 (+8/−3)	6.91 (+1.06/−0.27) ka	
JTS02 (142.836°E, 36.166°N, WD: −7998 m)							
	U1-S02	U1-S01	3.2 (+0.6/−0.1)	4.1 (±0.2)	9.5 (+2.2/−0.9)		AD 2011
	U2-S02		0.9 (+0.2/−0.1)	3.5 (±0.4)	1.4 (+0.8/−0.5)		
	U3-S02	U3-S01	3.0 (+0.5/−0.1)	4.0 (±0.4)	7.6 (+2.4/−1.1)		AD1677
	U4-S02	U4-S01	4.4 (+0.7/−0.1)	4.0 (±0.4)	11 (+3/−1)		AD 869
JTS03 (142.861°E, 36.194°N, WD: −7987 m)							
	U1-S03	U1-S02	1.3 (+0.3/−0.1)	0.20 (±0.04)	0.15 (+0.08/−0.05)		AD 2011
	U2-S03	U2-S02	0.5 (+0.2/−0.1)	0.15 (±0.04)	0.05 (+0.04/−0.02)		
	U3-S03	U3-S02	1.5 (+0.3/−0.1)	0.15 (±0.04)	0.16 (+0.09/−0.05)		AD1677
	U4-S03	U4-S02	2.1 (+0.4/−0.1)	0.15 (±0.04)	0.18 (+0.10/−0.06)		AD 869
JTS04 (142.938°E, 36.328°N, WD: −8002 m)							
	U1-S04	U1-S03	4.9 (+0.7/−0.1)	18.3 (±0.4)	43 (+9/−3)		AD 2011
	U2-S04	U2-S03	1.6 (+0.3/−0.1)	18.3 (±0.9)	12 (+4/−2)		
	U3-S04	U3-S03	2.2 (+0.4/−0.1)	18.3 (±0.9)	21 (+6/−3)		AD1677
	U4-S04	U4-S03	5.6 (+0.8/−0.1)	18.3 (±0.9)	45 (+11/−4)		AD 869
	U5-S04		5.7 (+0.9/−0.1)	2.1 (±0.3)	7.3 (+2.4/−1.2)		
JTS05 (142.999°E, 36.403°N, WD: −7972 m)							
	U1-S05	U1-S04	2.9 (+0.5/−0.1)	7.2 (±0.3)	12 (+3/−1)		AD 2011
	U2-S05	U2-S04	0.9 (+0.2/−0.1)	5.2 (±0.5)	3.1 (+1.4/−0.8)		
	U3-S05	U3-S04	1.6 (+0.3/−0.1)	5.2 (±0.5)	3.4 (+1.4/−0.8)		AD1677
JTS06 (143.103°E, 36.535°N, WD: −7820 m)							
	U1-S06		2.7 (+0.5/−0.1)	1.0 (±0.1)	2.1 (+0.6/−0.3)		AD 2011
JTS07 (143.315°E, 36.766°N, WD: −7651 m)							
	U1-S07		2.3 (+0.4/−0.1)	6.1 (±0.2)	9.3 (+2.3/−1.0)		AD 2011
JTS08 (143.396°E, 36.856°N, WD: −7686 m)							
	U1-S08	U1-S05	4.6 (+0.7/−0.1)	3.2 (±0.2)	12 (+3/−1)		AD 2011
JTS09 (143.402°E, 36.883°N, WD: −7701 m)							
	U1-S09	U4-S10	1.3 (+0.3/−0.1)	1.8 (±0.3)	1.2 (+0.6/−0.3)		AD 869
JTS10 (143.426°E, 36.914°N, WD: −7716 m)							
	U1-S10	U1-S11	1.4 (+0.3/−0.1)	1.8 (±0.1)	1.7 (+0.6/−0.3)		AD 2011
	U2-S10	U2-S11	1.4 (+0.3/−0.1)	1.8 (±0.3)	1.1 (+0.6/−0.3)		
	U3-S10	U3-S11	1.5 (+0.3/−0.1)	1.3 (±0.2)	0.89 (+0.48/−0.27)		
	U4-S10	U4-S04	1.7 (+0.3/−0.1)	1.1 (±0.2)	1.3 (+0.6/−0.4)		AD 869
JTS11 (143.447°E, 36.947°N, WD: −7722 m)							
	U1-S11	U1-S10	1.7 (+0.3/−0.1)	2.3 (±0.2)	1.9 (+0.7/−0.3)		AD 2011
	U2-S11	U2-S10	1.9 (+0.4/−0.1)	1.6 (±0.3)	2.4 (+1.0/−0.5)		
	U3-S11	U3-S10	1.3 (+0.3/−0.1)	1.4 (±0.2)	1.3 (+0.6/−0.3)		
	U4-S11	U4-S10	2.7 (+0.5/−0.1)	1.6 (±0.3)	3.7 (+1.4/−0.7)		AD 869
JTS12 (143.485°E, 37.002°N, WD: −7735 m)							
	U1-S12	U1-S11	1.5 (+0.3/−0.1)	4.3 (±0.2)	4.0 (+1.3/−0.6)		AD 2011
	U2-S12	U2-S11	1.3 (+0.3/−0.1)	4.0 (±0.4)	4.5 (+1.6/−0.8)		
	U3-S12	U4-S11	3.6 (+0.6/−0.1)	4.0 (±0.4)	9.4 (+2.8/−1.3)		AD 869

(Continued)

TABLE 1 | Continued

Basin	SBP Unit	Correlation inferred by DTW	Maximum thickness (m)	Area (km^2)	Volume ($\times 10^6$ m^3)	Age estimated from cores	Possible link to known large earthquakes
JTS13 (143.614°E, 37.171°N, WD: −7794 m)							
	U1-S13	U1-S12	2.2 (+0.4/−0.1)	10.2 (±0.3)	18 (+4/−2)		AD 2011
	U2-S13	U3-S12	3.2 (+0.5/−0.1)	10.2 (±0.6)	21 (+6/−2)		AD 869
JTS14 (143.726°E, 37.373°N, WD: −7829 m)							
	U1-S14	U1-S13	1.1 (+0.3/−0.1)	4.7 (±0.2)	2.9 (+1.0/−0.6)		AD 2011
	U2-S14	U2-S13	3.3 (+0.5/−0.1)	1.7 (±0.3)	3.7 (+1.4/−0.7)		AD 869
	U3-S14		1.9 (+0.4/−0.1)	0.89 (±0.20)	1.4 (+0.6/−0.4)		
JTS15 (143.740°E, 37.413°N, WD: −7826 m)							
	U1-S15	U1-S14	1.2 (+0.3/−0.1)	8.2 (±0.3)	4.1 (+1.6/−0.9)		AD 2011
	U2-S15		0.9 (+0.2/−0.1)	8.0 (±0.6)	3.8 (+1.8/−1.0)	AD1454/1611	AD1454
	U3-S15	U2-S14	3.6 (+0.6/−0.1)	8.0 (±0.6)	17 (+5/−2)	AD869	AD 869
	U4-S15		1.6 (+0.3/−0.1)	7.2 (±0.5)	7.2 (+2.5/−1.2)	2.25 (+0.40/−0.20) ka	2.4–2.6 ka (?)
	U5-S15		1.6 (+0.3/−0.1)	3.0 (±0.4)	2.2 (+1.0/−0.5)	4.02 (+1.03/−0.48) ka	
	U6-S15		1.6 (+0.3/−0.1)	1.1 (±0.2)	1.0 (+0.5/−0.3)	8.03 (+2.47/−1.09) ka	
JTS16 (143.860°E, 37.703°N, WD: −7556 m)							
	U1-S16	U1-S15	1.4 (+0.3/−0.1)	16.0 (±0.8)	9.2 (+3.7/−2.0)	AD 869	AD 869
	U2-S16		3.6 (+0.6/−0.1)	16.1 (±0.8)	34 (+8/−3)	25–40 ka	

The properties for the AD 2011 event are from Kioka et al. (2019).

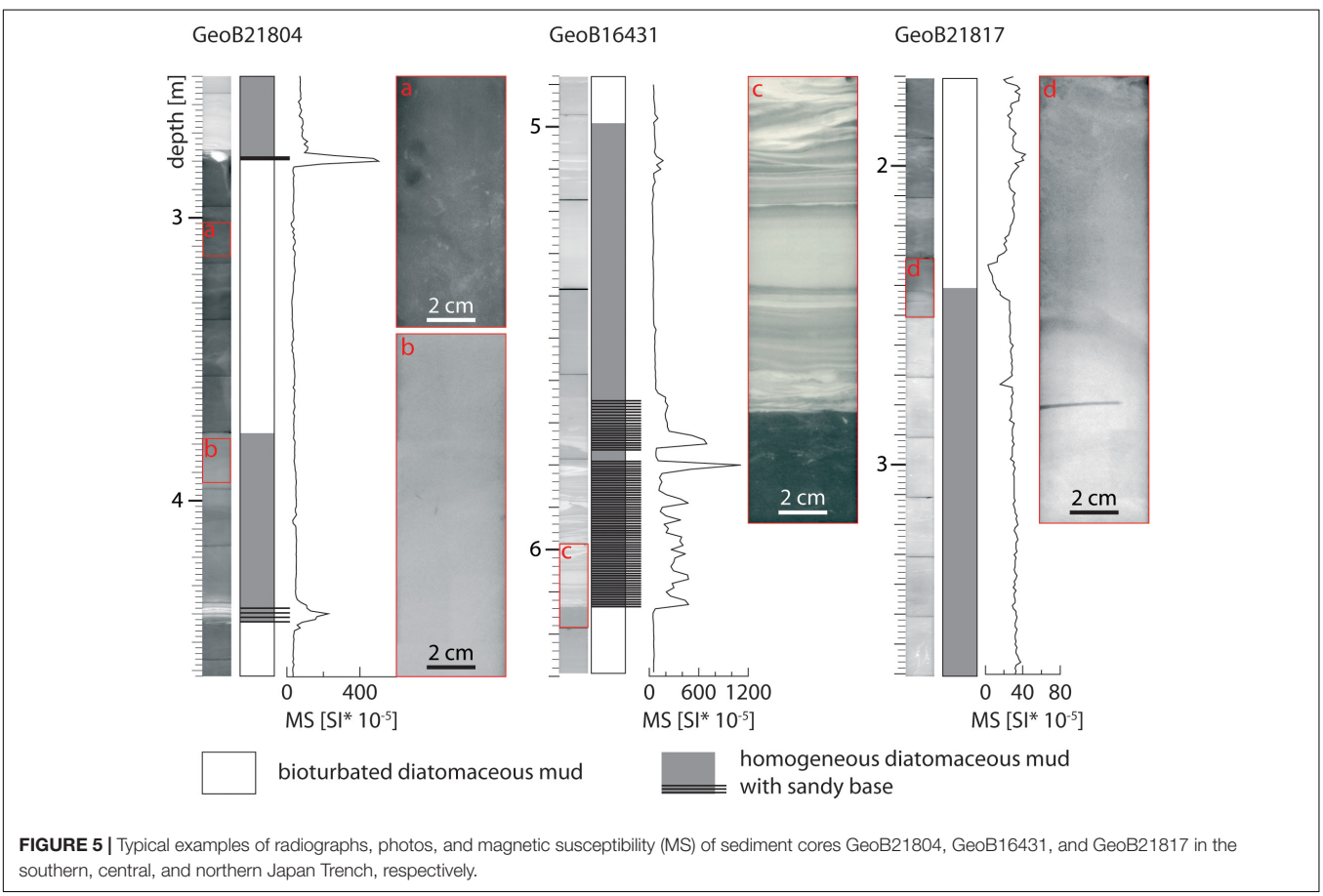


FIGURE 5 | Typical examples of radiographs, photos, and magnetic susceptibility (MS) of sediment cores GeoB21804, GeoB16431, and GeoB21817 in the southern, central, and northern Japan Trench, respectively.

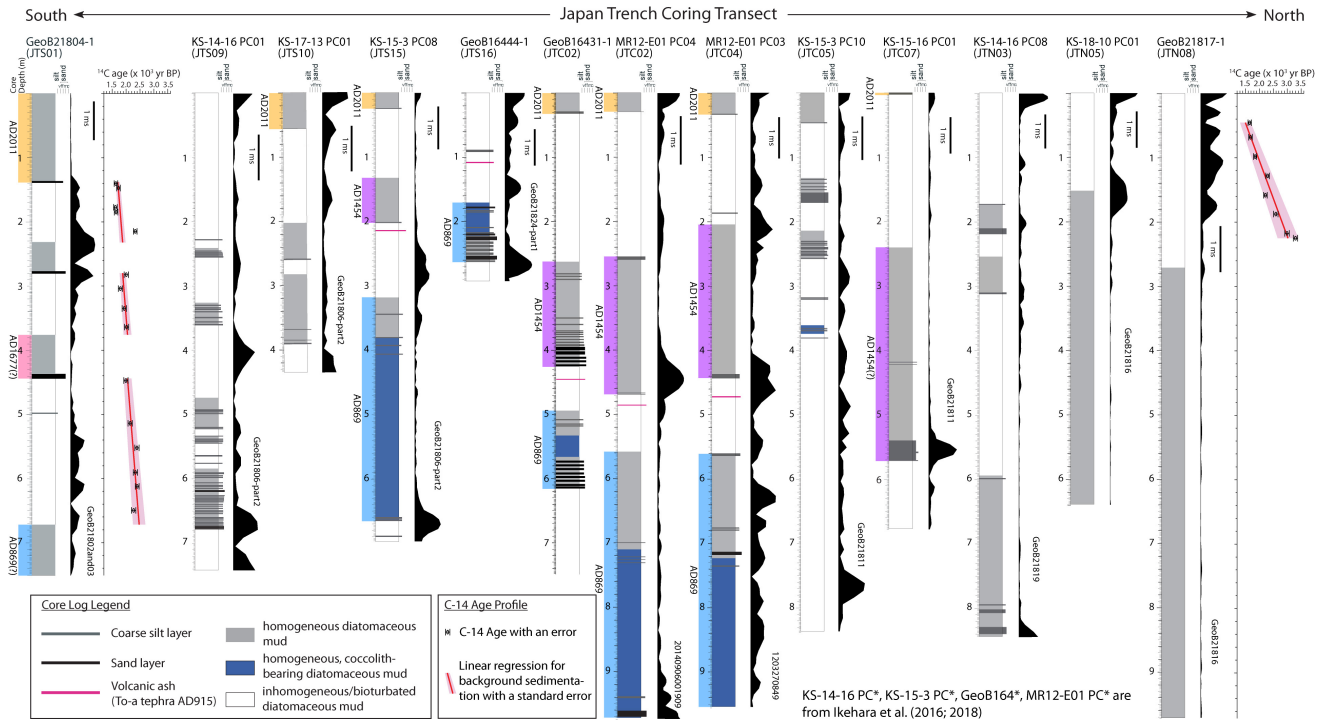


FIGURE 6 | Sediment cores taken at the trench-fill basins of Japan Trench identified in this study, wiggles of SBP data at the core locations, and 14C age profile. The cores GeoB21804, KS-17-13 PC01, KS-15-16 PC01, KS-18-10 PC01, and GeoB21817 are from this study, while the other cores are from previous studies (Ikehara et al., 2016, 2018; Bao et al., 2018). See **Figures 2–4** and **Supplementary Figure S1** for the locations of cores.

Similarly, the SBP data in the basin JTC05, which represents a local basin on a relative bathymetric high along the trench axis, did not image any acoustically transparent bodies even though thin event deposits are evidenced from the core KS-15-3 PC10 (Ikehara et al., 2018; **Figure 6**).

Despite reduced connectivity of basins along the central Japan Trench, our correlation suggests that several of the younger acoustically transparent deposits in a given trench-fill basin correlate well to respective deposits in its neighboring basins (**Figure 7**). For example, the acoustically transparent bodies U1-C02/U1-C04 and U2-C02/U2-C02 in the basin JTC02/JTC04 were correlated to corresponding acoustically transparent bodies throughout the basins JTC01 and JTC06–JTC11 (e.g., U2-C06/U2-C11 and U3-C06/U3-C11).

The deeper subsurface event stratigraphy in basins JTC01–JTC06 is mostly masked by unresolvable event-deposit thicknesses (e.g., JTC05; see above) or complex subsurface deformation structures (e.g., JTC02 comprising the area with described slump and co-seismic displacement into the trench (Kodaira et al., 2012; Strasser et al., 2013). In contrast, trench basins JTC07, JTC09, and JTC11 also image an older acoustically transparent body (U4), that can tentatively be dated to (3.8–4.9 ka) by extrapolating constant sedimentation rates estimated from inter-event background sedimentation in core KS-15-16 PC01 from basin JTC07. None of the identified acoustically transparent bodies can be correlated across the bathymetric high between basin JTC11 and JTC12, which also manifests a divide between different flow accumulation systems (**Figure 2**). The correlation of acoustically transparent bodies in the basins JTC12–JTC15 was not unique and cannot be verified by core data, due to absence of cores in this area. However, SBP data from basin JTC15, located south of petit-spot, document six acoustically transparent bodies clearly down to ∼35 ms TWT below the seafloor. Only one acoustically transparent deposit U4-C15 in the basin JTC15 can reliably be correlated by visual and DTW correlation to the deposit U1-C14 (i.e., event deposits with the largest areal extent in the central Japan Trench; **Table 2**) in JTC14 and perhaps to the deposits U2-C12 and U2-C13 in the basins JTC12 and JTC13, respectively.

Northern Japan Trench

The seafloor of the trench axis in the northern Japan Trench ranges between water depth of 7,400 and 7,620 m (**Figure 3C**). Most of the SBP data in the northern Japan Trench clearly imaged laterally continuous reflection signals down to 40–90 ms TWT (∼30–75 m) below the seafloor in the trench-fill basins, with the exception of basin JTN01, where the acoustic signal was strongly attenuated by a shallow subsurface body with hummocky surface, possibly linked to a mass-transport complex (**Figure 3C**). The SBP data imaged several acoustically transparent bodies of <1 to ∼15 ms TWT thick (**Figure 4**). We identified eight isolated trench-fill basins (JTN01–JTN08) in the northern Japan Trench that comprise 1–5 event deposits clearly imaged in SBP data (**Table 3** and **Figure 3C**). Unlike in the other parts of the

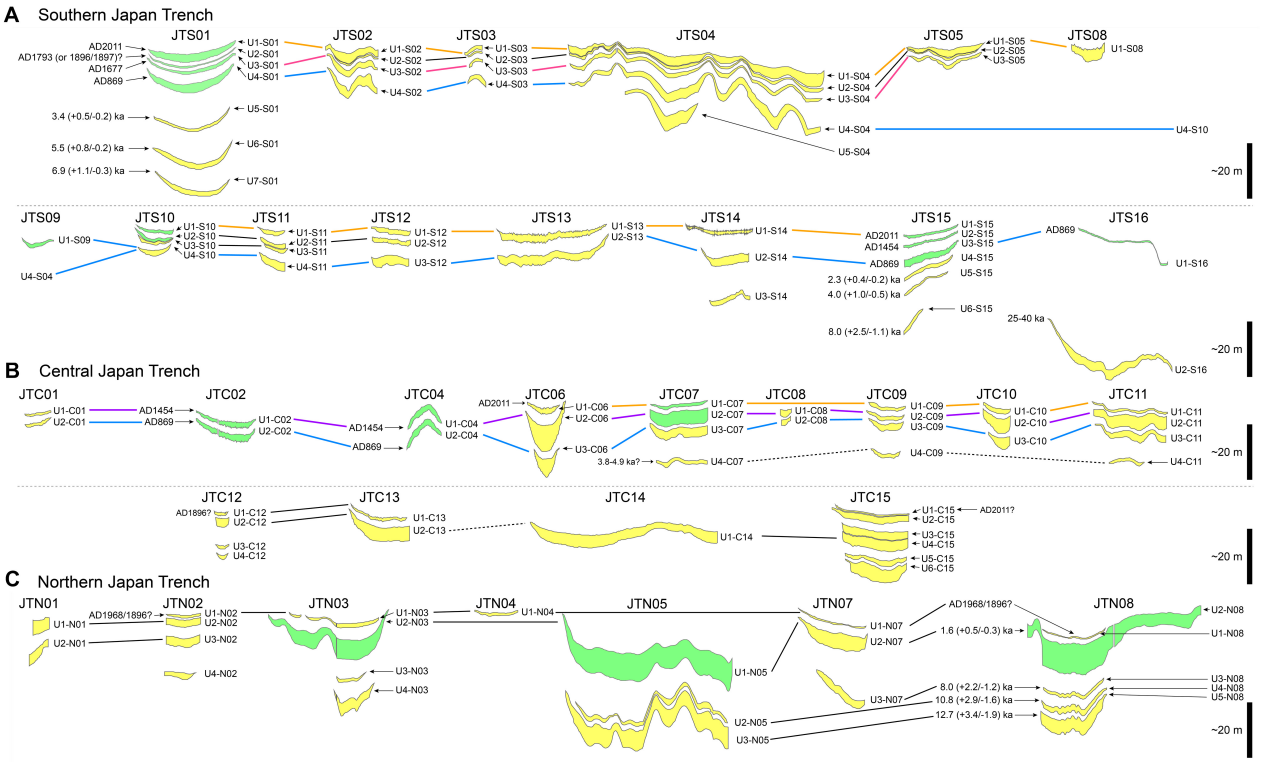


FIGURE 7 | Correlation of identified event deposit bodies between neighboring trench-fill basins in **(A)** the southern Japan Trench, **(B)** the central Japan Trench, and **(C)** the northern Japan Trench. The solid lines connecting individual identified event units between different basins indicate that the correlation is supported either by both image interpretation and DTW or evidence from cores, while the dash lines connecting individual identified event units indicate the correlation is expected from either image interpretation or DTW.

trench, the uppermost acoustic unit immediately below seafloor is either absent or not resolved (JTN01 and JTN05), or thin (0.6–1.4 m thickness) throughout all the SBP images in the northern Japan Trench.

At the northernmost basin JTN08, where flow accumulation is highest in the entire Japan Trench (**Figure 2**), five acoustically transparent bodies (U1-N08, U2-N08, …, U5-N08) were identified in SBP data (**Figures 3C**, **4**). Visual core description and magnetic susceptibility data (Strasser et al., 2017) and detailed analyses of radiograph images (this study; **Figure 5**) of core GeoB21817 taken from the depocenter of basin JTN08 documents mottled bioturbated diatomaceous mud (interpreted as background sediments) overlying a thick homogenous diatomaceous mud containing additional minor fine-sand lenses, foraminifera and pyrite framboids (below 2.7 mbsf to the base of core at 9.7 mbsf; interpreted as remobilized sedimentary event deposits; **Figures 5**, **6**). SBP-to-core correlation clearly documents that the thick acoustically transparent body U2-N08 correlates to the event deposit recovered below 2.7 m depth in core GeoB21817 (**Figure 4**). The very thin uppermost acoustically transparent body identified in SBP data immediately below the seafloor reflector (U1-N08) could not be validated in core data of GeoB21817, possibly due to coring disturbance in the uppermost part of the core or non-recovery of the sediment-waver interface (core overshoot).

Bulk OC ^{14}C data of bioturbated sediments overlying the homogenous diatomaceous mud within the core GeoB21817 indicate a mean sedimentation rate of 1.17 (+0.16/-0.12) m/kyr for background sedimentation in the basin JTN08 (**Figure 6** and **Supplementary Figure S2**), which is lower than that in the southernmost basin JTS01 [5.44 (+0.13/-0.09) m/kyr; this study] and upper 2.5 mbsf of JTC02 in the central Japan Trench (∼2.0 m/kyr; Bao et al., 2018). Extrapolating constant sedimentation rates and assuming no significant sediment loss in the uppermost part of the core, ages of acoustically transparent bodies U2-N08, U3-N08, U4-N08 and U5-N08 were estimated to be 1.62 (+0.49/-0.31) ka, 7.96 (+2.15/-1.15) ka, 10.77 (+2.89/-1.56), and 12.70 (+3.40/-1.87) ka, respectively. The acoustically transparent body U2-N08 [1.62 (+0.49/-0.31) ka] was thickest and had the largest volume [0.184 (+0.036/-0.010) km^3; **Table 3**] in the entire Japan Trench. We found similarly very thick acoustically transparent bodies U2-N03 [max. 8.4 (+1.2/-0.1) m thick] and U1-N05 [max. 9.6 (+1.4/-0.1) m thick], which were validated by sediment cores of KS-14-16 PC08 (Ikehara et al., 2018) and KS-18-10 PC01 in the basins JTN03 and JTN05, respectively (**Figure 6**). Basin-to-basin correlation suggests that the acoustically transparent body U2-N08 in the northernmost basin JTN08 can reliably be correlated to the acoustically transparent bodies U2-N07, U1-N05, and U2-N03 in the neighboring basins JTN07, JTN05, and JTN03, respectively

TABLE 2 | Longitude, latitude and water depth (WD) of modern depocenter, acoustically transparent SBP body units, correlation to neighboring SBP units inferred by DTW, maximum thicknesses, areal extents and volumes of identified event deposits, estimated ages from cores, and possible links to historically known large earthquakes at a given trench fill-basin in the central Japan Trench.

Basin	SBP Unit	Correlation inferred by DTW	Maximum thickness (m)	Area (km^2)	Volume ($\times 10^6$ m^3)	Age estimated from cores	Possible link to known large earthquakes
Central Japan Trench							
JTC01 (143.989°E, 37.953°N, WD: −7532 m)							
	NaN		0.2 (+0.1/−0.1)	2.0 (±0.1)	0.41 (+0.03/−0.03)		AD 2011
	U1-C01	U1-C02	0.9 (+0.2/−0.1)	2.0 (±0.3)	1.2 (+0.6/−0.4)	AD 1454/1611	AD 1454
	U2-C01	U2-C02	1.3 (+0.3/−0.1)	2.0 (±0.3)	1.3 (+0.6/−0.4)	AD 869	AD 869
JTC02 (144.006°E, 38.009°N, WD: −7569 m)							
	NaN		0.2 (+0.1/−0.1)	3.9 (±0.2)	0.79 (+0.04/−0.04)		AD 2011
	U1-C02	U1-C04	2.0 (+0.4/−0.1)	4.0 (±0.4)	5.1 (+1.8/−0.9)	AD 1454/1611	AD 1454
	U2-C02	U2-C04	2.8 (+0.5/−0.1)	3.6 (±0.4)	6.0 (+2.0/−1.0)	AD 869	AD 869
JTC03 (143.990°E, 38.022°N, WD: −7560 m)							
	NaN		0.2 (+0.1/−0.1)	0.7 (±0.1)	0.13 (+0.02/−0.02)		AD 2011
	U1-C03	U1-C02	1.7 (+0.3/−0.1)	0.7 (±0.2)	0.84 (+0.46/−0.27)		AD 1454
	U2-C03	U2-C02	1.7 (+0.3/−0.1)	0.7 (±0.2)	0.81 (+0.44/−0.26)		AD 869
JTC04 (143.995°E, 38.098°N, WD: −7558 m)							
	NaN		0.2 (+0.1/−0.1)	2.1 (±0.1)	0.42 (+0.03/−0.03)		AD 2011
	U1-C04	U2-C06	2.4 (+0.4/−0.1)	2.5 (±0.3)	3.5 (+1.3/−0.7)	AD 1454/1611	AD 1454
	U2-C04	U3-C06	2.4 (+0.4/−0.1)	2.4 (±0.3)	3.1 (+1.2/−0.6)	AD 869	AD 869
JTC05 (144.059°E, 38.298°N, WD: −7457 m)							
	NaN		0.2 (+0.1/−0.1)	1.8 (±0.1)	0.36 (+0.03/−0.03)		AD 2011
JTC06 (144.108°E, 38.644°N, WD: −7661 m)							
	U1-C06	U1-C07	2.0 (+0.4/−0.1)	1.3 (±0.2)	1.7 (+0.7/−0.4)		AD 2011
	U2-C06	U2-C07	9.4 (+1.4/−0.1)	2.5 (±0.3)	13 (+4/−2)		AD 1454
	U3-C06	U3-C07	6.9 (+1.0/−0.1)	0.7 (±0.2)	3.1 (+1.4/−0.8)		AD 869
JTC07 (144.130°E, 38.743°N, WD: −7622 m)							
	U1-C07	U1-C09	1.1 (+0.3/−0.1)	3.9 (±0.2)	3.1 (+1.0/−0.5)		AD 2011
	U2-C07	U1-C08	5.4 (+0.8/−0.1)	4.0 (±0.4)	17 (+5/−2)		AD 1454
	U3-C07	U2-C08	4.3 (+0.7/−0.1)	3.7 (±0.4)	10.3 (+3.1/−1.4)		AD 869
	U4-C07		2.0 (+0.4/−0.1)	3.5 (±0.4)	10.0 (+3.0/−1.4)	3.8–4.9 ka	3.8–4.1 ka (?)
JTC08 (144.148°E, 38.866°N, WD: −7456 m)							
	U1-C08	U2-C09	2.8 (+0.5/−0.1)	0.8 (±0.2)	1.9 (+0.9/−0.5)		AD 1454
	U2-C08	U3-C09	2.2 (+0.4/−0.1)	0.8 (±0.2)	1.4 (+0.7/−0.4)		AD 869
JTC09 (144.155°E, 38.836°N, WD: −7614 m)							
	U1-C09	U1-C10	1.7 (+0.3/−0.1)	2.5 (±0.2)	2.2 (+0.7/−0.4)		AD 2011
	U2-C09	U2-C10	1.6 (+0.3/−0.1)	2.5 (±0.3)	2.8 (+1.1/−0.6)		AD 1454
	U3-C09	U3-C10	2.3 (+0.4/−0.1)	1.9 (±0.3)	3.0 (+1.1/−0.6)		AD 869
	U4-C09		1.5 (+0.3/−0.1)	1.5 (±0.3)	2.4 (+1.0/−0.5)		3.8–4.1 ka (?)
JTC10 (144.152°E, 38.869°N, WD: −7632 m)							
	U1-C10	U1-C11	1.8 (+0.3/−0.1)	0.7 (±0.1)	0.87 (+0.32/−0.16)		AD 2011
	U2-C10	U2-C11	5.8 (+0.9/−0.1)	0.7 (±0.2)	3.1 (+1.4/−0.8)		AD 1454
	U3-C10	U3-C11	3.8 (+0.6/−0.1)	0.6 (±0.2)	1.7 (+0.8/−0.5)		AD 869
JTC11 (144.158°E, 38.904°N, WD: −7642 m)							
	U1-C11	U1-C10	1.3 (+0.3/−0.1)	4.3 (±0.2)	3.1 (+1.0/−0.6)		AD 2011
	U2-C11	U2-C10	5.1 (+0.8/−0.1)	4.6 (±0.4)	16 (+4/−2)		AD 1454
	U3-C11	U3-C10	4.2 (+0.7/−0.1)	4.6 (±0.4)	8.4 (+2.6/−1.2)		AD 869
	U4-C11		1.5 (+0.3/−0.1)	1.6 (±0.3)	1.6 (+0.7/−0.4)		3.8–4.1 ka (?)
JTC12 (144.215°E, 39.082°N, WD: −7440 m)							
	U1-C12	U1-C13	1.0 (+0.2/−0.1)	0.8 (±0.1)	0.51 (+0.23/−0.13)		AD 1896 (?)
	U2-C12	U2-C13	3.2 (+0.5/−0.1)	0.7 (±0.2)	1.3 (+0.7/−0.4)		
	U3-C12		1.8 (+0.3/−0.1)	0.7 (±0.2)	0.74 (+0.41/−0.24)		
	U4-C12		1.9 (+0.3/−0.1)	0.7 (±0.2)	0.65 (+0.37/−0.22)		

(Continued)

TABLE 2 | Continued

Basin	SBP Unit	Correlation inferred by DTW	Maximum thickness (m)	Area (km^2)	Volume ($\times 10^6$ m^3)	Age estimated from cores	Possible link to known large earthquakes
JTC13 (144.208°E, 39.136°N, WD: −7458 m)							
	U1-C13	U1-C12	1.2 (+0.3/−0.1)	1.6 (±0.1)	1.2 (+0.5/−0.2)		AD 1896 (?)
	U2-C13	U2-C12	6.3 (+0.9/−0.1)	2.2 (±0.3)	8.3 (+2.7/−1.3)		
JTC14 (144.204°E, 39.248°N, WD: −7462 m)							
	NaN		0.2 (+0.1/−0.1)	23.8 (±0.5)	4.8 (+0.1/−0.1)		AD 2011
	U1-C14	U4-C15	5.1 (+0.8/−0.1)	23.3 (±1.0)	69 (+15/−5)		
JTC15 (144.219°E, 39.423°N, WD: −7523 m)							
	U1-C15		0.7 (+0.2/−0.1)	12.0 (±0.4)	5.0 (+2.0/1.3)		AD 2011
	U2-C15		3.3 (+0.5/−0.1)	12.9 (±0.7)	28 (+7/−3)		
	U3-C15		3.1 (+0.5/−0.1)	11.0 (±0.7)	24 (+6/−3)		
	U4-C15	U1-C14	3.8 (+0.6/−0.1)	10.9 (±0.7)	35 (+8/−3)		
	U5-C15		1.7 (+0.3/−0.1)	8.9 (±0.6)	10.1 (+3.2/−1.5)		
	U6-C15		5.4 (+0.8/−0.1)	8.7 (±0.6)	25 (+6/−3)		

The properties for the AD 2011 event are from Kioka et al. (2019).

TABLE 3 | Longitude, latitude and water depth (WD) of modern depocenter, acoustically transparent SBP body units, correlation to neighboring SBP units inferred by DTW, maximum thicknesses, areal extents and volumes of identified event deposits, estimated ages from cores, and possible links to historically known large earthquakes at a given trench fill-basin in the northern Japan Trench.

Basin	SBP Unit	Correlation inferred by DTW	Maximum thickness (m)	Area (km^2)	Volume ($\times 10^6$ m^3)	Age estimated from cores	Possible link to known large earthquakes
Northern Japan Trench							
JTN01 (144.233°E, 39.571°N, WD: −7493 m)							
	U1-N01	U2-N02	5.7 (+0.9/−0.1)	1.4 (±0.1)	5.3 (+1.4/−0.6)		
	U2-N01	U3-N02	4.2 (+0.7/−0.1)	1.1 (±0.2)	3.5 (+1.4/−0.8)		
JTN02 (144.246°E, 39.648°N, WD: −7491 m)							
	U1-N02	U1-N03	0.6 (+0.2/−0.1)	2.9 (±0.2)	1.3 (+0.6/−0.4)		AD 1968/1896 (?)
	U2-N02	U1-N01	2.8 (+0.5/−0.1)	2.9 (±0.3)	6.4 (+2.1/−1.0)		
	U3-N02	U2-N01	3.7 (+0.6/−0.1)	2.5 (±0.3)	6.8 (+2.2/−1.1)		
	U4-N02		2.0 (+0.4/−0.1)	2.2 (±0.3)	2.5 (+1.0/−0.5)		
JTN03 (144.275°E, 39.777°N, WD: −7484 m)							
	U1-N03	U1-N02	1.4 (+0.3/−0.1)	6.6 (±0.3)	5.6 (+1.8/−0.9)		AD 1968/1896 (?)
	U2-N03	U1-N05	8.4 (+1.2/−0.1)	8.4 (±0.6)	40 (+10/−4)		2–3 century AD
	U3-N03		2.0 (+0.4/−0.1)	2.6 (±0.3)	2.8 (+1.1/−0.6)		
	U4-N03		6.3 (+0.9/−0.1)	3.0 (±0.4)	11 (+3/−2)		
JTN04 (144.295°E, 39.979°N, WD: −7517 m)							
	U1-N04	U1-N03	1.0 (+0.2/−0.1)	1.6 (±0.1)	1.0 (+0.4/−0.2)		AD 1968/1896 (?)
JTN05 (144.338°E, 40.137°N, WD: −7572 m)							
	U1-N05	U2-N08	9.6 (+1.4/−0.1)	23.3 (±1.0)	158 (+31/−9)		2–3 century AD
	U2-N05	U4-N08	2.1 (+0.4/−0.1)	20.8 (±0.9)	23 (+7/−3)		
	U3-N05	U5-N08	8.1 (+1.2/−0.1)	12.7 (±0.7)	69 (+15/−5)		
JTN06 (144.355°E, 40.174°N, WD: −7508 m)							
	U1-N06		5.6 (+0.9/−0.1)	4.0 (±0.4)	9.1 (+2.8/−1.3)		
JTN07 (144.401°E, 40.325°N, WD: −7609 m)							
	U1-N07	U1-N08	0.7 (+0.2/−0.1)	7.0 (±0.3)	2.2 (+1.2/−0.8)		AD 1968/1896 (?)
	U2-N07	U2-N08	6.5 (+1.0/−0.1)	7.6 (±0.6)	31 (+8/−3)		2–3 century AD
	U3-N07	U3-N08	3.4 (+0.5/−0.1)	5.5 (±0.5)	9.2 (+2.8/−1.3)		
JTN08 (144.408°E, 40.399°N, WD: −7623 m)							
	U1-N08	U1-N07	0.8 (+0.2/−0.1)	12.6 (±0.4)	4.8 (+2.3/−1.4)	AD 1968/1896	AD 1968/1896 (?)
	U2-N08	U2-N07	11.1 (+1.6/−0.1)	25.7 (±1.0)	184 (+36/−10)	1.62 (+0.49/−0.31) ka	2–3 century AD
	U3-N08	U3-N07	1.5 (+0.3/−0.1)	13.2 (±0.7)	9.9 (+3.5/−1.8)	7.96 (+2.15/−1.15) ka	
	U4-N08	U2-N05	2.3 (+0.4/−0.1)	12.5 (±0.7)	15 (+4/−2)	10.77 (+2.89/−1.56) ka	
	U5-N08	U3-N05	5.8 (+0.9/−0.1)	13.2 (±0.7)	51 (+12/−4)	12.70 (+3.40/−1.87) ka	

(**Figure 7**). This indicates that, at 1.62 (+0.49/-0.31) ka, a large volume [0.412 (+0.084/-0.025) km^3; **Table 3**] of event deposition took place over these basins. We also find positive correlation of deeper acoustically transparent bodies U3-N08, U4-N08, and U5-N08 in the basin JTN08, to U3-N07 in the basin JTN07 and U2-N05 and U3-N05 in the basin JTN05. The uppermost, thin, acoustically transparent body U1 correlates across all the basins in the northern Japan Trench, except for basins JTN01 and JTN05 where it is not resolved or absent. More southward correlation of these event deposit bodies to the neighboring basin JTC15 located in the northernmost part of the central Japan Trench, where the youngest event deposit in SBP data is linked to the AD 2011 Tohoku-oki earthquake (Kioka et al., 2019), is not supported by visual seismic facies correlation and DTW analysis.

DISCUSSION

We have studied, for the first time to our knowledge, the spatio-temporal distribution of thick sediment remobilization event deposits resolved by high-resolution subbottom profiling data of trench basins in the Japan Trench along and across its entire axis from 36.0°N to 40.5°N. In the uppermost 5–10 m subsurface depth of the acoustically imaged sedimentary sequences in the trench basins, SBP data interpretation is validated by sedimentological data and age constraints from several cores retrieved by conventional gravity and piston coring campaigns. SBP-to-core correlation demonstrates that most of the acoustically transparent bodies identified in SBP data represent event deposits composed of homogenous diatomaceous mud resulting from widespread sediment remobilization of unconsolidated surface sediments and link to the occurrence of major historical earthquakes (see green bodies and their stratigraphically correlated event deposits shown in **Figure 7**). For the deeper subsurface, our event-stratigraphy interpretation is solely based on acoustic facies interpretation, seismic stratigraphic mapping and correlation, and awaits further constraints and validation by deeper coring, that is planned to by conducted by the upcoming International Ocean Discovery Program (IODP) Expedition 386 in 2020 (Strasser et al., 2019) in the Japan Trench.

Spatial and Temporal Distribution of Event Deposits and Links to Past Earthquake Histories

Below, we first discuss the temporal and spatial extent of the earthquake-triggered event deposits found from SBP data with a focus on (i) testing how areal extent of event deposition in the trench links to rupture area and size distributions of historically documented large earthquakes and (ii) discussing possible earthquake scenarios for prehistoric events inferred from the sedimentary record. Our results reveal distinctly different event stratigraphies for the trench segments between north and south of the area characterized by the bathymetric high and the area affected by complicated structures such as petit spot volcanism between 39.0° and 39.5°N (Hirano et al., 2006). The nature of subducting oceanic lithosphere affected by petit-spot volcanism might also act as segment boundary of megathrust earthquakes, perhaps influencing different earthquake rupture mechanism and histories along the plate interface north and south of this structurally controlled divide. We thus separate our discussion between the southern and south-central part of the Japan Trench (starting with basins JTS01 through JTC11) and the northern Japan Trench (starting with basins JTN08 through JTN02).

Southern and South-Central Part of the Japan Trench

At the southernmost basin JTS01 in the southern Japan Trench, our SBP data document event deposits over the past ∼7 kyr. Funneling and focusing of the density flows through the proximal Nakaminato submarine canyon (**Figure 1**) transports larger amount of sediments into this basin than most other basins, as suggested by very high flow accumulation values (**Figure 2**) and high background sedimentation rates (**Supplementary Figure S3**). Based on our new age constraints from radiocarbon-dated background sedimentation rates and event-deposit basin-to-basin correlation, we document an event deposit of AD 1671 (+44/-52), recorded only in the southern-most trench basins JTS01–JTS05, which is interpreted to relate to the AD 1677 M_w8.3–8.6 Empo Boso-oki earthquake. The inferred rupture of this earthquake did not propagate much further north than the area drained by the Nakaminato canyon, suggesting a good fit between the mapped spatial distributions of its event deposits with the inferred rupture area (**Figure 1**; Takeuchi et al., 2007; Sawai et al., 2012).

Between the AD 2011 and the inferred AD 1677 event deposits, SBP data of the southernmost trench basin JTS01 evidence another sediment remobilization event with very limited spatial extend (only recorded in JTS01) that we date to AD 1846 (+22/-25). No major historical earthquake was reported within this time period. If we were to consider that dating uncertainties from a linearly extrapolating sedimentation rate from bulk organic radiocarbon data might have been underestimated (e.g., deviation of ^{14}C age at 215 cm of GeoB21804 core; **Figure 6** and **Supplementary Figure S2**), this event deposit might be related to either the AD 1793 February M7.6–8.2 Kansei, the AD 1896 January M7.3 Ibaraki-oki, or the AD 1897 August M7.7 Sanriku-oki earthquakes, which are all smaller earthquakes that have affected the source area of the JTS01 basin. However, we trust the age constraints and uncertainty estimates of the event deposit and, alternatively, interpret that such a locally recorded event deposit is not indicative for earthquake trigger. Indeed, the event deposit could also have been triggered by the AD 1856 Edo-Ansei typhoon that is known for the strongest typhoon within this possible time range (Sakazaki et al., 2015).

Remarkably, our results reveal that the thick event deposit (U4-S01) in the southernmost trench basin JTS01, as validated by a core and dated to AD 980 (+78/-157), correlates widely to acoustically transparent bodies within most of the basins in the southern Japan Trench and throughout basins JTC01–JTC11 in the central Japan Trench (**Figure 7**). Hence, this event deposit is extensively distributed in the trench-fill basins throughout the

southern Japan Trench and its spatial extent reaches northward up to the major bathymetric divide in the central Japan Trench at ∼39.0°N. As independently evidenced and dated from cores in the basins JTS15, JTS16, JTC02, JTC04, and JTC07 (Ikehara et al., 2016, 2018; Bao et al., 2018), this spatially extensive large-scale sediment remobilization event links to the AD 869 M_w≥8.6 Jogan earthquake.

Spatio-temporal mapping and basin-to-basin correlation of the other major historical earthquake (i.e., the AD 1454 M_w≥8.4 Kyotoku earthquake), which triggered sediment remobilization and event deposition in the central part of the Japan Trench (Ikehara et al., 2016), hint a constraint for the spatial extents of sediment remobilization. We reveal that this earthquake did not trigger as widespread sediment remobilization as the AD 2011 Tohoku-oki earthquake (Kioka et al., 2019) and AD 869 Jogan earthquake, because the correlative event deposits do not extend further southward than JTS15 (**Figure 7**). Nevertheless, in the central part of the Japan Trench, the respective event deposits of the AD 1454 earthquake are widely identified throughout basins JTC01 and JTC11 and thus across at least two different separated flow-accumulation systems (**Figure 2**). The event deposit of AD 1454 earthquake is thus distributed in the trench-fill basins between 37.4° and 38.9°N, which is further to the north than expected from the source area of AD 1454 earthquake (Sawai et al., 2015). The event deposit distribution of the AD 869 Jogan earthquake extends further to both the north and south than inferred from the source area of AD 869 earthquake (Sawai et al., 2012). This may suggest that (i) the AD 869 M_w≥8.6 earthquake remobilized a larger area of surface sediment than the AD 1454 earthquake, which is believed to be of similar magnitude, and/or (ii) the AD 869 earthquake may have actually ruptured a larger area than the AD 1454 earthquake, which agrees with a broad distribution for the AD 869 tsunami deposits as far as 40.5°N, suggesting the earthquake size is rather similar to the AD 2011 earthquake (Sawai et al., 2012; Namegaya and Satake, 2014). Interestingly, the event deposits of the AD 869 earthquake in the central part of the Japan Trench are thicker, comprising a larger total volume than that of the AD 2011 earthquake, as suggested from sediment cores taken between 38.0° and 38.1°N (Ikehara et al., 2016) and our volume estimates (see section "Export of Organic Carbon (OC) to the Hadal Trench by Large Earthquakes"). Given that the magnitude of the AD 2011 Tohoku-oki earthquake was larger than the inferred magnitude of AD 869 earthquake, we expect that the AD 869 earthquake guided different system of sediment routing and source and/or different mechanism of sediment supply from the AD 2011 earthquake for delivering remobilized surface sediment to the proximal trench. Or, event deposit thicknesses and volumes in the central Japan Trench may not be a straightforward indicator of earthquake magnitude, potentially because of complex and small-scale bathymetric differences, which are possibly enhanced by trench-sediment deformation by coseismic slip propagation to the trench (Kodaira et al., 2012) that affects trench-basin accommodation space and resulting deposition of remobilized sediment.

With respect to discussing possible earthquake scenarios for prehistoric earthquakes, our spatio-temporal event stratigraphy for the area south of 39.0°N reveals the most promising data from the deep subsurface of the basins JTS01, JTS15, and JTC07–JTC11. The 2.3 (+0.4/-0.2) ka event deposit identified in the basin JTS15 is probably related to the 2.4–2.6 ka earthquake that has been inferred from a tsunami deposit reported along the coast between the northern Fukushima and southern Miyagi Prefectures (e.g., Kusumoto et al., 2018). Yet, interpretation of an earthquake trigger for this event deposit may not be unique, because the correlation of the event deposit with a wide possible age range cannot be constrained by our basin-to-basin correlation. In contrast, an older event in the basin JTS15 [U5-S15, tentatively dated to 4.0 (+1.0/-0.5) ka], has an overlapping possible age range with the event deposit of 3.8–4.9 ka identified in the basin JTC07 (which further likely correlates across basins JTC09 and JTC11) and possibly U5-S01 (tentatively dated to 3.4 (+0.5/-0.2) ka) in the southernmost basin JTS01. If correlation can be confirmed by future IODP core analyses, this event could have similar spatial extent as the AD 2011 Tohoku-oki and the AD 869 Jogan earthquakes. Such an event is likely to correlate to either a 3.8 ka event found from tsunami deposits along the northern Miyagi coast (Hirakawa, 2012) or a 4.1 ka event reported from sediment cores at mid-slope terrace between 39.1° and 39.3°N (Usami et al., 2018). Alternatively, these reconstructed paleo-earthquake events might also all link to one single large megathrust earthquake, because the age ranges of the respective event deposits can overlap when considering dating uncertainties on the order of a few hundred years in these records.

Northern Japan Trench

North of 39.5°N, as compared to the southern and central Japan Trench, we found distinctly different stratigraphic successions characterized by lower sedimentation rates and fewer but thicker event deposits. We interpret that the uppermost very thin homogenous deposits imaged immediately below the seafloor reflection in the basins JTN02, JTN03, JTN04, JTN07, and JTN08 must relate to a very recent event, possibly either the AD 1968 M_w8.2–8.3 Tokachi-oki (Sanriku-oki Hokubu) earthquake or AD 1896 M_w8.0–8.4 Meiji Sanriku earthquake. These earthquakes were smaller in size than 2011 earthquake, which may explain that the resulting event deposits and total remobilized sediment volume are much smaller than those for the recent 2011 event found in the southern and central Japan Trench (Kioka et al., 2019). Furthermore, at the mid-slope area around 40.25°N, Molenaar et al. (2019) documented surface remobilization of very thin surface sediment associated with AD 1968 and AD 1896 earthquakes. This observation further supports our interpretation that the observed shallow-subsurface event deposits in the northern Japan Trench likely document the deposition of remobilized sediment related to one or the other of these earthquakes. However, this interpretation needs to be tested with high-resolution radionuclide dating on suitable cores not available to date.

The SBP data in the northern Japan Trench document very thick acoustically transparent bodies up to 11.1 (+1.6/-0.1) m. One of the thick event deposits, tentatively dated to 1.62 (+0.49/-0.31) ka in the JTN08 basin, is widely distributed in the basins JTN03, JTN05, JTN07, and JTN08 (**Figure 7**). Tsunami deposits of a 2nd–3rd Century large earthquake have been widely correlated along the Iwate coast between Yamada and Hirono Towns (Takada et al., 2016; see **Figure 1** for locations). This suggests that the 1.6 (+0.5/-0.3) ka event deposits identified in these basins may link to the 2nd–3rd Century AD event. We further identify deeper acoustically transparent bodies of 8.0 (+2.2/-1.2) ka, 10.8 (+2.9/-1.6) ka, and 12.7 (+3.4/-1.5) ka that are older than reported from tsunami deposits and marine sediment cores from slopes. These deposits can also represent event deposits linked to similarly large earthquakes, whereas alternate explanation such as canyon flushing of Ogawara canyon due to extreme flood events associated with rainfall condition change (e.g., Kawahata et al., 2017) and/or sea-level change or gas-rich deposits cannot be rejected as alternative interpretations. Only future coring by IODP expedition 386 will allow for testing these competing hypotheses based on detailed sedimentological and provenance analyses (Strasser et al., 2019).

Export of Organic Carbon (OC) to the Hadal Trench by Large Earthquakes

Having revealed spatial and temporal distribution of event deposits, we can quantify sediment volumes and OC contents of given event deposits linked to large earthquakes throughout the entire Japan Trench. The AD 2011 Tohoku-oki earthquake made spatially widespread remobilization of young surficial seafloor slope sediments and delivered event deposits of at least 0.187 (+0.045/-0.018) km^3 to the trench (Kioka et al., 2019). Similar to the 2011 event deposits, the AD 1454 and 869 event deposits also contain relatively young remobilized sediments with high OC content (Bao et al., 2018). From our results, we quantify a sediment volume of 0.064 (+0.019/-0.009) km^3 that was transported to the hadal trench after sediment remobilization within or around the area feeding the Nakaminato canyon, initiated by the AD 1677 M_w 8.3–8.6 Empo Boso-oki earthquake. The AD 1454 $M_w \geq 8.4$ Kyotoku earthquake remobilized surficial sediment over a widespread area resulting in a total volume of 0.068 (+0.022/-0.011) km^3 of event deposits in the hadal trench basins. The basins JTC06 (0.013 [+0.004/-0.002) km^3], JTC07 [0.017 (+0.005/-0.002) km^3], JTC11 [0.016 (+0.004/-0.002) km^3] document largest deposit volumes of the AD 1454 event in identified trench-bill basins, which agree with highest flow accumulation in the central Japan Trench (**Figure 8**). The AD 869 $M_w \geq 8.6$ Jogan earthquake triggered widespread sediment remobilization resulting in a total volume of 0.202 (+0.059/-0.026) km^3 of event deposits over more than 340 km along-strike the hadal trench. The basins JTS01 [0.040 (+0.010/-0.004) km^3], JTS04 [0.045 (+0.011/-0.004) km^3], JTS15 [0.017 (+0.005/-0.002) km^3] document largest deposit volumes of the AD 869 event, which can also be explained by highest flow accumulation among the identified basins in the southern and central Japan Trench (**Figure 8**). Interestingly, our results suggest that the AD 869 earthquake delivered a similarly large volume of remobilized sediment to the trench as did the AD 2011 earthquake. This may hint that, given that the sediment routing system does not change considerably through time, the AD 869 Jogan earthquake has a similar size to the AD 2011 Tohoku-oki earthquake that can generate similarly widespread remobilization of surficial slope sediments. Furthermore, the 2nd–3rd Century AD event delivered the largest volume of deposits in the last 2,000 years, yielding 0.412 (+0.084/-0.025) km^3 in the basins of the northern Japan Trench. Larger volumes of this event deposit in the basins JTN05 and JTN08 than JTN03 and JTN07 (**Table 3**) agree with high flow accumulation in bathymetry (**Figure 8**). It should be noted that sediment volume of the 2nd–3rd Century event deposit in the basin JTN08 [0.184 (+0.036/-0.010) km^3] alone is compatible to the total volume of event deposit of AD2011 M_w9.0–9.1 Tohoku-oki earthquake throughout the Japan Trench. This extremely large volume of deposit in the single basin might be due to funneling and focusing of the triggered muddy density flows through the proximal Ogawara canyon. All these findings indicate that eventual sediment supply to the trench is variable with different large earthquakes, suggesting various long-term rates of sediment flux to and filling of the trench basin along the Japan Trench.

By calculating the AD 2011 event-deposit total sediment volume and measuring OC content within the event deposits, Kioka et al. (2019) estimated that the giant AD 2011 Tohoku-oki earthquake delivered at least 1 Tg of OC to the hadal trench. Given that our results for sediment volume remobilized by older large earthquakes are comparable to or even larger than that for the AD 2011 earthquake, we also expect a large volume of export of OC to the trench associated with these previous earthquakes. Total organic carbon (TOC) contents within AD 1454 and AD 869 event deposits from the core GeoB16431-1 core are 0.99 ± 0.26 wt% and 0.65 ± 0.10 wt%, respectively (Bao et al., 2018). Here, we calculate masses of OC of event deposits using these TOC values, volume of a given event deposit, and a wide likely range of dry densities (800–1,200 kg/m^3). Total masses of OC within the AD 1677 Empo Boso-oki, AD 1454 Kyotoku, AD 869 Jogan, and 2–3 century event deposits are calculated to be 0.64 (+0.61/-0.31) Tg (10^{12} g), 0.68 (+0.68/-0.34) Tg, 1.32 (+1.03/-0.54) Tg, and 2.68 (+1.78/-0.97) Tg, respectively. As suggested by the large estimated volume of deposits, the AD 869 Jogan and 2–3 century earthquakes delivered large quantities of surficial seafloor sediment OC to the trench, which are compatible to or even larger than the carbon transfer to hadal trench triggered by the AD 2011 Tohoku-oki earthquake. These older event deposits contain relatively young remobilized sediments (Bao et al., 2018), indicating the occurrence of comparable remobilization and deposition processes. Therefore, we estimate that, at least 7.04 (+5.07/-2.89) Tg of OC remobilized from surficial slope seafloor sediments was exported to the hadal Japan Trench axis in the last 2,000 years, by the five historically known large earthquakes AD 2011, 1677, 1454, 869, and 2nd–3rd century earthquakes. This suggests that event deposits in the trench basins may play an important role as an OC sink during interseismic periods.

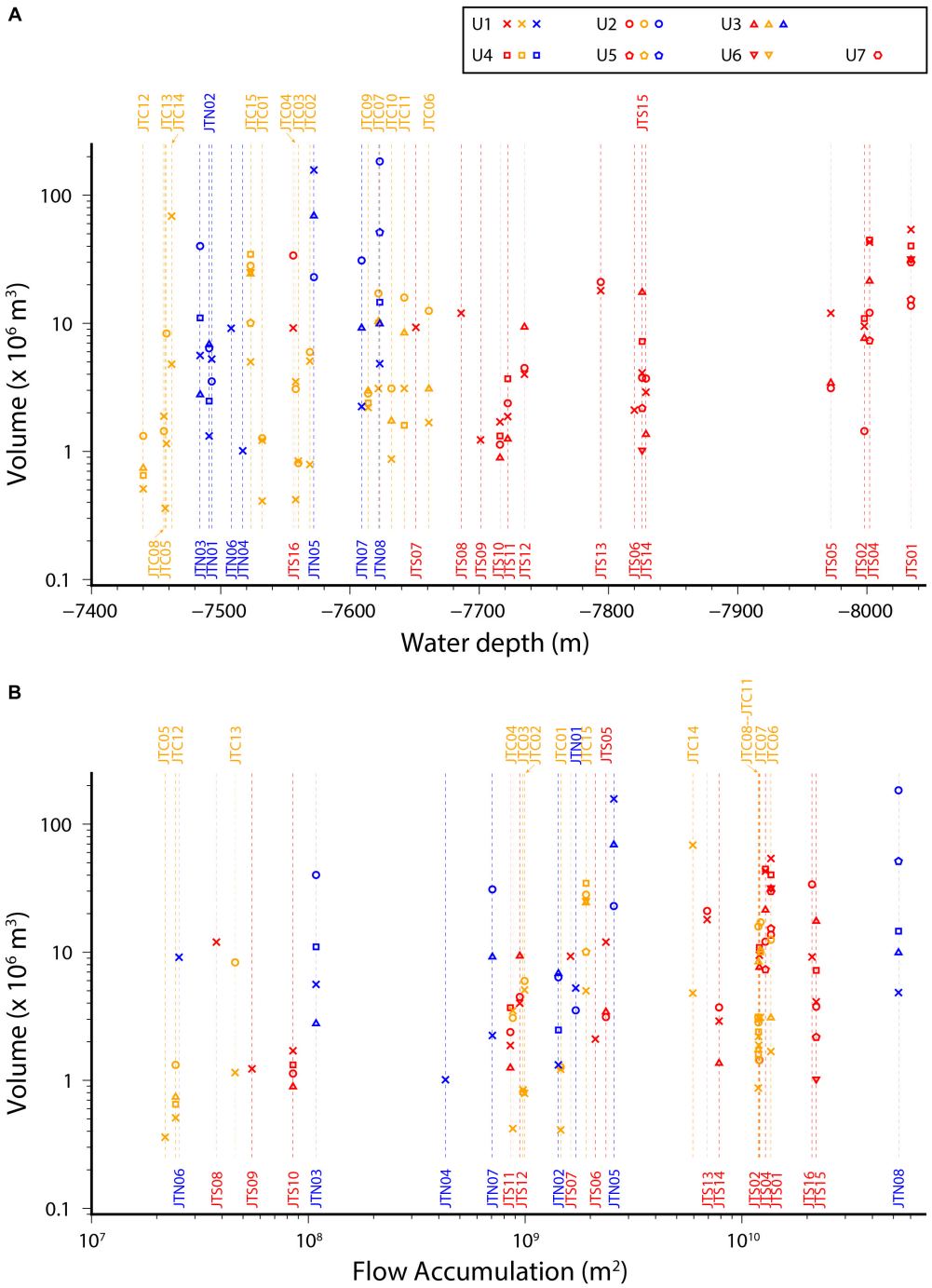


FIGURE 8 | (A) Relationship between volume of event deposit and modern water depth of depocenter at a given trench-fill basin. **(B)** Relationship between volume of event deposit and modern flow accumulation of modern depocenter at a given trench-fill basin. Red, orange, and blue plots represent the basins in the southern, central, and northern Japan Trench, respectively. Cross, circle, triangle, square, pentagon, inverted triangle, and hexagon plots represent the volumes of SBP units U1 (and uppermost deposits "NaN" in **Table 2**), U2, U3, U4, U5, U6, and U7, respectively. The data with volumes less than 0.3 × 10^6 m^3 are not shown.

We have also documented event deposits older than those related to the AD 869 and 2nd–3rd century earthquakes in the entire Japan Trench. We would thus expect similarly large quantities of OC supply to the trench by older large earthquakes perhaps throughout the Holocene, which could also influence the benthic communities at the hadal trench through the intensified supply of organic matter, but reserve final judgment for the future when further constraints are available from the upcoming IODP expedition. Nevertheless, the virtually instantaneous supply of OC to the hadal trench driven by large earthquakes brings the

majority of OC burial and carbon sequestration via eventual underthrusting on geological time scales. The hadal trench can thus be considered as a sink for global OC, which could account for several of the missing OC in global budget. It yet remains open to understand how much the buried OC accounts for being recycled by anaerobic degradation, being buried deep to be methanized (D'Hondt et al., 2002) or being subducted to contribute to the long-term carbon cycle and eventual CO_2 degassing through the proximal volcanic activity (Kerrick, 2001). Anyhow, our findings represent an important contribution of large earthquakes to long-term carbon cycling in the hadal zones that may have a broader span of significance yet to be discovered.

CONCLUSION

We have studied detailed event stratigraphy in an entire hadal trench for the first time to our knowledge, by integrating high-resolution bathymetry and highly dense dm-scale vertical resolution subbottom profiler (SBP) data, and sediment cores acquired during 2012–2018 over the entire hadal trench axis of the Japan Trench (36.0°–40.5°N). We identify 39 isolated trench-fill basins along the trench axis of the Japan Trench that contain a total of 115 individual SBP-resolvable acoustically transparent event deposits, documenting sediment remobilization of mostly diatomaceous mud. Spatio-temporal mapping and basin-to-basin correlation of the identified event deposits, along with SBP-to-core correlation and dating of cores retrieved from the upper parts of ∼10 m below the seafloor reveals that widely correlatable event deposits link to major historic large earthquakes such as the AD 2011 Tohoku-oki, AD 1454 Kyotoku, and AD 869 Jogan events.

Comparison between the areal extent of event deposits with inferred rupture areas and magnitude of the respective historical earthquakes suggests that our Japan Trench submarine paleoseismological approach can be used to roughly constrain areal extent of past M8+ earthquakes. Our data also suggest that only such large earthquakes trigger spatially extensive sediment remobilization that results in SBP-resolvable, thick event deposits across several trench-basins with different upslope flow network conditions. For these events, we could at least clearly separate smaller events from the event-stratigraphic record (exclusively for the southernmost trench basins) that link to M∼8.5 type earthquakes along the southernmost segment, and repeating spatially extensive large to giant (M8.4–9.1) earthquakes in the linked southern and central part of the Japan. However, detailed comparison between event-deposit distributions and rupture areas reported from literature also reveals that the two do not perfectly match. This highlights that large knowledge gaps remain in reconstructing rupture areas of past earthquakes, in understanding exact areal and subsurface-depth threshold conditions for earthquake induced surficial sediment remobilization, as well as in linking areal distribution and volume of remobilized sediment to earthquake parameters.

The lower part of the SBP data also documents several thick acoustically transparent bodies possibly dating back to the early and middle Holocene. Our results provide quantitative constraints of along-strike variation of sediment volumes redistributed by these episodic events along the entire trench axis. We find that the total volumes of event deposits triggered by the AD 869 Jogan and the prehistoric 2–3 century AD earthquakes are comparative to or even larger than that by the AD 2011 M_w 9.0–9.1 Tohoku-oki earthquake. Finally, we present a first-ever trench-wide quantification of OC translocation driven by these large earthquakes. We conclude that, at least 7 Tg of OC remobilized from surficial slope seafloor sediments was exported to the hadal Japan Trench axis in the last 2,000 years by large earthquakes. This highlights the significance of seismo-tectonic events for the long-term carbon cycle in hadal trenches.

DATA AVAILABILITY STATEMENT

Bathymetric data used in the paper are available at Bundesamt für Seeschifffahrt und Hydrographie (https://www.bsh.de/DE/DATEN/Ozeanographisches_Datenzentrum/Vermessungsdaten/Nordpazifischer_Ozean/nordpazifik_node.html) and JAMSTEC-DARWIN database (http://www.godac.jamstec.go.jp/darwin/e). All the other datasets generated for this study are available on request to the corresponding author.

AUTHOR CONTRIBUTIONS

MS and AK projected the study. AK analyzed all the data, created the figures, and drafted the manuscript. TS performed radiocarbon dating measurements and prepared **Figure 5**. KI provided radiographs of cores. All authors contributed to the acquisitions of data, discussion to this study, and provided feedback on the manuscript.

FUNDING

The R/V Sonne cruises were supported by the German Federal Ministry of Education and Research (BMBF) and German Research Foundation (DFG). The R/V Shinsei-Maru cruises were supported by Japan Agency of Marine-Earth Science and Technology (JAMSTEC) and Joint Usage/Research Center for Atmosphere and Ocean Science at the Atmosphere and Ocean Research Institute, The University of Tokyo. This work was supported by the Austrian Science Fund (FWF-P29678).

ACKNOWLEDGMENTS

The authors highly appreciate the effort of shipboard scientists and staffs of the R/V Sonne cruises SO251 Leg 1 and SO219A Leg 2, and R/V Shinsei-maru cruises KS-18-10, KS-17-13, KS-16-14, KS-15-16, KS-15-3, and KS-14-16 to acquire the data used in this work. The authors are also immensely grateful to the editor MC and the two reviewers for their valuable comments which significantly improved the quality and clarity of this manuscript. Processing and interpretation of SBP data were done helpfully using IHS Markit Kingdom software

(educational grant program), CWP/SU (Cohen and Stockwell, 2015) and Madagascar open-source software (Fomel et al., 2013). Bathymetric data were analyzed using Generic Mapping Tool (GMT) software (Wessel et al., 2013) and TopoToolbox (Schwanghart and Scherler, 2014).

SUPPLEMENTARY MATERIAL

The Supplementary Material for this article can be found online at: https://www.frontiersin.org/articles/10.3389/feart.2019.00319/full#supplementary-material

REFERENCES

Abma, R., and Kabir, N. (2006). 3D interpolation of irregular data with a POCS algorithm. *Geophysics* 71, E91–E97. doi: 10.1190/1.2356088

Arai, K., Inoue, T., Ikehara, K., and Sasaki, T. (2014). Episodic subsidence and active deformation of the forearc slope along the Japan trench near the epicenter of the 2011 tohoku earthquake. *Earth Planet. Sci. Lett.* 408, 9–15. doi: 10.1016/j.epsl.2014.09.048

Arai, K., Naruse, H., Miura, R., Kawamura, K., Hino, R., Ito, Y., et al. (2013). Tsunami-generated turbidity current of the 2011 Tohoku-Oki earthquake. *Geology* 41, 1195–1198. doi: 10.1130/G34777.1

Bao, R., Strasser, M., McNichol, A. P., Haghipour, N., McIntyre, C., Wefer, G., et al. (2018). Tectonically-triggered sediment and carbon export to the Hadal zone. *Nat. Commun.* 9:121. doi: 10.1038/s41467-017-02504-1

Berner, R. A. (1982). Burial of organic carbon and pyrite sulfur in the modern ocean; its geochemical and environmental significance. *Am. J. Sci.* 282, 451–473. doi: 10.2475/ajs.282.4.451

Bird, P. (2003). An updated digital model of plate boundaries. *Geochem. Geophys. Geosyst.* 4:1027. doi: 10.1029/2001GC000252

Boston, B., Moore, G. F., Nakamura, Y., and Kodaira, S. (2017). Forearc slope deformation above the Japan Trench megathrust: implications for subduction erosion. *Earth Planet. Sci. Lett.* 462, 26–34. doi: 10.1016/j.epsl.2017.01.005

Burdige, D. J. (2007). Preservation of organic matter in marine sediments: controls, mechanisms, and an imbalance in sediment organic carbon budgets? *Chem. Rev.* 107, 467–485. doi: 10.1021/cr050347q

Cadet, J. P., Kobayashi, K., Lallemand, S., Jolivet, L., Aubouin, J., Boulegue, J., et al. (1987). Deep scientific dives in the Japan and Kuril Trenches. *Earth Planet. Sci. Lett.* 83, 313–328. doi: 10.1016/0012-821X(87)90074-4

Chen, Y., Zhang, L., and Mo, L.-W. (2015). Seismic data interpolation using nonlinear shaping regularization. *J. Seism. Explor.* 24, 327–342.

Chester, F. M., Rowe, C., Ujiie, K., Kirkpatrick, J., Regalla, C., Remitti, F., et al. (2013). Structure and composition of the plate-boundary slip zone for the 2011 Tohoku-Oki Earthquake. *Science* 342, 1208–1211. doi: 10.1126/science.1243719

Clift, P., and Vannucchi, P. (2004). Controls on tectonic accretion versus erosion in subduction zones: implications for the origin and recycling of the continental crust. *Rev. Geophys.* 42:RG2001. doi: 10.1029/2003RG000127

Clift, P. D. (2017). A revised budget for Cenozoic sedimentary carbon subduction. *Rev. Geophys.* 55, 97–125. doi: 10.1002/2016RG000531

Cohen, J. K., and Stockwell, J. W. Jr. (2015). *CWP/SU: Seismic Un*x Release No. 44: An Open Source Software Package for Seismic Research and Processing*. Golden, CO: Colorado School of Mines.

Danovaro, R., Della Croce, N., Dell'Anno, A., and Pusceddu, A. (2003). A depocenter of organic matter at 7800m depth in the SE Pacific Ocean. *Deep Sea Res. Part I Oceanogr. Res. Pap.* 50, 1411–1420. doi: 10.1016/j.dsr.2003.07.001

Daubechies, I., Defrise, M., and De Mol, C. (2004). An iterative thresholding algorithm for linear inverse problems with a sparsity constraint. *Commun. Pure Appl. Math.* 57, 1413–1457. doi: 10.1002/cpa.20042

D'Hondt, S., Rutherford, S., and Spivack, A. J. (2002). Metabolic activity of subsurface life in deep-sea sediments. *Science* 295, 2067–2070. doi: 10.1126/science.1064878

Fomel, S., Sava, P., Vlad, I., Liu, Y., and Bashkardin, V. (2013). Madagascar: open-source software project for multidimensional data analysis and reproducible computational experiments. *J. Open Res. Softw.* 1:e8. doi: 10.5334/jors.ag

Fujiwara, T., dos Santos Ferreira, C., Bachmann, A. K., Strasser, M., Wefer, G., Sun, T., et al. (2017). Seafloor displacement after the 2011 Tohoku-oki Earthquake in the Northern Japan trench examined by repeated bathymetric surveys. *Geophys. Res. Lett.* 44, 833–839. doi: 10.1002/2017GL075839

Fujiwara, T., Kodaira, S., No, T., Kaiho, Y., Takahashi, N., and Kaneda, Y. (2011). The 2011 Tohoku-Oki earthquake: displacement reaching the trench axis. *Science* 334:1240. doi: 10.1126/science.1211554

Glud, R. N., Wenzhöfer, F., Middelboe, M., Oguri, K., Turnewitsch, R., Canfield, D. E., et al. (2013). High rates of microbial carbon turnover in sediments in the deepest oceanic trench on Earth. *Nat. Geosci.* 6, 284–288. doi: 10.1038/ngeo1773

Goldfinger, C. (2011). Submarine paleoseismology based on turbidite records. *Ann. Rev. Mar. Sci.* 3, 35–66. doi: 10.1146/annurev-marine-120709-142852

Goto, T., Satake, K., Sugai, T., Ishibe, T., Harada, T., and Gusman, A. R. (2019). Tsunami history over the past 2000 years on the Sanriku coast, Japan, determined using gravel deposits to estimate tsunami inundation behavior. *Sediment. Geol.* 382, 85–102. doi: 10.1016/j.sedgeo.2019.01.001

Hirakawa, K. (2012). Outsize tsunami sediments since last years along the Japan- and Kuril-Trench: a tentative idea on source and supercycle. *Kagaku* 82, 172–181.

Hirano, N., Takahashi, E., Yamamoto, J., Abe, N., Ingle, S. P., Kaneoka, I., et al. (2006). Volcanism in response to plate flexure. *Science* 313, 1426–1428. doi: 10.1126/science.1128235

Hydrographic and Oceanographic Department Japan Coast Guard, and JAMSTEC, (2011). Compilation of Tohoku-oki bathymetric data before the 2011 Tohoku-oki earthquake. *Seismol. Soc. Jpn News Lett.* 23, 35–36. doi: 10.1038/ncomms14044

Ide, S., Baltay, A., and Beroza, G. C. (2011). Shallow dynamic overshoot and energetic deep rupture in the 2011 Mw 9.0 Tohoku-Oki Earthquake. *Science* 332, 1426–1429. doi: 10.1126/science.1207020

Ikehara, K., Kanamatsu, T., Nagahashi, Y., Strasser, M., Fink, H., Usami, K., et al. (2016). Documenting large earthquakes similar to the 2011 Tohoku-oki earthquake from sediments deposited in the Japan Trench over the past 1500 years. *Earth Planet. Sci. Lett.* 445, 48–56. doi: 10.1016/j.epsl.2016.04.009

Ikehara, K., Usami, K., Kanamatsu, T., Arai, K., Yamaguchi, A., and Fukuchi, R. (2018). Spatial variability in sediment lithology and sedimentary processes along the Japan Trench: use of deep-sea turbidite records to reconstruct past large earthquakes. *Geol. Soc. Lond. Spec. Publ.* 456, 75–89. doi: 10.1144/SP456.9

Ishimura, D., and Miyauchi, T. (2015). Historical and paleo-tsunami deposits during the last 4000 years and their correlations with historical tsunami events in Koyadori on the Sanriku Coast, northeastern Japan. *Prog. Earth Planet. Sci.* 2:16. doi: 10.1186/s40645-015-0047-4

Jamieson, A. J., Fujii, T., Mayor, D. J., Solan, M., and Priede, I. G. (2010). Hadal trenches: the ecology of the deepest places on Earth. *Trends Ecol. Evol.* 25, 190–197. doi: 10.1016/j.tree.2009.09.009

Jones, D. O. B., Yool, A., Wei, C.-L., Henson, S. A., Ruhl, H. A., Watson, R. A., et al. (2014). Global reductions in seafloor biomass in response to climate change. *Glob. Chang. Biol.* 20, 1861–1872. doi: 10.1111/gcb.12480

Kanamatsu, T., Usami, K., McHugh, C. M. G., and Ikehara, K. (2017). High-resolution chronology of sediment below CCD based on Holocene paleomagnetic secular variations in the Tohoku-oki earthquake rupture zone. *Geochem. Geophys. Geosyst.* 18, 2990–3002. doi: 10.1002/2017GC006878

Kanamori, H. (1971). Seismological evidence for a lithospheric normal faulting — the Sanriku earthquake of 1933. *Phys. Earth Planet. Inter.* 4, 289–300. doi: 10.1016/0031-9201(71)90013-6

Kanamori, H. (1972). Mechanism of tsunami earthquakes. *Phys. Earth Planet. Inter.* 6, 346–359. doi: 10.1016/0031-9201(72)90058-1

Kanamori, H. (1977). The energy release in great earthquakes. *J. Geophys. Res.* 82, 2981–2987. doi: 10.1029/JB082i020p02981

Kawahata, H., Ishizaki, Y., Kuroyanagi, A., Suzuki, A., and Ohkushi, K. (2017). Quantitative reconstruction of temperature at a Jômon site in the Incipient Jômon Period in northern Japan and its implications for the production of early pottery and stone arrowheads. *Quat. Sci. Rev.* 157, 66–79. doi: 10.1016/j.quascirev.2016.12.009

Kawamura, K., Sasaki, T., Kanamatsu, T., Sakaguchi, A., and Ogawa, Y. (2012). Large submarine landslides in the Japan Trench: a new scenario for additional tsunami generation. *Geophys. Res. Lett.* 39:L05308. doi: 10.1029/2011GL050661

Kerrick, D. M. (2001). Present and past nonanthropogenic CO2 degassing from the solid earth. *Rev. Geophys.* 39, 565–585. doi: 10.1029/2001RG000105

Kioka, A., Schwestermann, T., Moernaut, J., Ikehara, K., Kanamatsu, T., McHugh, C. M., et al. (2019). Megathrust earthquake drives drastic organic carbon supply to the hadal trench. *Sci. Rep.* 9:1553. doi: 10.1038/s41598-019-38834-x

Kodaira, S., Nakamura, Y., Yamamoto, Y., Obana, K., Fujie, G., No, T., et al. (2017). Depth-varying structural characters in the rupture zone of the 2011 Tohoku-oki earthquake. *Geosphere* 13, 1408–1424. doi: 10.1130/GES01489.1

Kodaira, S., No, T., Nakamura, Y., Fujiwara, T., Kaiho, Y., Miura, S., et al. (2012). Coseismic fault rupture at the trench axis during the 2011 Tohoku-oki earthquake. *Nat. Geosci.* 5, 646–650. doi: 10.1038/ngeo1547

Koge, H., Fujiwara, T., Kodaira, S., Sasaki, T., Kameda, J., Kitamura, Y., et al. (2014). Friction properties of the plate boundary megathrust beneath the frontal wedge near the Japan Trench: an inference from topographic variation. *Earth Planets Space* 66:153. doi: 10.1186/s40623-014-0153-3

Kusumoto, S., Goto, T., Sugai, T., Omori, T., and Satake, K. (2018). Geological evidence of tsunamis in the past 3800 years at a coastal lowland in the Central Fukushima Prefecture, Japan. *Mar. Geol.* 404, 137–146. doi: 10.1016/j.margeo.2018.07.004

Lallemand, S. E., Schnürle, P., and Malavieille, J. (1994). Coulomb theory applied to accretionary and nonaccretionary wedges: possible causes for tectonic erosion and/or frontal accretion. *J. Geophys. Res. Solid Earth* 99, 12033–12055. doi: 10.1029/94JB00124

Lay, T., Kanamori, H., Ammon, C. J., Nettles, M., Ward, S. N., Aster, R. C., et al. (2005). The great Sumatra-Andaman Earthquake of 26 December 2004. *Science* 308, 1127–1133. doi: 10.1126/science.1112250

Leduc, D., Rowden, A. A., Glud, R. N., Wenzhöfer, F., Kitazato, H., and Clark, M. R. (2016). Comparison between infaunal communities of the deep floor and edge of the Tonga Trench: possible effects of differences in organic matter supply. *Deep Sea Res. Part I Oceanogr. Res. Pap.* 116, 264–275. doi: 10.1016/j.dsr.2015.11.003

Loveless, J. P., and Meade, B. J. (2010). Geodetic imaging of plate motions, slip rates, and partitioning of deformation in Japan. *J. Geophys. Res.* 115:B02410. doi: 10.1029/2008JB006248

MacInnes, B. T., Weiss, R., Bourgeois, J., and Pinegina, T. K. (2010). Slip distribution of the 1952 Kamchatka Great earthquake based on near-field tsunami deposits and historical records. *Bull. Seismol. Soc. Am.* 100, 1695–1709. doi: 10.1785/0120090376

McHugh, C. M., Kanamatsu, T., Seeber, L., Bopp, R., Cormier, M.-H., and Usami, K. (2016). Remobilization of surficial slope sediment triggered by the A.D. 2011 Mw 9 Tohoku-Oki earthquake and tsunami along the Japan Trench. *Geology* 44, 391–394. doi: 10.1130/G37650.1

McIntyre, C. P., Wacker, L., Haghipour, N., Blattmann, T. M., Fahrni, S., Usman, M., et al. (2017). Online 13C and 14C gas measurements by EA-IRMS–AMS at ETH Zürich. *Radiocarbon* 59, 893–903. doi: 10.1017/RDC.2016.68

Moernaut, J., Van Daele, M., Fontijn, K., Heirman, K., Kempf, P., Pino, M., et al. (2018). Larger earthquakes recur more periodically: new insights in the megathrust earthquake cycle from lacustrine turbidite records in south-central Chile. *Earth Planet. Sci. Lett.* 481, 9–19. doi: 10.1016/j.epsl.2017.10.016

Molenaar, A., Moernaut, J., Wiemer, G., Dubois, N., and Strasser, M. (2019). Earthquake impact on active margins: tracing surficial remobilization and seismic strengthening in a slope sedimentary sequence. *Geophys. Res. Lett.* 46, 6015–6023. doi: 10.1029/2019GL082350

Mori, N., Takahashi, T., Yasuda, T., and Yanagisawa, H. (2011). Survey of 2011 Tohoku earthquake tsunami inundation and run-up. *Geophys. Res. Lett.* 38:L00G14. doi: 10.1029/2011GL049210

Müller, M. (2007). *Information Retrieval for Music and Motion*. Berlin: Springer. doi: 10.1007/978-3-540-74048-3

Nagai, R., Kikuchi, M., and Yamanaka, Y. (2001). Comparative study on the source processes of recurrent large earthquakes in Sanriku-oki Region: the 1968 Tokachi-oki Earthquake and the 1994 Sanriku-oki Earthquake. *Zisin-II* 54, 267–280. doi: 10.4294/zisin1948.54.2_267

Nakamura, Y., Kodaira, S., Miura, S., Regalla, C., and Takahashi, N. (2013). High-resolution seismic imaging in the Japan Trench axis area off Miyagi, northeastern Japan. *Geophys. Res. Lett.* 40, 1713–1718. doi: 10.1002/grl.50364

Namegaya, Y., and Satake, K. (2014). Reexamination of the A.D. 869 Jogan earthquake size from tsunami deposit distribution, simulated flow depth, and velocity. *Geophys. Res. Lett.* 41, 2297–2303. doi: 10.1002/2013GL058678

Nunoura, T., Takaki, Y., Hirai, M., Shimamura, S., Makabe, A., Koide, O., et al. (2015). Hadal biosphere: insight into the microbial ecosystem in the deepest ocean on Earth. *Proc. Natl. Acad. Sci. U.S.A.* 112, E1230–E1236. doi: 10.1073/pnas.1421816112

O'Callaghan, J. F., and Mark, D. M. (1984). The extraction of drainage networks from digital elevation data. *Comput. Vis. Graph. Image Process.* 28, 323–344. doi: 10.1016/S0734-189X(84)80011-0

Oguri, K., Kawamura, K., Sakaguchi, A., Toyofuku, T., Kasaya, T., Murayama, M., et al. (2013). Hadal disturbance in the Japan Trench induced by the 2011 Tohoku–Oki Earthquake. *Sci. Rep.* 3:1915. doi: 10.1038/srep01915

Okamura, Y., and Namegaya, Y. (2011). Reconstruction of the 17th century Kuril multi-segment earthquake. *Annu. Rep. Act. Fault Paleoearthquake Res.* 11, 15–20.

Peng, G., Bellerby, R., Zhang, F., Sun, X., and Li, D. (in press). The ocean's ultimate trashcan: hadal trenches as major depositories for plastic pollution. *Water Res.* 168:115121. doi: 10.1016/j.watres.2019.115121

Sakazaki, T., Kano, Y., Ohmura, J., and Hattori, K. (2015). On the severe typhoon attacking edo region in 1856. *Sustain. Humanosphere* 11, 64–70.

Sakoe, H., and Chiba, S. (1978). Dynamic programming algorithm optimization for spoken word recognition. *IEEE Trans. Acoust.* 26, 43–49. doi: 10.1109/TASSP.1978.1163055

Satake, K. (2015). Geological and historical evidence of irregular recurrent earthquakes in Japan. *Philos. Trans. R. Soc. A Math. Phys. Eng. Sci.* 373:20140375. doi: 10.1098/rsta.2014.0375

Satake, K., and Atwater, B. F. (2007). Long-term perspectives on giant earthquakes and tsunamis at subduction zones. *Annu. Rev. Earth Planet. Sci.* 35, 349–374. doi: 10.1146/annurev.earth.35.031306.140302

Sawai, Y., Namegaya, Y., Okamura, Y., Satake, K., and Shishikura, M. (2012). Challenges of anticipating the 2011 Tohoku earthquake and tsunami using coastal geology. *Geophys. Res. Lett.* 39:L21309. doi: 10.1029/2012GL053692

Sawai, Y., Namegaya, Y., Tamura, T., Nakashima, R., and Tanigawa, K. (2015). Shorter intervals between great earthquakes near Sendai: scour ponds and a sand layer attributable to A.D. 1454 overwash. *Geophys. Res. Lett.* 42, 4795–4800. doi: 10.1002/2015GL064167

Schwanghart, W., and Scherler, D. (2014). TopoToolbox 2 – MATLAB-based software for topographic analysis and modeling in Earth surface sciences. *Earth Surf. Dyn.* 2, 1–7. doi: 10.5194/esurf-2-1-2014

Seno, T., Sakurai, T., and Stein, S. (1996). Can the Okhotsk Plate be discriminated from the North American plate? *J. Geophys. Res. Solid Earth* 101, 11305–11315. doi: 10.1029/96JB00532

Stein, S., and Okal, E. A. (2005). Speed and size of the Sumatra earthquake. *Nature* 434, 581–582. doi: 10.1038/434581a

Strasser, M., Ikehara, K., and Cotterill, C. (2019). Expedition 386 scientific prospectus: Japan trench paleoseismology. *Int. Ocean Disc. Prog.* 386, 1–57. doi: 10.14379/iodp.sp.386.2019

Strasser, M., Kolling, M., Ferreira, C., dos, S., Fink, H. G., Fujiwara, T., et al. (2013). A slump in the trench: tracking the impact of the 2011 Tohoku-Oki earthquake. *Geology* 41, 935–938. doi: 10.1130/G34477.1

Strasser, M., Kopf, A. J., et al. (2017). *Report and Preliminary Results of R/V SONNE Cruise SO251, Extreme Events Archived in the GEological Record of Japan's Subduction Margins (EAGER-Japan), Leg A SO251-1, Yokohama - Yokohama, 04.10.2016 – 15.10.2016, Leg B SO251- 2, Yokohama - Yokohama, 18.10.2016 – 02.11.2016*. Berichte: MARUM, 1–217.

Sun, T., Wang, K., Fujiwara, T., Kodaira, S., and He, J. (2017). Large fault slip peaking at trench in the 2011 Tohoku-oki earthquake. *Nat. Commun.* 8:14044. doi: 10.1038/ncomms14044

Takada, K., Shishikura, M., Imai, K., Ebina, Y., Goto, K., Koshiya, S., et al. (2016). Distribution and ages of tsunami deposits along the Pacific Coast of the Iwate Prefecture. *Active Fault Paleoearthq. Res.* 16, 1–52.

Takeuchi, H., Fuji, R., Mimura, N., Imamura, F., Satake, K., Tsuji, Y., et al. (2007). Survey of run-up height of Empo Boso-oki earthquake tsunami on the coast from Chiba prefecture to Fukushima prefecture. *Hist. Earthq.* 22, 53–59.

Tanioka, Y., and Satake, K. (1996). Fault parameters of the 1896 Sanriku Tsunami earthquake estimated from tsunami numerical modeling. *Geophys. Res. Lett.* 23, 1549–1552. doi: 10.1029/96GL01479

Tsuji, T., Kawamura, K., Kanamatsu, T., Kasaya, T., Fujikura, K., Ito, Y., et al. (2013). Extension of continental crust by anelastic deformation during the 2011 Tohoku-oki earthquake: the role of extensional faulting in the generation of a great tsunami. *Earth Planet. Sci. Lett.* 364, 44–58. doi: 10.1016/j.epsl.2012.12.038

Tsuji, Y., and Ueda, K. (1995). Evaluation of A.D. 1611 Keicho, A.D. 1677 Enpou, A.D. 1763 Houreki, A.D. 1793 Kansei, and A.D. 1856 Ansei Sanriku tsunamis. *Hist. Earthq.* 11, 75–106.

Tsuru, T., Park, J.-O., Miura, S., Kodaira, S., Kido, Y., and Hayashi, T. (2002). Along-arc structural variation of the plate boundary at the Japan Trench margin: implication of interplate coupling. *J. Geophys. Res. Solid Earth* 107:2357. doi: 10.1029/2001JB001664

Usami, K., Ikehara, K., Kanamatsu, T., and McHugh, C. M. (2018). Supercycle in great earthquake recurrence along the Japan Trench over the last 4000 years. *Geosci. Lett.* 5:11. doi: 10.1186/s40562-018-0110-2

von Huene, R., and Lallemand, S. (1990). Tectonic erosion along the Japan and Peru convergent margins. *Geol. Soc. Am. Bull.* 102, 704–720. doi: 10.1130/0016-76061990102<0704:TEATJA<2.3.CO;2

Wessel, P., Smith, W. H. F., Scharroo, R., Luis, J., and Wobbe, F. (2013). Generic mapping tools: improved version released. *Eos Trans. Am. Geophys. Union* 94, 409–410. doi: 10.1002/2013EO450001

Yanagisawa, H., Goto, K., Sugawara, D., Kanamaru, K., Iwamoto, N., and Takamori, Y. (2016). Tsunami earthquake can occur elsewhere along the Japan Trench-Historical and geological evidence for the 1677 earthquake and tsunami. *J. Geophys. Res. Solid Earth* 121, 3504–3516. doi: 10.1002/2015JB012617

Conflict of Interest: The authors declare that the research was conducted in the absence of any commercial or financial relationships that could be construed as a potential conflict of interest.

Copyright © 2019 Kioka, Schwestermann, Moernaut, Ikehara, Kanamatsu, Eglinton and Strasser. This is an open-access article distributed under the terms of the Creative Commons Attribution License (CC BY). The use, distribution or reproduction in other forums is permitted, provided the original author(s) and the copyright owner(s) are credited and that the original publication in this journal is cited, in accordance with accepted academic practice. No use, distribution or reproduction is permitted which does not comply with these terms.

frontiers in Earth Science

ORIGINAL RESEARCH
published: 05 December 2019
doi: 10.3389/feart.2019.00312

Provenance and Sediment Maturity as Controls on CO_2 Mineral Sequestration Potential of the Gassum Formation in the Skagerrak

Mette Olivarius[1], Anja Sundal[2], Rikke Weibel[1], Ulrik Gregersen[1], Irfan Baig[2], Tonny B. Thomsen[1], Lars Kristensen[1], Helge Hellevang[2] and Lars Henrik Nielsen[1]*

[1] Geological Survey of Denmark and Greenland (GEUS), Copenhagen, Denmark, [2] Department of Geosciences, University of Oslo, Oslo, Norway

OPEN ACCESS

Edited by:
Amanda Owen, University of Glasgow, United Kingdom

Reviewed by:
Maria Ansine Jensen, The University Centre in Svalbard, Norway
Adrian John Hartley, University of Aberdeen, United Kingdom

***Correspondence:**
Mette Olivarius
mol@geus.dk

Specialty section:
This article was submitted to Sedimentology, Stratigraphy and Diagenesis, a section of the journal Frontiers in Earth Science

Received: *31 March 2019*
Accepted: *08 November 2019*
Published: *05 December 2019*

Citation:
Olivarius M, Sundal A, Weibel R, Gregersen U, Baig I, Thomsen TB, Kristensen L, Hellevang H and Nielsen LH (2019) Provenance and Sediment Maturity as Controls on CO_2 Mineral Sequestration Potential of the Gassum Formation in the Skagerrak. Front. Earth Sci. 7:312. doi: 10.3389/feart.2019.00312

In order to meet the increasing demand to decarbonize the atmosphere, storage of CO_2 in subsurface geological reservoirs is an effective measure. To maximize storage capacity, various types of saline aquifers should be considered including dynamic storage options with open or semi-open boundaries. In sloping aquifers, assessment of the immobilization potential for CO_2 through dissolution and mineralization along the flow path is a crucial part of risk evaluations. The Gassum Formation in the Skagerrak is considered a nearshore CO_2 storage option with sloping layers, facilitating buoyant migration of CO_2 northwards along depositional and structural dip. In this study, petrographic data and provenance analysis provide the basis for estimating reactivity of the sandstones. Immobilization of CO_2 in the reservoir through fluid dissolution and mineral reactions reduces risk of leakage. Petrographic analyses are integrated with seismic and well-log interpretation to identify sedimentary facies and to estimate mineral distribution with corresponding reactivity in the proposed injection area. Here the Gassum Formation comprises south-prograding, shoreface-fluvial para-sequences, sourced from northern hinterlands. Pronounced differences in the mineralogical maturity in the studied area are identified and explained by the sediment transport distances and the type of sediment source. This is possible because the U-Pb ages of zircon grains in the sediments can be used to pinpoint the areas where they originate from in the Fennoscandian Shield, such as the Telemarkia or Idefjorden terranes. Albite and Fe-rich chlorite are identified as the most reactive mineral phases in the Gassum sand, of which feldspar comprises the largest weight fraction and the grain-coating chlorite has largest surface area. Their distribution is partly controlled by provenance, so their abundance decreases basinwards with increasing sediment maturity. The abundance of fluvial sandstones presumably increases northwards in basal parts of para-sequences, while shoreface sandstones comprise the top part of sandy units. CO_2 injected in the proposed area will migrate upwards within the reservoir, toward higher proportions of Telemarkian-derived sediment and up-dip along the seal, toward more immature sediments. Thus, the reactivity of sediments increases

in younger deposits and up depositional dip, while kinetic reaction rates will decrease in shallower, lower temperature regions. Identifying these parameters is important to estimate the CO_2 mineral sequestration potential as a function of sedimentary facies and ensure safe storage of CO_2. This approach can advantageously be applied to all reservoirs considered for CO_2 injection to improve the estimation of the possible CO_2 storage volume by taking the provenance dependence of the mineralization potential into account.

Keywords: CO_2 storage, reactive minerals, source to sink, zircon geochronology, depositional environments, petrography, diagenesis, reservoir quality

INTRODUCTION

Subsurface, brine-saturated sandstone reservoirs hold great potential for safe storage of anthropogenic CO_2. Upscaling carbon capture and storage is recommended by the Intergovernmental Panel on Climate Change (IPCC) as means to meet goals of reducing greenhouse gas emissions (Metz et al., 2005). In Scandinavia, the offshore storage potential is huge (Halland et al., 2011; Bergmo et al., 2013; Anthonsen et al., 2014), but under-utilized with only two operating storage sites (Eiken et al., 2011). Thorough geological reservoir characterization is essential in risk evaluations where not only the reservoir volume and seal quality must be taken into account, but also the dissolution capacity and reactivity of the reservoir rocks such that the mineral sequestration potential can be estimated. Highly reactive minerals can ensure the largest amount of CO_2 carbonatization and the dependence of the mineral sequestration potential on the sediment provenance has largely been overlooked hitherto. The provenance and sediment transport may strongly influence the distribution of the most reactive minerals, which is investigated in this study.

The main objective in the Upslope project is to improve reservoir characterization schemes and optimize storage (Upslope, 2019). Coupled modeling is applied to estimate trapping efficiency and migration distances in the further adaptation of suitable injection schemes, ultimately ensuring safe storage in open-boundary, prospective reservoirs. In order to estimate CO_2 plume retardation and immobilization potential, knowledge of sedimentary facies distribution, with varying reservoir properties and reaction potentials, is essential. In particular, the modal mineralogical variations are of importance regarding the most reactive minerals with respect to carbonatization of CO_2 (Palandri and Kharaka, 2004).

The Gassum Formation has been thoroughly investigated throughout onshore Denmark due to its good reservoir quality that makes it applicable for geothermal energy exploitation (Nielsen, 2003; Kristensen et al., 2016; Weibel et al., 2017a). This knowledge can be utilized in the Skagerrak to evaluate prospective storage sites for CO_2. The reservoir properties of the Gassum Formation are not well known in the Norwegian sector, but it is evident that the pressure and temperature conditions are suitable for CO_2 storage. The Gassum Formation comprises fluvial to marginal marine sandy deposits interbedded with mudstones in the study area located at the northern rim of the Norwegian-Danish Basin in the Skagerrak (**Figure 1**; Hamberg and Nielsen, 2000; Nielsen, 2003). The formation constitutes a sloping aquifer in this area (**Figures 2**, **3**) that holds great potential for CO_2 storage (e.g., Halland et al., 2011; Bergmo et al., 2013; Anthonsen et al., 2014). There is a need, however, to constrain the mineralogical composition and reservoir quality to evaluate aspects of migration-assisted immobilization. In this respect, evidence of provenance areas and diagenetic evolution is required. A prospective injection site in the south-central part of the study area is assessed as an example (**Figure 1**).

Variations exist in the composition and sediment maturity of the Gassum Formation in the Norwegian-Danish Basin (Weibel et al., 2017a). This study investigates if regional maturity trends can be identified by comparing the sediments along the northern basin margin and in the Farsund Basin with those deposited centrally in the basin. The objective is to identify geographical and stratigraphical trends in sediment maturity related to the sediment transport distance and the lithology in the provenance terrane. If such relationships exist, then the modal mineralogical composition, and subsequently reactivity, can be estimated in potential CO_2 injection areas. New data of zircon ages and petrography provide improved understanding of provenance and diagenesis in the Gassum Formation aquifer on the Norwegian continental shelf, which can be applied in predictions of CO_2 carbonatization here and elsewhere.

GEOLOGICAL SETTING

The Upper Triassic to Lower Jurassic sandstone-dominated Gassum Formation is widely distributed in the Norwegian-Danish Basin and is, therefore, the favorite target for exploitation of geothermal energy onshore Denmark. The formation was first defined for the Danish area by Larsen (1966) and redefined as the upper part of the Mors Group by Bertelsen (1978, 1980). Deposition of the Gassum Formation took place in shoreface, estuarine, fluvial, lagoonal and lacustrine environments in the northern and eastern parts of the Norwegian-Danish Basin during the Rhaetian, while the contemporary shallow marine mudstones belonging to the Vinding Formation were deposited in the basin center. The facies change from the underlying continental red beds was accompanied by a shift to a more humid climate, which was probably already initiated in late Ladinian times. Marine mudstones of the Fjerritslev Formation

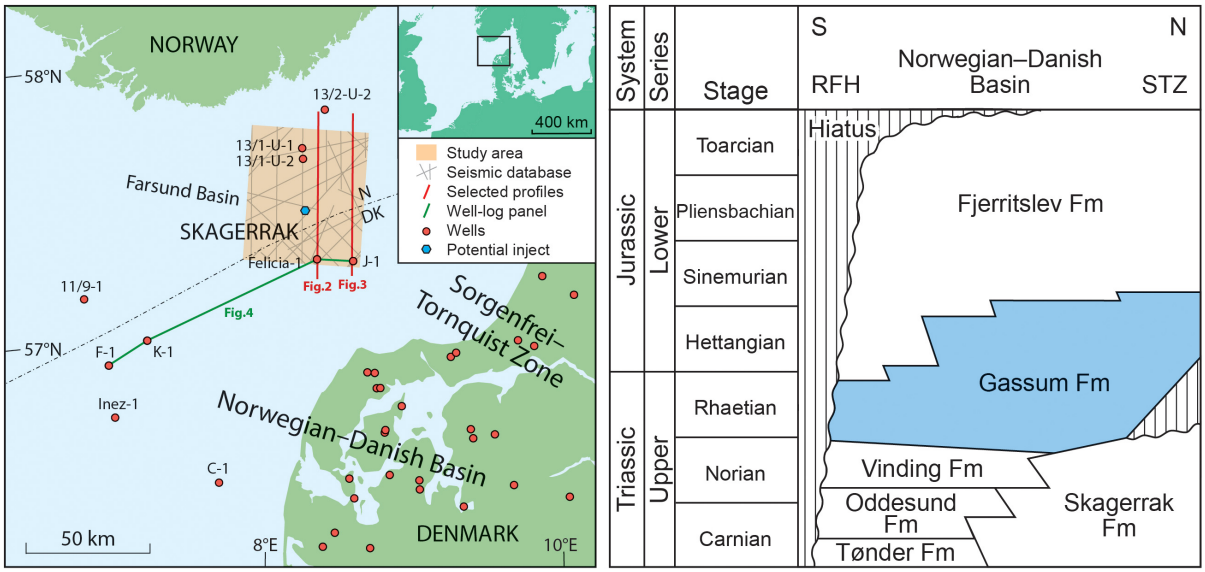


FIGURE 1 | The studied part of the Gassum Formation is located in the Skagerrak in the Norwegian-Danish Basin. The stratigraphic scheme depicts the basin from the Ringkøbing-Fyn High (RFH) to the Sorgenfrei-Tornquist Zone (STZ). The stratigraphy is based on Michelsen and Clausen (2002) and Nielsen (2003).

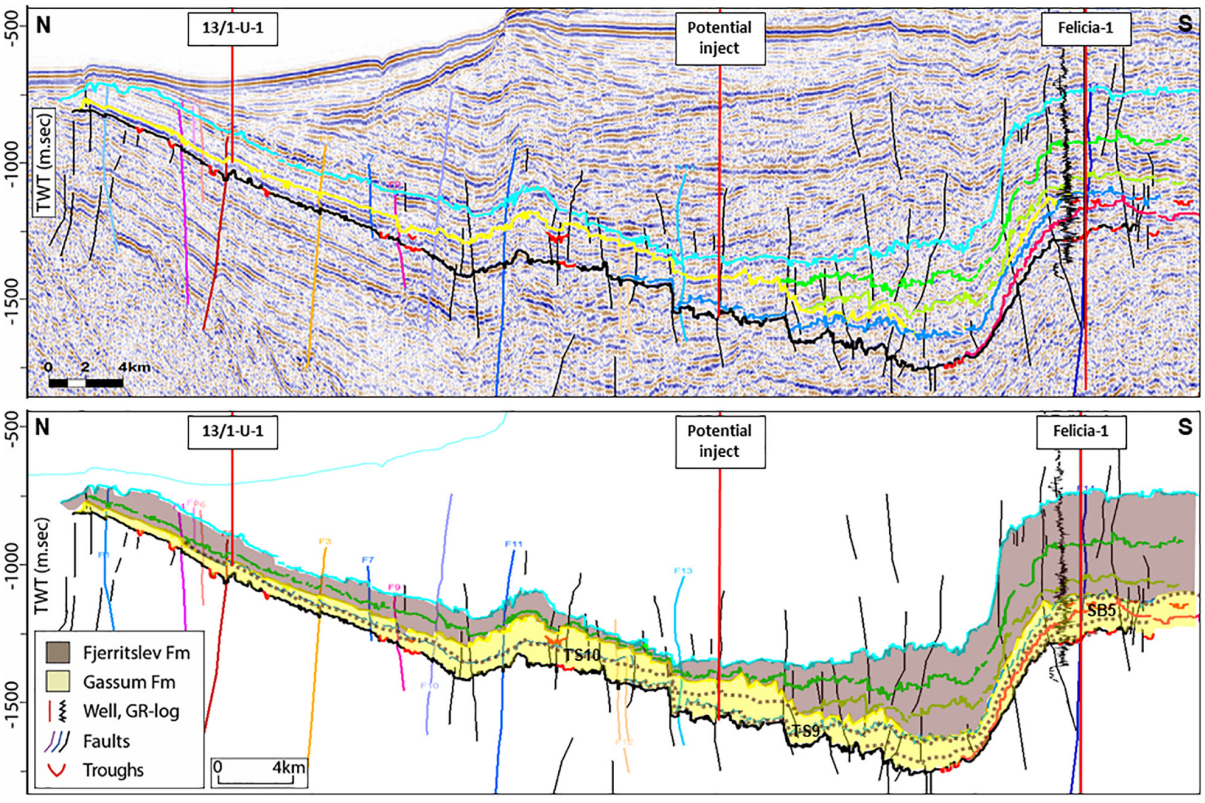


FIGURE 2 | Seismic profile from the Skagerrak showing that the Gassum Formation is sloping updip toward the north. The subtle troughs are possible channel structures. The 13/1-U-1 well and the potential injection site are projected (see **Figure 1**). The sequence boundary (SB5) and transgressive surfaces (TS9 and TS10) are interpreted in relation to the sequence stratigraphy by Nielsen (2003). The black faults are interpreted on this seismic profile only, whereas the colored faults tie between more seismic profiles. The northward onlapping internal seismic reflectors indicate that the lower part of the formation gradually disappears toward the basin margin.

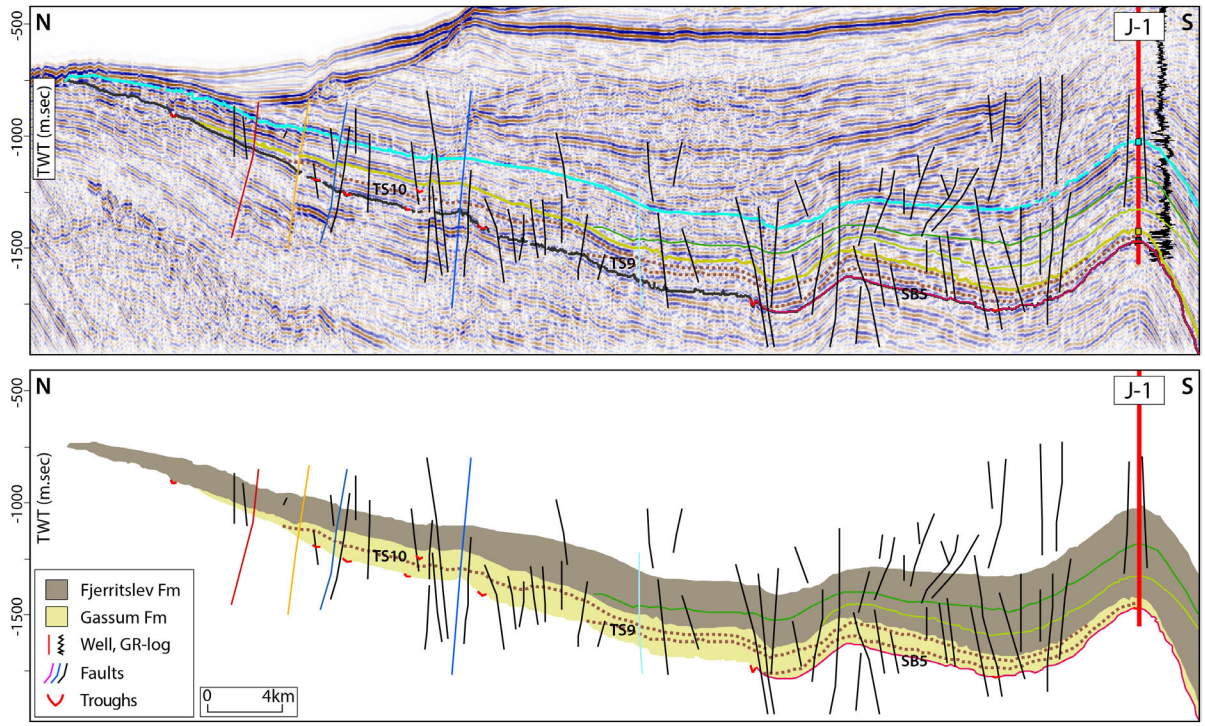


FIGURE 3 | Seismic profile from the Skagerrak located in the eastern part of the study area. The J-1 well is projected a short distance onto the profile (see **Figure 1**). See caption of **Figure 2** for further explanation.

were deposited during the early Jurassic while the deposition of sand moved northwards and the Gassum Formation was finally transgressed during the Early Sinemurian (Bertelsen, 1978, 1980; Michelsen, 1978; Hamberg and Nielsen, 2000; Nielsen, 2003; Lindström et al., 2009).

A Fennoscandian provenance of the Gassum Formation has been assumed based on the facies distribution in the basin (Bertelsen, 1980). The Fennoscandian Shield consists of an array of basement terranes formed at different times, which makes detrital zircon geochronology a powerful tool for interpreting the source areas of the sedimentary successions in the basin (Olivarius et al., 2014, 2017; Olivarius and Nielsen, 2016). The Paleozoic sediment cover in southwestern Sweden was removed during a middle Triassic uplift event and pronounced exhumation of southern Norway occurred during the Triassic where a succession of several kilometers thickness was eroded off (Rohrman et al., 1995; Japsen et al., 2016). Some Paleozoic sediments on the shield have been preserved such as in the Oslo Rift, but this is strictly local and it can be assumed that sediments constituted only a minor part of the exposed rocks of the Fennoscandian Shield during the Late Triassic.

The shield area positioned closest to the Skagerrak comprises the Sveconorwegian Orogen in southern Norway and Sweden, which consists of the Telemarkia Terrane, the Idefjorden Terrane and the Eastern Segment that formed at 1.52–1.48 Ga, 1.66–1.52 Ga, and 1.80–1.64 Ga, respectively (Bingen and Solli, 2009). Intrusions formed at 1.47–0.91 Ga and metamorphism occurred at 1.14–0.90 Ga in the Sveconorwegian belt and most pronouncedly in the Telemarkia Terrane (Bingen et al., 2008). The Idefjorden Terrane consists mostly of calc-alkaline plutonic and volcanic rocks and the Telemarkia Terrane is also primarily composed of plutonics and volcanics, where calc-alkaline signatures often are found in the felsic plutonic rocks (Brewer et al., 1998; Bingen et al., 2005). However, southeastern parts of the Telemarkia Terrane is a gneissic complex (Andersen et al., 2007). Clastic sediments formed in Pre-Sveconorwegian and early Sveconorwegian basins in both these terranes and they have mostly Sveconorwegian zircon ages, but also some older (Åhäll et al., 1998; Bingen and Solli, 2009). Magmatic zircon ages of 0.50–0.42 Ga are present in the Upper and Uppermost Allochthons in the Caledonian Orogen, whereas the Middle and Lower Allochthons have older ages of which most correspond to the basement windows in southern Norway of 1.69–1.62 Ga since these terranes are endemic to Fennoscandia (Bingen and Solli, 2009). Late Carboniferous to early Permian magmatism at 0.30–0.28 Ga caused extrusion of lavas in the Oslo Graben (Heeremans and Faleide, 2004).

MATERIALS AND METHODS

There are few wells and sparse core data available from the offshore parts of the Gassum Formation in the Skagerrak, especially from the Norwegian side. In the vicinity of the proposed storage area, only the well 13/1-U-1 was cored and

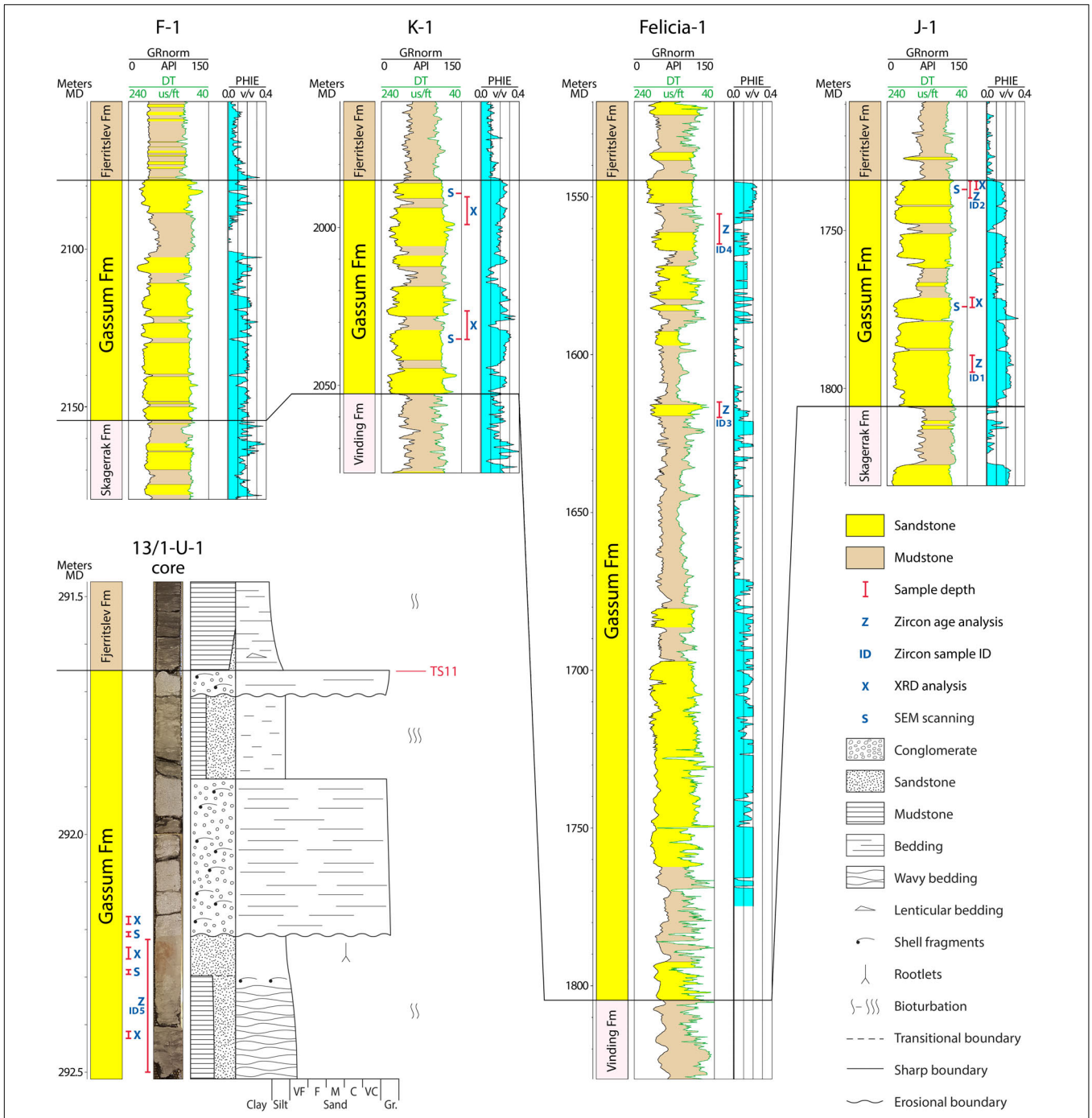


FIGURE 4 | Lithological columns of well-sections of the Gassum Formation with wireline logs and indicated sample depths. The lithostratigraphy is based on Nielsen and Japsen (1991). A sedimentological log of the cored section from the 13/1-U-1 well is shown alongside the core photos. Locations are shown in **Figure 1**. TS11 is a transgressive surface.

penetrates the top-most part of the Gassum Formation, as interpreted here (**Figures 2**, **4**). There is a continuous cored section through c. 170 m of the overlying Fjerritslev Formation and across the Gassum/Fjerritslev boundary. The nearest wells that have penetrated the Gassum Formation comprise the Felicia-1, J-1 and K-1 wells, from which only cuttings material and a few small sidewall cores are available. The reported depths are in meters below reference level (kelly bushing or rotary table).

Twelve samples were prepared as thin sections, including core from 13/1-U-1, cuttings from Felicia-1 and sidewall cores from J-1 and K-1. Seven samples were used for powder X-ray diffraction (XRD) analysis, including core from 13/1-U-1 and

cuttings from J-1 and K-1 (**Figure 4**). Five samples were selected for zircon age analysis comprising core from 13/1-U-1 and cuttings from Felicia-1 and J-1. The sample preparation requires up to 300 g of material to obtain a sufficient number of zircon grains, so a larger depth range was sampled than for the other types of analyses.

Polished thin sections were prepared with blue epoxy impregnation for easy porosity identification. The sidewall cores contained drilling mud with barite and mixed clays, and many grains in the samples were fractured during drilling, still, it was possible to characterize the rock texture. Grain-size distributions were obtained by measurements of minimum 100 grains. Grain size was determined according to the Wentworth scale (Wentworth, 1922) and sorting according to Folk (1966). Thin sections were studied by optical microscopy and scanning electron microscopy (SEM). Samples were carbon coated and examined at the University of Oslo SEM laboratory, using a Hitachi SU5000 FE-SEM (Schottky FEG) instrument including low-vacuum mode and in-lens SE-detector. Semi-quantification of mineralogy was performed as elemental analysis where the coloration is produced by mixing the colors of each element that is measured in each mineral.

The XRD analyses were performed on bulk samples of micronized sand and clay (Mc Crone mill) using a Bruker D8 Advance instrument applying CuKα radiation with Lynxeye detector and 90-position sample changer for high sample throughput. Bruker Eva software was used for phase identification (COD and PDF databases), and Profex BGMN for phase quantification applying Rietveld refinement. For core samples, the bulk mineral content estimated as weight percentage (wt.%) is representative contrary to sidewall core and cuttings samples where the clay, salt and sheet silicate contents are not representative due to contamination with drilling mud additives (e.g., gypsum, bentonite, barite). Thus, refinement results are normalized for the sand fraction as relative quartz/plagioclase (albite, oligoclase)/K-feldspar (intermediate microcline) contents.

Zircon U-Pb geochronological analyses were carried out at GEUS by laser ablation inductively coupled plasma mass spectrometry (LA-ICPMS), using a NWR 213 laser ablation instrument coupled to an Element2 magnetic sector-field ICPMS. The cuttings samples were first washed to remove drilling mud, then crushed and sieved to extract zircons from the 45–750 μm grain size fraction. The zircon grains were handpicked from heavy mineral concentrates obtained by density sorting using a Holman-Wilfley water-shaking table, and then embedded in epoxy, imaged by SEM at GEUS, and analyzed by LA-ICPMS. The zircons were ablated for 30 s in an air-tight helium-flushed chamber using a focused laser beam with a diameter of 25 μm, a repetition rate of 10 Hz and an output energy of ∼10 J/cm^2. The liberated material was transported through inert Tygon tubing by the helium carrier gas to the mass spectrometer for isotopic determination. To minimize instrumental drift, a standard-sample-standard analysis protocol was followed, bracketing the zircon analyses by measurement of the zircon standard GJ-1 (Jackson et al., 2004). For quality control, two secondary zircon standards were used, viz. Plešovice (Slama et al., 2008) and Harvard 91500 (Wiedenbeck et al., 1995, 2004), both yielding an average age accuracy and precision (2σ) within 3% deviation. Data reduction was performed using the Iolite software (Hellström et al., 2008; Paton et al., 2011; Petrus and Kamber, 2012). $^{207}Pb/^{206}Pb$ ages were used for zircons older than 700 million years (Ma), whereas $^{206}Pb/^{238}U$ ages were used for younger zircons, because the $^{206}Pb/^{238}U$ ages yield more robust ages and lower uncertainties (2σ) below 700 Ma. Common-lead correction was applied to a subset of the analyses when required, using measured mass 204 (i.e., $^{204}Hg + {}^{204}Pb$) corrected for Hg through the $^{202}Hg/^{204}Hg$ natural abundance ratio. Combined histogram and probability-density plots were produced through the software jAgeDisplay (Thomsen et al., 2016).

RESULTS

Sedimentology

In the Norwegian area, the Gassum Formation has only been drilled in the Farsund Basin by the 13/1-U-1 well, whereas the 13/1-U-2 and 13/2-U-2 wells did not reach the formation so no well logs exist from the northern part of the study area. The lowermost part of the 13/1-U-1 core is thus of great importance. Sedimentological investigation of the core with base at 292.52 m reveals that the lowermost 22 cm consists of heterolithic sand- and mudstone with wavy bedding and moderate bioturbation (**Figure 4**). Shell fragments occur near the top of the heterolith where there is a gradual transition to 9 cm of very fine-grained to silty sandstone displaying rootlets near the top. After an erosional boundary follows a 33 cm thick conglomerate with granule-sized clasts and abundant shell fragments. A sharp boundary marks the shift to the overlying 17 cm of sandstone-mudstone heterolith with abundant bioturbation, which is followed by an erosive boundary to the uppermost 5 cm of the formation that comprises a conglomerate with abundant shell fragments. The bivalve *Gryphaea Arcuata* (Lamarck) is identified in the core and is common in the Lower Sinemurian shallow-marginal marine deposits of southern Sweden (Troedsson, 1951). The lower c. 37 m of the overlying Fjerritslev Formation consists of an upward-coarsening para-sequence with beds of lenticular bedded silty mudstones, thin siltstones and very fine-grained sandstones that are moderate to intensely bioturbated. Based on the palynomorph assemblage, the succession is correlated to the Lower Sinemurian Bucklandi–Semicostatum zone (Smelror et al., 1989; Dybkjær, 2019, pers. comm.). A sharp boundary is present on top of this sequence after which a thick succession of stratified mudstones were deposited.

The combination of bioturbated, wavy bedded heteroliths, fine-grained sandstones with rootlets and conglomerates with shell debris suggest a vegetated paralic environment subjected to repeated flooding. The conglomerates with their erosive bases and high abundance of reworked shells are interpreted as lags formed during transgressive marine erosion. The boundary to the overlying deeper marine deposits is correlated to the transgressive surface TS 11, which occurs at the top of marine sandstones in parts of the basin and defines the top of the Gassum Formation

in more proximal located wells in the Fjerritslev Trough and on the Skagerrak-Kattegat Platform (Nielsen, 2003).

The seismic stratigraphic interpretation uses the sequence stratigraphic framework made by Nielsen (2003) for the Gassum Formation. The interpreted seismic lines in the study area are shown by their surface trace in **Figure 1**, and they tie to a regional grid that can be followed to the onshore part of the basin where more well data and cores exist. The internal seismic reflectors of the Gassum Formation in the study area include the regional mid-Rhaetian sequence boundary SB5 and the Hettangian transgressive surfaces TS9 and TS10. These surfaces show northward onlap, and the upper part of the Gassum Formation shows younging in the same direction (**Figures 2**, **3**) as also indicated by the Lower Sinemurian bivalves and palynomorphs found in the 13/1-U-1 core as described above, in contrast to the Hettangian age of the top of the Gassum Formation in J-1 identified by ostracods of the *O. aspinata* Zone (Michelsen, 1975). This conforms with the distal-proximal development seen elsewhere in the basin (Nielsen, 2003) and indicates that the lower part of the formation gradually pinches out toward the north and that the formation top is highly diachronous getting younger near the basin margin similar to what is observed in other parts of the basin (Nielsen, 2003; Weibel et al., 2017a). The identified seismic morphological troughs are possible channel systems (**Figure 5**), which suggest that fluvial deposits become more abundant toward the north in accordance with the overall sequence stratigraphic model. The interpretation focused on small U-shaped troughs, which were possibly not caused by faulting as seen by their position away from the faults, whereas apparent trough structures associated with faults have not been mapped since they may be caused by the faulting. The troughs occur where channels would be expected, which is along the base of sequence boundaries and para-sequences. A few of the troughs seem to coincide with the base of fluvial channels interpreted in Felicia-1 (**Figure 2**).

For the F-1, K-1, Felicia-1, and J-1 wells, the depositional environments have been interpreted based on well-log patterns, samples of cuttings and sidewall cores and palynological analyses since no conventional cores are available. The intercalated sandstone-mudstone succession in the upper part of the formation above SB5 has been interpreted as thin shoreface sandstones and marine mudstones formed in response to small sea-level fluctuations (**Figure 6**), which are also identified in other parts of the basin (Hamberg and Nielsen, 2000; Nielsen, 2003). The well-log pattern of a shoreface sandstone is typically sharp-based and blocky to funnel-shaped reflecting that it rests on a wave-scoured surface and consists of several thin sandstone units that may be almost amalgamated or separated by shoreface-offshore transition zone heteroliths. The thicker sandstone bodies near the base of the Gassum Formation in the F-1, Felicia-1, and J-1 wells display gamma-ray signatures that resemble estuarine sandstones as seen by their thick development and variable internal log pattern with bell- and funnel-shaped motifs due to the heterolithic component. The methodology for interpretation of facies associations from well-log patterns in the Gassum Formation is described in detail by Hamberg and Nielsen (2000) and Nielsen (2003), and the sequence stratigraphic surfaces are identified in accordance with Van Wagoner et al. (1990). The mid-Rhaetian sequence boundary SB5 occurring basin-wide in the Norwegian-Danish Basin typically cuts into marine mudstones. It is placed below estuarine deposits in F-1 and J-1 and it is traced to the base of thin shoreface deposits in K-1

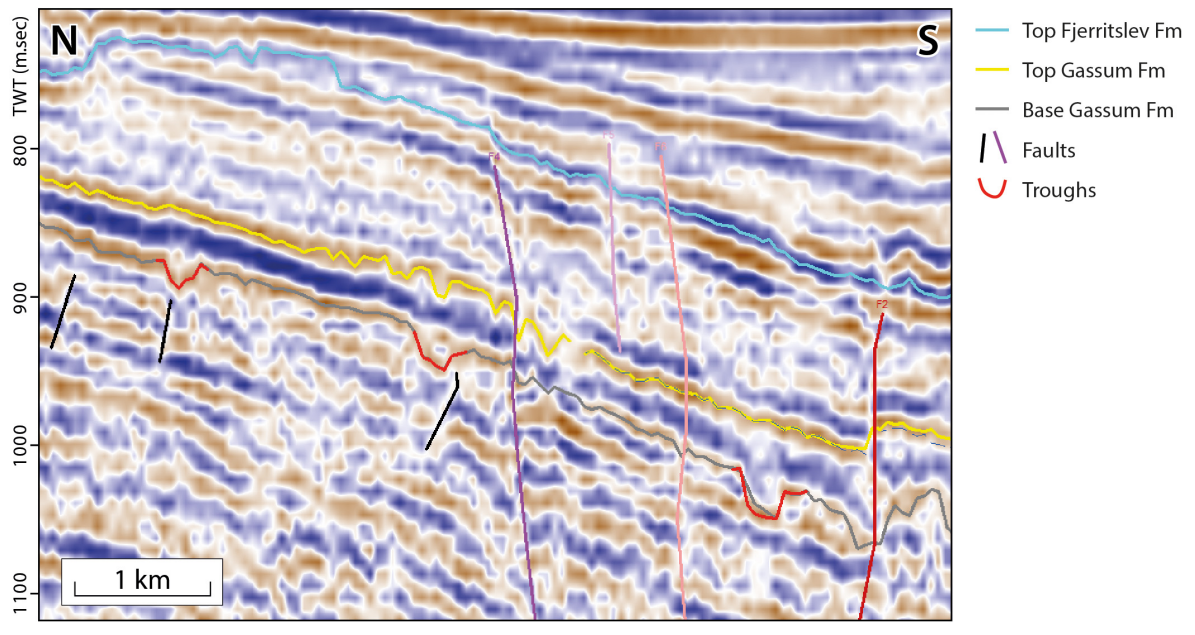


FIGURE 5 | Examples of seismic troughs, which are common in the study area and represent possible channel structures. The figure presents a close-up of the northern end of **Figure 2**.

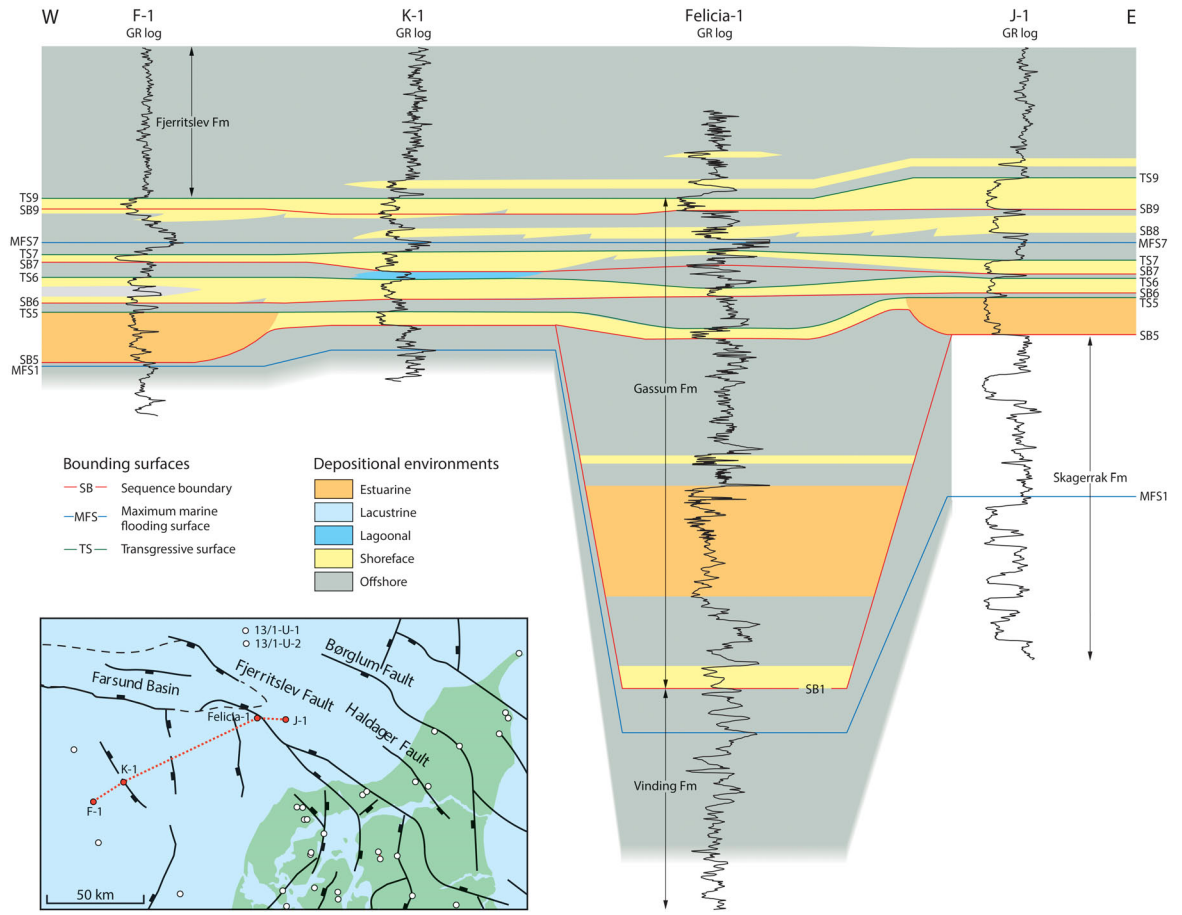


FIGURE 6 | Interpreted sequence stratigraphy and depositional environments of the Gassum Formation in the Skagerrak tied to the framework defined in wells onshore Denmark by Nielsen (2003). Oblique depositional dip section. The MWD-GR (measured while drilling – gamma ray) log is used for Felicia-1 since this is the most reliable because caving occurred during drilling.

and Felicia-1 (**Figure 6**). The overall pattern of the sequences of marine sandstones and mudstones overlying SB5 in the study area is backstepping in accordance with the general pattern in the basin with sequence boundaries marking the base of the sandstones and transgressive surfaces at their top. The latest Rhaetian basin-wide marine maximum flooding surface MFS7 is marked by claystones with extraordinarily high gamma-ray response (Nielsen, 2003).

The formation is much thicker in the Felicia-1 well compared to the three other wells in the area, which is interpreted as caused by deposition in the rim syncline of the closely located salt structure (Vejbæk and Britze, 1994). According to the seismic interpretation, the oldest part of the Gassum Formation below SB5 in the study area only occurs in the Felicia-1 area (**Figures 2**, **6**) since accommodation space was produced by the salt pillow forming to the southwest of the well, which caused the formation of a local basin. This lower part of the succession in Felicia-1 is not considered in this study since it is not present in the proposed injection area. In the 13/1-U-1 well, only the uppermost 86 cm of the Gassum Formation was penetrated, so the depositional facies in the deeper part are unknown, but fluvial deposits are likely to prevail in accordance with the general depositional pattern found in the basin (Nielsen, 2003) since the well is positioned more proximal to the Fennoscandian Shield than the other studied wells.

Based on these new findings, it was possible to construct a schematic north-south cross-section of the Gassum Formation from the Sorgenfrei-Tornquist Zone to the Norwegian-Danish Basin (**Figure 7**). The interpreted sequence-stratigraphic surfaces and depositional environments in J-1 are used as the southern end-point and the transgressive lag overlaying subaerial deposits in 13/1-U-1 comprises the northern end-point, where the proposed injection site is projected onto this schematic section (**Figures 4**, **6**). It is inferred that the predominance of shoreface sandstones in the central part of the basin is replaced by fluvial sandstones with fewer intercalated mudstones toward the basin margin. The marine mudstones are dominant toward the south, whereas lacustrine mudstones may be present between the fluvial sandstones to the north. The distal parts of the youngest shoreface sandstone layers in the study area passes laterally into time-equivalent marine mudstones that form part of the lower Fjerritslev Formation, which together with the

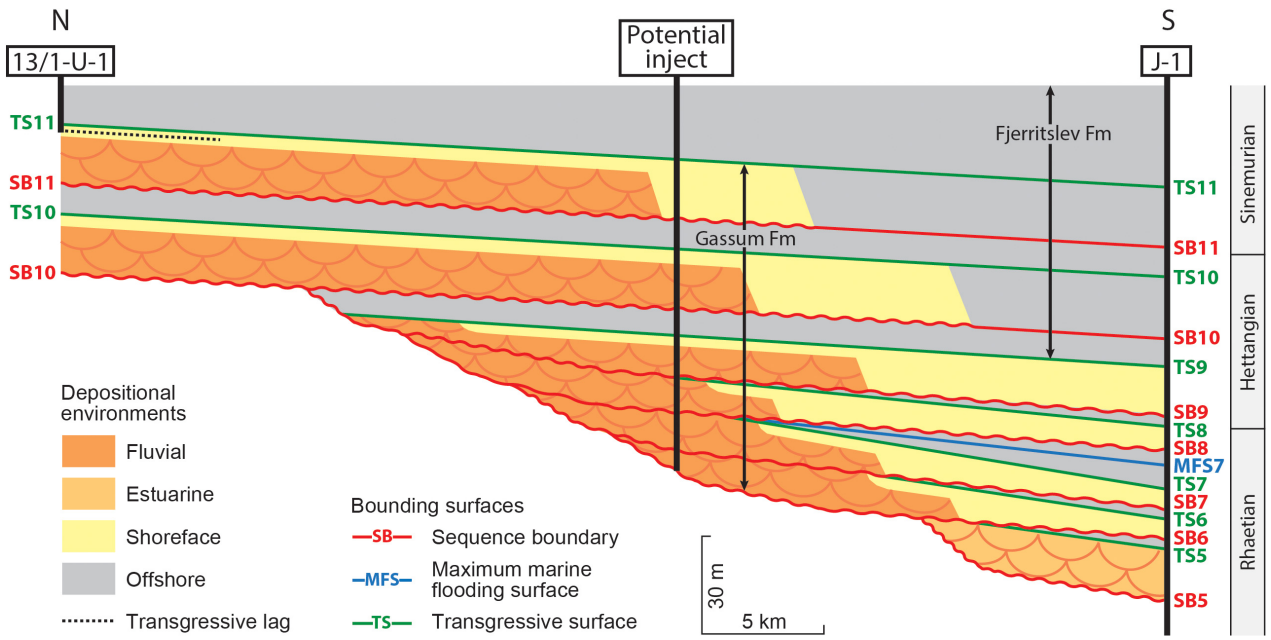


FIGURE 7 | Schematic north-south section from the Sorgenfrei-Tornquist Zone offshore Norway to the Norwegian-Danish Basin offshore Denmark. The sequence stratigraphic framework made by Nielsen (2003) is applied. The potential injection site is projected (see **Figure 1**).

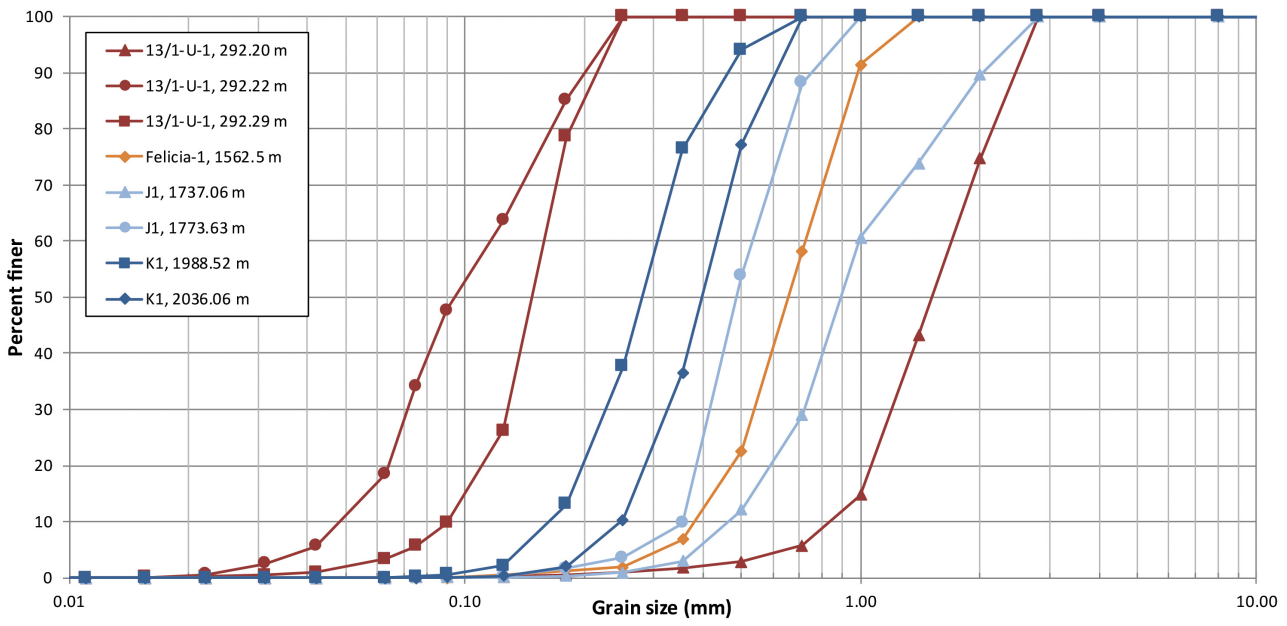


FIGURE 8 | Grain-size distributions of the Gassum Formation in the Skagerrak measured in thin sections.

northern onlap and pinch-out of the lower parts of the formation cause variations in the thickness of the Gassum Formation (**Figure 7**). These observations are in accordance with the consistent facies development that is documented in the onshore Danish area (Hamberg and Nielsen, 2000; Michelsen et al., 2003; Nielsen, 2003).

Petrography and Diagenesis

The studied sidewall core samples from the J-1 and K-1 wells and the cuttings sample from the Felicia-1 well represent a large spectrum of grain sizes ranging from fine- to very coarse-grained sandstones that are moderately to well sorted (**Figure 8**). Quartz is the dominant detrital component and feldspar consisting of

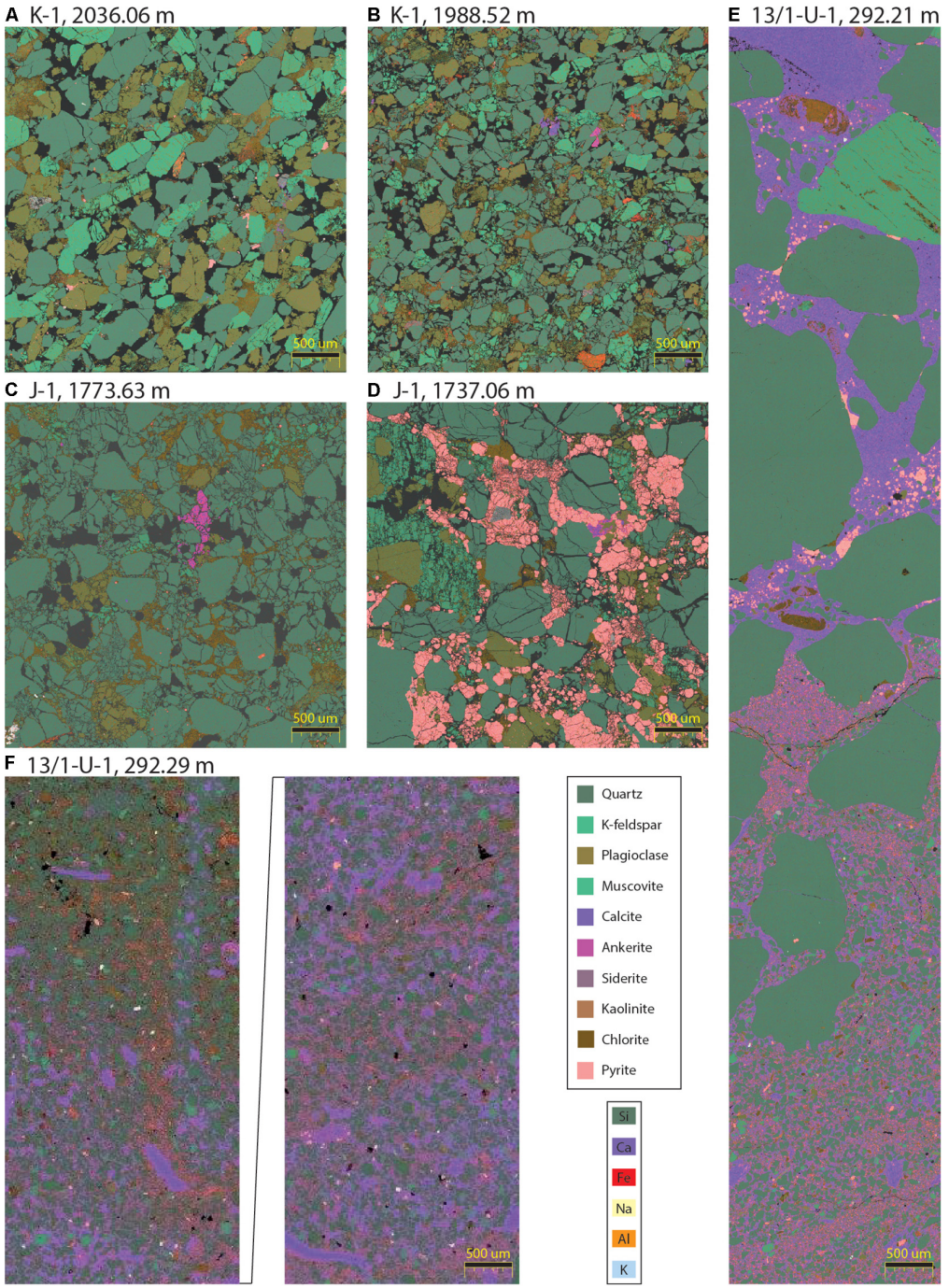


FIGURE 9 | Mineral semi-quantification by SEM element scanning. **(A–D)** Sandstones from sidewall cores from the K-1 and J-1 wells are dominated by quartz grains besides plagioclase/albite and K-feldspar grains, whereas authigenic phases occur in small amounts except for pyrite cement in D that may represent a local pyrite concretion. **(E)** The conglomerate in the 13/1-U-1 core contains clasts of quartz, feldspar, fossil fragments and chlorite ooids embedded in ankerite cement. **(F)** The lower sandstone in the 13/1-U-1 core is cemented by low-Fe calcite.

K-feldspar and plagioclase/albite is abundant in most samples (**Figure 9**). Quartz grains with undulatory extinction is a minor to common component, especially among the largest grains, and polycrystalline quartz grains occur. Mica minerals, heavy minerals and rock fragments are rare, except for the upper sample from J-1 in which rock fragments are common. Rare glauconite and organic matter are found in the samples from K-1. Most of the sandstones are porous (**Figures 9**, **10A**).

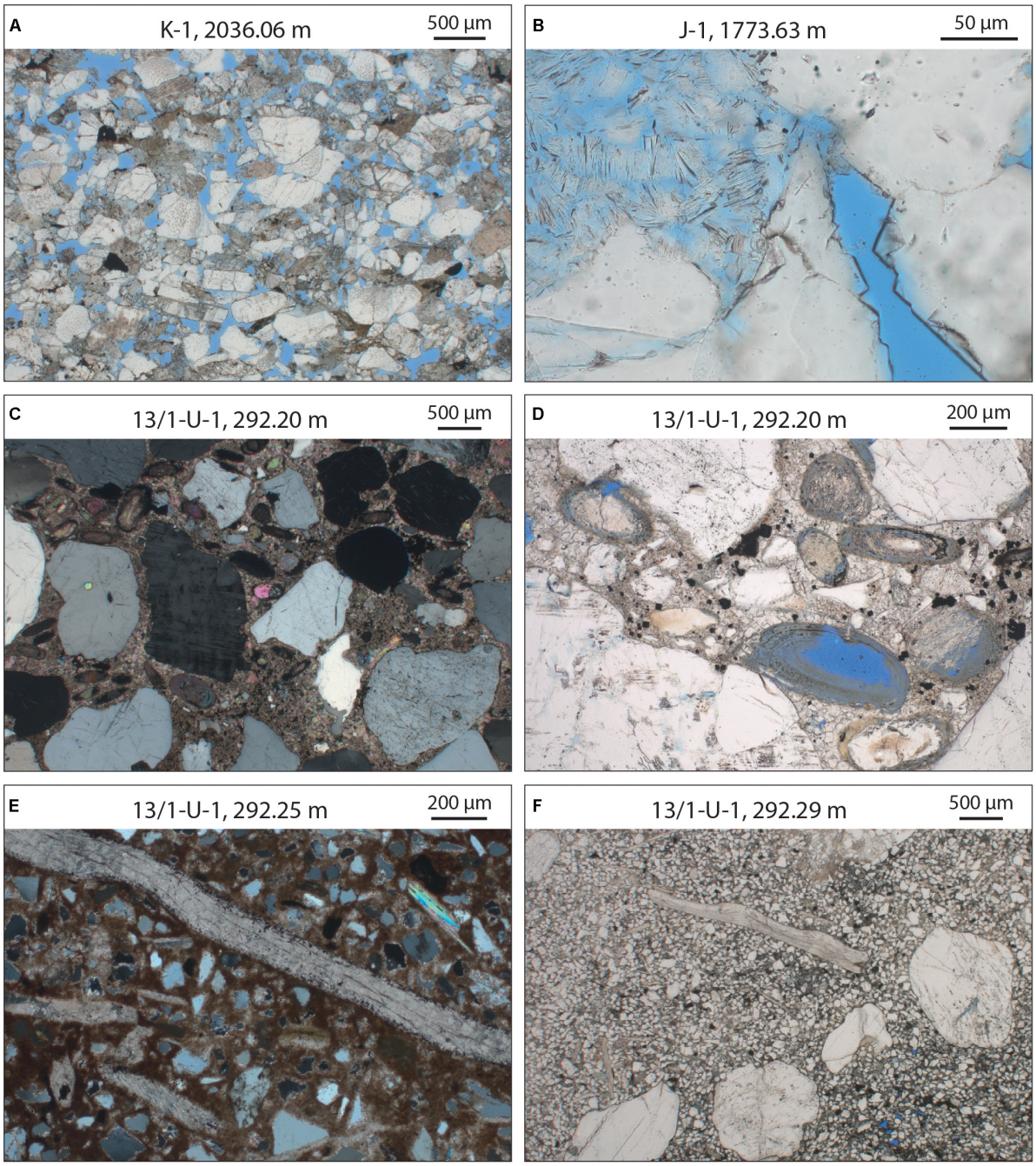


FIGURE 10 | Petrographic characteristics of the sampled sandstones. **(A)** Porous sandstone composed primarily of quartz and feldspar. **(B)** Thin quartz overgrowths enclosing kaolinite booklets. **(C)** Conglomerate with quartz and feldspar grains and chlorite ooids embedded in ankerite cement (crossed nicols). **(D)** Close-up of chlorite ooids. **(E)** Sandstone below the conglomerate with common shell fragments and siderite-ankerite cement (crossed nicols). **(F)** The lower part of the sandstone contains large grains dispersed in fine-grained sandstone with siderite-calcite cementation.

Thin quartz overgrowths is a recurrent authigenic phase and kaolinitic pore-fill is rare to common (**Figure 10B**). Minor to rare chlorite is found in most samples, sometimes as a patchy grain coating, and minor to rare illite has formed in the lower sample from K-1. Anatase and pyrite are minor to rare phases, except from the upper sample from J-1 that contains abundant pyrite cement (**Figure 9D**). Minor to common ankerite cement has formed in confined areas in the lower sample from J-1, where it has partly replaced some of the quartz grains and especially plagioclase and K-feldspar grains. K-feldspar overgrowths and albitization of microcline and oligoclase are occasionally observed. Some feldspar dissolution has occurred

in all samples and kaolinite booklets have formed in some of the secondary pores. Concerning the timing, anatase and pore-filling pyrite formed after kaolinite precipitation and feldspar dissolution. Anatase, pyrite and kaolinite formed prior to quartz overgrowths. The ankerite cement precipitated after some of the quartz cement and the quartz growth continued afterward.

The conglomerate in the 13/1-U-1 core (**Figure 4**) is studied in detail at its base at 292.21 m, where it is poorly sorted and contains grains and fossil fragments with lengths up to 5 mm (**Figure 9E**). The detrital components comprise primarily quartz and feldspar grains that are mostly 1–2 mm long, of which the quartz grains display rounded quartz overgrowths (**Figure 10C**). Many of the quartz grains have undulatory extinction, and plutonic rock fragments and polycrystalline quartz grains are present. The finer fraction contains also quartz and feldspar besides rare ilmenite, zircon, and abundant chlorite ooids that are 100–700 μm long. The ooids consist of a number of chamosite layers around nuclei of mica, quartz or feldspar that in most cases have been partly or fully replaced by ankerite (**Figure 10D**). The ooids were compacted prior to the pervasive ankerite cementation. The ankerite cement is sparry and has replaced fossil fragments and partly some detrital grains. Euhedral pyrite crystals are in some places abundant within the ankerite cement and tiny siderite rhombs and apatite crystals occur locally. Grain-coating chlorite occurs in some places and is thicker in embayments. Kaolinite has locally replaced grains, and secondary porosity has formed by partial dissolution of feldspar and the nuclei of ooids.

Quartz is the dominant detrital phase and feldspar is common in the moderately sorted, very fine-grained sandstone right beneath the erosional base of the conglomerate (**Figures 4**, **8**). Muscovite, chlorite and ilmenite grains and organic matter occur in minor amounts, whereas glauconite is minor to rare and zircon is rare. Shell fragments are common and up to 1 mm long and consists of low-Fe calcite (**Figure 10E**). Abundant siderite rhombs are dispersed in the pervasive ankerite cement, which has also formed within some of the dissolved nuclei of the rhombs. Tiny fragments of especially kaolinite, muscovite and quartz are present within the cement. Irregular chlorite coatings are found in some places and are thickest in embayments. Thin quartz overgrowths and albitization of K-feldspar is found locally. Further down, the sandstone becomes fine-grained and moderately well to well sorted (**Figure 8**), without considering the over-sized clasts of quartz and feldspar that are up to 2 mm long (**Figure 10F**). These large quartz grains have rounded overgrowths and some have undulatory extinction. Fossil fragments are common and consist of variating calcite and Fe-calcite. At 292.29 m, the pore-filling cement consists of low-Fe calcite (**Figure 9F**) with abundant siderite rhombs, framboidal pyrite and kaolinitic-illitic clay. Degraded biotite occurs in minor amounts and Fe-rich chlorite coatings occur locally. The heterolith at the base of the 13/1-U-1 core has a detrital composition that is comparable to the sandstone above but without carbonate cementation. Shell fragments are much less abundant and oversized clasts are not present. Some of the quartz grains have undulatory extinction.

TABLE 1 | Reservoir properties of the Gassum Formation based on well-log analysis.

Well	F-1	K-1	Felicia-1	J-1
Gross thickness	76 m	67 m	260 m	72 m
Net sandstone thickness	51 m	46 m	118 m	56 m
Net/Gross ratio	0.67	0.69	0.45	0.78
Porosity of sandstone	17–23%	20–28%	15–25%	18–25%

Reservoir Properties

The reservoir properties are estimated by well-log analysis where a porosity cutoff of 15% is used to define the sandstone intervals. For the F-1, K-1, and J-1 wells, the reservoir properties are comparable with a net sandstone thickness of 46–56 m, a net/gross ratio of 0.67–0.78 and a porosity range of 17–28% (**Table 1**). The much thicker succession encountered in the Felicia-1 well constitutes a special case with its net sandstone thickness of 118 m, net/gross ratio of 0.45 and porosity range of 15–25%. However, much caving occurred when the well was drilled, so the estimated reservoir properties of Felicia-1 may be subject to greater uncertainty than for the other wells. The available sidewall cores were not large enough for core analysis and the sandstones have become too crushed and deformed during drilling and sampling of the sidewall cores to make a reliable petrographic quantification of porosity.

Zircon Geochronology

The zircon age results are illustrated in **Figure 11** and the full dataset can be found in the online **Supplementary Table S1**. The zircon age distributions of the analyzed sandstones show that the sediment is derived from the Fennoscandian Shield where rocks with corresponding zircon ages are present, but some of their derived sediments may have been reworked prior to the deposition in the Skagerrak. Marked differences occur between some of the samples, showing that sediments were distributed differently in the basin during each of the depositional events. The zircon ages from the Gassum Formation are compared with published ages from the Fennoscandian Shield compiled by Bingen and Solli (2009).

The zircon age distribution of the lower sample from the J-1 well (Sample ID 1) has a broad age span with several age populations and associated prominent age peaks. The peak at 1.64 Ga corresponds to rocks included in the Caledonian Orogen domain and basement windows of central southern Norway, and the 1.49–1.48 Ga peak coincides with the formation of the Telemarkia Terrane in southernmost Norway. The younger Mesoproterozoic age peaks correspond to the magmatic and metamorphic ages associated with the Sveconorwegian Orogeny, which are far more abundant in the Telemarkia Terrane than in the Idefjorden Terrane and the Eastern Segment. Some of the zircons in the sample record ages that match the formation ages of the Idefjorden Terrane and the Eastern Segment. This is the only sample that contains zircon grains that record the Svecofennian Orogen/Transscandinavian Igneous Belt and the Oslo Graben areas, although these grains are few. Furthermore,

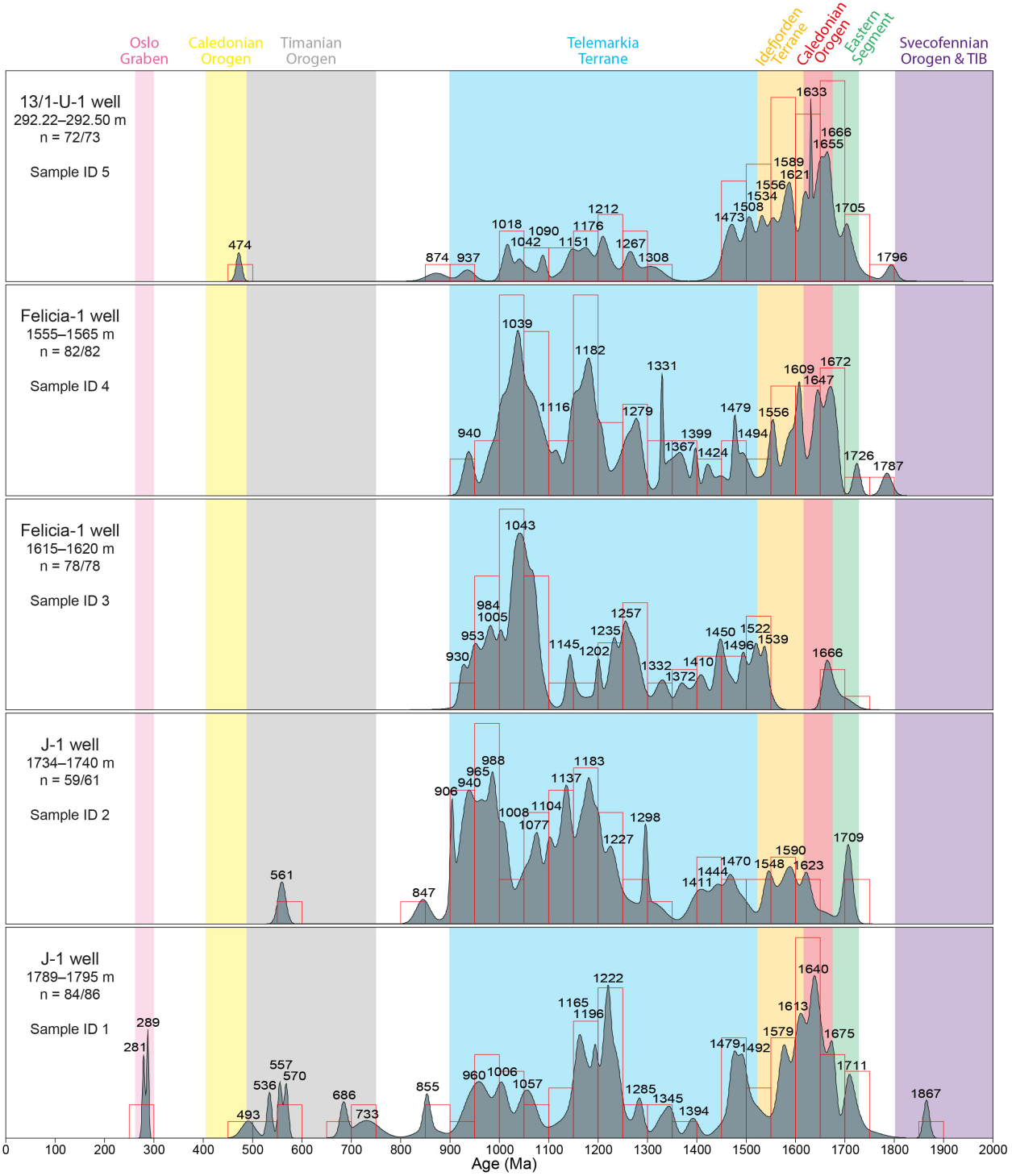


FIGURE 11 | U-Pb ages of zircon grains from the Gassum Formation in the Skagerrak plotted as probability density distributions and histograms. The number of employed concordant ages (discordance < 10%) out of the total number of measured ages is given by "n." See **Figure 4** for sampling positions in the wells and **Figure 12** for location of the wells and basement terranes.

this is the only sample with zircon ages that coincide with the age of the Timanian Orogen (c. 0.75–0.49 Ga) occurring far to the northeast. This orogen was eroded during the Cambrian-Ordovician and some of the produced detritus was deposited in southern Norway where it is outcropping in some areas (Slama, 2016).

The provenance of the three shoreface sandstones (Sample ID 2–4) is comparable and the zircon age distributions show that a large majority of the sediment is supplied from the Telemarkia Terrane in southernmost Norway, from which the Sveconorwegian ages are especially abundant in the samples. Some of the zircon ages also correspond to the Idefjorden Terrane, the Eastern Segment and the Caledonian Orogen domain including inherited ages and basement windows. Such zircons occur in small amounts in these sandstones and are most abundant in the upper sample from the Felicia-1 well (Sample ID 4). A single zircon grain with an age that matches the Timanian Orogen is found in the upper samples from the J-1 well (Sample ID 2).

The zircon age distribution of the sample from the 13/1-U-1 well (Sample ID 5) has its three most prominent age peaks at 1.67–1.63 Ga corresponding to ages in the middle and lower Caledonian allochthons and in basement windows in the Caledonian Orogen domain. Ages comparable to the Idefjorden Terrane and the Telemarkia Terrane are also common in the sample. This is the only sample where a zircon grain with age matching the timing of the Caledonian Orogen is found (0.47 Ga).

DISCUSSION

Provenance Signals

The interpreted source areas based on zircon ages from the Gassum Formation are shown in three scenarios in **Figure 12**. The lowstand scenario is based on the estuarine sandstone from J-1, whereas the highstand scenario merges the three shoreface sandstones from J-1 and Felicia-1 since they are of comparable provenance, and the transgressive scenario is based on the sandstone sample from 13/1-U-1. The thickness of the arrows indicates relative amounts of sediment supplied from each area. However, uncertainties are associated with this estimate, such as the variations in zircon fertility in the source areas and the hydraulic sorting occurring during transport (e.g., Malusà et al., 2016). Furthermore, the possibilities of reworking of older sediments and contamination of cuttings samples must be considered.

In the underlying Lower to Upper Triassic Skagerrak Formation, input from reworked Paleozoic sediments is observed in the Lower Triassic part of the formation where Caledonian zircon grains indicate a supply of reworked Silurian–Devonian sediments whereas this is not found in the upper part of the formation (Olivarius and Nielsen, 2016). This means that the deep erosion that occurred in southern Norway and southwestern Sweden during the Triassic has probably removed the majority of the Paleozoic sediment cover prior to the deposition of the Gassum Formation (Rohrman et al., 1995; Japsen et al., 2016).

The possibility of contamination of the cuttings samples from Felicia-1 and J-1 by cavings from younger deposits must be considered. For Felicia-1, it is known that caving occurred during drilling, whereas the caliper log from J-1 indicates a minimal amount of caving. The overlying Fjerritslev Formation is thickly developed in these areas (**Figures 2**, **3**) and presumably too fine-grained to contain zircons of sufficient size for U-Pb analysis, so cavings from this formation may not induce bias to the analyzed zircon age distributions. This assumption is based on knowledge of the Fjerritslev Formation, which consists mostly of claystone and contains siltstone laminae in some intervals besides few very fine-grained sandstones (Schmidt, 1985; Michelsen et al., 2003). The smallest zircon grains of less than 45 μm were sieved out of the samples prior to the U-Pb analyses so part of the possible silt-sized contamination would have been removed by this method. The possibly remaining contamination with coarse silt and very fine sand is assumed not to contain zircons since the settling equivalence that exists between light and heavy mineral grains means that the zircon grains in a sediment are smaller than the quartz grains (Garzanti et al., 2008). Furthermore, most of the zircons that have been extracted from the sediments are sand-sized (**Supplementary Figure S1**). The consistent provenance signal found in the zircon grains from the three shoreface sandstones is significantly different from the estuarine provenance signal from the fourth cuttings sample, which also indicates that cuttings contamination has not caused a significant artificial modification of the provenance signal. The most coarse-grained intervals of the Fjerritslev Formation have been deposited at the lower shoreface and therefore presumably have quite similar provenance signature as the shoreface sandstones in the upper part of the Gassum Formation, meaning that a zircon contamination would probably not even have changed the provenance signal much.

The provenance area of the estuarine sandstone (Sample ID 1) is rather large since the zircon grains originate from both southernmost Norway, central southern Norway and southwestern Sweden (**Figures 11**, **12**). This is the only sample with zircon ages matching the Svecofennian Orogen, the Timanian Orogen and the Oslo Graben, which shows that the source area is larger for this sample than for the remaining samples. The results indicate that the closer positioned sediment source areas supplied more sediment than the more distant source areas. This may be inferred from the larger amount of zircon ages matching the Telemarkia Terrane than the more northern Caledonian Orogen and from the progressively lower amount of zircon ages that correspond to the Idefjorden Terrane, the Eastern Segment and the Svecofennian Orogen, respectively. This may be because these three terranes are located progressively further away toward the northeast. Only a few ages coincide with the age of the Oslo Graben, which is probably because the zircon fertility is low in these extrusive rocks (Corfu et al., 2015). Timanian ages have not been encountered elsewhere in the Norwegian-Danish Basin (Olivarius and Nielsen, 2016), and such ages are rare in Fennoscandia since they correspond to the Timanian Orogen far to the northeast, which was eroded in Cambrian-Ordovician time where sediment was transported toward the southwest (Slama, 2016). These sediments are preserved locally in southern Norway, so it is likely that they have supplied detritus to proximal parts of the Gassum Formation in the study area. The reworking of such sediments would have increased the mineralogical maturity as observed for this sample.

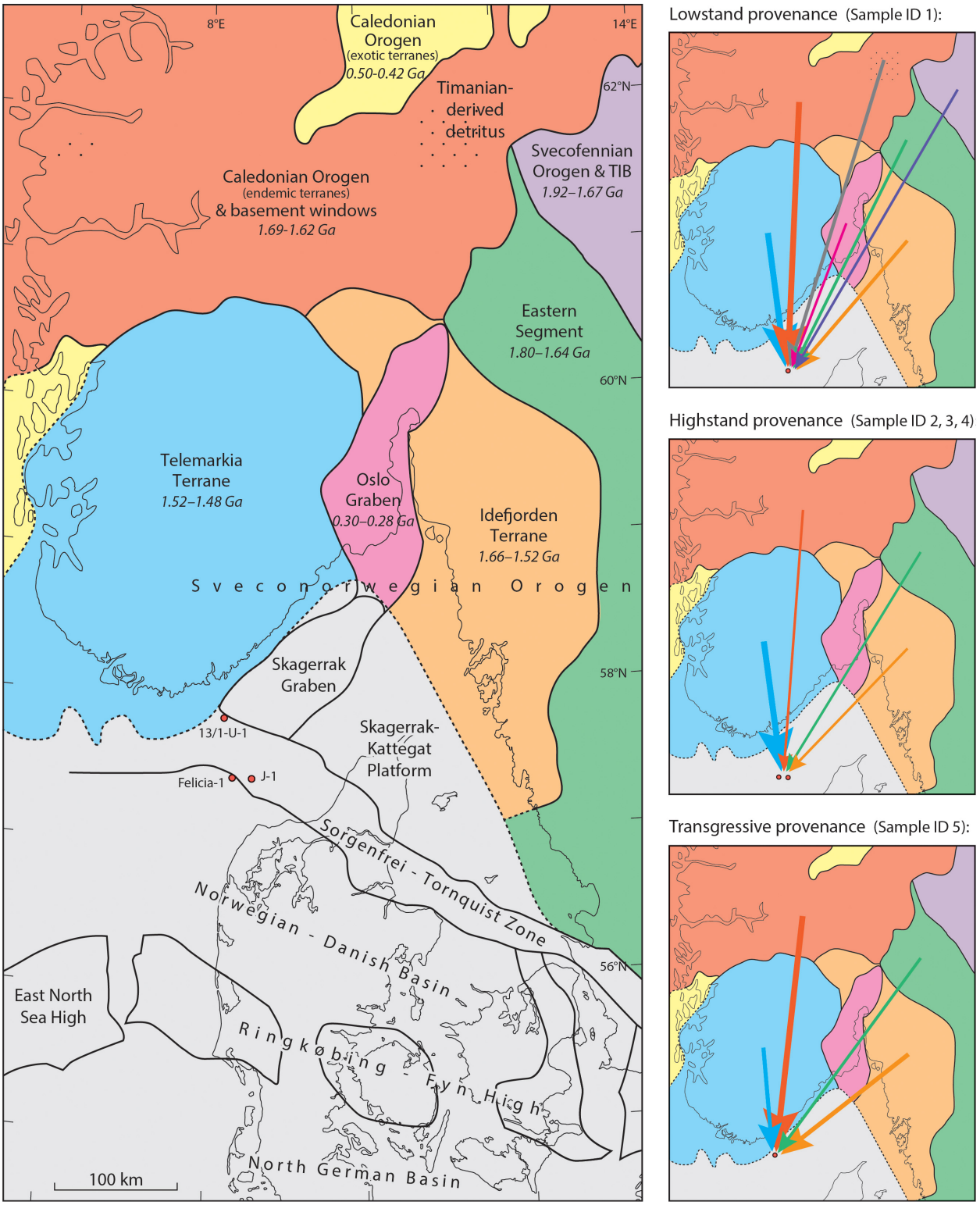


FIGURE 12 | Structural configuration of southern Scandinavia with the area of Triassic deposition shown in gray and indication of magmatic zircon ages of the major basement provinces in billion years (Ga). The map is based on Nielsen (2003), Heeremans and Faleide (2004), Lahtinen et al. (2008), Bingen and Solli (2009), Erlström and Sivhed (2012), Jarsve et al. (2014), and Slama (2016). The provenance interpretations are shown on the miniature maps where the thickness of the arrows is an indicator of the relative amount of sediment supplied from each terrane.

The prominent Telemarkian zircon age population found in all the shoreface sandstones (Sample ID 2–4) imply that the sediment was supplied almost exclusively from the southernmost Norway, which reveals a short transport distance from source to sink for most of the sediment. This is in accordance with the mineralogical immaturity of the sandstone in the sidewall core from the J-1 well at 1737.06 m, which corresponds to the upper zircon age sample from this well (Sample ID 2). Although the shoreface and transgressive samples (Sample ID 2–5) have quite similar age span, the relative proportion between the age populations is distinctly different, where the Telemarkian ages dominate the shoreface sandstones (Sample ID 2–4) and Caledonian and Idefjorden ages are dominant in the transgressive sandstone (Sample ID 5).

It is not surprising that young zircon ages corresponding to the timing of the Caledonian Orogeny are almost absent in the samples since only a limited amount of zircons was formed during this event. However, the inherited Paleoproterozoic zircon ages in the Caledonian Orogen are abundant in the estuarine and transgressive samples (Sample ID 1 and 5) indicating that favorable conditions for supplying sediment from central southern Norway to this part of the basin were present in these depositional environments. In the transgressive lag, reworking of the mineralogically immature sediments is a likely source of some of the deposited sediment as indicated by the content of coarse-grained quartz and feldspar grains in a very fine-grained matrix, and the quartz grains have rounded quartz overgrowths indicative of reworking of previous sandstones.

Temperature Indicators

The petrographic observations and reservoir properties extracted from the limited amount of samples and well logs that are available from the study area are in accordance with the detailed knowledge obtained for the Gassum Formation in the onshore Danish area (Kristensen et al., 2016; Weibel et al., 2017a,b). The new results are considered valid, but they represent individual examples of the reservoir and do not express the full variation that occur within the formation. Therefore, the average reservoir data from the onshore part of the formation are given in **Figure 13** to show the general characteristics of the depositional environments at different burial depths, and these results are assumed to concur with the sediment in the study area, except for the differences related to decreasing sediment maturity when approaching the source areas.

The petrographic relationships in the study area indicate that kaolinite has precipitated early during burial, which is in accordance with interaction with flowing meteoric water for its formation, and it sets limits on the maximum burial temperature since kaolinite is unstable at temperatures above c. 130°C when K-feldspar is present (Bjørlykke et al., 1986; Bjørlykke, 1998). Siderite normally precipitates early during burial (Morad, 1990; Hervig et al., 1995; Weibel et al., 2017b) and the presence of siderite means that the sandstones presumably not have been buried deeper than c. 3 km (c. 100°C). This is evident by the decreasing amount of siderite in the Gassum Formation onshore Denmark with increasing depth and its disappearance at a maximum burial depth of c. 3 km (Weibel et al., 2017b).

The thin macroquartz overgrowths signify that the sandstones were subjected to temperatures of c. 80–100°C since the onset of macroquartz formation normally occurs in this range, whereas it becomes extensive at higher temperatures (Bjørlykke et al., 2009; Weibel et al., 2010). The petrographic relationship between quartz overgrowths and ankerite cement shows that ankerite began precipitating after quartz, which is also observed in the Gassum Formation onshore Denmark (**Figure 13**), where it corresponds to a maximum burial depth of at least c. 2 km (c. 70°C). This is in accordance with other studies showing that the formation of ankerite normally requires temperatures of at least 75–80°C (Fisher and Land, 1986; Burley et al., 1989). The incipient albitization of some of the K-feldspar grains indicates that the sandstones have been exposed to temperatures of at least c. 65°C and not above c. 130°C where the albitization process would be almost complete (Bjørlykke et al., 1986; Saigal et al., 1988; Aagaard et al., 1990).

In conclusion, the diagenetic alterations observed in the sandstones give a consistent picture of the burial history and show that the Gassum Formation in the Skagerrak was subjected to maximum burial temperatures of c. 80–100°C corresponding to maximum burial depths of c. 2.3–3.0 km prior to structural inversion. This is in accordance with the thickness of the succession removed by Cenozoic exhumation that has been estimated by basin modeling based on sonic data to be 800 m for the Felicia-1 and J-1 wells and 600 m for the K-1 well (Japsen and Bidstrup, 1999; Japsen et al., 2007; Baig et al., 2019).

Reservoir Quality

The lack of core material makes it impossible to directly measure the porosity and permeability of the sandstones in the proposed injection area. However, the observed diagenetic development corresponding to maximum burial depths of c. 2.3–3.0 km can be used to compare the studied sandstones in nearby wells in the Skagerrak with their onshore equivalents where the Gassum Formation has been studied in detail based on core material from Danish wells. The results show that sandstones having been buried to this depth interval have average porosities of 22–32% and average gas permeabilities of 112–2757 mD, depending on their depositional environment (**Figure 13**). This porosity interval is higher than the porosities of 15-25% interpreted from Felicia-1 and J-1 well-logs (**Table 1**). However, both approaches give porosities that are sufficiently high for CO_2 injection. According to the applied sequence stratigraphic model, supported by the detailed seismic interpretation, the formation contains progressively more fluvial sandstones and less shoreface sandstones northwards across the Skagerrak (**Figure 7**). According to observations from the onshore facies, this would result in higher permeability due to both larger grain size and less cementation (Kristensen et al., 2016; Weibel et al., 2017a). This is in accordance with the medium to very coarse grain-size of the sandstones encountered in

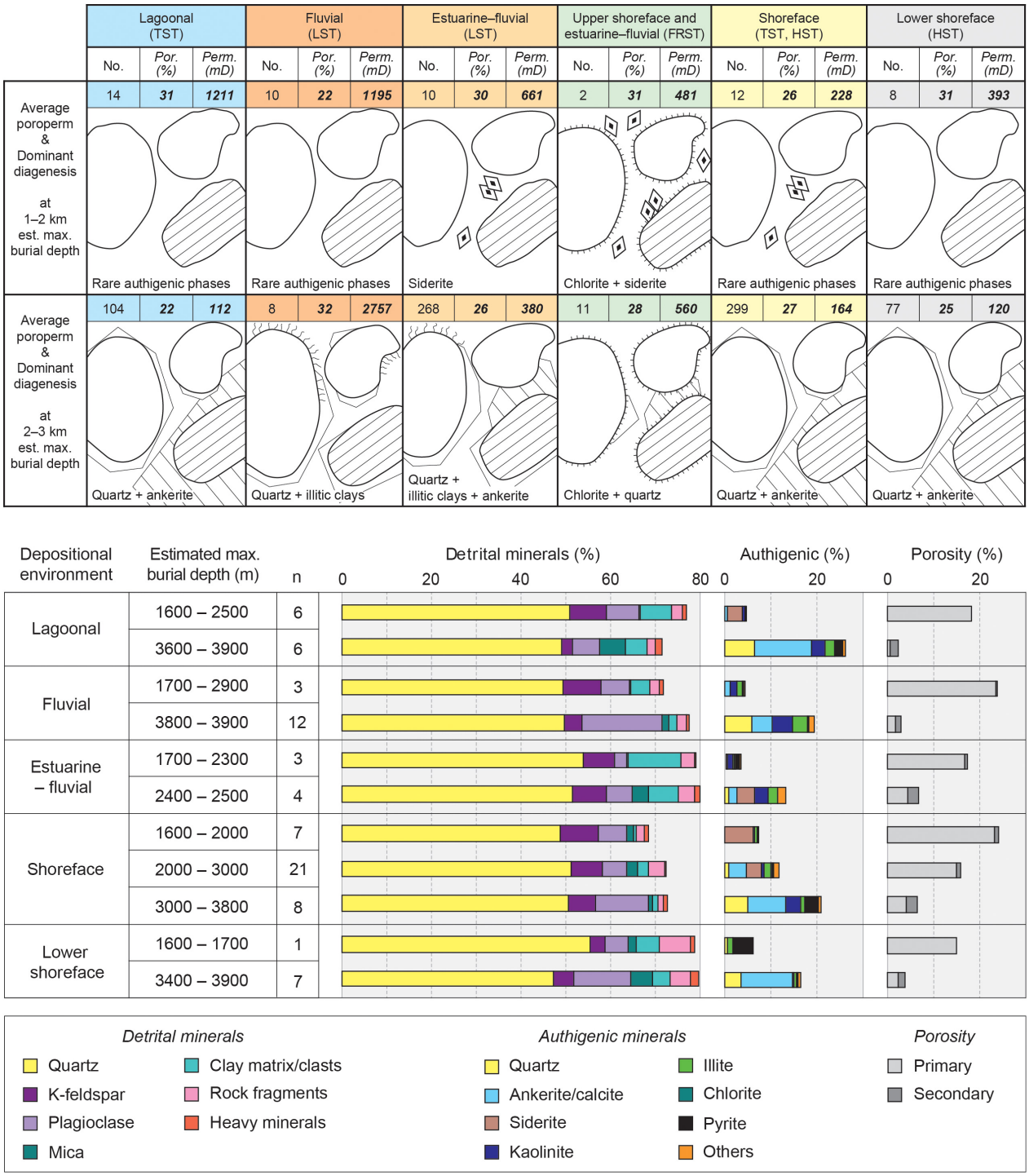


FIGURE 13 | Overview of the typical diagenetic alterations occurring in the different depositional environments and the resulting average porosity and permeability for estimated maximum burial depths of sandstones from the Gassum Formation onshore Denmark. The mineralogy is quantified by petrographic point counting. Modified from Weibel et al. (2017a). TST, transgressive systems tract; LST, lowstand systems tract; FRST, forced regressive systems tract; HST, highstand systems tract.

Felicia-1 and J-1 (**Figure 8**), whereas fine-grained sandstones are most abundant onshore Denmark followed by medium-grained sandstones while coarse-grained sandstones are rare (Weibel et al., 2017a). It is thus assumed that the net/gross ratio increases northwards due to deposition of less marine mud and more local sand, so all points toward that the

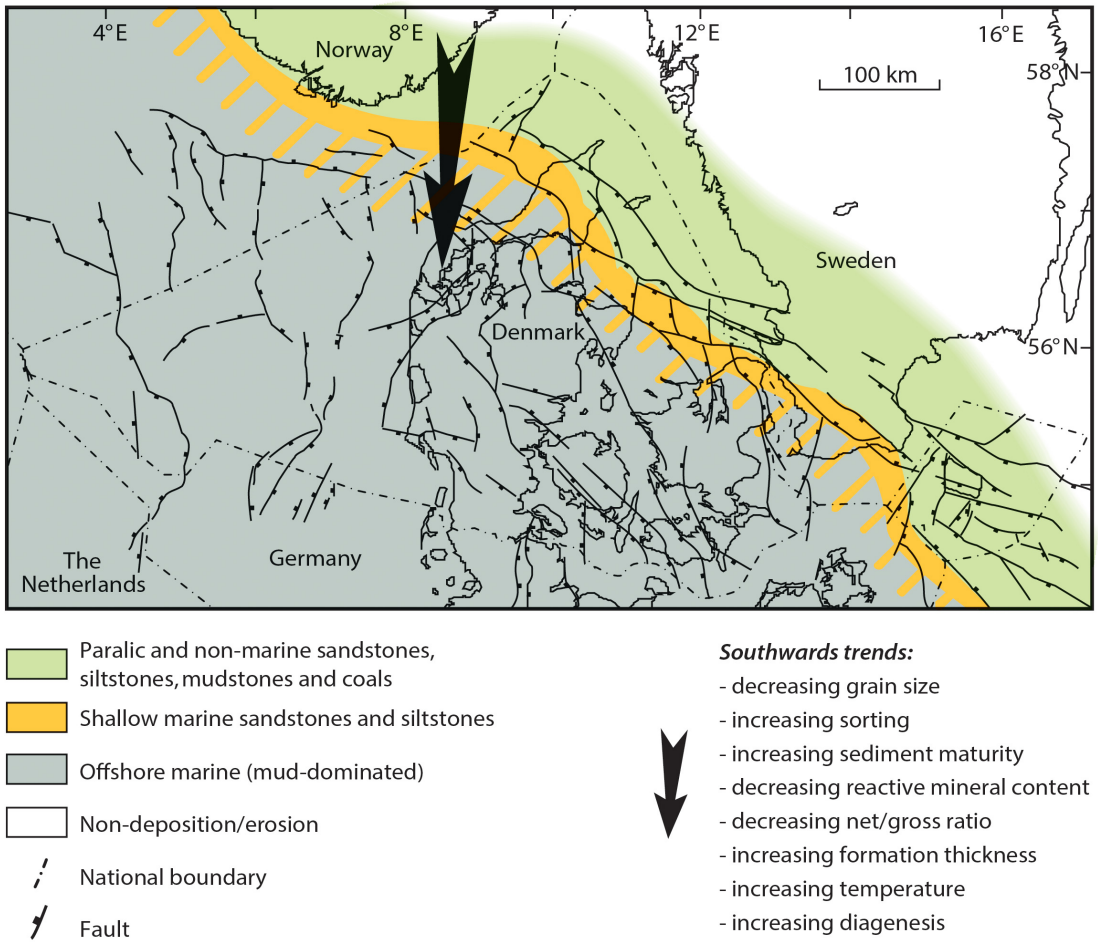


FIGURE 14 | Hettangian paleogeography from Michelsen et al. (2003) corresponding to the time when the upper part of the Gassum Formation was deposited. The facies belts shifted back and forth corresponding to repeated sea-level changes. The observed directional trends that influence the reservoir quality in the study area are listed.

storage volume within the formation increases in a northerly direction. However, the seismic interpretation shows that the total thickness of the formation decreases in the northernmost part of the study area (**Figures 2**, **3**). All these directional trends that affect the reservoir quality are summarized in **Figure 14** based on the results of this study compared to the findings of Weibel et al. (2017a,b). Comparable reactivity-related maturity trends of time-equivalent sediments deposited along the rim of the Fennoscandian Shield in the North Sea and Norwegian Sea may be assumed.

The sediments were only subjected to initial mesogenesis and a limited residence time at maximum burial before the Neogene inversion. Thus, the quartz overgrowths are thin and only minor amounts of authigenic clays were formed. The reservoir quality is therefore expected to be good in the Gassum Formation in the Skagerrak. Locally, pore-filling carbonate-cemented intervals occur in the onshore part of the formation, but they are mostly thin and associated with shell layers (Weibel et al., 2017a). The cemented interval observed in the 13/1-U-1 well is caused by abundant shell fragments, which are a result of the deposition as a transgressive lag. Observations from the more southern and eastern part of the formation show that pore-filling carbonate is most abundant in intervals of the shoreface and lagoonal depositional environments, but it also occurs in fluvial deposits (**Figure 13**; Weibel et al., 2017a,b). Only thin intervals of the sandstones are presumed to be pervasively carbonate cemented in the study area due to the limited mesogenesis that has affected the sandstones prior to structural inversion, especially in the northern part of the area, and the carbonate cement abundance probably decreases northwards since the formation most likely is more fluvially dominated toward the north (**Figure 7**).

Reservoir Characterization at CO_2 Injection Site

The tentative injection site considered here is located in the Sorgenfrei-Tornquist Zone in the southern part of the study area (**Figure 1**). This position secures a long possible migration path

within the inclined sandstone layers of the Gassum Formation. The potential injection site is located north of the F-1, K-1, Felicia-1, and J-1 wells and south of the 13/1-U-1 well. The net/gross ratio of 0.45–0.78 in the southern wells is likely to be higher at the injection site due to its location that is more proximal to the source area. The thickly developed succession in Felicia-1 constitutes an outlier in the central Skagerrak with its thickness of 260 m (**Table 1**). However, the seismic mapping shows that the Gassum Formation has large thicknesses of c. 100–150 centrally in the study area and is extra thick at the injection site due to faulting and therefore has the potential to store large amounts of CO_2 (**Figures 2**, **7**). The formation is here located at 1545–1675 ms TWT corresponding to about 1850–2130 m depth, indicating that the net sandstone thickness is in the order of 130–180 m and that the reservoir temperature is in the range of 60–80°C.

It is likely that fluvial sandstones are more abundant at the injection site than in the southern wells due to its more proximal position (**Figure 7**). This is supported by the findings of Nielsen (2003), who presented a detailed sequence stratigraphic interpretation onshore Denmark based on well logs and cores. Furthermore, in the study area, possible channel features are recognized along the base of (para)-sequences as troughs on seismic profiles (**Figure 5**). Inferred dominating channel orientation (i.e., north-south, semi-parallel with most lines), sand-sand contacts and low relief make quantification of channelization difficult. The transgressive succession in the 13/1-U-1 well shows that a marine incursion to the northern part of the study area occurred, as evident by the content of glauconite and chlorite ooids. The transgressive lag marks the end of sand deposition in this area due to the back-stepping coastline. This succession was probably deposited in an estuary where the fine-grained material was supplied by erosion of shoreface deposits and the coarser grains were transported by rivers from the north. The grains are characterized by large feldspars, plutonic rock fragments, quartz with undulatory extinction, polycrystalline quartz and quartz with rounded overgrowths, suggesting a combination of first and second cycle sand grains. The high amount of Fe-rich authigenic phases in the conglomerate, including chamosite, pyrite, siderite and pervasive ankerite, may have formed in response to the dissolution of mafic minerals, or they may have precipitated due to high supply of iron from rivers entering the sea similar to glauconite formation (Ehrenberg, 1993). The presence of rootlets in the sandstone below the conglomerate shows that subaerial exposure occurred at this time, which may explain dissolution of feldspar grains and kaolinite precipitation. Flooding of these subaerially exposed sediments by the generally fluctuating sea-level (Haq et al., 1988; Nielsen, 2003) resulted in reworking of large clasts, which occur in the conglomerate and also are found in small quantities in the very fine- to fine-grained sandstone with traces of glauconite.

The northwards on-lapping internal seismic reflectors at base of the Gassum Formation in the study area in combination with the identification of the Lower Sinemurian TS11 topping the formation in 13/1-U-1 and disappearing toward the south show that the Gassum Formation is younging toward the north (**Figures 2–4**, **7**). The general back-stepping of the basin margin that occurred during deposition of the upper part of the Gassum Formation (Nielsen, 2003) means that the shoreface belt and coastal plain moved northwards. Therefore, this was probably the prevalent mechanism of sandstone deposition in the upper part of the succession at the injection site, whereas fluvial sandstones presumably dominate in the lower part. Based on the grain sizes found in the sandstones, varying from mostly fine- to medium-grained onshore Denmark and in the distally located K-1 well to coarse-grained in the Felicia-1 well and medium- to very coarse-grained in the J-1 well, it is concluded that the grain size increases toward the north due to the shorter transport distance from the provenance. Thus, coarse-grained shoreface sandstones are estimated to be the predominant reservoir constituent at the injection site, and they are probably coarsening-upwards hence being medium-grained or perhaps fine-grained at their base. The well-log analysis is based on old logs, so it is possible that the porosities have been underestimated (**Table 1**) since larger porosities are indicated by the texture and grain size of the sandstones (**Figures 8–10**). Porosities of 22–28% and permeabilities of 200–600 mD are therefore suggested for the injection site when also taking the onshore equivalents into account (**Figure 13**).

Albite, oligoclase and chamosite are the most reactive mineral phases with respect to carbonatization of CO_2, so the amount, distribution and surface area of these minerals in the sandstones at the injection site are of importance. The average plagioclase content of c. 10 vol% in the Gassum Formation onshore western Denmark (Weibel et al., 2017a) is assumed to be higher in the Skagerrak due to the proximity to the source area. Hence, a total albite + oligoclase content of 15 wt.% is estimated for the injection site, which is in accordance with the abundance indicated by the element scans (**Figure 9**). Chamosite occurs as thick concentric coatings in abundant ooids, forming part of the conglomerate in the 13/1-U-1 well (**Figure 10D**), and as discontinuous coats on grains in both the sandstone and conglomerate. Small amounts of chlorite also occur in sandstones from the K-1 and J-1 wells. Patchy chlorite coatings are also present in some of the sandstones onshore Denmark and continuous chamosite coatings are ubiquitous in shoreface and estuarine-fluvial sandstones in a forced regressive systems tract in the upper part of the formation (Weibel et al., 2017a). This could be a regional phenomenon as the coatings are present in both of the two wells where this interval has been drilled. The reactive surface area of this grain-coating chamosite is considerably larger than the surface area of the feldspar grains.

Mineral CO_2 Sequestration Potential

To ensure supercritical conditions for CO_2 during injection, prospective reservoirs are located deeper than 800 m. A suitable injection area is indicated in **Figures 1**, **2**, where the top of Gassum Formation is at c. 1850 m depth. There are no lithological data from this area, and reservoir properties must be inferred from seismic interpretation and extrapolated from the nearest wells (i.e., 13/1-U-1, Felicia-1, J-1, and K-1).

Injected CO_2 will rise to the top of the reservoir and migrate up-dip toward the north, within a progradational para-sequence

capped by a transgressive surface and overlain by mudstones of the Fjerritslev Formation. According to the depositional model, a CO_2 plume will sweep through lower to upper shoreface deposits i.e., from fine- to medium-grained to coarse-grained sandstones. The most reactive phases in the observed mineral assemblages, with respect to carbonatization of CO_2, are albite, oligoclase and chamosite (Palandri and Kharaka, 2004). Trace minerals may also contribute cations to the solution, depending on reducing/oxidizing potential of injected fluids. Plagioclase contents are in the order of 6–15 wt.% (estimated from XRD data, **Supplementary Figure S2**, and SEM element scans, **Figure 9**) in porous samples representative of reservoir sandstone, of which oligoclase constitutes a minor fraction of assumed 3 wt.%, while most grains are albite. Chamosite (Fe-endmember of chlorite) contents are in the order of 1–2 wt.% (estimated from XRD). Total reaction potential with cations provided to solution by albite (Na), oligoclase (Ca, Na) and chamosite (Fe, minor Mg) were estimated for shoreface reservoir sandstone with 25% porosity (mass balance method described by Hellevang et al., 2013). Comparing more reactive sediment (12 wt.% albite, 3 wt.% oligoclase and 2 wt.% chamosite) with a less reactive case (6 wt.% albite, 0 wt.% oligoclase and 1 wt.% chamosite), the total carbonatization potential for CO_2 precipitated as siderite, calcite and dawsonite ranges between 2.28 and 5.29 mol/L formation water. Disregarding dawsonite (as its relevance is somewhat disputed, e.g., Hellevang et al., 2005), the mineralization potential would be between 0.47 and 1.1 mol/L.

High salinities, in the order of 100–200 g/l, are reported for formation water in the Gassum Formation in the Danish Basin (Laier, 2008; Holmslykke et al., 2019). However, the data and established salinity-depth correlations may not be representative for the suggested injection site. The reported water chemistries are affected by deeper burial and proximity to thick, underlying Zechstein salt deposits, as well as super-saline Triassic porewaters. There are no formation water data from the 13/1-U-1 well, which would be most representative for the suggested injection site. It is likely that formation waters in the injection area are much less saline, given the nearshore location, the longer distance to salt deposits and the structural setting with a landwards slope. CO_2 experiments with sandstones from the Gassum Formation from central parts of the basin have shown small reaction potential during the experiment period (Weibel et al., 2014). However, the higher feldspar and chlorite contents and presumed less saline brines at the basin margin makes this area more prospective regarding carbonatization potential. Given relatively warm reservoir conditions ($>80°C$), the mineralization potential in a time frame of some hundred years is likely to be relevant (>5.5 kg CO_2 per m^3 reservoir), although not very high. Immobilization of CO_2 by dissolution and mineralization may also be optimized with respect to spreading in different sedimentary facies settings by means of adapted injection strategies (Sundal et al., 2015).

The content of reactive phases is higher in less mature sediment, as plagioclase is more intact. Also, in sediment derived from the Telemarkia Terrane, metamorphic rocks of greenschist facies in southern regions are likely to contribute with more chlorite and albite compared to sediments from the Idefjorden Terrane. Thus, the total mineral reaction potential, although probably moderate, increases toward the top of the reservoir and toward more proximal parts in the study area. Varying grain size in different sedimentary facies and heterogeneity will also affect the reactive contact areas and overall mineralization potential. Generally, there are good prospects for migration-assisted storage in the Gassum Formation. The reservoir properties are presumably ideal, allowing for effective injection and for CO_2 to migrate upslope, becoming immobilized through structural, residual and dissolution trapping, while an open boundary allows for efficient pressure dissipation.

There is a general lack of data, which is the main challenge in this area and in many other prospective CO_2 reservoirs, as data collection from uneconomical saline aquifers is rather limited. Hence, it is important to utilize regional knowledge to delineate relevant trends both in a traditional sense for reservoir properties and also with respect to reactivity. As provenance shifts with time and causes a more reactive mineral assembly, it is inferred to change upwards in the studied succession. The major novelty of the approach is to use provenance analysis to help determining the reactivity of the reservoir rocks, which has not been considered before although this can provide important information. Also, the extrapolation of facies belts and evaluation of the effect of burial diagenesis on reservoir properties is new for this part of the basin, and a valuable addition to the overall estimation of storage potential available to Europe.

CONCLUSION

Sedimentary facies and mineral assemblages provide constraints on the reaction potential for CO_2 in the Gassum Formation. Detailed delineation of stratigraphic surfaces and evaluation of sediment provenance have not previously been presented for this area. Linking reactivity to provenance and sediment maturity proved to be a useful tool to point out immobilization potentials in different parts of the reservoir. Corresponding basinward maturity trends are presumed to be present along the rim of the Fennoscandian Shield in the North Sea and Norwegian Sea.

The source area extent decreases with time through the succession, providing more reactive minerals and sediment with higher potential for mineralization of CO_2 in the top part of the reservoir. CO_2 is buoyant and will rise upwards, meaning that CO_2 migration will occur mostly in lower to upper shoreface facies within relatively immature, fine- to coarse-grained sand of increasing reactivity up depositional dip (closer to source areas). Temperature and reaction kinetics will decrease in shallower parts, however, and the total mineralization potential is moderate (>5.5 kg CO_2 per m^3).

The largest provenance area with zircons supplied from seven different basement terranes in the Fennoscandian Shield is found in the sample with the most mature mineralogy, reflecting the longer transport distance during this estuarine lowstand setting, which may partly be related to recycling of sediments. The highstand setting of the shoreface sandstones has resulted in immature mineralogy due to predominant sediment transport from the adjacent Telemarkia Terrane. The most reactive

phases with regards to mineral sequestration of CO_2 comprise albite, oligoclase and chlorite. The feldspar content decreases southwards due to mechanical breakdown and weathering, whereas chlorite coatings and ooids are most abundant in the northern and upper part of the formation, presumably because they are sourced by alteration of unstable heavy minerals or by iron from rivers. Provenance including mineralogy and transport distance exerts a stronger influence on total reactivity than the sedimentary facies setting (fluvial vs. shoreface).

Based on observed diagenetic alterations, the maximum burial depths prior to structural inversion are estimated to be within 2.3–3.0 km. Thus, burial diagenesis has not reduced the reservoir quality drastically. Pore-filling carbonate cementations occur only locally. From the proposed injection area, CO_2 would move into progressively more mineralogically immature sediments with presumed excellent reservoir quality.

DATA AVAILABILITY STATEMENT

All datasets generated for this study are included in the article/**Supplementary Material**.

AUTHOR CONTRIBUTIONS

MO and AS wrote the manuscript with support from the other authors. MO, AS, and RW did the petrographic work. UG and IB performed the seismic interpretation. TT was in charge of the zircon age analyses. MO made the provenance interpretation. LK did the well-log interpretation. AS and HH made the reactivity estimates. LN performed the sedimentological work.

FUNDING

This contribution is part of the CO_2-Upslope project that is funded by CLIMIT and the Research Council of Norway under grant #268512.

ACKNOWLEDGMENTS

We would like to acknowledge NPD, Sintef and Atle Mørk for access to the 13/1-U-1 core, and GEUS for providing samples from K-1, J-1 and Felicia-1. Thanks to B. G. Haile, T. Naidoo, S. Simonsen, M. Heeremans, L. H. Line and S. Akhavan at the Department of Geosciences at UiO and S. H. Serre, M. Alaei, M. Leth, J. L. Bendtsen, and J. Halskov at GEUS for technical assistance and discussions. The reviewers and editor are thanked for valuable advice that helped improve the manuscript.

SUPPLEMENTARY MATERIAL

The Supplementary Material for this article can be found online at: https://www.frontiersin.org/articles/10.3389/feart.2019.00312/full#supplementary-material

FIGURE S1 | Cathodoluminescence photo of detrital zircon grains from the Gassum Formation used for U-Pb age dating.

FIGURE S2 | X-ray diffraction results of samples from the Gassum Formation in the Skagerrak.

TABLE S1 | Zircon U-Pb age data from the Gassum Formation in the Skagerrak.

REFERENCES

Aagaard, P., Egeberg, P. K., Saigal, G. C., Morad, S., and Bjørlykke, K. (1990). Diagenetic albitization of detrital K-feldspars in jurassic, lower cretaceous and tertiary clastic reservoir rocks from offshore Norway, II. Formation water chemistry and kinetic considerations. *J. Sediment. Petrol.* 60, 575–581. doi: 10.1306/212f91ec-2b24-11d7-8648000102c1865d

Åhäll, K. I., Cornell, D. H., and Armstrong, R. (1998). Ion probe zircon dating of metasedimentary units across the Skagerrak: new constraints for early mesoproterozoic growth of the Baltic Shield. *Precambrian Res.* 87, 117–134. doi: 10.1016/s0301-9268(97)00059-4

Andersen, T., Griffin, W. L., and Sylvester, A. G. (2007). Sveconorwegian crustal underplating in southwestern Fennoscandia: LAM-ICPMS U-Pb and Lu-Hf isotope evidence from granites and gneisses in Telemark, southern Norway. *Lithos* 93, 273–287. doi: 10.1016/j.lithos.2006.03.068

Anthonsen, K. L., Aagaard, P., Bergmo, P. E. S., Gislason, S. R., Lothe, A. E., Mortensen, G. M., et al. (2014). Characterisation and selection of the most prospective CO2 storage sites in the Nordic region. *Energy Procedia* 63, 4884–4896. doi: 10.1016/j.egypro.2014.11.519

Baig, I., Faleide, J. I., Mondol, N. H., and Jahren, J. (2019). Burial and exhumation history controls on shale compaction and thermal maturity along the Norwegian North Sea basin margin areas. *Mar. Pet. Geol.* 104, 61–85. doi: 10.1016/j.marpetgeo.2019.03.010

Bergmo, P. E. S., Polak, S., Aagaard, P., Frykman, P., Haugen, H. A., and Bjørnsen, D. (2013). Evaluation of CO2 storage potential in skagerrak. *Energy Procedia* 37, 4863–4871. doi: 10.1016/j.egypro.2013.06.396

Bertelsen, F. (1978). The upper triassic – lower jurassic vinding and gassum formations of the Norwegian-Danish Basin. *Geol. Surv. Denmark Ser. B* 3:26.

Bertelsen, F. (1980). Lithostratigraphy and depositional history of the Danish Triassic. *Geol. Surv. Denmark Ser. B* 4:59.

Bingen, B., Nordgulen, Ø, and Viola, G. (2008). A four-phase model for the sveconorwegian orogeny, SW Scandinavia. *Nor. J. Geol.* 88, 43–72.

Bingen, B., Skår, Ø, Marker, M., Sigmond, E. M. O., Nordgulen, Ø, Ragnhildstveit, J., et al. (2005). Timing of continental building in the sveconorwegian orogen, SW Scandinavia. *Nor. J. Geol.* 85, 87–116.

Bingen, B., and Solli, A. (2009). Geochronology of magmatism in the caledonian and sveconorwegian belts of Baltica: synopsis for detrital zircon provenance studies. *Norw. J. Geol.* 89, 267–290.

Bjørlykke, K. (1998). Clay mineral diagenesis in sedimentary basins – a key to the prediction of rock properties. Examples from the North Sea Basin. *Clay Minerals* 33, 15–34. doi: 10.1180/claymin.1998.033.1.03

Bjørlykke, K., Aagaard, P., Dypvik, H., Hastings, D. S., and Harper, A. S. (1986). "Diagenesis and reservoir properties of jurassic sandstones from the hahenbanken area, offshore mid Norway," in *Habitat of hydrocarbons on the Norwegian continental shelf*, ed. A. M. Spencer, (London: Graham & Trotman Ltd.), 275–286.

Bjørlykke, K., Jahren, J., Mondol, N. H., Marcussen, Ø, Croize, D., Peltonen, C., et al. (2009). Sediment compaction and rock properties. *Search Discov. Article* 50192, 1–8.

Brewer, T. S., Daly, J. S., and Åhall, K.-I. (1998). Contrasting magmatic arcs in the palaeoproterozoic of the south-western Baltic Shield. *Precambrian Res.* 92, 297–315. doi: 10.1016/s0301-9268(98)00079-5

Burley, S. D., Mullis, J., and Matter, A. (1989). Timing diagenesis in the tartan reservoir (UK North Sea): constraints from combined cathodoluminescence microscopy and fluid inclusion studies. *Mar. Pet. Geol.* 6, 98–120. doi: 10.1016/0264-8172(89)90014-7

Corfu, F., Larsen, B. T., and Ganerød, M. (2015). "Geochronology of Krogskogen rombporphyry lavas by U-Pb and Ar-Ar and relations to Oslo Rift chronology," in *31st Geological Winter Meeting, Abstracts and Proceedings of the Geological Society of Norway*, (Stavanger).

Ehrenberg, S. N. (1993). Preservation of anomalously high porosity in deeply buried sandstones by grain-coating chlorite: examples from the Norwegian continental shelf. *Am. Assoc. of Pet. Geol. Bull.* 77, 1260–1286.

Eiken, O., Ringrose, P., Hermanrud, C., Nazarian, B., Torp, T. A., and Høier, L. (2011). Lessons learned from 14 years of CCS operations: sleipner. In salah and snøhvit. *Energy Procedia* 4, 5541–5548. doi: 10.1016/j.egypro.2011.02.541

Erlström, M., and Sivhed, U. (2012). Pre-Rhaetian Triassic strata in Scania and adjacent offshore areas –stratigraphy, petrology and subsurface characteristics. *Geological Survey of Sweden Rapporter och meddelanden* 132:74.

Fisher, R. S., and Land, L. S. (1986). Diagenetic history of eocene wilcox sandstones, South-Central Texas. *Geochim. t Cosmochim. Acta* 50, 551–561. doi: 10.1016/0016-7037(86)90104-3

Folk, R. L. (1966). A review of grain-size parameters. *Sedimentology* 6, 73–93. doi: 10.1111/j.1365-3091.1966.tb01572.x

Garzanti, E., Andò, S., and Vezzoli, G. (2008). Settling equivalence of detrital minerals and grain-size dependence of sediment composition. *Earth Planet. Sci. Lett.* 273, 138–151. doi: 10.1016/j.epsl.2008.06.020

Halland, E. K., Gjeldvik, I. T., Johansen, W. T., Magnus, C., Meling, I. M., Pedersen, S., et al. (2011). *CO2 storage atlas Norwegian North Sea*. Stavanger: Norwegian Petroleum Directorate, 163.

Hamberg, L., and Nielsen, L. H. (2000). Shingled, sharp-based shoreface sandstones: depositional response to stepwise forced regression in a shallow basin, upper triassic gassum formation, denmark. *Geol. Soc. Lon. Spec. Publications* 172, 69–89. doi: 10.1144/gsl.sp.2000.172.01.04

Haq, B. U., Hardenbol, J., and Vail, P. R. (1988). "Mesozoic and Cenozoic chronostratigraphy and cycles of sea-level change," in *Sea Level Changes: An Integrated Approach*, ed. C. K. Wilgus, (Houston: SEPM Special Publication).

Heeremans, M., and Faleide, J. I. (2004). Late Carboniferous-Permian tectonics and magmatic activity in the Skagerrak, Kattegat and the North Sea. *Geol. Soc. Lon. Spec. Publications* 223, 157–176. doi: 10.1144/gsl.sp.2004.223.01.07

Hellevang, H., Aagaard, P., Oelkers, E. H., and Kvamme, B. (2005). Can dawsonite permanently trap CO2? *Environ. Sci. Technol.* 39, 8281–8287. doi: 10.1021/es0504791

Hellevang, H., Pham, V. T. H., and Aagaard, P. (2013). Kinetic modelling of CO2–water–rock interactions. *Int. J. Greenhouse Gas Control* 15, 3–15. doi: 10.1016/j.ijggc.2013.01.027

Hellström, J., Paton, C., Woodhead, J., and Hergt, J. (2008). "Iolite: Software for spatially resolved LA- (quad and MC) ICPMS analysis," in *Laser Ablation ICP–MS in the Earth Sciences: Current Practices and Outstanding Issues. Mineral*, ed. P. Sylvester, (Quebec: Assoc. of Canada), 343–348.

Hervig, R. L., Williams, L. B., Kirkland, I. K., and Longstaffe, L. J. (1995). Oxygen isotope microanalyses of diagenetic quartz: possible low temperature occlusion of pores. *Geochim. Cosmochim. Acta* 59, 2537–2543. doi: 10.1016/0016-7037(95)00148-4

Holmslykke, H. D., Schovsbo, N. H., Kristensen, L., Weibel, R., and Nielsen, L. H. (2019). Characterising brines in deep Mesozoic sandstone reservoirs, Denmark. *Geol. Surv. Denmark Greenland Bull.* 43:e2019430104.

Jackson, S. E., Pearson, N. J., Griffin, W. L., and Belousova, E. A. (2004). The application of laser ablation-inductively coupled plasma-mass spectrometry to in situ U–Pb zircon geochronology. *Chem. Geol.* 211, 47–69. doi: 10.1016/j.chemgeo.2004.06.017

Japsen, P., and Bidstrup, T. (1999). Quantification of late Cenozoic erosion in Denmark based on sonic data and basin modelling. *Bull. Geol. Soc. Denmark* 46, 79–99.

Japsen, P., Green, P. F., Bonow, J. M., and Erlström, M. (2016). Episodic burial and exhumation of the southern baltic shield: epeirogenic uplifts during and after break-up of Pangaea. *Gondwana Res.* 35, 357–377. doi: 10.1016/j.gr.2015.06.005

Japsen, P., Green, P. F., Nielsen, L. H., Rasmussen, E. S., and Bidstrup, T. (2007). Mesozoic-cenozoic exhumation events in the eastern North Sea Basin: a multi-disciplinary study based on palaeothermal, palaeoburial, stratigraphic and seismic data. *Basin Res.* 19, 451–490. doi: 10.1111/j.1365-2117.2007.00329.x

Jarsve, E. M., Maast, T. E., Gabrielsen, R. H., Faleide, J. I., Nystuen, J. P., and Sassier, C. (2014). Seismic stratigraphic subdivision of the triassic succession in the Central North Sea; integrating seismic reflection and well data. *J. Geol. Soc.* 171, 353–374. doi: 10.1144/jgs2013-056

Kristensen, L., Hjuler, M. L., Frykman, P., Olivarius, M., Weibel, R., Nielsen, L. H., et al. (2016). Pre-drilling assessments of average porosity and permeability in the geothermal reservoirs of the Danish area. *Geothermal Energy* 4, 1–27.

Lahtinen, R., Garde, A. A., and Melezhik, V. A. (2008). Paleoproterozoic evolution of Fennoscandia and Greenland. *Episodes* 31, 20–28. doi: 10.18814/epiiugs/2008/v31i1/004

Laier, T. (2008). *Chemistry of Danish saline formation waters relevant for core fluid experiments. Fluid chemistry data for lab experiments related to CO2 storage in deep aquifers. Geological Survey of Denmark and Greenland*. Report 2008/48. Karbunya St: GEUS

Larsen, G. (1966). Rhaetic-Jurassic-Lower Cretaceous sediments in the Danish Embayment. *A heavy-mineral study. Geol. Surv. Denmark Ser.* 2:127.

Lindström, S., Vosgerau, H., Piasecki, S., Nielsen, L. H., Dybkjær, K., and Erlström, M. (2009). Ladinian palynofloras in the Norwegian–Danish Basin: a regional marker reflecting a climate change. *Geol. Surv. Denmark Greenland Bull.* 17, 21–24.

Malusà, M. G., Resentini, A., and Garzanti, E. (2016). Hydraulic sorting and mineral fertility bias in detrital geochronology. *Gondwana Res.* 31, 1–19. doi: 10.1016/j.gr.2015.09.002

Metz, B., Davidson, O., De Coninck, H., Loos, M., and Meyer, L. (2005). *Carbon dioxide capture and storage. IPCC Special Report*. Geneva: IPCC, 431.

Michelsen, O. (1975). Lower jurassic biostratigraphy and ostracods of the danish embayment. *Geol. Surv. Denmark II Række Ser.* 104:287.

Michelsen, O. (1978). Stratigraphy and distribution of Jurassic deposits of the Norwegian–Danish Basin. *Geol. Sur. Denmark Ser. B* 2:28.

Michelsen, O., and Clausen, O. R. (2002). Detailed stratigraphic subdivision and regional correlation of the southern Danish Triassic succession. *Mar. Pet. Geol.* 19, 563–587. doi: 10.1016/s0264-8172(02)00028-4

Michelsen, O., Nielsen, L. H., Johannessen, P. N., Andsbjerg, J., and Surlyk, F. (2003). Jurassic lithostratigraphy and stratigraphic development onshore and offshore Denmark. *Geol. Sur. Denmark Greenland Bull.* 1, 147–216.

Morad, S. (1990). Mica alteration reactions in Jurassic reservoir sandstones from the Haltenbanken area, offshore Norway. *Clays Clay Minerals* 38, 584–590. doi: 10.1346/ccmn.1990.0380603

Nielsen, L. H. (2003). Late triassic – jurassic development of the danish basin and the fennoscandian Border Zone, southern scandinavia. *Geol. Surv. Denmark Greenland Bull.* 1, 459–526.

Nielsen, L. H., and Japsen, P. (1991). Deep wells in Denmark 1935–1990. lithostratigraphic subdivision. *Geol. Surv. Denmark Ser. A* 31:178.

Olivarius, M., and Nielsen, L. H. (2016). Triassic paleogeography of the greater eastern Norwegian-Danish Basin: constraints from provenance analysis of the Skagerrak Formation. *Mar. Pet. Geol.* 69, 168–182. doi: 10.1016/j.marpetgeo.2015.10.008

Olivarius, M., Rasmussen, E. S., Siersma, V., Knudsen, C., Kokfelt, T. F., and Keulen, N. (2014). Provenance signal variations caused by facies and tectonics: zircon age and heavy mineral evidence from miocene sand in the north-eastern North Sea Basin. *Mar. Pet. Geol.* 49, 1–14. doi: 10.1016/j.marpetgeo.2013.09.010

Olivarius, M., Weibel, R., Friis, H., Boldreel, L. O., Keulen, N., and Thomsen, T. B. (2017). Provenance of the Lower Triassic Bunter Sandstone Formation: implications for distribution and architecture of aeolian vs. fluvial reservoirs in the North German Basin. *Basin Res.* 29(Suppl. 1), 113–130. doi: 10.1111/bre.12140

Palandri, J. L., and Kharaka, Y. K. (2004). *A Compilation of Rate Parameters of Water-Mineral Interaction Kinetics for Application to Geochemical Modeling (No. OPEN-FILE-2004-1068)*. Menlo Park CA.: Geological Survey.

Paton, C., Hellstrom, J. C., Paul, P., Woodhead, J. D., and Hergt, J. M. (2011). Iolite: freeware for the visualisation and processing of mass spectrometric data. *J. Anal. Atomic Spectrometry* 26, 2508–2518.

Petrus, J. A., and Kamber, B. S. (2012). VizualAge: a novel approach to laser ablation ICP-MS U-Pb geochronology data reduction. *Geostand. Geoanal. Res.* 36, 247–270. doi: 10.1111/j.1751-908x.2012.00158.x

Rohrman, M., van der Beek, P., Andriessen, P., and Cloeting, S. (1995). Meso-Cenozoic morphotectonic evolution of southern Norway: neogene domal uplift

inferred from apatite fission track thermochronology. *Tectonics* 14, 704–718. doi: 10.1029/95tc00088

Saigal, G. C., Morad, S., Bjørlykke, K., Egeberg, P. K., and Aagaard, P. (1988). Diagenetic albitization of detrital K-feldspar in Jurassic. *J. Sediment. Petrol.* 58, 1003–1013.

Schmidt, B. J. (1985). Clay mineral investigation of the rhaetic-jurassic-lower cretaceous sediments of the Børglum 1 and Uglev 1 wells. *Denmark. Bull. Geol. Soc. Denmark* 34, 97–110.

Slama, J. (2016). Rare late neoproterozoic detritus in SW Scandinavia as a response to distant tectonic processes. *Terra Nova* 28, 394–401. doi: 10.1111/ter.12232

Slama, J., Kosler, J., Condon, D. J., Crowley, J. L., Gerdes, A., Hanchar, J. M., et al. (2008). Plesovice zircon - a new natural reference material for U-Pb and Hf isotopic microanalysis. *Chem. Geol.* 249, 1–35. doi: 10.1016/j.chemgeo.2007.11.005

Smelror, M., Jacobsen, T., Rokoengen, K., Bakke, S., Bø, R., Goll, R. M., et al. (1989). *Shallow Drilling Farsund Subbasin: Main Report. IKU report 21*. Trondheim: Institute for Continental Shelf Research.

Sundal, A., Miri, R., Ravn, T., and Aagaard, P. (2015). Modelling CO2 migration in aquifers; considering 3D seismic property data and the effect of site-typical depositional heterogeneities. *Int. J. Greenhouse Gas Control* 39, 349–365.

Thomsen, T. B., Heijboer, T., and Guarnieri, P. (2016). jAgeDisplay: software for evaluation of data distributions in U-Th-Pb geochronology. *Geol. Surv. Denmark Greenland Bull.* 35, 103–106.

Troedsson, G. (1951). *On the Höganäs series of Sweden (Rhaeto-Lias)*. Lund: C.W.K. Gleerup, 268.

Upslope (2019). Optimized CO2 Storage in Sloping Aquifers. The CO2-Upslope Project is Funded by the CLIMIT-Programme, Grant Number 268512. Available at: www.mn.uio.no/geo/english/research/projects/upslope (accessed November 15, 2019).

Van Wagoner, J. C., Mitchum, R. M., Campion, K. M., and Rahmanian, V. D. (1990). Siliciclastic sequence stratigraphy in well logs, cores, and outcrops: concepts for high-resolution correlation of time and facies. *Am. Assoc. Pet. Geol. Methods Explor. Ser.* 7:55. doi: 10.1306/Mth7510

Vejbæk, O. V., and Britze, P. (1994). *Geological Map of Denmark 1:750.000. Top pre-Zechstein (two-way traveltime and depth)*. Map Series 45. Copenhagen: Geological Survey of Denmark, 8.

Weibel, R., Friis, H., Kazerouni, A. M., Svendsen, J. B., Stokkendal, J., and Poulsen, M. L. K. (2010). Development of early diagenetic silica and quartz morphologies – Examples from the Siri Canyon. Danish North Sea. *Sediment. Geol.* 228, 151–170. doi: 10.1016/j.sedgeo.2010.04.008

Weibel, R., Kjøller, C., Bateman, K., Laier, T., Nielsen, L. H., and Purser, G. (2014). Carbonate dissolution in mesozoic sand- and claystones as a response to CO2 exposure at 70°C and 20 MPa. *Appl. Geochem.* 42, 1–15. doi: 10.1016/j.apgeochem.2013.12.006

Weibel, R., Olivarius, M., Kristensen, L., Friis, H., Hjuler, M. L., Kjøller, C., et al. (2017a). Predicting permeability of low-enthalpy geothermal reservoirs: a case study from the upper triassic - lower jurassic gassum formation. Norwegian–Danish Basin. *Geothermics* 65, 135–157. doi: 10.1016/j.geothermics.2016.09.003

Weibel, R., Olivarius, M., Kjøller, C., Kristensen, L., Hjuler, M. L., Friis, H., et al. (2017b). The influence of climate on early and burial diagenesis of Triassic and Jurassic sandstones from the Norwegian–Danish Basin. *Depos. Rec.* 3, 60–91. doi: 10.1002/dep2.27

Wentworth, C. K. (1922). A scale of grade and class terms for clastic sediments. *J. Geol.* 30, 377–392. doi: 10.1086/622910

Wiedenbeck, M., Allé, P., Corfu, F., Griffin, W. L., Meier, M., Oberli, F., et al. (1995). Three natural zircon standards for U-Th-Pb, Lu-Hf, trace element and REE analyses. *Geostand. Newslett.* 19, 1–23. doi: 10.1111/j.1751-908x.1995.tb00147.x

Wiedenbeck, M., Hanchar, J. M., Peck, W. H., Sylvester, P., Valley, J., Whitehouse, M., et al. (2004). Further characterisation of the 91500 zircon crystal. *Geostand. Geoanal. Res.* 28, 9–39. doi: 10.1111/j.1751-908x.2004.tb01041.x

Conflict of Interest: The authors declare that the research was conducted in the absence of any commercial or financial relationships that could be construed as a potential conflict of interest.

Copyright © 2019 Olivarius, Sundal, Weibel, Gregersen, Baig, Thomsen, Kristensen, Hellevang and Nielsen. This is an open-access article distributed under the terms of the Creative Commons Attribution License (CC BY). The use, distribution or reproduction in other forums is permitted, provided the original author(s) and the copyright owner(s) are credited and that the original publication in this journal is cited, in accordance with accepted academic practice. No use, distribution or reproduction is permitted which does not comply with these terms.

Advantages of publishing in Frontiers

OPEN ACCESS
Articles are free to read for greatest visibility and readership

FAST PUBLICATION
Around 90 days from submission to decision

HIGH QUALITY PEER-REVIEW
Rigorous, collaborative, and constructive peer-review

TRANSPARENT PEER-REVIEW
Editors and reviewers acknowledged by name on published articles

Frontiers
Avenue du Tribunal-Fédéral 34
1005 Lausanne | Switzerland

Visit us: www.frontiersin.org
Contact us: info@frontiersin.org | +41 21 510 17 00

REPRODUCIBILITY OF RESEARCH
Support open data and methods to enhance research reproducibility

DIGITAL PUBLISHING
Articles designed for optimal readership across devices

FOLLOW US
@frontiersin

IMPACT METRICS
Advanced article metrics track visibility across digital media

EXTENSIVE PROMOTION
Marketing and promotion of impactful research

LOOP RESEARCH NETWORK
Our network increases your article's readership